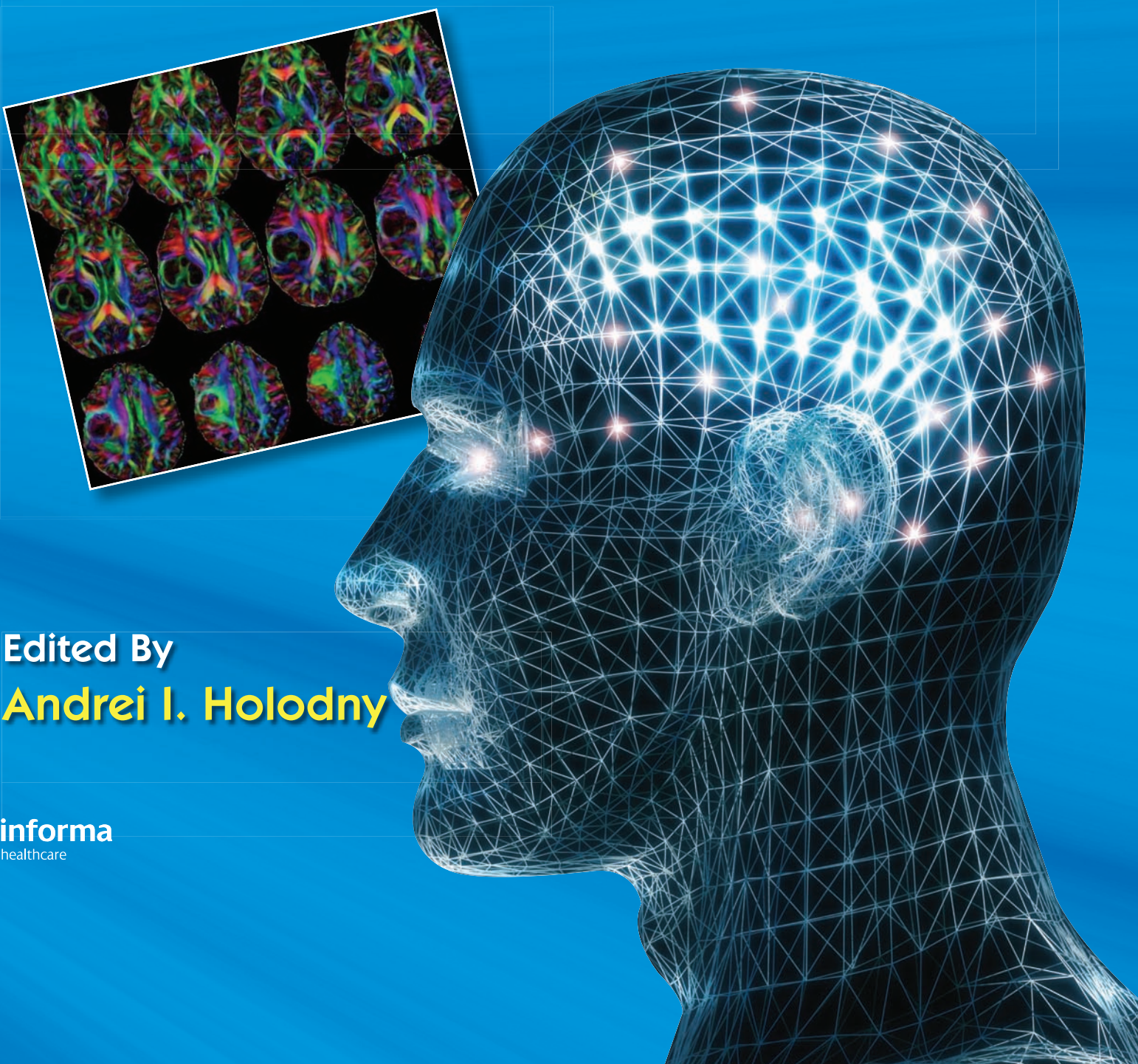


FUNCTIONAL NEUROIMAGING

A Clinical Approach



Edited By
Andrei I. Holodny

informa
healthcare

FUNCTIONAL NEUROIMAGING

FUNCTIONAL NEUROIMAGING

A Clinical Approach

Edited By
Andrei I. Holodny
Memorial Sloan-Kettering Cancer Center
New York, New York, USA

informa
healthcare

New York London

Informa Healthcare USA, Inc.
52 Vanderbilt Avenue
New York, NY 10017

© 2008 by Informa Healthcare USA, Inc.
Informa Healthcare is an Informa business

No claim to original U.S. Government works
Printed in the United States of America on acid-free paper
10 9 8 7 6 5 4 3 2 1

International Standard Book Number-10: 0-8493-7056-6 (Hardcover)
International Standard Book Number-13: 978-0-8493-7056-4 (Hardcover)

This book contains information obtained from authentic and highly regarded sources. Reprinted material is quoted with permission, and sources are indicated. A wide variety of references are listed. Reasonable efforts have been made to publish reliable data and information, but the author and the publisher cannot assume responsibility for the validity of all materials or for the consequence of their use.

No part of this book may be reprinted, reproduced, transmitted, or utilized in any form by any electronic, mechanical, or other means, now known or hereafter invented, including photocopying, microfilming, and recording, or in any information storage or retrieval system, without written permission from the publishers.

For permission to photocopy or use material electronically from this work, please access www.copyright.com (<http://www.copyright.com/>) or contact the Copyright Clearance Center, Inc. (CCC) 222 Rosewood Drive, Danvers, MA 01923, 978-750-8400. CCC is a not-for-profit organization that provides licenses and registration for a variety of users. For organizations that have been granted a photocopy license by the CCC, a separate system of payment has been arranged.

Trademark Notice: Product or corporate names may be trademarks or registered trademarks, and are used only for identification and explanation without intent to infringe.

Library of Congress Cataloging-in-Publication Data

Functional neuroimaging : a clinical approach / edited by Andrei I. Holodny.
p. ; cm.

Includes bibliographical references and index.

ISBN-13: 978-0-8493-7056-4 (hardcover : alk. paper)

ISBN-10: 0-8493-7056-6 (hardcover : alk. paper)

1. Brain—Magnetic resonance imaging. I. Holodny, Andrei I.

[DNLM: 1. Nervous System Diseases—diagnosis. 2. Diagnostic Imaging. 3. Diagnostic Techniques, Neurological. 4. Nervous System Physiology. 5. Neurosurgical Procedures. WL 141 F9796 2008]
RC386.6.M34F865 2008

616.8'047548—dc22

2008013279

**For Corporate Sales and Reprint Permissions call 212-520-2700 or write to: Sales Department,
52 Vanderbilt Avenue, 16th floor, New York, NY 10017.**

Visit the Informa Web site at
www.informa.com

and the Informa Healthcare Web site at
www.informahealthcare.com

*To my loving wife Maria and to my wonderful children
Elena and Sergei — you make it all worth while.*

—A. Holodny

Preface

It would not be an exaggeration to say that functional neuroimaging has caused a revolution in the way that humankind studies brain function. This modality has been adopted almost universally by clinicians who endeavor to understand how the brain works, including radiologists, clinical psychologists, psychiatrists, neurologists, and neurosurgeons, as well as basic scientists, such as cognitive neuroscientists, theoretical biologists, and physiologists. The main attraction of functional neuroimaging as a method is that it can depict not only the detailed anatomy of the brain but also brain function. In addition, functional images can be superimposed on high-resolution routine anatomical MR images to improve the localization of functional data.

Notwithstanding the immense increase in the use of functional neuroimaging, it seems to me that this exceptionally powerful technique is still underutilized in the clinical arena and that it could be put to use much more forcefully for the benefit of our patients. Why would anyone operate on a patient with a brain tumor adjacent to the prefrontal gyrus without first performing an fMRI to clearly depict the relationship of the tumor with the motor cortex?

Functional imaging of the brain has been embraced to a much greater extent by our colleagues in the basic sciences. Perhaps this is natural, since one needs basic scientists to work out the details of any new method as well as to optimize various parameters before a technique can be applied in the clinical setting. However, the labor of the basic scientists has already established enough of a foundation for us to vigorously promote functional imaging into mainstream clinical imaging.

A number of outstanding books are available on functional imaging that are geared toward the needs of basic scientists. However, it appears to me that there is a relative paucity of publications dedicated to the requirements of clinicians. Therefore, the present humble opus will focus on practical needs of clinicians who already use or who will come to use these wonderful techniques. It is my sincere wish to make this topic understandable and immediately applicable to practicing radiologists, neurologists, neurosurgeons, and others in the clinical arena, so that they can use the techniques described herein to the benefit of their patients.

Observing trends, it appears likely that functional neuroimaging will become an integral part of the clinical imaging armamentarium. I cannot recall how many times neurosurgeons walked up to me after hearing a talk on fMRI and asked me, “What you

showed was really great, but how can I get my guys to do this?” To this end I will attempt to present functional neuroimaging in a manner that is understandable to a clinician and immediately applicable to his or her practice.

One of the most difficult tasks that a scientific writer can undertake is to describe complex physics and math in a manner digestible for clinical physicians, who are expert in their own respective fields but do not have Ph.D.’s in the “hard” sciences. In this book, my colleagues and I have endeavored to overcome this barrier. I believe that it is absolutely essential to understand the physical and physiological underpinnings of functional neuroimaging. Failure to appreciate an advanced imaging technique as anything more than a “black box” and not being cognizant of the physical and physiological processes that underpin this technique will inevitably lead to clinical errors. Therefore, we presented the physics of these complex imaging technologies not only “for completeness’ sake” but with a practical, clinical goal in mind.

In writing this book, we sought to limit the number of equations. Where equations are presented, we sought to describe their meaning and significance in words. We also sought to present complicated concepts in a comprehensible manner, occasionally with attempts at humor.

The current book stems from the founding of the American Society of Functional Neuroradiology, with which I had the honor of being associated from its inception. The outline of the book mirrors the topics that the founders of this society considered salient and that were highlighted during the first annual meeting of this society. A vast majority of the authors were instrumental in the establishment of this society as well.

I would also like to welcome our clinical colleagues from disciplines other than neuroradiology, since many of them are also involved in various facets of neuro-imaging. As an example of cooperation between disciplines, I can bring forward the case of the collaborative effort of neuroradiologists and representatives from organized neurology, psychology, as well as general radiology in the most successful endeavor of bringing about a CPT code for BOLD fMRI.

Notwithstanding the more clinical trajectory, I would also like to emphasize my respect and appreciation for the basic scientists who labor for the advancement of functional neuroimaging. It seems to me that the situation that has arisen is ripe for cooperation and collaboration between the clinicians and the basic scientists in the field of functional neuroimaging and that we can work together for the advancement of the field and for the betterment of the lot of our patients. This has always been my personal experience. In this book, I will present already successful and future examples of such cooperation.

*Andrei I. Holodny, MD
New York, NY
February 4, 2008*

Contents

Preface	v
Contributors	ix

1. Physical Principles of BOLD fMRI—What Is Important for the Clinician	1
<i>Andrei I. Holodny and Bob L. Hou</i>	
2. Preparing the Patient for the fMRI Study and Optimization of Paradigm Selection and Delivery	13
<i>Nicole M. Petrovich Brennan</i>	
3. Methods of Analysis	23
<i>Kyung K. Peck</i>	
4. Fact or Artifact?	37
<i>John F. Kaufman and Joseph A. Maldjian</i>	
5. Language	51
<i>Jay J. Pillai</i>	
6. Vision and Higher Cortical Function	67
<i>Sonia Gill, John Ulmer, and Edgar A. DeYoe</i>	
7. <i>Cortical Plasticity</i>	81
<i>Andrei I. Holodny</i>	
8. Functional Image-Guided Neurosurgery	91
<i>Cameron W. Brennan and Nicole M. Petrovich Brennan</i>	
9. <i>Development and Developmental Disorders</i>	107
<i>Adam P. Wallach</i>	
10. Neurodegenerative Disorders	129
<i>Lihong Wang and Jeffrey R. Petrella</i>	

11. Diffusion Imaging and Tensor Physics for the Clinician	161
<i>Richard Watts</i>	
12. Diffusion-Weighted Imaging in Stroke	177
<i>Pamela W. Schaefer and William A. Copen</i>	
13. Diffusion Imaging in Brain Tumors and Treatment Response	201
<i>Shareef Riad, Andrei I. Holodny, and Suresh K. Mukherji</i>	
14. DTI of Developmental and Pediatric Disorders	217
<i>Michael J.J. Kim and James M. Provenzale</i>	
15. DTI of Neurodegenerative Disorders	233
<i>Sumei Wang, John H. Woo, and Elias R. Melhem</i>	
16. Perfusion Imaging	249
<i>Jonathan P. Dyke</i>	
17. Perfusion Imaging: Physical Principles and Applications in the Brain	273
<i>Meng Law</i>	
18. Magnetoencephalography	309
<i>Timothy P.L. Roberts, Christopher Edgar, and Erin Simon Schwartz</i>	
<i>Index</i>	<i>329</i>

Contributors

Cameron W. Brennan Department of Neurosurgery, Memorial Sloan-Kettering Cancer Center, New York, New York, U.S.A.

Nicole M. Petrovich Brennan Department of Radiology, Memorial Sloan-Kettering Cancer Center, New York, New York, U.S.A.

William A. Copen Department of Radiology, Division of Neuroradiology, Massachusetts General Hospital, Boston, Massachusetts, U.S.A.

Edgar A. DeYoe Department of Radiology, Medical College of Wisconsin, Milwaukee, Wisconsin, U.S.A.

Jonathan P. Dyke Citigroup Biomedical Imaging Center, Weill Cornell Medical College, New York, New York, U.S.A.

Christopher Edgar Children's Hospital of Philadelphia, Philadelphia, Pennsylvania, U.S.A.

Sonia Gill Department of Radiology, Medical College of Wisconsin, Milwaukee, Wisconsin, U.S.A.

Andrei I. Holodny The Neuroradiology Section and the Functional MRI Laboratory, Department of Radiology, Memorial Sloan-Kettering Cancer Center, New York, New York, U.S.A.

Bob L. Hou The Neuroradiology Section and the Functional MRI Laboratory, Department of Radiology, Memorial Sloan-Kettering Cancer Center, New York, New York, U.S.A.

John F. Kaufman Department of Radiology, Wake Forest University Medical Center, Winston-Salem, North Carolina, U.S.A.

Michael J.J. Kim Department of Radiology, Memorial Sloan-Kettering Cancer Center, New York, New York, U.S.A.

Meng Law Departments of Radiology and Neurosurgery, Mount Sinai Medical Center, New York, New York, U.S.A.

Joseph A. Maldjian Department of Radiology, Wake Forest University Medical Center, Winston-Salem, North Carolina, U.S.A.

Elias R. Melhem Department of Radiology, Division of Neuroradiology, Hospital of the University of Pennsylvania, Philadelphia, Pennsylvania, U.S.A.

Suresh K. Mukherji Department of Radiology, University of Michigan, Ann Arbor, Michigan, U.S.A.

Kyung K. Peck Functional MRI Laboratory, Department of Radiology, Memorial Sloan-Kettering Cancer Center, New York, New York, U.S.A.

Jeffrey R. Petrella Department of Radiology, Duke University, Durham, North Carolina, U.S.A.

Jay J. Pillai The Russell H. Morgan Department of Radiology and Radiological Science, Johns Hopkins University School of Medicine, and The Johns Hopkins Hospital, Baltimore, Maryland, U.S.A.

James M. Provenzale Department of Radiology, Duke University Medical Center, Durham, North Carolina, U.S.A.

Timothy P.L. Roberts Children's Hospital of Philadelphia, Philadelphia, Pennsylvania, U.S.A.

Shareef Riad The Functional MRI Laboratory, Department of Radiology, Memorial Sloan-Kettering Cancer Center, New York, New York, U.S.A.

Pamela W. Schaefer Department of Radiology, Division of Neuroradiology, Massachusetts General Hospital, Boston, Massachusetts, U.S.A.

Erin Simon Schwartz Children's Hospital of Philadelphia, Philadelphia, Pennsylvania, U.S.A.

John Ulmer Department of Radiology, Medical College of Wisconsin, Milwaukee, Wisconsin, U.S.A.

Adam P. Wallach Department of Radiology, Neuroradiology Division, Memorial Sloan Kettering Cancer Center, New York, New York, U.S.A.

Richard Watts Department of Physics and Astronomy, University of Canterbury, Christchurch, New Zealand

Lihong Wang Brain Imaging and Analysis Center, Duke University Medical Center, Durham, North Carolina, U.S.A.

Sumei Wang Department of Radiology, Division of Neuroradiology, Hospital of the University of Pennsylvania, Philadelphia, Pennsylvania, U.S.A.

John H. Woo Department of Radiology, Division of Neuroradiology, Hospital of the University of Pennsylvania, Philadelphia, Pennsylvania, U.S.A.

1

Physical Principles of BOLD fMRI—What Is Important for the Clinician

ANDREI I. HOLODNY and BOB L. HOU

*The Neuroradiology Section and the Functional MRI Laboratory, Department of Radiology,
Memorial Sloan-Kettering Cancer Center, New York, New York, U.S.A.*

INTRODUCTION

In order to correctly interpret clinical blood oxygenation-level dependent (BOLD) functional magnetic resonance imaging (fMRI) studies, it is essential to appreciate the MRI physics of this technique. There are many books with thorough descriptions of the complicated physical principles of fMRI; however, in the present chapter, we hope to describe these important physical concepts in language geared toward clinicians. Readers who wish to know more about this broad subject are referred to the books: 1 to 6 in references.

THE MRI MAGNET

To obtain good quality fMRI studies it is necessary to use a superconductive magnet (usually at 1.5 or 3 T) with high-field homogeneity. The higher the magnetic field strength, the better the magnet is for fMRI studies, since the BOLD fMRI signal increases as the square of the difference in field strength. Therefore, a 3-T magnet will produce an fMRI BOLD signal approximately four times greater than a 1.5-T system.

Before obtaining an fMRI scan on a patient, the magnetic field must be adjusted (or “shimmed”) to obtain as uniform a

magnetic field as possible. Likewise, the gain of the transmitter and receiver in the MRI scanner must be optimized. In contemporary scanners of most manufacturers, this can be accomplished by the auto pre-scan mode.

MRI CONTRAST MECHANISMS

The three major tissue contrast mechanisms important for our discussion of BOLD fMRI are T1, T2, and T2*. T1 is the longitudinal relaxation time or spin-lattice relaxation time, caused by the interaction between the spin and its environment. T2 is the transverse relaxation time or spin-spin relaxation time in a homogeneous local magnetic field, caused by the interaction between the spin and other nearby spins. T2* is the transverse relaxation time or spin-spin relaxation time in a nonhomogeneous local magnetic field. Usually T1- and T2-weighted images are used for anatomical studies, i.e., displaying tissue and/or tumor structures in the brain. T2*-weighted images are used in BOLD fMRI to investigate brain function.

The raw data for generating T1- and T2-weighted images are usually acquired using a spin echo (SE) pulse sequence. There are two RF pulses in the SE pulse sequence. The first one, with a flip angle of 90°, is an excitation pulse used for transverse magnetization and the

second (180°) is a refocusing pulse to reverse the spin phase and generate the SE.

T 2^* -weighted images are usually obtained using a gradient echo (GE) pulse sequence. A GE pulse sequence has only one RF pulse with a flip angle (α) for excitation of the signal and uses gradient pulses to refocus the spin phase and generate an echo (i.e., “gradient echo”).

For our purposes, the main difference between the SE sequences (usually used to acquire T1 and T2) and the GE sequence (usually used to acquire T 2^*) is that the GE sequence is much more affected by local field inhomogeneities. T 2^* depends not only on the inherent T2 of the tissues but also on the additional relaxation time resulting from an inhomogeneous local magnetic field. Local magnetic field inhomogeneities can be generated by many things, including metal, blood products, and air-tissue interface. Since the SE sequences have a refocusing pulse, they are less affected by local field inhomogeneities, whereas the lack of a refocusing pulse on the GE sequences causes the artifacts created by the field inhomogeneities to become more prominent or to “bloom” (Fig. 1). Usually, such artifacts are a nuisance (for example, artifacts caused by dental work) and MRI sequences are optimized to minimize their effect; however, the BOLD fMRI sequence, on the other hand, will actually use the local field inhomogeneities caused by the different states of hemoglobin to create images of brain function (Fig. 2).

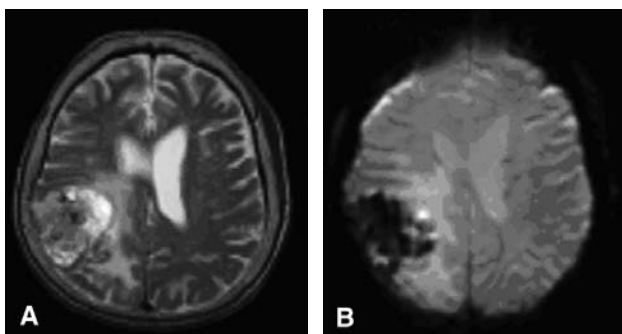


Figure 1 (A) SE T2-weighted images (TR/TE/flip angle = 3800 ms/102 ms/90°) from a 3-T scanner for a patient with a tumor in the right parietal lobe. (B) GE T 2^* -weighted images (TR/TE/flip angle = 4000 ms/30 ms/90°) of the same patient. The main difference between the two images is that there is a large signal dropout on the T 2^* sequence in the area of the tumor. This is caused by small local field inhomogeneities in the tumor caused by microcalcifications and small hemorrhages. The SE sequence is less sensitive to these small local field inhomogeneities. Therefore, the tumor exhibits signal intensity close to that of the normal brain. However, the T 2^* sequence is very sensitive to these local field inhomogeneities, which causes rapid spin-spin relaxation and a prominent dropout in signal.

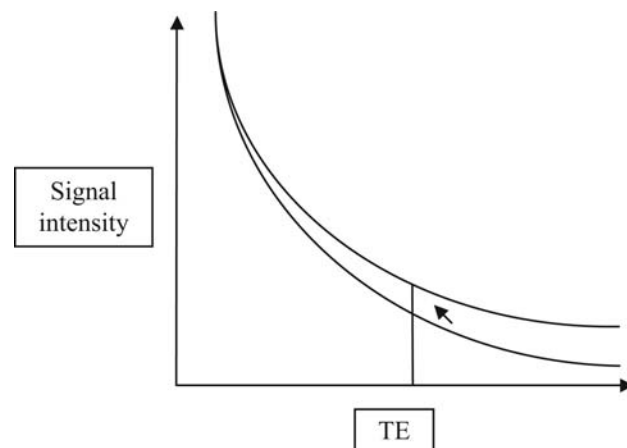


Figure 2 The physical basis for BOLD fMRI. T 2^* decay curves show that the signal (S) will vary according to the presence or absence of field inhomogeneities. At time = TE, the signal intensity (S) is different. The presence of field inhomogeneities causes the signal to drop (arrow). BOLD fMRI uses this principle since deoxygenated hemoglobin is paramagnetic and causes a much large signal dropout than oxygenated hemoglobin. Hence a relative increase of dHb concentration in blood leads to a magnetic susceptibility effect and a dropout in T 2^* signal.

T 2^* AND BOLD fMRI Signal

One physiological source that strongly influences the T 2^* value in a human brain is hemoglobin (Hb), especially, the difference between oxygenated hemoglobin (HbO₂) and deoxygenated hemoglobin (dHb) in blood. dHb has a paramagnetic species of iron due to the four unpaired electrons, which produces a large magnetic susceptibility effect. On the other hand, HbO₂ is a diamagnetic molecule with a small magnetic susceptibility effect. Hence a relative increase of dHb concentration in blood leads to a corresponding increase in the distortion of the local magnetic field due to the magnetic susceptibility effect. Therefore, the protons in or next to the blood in veins and capillaries with high dHb content lose the coherent phase faster, making the T 2^* value shorter and leading to a dropout of signal. Therefore, employment of a T 2^* sequence will serve to highlight the difference between dHb and HbO₂.

Ogawa et al. in 1990 (7–9) published three papers on fMRI based on the change of dHb concentration in the veins due to brain neuronal activity. Although the first fMRI of human brain, described by Belliveau et al. in 1991 (10), used an exogenous gadolinium-based contrast agent, this technique was rapidly superseded by the method from Ogawa who used the dHb molecule as an endogenous contrast agent for brain functional imaging. Ogawa's results showed that the observed T 2^* change through the microvascular MR signal was linked to the presence of blood

deoxygenation and that relative changes in dHb cause a “blood oxygen-level dependent” or a “BOLD” effect.

The sensitivity of BOLD contrast allows fMRI to be performed in an individual subject with temporal resolution on the order of a second and spatial resolution of 2 mm or less in almost all cortical structures of a human brain. Since current BOLD fMRI technology can indirectly measure neuronal activity in real time, it is capable of noninvasive investigation of functional attributes of the brain while performing a certain task. The BOLD fMRI has developed to become one of dominated methods for functional brain imaging.

HOW BOLD fMRI IS DIFFERENT FROM ROUTINE MR IMAGING SEQUENCES

It is important to understand that the way that one acquires images for BOLD fMRI differs from routine MRI sequences (such as T1, T2, and FLAIR) in a number of fundamental ways. First, routine brain imaging sequences typically take a number of minutes to acquire. This allows one to acquire high-resolution images of the brain, generally with a matrix of 256×256 or higher. On the other hand, for BOLD fMRI one is not so much interested in spatial resolution, rather the goal of BOLD is to measure the changes in signal intensity in each voxel over short periods. In order to accomplish this, one needs to scan the entire brain (or at least the area of the brain in which one is interested) multiple times with the time of each acquisition being on the order of two to four seconds. To acquire images of the entire brain every few seconds, one is forced to use a very rapid technique (typically echo planar imaging, EPI) and to sacrifice resolution. Typically, fMRI images are acquired using a 64×64 or 128×128 matrix.

Second, when one acquires routine scans of the brain, one assumes that the signal intensity will not change over the time of acquisition. On the other hand, when acquiring BOLD data, one actually focuses on the small changes in signal intensity that occur in each voxel during the acquisition. Typically, one compares two different conditions, such as rest and finger tapping, which is known as a paradigm. The simplest functional paradigm is known as a “boxcar paradigm,” during which the subject or patient performs a task for a period of time and then rests for a period of time. This “on (= task period)” and “off (= rest period)” sequence is repeated a number of times. One then performs a statistical analysis of the data to determine if the change in signal intensity correlates to the paradigm.

WHY DOES THE MR SIGNAL CHANGE WITH AN INCREASE IN NEURONAL ACTIVITY?

The main idea behind BOLD fMRI is that when there is an increase in neuronal activity in a part of the brain, that part

will show a change in signal intensity that can be detected by MRI. Neuronal activity is associated with many complex physiological processes in which metabolic byproducts, cerebral blood flow (CBF), cerebral blood volume (CBV), cerebral metabolic rate of oxygen (CMRO_2), and blood oxygenation all combine to create the BOLD effect in fMRI.

The change over time in the BOLD fMRI signal intensity that one observes can be termed the hemodynamic response, and mathematical models of the response are called the hemodynamic response function (HDRF). In-depth basic science work has led to the establishment of a quantitative model relating the BOLD signal to CBF, CBV, and CMRO_2 . Understanding how these three parameters interplay to create the HDRF will allow one to appreciate how the BOLD signal produced as well as to understand how the BOLD signal is modified in pathological conditions. The standard model to explain the HDRF was developed by Buxton et al. (11) and is known as the “Balloon Model.”

Essentially what occurs is that an increase in neuronal activity leads to two processes. First, there is an increase in the local metabolic rate of oxygen (CMRO_2) that leads to an increase in oxygen extraction. This, in turn, leads to an increase in deoxyhemoglobin (dHb), which is paramagnetic. Such an increase in paramagnetic deoxyhemoglobin (had it been the only process to occur) would have led to a drop in fMRI signal intensity since the presence of a paramagnetic substance causes more rapid $T2^*$ dephasing and a drop in signal intensity. However, neuronal activity also causes a concomitant increase in blood flow (CBF), which actually overshoots the increased demand for oxygen. This overshoot leads to an influx of oxygenated blood, an increase in oxyhemoglobin (HbO_2) over and above the decrease in oxyhemoglobin caused by oxygen extraction and a consequential dilution of deoxyhemoglobin. Since there is now less paramagnetic deoxyhemoglobin, there is less dephasing of the $T2^*$ signal and a consequential increase in fMRI signal (Fig. 3).

The reason for the overshoot in blood flow (CBF) is unclear. Some recent results have suggested that the increase in CBF following neural activity is not because of the metabolic demands of the brain region, but rather is driven by the presence of neurotransmitters, especially glutamate (12,13).

The image intensity for a given voxel in the brain can therefore significantly increase if more oxygenated blood enters this region and fills the venous bed. This assumes, however, that cortical activation causes local vasodilation and an increase in CBF. If there is no increase in the CBF due to an increase in neuronal activity, the changes in oxygen consumption may lead to no change or even a decrease in BOLD fMRI signal intensity.

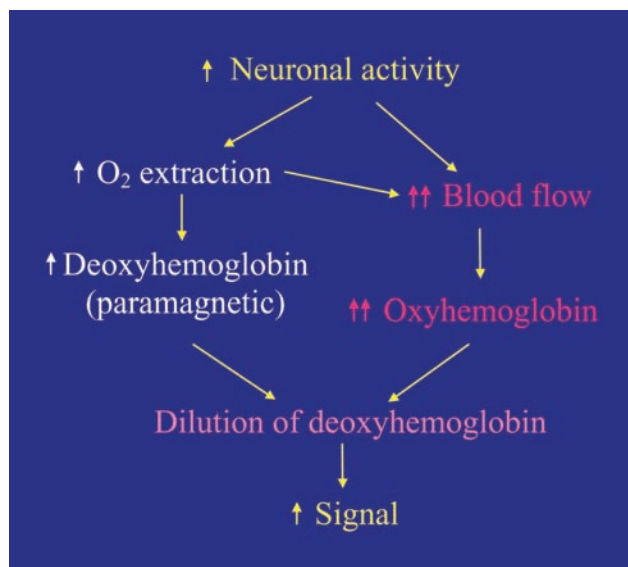


Figure 3 A schematic that illustrates why there is an increase in BOLD signal following an increase in neuronal activity.

This last point is becoming more important in the clinical arena as we use BOLD fMRI to study pathological conditions. There are a number of conditions where the vasculature to the brain is abnormal and will not respond normally to an increase in neuronal activity, for example, arteriovenous malformations, high-grade gliomas with tumor neovasculature (Fig. 4), or high-grade vascular stenosis. All of these can potentially affect or even negate the BOLD fMRI signal, and it is important for the clinician who is interpreting the fMRI scan to be cognizant of these potential pitfalls (14–16).

A detailed analysis of the HRF reveals that the fMRI signal drops below the baseline twice: there is an initial dip in the signal intensity at the beginning and a prolonged poststimulus undershoot (Fig. 5). The initial dip in signal

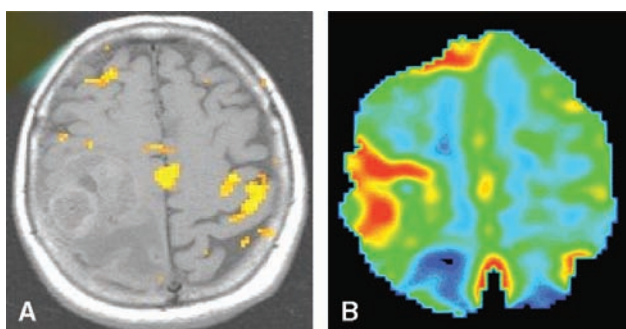


Figure 4 (A) The fMRI BOLD activation volume much smaller on the side with the tumor. (B) This decrease in fMRI activation volume was shown to correlate to the presence of abnormal tumor neovasculature (as shown by relative cerebral volume). *Source:* From Ref. 25.

appears to be related to the increase in CMRO₂ before the increase in CBF. During this short period, the increase in oxygen consumption prior to the increase in blood flow leads to an increase in dHb and a decrease in HbO₂, which causes a decrease in the BOLD signal. The initial dip is occasionally not seen on a 1.5-T scanner. The poststimulus undershoot usually can be detected if a boxcar stimulation with a rest period of longer than 20 seconds is applied. The poststimulus undershoot can be explained by the slow return of the CBV to prestimulus levels. After the conclusion of the stimulus, the CBV value remains higher than the baseline even as both the CMRO₂ and the CBF

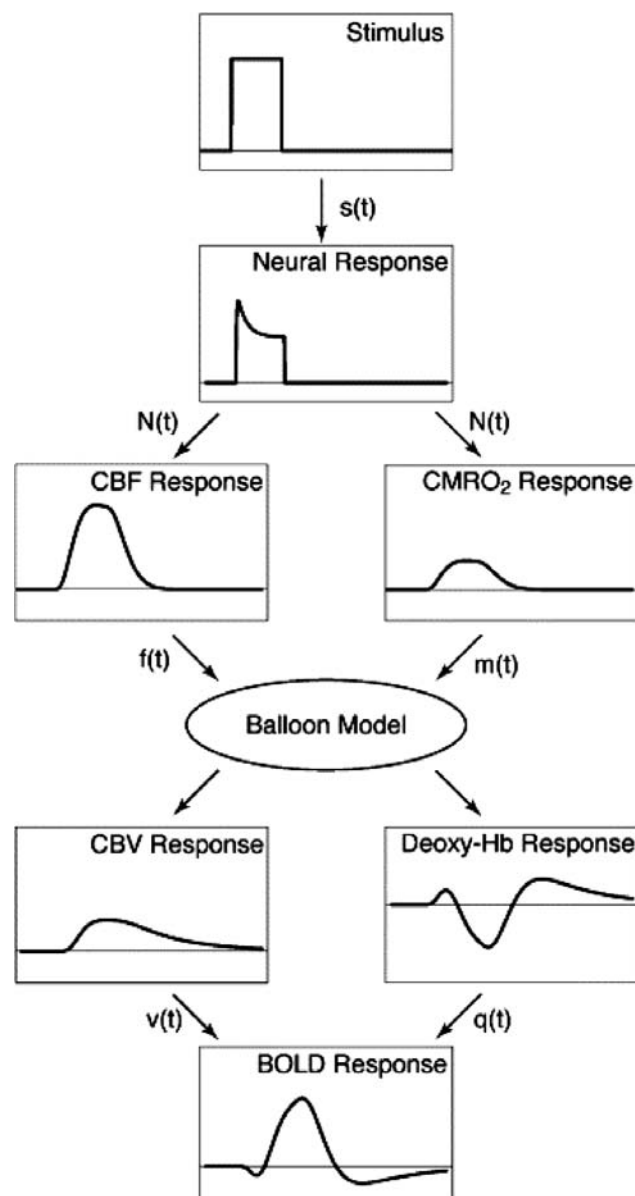


Figure 5 A diagram of the Balloon model with the steps and corresponding time responses from neuronal stimulation to BOLD signal. *Source:* From Ref. 11.

return to their respective baselines. Therefore, even after the conclusion of the stimulus, the dHb concentration will be higher than the baseline, which will result in a negative BOLD signal (i.e., “undershoot”) until the CBV value returns to the baseline (Fig. 5) (11).

STATISTICAL ANALYSIS OF THE BOLD fMRI DATA

Having understood how the BOLD signal changes over time in each voxel, we can proceed to how one actually produces an fMRI “map.” Once the data is acquired, it must be analyzed to see which voxels are “active.” From the fMRI data, we can generate a signal intensity curve over time for each voxel in the brain. This signal intensity-time curve must then be compared with the stimulus to see if there is a correlation between the two. There are many different statistical ways to solve this problem, which range from the simple to the very complex. A commonly used method is to see if there is a “correlation” between the signal change in a specific voxel and the timing of the paradigm. (For methods of analysis please see chap. 3 by Peck.)

Essentially, if a signal “correlates significantly” with the paradigm for a specific voxel, then that pixel is considered active. Figure 6 represents a patient who has undergone a paradigm during which he is asked to move his tongue and then to rest. The time when he moves his tongue is depicted by the red line. When he moves his tongue, the red line is elevated; when he is resting, the line drops back to zero. The blue line represents the signal change over time (hemodynamic response time series, HRTS). On the top graph, the BOLD signal changes in concert with the tongue movement: when the subject is moving his tongue, the signal increases. When he rests, the signal reverts to baseline. This voxel corresponds to the known location of the motor homunculus of the tongue. Therefore, this voxel would be considered to be active and is depicted in yellow. On the other hand, the lower graph is of a voxel that has nothing to do with tongue movement. Even visual inspection demonstrates that there is no correlation between the BOLD signal (in blue) and the paradigm (in red). Therefore, this voxel is not depicted in yellow.

Most commercial and noncommercial products allow the user to vary the parameters (such as the correlation coefficient or the p value) to display varying degrees of correlation. For example, in Figure 6, the voxels passing a

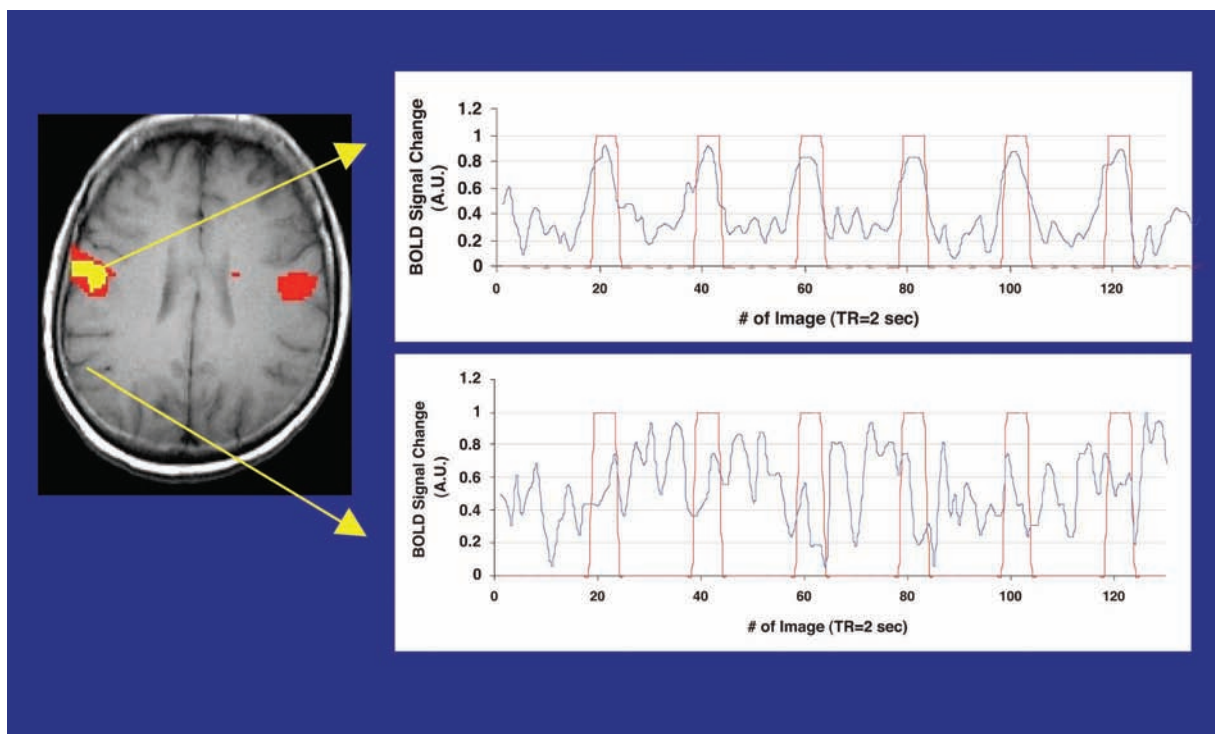


Figure 6 Relationship between a motor tongue paradigm and signal intensity in significant versus not significant voxels. The paradigm is depicted by the red line. When the patient moves his tongue, the red line is elevated to 1; when he is resting, the line drops back to zero. The blue line represents the signal change over time. On the top graph, the BOLD signal changes in concert with the tongue movement: when the subject is moving his tongue, the signal increase. When he rests, the signal reverts to baseline. This voxel corresponds to the known location of the motor homunculus of the tongue. Therefore, this voxel would be considered to be “active” and is depicted in yellow. One the other hand, the lower graph is of a voxel that has nothing to do with tongue movement. Even visual inspection demonstrates that there is no correlation between the BOLD signal (in blue) and the paradigm (in red). Therefore, this voxel is not depicted in yellow.

statistical threshold is depicted in red and yellow, while yellow represents a higher correlation.

Most products also allow one to view the actual HRTS for each voxel. Review of the HRTS is especially important if one gets unexpected results. Occasionally, review of the actual HRTS data (for example, if the percent change in a voxel is greater than 5%) will allow one to catch artifacts such as motion artifact. Obviously, the patterns of all voxels in the activation volume should be similar to the one of the designed boxcar stimulation so that the voxels can be designated as “activated” by passing the statistical significant threshold, i.e., a larger “ r ”. Figure 7 is an example of the HRTS (in black) for nine voxels versus the bilateral finger-tapping paradigm (in red). Among the nine voxels, only six pass the statistical significant threshold so that only these six voxels can be considered active.

SOME THOUGHTS ON STATISTICAL SIGNIFICANCE

The main goal of fMRI analysis is to determine which voxels in the brain are active or in other words are associated

with the task being performed by the patient and (presumably, without getting into deep philosophical issues) are the parts of the brain that are actually causing the activity performed by the patient. All of these methods of analysis must determine which voxels are “statistically significant.” Also, the vast majority allows the operator (the technologist, physicist, psychologist, or physician who is interpreting the study) to adjust this parameter. Consequently, one can view the data at different p values, for example.

The problem is that there is no set p value (or r value or any other statistical test) that is universally accepted as the threshold that one should set when analyzing fMRI data. In everyday clinical practice, one usually adjusts the p value until the image “looks right,” or in other words the area of interest is clearly seen and activity in spurious areas is minimized. For purists, this may appear to be scientifically unsatisfactory; however, it does generally serve to answer the clinical question at hand—for example, telling the neurosurgeon where Broca’s area is in relation to the tumor.

In fact, the issue of finding a single optimal statistical test may be unsolvable in principle: it would appear axiomatic that certain people are stronger “activators” than others. For example, vasculature in younger people

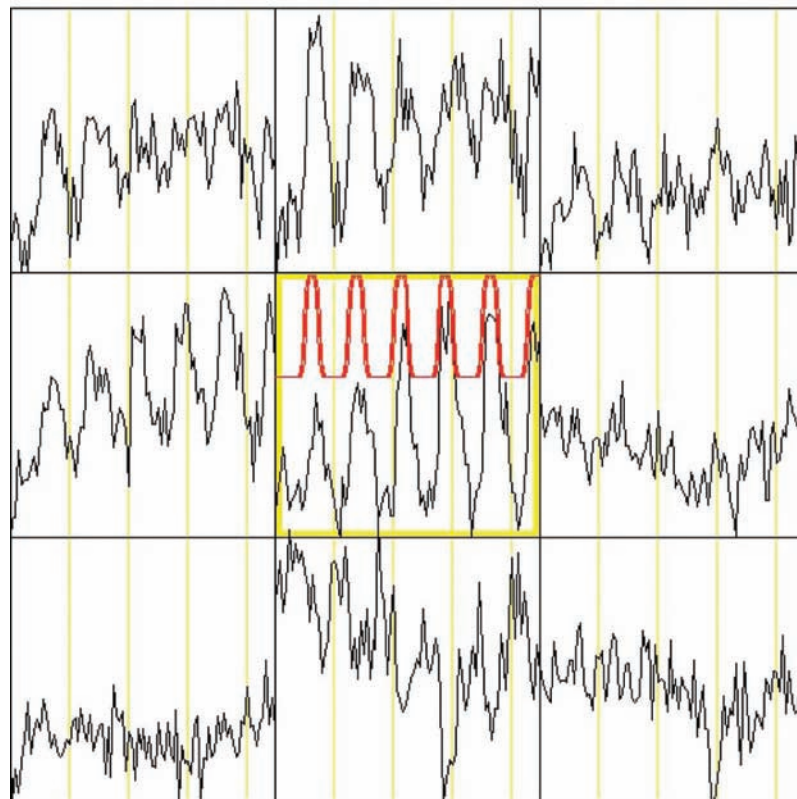


Figure 7 The hemodynamic response time series (in black) for nine voxels (shown in 9 black boxes) versus a bilateral finger-tapping boxcar paradigm (in red). Only six voxels (all of the voxels in the top row, the first two voxels in the second row, and the second voxel in the third row) pass the statistical significant threshold and can be considered “active.”

is more reactive than in older individuals (17). Therefore, interpretation of fMRI data may actually be more “art” rather than “science.”

In the vast majority of cases, adjusting the statistical values to make the image “look better” does not affect the localization of an eloquent cortex. However, in many cases, the laterality index (which serves to determine the language laterality) can be affected by the choice of p value (Fig. 8). In interpreting clinical fMRI data, one must be cognizant of this rare possibility (18).

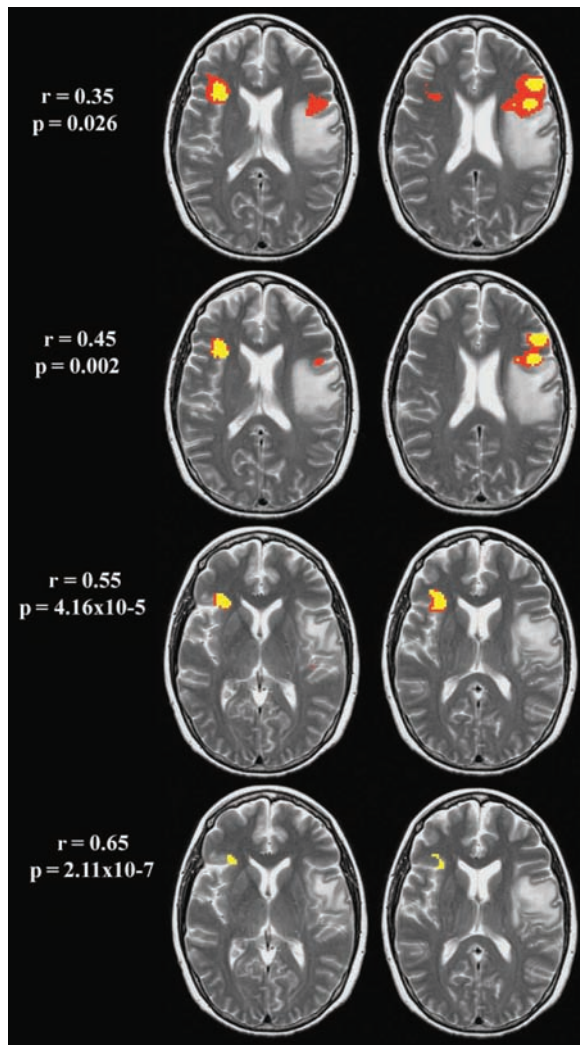


Figure 8 Rarely the choice of threshold can affect the language laterality index. Axial T2-weighted images with coregistered fMRI data in a patient with a left frontal tumor performing the letter fluency task. The fMRI data is presented at different thresholds. At less stringent thresholds ($r < 0.55$), the language LI is bilateral, whereas at more stringent ($r > 0.55$) thresholds, the LI shifts to the right side. This right-handed patient showed signs of moderate aphasia preoperatively and mild aphasia and dysarthria postoperatively, clinically suggesting a significant left language component.

BOLD fMRI SIGNAL MEASUREMENTS: GE EPI AND SE EPI PULSE SEQUENCES

A GE EPI sequence, due to its high sensitivity to change in the $T2^*$ value, is the most commonly used acquisition method to detect the BOLD effect. As we mentioned previously, dHb concentration leads to an increase in the magnetic susceptibility, which induces a localized, inhomogeneous magnetic field.

Another method to obtain the BOLD fMRI signal is to use an SE pulse sequence. SE BOLD signal does not include the contribution from venous blood so that the signal is considerably smaller than the one from GE BOLD signal. This is one of major reasons why the GE sequence is more commonly used for magnets at 1.5 T since even for the GE BOLD the fMRI signal is only 1% to 5%, which is barely larger than the thermal noise in the brain.

However, the SE EPI has advantages compared with GE BOLD. First, when one employs SE EPI, the BOLD signal originates from the capillaries, which are located in direct proximity to the neuronal activity. On the other hand, when one uses GE EPI, the BOLD signal picks up contribution from both the capillary bed and the venules, which are at a small distance from the neuronal activity. Hence, SE EPI can potentially detect the location of an eloquent cortex more accurately. Second, the SE EPI sequence is less sensitive to the susceptibility artifacts such as from prior surgery, metallic artifacts, prior hemorrhage, or the air-bone interface (such as the inferior frontal lobes or the temporal lobes). Therefore, one may wish to consider using the SE EPI sequence to detect BOLD activity near the sinuses, the skull base, and adjacent to surgical beds.

Theoretic calculations of the contributions to the BOLD signal from vessels of differing diameters for both the SE and GE sequences are depicted in Figure 9 (19,20). The results suggested that the BOLD signal using GE EPI is much larger than the BOLD signal with SE EPI because of the significant contribution to the GE BOLD signal from the blood vessels with the radius larger than 10 μm (venules and veins).

To obtain BOLD fMRI signal with high sensitivity (i.e., high signal-to-noise ratio) and high spatial and temporal resolutions, we need to apply optimum acquisition parameters. In Table 1, we have listed the most important parameters used in a GE EPI and a SE EPI pulse sequence for a 1.5-T or a 3.0-T scanner.

PRACTICAL CONSIDERATIONS IN BOLD fMRI

The main advantages of BOLD fMRI as a technique to image brain activity include (i) no need for injection of radioactive isotopes (as in PET), (ii) the total scan time required can be relatively short, i.e., on the order of few

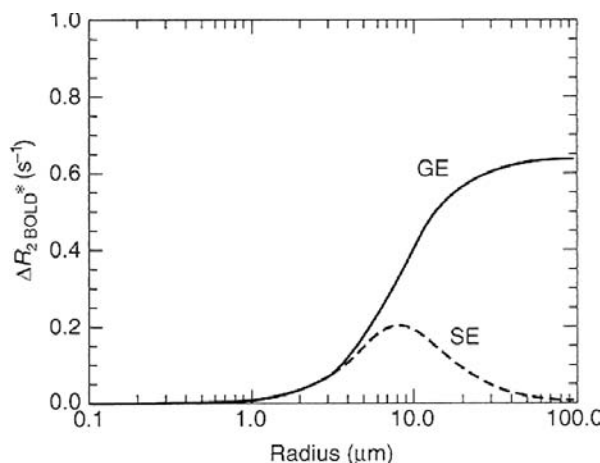


Figure 9 Simulated GE and SE BOLD signal versus blood vessel radius (μm). The results suggested that the GE BOLD signal is much larger than the SE BOLD due to the significant contribution to the GE BOLD signal from the blood vessels with the radius larger than $10 \mu\text{m}$ (venules and veins). Abbreviations: GE, gradient echo; SE, spin echo; BOLD, blood oxygenation-level dependent. Source: From Refs. 19 and 20.

minutes per run (depending on the paradigm), (iii) the in-plane resolution of the functional image can be as low as $2 \times 2 \text{ mm}$, although resolutions less than 2 mm are possible for a small area of coverage (i.e., few slices), (iv) MRI scanners [as opposed to MEG (magnetoencephalography) machines] are readily available.

The main limitation of BOLD fMRI is the relatively poor temporal resolution (on the order of seconds) compared with techniques such as EEG and MEG. EEG and MEG techniques directly measure electrical activity caused by neuronal discharges, while fMRI measures changes in blood vessels, which has a longer response time.

BOLD fMRI studies are often limited by susceptibility artifacts. Since the BOLD sequence is optimized to maximize susceptibility (to highlight the difference between dHb and HbO₂), susceptibility artifacts seen on such scans are often worse than on routine SE images. This is especially true in brain regions close to an air-bone interface, a

postoperative cavity, or dental work. Thus, there are some problems in observing BOLD fMRI activity in the orbito-frontal cortex, the medial temporal cortices, and any eloquent area covered by or adjacent to either metal or a surgical cavity (21). This is why it is essential to review the source images (the BOLD fMRI scan superimposed on the T2* scan) and not only the completed and analyzed study with the BOLD fMRI data superimposed on high-resolution T1-weighted images. If one foregoes this essential step, one may be lulled to think that there is a lack of BOLD fMRI activity, when, in fact, this activity is whipped out by susceptibility artifact.

When interpreting BOLD fMRI studies, it is crucial to appreciate that an area of activation may actually represent a large draining vein rather than a capillary bed near the site of neuronal activation. The BOLD signal is only an indirect measure of neural activity and is therefore susceptible to influence by nonneural changes in the oxygenation of hemoglobin. Hence, it is indispensable to review the high-resolution study to exclude the presence of a large draining vein.

Different brain areas may have different hemodynamic responses, which would not be accurately reflected by any model-dependent method, including the standard and manufacturer supplied methods of analysis. More complicated statistical methods, which do not assume a likely response such as principle component analysis (22) and independent component analysis (23), have been proposed.

AN EXAMPLE: BOLD fMRI SIGNAL FOR A BILATERAL FINGER-TAPPING TASK

As an example to illustrate how the BOLD fMRI signal is generated, we will examine the dHb-induced T2* change in vascular bed of primary motor cortex (PMC). To identify the PMC, we will ask the patient (or subject) to perform bilateral finger-tapping stimulation, using a block paradigm with “activation” and “rest” cycles during the imaging acquisition. During the activation periods (each lasting 20 seconds), the patients will tap their fingers in both

Table 1 Parameters Used in a GE EPI and a SE EPI Pulse Sequence for a 1.5-T or a 3.0-T Scanner to Obtain Optimum BOLD fMRI Signal

	TR (ms)	TE (ms)	Flip angle (in degrees)	Matrix size	Slice thickness (mm)
1.5-T GE	1500–4000	40–60	60–90	128×128	4–6
1.5-T SE	1500–4000	80–100	$\alpha_1 = 90$ $\alpha_2 = 180$	128×128	4–6
3.0-T GE	1500–4000	30–40	60–90	128×128	4–6
3.0-T SE	1500–4000	65–75	$\alpha_1 = 90$ $\alpha_2 = 180$	128×128	4–6

Abbreviations: GE, gradient echo; EPI, echo planar imaging; SE, spin echo.

hands at the rate of approximately 1 Hz (one tap per second). During the rest period (each again lasting 20 seconds), the patients will lie still and not move their fingers. The length of the activation and rest periods can vary both between and within each paradigm. The activation and rest periods will be repeated a number of times—typically three to five. During the stimulation period, the observable T₂* signal is modulated by an overabundance of HbO₂ with respect to the more paramagnetic dHb in the capillary and venous beds directly adjacent to the active neurons during the activation periods. This overabundance produces a change of a local magnetic gradient field. The neuronal activation leads to an increase in CBF, CBV, and oxygen delivery. As CBF increased more than CMRO₂, oxygen delivery quickly exceeded the slight increase in local oxygen consumption due to the neuronal activity. The net effect was a surplus in the amount of HbO₂ delivered to any activated voxel in the PMC. As the delivered oxygen exceeds the local oxygen consumption, the capillary and venous beds filled with a higher ratio of HbO₂ to dHb compared to when the cortices were at rest. This larger amount of diamagnetic HbO₂ meant less effect on the local magnetic field, a longer T₂*, and leads to an increased signal on the T₂*-weighted images for the voxels of the PMC. The actual volume of hemoglobin in the brain is quite small (a few percent); however, the T₂* effects extended for microns beyond the vascular bed because magnetic susceptibility has a relatively long-range effect. This leads to an approximately 1% to 5% increase in the T₂*-induced image intensity for the finger-tapping task in a 1.5-T scanner. Figure 10 shows the identification of the finger homunculus in the PMC in a normal volunteer. The subject performed a bilateral finger-tapping paradigm. The red and yellow areas depict the localization of where changes in the BOLD fMRI signal correlated to the finger-tapping paradigm to a statistically significant degree.

AN EXPLANATION AT A COCKTAIL PARTY

Occasionally, we are asked to explain what we do by people who are not specialists in MRI, and yes, this does occasionally occur at cocktail parties. Clearly, our interlocutors at such events are not really interested in T₂* relaxation or the relationship between oxyhemoglobin and deoxyhemoglobin. What are we to do? One explanation that I have come up with that seems to satisfy most is the following. (Disclaimer—we blushingly and profusely beg forgiveness for the inaccuracies of the following from any physicist who may actually read further.) On a more serious side, we have found that the below explanation actually works quite well for patients and their families who are undergoing fMRI to identify eloquent cortices prior to brain tumor resection.

“When I move the finger of my hand, the part of the brain that is controlling this action is working harder and



Figure 10 BOLD fMRI of the motor homunculus. Three-dimensional, axial, and coronal views of the identification of the finger homunculus in the primary motor cortex in a normal volunteer. The subject performed a bilateral finger-tapping paradigm. The red and yellow areas depict the localization of where changes in the BOLD fMRI signal correlated to the finger-tapping paradigm to a statistically significant degree.

needs more blood, which carries oxygen and other nutrients. We all know that blood has hemoglobin, which has an iron atom in it. (Most people remember these from high school biology.) We also know that an iron atom is a small magnet. Well what we do is detect an increase in the number of such small magnets (iron atoms in the hemoglobin molecules) using our *magnetic resonance imaging machine*.”

Again, we beg forgiveness; however, it seems to me that the vast majority of non-MRI experts who have heard this came up with at least a small appreciation for what we do. This explanation has also served to put at ease many of our patients who are often scared and confused prior to their fMRI exam.

INTRAVENOUS BOLUS TRACKING AND ARTERIAL SPIN LABELING FOR THE STUDY OF BRAIN FUNCTION

Perfusion MRI, which measures the change of regional CBF due to neuronal activity, can also be applied to study brain function. Two perfusion fMRI methods have been

developed for measuring CBF. The first technique that employed this method was intravenous bolus tracking. This method relies on the intravenous injection of a magnetic compound, such as a gadolinium-containing contrast agent, and on measuring its T2*-weighted signal as it perfuses through the brain over a short period (~1 minute). Certain metal elements such as gadolinium and dysprosium have an inherently high magnetic susceptibility relative to tissue or air. Areas perfused with the magnetic compound show less signal intensity as the compound creates a magnetic inhomogeneity between the intravascular space and the extravascular space that decreases the T2* signal. The magnetic compound may be injected once during the control and once during the activation tasks, and the relative differences in blood flow between the two states is determined from the perfusion images in two injections. Belliveau et al. (10) used the technique to create the first functional magnetic resonance maps of human visual stimulation. They imaged the occipital lobe after injecting gadolinium-DTPA once during darkness and again during a flashing light to map the visual response. They made a statistical comparison between images obtained during visual stimulation versus those obtained during darkness to generate functional images.

Although gadolinium-based contrasts are not radioactive, the number of boluses that can be given to an individual is limited by the potential for kidney toxicity with repeated tracer administration. The advantage of applying this method is its high sensitivity, which is one order higher than the one from BOLD contrast for a 1.5-T scanner.

Arterial spin labeling (ASL) is the second perfusion method used to investigate brain function. It is a T1-weighted noninvasive technique where intrinsic hydrogen atoms in arterial water outside of the slice of interest are magnetically tagged ("flipped") and are then imaged as they enter the slice of interest in the brain. By magnetic labeling the proximal blood supply using ASL, the associated signal is proportional to the CBF or perfusion. This method provides more quantitative physiological information than BOLD signal since it measures CBF directly and has the same sensitivity for detecting task-induced changes. ASL measures the change of CBF whereas BOLD measures the change of oxygen level in the blood.

ASL is noninvasive, does not involve an IV bolus injection, and can thus be repeatedly performed multiple times in an individual subject. Also, absolute regional blood flow can be measured, which cannot be easily measured with BOLD-fMRI or bolus tracking that requires an estimation of the arterial input function. Figure 11 shows an example of using ASL to identify the cortex involved in visual activity (24).

At this point, ASL has some limitations in that it takes several minutes to acquire information on a limited number of slices. Therefore, one is limited to study of a single

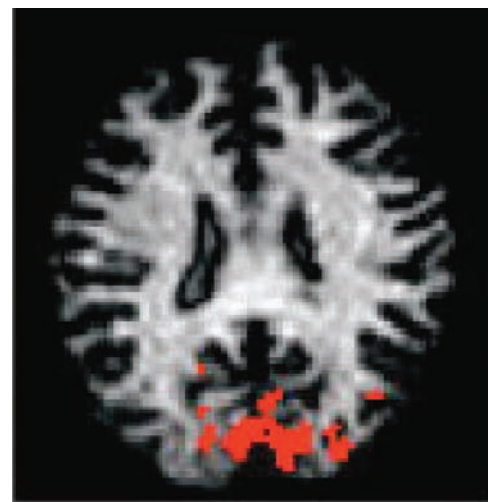


Figure 11 The image shows CBF changes (red) in the visual cortex during a visual paradigm using arterial spin labeling. Abbreviation: CBF, cerebral blood flow. Source: From Ref. 24.

region of the brain. Also, due to low inherent signal-to-noise ratio, it is necessary to obtain a large number of data points (which translates into long scanning times) to make a valid statistical statement on a given subject. Thus, in order for this technique to reach its potential, we need to await technical improvements in scanner technology.

CONCLUSION

In order to optimally apply BOLD fMRI well to the clinical situation, one needs a solid understanding of physics, statistics, neurology, and anatomy. Optimizing the protocol for data acquisition and processing is very important. Lack of understanding of the mechanisms that underlie BOLD fMRI (or treating BOLD fMRI simply as a "black box") can lead to errors in the clinical arena. Hopefully, this chapter will lead the reader to appreciate the physics and physiology of fMRI, which will translate into an improvement in clinical care for our patients.

REFERENCES

1. Buxton RB. Introduction to Functional Magnetic Resonance Imaging. Principles and Techniques. Cambridge, U.K.: Cambridge University Press, 2002.
2. Moonen CTW, Bandettini PA, eds. Functional MRI. Berlin: Springer, 2000.
3. Jezzard P, Matthews PM, Smith SM, eds. Functional MRI: An Introduction to Methods. Oxford, U.K.: Oxford University Press, 2001.
4. Huettel SA, Song AW, McCarthy G. Functional Magnetic Resonance Imaging. 1st ed. Sunderland, MA: Sinauer Associates Inc. 2004.

5. Tofts P. Quantitative MRI of the Brain. Measuring Changes caused by Disease. Chichester, U.K.: Wiley, 2003.
6. Bradley WG, Stark DD. Magnetic Resonance Imaging. 3rd ed. St Louis: Mosby Inc, 1999.
7. Ogawa S, Lee T-M, Nayak AS, et al. Oxygenation-sensitive contrast in magnetic resonance image of rodent brain in high magnetic fields. *Magn Reson Med* 1990; 14:68–78.
8. Ogawa S, Lee T-M, Kay AR, et al. Brain magnetic resonance imaging with contrast dependent on blood oxygenation. *Proc Natl Acad Sci U S A* 1990; 87:9868–9872.
9. Ogawa S, Lee TM. Magnetic resonance imaging of blood vessels at high fields: in vivo and vitro measurements and image stimulation. *Magn Reson Med* 1990; 16:9–18.
10. Belliveau JW, Kennedy DN Jr., McKinstry RC, et al. Functional mapping of the human visual cortex by magnetic resonance imaging. *Science* 1991; 254:716–719.
11. Buxton RB, Uludag K, Dubowitz DJ, et al. Modeling the hemodynamic response to brain activation. *NeuroImage* 2004; 23:S220–S233.
12. Logothesis NK, Pauls J, Augath M, et al. Neurophysiological investigation of the basis of the fMRI signal. *Nature* 2001; 412:150–157.
13. Logothesis NK, Wandell BA. Interpreting the BOLD signal. *Annu Rev Physiol* 2004; 66:735–739.
14. Holodny AI, Schulder M, Liu WC, et al. Deceased BOLD functional MR activation of the motor and sensory cortices adjacent to a glioblastoma multiforme: implications for fMRI guided neurosurgery. *Am J Neuroradiol* 1999; 20:609–612.
15. Holodny AI, Schulder M, Liu WC, et al. The effect of brain tumors on BOLD fMRI activation in the adjacent motor cortex: implications for image-guided neurosurgery. *Am J Neuroradiol* 2000; 21:1415–1422.
16. Ulmer JL, Hacein-Bey L, Mathews VP, et al. Lesion-induced pseudo-dominance at functional magnetic resonance imaging: implications for preoperative assessments. *Neurosurgery* 2004; 55:569–579.
17. Chen C, Hou BL, Holodny AI. Effect of age and tumor grade on BOLD fMRI in preoperative assessment of glioma patients. *Radiology* (in press).
18. Ruff IM, Petrovich Brennan NM, Peck KK, et al. Assessment of the language laterality index in brain tumor patients using fMRI: effects of thresholding, task selection and prior surgery. *Am J Neuroradiol* 2008; 29(3):528–535.
19. Kennan RP, Zhong J, Gore JC. Intravascular susceptibility contrast mechanisms in tissues. *Magn Reson Med* 1994; 31(1):9–21.
20. Weisskoff RM. Basic theoretical models of BOLD signal change. In: Moonen CWT, Bandettini PA, ed. *Functional MRI*. Berlin: Springer-Verlag, 1999:P115–P123.
21. Kim MJ, Holodny AI, Hou BL, et al. The effect of prior surgery on blood oxygen level-dependent functional MR imaging in the preoperative assessment of brain tumors. *Am J Neuroradiol* 2005; 26(8):1980–1985.
22. Viviani R, Grön G, Spitzer M. Functional principal component analysis of fMRI data. *Hum Brain Mapp* 2005; 24:109–129.
23. McKeown MJ, Makeig S. Analysis of fMRI data by blind separation into independent spatial components. *Hum Brain Mapp* 1998; 6(3):160–188.
24. Lu H, Donahue MJ, van Zijl PC. Detrimental effects of BOLD signal in arterial spin labeling fMRI at high field strength. *Magn Reson Med* 2006; 56:546–552.
25. Hou BL, Bradbury M, Peck KK, et al. Effect of brain tumor neovasculature defined by rCBV on BOLD fMRI activation volume in the primary motor cortex. *NeuroImage* 2006; 32:489–497.

2

Preparing the Patient for the fMRI Study and Optimization of Paradigm Selection and Delivery

NICOLE M. PETROVICH BRENNAN

Department of Radiology, Memorial Sloan-Kettering Cancer Center, New York, New York, U.S.A.

INTRODUCTION

Functional magnetic resonance imaging (fMRI) has gained both popularity and credibility. Because the neural activity and response to a wide variety of stimuli can be assayed noninvasively, fMRI is employed to study everything from consciousness to pain management (1,2). Use of fMRI in patients with neurological maladies deserves special attention. Such patients may have difficulty understanding instructions, tend to demonstrate more head motion than the average control subjects (3), may have altered physiology affecting their hemodynamic responses (4,5), and are generally more anxious overall. In this chapter we will consider a subsection of these concerns. We will mainly focus on the design of fMRI paradigms in terms of clinical treatment goals, delivery of chosen paradigms to the patient, and patient preparation and monitoring. We will see that each of these components is important in maximizing ones likelihood of obtaining an accurate and representative map of function.

Currently, clinical fMRI is dominated by neurosurgical planning and patient treatment counseling. To this end, fMRI paradigms should be designed to answer the clinical questions of concern to neurosurgeons and neurologists. Clinicians often use fMRI when deciding whether to offer a neurosurgical procedure or assessing risk in neurological

treatments. To design the most appropriate fMRI paradigms for this clinical context, it is useful to review the functional neuroanatomy of speech and motor function, as these systems are those commonly mapped using fMRI. A working knowledge of functional neuroanatomy is useful in choosing appropriate patient paradigms. The following is a review of the basic principles of functional anatomy necessary for the design of fMRI paradigms.

FUNCTIONAL NEUROANATOMY

Language

In most right-handed individuals, language is the purview of the left hemisphere. There is some debate about how complete this specialization is, particularly in left-handed people where fMRI maps of language are more likely to display codominance (bihemispheric) or right-hemisphere dominance (6–8). Further, scientists continue to subdivide linguistic subcomponents with ever-increasing anatomic precision. However, current clinical fMRI of language relies mostly on hemispheric language dominance and gross spatial localization of language areas.

Language can be roughly subdivided into productive and receptive areas or frontal and tempoparietal areas,

respectively. Classically, the left-hemispheric frontal areas have been termed “Broca’s area” and the left-hemispheric posterior superior temporal areas termed “Wernicke’s area.” However, especially in the case of Wernicke’s area, the precise anatomical areas that subserve speech function as a whole are not well defined. Further, there can be considerable variability from person to person in the anatomical specialization of language anatomy. As a result, we will discuss these areas in terms of frontal systems (generally responsible for productive speech) and temporo-occipital systems (generally responsible for receptive speech).

Frontal Language Areas

The frontal speech areas mostly comprise the inferior frontal gyrus (pars triangularis and pars opercularis) of the left hemisphere (Fig. 1A). Broadly, the frontal speech area is involved in speech production. Lesions to this area produce a halting, expressive, or nonfluent aphasia (also termed “Broca’s aphasia”). Most commonly, patients with expressive aphasias perform well on measures of speech comprehension but display agrammatic or telegraphic speech (simplified, staccato-like sentences).

Temporal Language Areas

The dominant temporal speech areas reside mostly in the posterior superior temporal gyrus of the left hemisphere (Fig. 1B). Temporal systems drive receptive speech such as

comprehension. Lesions to this area produce fluent aphasias where the patient speaks with normal inflection, rate, and cadence but with impaired meaning (i.e., word salad). Lesions to this area can also result in word-finding difficulty and impaired confrontation naming (picture naming).

Figure 2 shows a map of language function in a healthy control subject during an auditory responsive naming language task. (The patient responded to aurally presented questions. Question: “What do you shave with?” Response: “A razor.”). Aside from Wernicke’s area, auditory stimuli will activate the primary auditory cortex, located bilaterally in the transverse temporal gyrus, also known as Heschl’s gyrus. Figure 3 demonstrates similar putative areas during a productive (verb generation) language task. There is significant functional overlap in the areas activated during “targeted” language tasks (targeted to frontal or posterior language systems). This will be discussed in more detail later in the chapter.

It should be noted that while the aforementioned are the major language centers in the brain, there are many secondary language areas that activate consistently on an fMRI map. These include (but are not limited to) middle frontal gyrus, middle and inferior temporal gyri, and supramarginal and angular gyri. For example, Figure 3 clearly demonstrates prominent activation in the left middle frontal gyrus. These areas should not be discounted as their contribution to essential speech function can be significant and their role in linguistics is being increasingly well defined.

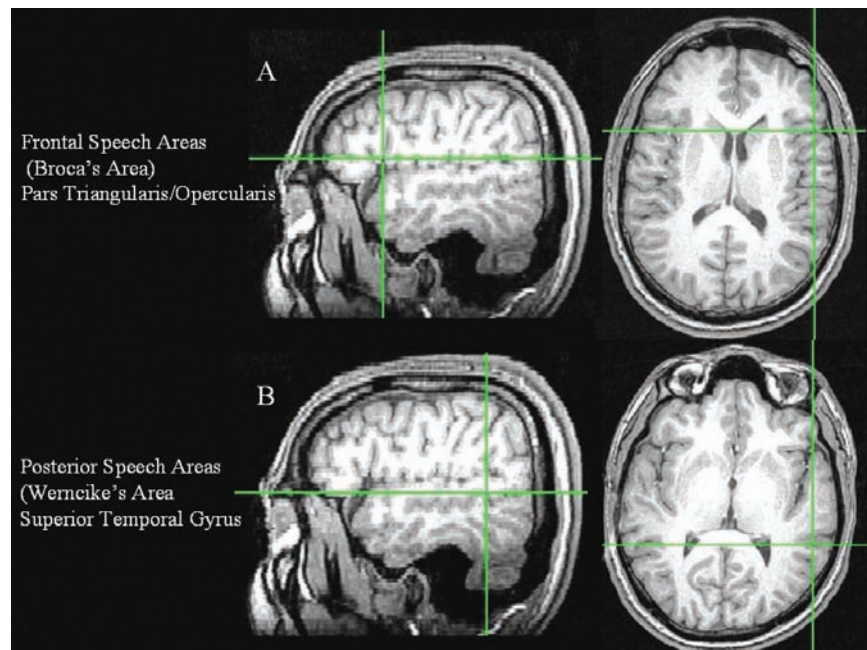


Figure 1 Basic language anatomy. **(A)** Putative anatomical definition of frontal speech areas and **(B)** posterior speech areas.

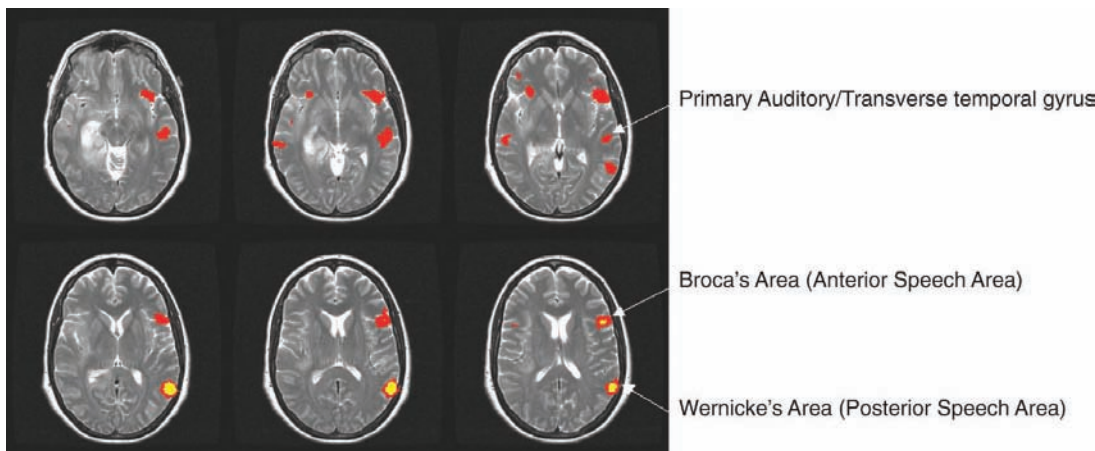


Figure 2 Language map during a semantic fluency task in a patient with a glioma. A well-lateralized left-dominant language map showing robust frontal (Broca's area) and posterior (Wernicke's area) language areas during an auditory responsive naming task. Auditory stimuli also activate the primary auditory cortex, located bilaterally in the transverse temporal gyrus, also known as Heschl's gyrus. The patient was asked to generate words to a given aural descriptor, e.g., “What do you shave with?” The patient would covertly answer, “a razor”.

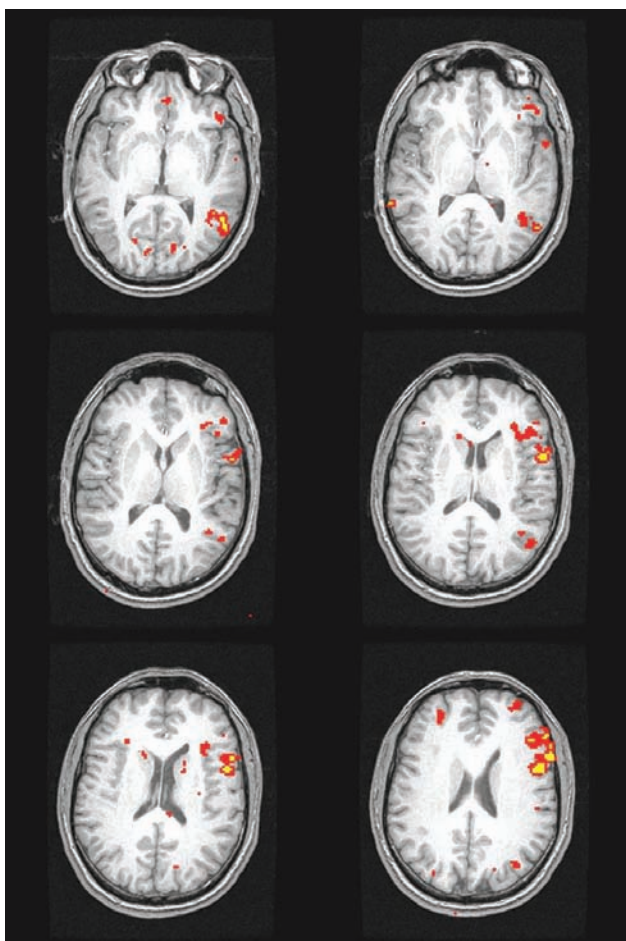


Figure 3 Language map during a productive task (verb generation) in a healthy control subject. The subject silently generated verbs to aurally presented nouns.

Motor Areas

The sensory/motor system is organized topographically. This means that each portion of the body has a specific location on the cortex. The classical version of this homunculus places the foot and leg directly adjacent to the interhemispheric fissure, the hand lateral to the foot, and the face at the most lateral level (Fig. 4). A more detailed view of the location of motor hand in the “reverse or upside-down omega area” in the axial plane is shown in Figure 5, so called because the motor homunculus has the appearance of an upside-down omega, although this appearance can be variable. Understanding the anatomy of the motor homunculus is important in choosing the appropriate fMRI paradigm. It is essential to review prior films to ascertain the location of the lesion with respect to the different parts of the motor strip when selecting which paradigm to perform. Performing generic paradigms may lead to ambiguous results. For example, performing a finger-tapping paradigm may not be useful in determining the location of the motor strip if the lesion is adjacent to the tongue motor homunculus. Therefore, one should choose the paradigm that would identify the location of the specific motor cortex, which is in closest proximity to the lesion. Often, the motor strip is not perpendicular, but rather is oblique to the scanning plane, which makes following it problematic over multiple slices. Consequently, if the fMRI study unambiguously identifies the hand motor homunculus, it is not necessarily true that the reader will be able to clearly identify the tongue motor homunculus located some slices caudad. Therefore, it is essential to perform the appropriate fMRI paradigm to be able to identify the specific part of the motor homunculus, which is adjacent to the lesion.

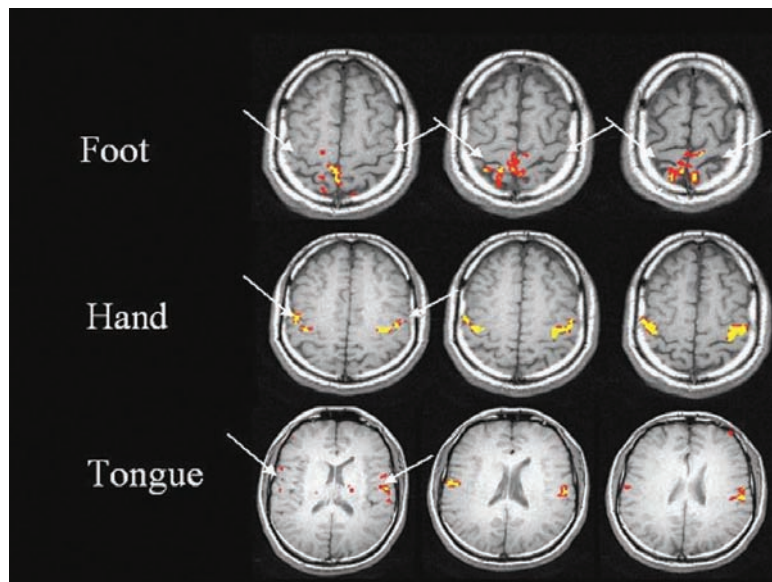


Figure 4 Motor fMRI maps representing three major areas on the motor homunculus. Foot activates medially, hand lateral to foot, and face/tongue at the most lateral position. Keeping the homunculus in mind when designing fMRI paradigms is important in surgical decision making. Abbreviation: fMRI, functional magnetic resonance imaging.

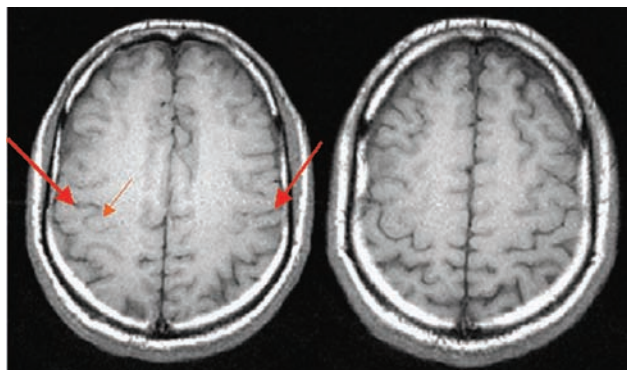


Figure 5 The motor and sensory gyri in the axial plane. The red arrows indicate the location of the central sulcus. The orange arrow demonstrates the location of the “hand omega” anatomy, typically suggesting the location of hand motor.

In addition, it is important to select the proper paradigm prior to initiation of the fMRI scan itself, so that the patient (especially those with neurological deficits) will be able to practice and feel comfortable with the selected paradigm. Some of these motor paradigms, such as lip pursing or tongue motion may be difficult to explain once the patient is in the scanner.

Not all patients with lesions in the perirolandic cortex are referred for motor strip localization. Many patients with medial frontal lesions are mapped to localize the supplementary motor area (SMA) in the superior frontal gyrus. The SMA is generally responsible for planning

motor movements. It is divided into two major portions, the SMA proper and the pre-SMA, just anterior (Fig. 6). The SMA proper is generally responsible for planning motor movements and the pre-SMA is generally involved in linguistic planning (9). SMA localization using fMRI is important as the anatomical boundaries are vague and

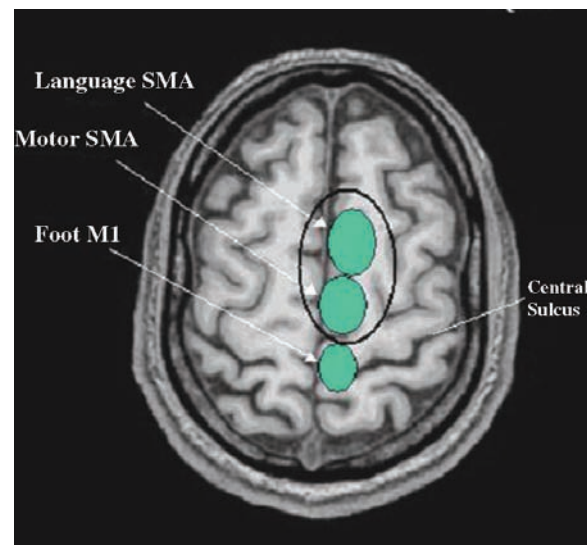


Figure 6 Supplementary motor area. The supplementary motor area is subdivided grossly into two major areas. The more anterior portion has a linguistic role and the more posterior area subserves motor planning. The expected location of foot is also indicated.

surgical insult can result in paresis or muteness. Interestingly, these deficits tend to resolve fairly quickly (on the order of weeks in many cases). Further, in our experience, it can be difficult to get a response in the SMA during intraoperative electrocorticography, placing even more importance on the fMRI localization.

fMRI PARADIGM SELECTION FOR PATIENTS

Given this knowledge of functional neuroanatomy, one can start to consider which areas to target with an fMRI paradigm based on the location of a lesion. These decisions can be straightforward and they can be nuanced. For example, lesions in perirolandic regions generally call for motor and or sensory paradigms. However, while SMA may activate with most sensory motor paradigms (passive hand stimulation, for example), in our experience, volitional patient-directed tasks (for example, finger tapping) more robustly activate this area. Further, it is important to know the handedness of the referred patient as right-hemispheric lesions seemingly indicating motor fMRI paradigms may also require language measurements if the patient is left-handed. Left-handed patients are more likely to be codominant or right dominant for language and the inclusion of language tasks may not be evident without a thorough history.

In selecting the proper paradigm, it is important to evaluate the patient's clinical condition while interviewing the patient prior to initiation of the fMRI scan. An obvious example is a patient with a lesion in the expected location of the hand homunculus in whom the neurosurgeon is interested in determining the location of the motor strip. However, if pre-fMRI evaluation reveals that the patient's hand is paralyzed, asking the patient to tap his/her fingers would not lead to interpretable fMRI results. Alternative strategies maybe to perform motor paradigms of a different motor system (such as foot or tongue) or to perform a sensory hand paradigm of the hand. Armed with fMRI results from the alternative paradigm, one would then extrapolate the location of hand motor homunculus.

Lastly, if the fMRI is being ordered for neurosurgical planning, it is important to consider the neurosurgeon's goals and to tailor the paradigms to these specific goals. The most basic decision that the neurosurgeon must undertake is weather or not to attempt a resection. If it can be demonstrated that the lesion is located in an essential, eloquent cortex, the neurosurgeon may decide to forego an attempted resection and biopsy the lesion. For example, it may be difficult to tell, whether a lesion is located in the precentral gyrus or within the posteriomost aspect of the middle frontal gyrus. If the fMRI demonstrates the former, the neurosurgeon may settle for a

biopsy, whereas, if the fMRI demonstrates the latter, the neurosurgeon may decide on a resection.

Another area where fMRI may be crucial to the neurosurgeon in making a decision as to whether or not to operate is in patients with lesions possibly involving the dominant language cortices. In our institution, such patients are frequently referred for language mapping. Right-handed individuals are almost always left language-dominant; however, left-handed or ambidextrous individuals are much more often right language-dominant or of mixed dominance. Therefore, in left-handed individuals, it is often unclear if a lesion involves the dominant Broca's or Wernicke's area, which is a clear indication for a language fMRI study.

Lesions in the insula have produced speech apraxia and word-finding difficulty and this has suggested an insular role in language in some people (10). However, most of these patients are also mapped intraoperatively using electrocorticography during an awake craniotomy. This procedure often begins with the surgeon stimulating motor cortex (to establish a current threshold) and subsequently mapping language. As a result, many surgeons also request tongue motor-mapping fMRI as a guide to this portion of intraoperative mapping despite the fact that the main aim of the fMRI is language related.

Common Patient fMRI Paradigms

There are no standard fMRI paradigms for patients. From a scientific standpoint this is troublesome as it introduces a significant amount of variability from study to study and only broad comparisons among study results are appropriate. However, from a clinical perspective, having no standard battery of tasks is extremely advantageous as the investigator has flexibility in choosing or designing a task that the patient can perform correctly. This is paramount. If the patient cannot adequately perform the task, the interpretation of the resultant map becomes highly questionable. The following are guidelines based on commonly used fMRI tasks. Keep in mind, however, that the best fMRI protocol for a given patient may require some creativity. Very aphasic patients may need modified versions of the language tasks detailed below. In extreme cases, tailored paradigms can be designed specifically to the single category of speech that is preserved in a globally aphasic patient (autobiographical questions, for example).

Language Systems

Productive speech tasks are generally tasks that require the patient to generate words. These are categorically considered fluency tasks. Verb generation is a commonly used fMRI paradigm. The patient is presented with nouns

either visually or aurally and she/he is asked to silently generate (to avoid head motion) verbs to the given nouns.

During a phonemic fluency task, patients are given a letter and asked to generate words that begin with that letter. A similar task involving categories requires that the subject generate words to the given category (fruits, vegetables, etc.). This task is termed a “semantic fluency task” and has the advantage of also tapping into posterior areas in their participation of semantic judgments.

Receptive speech tasks generally involve reading, listening to aurally presented words, or filling in visually presented sentences with the appropriate word. The advantage of this last task is that performance measures can be built in. The patient is presented a sentence like, “Bill gives haircuts and shampoos. He is a ____.” and the patient is presented with four choices, (A) a butcher (B) a barber (C) a doctor (D) a boy. The patient can then press a button corresponding to the correct answer and the investigator has a measure of the patient’s performance during a task. Good patient performance is crucial for an interpretable language map and the investigator should build in performance measures wherever possible.

It should be noted that regardless of the target of the language task, most language tasks will activate both frontal and posterior language areas to some degree. These areas are highly cooperative. However, in our experience it can be more difficult to measure posterior language areas than frontal language areas. It may be that the posterior language areas are somewhat more distributed (superior temporal, middle temporal, and supramarginal and angular gyri all participate to some extent in receptive language). This distributive nature may mean that the detection of a reproducible fMRI signal requires significant statistical power (in the form of fMRI task repetitions) to detect it reliably.

Price et al. (11) suggests that nonperiodic temporal sampling during fMRI acquisition may help detect temporoparietal language areas. In this technique, either the stimuli or the baselines are designed such that there are no integer-multiples of the repetition time (TR). In this way, the first image of each stimulation epoch does not occur at the same point in the TR each time. This minimizes contribution of systematic periodic artifacts (like scanner noise) and/or physiological noise (heart rate and respiration) and allows more robust detection of small fMRI signals.

Motor Systems

Commonly used paradigms to localize the motor strip include finger tapping, tongue motion, and sensory foot stimulation. In the finger-tapping task, patients are asked to sequentially tap their fingers avoiding arm or shoulder motion. Patients whose distal limbs are weak can open and

close the fist with similar fMRI results. The sequential motion of the fingers from thumb to pinky finger or other more complicated sequencing will also capture premotor areas as well as the primary motor gyrus.

During tongue movement, patients are asked to keep their teeth closed (to avoid head motion) and make a small sweeping motion of their tongue against the back of their teeth. The mouth, lips, and tongue area of the motor homunculus has so much cortical space dedicated to it relative to other parts of the body, only a small movement of the tongue is required to measure a strong fMRI signal. Further, large mouth movements should be avoided, as it is difficult to keep one’s head still during the tongue motion task regardless of the extent of the motion.

Foot stimulation is generally done with a passive sensory stimulation procedure to avoid head motion. These results (as with passive sensory hand stimulation) should be interpreted with caution, as the centroid of fMRI activity will represent the location of the sensory gyrus and not the motor gyrus. In our experience, asking patients to tap or wiggle their toes produces excessive head motion regardless of the extent of the restraint and padding. Further, the type of head motion with this task tends to be in the z (or inferior to superior) direction when scanning the more common axial plane, which is often difficult for statistical programs to extract.

In general, passive sensory paradigms can be substituted for motor paradigms in the event that the patient is paretic. Even given the very weak but not paretic patient, the investigator should consider a passive sensory paradigm to avoid the head motion associated with struggling to move the affected limb. (Head motion comes up consistently when designing paradigms as it can be very problematic in statistical analysis and may render the experimental run void. It goes without saying that it should be avoided wherever possible.) There is generally such sufficient neuronal reciprocity in the sensory motor system that the motor gyrus will also activate during fMRI of passive sensory stimulation of the hand, for example.

Block Design Vs. Event-Related Designs

Every fMRI paradigm (for clinical purposes) requires both resting and active states. The most common paradigm design for use in patients is termed “block design” and consists of a periodic (or nonperiodic) presentation of stimuli in blocks (Fig. 7). For example, in a typical block-designed finger-tapping protocol, the patient alternates between fixation on a crosshair on a screen for 20 seconds and finger tapping for 20 seconds. Many paradigms repeat this cycle for five or six trials.

Event-related designs are another common stimulus presentation where the patient or subject performs a single short event followed by rest of a short or longer duration

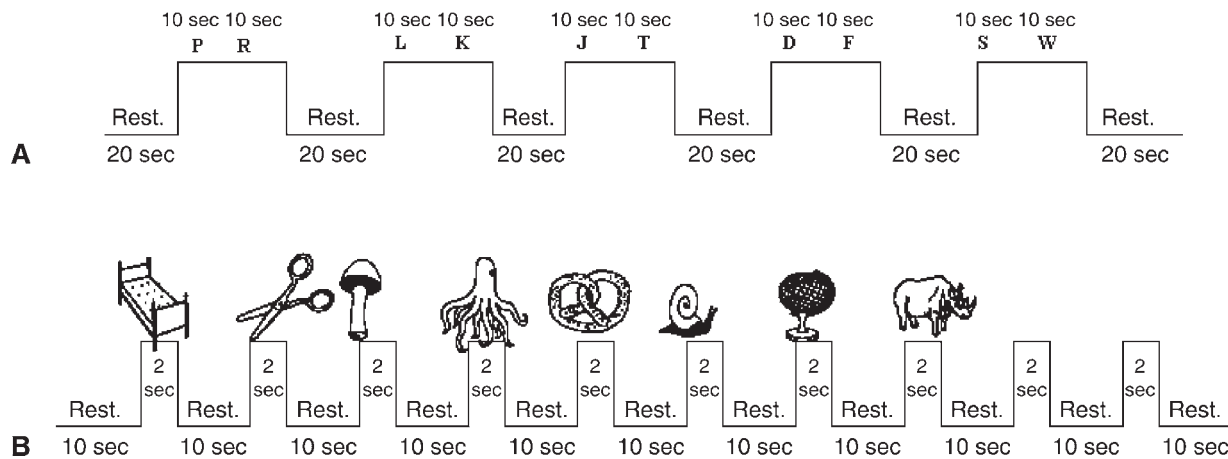


Figure 7 Common paradigm designs. (A) Block design for a phonemic fluency paradigm. Letters are examples of stimuli that could be presented to a patient aurally or on a screen for 10 seconds each, as indicated. Block design is much preferred in patient populations. It averages images of the two epoch types (stimulation and rest). As a result, the fMRI signal is better detected than with (B) event-related designs where the details of the fMRI BOLD signal can be better measured. Event-related designs can be statistically equivalent but require many repetitions, and patients tend not to perform as well overall with event-related designs, in our experience. An event-related picture-naming paradigm is shown. Paradigm designs are the simplest periodic form. Ideally, paradigms should be designed with a variable interstimulus interval to maximize detection of weak signals. Abbreviations: fMRI, functional magnetic resonance imaging; BOLD, blood oxygenation level dependent. Source: From Ref. 12.

(rapid event-related and event-related, respectively). This type of paradigm design is used when the investigator is interested in the neural response to a single event or the hemodynamic response to a single event is desired. [An example of an event-related picture-naming paradigm with standardized pictures from the Boston Diagnostic Aphasia Examination is shown in Fig. 7 (12).] Event-related paradigms are not as commonly used with patients. Block designs are effective at detecting an averaged fMRI signal as the patient performs many repetitions of the same type of event over time. This type of detection is advantageous in patients where there may be variable performance, dysfunctional hemodynamics, and greater than average head motion. Event-related paradigms are better at estimating the details of a particular hemodynamic response (13). Because it involves single events separated by rest, these paradigms are often long and laborious for patients. The long length of the experiment is often necessary to obtain the same or similar statistical power as the block design where the averaged images in an epoch afford greater statistical significance.

Baseline Tasks

The choice of baseline task is an important consideration. In all fMRI studies, the bigger the difference between the baseline and the activation period the stronger the fMRI signal. To this end, the simplest baseline choice is a fixation cross where the patient is instructed to fixate on the cross. Occasionally, it is appropriate to “raise” the

baseline and place a contrasting task instead of true rest to extract a particular neural region. Baselines can involve tasks that will extract primary sensory areas not of interest to the final results. By design, most statistical analyses are asked to show activity that is unique to the stimulus periods and not the rest periods. If an event happens during both the rest period and the stimulation period, there will be no significant change in gray scale values and no subsequent fMRI activity. For example, during an aurally presented language task, a tone can be placed in the baseline such that the primary auditory signal (transverse temporal gyrus) happens in both the stimulation and baseline periods and is extracted. This is of particular advantage when trying to localize Wernicke’s area (or the main posterior language center) as the two areas are in close proximity to one another.

However, manipulating the baseline task can be perilous. Peck et al. (14) investigated the use of picture naming and nonsense objects in the investigation of syntax in sentence completion. They found that activity in Broca’s area was obscured by use of picture naming as compared with nonsense objects that simply extracted primary visual fMRI activity.

PREPARING THE PATIENT FOR THE fMRI STUDY

The quality of the fMRI result is only as good as the patient’s performance (15). Patients are often anxious because they are impaired and not sure how their

impairment will affect the fMRI results. Patients need to be familiarized with the task, particularly with the rest/perform nature of the task. Elderly patients can have difficulty in understanding the silent/covert performance of many language tasks. In all cases, careful patient preparation will translate to a much more accurate and reliable fMRI map.

Most fMRI tasks are amenable to practice versions. These practice versions can be loaded onto a laptop so that the patient can run through a shortened version of the identical task that they will be expected to perform. These trial runs should be put together with similar but different stimuli (words or letters) than the real task as patients can habituate (truncate their neural response) to previously seen stimuli. The trial tasks can also serve as a good predictor of the patient's abilities. If easier versions of fMRI tasks are made ahead of time, they can be easily substituted for patients having obvious trouble with a harder task set.

Once the patient is in the MRI scanner doing the tasks, it is sometimes helpful to give the patient intermittent instructions or encouragement over headphones. While this may seem superfluous, patient's performance may improve once they are reassured that they are performing the task correctly. For those institutions with real-time fMRI analysis software on their MRI scanner, the investigator can, for example, even give the patient an idea of their performance in terms of head motion. Careful patient preparation relaxes patients and may decrease the amount of head motion. Also, elderly patients may particularly benefit from intermittent reiteration of the instructions over headphones given common issues with working memory. All things considered, while fMRI is commonplace to the investigator, it is important to remember that not only are the procedures, sights, and sounds unfamiliar to the patient, the patient is generally not entirely sure how their doctor will use the map of their brain function. It is our responsibility to be sensitive to our patients in this respect.

MONITORING PATIENT PERFORMANCE

There are a variety of ways to add confidence that the patient is actually performing the task correctly. The easiest, of course, is visual inspection. Paradigms like finger tapping are amenable to this type of monitoring. In our institution, certain patients are given squeeze balls that record the magnitude of their motor response during the acquisition. These parameters are nicely documented in the patient's record and can be referred to if a retrospective study requires such. Sensory paradigms are likewise easy to monitor as the investigator is generally timing the passive stimulation themselves.

Language paradigms however are more difficult to monitor. Building language paradigms that are "forced choice" (where the patient must make a response) are a good way to ensure that the patient is performing the task and to record the error rate for consideration in the postprocessing. MRI-compatible button boxes are ideally suited for this type of observation. The boxes tend to have large buttons that are few in number so as not to confuse a patient who is already disoriented and not able to see their hands. In keeping with this, patients with sensory lesions have difficulty using button boxes because of their difficulty with proprioception and sensation.

Using vocalized speech paradigms has become an exciting possibility in clinical fMRI only recently. With the advent of sophisticated motion correction algorithms and a plethora of ways to avoid excessive head motion during the fMRI acquisition (including coaching the patient to speak like a ventriloquist and securing their head with tape and foam padding and in some cases face masks) vocalized speech fMRI is now possible (16). The statistical analysis of vocalized speech fMRI takes advantage of the delay in the hemodynamic response (6–30 seconds) following a neural event. Using an event-related paradigm, the patient can vocalize their response to a single or near-single stimulus. The images following the acquisitions where the patient actually spoke are analyzed for the hemodynamic response. The images where the patient actually spoke are discarded as they often contain unacceptable amounts of head motion.

Vocalized speech paradigms are not without their difficulties. Of course, all the usual caveats about using event-related paradigms in patients still apply. Further, anytime head motion grossly changes the position of the head over time will be a problem statistically regardless of whether the "active" images are extracted. Additionally, while overt responses can theoretically be recorded and inspected, it can be difficult to hear patients over the gradient noise regardless of the quality of the microphone. Individual institutions should experiment with their particular system to find what works best. Lastly, vocalized speech fMRI may skew the measurement of the laterality index. Because auditory and motor systems are bilaterally represented, hemispheric measurements of language laterality maybe affected by vocalized speech fMRI paradigms.

SUMMARY

Choosing the appropriate fMRI paradigms to assay the most relevant functional networks is an important aspect of clinical fMRI. For the purpose of neurosurgical planning, measures of fMRI localization of function are deliberately coarse as neurosurgical practice does not, to date, generally support the sparing of finely subdivided

cognitive substrates. As a result, with a general knowledge of functional neuroanatomy the choice/design of appropriate fMRI paradigms is fairly straightforward. Patient training, monitoring, and encouragement are equally important in increasing the likelihood of an accurate/reliable fMRI map of function. For neurosurgical planning, vocalized speech paradigms should be used when possible but should be interpreted with caution in terms of language lateralization.

REFERENCES

1. Peyron R, Laurent B, Garcia-Larrea L. Functional imaging of brain responses to pain. A review and meta-analyses. *Neurophysiol Clin* 2000; 30(5):263–288.
2. Bernat JL. Chronic disorders of consciousness. *Lancet* 2006; 367(9517):1181–1192.
3. Krings T, Reinges MH, Erberich S, et al. Functional MRI for presurgical planning: problems, artefacts, and solution strategies. *J Neurol Neurosurg Psychiatry* 2001; 70(6):749–760.
4. Holodny AI, Schulder M, Liu WC, et al. The effect of brain tumors on BOLD functional MR imaging activation in the adjacent motor cortex: implications for image-guided neurosurgery. *AJNR* 2000; 21(8):1415–1422.
5. Hou BL, Bradbury M, Peck KK, et al. Effect of brain tumor neovasculature defined by rCBV on BOLD fMRI activation volume in the primary motor cortex. *Neuroimage* 2006; 32(2):489–497.
6. Knecht S, Drager B, Deppe M, et al. Handedness and hemispheric language dominance in healthy humans. *Brain* 2000; 123(pt 12):2512–2518.
7. Issacs KL, Barr WB, Nelson PK, et al. Degree of handedness and cerebral dominance. *Neurology* 2006; 66(12):1855–188.
8. Knecht S, Deppe M, Drager B, et al. Language lateralization in healthy right-handers. *Brain* 2000; 123(pt1):74–81.
9. Van Oostende S, Van Hecke P, Sunaert S, et al. FMRI studies of the supplementary motor area and the preomotor cortex. *Neuroimage* 1997; 6(3):181–190.
10. Dronkers NF. A new brain region for coordinating speech articulation. *Nature* 1996; 384(6605):159–161.
11. Price CJ, Veltman DJ, Ashburner J, et al. The critical relationship between the timing of stimulus presentation and data acquisition in blocked designs with fMRI. *Neuroimage* 1999; 10(1):36–44.
12. Goodglass H, Kaplan E. *The Assessment of Aphasia and Related Disorders*. 2nd ed. Philadelphia, PA: Lea & Febiger, 1983.
13. Birn RM, Cox RW, Bandettini PA. Detection versus estimation in event-related fMRI: choosing the optimal stimulus timing. *Neuroimage* 2002; 15(1):252–264.
14. Peck KK, Wierenga CE, Moore AB, et al. Comparison of baseline conditions to investigate syntactic production using functional magnetic resonance imaging. *Neuroimage* 2004; 23(1):104–110.
15. Price CJ, Friston KJ. Scanning patients with tasks they can perform. *Hum Brain Mapp* 1999; 8(2–3):102–108.
16. Huang J, Carr TH, Cao Y. Comparing cortical activations for silent and overt speech using event-related fMRI. *Hum Brain Mapp* 2002; 15(1):39–53.

3

Methods of Analysis

KYUNG K. PECK

*Functional MRI Laboratory, Department of Radiology, Memorial Sloan-Kettering Cancer Center,
New York, New York, U.S.A.*

INTRODUCTION

Since the discovery in the early 1990s, functional MRI (fMRI) has been increasingly utilized as a technique to investigate human brain function. With this neuroimaging technique, a rapidly increasing number of studies have been published that attempt to image the brain function obtained during specific functional tasks including motor, sensory, and cognitive tasks. Recently, fMRI has expanded into a variety of clinical applications. The most direct clinical application in which fMRI is already playing an important role is presurgical mapping for patients with brain tumors near functional cortical areas (1–3).

One of the most significant challenges in fMRI is to be able to accurately identify the small amplitude blood oxygenation level-dependent (BOLD) (4) signal. Typically, the BOLD fMRI signal measures only a few percentage changes for activation in the sensorimotor system and is even smaller for higher cognitive tasks. The problem is compounded by the fact that BOLD signal is easily obscured by undesirable noises (5).

After acquiring fMRI data, proper processing steps must be taken to optimize the signal, which is associated with specific functional tasks, and to minimize the noise-related signal. This is essential because the statistical analysis is greatly affected by the preprocessed data. Nowadays, commercial software allows real-time processing and analyzing of fMRI data while the patient is still in

the scanner (6). While this procedure plays an important role in clinical application where time is limited, it has its limitations. In the clinical setting, many patients are neurologically impaired and exhibit increased voluntary movements and inconsistent task performance compared with healthy control subjects (7). Such problems can lead to spurious results and misinterpretation of fMRI data. As a result, offline data preprocessing and statistical analysis are critical to achieving accurate results for which various fMRI software packages are available, each having its own strengths and weaknesses (8).

Even though general agreement exists on how to process fMRI data (e.g., algorithms to detect head motion and correction), the theory and practicalities associated with data processing are complex and constantly evolving. A number of important issues such as choosing statistical tests and thresholds remain.

PREPROCESSING: IMPROVING IMAGE QUALITY

The goal of preprocessing is to reduce artifactual signal variance in the voxel time series that is not associated with the subject's functional task and to improve the detectability of neurally induced changes. Preprocessing steps generally encompass image reconstruction, slice-timing correction, motion correction, spatial smoothing, and spatial normalization.

Quality Assessment

In the clinical fMRI, prior to the acquisition of fMRI data, it is important to assess the clinical status of the patient to determine if he/she will be able to perform the planned fMRI procedures (9). For example, the fMRI data of a patient with aphasia or motor deficits may contain more motion artifacts because of their physical deficit than healthy normal subjects. A patient with severe depression may not perform cognitive tasks like healthy normal subjects. Recognizing issues such as motion artifacts and weak task performance in advance allows for customization of the analytical approach on the basis of the patient's deficit. These issues can be greatly minimized with careful instruction and practice prior to the scan. In addition, a simple signal-to-noise ratio (SNR) measurement of scanner stability will be beneficial prior to the functional imaging (10).

After acquisition, the fMRI data is converted from a raw data format into individual images or groups of images, which can then be read by existing software packages. This process of converting raw data sets into images is called image reconstruction. Performing the image quality checks at multiple points in the preprocessing stream is essential, although it may be time consuming (Fig. 1). During the image quality check, various types of artifacts related to data acquisition, head motion, and data analysis can be noticed. Data acquisition-related artifacts

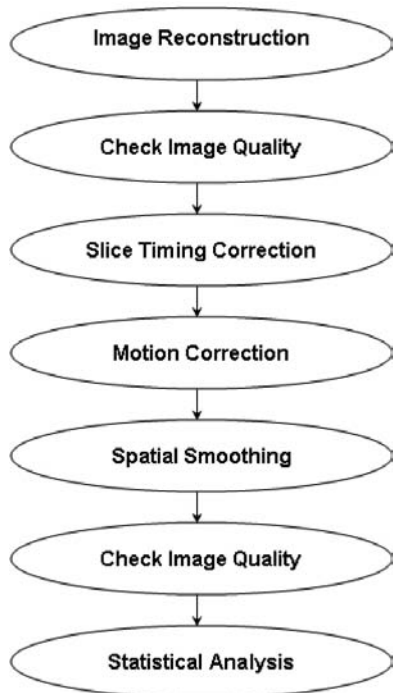


Figure 1 Preprocessing stream for fMRI data. Abbreviation: fMRI, functional magnetic resonance imaging.



Figure 2 White pixel noise leading MR artifacts. Wavelike (A) or stripe (B) artifacts superimposed onto the T2*-weighted image are visible. Commercial software displaying real-time images can monitor this problem. Images contaminated by the noise should be removed before proceeding. Abbreviation: MR, magnetic resonance.

include image distortion due to field inhomogeneous and signal drops due to white pixel noise. Subject-related artifacts include head motion (11) and physiological motion, such as respiration and pulsation (12,13). Viewing the images in "cine mode" and checking temporal variations in the time series often reveal obvious problems, including white pixel noise (Fig. 2) or abrupt patient head motion (Fig. 3). Such images should be eliminated prior to further steps.

Beyond these artifacts, a low-frequency drift (0.0–0.015 Hz), also called a linear trend, in the fMRI time

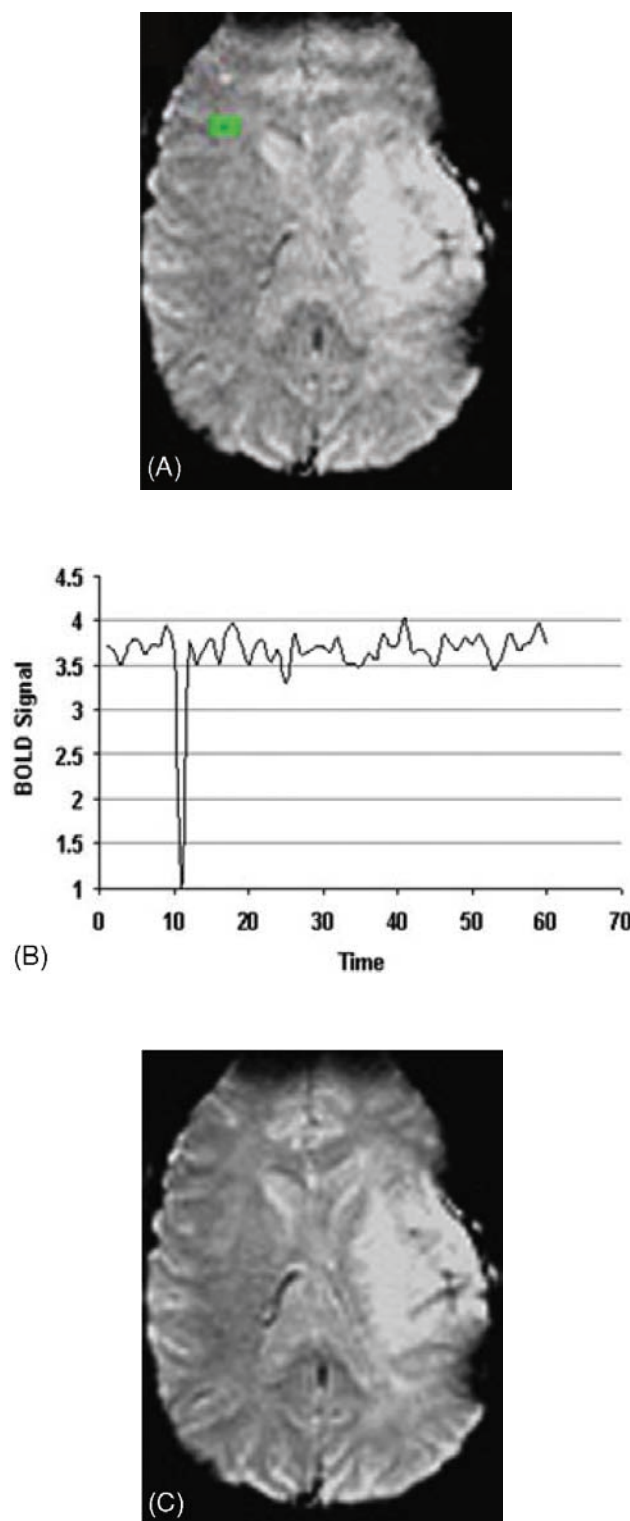


Figure 3 (A) Degraded image is shown. (B) Spike in the image time series. A spike in the data (at time = 11 seconds) causes a signal dropout and may signify that abrupt motion has occurred during images acquisition. (C) After removal of the spike during the postprocessing, image quality is improved. Abbreviation: BOLD, blood oxygenation level dependent.

series is frequently observed (Fig. 4). The cause could be the magnet (e.g., warming up), subject related (e.g., head slowly settling), or a possible leak in the vacuum pack that keeps the head still. A previous study showing a significant drift from cadavers and nonhomogeneous phantoms implied that scanner instabilities may be the major cause of the drift (14). Several methods including using linear models (15), low-order polynomial models (16), and spline models (17) are introduced to remove the drift.

Slice-Timing Correction

The “slice timing” problem refers to a continuous ascending/descending gradient echo-planar imaging sequence in which, for example, the top slice is acquired at a time equal to the repetition time (TR) later than the bottom slice. For example, with a TR of 2000 milliseconds, the first slice is nearly two seconds earlier than the last slice. Since the hemodynamic response reaches its maximum in about six seconds, two seconds can make a significant difference. This becomes an issue in event-related designs where stimulus durations that elicit BOLD hemodynamic responses lasting only a couple of seconds are used. While no satisfactory solutions exist to the questions of appropriateness and timing of slice-timing correction, some common sense guidelines can help one decide how to proceed. When TR is small (e.g., <2 seconds), slice-timing correction is usually not necessary since the time that passes between the acquisition of adjacent volumes is almost negligible. When TR is four seconds and a block paradigm is used, conditions most frequently experienced in clinical fMRI, it is not necessary to apply slice-timing correction. If TR is greater than two seconds and the head motion is large, then performing motion correction can be applied before the slice-timing correction. Slice-timing correction will determine the midpoint slice in the acquisition and temporally interpolate all the other slices to this point, thus interpolating the data as if the slices were acquired simultaneously.

Motion Correction

Head Motion

Head motion during the fMRI experiment poses the biggest practical problem, especially in clinical fMRI. Random motion of the subject appears as additive noise in the voxel time series and decreases the detectability of functional activation. Since the BOLD signal of interest is small and the data analysis is based on the voxel time series, even small head movement (1 ~ 2 mm) can confound statistical analysis (18). Artifacts due to head movement are present when voxels of higher signal intensity are shifted into positions occupied by voxels with

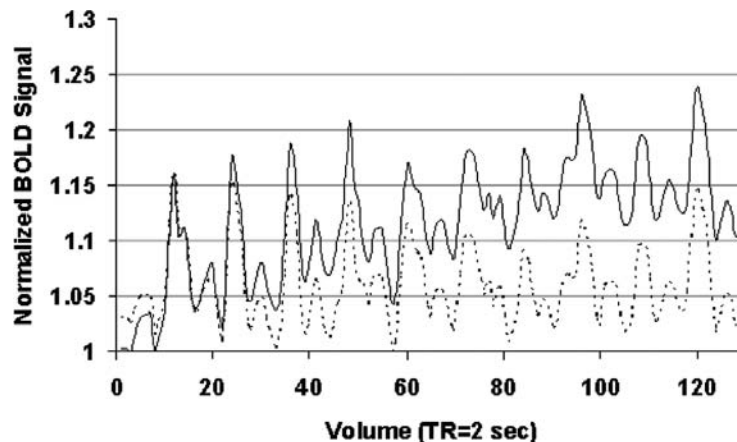


Figure 4 Temporal drift (*solid line*) is evident in a voxel time series. The baseline of the signal is changing over the course of the scan. Dotted line is obtained after removing the trend using a linear model. The trend can be included as regressors of no interest in statistical analysis at a later stage.

lower signal intensity. If two neighboring voxels differ in intrinsic brightness by 20%, then a motion of 10% of a voxel dimension can result in a 2% signal change, which is comparable to the BOLD signal change at 1.5 T, subsequent to neural activation (19). The problem can be severe in areas lying close to high-contrast boundary in the brain image, where movement-related changes in image intensity can be large. An example illustrates that motion in the axial plane typically has a ring-like spatial appearance at the edges of the brain and high-contrast regions of the brain after statistical analysis (Fig. 5).

Motion Correction

Head motion is more easily prevented than corrected, which has led to the development of devices for immobilizing

the head (20) as well as motion correction algorithms for preprocessing prior to statistical analysis (21–27). Even though such efforts are made to minimize subject head motion, it is not currently possible to correct for severe or rapid movement. It is essential to emphasize keeping the head still during patient instruction prior to the fMRI scan and to remind the patient during the scan. Furthermore, maximizing the patient's comfort greatly improves the chances of completing a whole session without excessive motion.

If head motion occurs notwithstanding our efforts, a number of strategies can be employed to attempt to overcome this artifact. The first step of motion correction entails estimating 3D movement parameters (the set of three translocation and three rotation parameters) that are required to minimize differences between each functional volume and a target volume. One can choose the target volume at the first time point or the middle time point of the scan, and then register all remaining volumes against the target volume. Next, the sum of absolute intensity differences between voxels in the corrected and target volumes is calculated. Estimated rotation and translation over the time necessary to align the volumes against the reference volume can be plotted (Fig. 6). The six motion parameters could be included in the statistical model and used to detrend the data against correlation with the movements (28). This approach using motion parameters as a regressor can be used to minimize motion-correlated false-positive activation. However, this approach can cause increased false-negative pixels if the task-correlated motion is the main concern. Following motion correction, the fMRI data should be checked by looking at the motion parameter plots and viewing the images in "cine mode" to evaluate whether the mismatch between slices has improved.

Three-dimensional volume registration is generally useful for intra- and intersession alignment. However, this

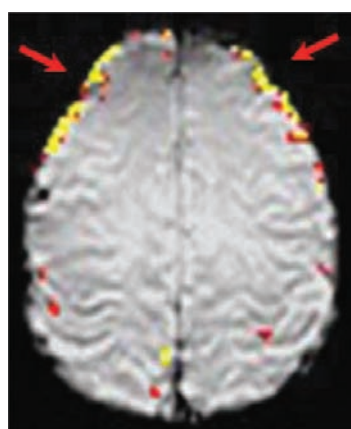


Figure 5 False-positive activated pixels due to a motion are presented around the frontal edges. Over 6% signal change was observed in these pixels. The fMRI data was obtained during a bilateral finger-tapping task. Average percentage signal change in the primary motor cortex was 3%. Abbreviation: fMRI, functional magnetic resonance imaging.

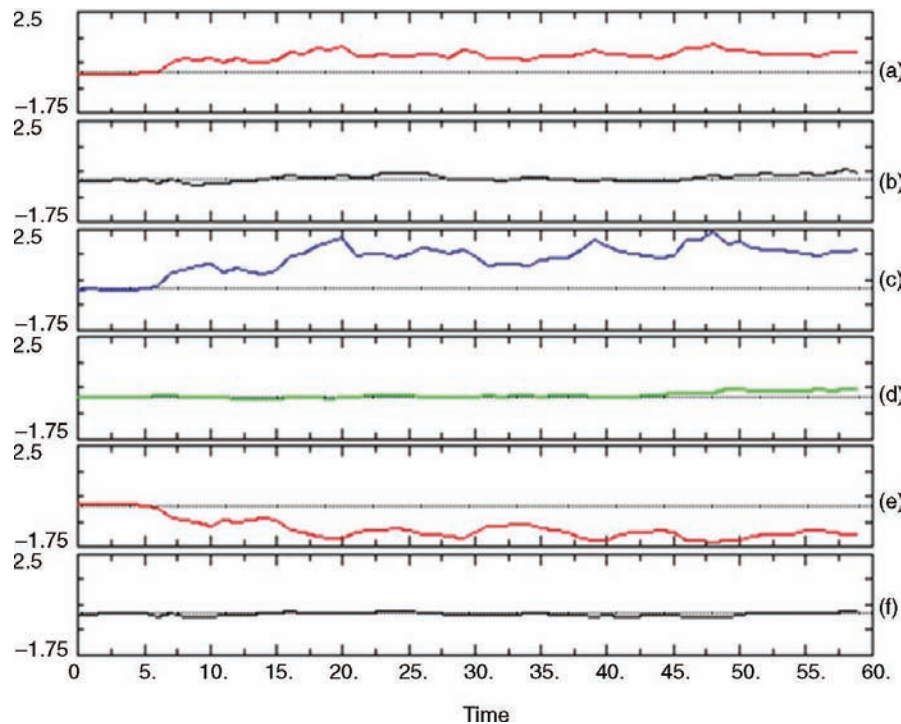


Figure 6 An example of plots of head motion with six motion parameters. (a) $\Delta A\text{-}P$ (mm): displacement in the anterior-posterior (A-P) direction; (b) $\Delta R\text{-}L$ (mm): displacement in the right(R)-left(L) direction; (c) $\Delta I\text{-}S$ (mm): displacement in the inferior(I)-superior(S) direction; (d) yaw (degree): rotation about the A-P; (e) pitch (degree): rotation about the R-L; (f) roll (degree): rotation about the I-S axis. The plot was obtained using AFNI software (21).

approach cannot correct motions that occur within time equal to or less than the TR since this approach assumes a rigid movement of the entire volume. This inability of current technology to correct motion, which occurs at a time faster than the length of the TR, emphasizes the importance of having the patient hold as still as possible.

Motion artifacts due to global motions can be detected during scanning and also corrected during data reconstruction by using navigator echo as indicators of movements acquired during scanning (29).

Task-Correlated Motion Artifacts

Other than randomly occurring rigid head motion, task-associated nonrigid motion can also lead to MR signal artifacts that appear as a false-activation signal (30). The classical example is when a patient moves his/her head when vocalizing the fMRI paradigm and stops moving her/her head during the rest periods. There is no good method to correct for such data and it should be discarded. An event-related paradigm using a vocalized speech task, for example, suffers from a class of task-correlated signal changes arising from speech. The signal changes due to speech-correlated motion usually occur in the first three to four seconds after speaking begins (31,32) (Fig. 7). The BOLD hemodynamic response to a functional task typically has a delay of three to six seconds before onset, and

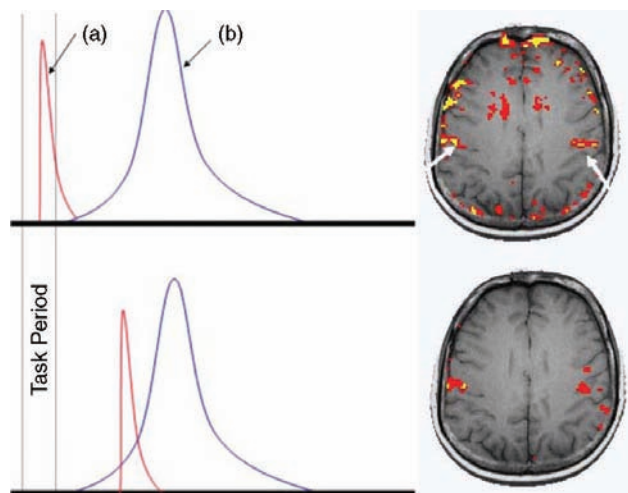


Figure 7 Stimulus correlated motion during speech task. Without removing the speech-induced signal, significant false-positive pixels are observed in the frontal regions (*top image*). However, by using the intrinsic difference between the speech-induced signal (**a**) and BOLD signal (**b**), artifactual activation can be minimized (*bottom image*) without losing vocalized speech-related motor activity (*arrow*). If these two curves overlap (*bottom left*), there is a great chance to increase false-negative pixels. Abbreviation: BOLD, blood oxygenation level dependent.

the peak is reached around four to six seconds. The inherent difference in the time scales of BOLD and speech-induced signal changes has been used to remove speech-correlated motion artifacts by discarding the first few images after voice production (33).

It is important to note that giving the patient proper instructions prior to imaging and emphasizing the direct benefit from the fMRI procedure are most important in minimizing head motion. In patients with paresis, different paradigms could be used to minimize artifacts while keeping functional information intact. Examples include passive movement or sensory stimulation rather than applying voluntary movement tasks. For patients with aphasia, a covert task using a block paradigm (during which the patient does not vocalize his/her response, but instead responds silently) can be ideal.

Spatial Smoothing

Two main reasons exist for smoothing fMRI data. First, smoothing increases the SNR by suppressing the high-frequency noise and enhancing the low-frequency signal. This is due to the fact that neurophysiologic effects in the region widen over a few millimeters and have relatively low frequency. Parrish (5) demonstrated the positive effects of spatial smoothing on functional SNR. Second, smoothing reduces intersubject variability in anatomy, which increases the sensitivity of group analyses.

Spatial smoothing is a procedure by which data points are averaged with their neighbors in an image, thus blurring

sharp edges in smoothed data. Spatial smoothing can be performed by convolving the image with a point spread function using a Gaussian kernel with a width between 4- and 8-mm of full width half maximum (FWHM). The Gaussian function can be written as

$$F(x, y, z) = e^{\left\{ -\left(\frac{x^2}{2S_x^2} + \frac{y^2}{2S_y^2} + \frac{z^2}{2S_z^2} \right) \right\}}$$

where S_x , S_y , and S_z are the standard deviations of the Gaussian in each direction. A good estimation of a smoothing can be given by the FWHM of the Gaussian kernel. The standard deviation can be calculated using a relation of $S = \text{FWHM} \times 0.425$. For example, when smoothing an image of resolution $3 \times 3 \times 4 \text{ mm}^3$ with a kernel of 4 mm, the required values for S_x , S_y , and S_z are 0.57, 0.57, and 0.25, respectively. To perform the smoothing, a matrix of the same size as the image is formed. This image is then convolved with the smoothing matrix. Using this approach, the signal from each voxel spreads out to surrounding voxels. The optimal width of the smoothing filter determines the extent of blurring and is chosen to closely match the size of the region, which is activated (34). The FWHM can be measured in each direction as follows:

FWHM_x = Left to right smoothness

FWHM_y = Anterior to posterior smoothness

FWHM_z = Superior to inferior smoothness

Figure 8 shows functional maps with different spatial smoothing kernel sizes.

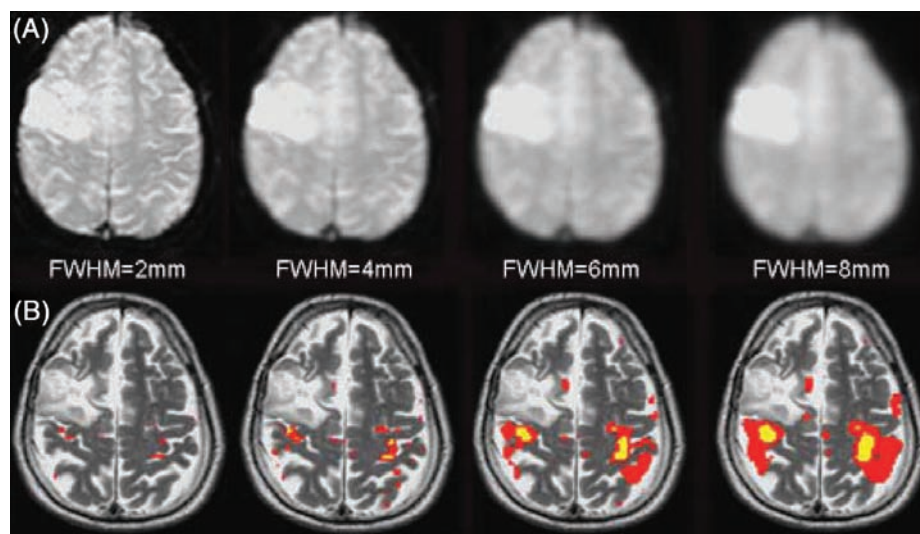


Figure 8 The effect of smoothing on BOLD activity. Top images (A) show the effect of smoothing on T2* image, which increases blurring. The data was acquired using 1.5 T (TR = 4 seconds, TE = 60 seconds, matrix = 128 × 128, FOV = 240 mm). Bottom images (B) show functional activity obtained during bilateral finger tapping and overlaid onto the anatomical T2-weighted images. Spatial smoothing blurs the sharp edges, causing reduced spatial resolution that tends to spread out the activation and eventually decrease the BOLD signal magnitude. Abbreviation: BOLD, blood oxygenation level dependent.

BOLD signal change due to some paradigms such as language or cognitive tasks is relatively small compared with signal change due to motor-sensory tasks. For example, if an fMRI for presurgical planning attempts to map the primary motor cortex, which may be in the order of a few mm across, it is better to use narrow smoothing, or even no smoothing since a robust BOLD signal in the region can be obtained without blurring. One to two voxels for FWHM filter widths are commonly used. The BOLD response in the motor-sensory system is generally large (usually 2–6%) so that robust activated voxels are easily detectable in an expected location (Fig. 8). However, very often, the BOLD response is much weaker (usually 1–3%) from the Broca's area and/or Wernicke's area activated during language tasks. To detect small signal change, relatively large kernel size could be beneficial in these regions. Bigger kernel size is recommended to increase SNR, thus increasing the chance of retaining voxels responding to functional tasks. As a result, the reliability of detection of the motor region is generally greater than that of language regions.

After spatial smoothing, spatial normalization (35,36) can be employed if necessary. This method transforms (stretching or shrinkage) an individual brain image onto a template space defined by a template image and then minimizes the difference between these two images. This procedure is required for intersubject averaging and statistical comparison between different groups and when standard coordinates are required to specify regions of activation. One drawback of this procedure is that as the template is typically derived from normal brains, transformations for a patient's brain with a tumor, for example, can lead to image distortion at the site of the tumor where the brains to be normalized have areas of signal intensity that are very different compared with the corresponding area of the template brain. In other words, this procedure may distort the location of intact tissue to diminish the contribution of the lesion. If fMRI is performed for presurgical planning, for example, spatial normalization should not be used since keeping intact anatomical and functional information essential and the possibility of adding confounding effects must be eliminated.

POSTPROCESSING: IDENTIFYING BRAIN ACTIVATION

Once fMRI data have been through a variety of preprocessing steps, statistical methods to identify activated regions associated with subject's task can be performed in the postprocessing stage. When these statistics are

calculated for each pixel in the brain, and the resulting statistics are presented in an image in which intensity or color is used to represent the statistical value, the resulting image is called a "statistical map" of brain activation. In such methods, either correlation or linear modeling algorithms are used. Two goals of postprocessing are (i) to identify the activated regions and (ii) to minimize additional residual noise and artifact-related false-positive pixels in the image in order to only extract function-related signal changes. From a statistical point of view, the analysis of fMRI can be divided broadly into two types: the first is called hypothesis driven and is model based for the BOLD response; the other is called data driven and is model-free based. Hypothesis-driven analysis includes parametric tests (require assumptions about the hemodynamic response timing and shape and about the noise characteristics) such as *t* test (37), cross-correlation (38), and general linear model (GLM) (39). Nonparametric tests include the Kolmogorov-Smirnov (K-S) test (40). Data-driven analysis that does not make assumptions regarding the shape or timing of the BOLD response to stimulation includes principle component analysis (PCA) (41,42) and independent component analysis (ICA) (43,44). PCA and ICA are rarely used in practical fMRI data analysis.

Statistical Analysis

Hypothesis-driven analysis is the most commonly used approach in fMRI. It presupposes some model for the fMRI-measured response to neural activation. The chosen model is fit to the data using some form of regression analysis. For this, a null hypothesis is set and one sets out to determine whether or not the experimental conditions influence the BOLD fMRI signal. A statistical *p* value verifies the evidence against the null hypothesis. If the null hypothesis is rejected when *p* < 0.001, then the false-positive rate is less than 0.001. This says that there is less than a 1 in 1000 chance that the activation that we see is due to random chance. The resulting activation map is the set of pixels that fit the response model with the significant *p* value.

Student's *t* Test

The simplest statistical test that can be used in fMRI is Student's *t* test. The *t* test assumes that each number in each group is independent and that the numbers form a Gaussian distribution. This method involves subtracting two mean intensities obtained from two conditions for each voxel. The two conditions could be stimulus versus rest or stimulus A versus stimulus B. An example of *t* test

using stimulus versus rest paradigm is given as following. One mean value is obtained by averaging all temporal responses acquired during the stimulus period. Another mean value is obtained by averaging all the temporal responses acquired during the rest period. To determine whether a voxel is activated or not, the mean intensities are subtracted. Voxels with significant difference in the mean intensities between two conditions are identified as being activated. The t value is calculated as

$$t = \frac{\bar{x}_{\text{task}} - \bar{x}_{\text{rest}}}{\sqrt{\frac{\sigma_{\text{task}}^2}{N_{\text{task}}-1} + \frac{\sigma_{\text{rest}}^2}{N_{\text{rest}}-1}}}$$

where x_{task} and x_{rest} refer to the set of data points that correspond to the task and the rest periods, respectively. \bar{x}_{task} and \bar{x}_{rest} are the mean of the data x_{task} and x_{rest} , respectively. N_{task} and N_{rest} refer to the number of time points that corresponds to the task and the rest periods, respectively. σ_{task}^2 and σ_{rest}^2 are the variance of the data x_{task} and x_{rest} , respectively.

The t value obtained can then be converted to a probability value, p , based on the degree of freedom. Usually, two-tailed tests can be applied for the joint probability of a positive or negative effect. In this way, a color-coded map can be obtained based on the computed t and p values for each voxel in the brain.

One drawback of this method is the assumption that temporal measurement of a given voxel can be divided into the two regions, which are condition A and condition B. There is one- to two-second BOLD hemodynamic response delay time after stimulation. Therefore, one could shift the onset of all blocks. However, this approach is not ideal because changes in the BOLD hemodynamic response in each block are not consistent in most cases. Additionally, the linear trend and/or head motion that occurred during resting period will cause increased signal change and therefore will reduce the mean difference between the task and resting period. This will significantly affect t test result.

Correlation Analysis

Correlation analysis is the most widely used method for analysis of block paradigms. Correlation analysis (38) computes the correlation between two variables, a modeled hemodynamic response (called reference waveform that has the shape of the expected BOLD response) and the each observed voxel time series (Fig. 9). The reference waveform is obtained from the experimental design.

The correlation coefficient γ_{xy} is a measure of the correlation between the modeled reference waveform x

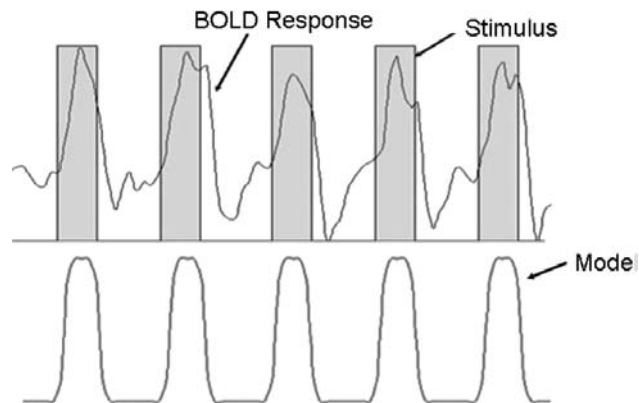


Figure 9 Correlation analysis. Correlation coefficients are calculated between the observed BOLD response that is obtained during the stimulus period (color) and the modeled reference waveform. A boxcar waveform, which is often convolved with an estimated HRF, can be used to yield the reference waveform. Several functions have been used to model the response, including the Poisson distribution curve (55), Gaussian (56), or Gamma (57,58). Abbreviation: BOLD, blood oxygenation level dependent.

and the observed voxel time series y , and is defined by

$$\gamma_{xy} = \frac{\sum (x - \bar{x})(y - \bar{y})}{\sqrt{\sum (x - \bar{x})^2 \sum (y - \bar{y})^2}}$$

where \bar{x} and \bar{y} refer to the mean of x and y , respectively. The summation is taken over all the time points in the waveform. The resulting correlation coefficient, γ value can have values ranging from 1.0 (for perfect positive correlation) to -1.0 (perfect negative correlation). Voxels with a large correlation coefficient are considered active (Fig. 10). A critical part of this method is the choice of the reference waveform, which is correlated with the observed signal. However, due to many unknown factors in measuring the brain-activation patterns, including a delayed response between regions, it is difficult to indicate which reference waveform is the best.

Unlike the t test, correlation analysis uses information about the shape of the hemodynamic response and can incorporate hemodynamic response function (HRF) to predict time course more accurately. Specifically, the reference waveform can take into account the rise and fall times in the hemodynamic response. BOLD response takes about six to eight seconds to reach its time to peak after the onset of neuronal activity. Following the offset of neuronal activity, the hemodynamic response falls over an additional six to eight seconds and then stabilizes at a below-baseline level. Aguirre (40) demonstrated variability of the hemodynamic response between subjects and within the subject.

One shortcoming of both t test and correlation methods is that one has to assume that there is no variability of the

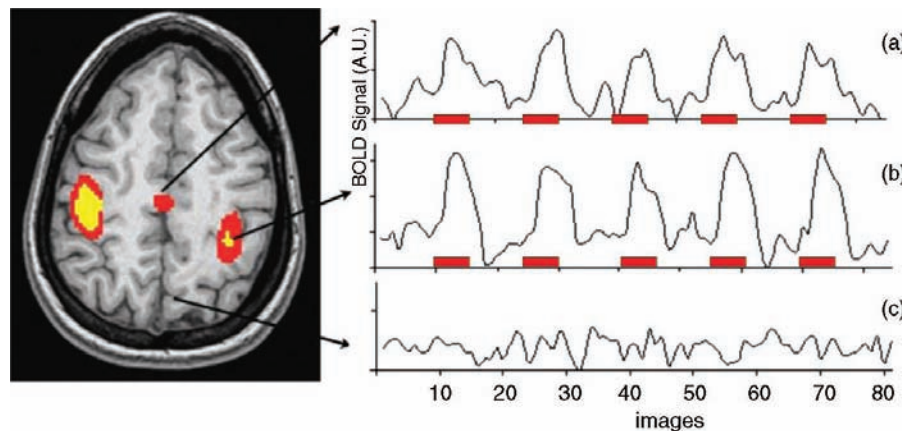


Figure 10 Correlation analysis. An example of activation in the PMC and SMA observed during bilateral finger movement (TR = 2-seconds, 10-sec stimulus on/20-sec stimulus off). Regions with correlation score higher than 0.6 and 0.7 are displayed in red and yellow, respectively. The time courses are obtained from the (a) SMA, (b) PMC, and (c) a region of no interest. Stimulus period is marked as red and the rest period is between red marks. Abbreviations: PMC, primary motor cortex; SMA, supplementary motor area; BOLD, blood oxygenation level dependent.

hemodynamic response of all voxels in the brain, which is not true. There may be some intrinsic hemodynamic delays between regions in the brain. A time-shifted correlation analysis was used to map the retinotopic organization of visual cortex (45). In this study, voxel correlation coefficients were calculated with a larger number of delay times. Voxels with maximum correlation larger than the threshold were included in the brain map.

Deconvolution Analysis

A popular method of analyzing event-related fMRI data is the deconvolution analysis (46). The goal of this analysis is to find the shape and amplitude of the HRF in each voxel. In fMRI, observed time series data as the output $Z(t)$ can be expressed as the convolution between the HRF and the stimulus as the input $f(t)$. Conventionally, this can be written:

$$Z(t) = \text{HRF} \otimes f(t)$$

One always knows the stimulus timing (when exactly the paradigms are performed by the patient). Therefore, we can determine the time series data by convolving the stimulus timing with the modeled HRF. Alternatively, we can determine the HRF by deconvolving the time series data with the stimulus timing. One knows when stimulus began, but one does not precisely know what should be the response.

In practice, however, the actual observed response can be written as

$$Z(t) = \alpha + \alpha_1 \times t + \beta \times \sum_{n=0}^T h(n\Delta t) \times f(t - n\Delta t) + \varepsilon(t)$$

with baseline α , baseline drift term $\alpha_1 \times t$, HRF $h(n\Delta t)$, stimulus function $f(t - n\Delta t)$, and noise term $\varepsilon(t)$. Deconvolution analysis can perform linear least squares, for

example, to fit time series models, $h(n\Delta t)$ to each voxel time series $Z(t)$. Most common use in fMRI is measuring each voxel's $h(n\Delta t)$, assuming the stimulus input function is known. Assuming white noise with a Gaussian distribution, the statistical significance of the regression can be calculated using F statistics. Goodness of fit of multiple linear regressions with the voxel time series can be measured using R^2 .

Unlike the previously described t test and correlation analyses in which the shape of the modeled hemodynamic response is already assumed, deconvolution analysis does not assume the shape of the impulse response and models the response in an unconstrained fashion. This is significant in pathology, especially in stroke and tumor patients where the shape of the hemodynamic response may differ from normals. Another advantage of this method is that it allows for exploration of the temporal pattern of the hemodynamic response in the cortical regions (Fig. 11). However, it is necessary to have enough time points to resolve the shape of the HRF.

General Linear Model (GLM)

GLM (47) is a broad term for a modeling approach that includes any modeling methods that can be transformed into regression models. Therefore, traditional regression analysis, analysis of variance (ANOVA), and deconvolution are special cases of the GLM. This approach attempts to determine the correct linear combination of explanatory variables (e.g., hemodynamic response due to a subject's task performance, confounding effects due to motion, respiratory and cardiac dynamics) that account for the temporal response observed at each voxel during an experiment.

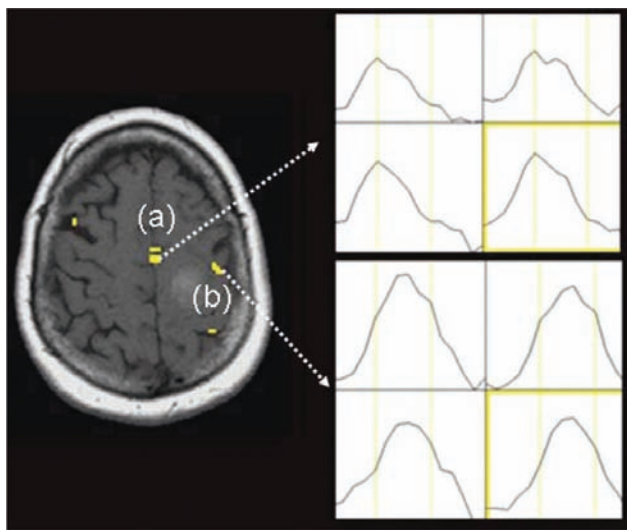


Figure 11 Activation and impulse response function obtained from the deconvolution analysis. A threshold of $R^2 > 0.5$ was applied to show significantly activated pixels in the (a) supplementary motor area and the (b) primary motor cortex. Deconvolution analysis implemented in AFNI (21) was used.

The idea behind this method is that the observed data is equal to a weighted combination of several variables plus the error term. The weights reflect that how much each variable contributes to the data. The goal of this method is to find what combination of weights serves to minimize the error term. Let t denote the number of time point measurements per voxel and S_t denote the measurement (e.g., neurophysiologic response) at some voxel at time t . Assume that there are j number of explanatory variables in this model. Let f_{tj} denote the value of the j th explanatory variable at time t . α_j denotes the scaling parameter (or parameter weights) for the j th explanatory variable. ε_j denotes the residual error term associated with the linear model fit at the same voxel at time t . With these definitions, the model can be written as:

$$\begin{pmatrix} S_1 \\ S_2 \\ \vdots \\ S_t \end{pmatrix} = \begin{pmatrix} f_{11} & f_{12} & f_{1j} \\ f_{21} & f_{22} & f_{2j} \\ \vdots & \vdots & \vdots \\ f_{t1} & f_{t2} & f_{tj} \end{pmatrix} \times \begin{pmatrix} \alpha_1 \\ \alpha_2 \\ \vdots \\ \alpha_j \end{pmatrix} + \begin{pmatrix} \varepsilon_1 \\ \varepsilon_2 \\ \vdots \\ \varepsilon_j \end{pmatrix}$$

In this equation, one can estimate best-fit parameters (α_j) to minimize differences between measurement and modeled response using the least sum of square algorithm.

Additionally, the K-S test, a nonparametric test, has been used in fMRI studies (48,49). This test determines if two data sets differ significantly and has the advantage of making no assumption about the distribution of data. However, it has been argued that the K-S test is formally

unable to support inferences of interest to most neuro-imaging studies and has reduced sensitivity compared with parametric methods (40).

Interpretation of Statistical Maps

Draining Vein

One of major considerations for fMRI map interpretation is to distinguish between spots of small parenchymal venules and cortical activation that are in close proximity to these sites (maximally 1.5 mm apart) and large draining veins remote from the active parenchyma (50,51). This consideration becomes especially important as fMRI for presurgical mapping of functional cortical areas is performed (52). The most common approach used to differentiate between draining veins and functional sites has been visual inspection in correlation with high-resolution anatomic images (Fig. 12).

Susceptibility Artifacts

Another consideration is the susceptibility artifacts that are often found at junctions between air and tissue, such as orbitofrontal cortex from the sinuses. These become a more pressing problem in patients with prior brain surgery

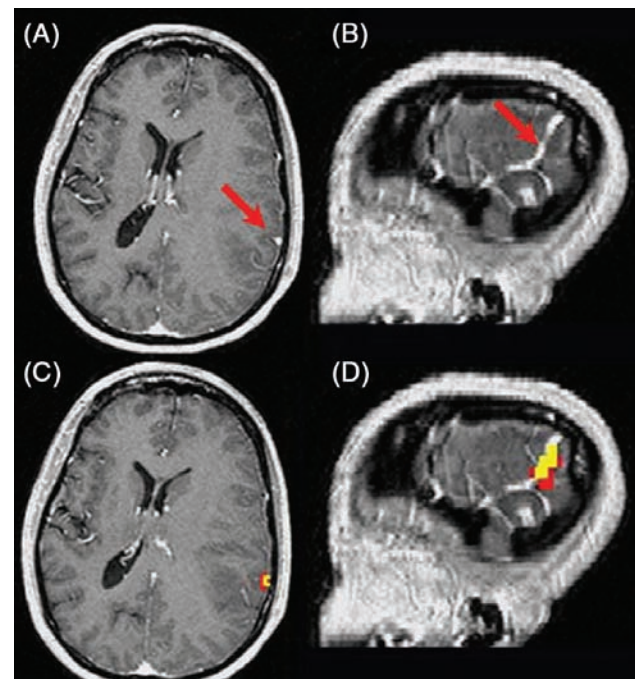


Figure 12 Draining vein effect. (A, B) The draining vein (arrow) in an axial and in a sagittal plane, respectively. (C, D) Artifactual activation on the vein in an axial and in a sagittal plane, respectively. An averaged signal change of 4.9% is measured in the area.

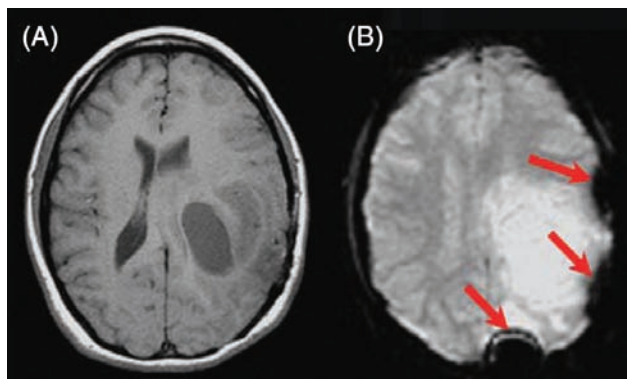


Figure 13 Susceptibility artifacts due to a prior surgery. The presence of titanium plates to secure skull flaps, metallic staples to close surgical resections, and hemorrhage from the surgery or from the tumor can increase in the susceptibility artifact. Susceptibility artifacts due to prior surgery are evident in the T2* image (B), but not visible in the T1 image (A).

(Fig. 13). It has been reported that in brain tumor patients, prior surgery can affect the accuracy of the fMRI activation map (53).

Multiple Comparison Correction

Another central concern of fMRI data analysis is called “multiple comparisons.” The voxel-wise p values do not account for the number of voxels tested. Therefore, one needs to control for the error rate, which reflects false-positive results for any voxel. False-negative activations (i.e., no activation visible at regions where it should be) are of particular concern when using fMRI in the presurgical planning of tumor resection. If, for example, 10,000 statistical tests are performed, a 1% false-positive rate (type I error) indicates that 100 voxels are “activated” due to chance fluctuation. To address such a problem, the threshold for significance has to be adjusted for the number of voxels. However, the voxel-wise statistics do not account for covariance of voxels across space and for noise in the brain that is not spatially independent.

The most straightforward method of limiting the number of type I errors associated with multiple comparisons is the Bonferroni correction. This method decreases the critical p value in proportion to the number of comparisons being made. For an overall test at the α significance level, one could select individual voxels among N total voxels as active if $p \leq \alpha/N$. For example, if there are 10,000 voxels in the brain and one wants to have α significance level of 0.01, the p value of the test should be set at $0.01/10,000 = 10^{-6}$. However, such a stringent value could remove some true positive pixels. For example, if the degree of freedom is 90, this corresponds to a t -statistic threshold of 5.1. If the noise standard deviation is about 2% of the baseline signal, this

means that imaging would detect BOLD signal changes of about 1.1% ($=2\% \times 5.1\sqrt{90}$). 1.5 T is the most common field strength which is used in the clinical setting, and the BOLD signal change of 1.1% is a reasonable value to set for the primary and secondary motor regions during, for example, finger-tapping tasks. However, it may not be a reasonable value when detecting other regions, for example, cognitive related regions, where percent signal changes of lower than 1% are usual. In other words, such voxel-wise detection methods are good at detecting large BOLD signal changes. A drawback of the methods is that there is a potential to remove a large region of activation in which each voxel has only a small signal change.

Another drawback of the Bonferroni correction is that it is overly conservative since it does not account for correlations between adjacent voxels. Neighboring voxels are not statistically independent because they are spatially and temporally smoothed prior to statistical analysis. Alternatively, a combined analysis using both Bonferroni and cluster thresholding was introduced by Forman (54). In this method, voxel-wise tests are adjusted by accepting as active only those voxels that lie in a cluster of voxels of at least a specified size with a test statistic above the threshold. As another approach, Gaussian random field theory accounts for image smoothness and dependence (22,34) when correcting for multiple comparisons, while controlling for the nonindependence of the data is introduced.

CONCLUSION

It is clear that application of different statistical thresholds to define the volume of the eloquent cortex would lead to different results. For example, in evaluating the motor cortex, if one uses a lower correlation coefficient or a lower significance (p value), the volume of activation, which defines the motor cortex, would be larger. This would be of critical importance to the surgeon, especially when the tumor to be resected overlaps with one volume of activation but not with the other. Figuring out which correlation r value and p value are optimal when defining the volume of activation is yet to be resolved and the answer will not likely be straightforward. However, by following steps described in the previous sections, including proper preprocessing, statistical tests, and removing false positives and negatives due to various artifacts, fMRI can become a useful tool in the clinical and research settings.

RECOMMENDED READING MATERIALS

Books by the following authors are recommended for further reading on fMRI technical and methodological issues: Bandettini and Moonen (59), Jezzard et al. (60), and Boxtom (61).

REFERENCES

1. Korvenoja A, Kirveskari E, Aronen H, et al. Sensorimotor cortex localization: comparison of magnetoencephalography, functional MR imaging, and intraoperative cortical mapping. *Radiology* 2006; 241:213–222.
2. Petrella J, Shah L, Harris K, et al. Preoperative functional MR imaging localization of language and motor areas: effect on therapeutic decision making in patients with potentially resectable brain tumors. *Radiology* 2006; 240:793–802.
3. Jacobs A, Kracht L, Gossman A, et al. Imaging in neurooncology. *NeuroRx* 2005; 2:333–347.
4. Ogawa S, Lee T, Nayak A, et al. Oxygenation-sensitive contrast in magnetic resonance image of rodent brain at high magnetic field. *Magn Reson Med* 1990; 14:68–78.
5. Parrish T, Gitelman D, LaBar K, et al. Impact of signal to noise on functional MRI. *Magn Reson Med* 2000; 44: 925–932.
6. Thesen S, Henselmann N, Muller E, et al. BOLD magnetic resonance imaging in real time. *Electromedica* 2000; 68: 45–52.
7. Price C, Crinion J, Friston K. Design and analysis of fMRI studies with neurologically impaired patients. *JMRI* 2006; 23:816–826.
8. Gold S, Christian B, Arndt S, et al. Functional MRI statistical software packages: a comparative analysis. *Hum Brain Mapp* 1998; 6:73–84.
9. Bogomolny D, Petrovich N, Hou B, Peck K, et al. Functional MRI in the brain tumor patient. *Top Magn Reson Imag* 2004; 15:325–335.
10. Weisskoff R. Simple measurement of scanner stability for functional NMR imaging of activation in the brain. *Magn Reson Med* 1996; 36:643–645.
11. Thacker N, Burton E, Lacey A, et al. The effects of motion on parametric fMRI analysis techniques. *Physiol Meas* 1999; 20:251–263.
12. Frank L, Buxton E, Wong E. Estimation of respiration-induced noise fluctuations from undersampled multislice fMRI data. *Magn Reson Med* 2001; 45:635–644.
13. Dagli M, Ingeholm J, Haxby J. Localization of cardiac-induced signal change in fMRI. *Neuroimage* 1999; 9: 407–415.
14. Smith A, Lewis B, Ruttmann U, et al. Investigation of low frequency drift in fMRI signal. *Neuroimage* 1999; 9:526–533.
15. Bullmore E, Brammer M, Williams S, et al. Statistical methods of estimation and inference for functional MMR image analysis. *Magn Reson Med* 1996; 35:261–277.
16. Mattay V, Frank J, Santha A, et al. Whole brain functional mapping with isotropic MR imaging. *Radiology* 1996; 201:399–404.
17. Genovese C. A time-course model for fMRI data. Paper presented at: International Society for Magnetic Resonance in Medicine meeting, May, 1669, 1997; Vancouver, Canada.
18. Friston KJ, Williams S, Howard R, et al. Movement-related effects in fMRI time-series. *Magn Reson Med* 1996; 35: 346–355.
19. Cox RW, Jesmanowicz A. Real-time 3D image registration for functional MRI. *Magn Reson Med* 1999; 42:1014–1018.
20. Edward V, Windischberger C, Cunnington R, et al. Quantification of fMRI artifact reduction by a novel plaster cast head holder. *Hum Brain Mapp* 2000; 11:207–213.
21. Cox RW. AFNI: software for analysis and visualization of functional magnetic resonance neuroimages. *Comput Biomed Res* 1996; 29(3):162–173.
22. Friston K, Ashburner J, Frith C, et al. Spatial registration and normalization of images. *Hum Brain Mapp* 1995; 3:165–189.
23. Jiang A, Kennedy D, Baker J, et al. Motion detection and correction in functional MR imaging. *Hum Brain Mapp* 1995; 3:224–235.
24. Collins DL, Evans AC, Holmes C, et al. Automatic 3D intersubject registration of MR volumetric data in standardized Talairach space. *J Comput Assist Tomogr* 1994; 18:192–205.
25. Eddy WF, Fitzgerald M, Noll DC. Improved image registration by using Fourier interpolation. *Magn Reson Med* 1996; 36:923–931.
26. Bannister P, Brady J, Jenkinson M. Integrating temporal information with a non-rigid method of motion correction for functional magnetic resonance images. *Image Vis Comput* 2007; 25:311–320.
27. Woods RP, Cherry SR, Mazziotta JC. Rapid automated algorithm for aligning and reslicing PET images. *J Comput Assist Tomogr* 1992; 16:620–633.
28. Bullmore E, Brammer M, Rabe-Hesketh S, et al. Methods for diagnosis and treatment of stimulus-correlated motion in generic brain activation studies using fMRI. *Hum Brain Mapp* 1999; 7:38–48.
29. Ramsey NF, Van den Brink JS, Van Muiswinkel AM, et al. Phase navigator correction in 3D fMRI improves detection of brain activation: quantitative assessment with a graded motion activation procedure. *Neuroimage* 1998; 8:240–248.
30. Hajnal J, Myers R, Oatridge A, et al. Artifacts due to stimulus correlated motion in functional imaging of the brain. *Magn Reson Med* 1994; 31:283–291.
31. Birn RM, Bandettini PA, Cox RW, et al. Magnetic field changes in the human brain due to swallowing or speaking. *Magn Reson Med* 1998; 40:55–60.
32. Birn RM, Bandettini PA, Cox RW, et al. Event-related fMRI of tasks involving brief motion. *Hum Brain Mapp* 1999; 7:106–114.
33. Barch DM, Sabb FW, Carter CS, et al. Overt verbal responding during fMRI scanning: empirical investigations of problems and potential solutions. *Neuroimage* 1999; 10:642–657.
34. Worsley K, Friston K. Analysis of fMRI time-series revisited-again. *Neuroimage* 1995; 2:173–181.
35. Ashburner J, Friston K. Nonlinear spatial normalization using basis functions. *Hum Brain Mapp* 1999; 7:254–266.
36. Brett M, Leff A, Rorden C, et al. Spatial normalization of brain images with focal lesions using cost function masking. *Neuroimage* 2001; 14:486–500.
37. Henriksen O, Larsson H, Ring P, et al. Functional MR imaging at 1.5T. *Acta Radiol* 1993; 34:101–103.
38. Bendettini P, Jesmanowicz E, Wong E, et al. Processing strategies for time-course data sets in functional MRI of the human brain. *Magn Reson Med* 1993; 30:161–173.

39. Friston K, Holmes A, Worsley K, et al. Statistical parametric maps in functional imaging: a general linear approach. *Hum Brain Mapp* 1995; 3:165–189.
40. Aguirre G, Zarahn E, D'Esposito M. A critique of the use of the Kolmogorov-Smirnov (KS) statistic from the analysis of BOLD fMRI data. *Magn Reson Med* 1998; 39: 500–505.
41. McKeown M, Makeig S, Brown G, et al. Analysis of fMRI data by blind separation into independent spectral components. *Hum Brain Mapp* 1998; 6:160–188.
42. Lai S, Fang M. A novel local PCA-based method for detecting activation signals in fMRI. *Magn Reson Imag* 1999; 17:827–836.
43. Andersen AH, Gash DM, Avison MJ. Principle component analysis of the hemodynamic response measured by fMRI: a generalized linear systems framework. *Magn Reson Imag* 1999; 17:795–815.
44. Friston K, Phillips J, Chawla D, et al. Nonlinear PCA: characterizing interactions between modes of brain activity. *Phil Trans R Soc Lond B Biol Sci* 2000; 355:135–146.
45. DeYoe EA, Bandettini P, Neitz J, et al. Functional magnetic resonance imaging of the human brain. *J Neurosci Method* 1994; 54:171–187.
46. Saad Z, Chen G, Reynolds R, et al. FIAC Analysis According to AFNI and SUMA. *Hum Brain Mapp* 2006; 27:417–424.
47. Friston K, Jezzard P, Turner R. Analysis of functional MRI time-series. *Hum Brain Mapp* 1998; 6:283–300.
48. Cramer S, Moore C, Finklestein S, et al. A pilot study of somatotopic mapping after cortical infarct. *Stroke* 2000; 31:668–671.
49. Kanwisher N, Chun M, McDermott J, et al. Functional imaging of human visual recognition. *Cog Brain Res* 1996; 5:55–67.
50. Turner R. How much cortex can a vein drain? Downstream dilution of activation-related cerebral blood oxygenation changes. *Neuroimage* 2001; 16:1062–1067.
51. Frahm J, Merboldt K, Hanicke W, et al. Brain or vein: oxygenation or flow? On signal physiology in functional MRI of human brain activation. *NMR Biomed* 1994; 7:445–453.
52. Krings T, Reinges M, Erberich S, et al. Functional MRI for presurgical planning: problems, artifacts, and solution strategies. *J Neurol Neurosurg Psychiatry* 2001;70:749–776.
53. Kim M, Holodny A, Hou B, et al. The effect of prior surgery on BOLD fMRI in the pre-operative assessment of brain tumors. *AJNR Am J Neuroradiol* 2005; 26:1980–1985.
54. Forman S, Cohen J, Fitzgerald M, et al. Improved assessment of significant activation in functional magnetic resonance imaging (fMRI): use of a cluster-size threshold. *Magn Reson Imag* 1995; 33:636–647.
55. Friston K, Ashburner J, Frith C, et al. Spatial registration and normalization of images. *Hum Brain Map* 1995; 3: 165–189.
56. Rajapakse J, Kruggel F, Maisog J, et al. Modeling hemodynamic response for analysis of functional MRI time series. *Hum Brain Mapp* 1998; 6:283–300.
57. Lange N, Zeger S. Non-linear Fourier time series analysis for human brain mapping by functional magnetic resonance imaging. *J R Stat Soc Appl Stat* 1997; 46:1–29.
58. Cohen MS. Parametric analysis of fMRI data using linear system methods. *Neuro Image* 1997; 6:93–103.
59. Bandettini P, Moonen C, Aguirre G. *Functional MRI*. Berlin: Springer, 1999.
60. Jezzard P, Matthews P, Smith S. *Functional MRI: An Introduction to Methods*. Oxford: Oxford University Press, 2003.
61. Buxton R. *Introduction to Functional Magnetic Resonance Imaging: Principles and Techniques*. Cambridge: Cambridge University Press, 2002.

4

Fact or Artifact?

JOHN F. KAUFMAN and JOSEPH A. MALDJIAN

Department of Radiology, Wake Forest University Medical Center, Winston-Salem, North Carolina, U.S.A.

INTRODUCTION

Artifacts are observed in any imaging technique, and functional magnetic resonance imaging (fMRI) is no exception. However, artifacts in fMRI are often hidden in the final results and only uncovered through careful scrutiny of the data and processing steps. Therefore, careful technique and preparatory measures against artifacts are very important in fMRI to avoid incorrect conclusions.

Artifacts introduced in an fMRI experiment often result in reduced sensitivity and false negatives. Additionally, if artifactual signal is correlated with the fMRI task, false-positive activations may be seen. Both of these could prove disastrous in an experiment or clinical scenario if unrecognized.

Some of the artifacts seen uniquely or prominently in fMRI are presented, including artifacts related to noise from various sources, data acquisition, motion, and processing steps. Additional artifacts from general magnetic resonance imaging (MRI) may also be seen but are not discussed in this chapter.

NOISE

Noise is unwanted signal that obscures the blood oxygen level-dependent (BOLD) contrast being observed and results in reduced sensitivity. BOLD changes are very small (5–7% at 1.5T) compared with baseline signal (1),

and relatively small amounts of noise can hide BOLD changes and potentially cause false-negative results. This problem can be reduced by either increasing the signal or reducing the noise, i.e., improving the signal-to-noise ratio (SNR).

Noise can be categorized into random and structured types. Random noise is evenly distributed throughout the frequency spectrum. Sources of random noise include scanner electronics and thermal noise (2). SNR may be improved for random noise by increasing the magnet strength, improving detector coils, or averaging multiple acquisitions. Low-pass filters or spatial smoothing algorithms may also be applied to reduce high-frequency random noise.

Structured noise is nonrandom and unevenly distributed in the frequency spectrum. It can also vary depending on position within the brain. The nonrandom distribution violates statistical assumptions based on Gaussian noise models. Sources of structured noise include scanner drift and various physiologic processes.

For structured noise, SNR is worsened rather than improved by increasing the magnetic field strength or increasing receiver sensitivity (3). Therefore, different strategies have been developed to deal with structured noise. In addition to reducing sensitivity to BOLD contrast, if structured noise is correlated with the fMRI task, it may also act as a confound and produce false-positive activation.

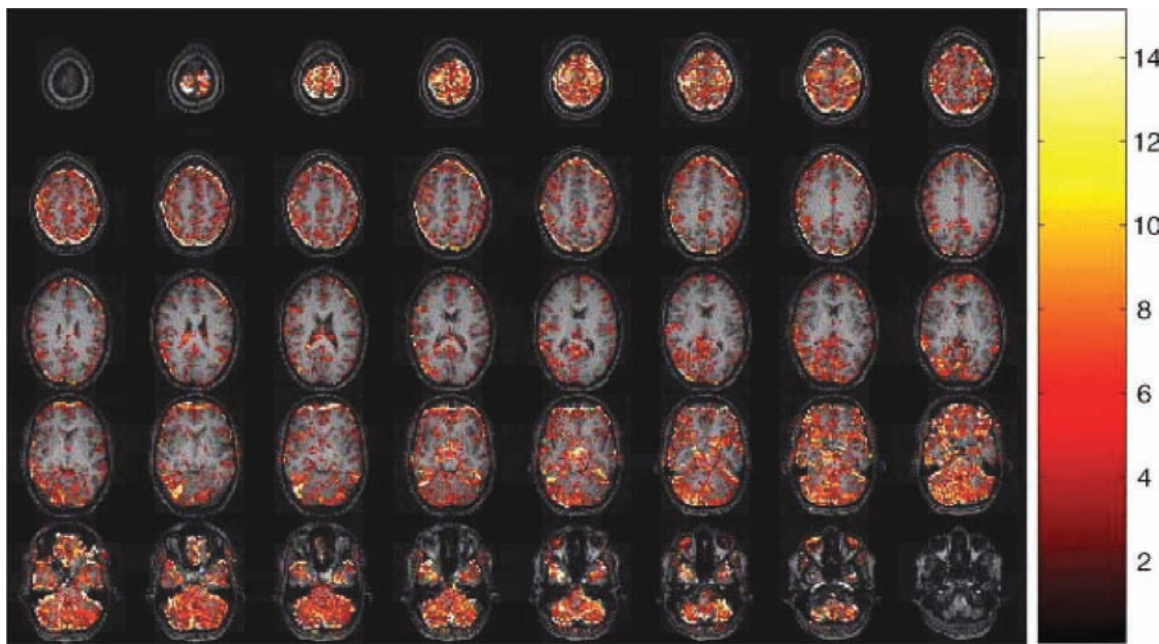


Figure 1 Low-frequency noise. Effects of low-frequency noise are seen at the edges of the brain. *Source:* From Ref. 4.

Scanner Drift

Scanner drift is a commonly observed source of low-frequency structured noise in fMRI. It has been suggested that it may be due to gradually progressing motion such as the subject's head sinking into padding or some kind of physiologic change. However, it has also been observed in cadavers and phantoms (4,5). It may represent slowly changing local B₀ magnetic field strength over the course of the experiment related to eddy current production or heating of the equipment over time (5). It is seen as signal change occurring predominantly at the edges of the brain (Fig. 1) (4).

One way to remove this low-frequency noise is through high-pass digital filtering. Digital filters are used in signal processing to enhance, attenuate, or otherwise alter certain frequencies within a signal. Filters may be designed to eliminate frequencies greater than a given cutoff (low-pass filter) or less than a given cutoff (high-pass filter). Targeted filters may be used to eliminate specific frequencies (band-reject filter) or to preserve specific frequencies (band-pass filter). Care should be taken in selecting the filter cutoff frequency so that it does not also remove the BOLD signal.

Another way to reduce the effects of scanner drift is through dynamic B₀ field mapping. This involves acquiring a B₀ field map with each run and applying a warp correction to the corresponding images. Additionally, functional techniques such as flow-sensitive alternating inversion recovery (FAIR) and arterial spin-labeling (ASL) are less affected by scanner drift (5,6).

Noise Due to Physiologic Activity

Normal physiologic processes can produce structured noise in fMRI experiments. Examples include cardiac and respiratory activity, swallowing, eye movements, and baseline neuronal activity (7–9). The highest amplitude and most frequently observed physiologic signal changes are from cardiac and respiratory activity. Figure 2 shows

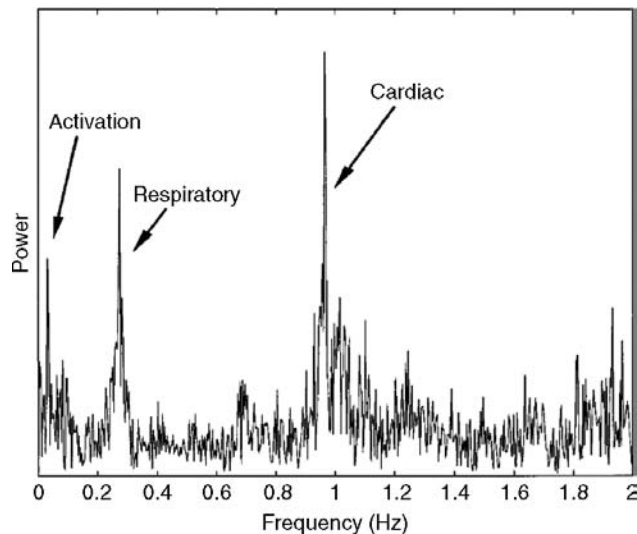


Figure 2 Physiologic noise frequencies. A power spectrum analysis of fMRI data shows characteristic peaks corresponding to cardiac and respiratory activity. The task activation is seen at lower frequencies. Abbreviation: fMRI, functional magnetic resonance imaging. *Source:* From Ref. 14.

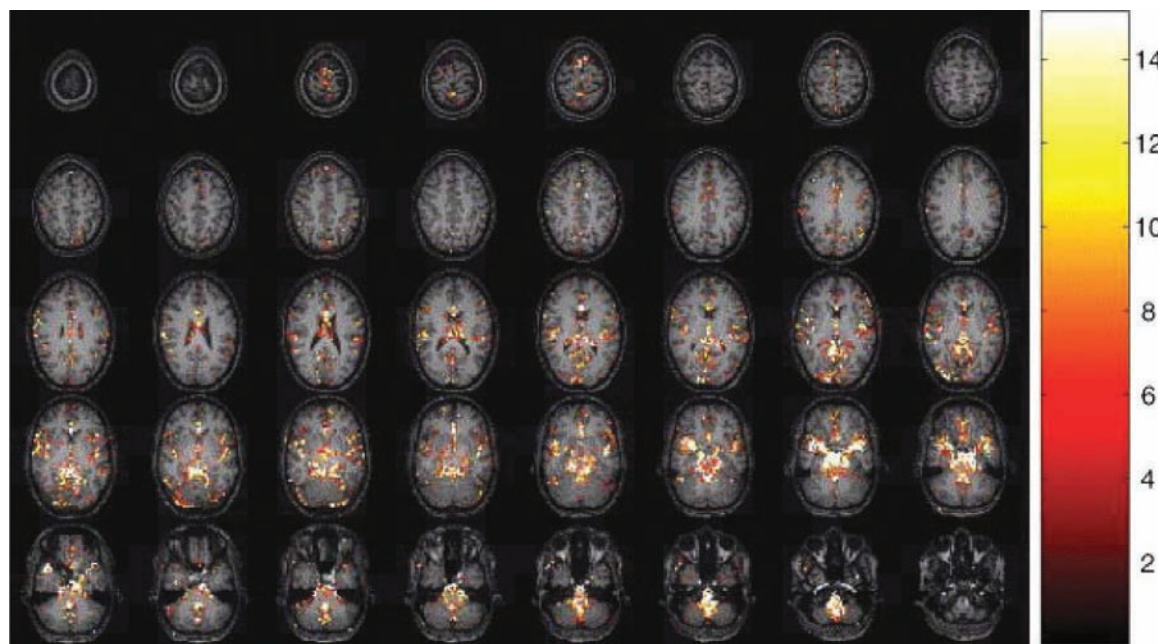


Figure 3 Cardiac-induced noise. Effects of cardiac activity are seen near larger vessels such as the Circle of Willis and middle cerebral arteries. *Source:* From Ref. 4.

cardiac and respiratory activity frequencies on a power spectrum of fMRI data.

Signal changes corresponding to cardiac activity are observed at frequencies near 1.0 to 1.7 Hz, corresponding to a normal heart rate of 60 to 100 beats/min. Instead of a single frequency, there is often a small range of frequencies observed because the heart rate normally varies over time. Signal changes tend to be seen around major intracranial arteries and near cerebrospinal fluid (CSF) spaces (Fig. 3) (4,10).

The motion of pulsating arteries causes vibrations of adjacent structures resulting in perivascular signal variation. Additionally, flow artifacts are seen around the vessels. During systole, there is increased blood volume delivery to the brain. Because the cranium is fixed in size, the increase in blood volume causes compression and shifting of the brain as well as CSF pulsations through the foramen magnum, involving the cisterns (11).

Respiratory noise is present at 0.25 to 0.33 Hz, corresponding to a normal respiratory rate of 15 to 20 breaths/min. There is also a range of frequencies for respiratory activity due to normal variations in respiratory rate. Signal changes due to respiratory activity tend to be localized around venous structures and in the ventricles (Fig. 4) (4,12).

Changes near the venous structures may be the result of increased central venous return and cardiac output during inspiration (12). Additionally, chest motion causes non-linear fluctuations in the B0 magnetic field, which may result in signal changes more generally in the brain (13).

Cardiac and respiratory signal variations are typically seen at higher frequencies than BOLD activation. This suggests that one could simply use a low-pass filter to eliminate these contaminants. However, cardiac signal tends to be undersampled and aliased to lower frequencies. Thus, a simple low-pass filter will not remove it. Depending on the time to repeat (TR), either all or a portion of the respiratory frequency range may also be aliased. Additionally, there are harmonics of cardiac and respiratory signals at even higher frequencies that are also aliased.

Physiologic noise may be removed by a variety of techniques (4,14–18).

Global Signal Change

There is a level of baseline activity present in the brain at rest, when no task is being performed. Changes in this baseline activity (or resting state) may be seen during the course of an experiment. The associated fMRI signal changes are known as global signal changes. This may affect the results of the experiment. For example, if increased baseline activity is seen during the task, diffuse brain activation will be seen (Fig. 5A).

This activation is usually interpreted as artifact and several methods have been devised to remove changes in whole-brain activity from the experimental data prior to processing. These methods usually involve subtracting out the mean change in whole-brain activity between the task and control acquisitions. However, doing this also results in reduced sensitivity to true BOLD changes and

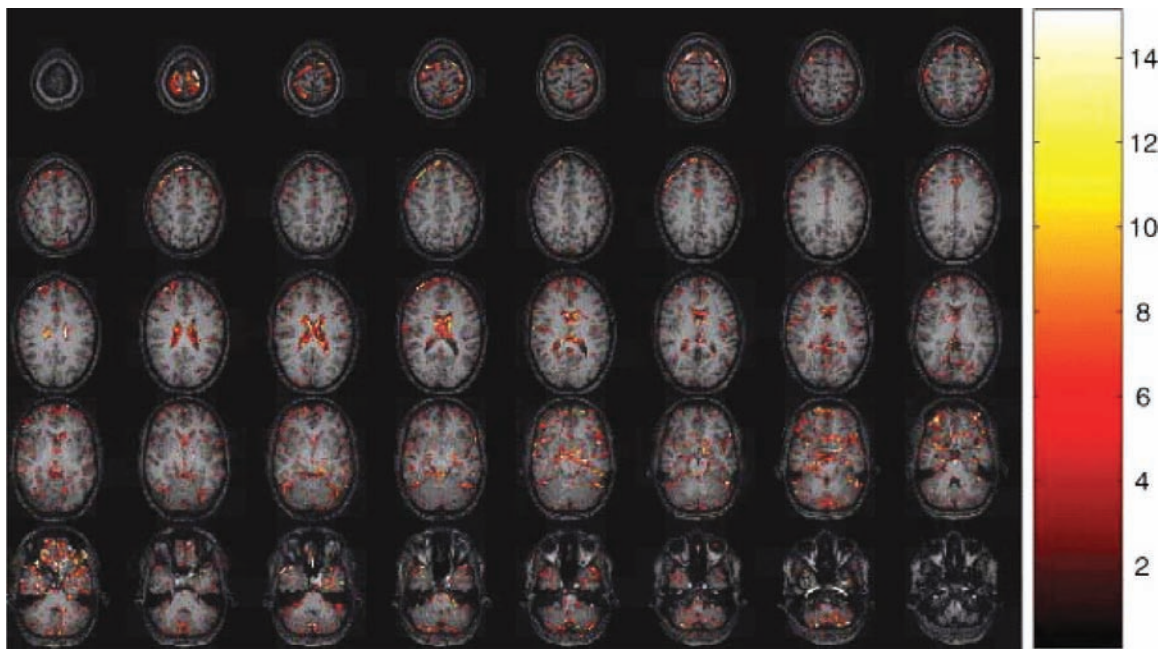


Figure 4 Respiratory-induced noise. Effects of respiratory activity are seen near larger veins, in the ventricles, and at the brain edges. Source: From Ref. 4.

may cause deactivation of signal in areas that are not correlated, or only weakly correlated, with the task (Fig. 5B). These areas of deactivation often include white matter, which should not experience any true BOLD change during the experiment. To adjust for this, the amount of applied correction may be reduced for white matter.

Another possibility is that the activation signal seen with global signal changes is not an artifact and should not be removed. The global activation signal may represent a true generalized increase in neural activity that occurs as a result of the task stimulus.

Scanner Acoustic Noise

Another source of noise in fMRI experiments is sound within the MRI suite that is heard by the subject. Sound is produced by the scanner during data acquisition from gradient switching. Fluctuating currents in the gradient coils result in Lorentz forces producing vibrations and sound (19). This noise is more pronounced during echo-planar imaging (EPI) due to the rapid rate and higher amplitude-gradient switching. Sound levels may reach up to 130 dB at 1.5T using EPI sequences (20) and increase at higher field strengths. Ambient noise within the room from various sources also may contribute to a small degree, perhaps having an influence during silent periods (21).

In addition to concerns of exposing the subject to high-amplitude sound, acoustic noise may also affect the fMRI data. These effects are presumed to result in reduced sensitivity rather than false-positive activation since the

acoustic noise is similar during stimulus and control acquisitions. Acoustic noise produces activation in the primary auditory cortex (22). Activation may also be produced in the secondary auditory cortex (21). This reduces sensitivity to BOLD activation during auditory experiments by increasing baseline signal and through partial saturation of the hemodynamic response (HR) in these regions (22,23). Additionally, alteration of activation signal may be seen with experiments evaluating nonauditory regions (e.g., visual and motor cortices), possibly the result of attention effects (21,24–27).

Several strategies have been devised to reduce the effects of scanner acoustic noise. One strategy is hardware modifications to reduce the amount of noise produced during scanning (28–30). Sound reaching the subject may be reduced with equipment insulators, earplugs/earmuffs, etc., or through active noise cancellation techniques (21). Quieter pulse sequences (such as burst imaging) and digital filters have also been suggested to reduce scanner noise (21).

The effect of acoustic noise on the BOLD activation signal may also be reduced through clever experimental designs. Since most of the scanner noise is produced during the acquisition sequence when gradient switching occurs, a silent period may be introduced into the experimental paradigm during which no acquisitions are performed. During the silent period, the stimulus is presented and the HR is initiated in the absence of scanner noise (31). The acquisition sequence is then performed to capture the BOLD signal. This is possible because of the several-second delay between a stimulus and the HR.

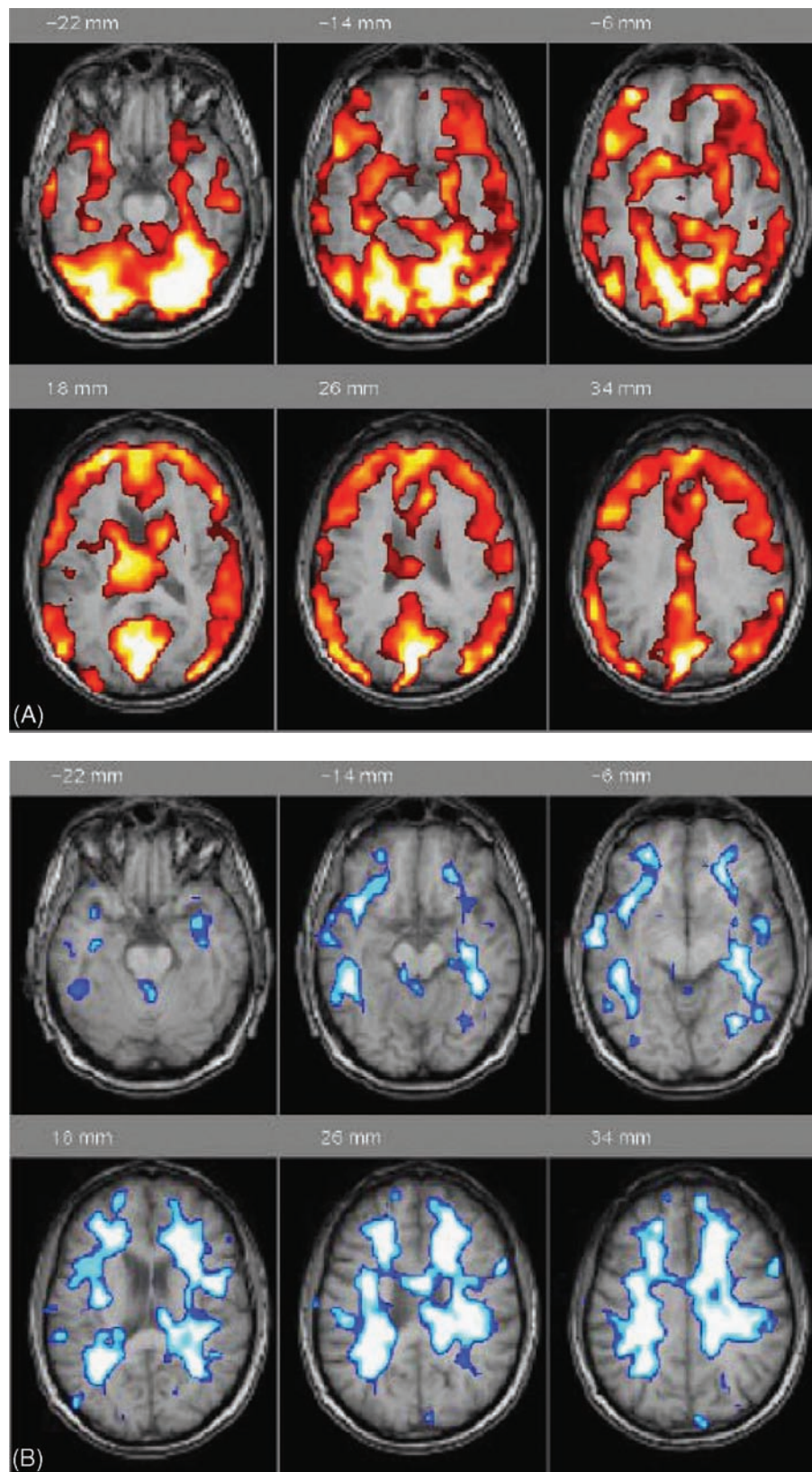


Figure 5 Global signal change. (A) Diffuse activation in gray matter is seen due to increased baseline activity during the task. (B) Following correction for global activation signal, diffuse deactivation is seen predominantly in white matter.

One potential problem with this strategy is that the noise produced by the acquisition sequence will produce its own delayed HR during the next silent period, which will elevate baseline signal and reduce sensitivity (21,32). This may be remedied by using a long silent period, enough to let the acquisition-induced HR decay to baseline levels before the next stimulus is presented (21,31). The delayed HR produced by sound at the beginning of an acquisition sequence may also affect signal observed at the end of the sequence (21,32). This may be addressed by making the acquisition time short enough to avoid the HR (21,31).

IMAGE ACQUISITION ARTIFACTS

Rapid imaging methods are needed in fMRI to achieve high temporal resolution. Because of this, sequences such as EPI and spiral imaging are used. However, these sequences suffer from some disadvantages including reduced spatial resolution and lower SNR. They are also both subject to a variety of acquisition artifacts, unique or more prominent with these sequences (33,34). These artifacts may reduce sensitivity to BOLD contrast in areas of interest as well as potentially introducing false-positive activations.

Susceptibility Artifacts

Magnetic susceptibility is a measure of the amount of magnetization induced in a tissue in the presence of an applied external magnetic field. Different tissues or structures have different magnetic susceptibilities. When tissues with large differences in magnetic susceptibility are placed in close proximity, distortions in the local magnetic field may arise and produce artifact. The most common sites for these artifacts are at tissue-air or tissue-bone interfaces because of the rapid transition among different magnetic susceptibilities.

Two types of artifact may occur as a result of susceptibility differences. One type is the result of protons in the region experiencing a change in resonance frequency because of the difference in local magnetic field strength (35). In EPI, this results in spatial misallocation of their signals and geometric distortion along the phase-encode direction (34). In spiral imaging it presents as blurring rather than misallocation (34). This artifact may be reduced by obtaining a field map prior to the study and applying a correction to the subsequent images (36).

Another type of susceptibility artifact is T2*-induced intravoxel dephasing. This produces local reduction of signal and results in decreased sensitivity to BOLD changes. Because BOLD contrast is detected by observing T2* change, fMRI imaging sequences are naturally prone to this artifact. This artifact may be reduced by using thinner slices, by increasing the resolution, by reducing the TE, or by using z-shimming techniques (37–39).

Intravoxel dephasing causes reduced signal in the inferior frontal and temporal lobes (40) and can result in decreased sensitivity to BOLD activation and potentially, false negatives in these regions (41). This effect may also be seen locally near paramagnetic substances such as blood products. This can be problematic in fMRI examinations for preoperative planning such as when a tumor or vascular malformation contains blood products and reduces signal in adjacent tissue. Signal-intensity maps have been developed to display regions of reduced signal due to susceptibility artifact (Fig. 6). These maps have been used clinically and, in some cases, resulted in changes in interpretation of fMRI studies (42).

N/2 Ghosting

N/2 (or Nyquist) ghosting is an artifact unique to EPI. It manifests as a “ghost” of the real image displaced by half the field of view in the phase-encode direction (33,34). It is the result of the zigzag pattern of EPI data acquisition with alternating positive and negative frequency-encoding gradients. If the echoes are acquired slightly off center, i.e., the middle of the echo is not at the middle of the acquisition time period, the odd and even lines of k-space will be staggered after time reversing the negative frequency-encoded lines (43). Since odd and even echoes each sample N/2 data points, or half the Nyquist rate of sampling, the artifact is seen as a “ghost” image shifted by N/2 pixels (44). N/2 ghosting may be caused by eddy currents, magnetic field inhomogeneities, susceptibility, or chemical shift (43). Additional sources of N/2 ghosting are timing errors between the gradient and data sampling and temporal asymmetries in the analogue filter (45). If uncorrected, N/2 ghosting may result in artifactual signal outside the head or at the overlap of the ghost and the real image (Fig. 7). The artifact is commonly reduced using a calibration scan obtained at the beginning of the EPI sequence with the phase-encode gradient turned off (34).

Latency Differences and the Slice-Timing Effect

Response latency is the amount of delay between a stimulus and the observed HR. Latency may be variable in different regions of the brain (46). When a canonical hemodynamic response function (HRF) is used as the regressor in modeling an event-related fMRI experiment, latency differences cause mismatching of data to the model and reduction in the observed signal amplitude (47).

The slice-timing effect is an artifact seen in event-related fMRI studies due to the nonsimultaneous acquisition of slices within a 3D image volume. Because slices are obtained in a sequential or interleaved order with time passing between the acquisitions, slices obtained later will

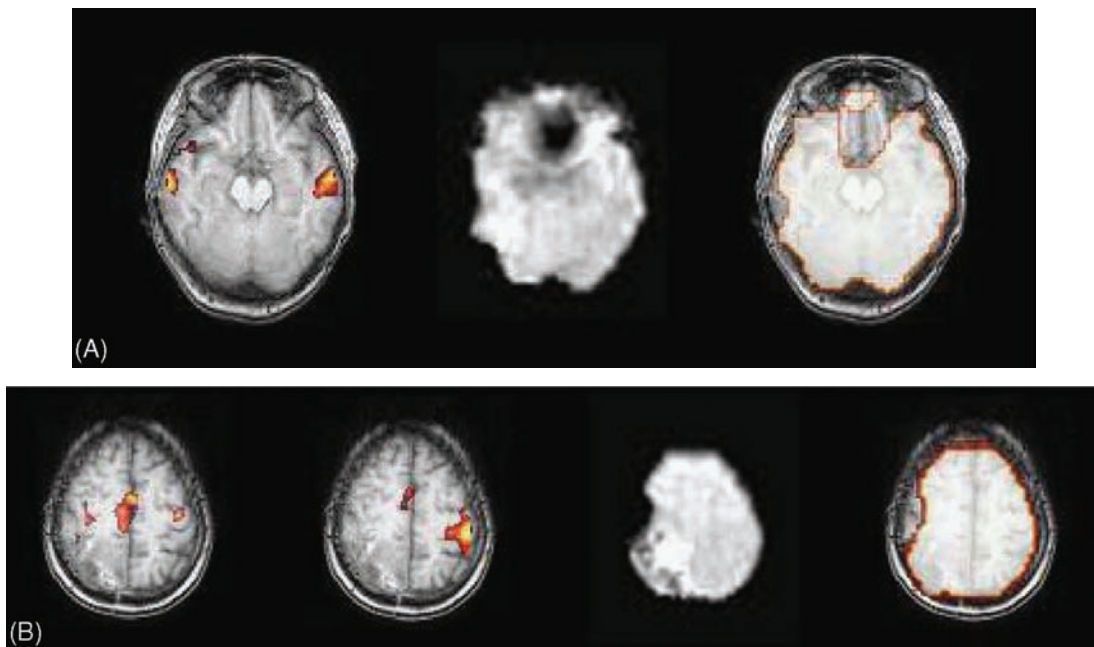


Figure 6 Susceptibility artifact. Images demonstrating susceptibility induced artifact in a patient who has had a right craniotomy. (A) An activation map for a verbal task is shown with corresponding EPI image and signal-intensity map (SIM). An area of postsurgical susceptibility induced signal loss is seen in the lateral right temporal lobe, which reduces the activation signal on the right compared to the contralateral side. (B) Images in the upper brain for left and right-sided motor tasks show reduced signal in the right motor cortex compared with the contralateral side due to EPI signal loss on the right. Abbreviation: EPI, echo planar imaging.

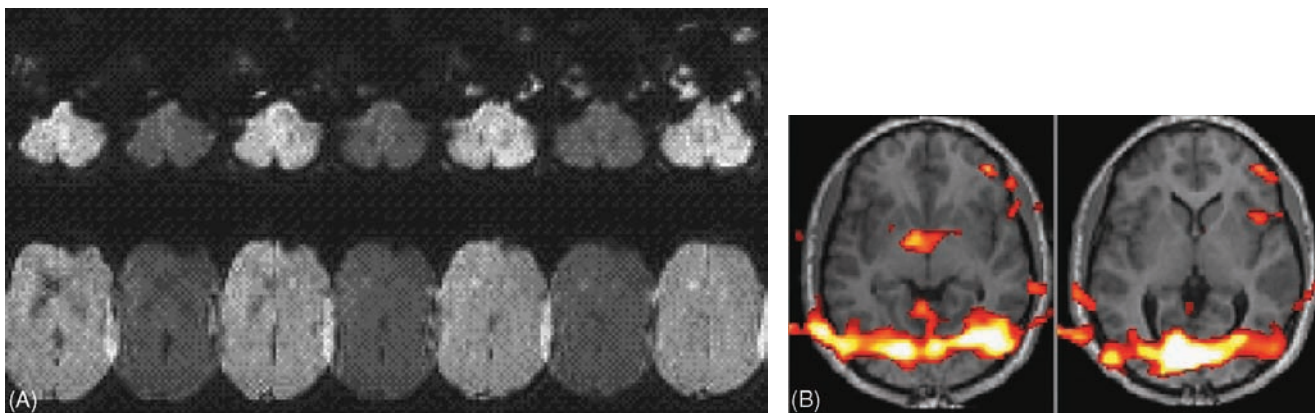


Figure 7 Nyquist ghost artifact. (A) A ghost of the EPI image is seen displaced by half the field of view in the phase encode direction. This has resulted in overlap at the lateral margins of the image. (B) Activation map following a visual task shows appropriate activity posteriorly and artifactual activation at the lateral margins of the brain as well as outside the brain. Abbreviation: EPI, echo planar imaging.

sample the HR at a slightly later time. This is similar to having latency differences between the slices and results in progressive phase shifting of the HR. Because the statistical analysis assumes all slices are obtained at the same time, the measured amplitude of the HR will be different depending on slice location. For example, when slices are obtained sequentially from cranial to caudal and the HRF regressor is synchronized with the top slice, signal will be progressively reduced in the lower

slices (Fig. 8) (48). This is the result of a progressively worsening fit with the HRF model with lower slices.

One method of correcting this problem is through the use of multiple regressors in the model to account for phase differences. This can be done by using a Fourier basis set or the canonical HRF and its derivatives as basis functions for the regression (46,47). Another method is to use interpolation to phase-shift the signals from different slices back into alignment (48,49).

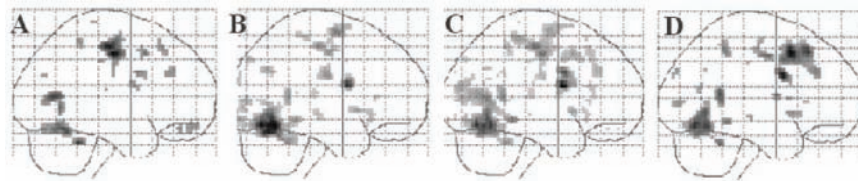


Figure 8 The slice-timing effect. (A) Reduced activation is seen in the lower brain when slices are obtained from cranial to caudal. (B) Reduced activation is seen in the upper brain when slices are obtained from caudal to cranial. (C) and (D) show more homogeneous activation following multiple regressors and interpolation correction methods respectively. Source: From Ref. 48.

MOTION

To improve the SNR in fast imaging techniques such as EPI, multiple images taken over a period of time must be averaged. However, this increases susceptibility to motion. Even with proper restraints and patient cooperation, small head movements may still be present and result in artifacts in the fMRI study.

Motion may occur during the acquisition of a single 3D image volume or between image volume acquisitions. If the motion is correlated with the task, false-positive BOLD contrast changes may be identified (50). If uncorrelated with the task, noise is introduced, which may obscure true BOLD signal.

Rigid-Body Motion Artifact

Rigid-body motion is movement that results in a change in location or orientation of an object while maintaining the object's shape. This contrasts with nonrigid motion in

which individual elements within an object are shifted relative to other elements in the same object, so the overall structure is not maintained. Rigid-body motion is described by six parameters: translational motion along the x-, y-, and z-axes and rotational motion about these same axes. Estimating and correcting for rigid-body motion involve determining these six parameters.

Rigid-body motion in an fMRI experiment is the result of subject movement between 3D volume acquisitions. This causes shifts in the locations of voxels relative to their counterparts in the previous scan and can result in the false-signal variation if two voxels with different signal become overlaid. This effect is most pronounced at the edges of the brain, because of the abrupt changes in signal strength between gray matter and CSF, resulting in “edge artifact”. Figure 9 demonstrates false-positive activation at the brain edges produced by rigid-body motion correlated with the fMRI task.

Rigid-body motion is correctable through the process of registration. Registration may be used to correct for

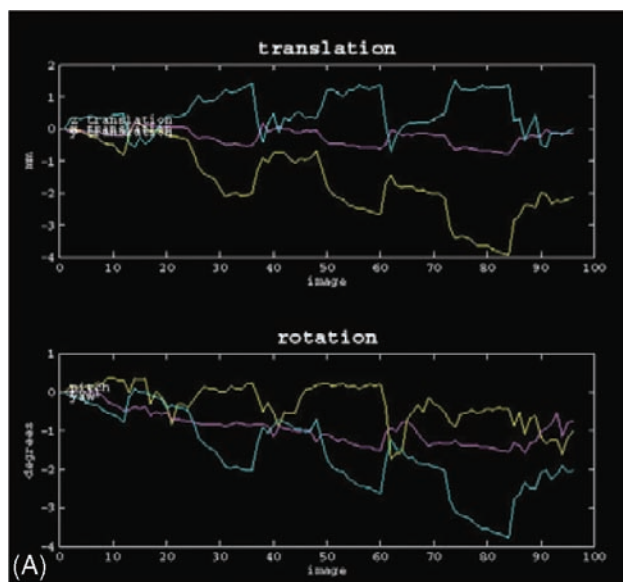
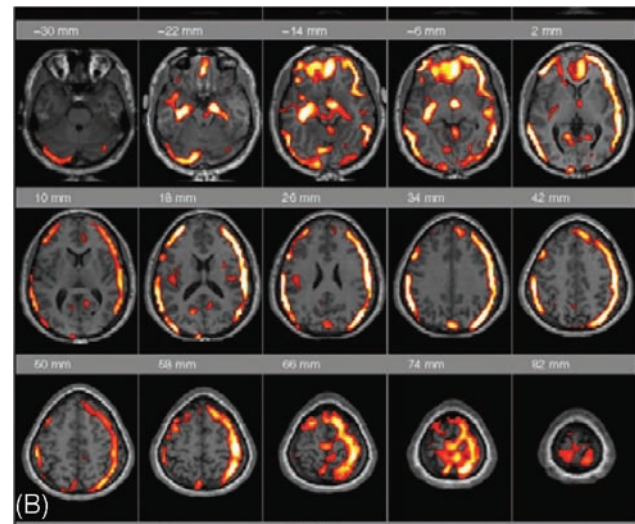


Figure 9 Rigid-body motion artifact. (A) Periodic translational and rotational motion is seen. (B) Artifactual activation is seen at the edges of the brain.



motion within an fMRI time series or motion between different imaging series in the same patient. Within a time series, registration uses one of the image volumes as a reference and compares the other volumes to it. The six motion parameters for each volume are estimated through an iterative process and then inversely applied to bring the images back into alignment with the reference. Various software packages are available to provide image registration (51).

Residual Motion Artifact

Even following rigid-body motion correction, residual motion artifacts may persist (52). Similar to rigid-body motion, signal changes are seen at the edges of the brain (Fig. 10) (4).

One potential cause of this is geometric distortions due to magnetic field inhomogeneity (34,53). These distortions may be fixed with respect to the scanner or can change with differing positions of the subject within the scanner (53). In the first case, motion causes the same structure to be exposed to different magnetic field strengths at different times as a result of being in differing positions in the inhomogeneous field. In the second case, fluctuating geometric distortions induced by subject motion result in spatially dependent signal variations. Additionally, changes in susceptibility effects as a result of reorientation within the magnetic field can result in

false-positive activation in locations adjacent to air and bone that persist after rigid-body correction (54).

Following motion, the signal will also be affected by previous positions of the head within the field as different degrees of spin saturation will be present depending on the varying magnetic field exposure at different locations. This is primarily observed with short TRs in the order of T1 and has been termed the “spin-history effect” (52). In most fMRI experiments, however, the TR is long enough for spin-excitation history not to be a problem.

These effects may be reduced by improving homogeneity of the magnetic field through shimming. Another approach is to remove any signal change that correlates with motion as determined by the registration parameters. Unfortunately, if the motion is correlated with the task, this correction will remove true activation signal as well.

PREPROCESSING ARTIFACTS

Several artifacts may be introduced during preprocessing. Preprocessing includes realignment of images using rigid-body registration, normalization of images to a common reference space, segmentation, and spatial smoothing algorithms. Since these artifacts may be difficult to recognize and characterize after data analysis, it is extremely important to view images after preprocessing to make sure no visible abnormality has occurred before proceeding.

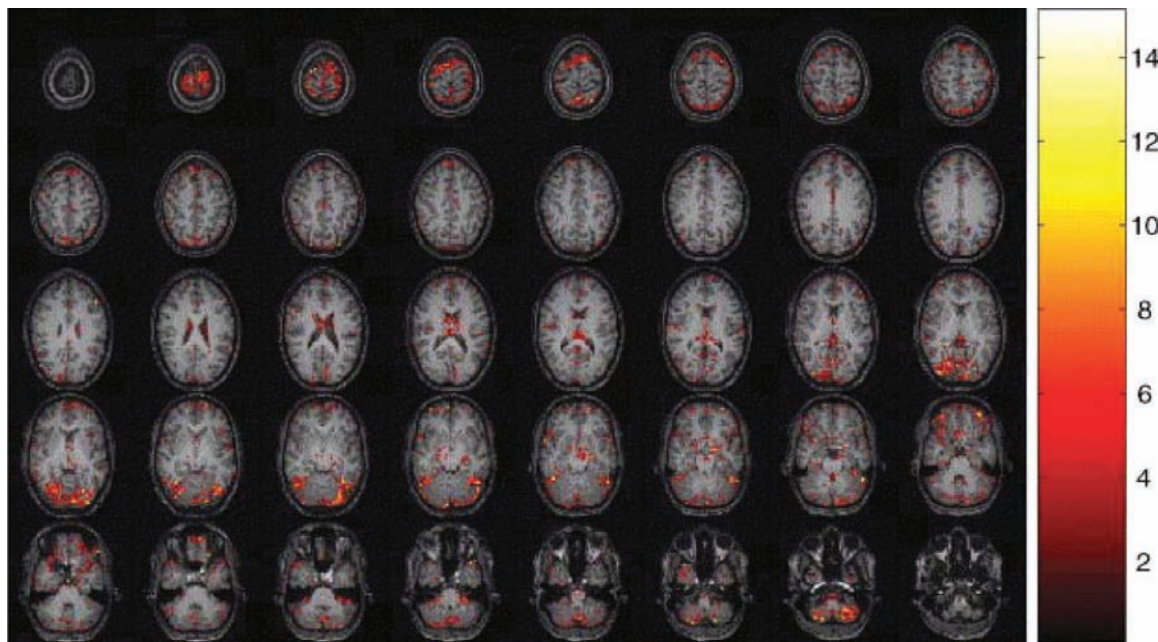


Figure 10 Residual motion artifact. Effects of residual movement are seen near the edges of the brain. Source: From Ref. 4.

Registration

One way artifacts may be introduced in rigid-body registration is during the interpolation step. Interpolation is necessary for estimating subvoxel signal intensities. When images are moved during registration, the adjustments are not necessarily made in single-voxel increments. Because of this, the images must be resampled to subvoxel resolution and interpolation must be made from the neighboring voxels to determine the value at a new position. Since interpolation schemes are imperfect due to computational time restraints, a certain inaccuracy is introduced, and this may result in spurious signal change (55).

Another way artifacts may occur is by faulty registration due to the influence of task-related BOLD signal. A BOLD signal change may be interpreted as a morphologic difference in the image by the registration algorithm. Therefore, the image may be incorrectly shifted because of the perceived morphologic difference. This tends to occur with less robust methods of registration such as “least squares” and appears to be less of a problem with methods such as “mutual information” (56).

Normalization

Normalization, or warping, is performed to bring images into a common reference space so that they may be

compared. In addition to rigid-body adjustments and zooms, the image is subjected to nonlinear warps to focally stretch regions of the brain to match a reference image as closely as possible. This allows voxel-level comparisons between subjects. However, artifacts may be introduced during normalization, and it is important to look at images following the procedure to identify any obvious errors.

Focal morphologic abnormalities within the brain may produce errors in normalization. For example, focal encephalomalacia may cause the subjacent normal tissue to be stretched to fill the gap in an effort by the warping procedure to match the brain with a normal reference image (Fig. 11). Spatial regularization techniques may be used to reduce large amounts of voxel repositioning.

Segmentation

Segmentation may be performed as part of the normalization process or in voxel-based morphometry (VBM) to separate gray matter, white matter, and CSF. Artifact may result from improper segmentation. An example is misrepresenting a voxel as gray matter when it is in fact white matter (Fig. 12). This could result in incorrect interpretation of a change in gray matter volume between two scans in a VBM analysis.

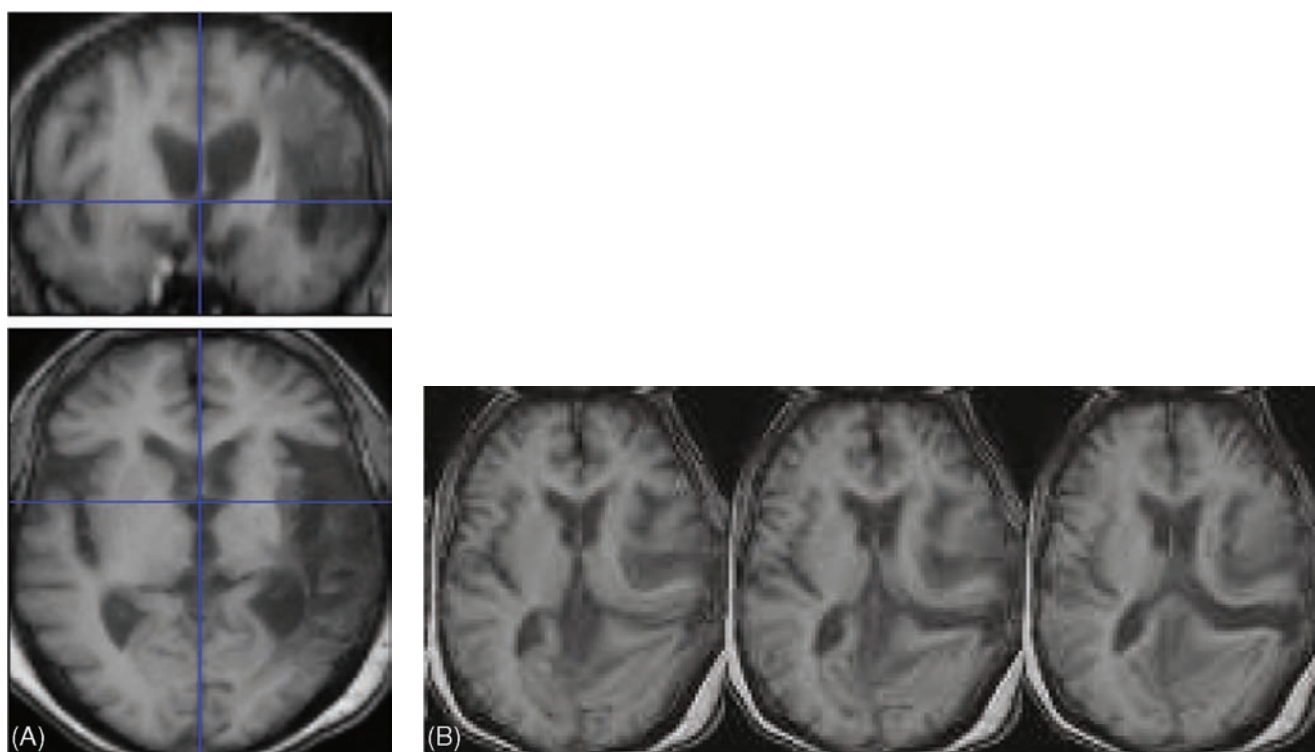


Figure 11 Normalization artifact. (A) Encephalomalacia is seen in the left temporal lobe and insular region. (B) Following normalization, the surrounding tissue and left lateral ventricle have been stretched to fill in the region of encephalomalacia.

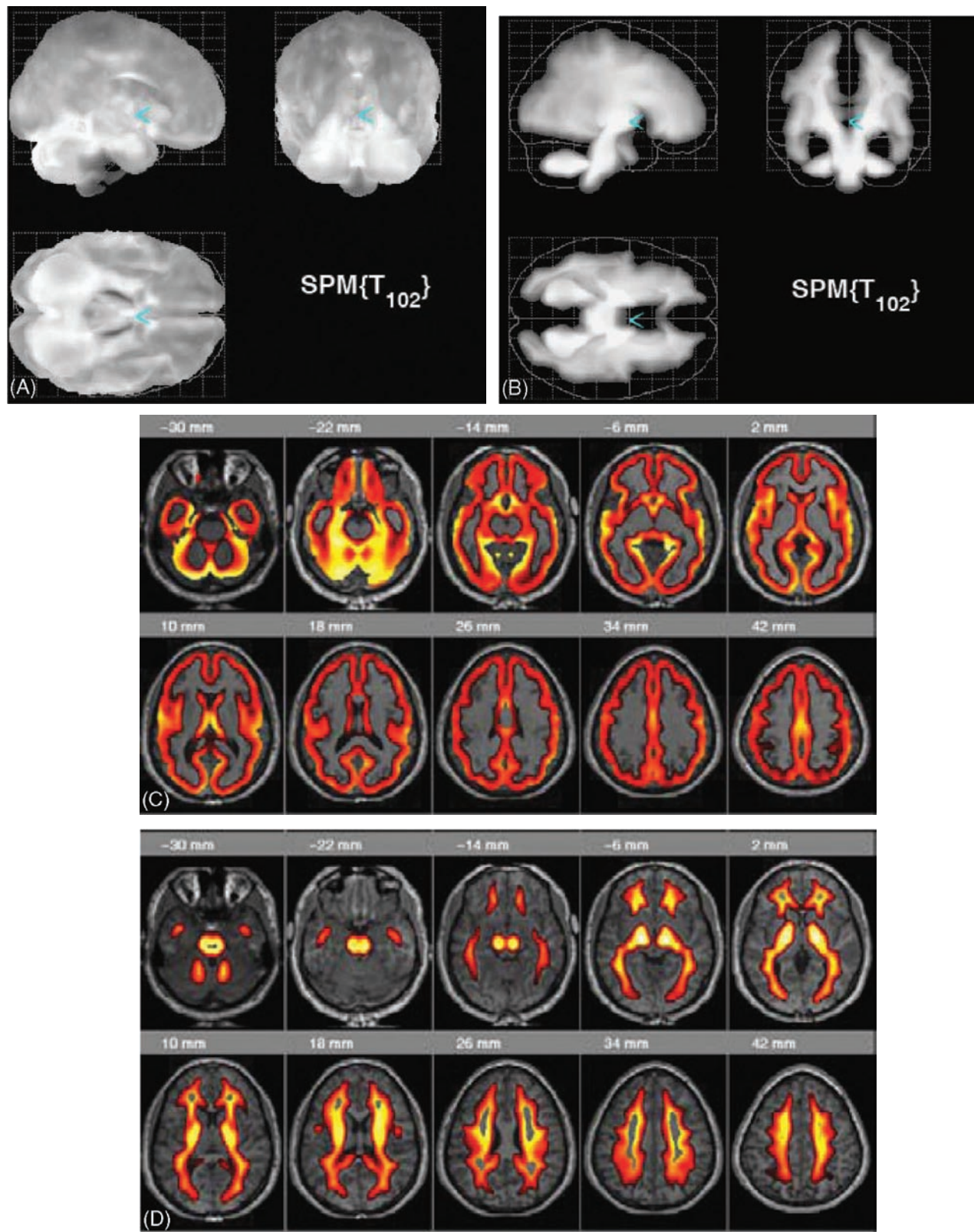


Figure 12 Segmentation artifact. This is an extreme example in which the white matter segmentation map has been mislabeled as grey matter and compared to a grey matter map. (A) The gray matter segmentation map. (B) The mislabeled white matter segmentation map. (C) Subtraction map following group comparison of (A) and (B) showing artifactual differences in gray matter. (D) Negative contrast shows artifactual differences in white matter.

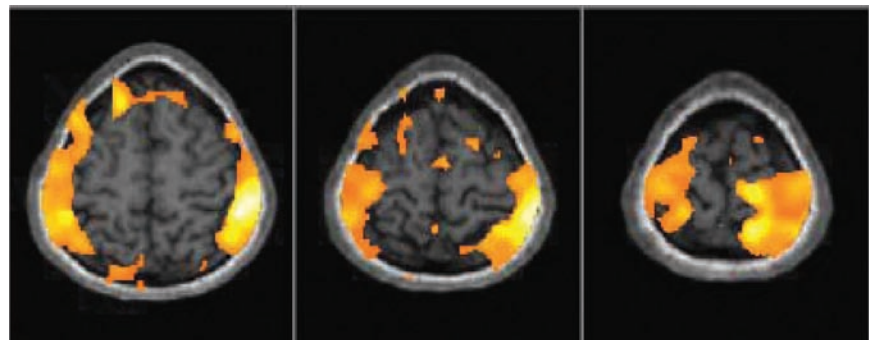


Figure 13 Smoothing artifact. Activation is seen outside the brain as a result of smoothing.

Smoothing

Another method of removing high-frequency noise is through smoothing. This is done by applying a smoothing kernel to an image in the spatial domain. It has a similar effect to applying a low-pass filter in the frequency domain. This improves the SNR and allows the application of Gaussian random field theory to data analysis. However, smoothing also reduces spatial resolution and can introduce artifact as a result of signal averaging. This is especially problematic at tissue interfaces and at the edges of the brain. Smoothing may enlarge the image by spreading its edges outward and may result in signal outside the brain when overlaid on an unsmoothed anatomic image (Fig. 13).

ACKNOWLEDGMENT

Research support was provided by R01EB004673 and EB004673-02S1.

REFERENCES

- Bernal B, Altman NR. Auditory functional MR imaging. *AJR Am J Roentgenol* 2001; 176(4):1009–1015.
- Bellon EM, Haacke EM, Coleman PE, et al. MR artifacts: a review. *AJR Am J Roentgenol* 1986; 147(6):1271–1281.
- Kruger G, Glover GH. Physiological noise in oxygenation-sensitive magnetic resonance imaging. *Magn Reson Med* 2001; 46(4):631–637.
- Lund TE, Madsen KH, Sidaros K, et al. Non-white noise in fMRI: does modelling have an impact? *Neuroimage* 2006; 29(1):54–66.
- Smith AM, Lewis BK, Ruttimann UE, et al. Investigation of low frequency drift in fMRI signal. *Neuroimage* 1999; 9(5):526–533.
- Wang J, Aquirre GK, Kimberg GY, et al. Arterial spin labeling perfusion fMRI with very low task frequency. *Magn Reson Med* 2003; 49(5):796–802.
- Beauchamp MS. Detection of eye movements from fMRI data. *Magn Reson Med* 2003; 49(2):376–380.
- Birn RM, Bandettini PA, Cox RW, et al. Magnetic field changes in the human brain due to swallowing or speaking. *Magn Reson Med* 1998; 40(1):55–60.
- Weisskoff RM, Baker J, Belliveau J, et al. What's in the Noise? Proceedings of the 12th Annual Meeting of the Society of Magnetic Resonance in Medicine, New York 1993:7.
- Dagli MS, Ingeholm JE, Haxby JV. Localization of cardiac-induced signal change in fMRI. *Neuroimage* 1999; 9(4):407–415.
- Feinberg DA. Modern concepts of brain motion and cerebrospinal fluid flow [comment]. *Radiology* 1992; 185(3):630–632.
- Windischberger C, Langenberger H, Sycha T, et al. On the origin of respiratory artifacts in BOLD-EPI of the human brain. *Magn Reson Imaging* 2002; 20(8):575–582.
- Raj D, Anderson AW, Gore JC. Respiratory effects in human functional magnetic resonance imaging due to bulk susceptibility changes. *Phys Med Biol* 2001; 46(12):3331–3340.
- Frank LR, Buxton RB, Wong EC. Estimation of respiration-induced noise fluctuations from undersampled multi-slice fMRI data. *Magn Reson Med* 2001; 45(4):635–644.
- Glover GH, Li TQ, Ress D. Image-based method for retrospective correction of physiological motion effects in fMRI: RETROICOR. *Magn Reson Med* 2000; 44(1):162–167.
- Kruggel F, von Cramon DY, Descombes X. Comparison of filtering methods for fMRI datasets. *Neuroimage* 1999; 10(5):530–543.
- Friston KJ, Glaser DE, Henson RN, et al. Classical and Bayesian inference in neuroimaging: applications. *Neuroimage* 2002; 16(2):484–512.
- Thomas CG, Harshman RA, Menon RS. Noise reduction in BOLD-based fMRI using component analysis. *Neuroimage* 2002; 17(3):1521–1537.
- Mansfield P, Glover PM, Beaumont J. Sound generation in gradient coil structures for MRI. *Magn Reson Med* 1998; 39(4):539–550.
- Ravicz ME, Melcher JR, Kiang NY. Acoustic noise during functional magnetic resonance imaging. *J Acoust Soc Am* 2000; 108(4):1683–1696.
- Moelker A, Pattynama PM. Acoustic noise concerns in functional magnetic resonance imaging. *Hum Brain Mapp* 2003; 20(3):123–141.

22. Bandettini PA, Jesmanowicz A, Van Kylen J, et al. Functional MRI of brain activation induced by scanner acoustic noise. *Magn Reson Med* 1998; 39(3):410–416.
23. Di Salle F, Formisano E, Seifritz E, et al. Functional fields in human auditory cortex revealed by time-resolved fMRI without interference of EPI noise. *Neuroimage* 2001; 13(2): 328–338.
24. Cho ZH, Chung ST, Chung JY, et al. A new silent magnetic resonance imaging using a rotating DC gradient. *Magn Reson Med* 1998; 39(2):317–321.
25. Elliott MR, Bowtell RW, Morris PG. The effect of scanner sound in visual, motor, and auditory functional MRI. *Magn Reson Med* 1999; 41(6):1230–1235.
26. Loenneker, T., Hennel F, Ludwig U, et al. Silent BOLD imaging. *MAGMA* 2001; 13(2):76–81.
27. Mazard, A., Mazoyer B, Etard O, et al. Impact of fMRI acoustic noise on the functional anatomy of visual mental imagery. *J Cogn Neurosci* 2002; 14(2):172–186.
28. Edelstein WA, Heden RA, Mallozzi RP, et al. Making MRI quieter. *Magn Reson Imaging* 2002; 20(2):155–163.
29. Katsunuma A, Takamori H, Sakakura Y, et al. Quiet MRI with novel acoustic noise reduction. *MAGMA* 2002; 13(3): 139–144.
30. Mansfield P, Chapman BL, Bowtell R, et al. Active acoustic screening: reduction of noise in gradient coils by Lorentz force balancing. *Magn Reson Med* 1995; 33(2): 276–281.
31. Amaro E Jr., Williams SC, Shergill SS, et al. Acoustic noise and functional magnetic resonance imaging: current strategies and future prospects. *J Magn Reson Imaging* 2002; 16(5):497–510.
32. Talavage TM, Edmister WB, Ledden PJ, et al. Quantitative assessment of auditory cortex responses induced by imager acoustic noise. *Hum Brain Mapp* 1999; 7(2):79–88.
33. Edelman RR, Wielopolski P, Schmitt F. Echo-planar MR imaging [comment]. *Radiology* 1994; 192(3):600–612.
34. Jezzard P, Clare S. Sources of distortion in functional MRI data. *Hum Brain Mapp* 1999; 8(2–3):80–85.
35. Lipschutz B., Friston KJ, Ashburner J, et al. Assessing study-specific regional variations in fMRI signal. *Neuroimage* 2001; 13(2):392–398.
36. Jezzard P, Balaban RS. Correction for geometric distortion in echo planar images from B0 field variations. *Magn Reson Med* 1995; 34(1):65–73.
37. Glover GH. 3D z-shim method for reduction of susceptibility effects in BOLD fMRI. *Magn Reson Med* 1999; 42(2): 290–299.
38. Jesmanowicz A, Biswal B, Hyde JS. Reduction in GR-EPI intravoxel dephasing using thin slices and short TE. *Proc Int Soc Magn Reson Med* 1999:1619.
39. Yang QX, Williams GD, Demeure RJ, et al. Removal of local field gradient artifacts in T2*-weighted images at high fields by gradient-echo slice excitation profile imaging. *Magn Reson Med* 1998; 39:404–409.
40. Ojemann JG, Akbudak E, Snyder AZ, et al. Anatomic localization and quantitative analysis of gradient refocused echo-planar fMRI susceptibility artifacts. *Neuroimage* 1997; 6(3):156–167.
41. Devlin JT, Russell RP, Davis MH, et al. Susceptibility-induced loss of signal: comparing PET and fMRI on a semantic task. *Neuroimage* 2000; 11(6 pt 1):589–600.
42. Strigel RM, Moritz CH, Haughton VM, et al. Evaluation of a signal intensity mask in the interpretation of functional MR imaging activation maps. *AJR Am J Neuroradiol* 2005; 26(3):578–84.
43. Buonocore MH, Gao L. Ghost artifact reduction for echo planar imaging using image phase correction. *Magn Reson Med* 1997; 38(1):89–100.
44. Grieve SM, Blamire AM, Styles P. Elimination of Nyquist ghosting caused by read-out to phase-encode gradient cross-terms in EPI. *Magn Reson Med* 2002; 47(2):337–343.
45. Porter DA, Calamante F, Gadian DG, et al. The effect of residual Nyquist ghost in quantitative echo-planar diffusion imaging. *Magn Reson Med* 1999; 42(2):385–392.
46. Friston KJ, Fletcher P, Josephs O, et al. Event-related fMRI: characterizing differential responses. *Neuroimage* 1998; 7(1): 30–40.
47. Calhoun VD, Stevens MC, Pearlson GD, et al. fMRI analysis with the general linear model: removal of latency-induced amplitude bias by incorporation of hemodynamic derivative terms. *Neuroimage* 2004; 22(1):252–257.
48. Henson RN, Büchel C, Josephs O, et al. The slice-timing problem in event-related fMRI. *NeuroImage* 1999; 9: S125.
49. Calhoun V, Golay X, Pearlson G. Improved fMRI slice timing correction: interpolation errors and wrap-around effects. *Proceedings, ISMRM, 9th Annual Meeting*, Denver, CO 2000:810.
50. Hajnal JV, Myers R, Oatridge A, et al. Artifacts due to stimulus correlated motion in functional imaging of the brain. *Magn Reson Med* 1994; 31(3):283–291.
51. Oakes TR, Johnstone T, Ores Walsh KJ, et al. Comparison of fMRI motion correction software tools. *Neuroimage* 2005; 28(3):529–43.
52. Friston KJ, Williams S, Howard R, et al. Movement-related effects in fMRI time-series. *Magn Reson Med* 1996; 35(3): 346–355.
53. Andersson JL, Hutton C, Ashburner J, et al. Modeling geometric deformations in EPI time series. *Neuroimage* 2001; 13(5):903–919.
54. Wu DH, Lewin JS, Duerk JL. Inadequacy of motion correction algorithms in functional MRI: role of susceptibility-induced artifacts. *J Magn Reson Imaging* 1997; 7(2):365–370.
55. Grootoont S, Hutton C, Ashburner J, et al. Characterization and correction of interpolation effects in the realignment of fMRI time series. *Neuroimage*, 2000; 11(1):49–57.
56. Freire L, Mangin JF. Motion correction algorithms may create spurious brain activations in the absence of subject motion. *Neuroimage* 2001; 14(3):709–722.

5

Language

JAY J. PILLAI

The Russell H. Morgan Department of Radiology and Radiological Science, Johns Hopkins University School of Medicine, and The Johns Hopkins Hospital, Baltimore, Maryland, U.S.A.

THE BOLD PRINCIPLE IN A NUTSHELL AND ITS SIGNIFICANCE

The blood oxygen level-dependent (BOLD) principle is the underlying concept that forms the foundation for the current practice of functional magnetic resonance imaging (fMRI). This concept was first described by Dr. Ogawa and colleagues in the early 1990s and relates to the mismatch between the oxygen delivery to the microvasculature adjacent to neuronal activation and the actual oxygen utilization by the activated cerebral tissue (1). From a practical standpoint, the intrinsic paramagnetic contrast agent, deoxyhemoglobin, forms the basis for BOLD contrast. Deoxyhemoglobin is associated with signal loss on heavily T2*-weighted [such as gradient-recalled echo (GRE)] echo-planar images. After an “initial dip” in signal intensity associated with increased oxygen extraction by the activated cerebral tissue, a rapid rise in signal intensity is noted on T2* GRE echo-planar images to a maximal level approximately five seconds later (2). This rise in signal intensity is secondary to a net decrease in deoxyhemoglobin concentration resulting from an increase in oxyhemoglobin concentration. While BOLD fMRI thus does not directly measure neural activation, it indirectly does so by assessing the associated regional blood flow changes in the adjacent microvasculature. This indirect but entirely noninvasive approach to determine

cortical activation has made a substantial impact on the scientific study of language processing in both healthy individuals and patients with neurological disease; furthermore, this technique is increasingly playing a major role in the diagnostic evaluation and clinical management of patients with brain lesions near eloquent language cortex who are candidates for neurosurgical intervention.

fMRI DATA ANALYSIS AND LANGUAGE PARADIGM DEVELOPMENT

In fMRI, we can exploit the BOLD principle by evaluating regional blood flow changes associated with performance of various sensorimotor and cognitive tasks. The actual task design can be generally considered to be one of two basic types: block design (also known as state-related, boxcar, or epoch design) or event-related design. In the former, alternating on-off states (i.e., activation vs. rest) are typically used with each alternating condition conducted for generally 15 to 30 seconds. Repeated stimulus presentation during each condition (i.e., epoch) is usually conducted, and this results in generally high statistical power. Stimulus presentation can be either visual or auditory; visual stimulus presentation is achieved either through use of video goggles for display of digital images or via an LCD or other type of projector in conjunction with mirrors. Auditory stimulus presentation is accomplished through use of

headphones. Various stimulus presentation programs are available through different software vendors. Triggering of the MR scanner by the stimulus presentation device is also possible, as is EEG-triggering when MRI-compatible electrodes are used. In this chapter, we will only discuss language activation paradigms and specifically, only commonly used ones for clinical purposes. In the field of cognitive neuroscience, however, hundreds of different paradigms have been developed by investigators exploring different aspects of language and memory function with fMRI. In general, however, the control states that alternate with the activation blocks consist of stimuli that control for all aspects of task performance except the specific cognitive aspect that is being studied in the activation task. For example, if visual stimulus presentation is desired, and the paradigm involves an object-naming task (in which a picture of an object is presented and two possible names for the depicted object are presented below the picture) in the activation state, then the control state should include stimuli that exactly match the stimuli in the task block in terms of overall visual stimulation (luminosity, visual complexity), lexical/linguistic component (i.e., letters and words should be included in both task and control blocks), and motor component (i.e., if button presses on a lap-held keypad are used to monitor task performance, then the same number of button presses should be expected in the control blocks as in the activation blocks). The object-naming component should be the only feature/variable that is not included in both task and control stimuli. Depending on how effective the control states are, the activation patterns that are observed will vary accordingly. Thus, optimization of paradigm design is very important to ensure accuracy of activation in cortical regions that are important to the particular cognitive function of interest.

Event-related paradigms, which are quite different in that very brief stimuli, are used at unpredictable and usually irregular intervals. These stimuli are often very short compared with typical block design paradigms and may even be less than 100 milliseconds in duration. However, just as in block design paradigms, it is difficult to generalize; the specific details of cognitive paradigms vary tremendously from task to task. Often the statistical power is lower than that of a comparable block design paradigm, and for this reason most clinical applications of fMRI rely on block design paradigms. However, for certain applications, event-related designs may be very useful, such as with EEG-triggered fMRI.

A variety of statistical analysis approaches exist to deal with the enormous amount of raw data that is usually acquired during a typical fMRI run. With single-shot echo-planar imaging (ssEPI) or equivalent ultrafast imaging techniques (e.g., spiral imaging), one can generally obtain whole brain coverage with acquisition of 20 to 30 images from skull base to vertex every three to five seconds.

During a typical five- to six-minute paradigm, thousands of raw images are thus obtained. A voxel-by-voxel analysis of the signal intensity changes that occur over time (i.e., fMRI time series) must be conducted to obtain fMRI activation maps. These maps are actually statistical probability maps that are obtained through extensive statistical analysis and then overlaid on 3D structural brain image sets. There are numerous approaches to fMRI data analysis, and, unfortunately, there has been little progress made to date with respect to national standardization of fMRI data processing approaches. In general, t-test, cross-correlation, general linear model (GLM) and independent component analysis methods have been used. The GLM is the most commonly used approach worldwide at this time, and the most popular software package utilizing this approach has been statistical parametric mapping (SPM) (SPM—SPM99 through SPM5), which is a software package developed by the Wellcome Department of Cognitive Neurology in London (3). The GLM assumes that the experimental data are composed of a linear combination of different model factors, along with uncorrelated noise (4). However, many other commercial and institutional internally developed statistical software packages are available. An alternative approach to statistical analysis is the independent components analysis (ICA), which is a data-driven analysis method that identifies spatially stationary sets of voxels whose activity varies together over time and is maximally distinguishable from that of other sets (4).

TYPICAL LANGUAGE PARADIGMS USED IN CLINICAL PRACTICE

Although the exact types of paradigms used varies from one institution to the next, in general multiple language paradigms need to be used for accurate language lateralization and localization. If only a single paradigm is used, false-negative results can be problematic. This is true because different language paradigms activate different cortical regions involved in different aspects of language processing. For this reason, it is essential to include both receptive and expressive speech paradigms for accurate lateralization and localization of all critical language cortical areas. In addition, our group has demonstrated that in bilingual patients, for best lateralization, semantic language tasks are better than phonological tasks (5) and language tasks (particularly, in our experience, the phonological task) in the patient's native language produce better lateralization than tasks in the secondary language (5) (Fig. 1). This is especially true in late acquisition or low proficiency (in the second or nonnative language) bilinguals. At our institution, we have developed both English and Spanish versions of a noun-verb semantic

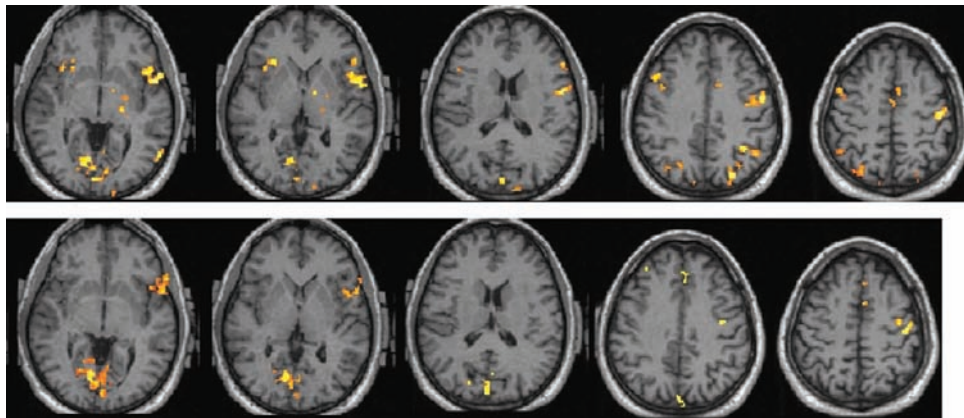


Figure 1 This figure demonstrates the difference in lateralization observed between comparable language tasks performed in a bilingual individual's native and nonnative languages: the top row demonstrates an English version of a phonological rhyming task in a primary Spanish, secondary English-speaking bilingual, while the bottom row demonstrates activation in a Spanish version of the same phonological language task—it is preferable to use a task in the native (primary) language for correct lateralization. Statistical thresholding is at $p < 0.001$ with 10 voxel spatial extent (clustering) threshold applied.

association task and a phonological rhyming task with very similar content in both languages for use in our Spanish-English bilingual population.

Typical language paradigms that are used include verb generation tasks, semantic decision tasks, phonological (rhyming) tasks, and passive listening or sentence reading tasks. The first three generally activate both expressive and receptive speech areas reliably, whereas the last two primarily activate receptive speech areas; in fact, passive listening tends to specifically activate only receptive speech areas, whereas sentence reading/comprehension tasks often also activate expressive speech cortices as well. At our institution, we have used a noun-verb semantic association task as well as a phonological rhyming task on our 1.5T-MRI systems (see Figs. 2, and 3 for descriptions of the noun-verb task, phonological task, and control tasks for both, respectively), and at 3T we have used a semantic decision task, rhyming task (see Fig. 4 for a description of the 3-T rhyming task), and passive listening task (these 3-T versions are vendor-provided) (6). We generally do not use verb generation tasks, despite ample evidence of its utility in the published literature pertaining to clinical language mapping, primarily because we are unable to monitor patient performance during this task. For all tasks, we use a lap-held keypad with right- and left-hand buttons to record responses; we monitor both patient response accuracy and latency of responses. We use visual stimulus presentation for all of our language tasks except for our passive listening task, which is obviously performed using auditory stimuli. We use video goggles for display of the visual stimuli and headphones for auditory stimulus presentation. It is extremely important to test patients for language proficiency either formally or informally outside the scanner environment to



Figure 2 In our noun-verb semantic association task at 1.5 T (internal institutionally developed paradigm), we present a noun on the upper half of each stimulus image as well as two verbs below it as shown in this figure. If the verb which is more closely semantically associated with the presented noun is located on the right side of the image, then the patient is asked to press the right-hand button on the hand-held keypad. If the verb which is more closely associated with the presented noun is located on the left side of the image, then the patient is expected to press the left-hand button.

determine suitability of various language paradigms, since many previously high-functioning patients may have recently experienced precipitous decreases in cognitive function as a result of their neurological diseases; this is especially true in brain tumor patients. In addition, testing while inside the bore of the scanner with practice items and reiteration of the instructions to ensure patient understanding of the tasks is essential. Patient response monitoring is also essential to ensure that the patients are actually performing the required tasks. We never sedate patients prior to fMRI studies because sedation will also adversely affect their performance of cognitive tasks and thereby decrease the diagnostic value of the resultant functional activation maps.

WEIGH PLAY

(A)

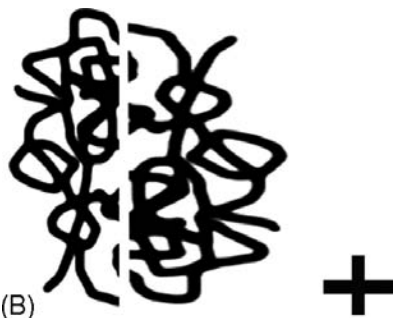


Figure 3 (A) In the phonological (rhyming) language task at 1.5 T (internal institutionally developed paradigm), a word pair is presented such as the one in this figure, which either rhymes or does not rhyme. If the pair does indeed rhyme, the patient is instructed to press the right-hand button on the keypad, whereas if the words do not rhyme, he or she is instructed to press the left button. (B) The control images for both the phonological (rhyming) and the noun-verb semantic association task at 1.5 T consist of abstract randomly configured “nonsense” line drawings with a plus sign located in either the lower right- or lower left-hand corner of the image. The patient is instructed to press the right button on the keypad if the plus sign is located on the right lower corner of the image and is expected to press the left button if the plus sign is located on the lower left-hand corner of the image. Thus, the control task controls for the visual input, decision making, and motor components of activation, thus isolating the actual semantic language function being tested.

In the semantic decision paradigm that we use on our 3T system, the task involves auditory stimulus presentation. Specifically, the name of an animal is mentioned and the button responses are dependent on whether or not the animal is native to the United States and whether the animal can be used by humans. In this case, the control task involves listening to a series of tones. If there are exactly two tones, the patient is instructed to press the right button. If not, the patient is asked to press the left button on the response keypad. Investigators have developed many different additional semantic decision tasks at institutions across the country, and all of these tasks tend to reproducibly activate expressive and receptive language cortex.

For the passive listening paradigm, alternating blocks of story listening and nonsense sounds are used for the task and control blocks, respectively. Other language tasks that others and we have used clinically include naming tasks and verb generation tasks. In the naming task, a picture of an object is presented visually and two words are presented below the picture. If the word on the left represents the name of the object, the patient is asked to press the left hand-button on the keypad; if the one on the



(A)



Figure 4 (A) This figure shows a typical word pair example from our rhyming task performed on our 3-T MRI system (vendor-provided commercially available paradigm). If the pair does indeed rhyme, the patient is instructed to press the right-hand button on the keypad, whereas if the words do not rhyme, he or she is instructed to press the left button. (B) On our 3-T system we use a different control task from the one we use on our 1.5-T systems, which consists of a series of line figures (sticks) in two rows. If the two patterns of sticks are identical, then the patient is asked to press the right button on the keypad; if the patterns are not identical, then the patient is supposed to press the left button.

right is the correct name of the object, then the right button is to be pressed. Advantages of such a dual-response paradigm include the ability to monitor patient task performance and the ability to standardize responses.

The verb generation task, in which a letter is presented and the patient is asked to silently generate a verb beginning with this letter, has the major limitation of not providing any means of monitoring patient task performance; thus, we tend to use this as a paradigm of last resort. We also prefer not to use the naming task if we can avoid it, because in our experience the activation seen in both patients and normal volunteers tends to be too widely spatially distributed to be of much clinical use in the assessment of language lateralization and critical localization. We have found that the semantic and phonological (rhyming) tasks tend to produce the best combination of reliable lateralization and activation of both expressive and receptive speech cortex. At 3T, more robust activation is generally seen because of the higher signal-to-noise ratio (SNR) resulting in more intense BOLD responses, and we have found that the passive listening task provides excellent selective receptive language (Wernicke's) localization.

Areas that are commonly activated include Broca's area [inferior frontal gyrus, Brodmann's areas (BA) 44,45], the classic expressive speech area, and Wernicke's area (superior temporal gyrus, BA 22), the classic receptive speech area. However, additional areas that are commonly activated include dorsolateral prefrontal cortex (middle frontal gyrus predominantly), supplementary motor area, angular and supramarginal gyri, and occasionally additional gyri of the frontal and temporal lobes. The exact distribution of activation varies according to the particular nature of the language task; thus, for accurate lateralization and localization of activation, based on our experience, at least two and preferably three tasks should be used (Fig. 5 shows differences in lateralization that can result from use of different language tasks). In addition, variation of the statistical threshold greatly affects the spatial distribution of activation; thus, it is essential that functional data be thresholded at more than one level to display the effects of thresholding on extent of activation. Our group has shown that more conservative thresholds, often with a correction for multiple comparisons, need to be applied for motor cortical mapping, but for language mapping, we tend to prefer to use less conservative statistical thresholds

when displaying the statistical parametric maps (7). Figures 6, 7, 8, and 9 show some of the expected areas of activation on passive listening, semantic decision, and rhyming (phonological language) tasks in a patient with a left frontal opercular low grade astrocytoma, as depicted on both standard axial and 3D structural images. Their clinical significance with regard to presurgical planning is also described in these figure legends.

Two essential caveats that a referring neurosurgeon needs to be aware of when fMRI language mapping is being performed are the following: (i) presence of activation in a cortical region does not necessarily imply that the cortical area is absolutely essential for language function (this essential nature of language cortex can be better assessed with direct intraoperative electrical cortical stimulation mapping with demonstration of speech arrest) and (ii) the absence of activation on a single language task does not mean that the cortical region being considered is not essential for any language function. The second issue can be considered in a different way: false-negative activation can be seen when only one language task is used, and thus more than one language task must be used to accurately assess both expressive and receptive language

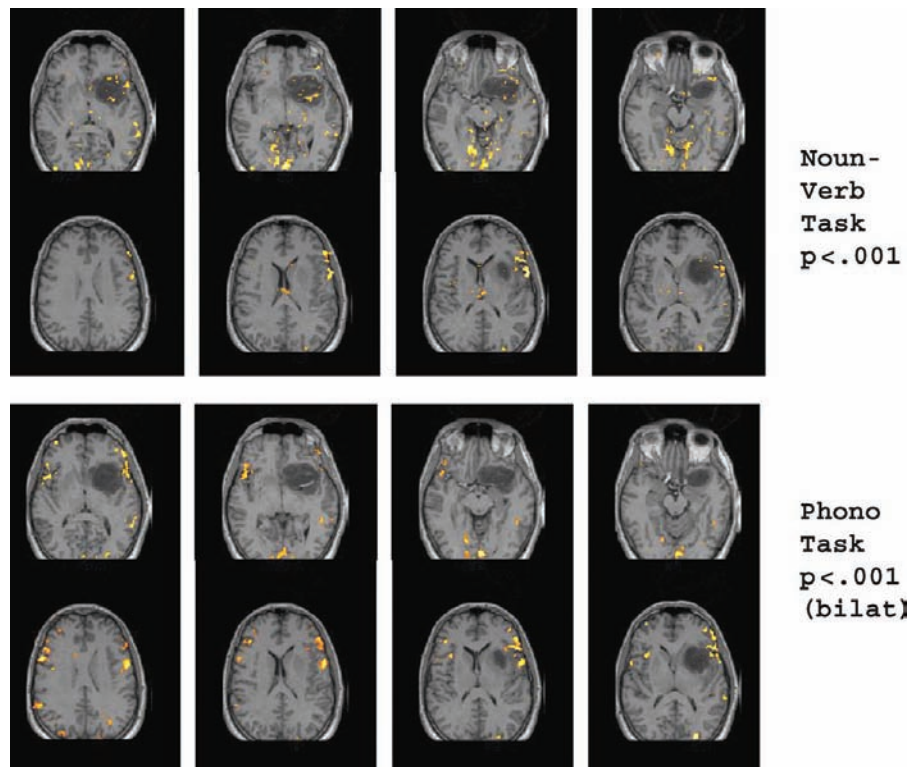


Figure 5 The top two rows of images display activation obtained during performance of the noun-verb semantic association task (developed at our institution) while the bottom two rows show activation during a phonological rhyming task at 1.5 T. This patient demonstrates a left-hemispheric tumor. All statistical thresholding is at $p < 0.001$, but on the noun-verb task, strong left frontal dominance is seen compared with bilateral expressive language representation in the phonological task. This highlights the need to perform at least two different language tasks for accurate language lateralization.

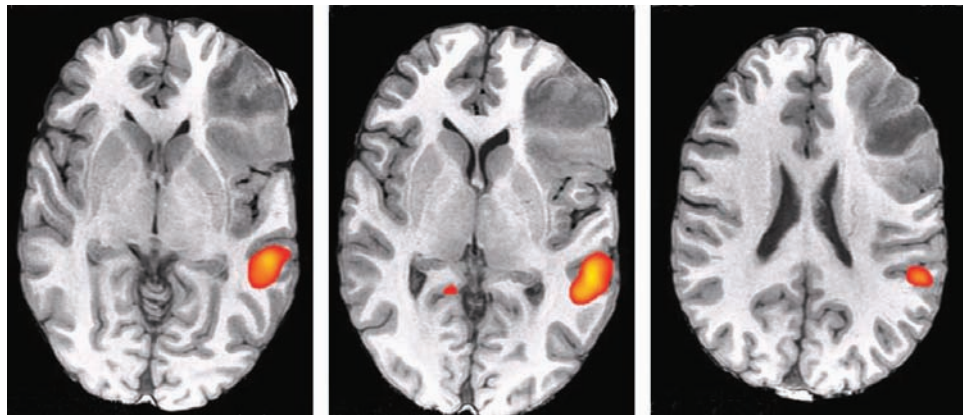


Figure 6 This figure shows activation overlaid on standard axial T1 3-D SPGR images during performance of a passive listening task by a patient with a left frontal low-grade glioma ($p < 0.05$). Only the receptive speech areas in the superior temporal gyrus demonstrate activation, but no activation within or adjacent to the left frontal opercular tumor is seen. The study was performed on a 3-T MRI scanner.

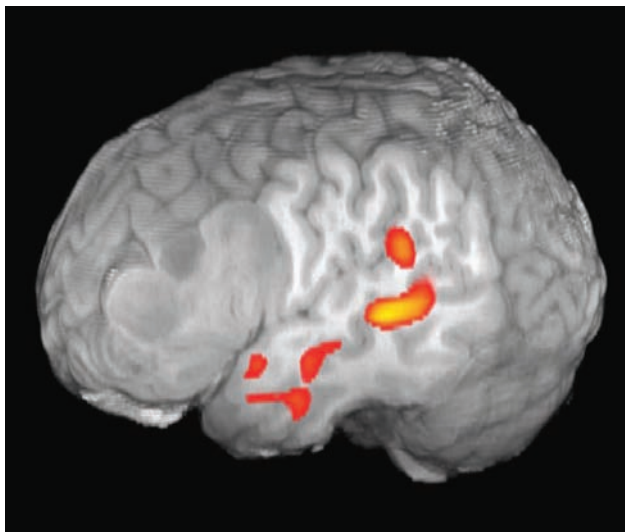


Figure 7 This figure shows a 3-D rendering of activation on the same task as depicted in Figure 6. Enlargement of the gyri in the left frontal opercular region (left inferior and middle frontal gyri) is seen secondary to tumor infiltration, but activation is only seen in the left temporal lobe in receptive speech cortex on this passive listening task performed on a 3-T MRI system, which tends to activate only receptive speech cortex. Thus, the patient is not at risk for developing a receptive (Wernicke's) aphasia with total tumor resection.

functions. In other words, a cortical region may be activated in one language task but not necessarily in all language tasks. While in the cognitive neurosciences type I errors (i.e., false positives) are the main concern, in clinical presurgical mapping type II errors (i.e., false negatives) are a much more prominent consideration because the main concern is the avoidance of resection of eloquent language cortex (8).

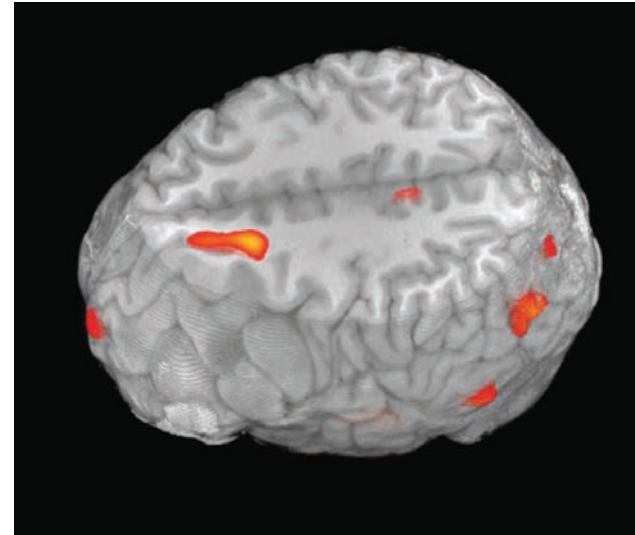


Figure 8 This figure shows activation during a semantic decision paradigm overlaid on T1-weighted 3-D SPGR images ($p < 0.05$, semantic decision task on 3-T MRI). Note the activation bordering on the superomedial aspect of the left frontal tumor on this 3-D overlay, separated by less than 1 cm. This represents eloquent cortex at risk for injury during a total resection of the tumor.

CLINICAL VALIDATION OF fMRI LANGUAGE PARADIGMS

Every institution needs to internally validate their language fMRI paradigms to be able to rely on them for presurgical language mapping. Unfortunately, no standardization of language paradigms currently exist nationwide, despite efforts of MRI scanner vendors to provide "canned"

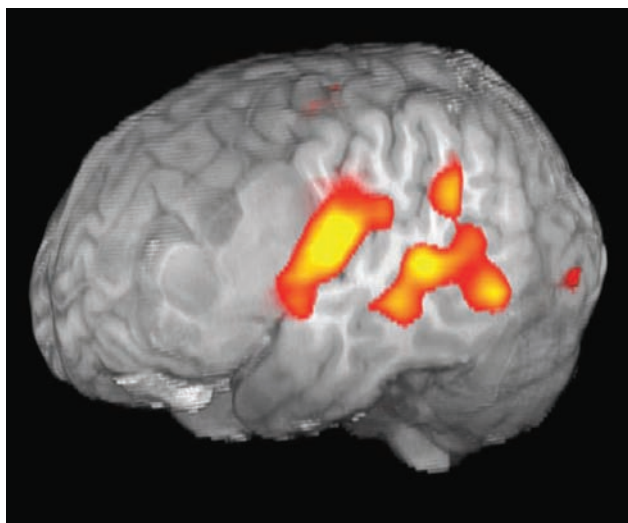


Figure 9 This figure shows activation during a rhyming paradigm overlaid on T1-weighted 3D SPGR images ($p < 0.05$, obtained on 3T MRI). Note the activation bordering on and actually involving the posterior aspect of the left frontal opercular tumor. This suggests that the patient is at risk for developing a Broca's aphasia if complete tumor resection is performed.

paradigms, particularly on newer 3T MRI systems, and despite national-level efforts to standardize paradigms through establishment of American College of Radiology published standards, educational efforts of the American Society of Functional Neuroradiology, and formulation of multicenter clinical trials designed to provide valuable correlative outcome analysis data. Every institution that conducts these studies has in one way or another attempted to internally validate their respective preferred techniques, and multiple published correlative studies have demonstrated that this is feasible. The Table 1 lists a variety of such published studies which have compared the results of language fMRI with those of intraoperative direct electrical cortical stimulation (DECS) mapping or Wada testing (intracarotid sodium amytal testing), and most of these studies have shown very high concordance rates, generally in the range of 85–100% (9–22).

Some of these studies will be described in this section. For example, in Rutten's series of 13 temporal lobe epilepsy patients, comparison was made between fMRI localization of language cortex using four tasks (verb generation, picture naming, verbal fluency, and sentence comprehension) and intraoperative DECS mapping (19). DECS failed in two patients and detected critical language areas in only eight of the remaining 11 patients (19). They found that correspondence between fMRI and DECS depended heavily on fMRI statistical thresholding and thus varied among patients and tasks; in addition, fMRI using a combination of three language tasks demonstrated 100% sensitivity in detecting all critical language areas

detected with DECS with high spatial accuracy in seven of the eight patients with diagnostic DECS data (19). In one patient, sensitivity was only 38% (19). Overall, specificity was 61%; fMRI was able to reliably predict the absence of critical language areas within the region exposed during surgery, but presence of activation at noncritical language sites (as determined with DECS) limited the predictive value of fMRI for the presence of critical language areas to 51% (19). The authors thus concluded that while these findings preclude replacement of DECS with fMRI, fMRI may be used to shorten the length of intraoperative DECS-mapping procedures and guide the necessary extent of craniotomy in epilepsy surgery cases (19).

Brannen's group studied the accuracy and reproducibility of fMRI word generation tasks in mapping Broca's area by comparing fMRI activation with awake DECS intraoperative language-mapping results and performing two iterations of the fMRI task, respectively (11). They noted activation in the inferior frontal gyri or middle frontal gyri or both in BA 9, 44, 45, or 46, unilaterally or bilaterally, with one or more of the tasks in 31 of the 34 patients, and the same gyri demonstrated activation in the second scan session (11). Furthermore, in those undergoing awake DECS mapping, the speech areas mapped intraoperatively corresponded to those areas of the brain activated during the fMRI word generation task (11). On the basis of their work, Brannen thus concluded that fMRI accurately and reliably maps Broca's area (11).

Ruge and colleagues have studied 21 patients with language and sensorimotor fMRI and compared the mapping results with those of intraoperative electrophysiology [somatosensory-evoked potential recordings (SSEP), DECS including stimulation of motor cortex in 15 patients, and of Broca's area and Wernicke's area in five patients] (12). In their study, in those patients for whom responses were obtained with both mapping methods, localization of function concurred in all cases (12). On the basis of their study results, the authors conclude that fMRI represents a reliable preoperative tool for the identification of language-sensitive areas (12).

In Hirsch's series, evaluation of a battery of multiple fMRI tasks through comparison with intraoperative electrophysiological measurements, the investigators found that in brain tumor patients, the sensitivity for identification of the putative Wernicke's area was 91% and for Broca's area 77%; the sensitivities were increased by use of multiple tasks (20). In all patients in whom both fMRI and intraoperative electrophysiological measurements yielded maps, the two maps were concordant (20).

Sabbah's group studied 20 epilepsy patients (9 right-handed and 11 left-handed, 14 with temporal lobe seizure focus, and 6 extratemporal), who all underwent both Wada testing and fMRI using a silent word generation paradigm (15). In this series, fMRI language lateralization

Table 1 Studies Comparing Language fMRI to DECS or Wada Testing

Reference No.	Number of patients	Type of fMRI task	Location of tumors/etiol.	Concordance with DECS	Concordance with Wada
9	22 epilepsy patients	semantic decision-tone discrim. task	NA	NA	22/22 for hemis. lateraliz. (correlation $r = 0.96$ for LI)
14	5 TLE patients	verbal fluency task	NA	NA	5/5
13	100 epilepsy patients	covert word generation	localization-rel. epilepsy	NA	91/100 language dominance
15	20 epilepsy patients	silent word generation task	partial epilepsy	NA	19/20
16	7 pediatric epilepsy patients	word generation task	partial epilepsy	1/1 concordant	6/6 concordant
17	7 epilepsy patients	language tasks	epilepsy	NA	7/7 concordant
18	23 patients	verb generation	tumors, etc.	10/11	12/12
19	13 patients	verb generation/ additional three language tasks	TLE	7/8	NA
20	125 patients; 43 intraop DECS, SSEP, or Wada	Multiple tasks (tactile, motor, language, and visual)	brain tumors	30/30	13/13
21	28 patients	motor, word generation, counting	—	28/28 (100% within 20 mm, 87% within 10 mm)	NA
12	21 patients	language and sensorimotor mapping	NA	intraop SSEP (21 pts.), intraop motor DECS (15 pts), intraop Broca's, Wernicke's DECS (5 pts)— all 100% concordance	NA
22	11 patients	visual word reading, visual verb generation, auditory verb generation, listening to words, text	eight tumors, one epilepsy, one benign cyst, one cavernous angioma	81% sensitivity/53% specificity for activation in direct contact with areas of DECS mapping	NA
11	34 patients	word generation task	NA	100% concordance in those undergoing DECS	NA

Abbreviations: fMRI, functional magnetic resonance imaging; DECS, direct electrical cortical stimulation; TLE, temporal lobe epilepsy; SSEP, somatosensory-evoked potential recordings.

was concordant with the Wada test in 19 of the 20 cases (15). One left-handed patient in their series demonstrated bilateral language fMRI activation but right-hemispheric language dominance on the Wada test (15). Right-hemispheric language lateralization was significantly correlated with left lateralized epilepsy ($p < 0.05$) in this series, but was not correlated with age at epilepsy onset, history of early brain injury (prior to six years of age), or lobe of seizure focus localization (15).

However, much of the concordance of fMRI results with Wada testing or intraoperative DECS mapping depends on the fMRI paradigm used. For example, in

Lehericy's study, in which three different language tasks were used to study a group of 10 patients with temporal lobe epilepsy, the semantic verbal fluency task produced frontal lobe activation asymmetry which correlated highly with Wada laterality indices (especially in the precentral/middle frontal gyrus/inferior frontal sulcus area), but the temporal lobe activation on this task did not correlate well with Wada test results (10). Similarly with a story listening task, high correlation between frontal lobe-activation asymmetry, but not temporal lobe-activation asymmetry, and Wada laterality indices was found; however, with a covert sentence repetition task, no such correlation was

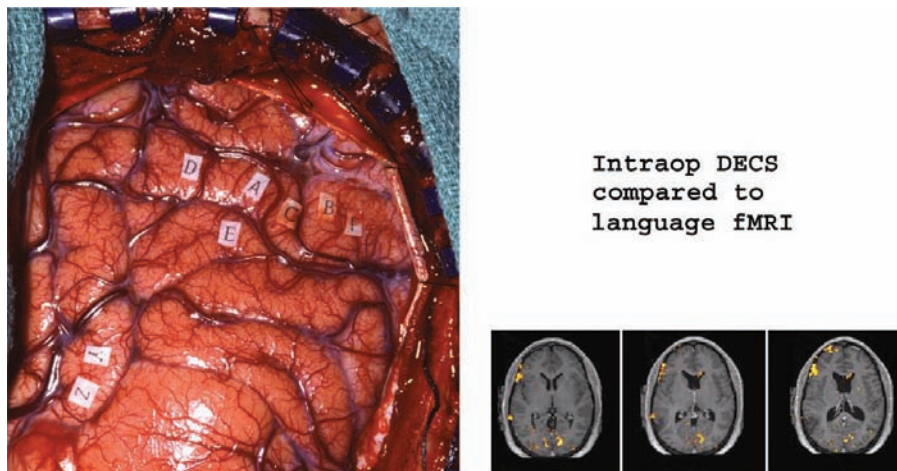


Figure 10 This figure shows a patient with a left parietal low-grade astrocytoma being mapped intraoperatively with direct electrical cortical stimulation—(DECS) mapping on the left with delineation of receptive speech cortex in the superior temporal gyrus (tagged as “Y” and “Z”), and on the right, activation during a noun-verb semantic association task is displayed with corresponding Wernicke’s activation seen lateral to the tumor margin, in addition to more robust Broca’s activation. The fMRI images do not follow radiologic convention, but rather are oriented to match the intraoperative view, so the left side of the image represents the patient’s left side.

found, but the story listening and the covert sentence repetition tasks increased the sensitivity of detection of posterior receptive language eloquent cortices (10). Thus, the degree of concordance of fMRI lateralization indices with the hemispheric language dominance determined by Wada depends on the particular fMRI tasks utilized (10).

However, unfortunately, not all such correlative studies have demonstrated high reliability of fMRI in the mapping of eloquent cortex. For example, Roux et al. have shown in their study of 14 right-handed patients with left-hemispheric tumors, comparing fMRI activation on naming and verb generation tasks with DECS results, that high variability in extent and locations of activation was present on both tasks, and overall imperfect correlation with DECS results was noted (23). The activated areas were located mainly in the left hemisphere in the middle and inferior frontal gyri, the superior and middle temporal gyri, and the supramarginal and angular gyri—typical areas seen on fMRI language activation tasks (23). Specifically, using $p < 0.005$ statistical threshold in frontal and temporoparietal areas, they found that sensitivity of the fMRI technique for the naming task was only 22% and for the verb generation task 36% (23). The specificity for fMRI was much higher—97% for the naming task and 98% for the verb generation task (23). Combining the two fMRI tasks, however, greatly increased the sensitivity (59%) while maintaining similar specificity (97%) (23). By using a less conservative statistical threshold of $p < 0.05$, higher sensitivity (66%) was achieved with only a minor reduction in specificity (91%) (23). Postoperative fMRI data (for cortical regions studied intraoperatively

with DECS) were in accordance with DECS results for six of eight patients, and complete agreement between pre- and postoperative fMRI results and DECS results was seen in only three of the eight patients in this series (23). Of course, one reason for the relatively poor correlation may have been the use of suboptimal language fMRI tasks in this series. In our experience, neither the naming nor the verb generation task has been particularly useful for language lateralization or localization because of the widely distributed nature of activated cortical regions on the naming tasks and the lack of adequate patient monitoring capability for the verb generation task.

Figure 10 demonstrates how we have internally validated fMRI at our institution through correlation of fMRI results with intraoperative cortical stimulation mapping results. This figure specifically shows how we can map the receptive speech cortex intraoperatively and visualize the corresponding fMRI activation in Wernicke’s area in a patient with a parietal lobe tumor.

In reality, prospective multicenter studies using identical paradigms and stimulus delivery systems, identical MRI scanner hardware and software, as well as standardized data processing and statistical analysis methods, and ample collection of normative data will be necessary to truly validate a variety of language fMRI paradigms for routine clinical use (24–26). Such multicenter studies are in progress and more are being formulated at present. When we obtain the aggregate results of such multicenter studies, hopefully the evidence will promote the integration of this presurgical language-mapping technique into the preoperative-planning algorithm at virtually every academic center in the nation. Currently, however, only

a small (but growing) number of centers perform these clinical studies routinely.

However, despite the fact that intraoperative cortical stimulation mapping and Wada testing are considered to be “gold standards” for language cortex localization and hemispheric language lateralization, respectively, these are far from perfect gold standards. For example, both are limited by the effects of sedation, which can obviously impair cognitive function. In addition, Wada testing only provides lateralization information and does not provide any localization information. Similarly, intraoperative standard cortical surface mapping approaches are limited in resolution and often do not allow adequate evaluation of cortex at the depth of sulci (although newer micro-electrode approaches and ultrasonic aspiration white matter tracking methods have overcome some of the limitations of standard cortical surface mapping approaches) (27). In addition, intraoperative mapping is clearly limited by the extent of craniotomy exposure and does not allow bihemispheric (whole brain) evaluation.

In addition, false negatives have been reported with intraoperative cortical stimulation mapping; for example, Shinoura et al. have shown in their study of six patients with brain tumors within or near the primary motor cortex that DECS demonstrated the location of the primary motor cortex in only five of six cases, whereas fMRI demonstrated the location in all six (28). Furthermore, in their study, intraoperative mapping provided equivocal information regarding the cortical representation of motor territories; specifically, during evaluation of cortical regions in close spatial proximity to the tumor margins, the motor representation areas were detected in only one of the six cases (28). In contrast, motor representation areas in close proximity to the tumor were detected by fMRI in four of six cases (28). Thus, intraoperative cortical stimulation mapping may actually have a low sensitivity for the detection of motor function in areas adjacent to brain neoplasms (28). Others, such as Bittar’s group have also reported false negatives with DECS (29).

Whole brain coverage and absence of sedation effects are major advantages of fMRI over these more invasive techniques. Although fMRI may effectively replace the Wada test for language lateralization (already established for this purpose at a number of centers around the country), it may not be ready for complete replacement because its utility for memory lateralization has not been fully established and clinically accepted. A number of centers, however, do use fMRI for memory lateralization as well, and internal validation of their memory activation paradigms through correlation with postsurgical memory outcome has been performed (30–33). Thus, overall, few centers have currently replaced the Wada test with fMRI, although in the near future such replacement may become a reality at a greater number of academic centers.

POTENTIAL PITFALLS OF LANGUAGE MAPPING WITH fMRI

fMRI does have some limitations of its own, and the neuroradiologist and neurosurgeon need to be aware of these to properly interpret the results of fMRI language-mapping studies. First of all, the recently described phenomenon of neurovascular uncoupling needs to be understood. This concept, which has been well described by Ulmer and colleagues at the University of Wisconsin, refers to the indirect nature of the BOLD response in terms of localization of actual neural activation (34,35). The BOLD principle describes the coupling of regional blood flow changes in the cerebral microvasculature (that are highly correlated with cognitive task performance) with actual neuronal activation in adjacent cerebral cortex. Any pathological process that alters regional hemodynamics can disrupt this coupling between the neural activity and the adjacent vascular response. This is particularly the case with brain tumors that may be responsible for angiogenesis/neovascularity or loss of normal vasoactivity. A similar scenario may be seen with arteriovenous malformations (AVMs) that may also alter regional hemodynamics. Thus, lesion-induced neurovascular uncoupling resulting in decreased fMRI activation in perilesional eloquent cortex, along with normal or increased activation in homologous brain regions, may falsely suggest contralateral hemispheric dominance and lesion-induced homotopic cortical reorganization (34,35). The solution to this problem is to use MR perfusion imaging (either dynamic susceptibility contrast perfusion imaging or arterial spin labeling approach can be used) to ensure that no significant alteration of perfusion within or adjacent to the lesion is present. If such substantial alteration of perfusion exists, then the interpretation of the fMRI activation map will be quite limited in terms of diagnostic value. If, on the other hand, no such substantial perfusion alteration is observed, then one can more confidently evaluate the activation maps without the concern regarding false-negative activation that may erroneously suggest presurgical homotopic reorganization (34,35).

In Lehericy’s series, 11 patients with left-hemispheric AVMs and 10 age-matched controls were studied with fMRI using verbal fluency, sentence repetition, and story listening tasks to determine whether cortical reorganization secondary to AVMs occurs and whether blood flow abnormalities associated with the AVMs may limit ability of the fMRI to correctly lateralize language function (36). While the controls all displayed typical left language dominance, only six patients demonstrated left-hemispheric dominance; five patients demonstrated right-hemispheric language lateralization, suggesting language cortical reorganization by fMRI (36). However, Wada results and/or postembolization fMRI in two of these five patients showed that the

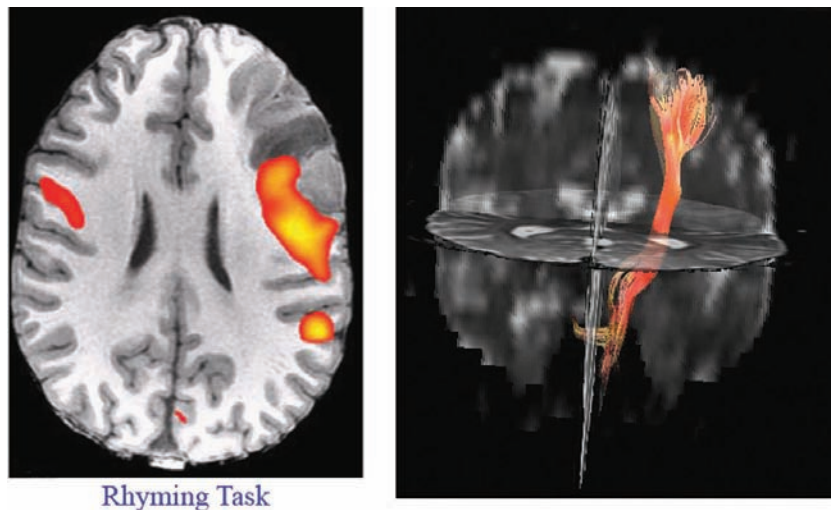


Figure 11 On the image on the left, expressive language activation is displayed in the left frontal lobe bordering on and extending into the left inferior frontal astrocytoma on a rhyming task, but the fiber-tracking (tractogram) image on the right shows an intact left corticospinal tract, unaffected by the infiltrating left frontal lobe tumor. This combined use of BOLD imaging and DTI (fiber-tracking) provides additional presurgical mapping information over either method alone. Thresholding for the rhyming task was at $p < 0.05$, and DTI was performed with 25 directions of diffusion encoding; both were obtained on a 3-T MRI system. Abbreviations: BOLD, blood oxygen level dependent; DTI, diffusion tensor imaging; MRI, magnetic resonance imaging.

abnormal laterality indices were at least partly secondary to severe flow abnormalities that likely impaired detection of BOLD signal (false negative activation) due to neurovascular uncoupling (36).

Another concern in presurgical language mapping is that underlying white matter tracts need to be assessed in addition to simply overlying eloquent cortex, since injury to these tracts by either pathologic processes or surgical intervention may result in similar neurological deficits as seen with cortical injury/resection. The integrity of these white matter tracts can be readily assessed with diffusion tensor imaging (DTI). While a full description of DTI and fiber-tracking (tractography) is beyond the scope of this chapter, Figure 11 shows how the combination of BOLD language cortical mapping and DTI may be useful for presurgical mapping in a patient with a left frontal glioma.

Some technical challenges often encountered in clinical fMRI involve patient motion artifacts and susceptibility artifacts, especially at higher field strengths (3T and beyond). A variety of methods to avoid or minimize motion artifacts have been used by academic centers performing fMRI. Thermoplastic masks, head stabilizers with bite bars (see Figure 12 for an example), or styrofoam beads have been used to limit head motion. Often, the patient's head is simply strapped using tape just to remind the patient to keep his head perfectly still. MRI simulators have been helpful in alleviating patient anxiety, which secondarily often leads to patient head bulk motion.

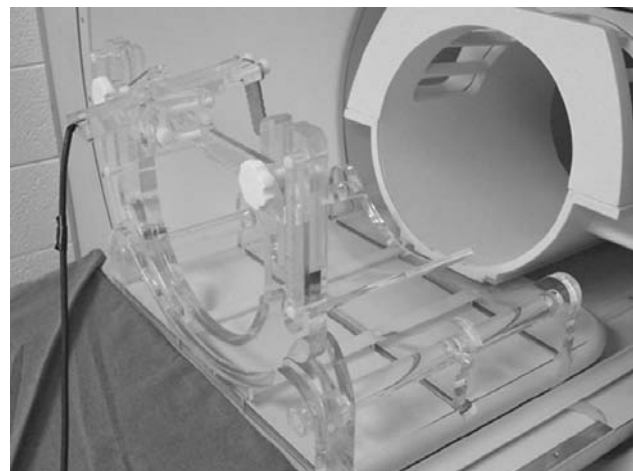


Figure 12 This is an example of a head stabilizer with a bite bar. Source: Photograph courtesy N. Yanasak, PhD, Medical College of Georgia/University of Georgia and UGA Human Neuroimaging Facility.

These simulators have been useful in borderline claustrophobic individuals and certainly in pediatric patients in that they have enabled the patients to acclimate to the high-acoustic noise of the typical high-field MRI scanner environment that tends to distract those who have never previously been inside the bore of a high-field MRI system. Real-time fMRI has been a recent advance that has become commercially available. Real-time fMRI is

usually not used for definitive data analysis but, rather, has been useful for determining endpoints for data collection to ensure that cumulative imaging data are adequate for a diagnostic clinical fMRI examination. Rotational and translational components of head motion can be plotted graphically on a millimeter scale to quantitate the degree of patient motion. If certain preestablished thresholds are exceeded during data acquisition, the study can be repeated before the patient actually leaves the MRI scanner table. Thus, real-time fMRI, which has recently been offered commercially by a number of MRI scanner vendors, particularly on their recent generation 3T systems, can help to minimize the number of technically suboptimal or nondiagnostic clinical fMRI examinations.

Magnetic susceptibility artifacts are also a major problem, particularly at very high field strengths and particularly when using single-shot echo GRE planar imaging, as is often the case in clinical fMRI. Ways to minimize susceptibility artifact in GRE images in general include reduction of slice thickness to decrease voxel size [shown to be effective in EPI also (37)] and reduction of echo time (TE) (38). In addition, rather than using GRE ssEPI for functional imaging, spiral imaging (especially spiral in/out) has been effective in reducing susceptibility artifacts (39). Multishot EPI is another approach that has been shown to be effective in improving BOLD fMRI by reducing such artifacts (40).

Furthermore, one needs to be aware of additional confounding variables that may affect BOLD contrast. For example, Hesselmann and colleagues noted in their study of 86 individuals that decreased intensity of activation in the left motor cortex occurs with increasing age, likely reflecting decreasing overall BOLD contrast with increasing age (41). In addition, Konrad and coworkers have shown in their study of 10 normal volunteers using block design and visually triggered sentence generation that clinical fMRI paradigm adaptation does not alter functional localizations but does change BOLD signal intensities and resultant hemispheric lateralization (42). Adaptation of cognitive paradigms (both stimulus presentation rate and degree of difficulty) to individual patient's cognitive capacities is often necessary in the clinical setting, and these investigators sought to determine the effects of such paradigm adaptation on BOLD language activation; they found that the most intense BOLD activations were obtained with either the highest stimulus presentation rate or with the maximum language production task (42).

BILINGUAL LANGUAGE REPRESENTATION

As the U.S. population becomes increasingly bilingual and multilingual with greater percentage of the population speaking languages other than English, greater interest in bilingual language processing has emerged. fMRI

provides an entirely noninvasive way of exploring bilingual language representation in the human brain. Specifically, the question of how one brain handles more than one language efficiently has been studied in some detail over the last decade. Numerous fMRI studies have explored the issue of language representation in bilingual individuals, in particular. While extensive discussion of these results is beyond the scope of this chapter, a few will be highlighted. Bilingual studies of language activation have generally demonstrated increased right-hemispheric (primarily frontal) activation in the nonnative language (L2) compared with the native language (L1).

Although most work with monolingual individuals using fMRI evaluation of language processing (semantic, phonological, and other subtypes of language processing) has demonstrated predominantly left-hemispheric areas of supratentorial activation, several studies show that poorly to moderately proficient late-acquisition bilinguals have a greater tendency to display right cerebral hemispheric activation in various language tasks. For example, in Dehaene's study of moderately fluent French (L1) and English (L2) bilingual subjects, these individuals listened to stories in both languages (43). In their study, left superior temporal sulcal activation was consistently seen during the L1 version of the language comprehension task, but variable bihemispheric activation (involving bilateral temporal and frontal regions) was seen during the L2 comprehension task (43). In addition, Calabrese's group has shown that while predominantly left prefrontal activation is present during both L1 and L2 processing in a word fluency paradigm right prefrontal activation is also present during L2 processing (44).

In a study of English-Mandarin bilinguals, Chee and colleagues noted bilateral inferior frontal activation in some subjects who were of low L2 proficiency and unilateral (left) prefrontal and parietal activation in others who were more proficient in L2; more proficient individuals thus displayed greater left lateralization (45). In a previous work conducted at our institution dealing with primary Spanish and secondary English speakers, we noted greater right-hemispheric activation (right frontal lobe activation) in the English version of the phonological (rhyming) task than with the Spanish phonological task (5). We, at least in part, attributed this observation to our subjects' moderate L2 proficiency or to the relatively late age at which they acquired their second language (5). In addition, the higher cognitive demands of task performance in L2 may account for the decreased lateralization of the supratentorial activation in L2 compared with L1 (5). A more recent work by Yokoyama and colleagues has shown that, in addition to proficiency in L2 and age of acquisition of L2, the complexity (in terms of grammatical construction) of language tasks also greatly affects fMRI activation patterns (46). In this group's study, brain

activation during processing of active and passive sentences in both L1 and L2 was studied in 36 Japanese-English bilinguals who were asked to determine whether a presented sentence was semantically plausible (46). They found that both L1 and L2 activated the left inferior frontal gyrus as well as the superior and middle temporal and parietal regions of the left hemisphere with greater activation in the pars triangularis, premotor area, and superior parietal lobule during presentation of passive sentences than active sentences in Japanese, but not in English (46). More importantly, their results suggested that, although late bilinguals in general use similar cortical regions to comprehend both L1 and L2, when they are presented with structurally complex sentences, the involvement of the regions differ between L1 and L2 (46).

Our group has shown that a divergence in fMRI activation topography existed in a cohort of highly educated Spanish-English bilinguals between semantic and phonological language tasks performed in their nonnative language (L2, English) but not in their primary language (L1, Spanish); this suggests that neural networks used for semantic and phonological language processing may be less similar in L2 than in L1 in moderate proficiency late acquisition Spanish-English bilinguals (5). Furthermore, we have shown that in a similar Spanish-English (L1-L2) bilingual cohort, English versions of the same noun-verb semantic association and phonological rhyming tasks produced greater left cerebellar hemispheric lateralization than the Spanish versions, although both resulted in left cerebellar hemispheric dominance in contradistinction to typical right cerebellar hemispheric dominance in monolinguals (47). The role of the cerebellum in language processing is thus not to be underestimated.

RESEARCH APPLICATIONS OF LANGUAGE fMRI AND FUTURE DIRECTIONS

A wide variety of research applications of language fMRI have been described in the cognitive neuroscience literature. Perhaps the most interesting applications have been in the realm of brain plasticity; some of this work relates to normal volunteers undergoing different learning processes. However, clinical fMRI research relating to brain plasticity has also been performed in patients with a variety of brain lesions, including infarcts, tumors, and AVMs.

For example, Holodny and colleagues have described a case of a patient with a left inferior frontal lobe glioma in which fMRI language paradigms have produced activation of a Broca's area homologue in the right frontal lobe in addition to expected activation in Wernicke's area in the left hemisphere (48). The authors suggest that tumor infiltration of the left frontal operculum resulted in language cortical reorganization with interhemispheric trans-

fer of the expressive speech area (Broca's area) to the right (48).

Vikingstad's group studied five right-handed adults with left-hemispheric AVMs involving language cortical (perisylvian) regions as well as right-handed stroke patients recovering from aphasia and right-handed normal controls with fMRI using silent picture naming and verb generation tasks (49). They found primarily right-hemispheric lateralization in the AVM group compared with left-hemispheric lateralization in the control group; interestingly, the right-hemispheric activation and overall rightward shift in language network (dominance) in the AVM group exceeded that of the stroke patient group in whom damage to left-hemispheric language areas occurred in adulthood (49). They suggested that their data provided evidence of effective plasticity in the developing human brain compared with the mature brain response to injury (49). Lazar and coworkers have also reported evidence, both from Wada testing with super-selective injections into the frontal and temporal lobes and from fMRI of interhemispheric transfer of language in patients with left frontal AVMs (50).

Some fascinating work has been conducted in the area of pediatric language plasticity. For example, Hertz-Pannier and colleagues have reported the case of a boy, who at an age of five years and six months developed intractable epilepsy secondary to Rasmussen's encephalitis of the left hemisphere (51). In the first fMRI study using a word fluency task, he demonstrated left-hemispheric language dominance (51). Following left hemispherotomy at nine years, and subsequent aphasia and alexia, the patient rapidly recovered receptive language, but slower and incomplete recovery of expressive speech and reading was noted (51). On a postoperative fMRI obtained at 10 years 6 months, shift of language dominance to the right hemisphere was observed on both expressive and receptive language fMRI tasks with activation in homologous regions (inferior frontal, temporal, and parietal cortex) to those seen preoperatively on the right; the authors suggest that reorganization within a preexisting bilateral language network occurred and further suggest that the classical limit for critical period of language acquisition may actually exceed six to seven years, contrary to conventional wisdom (51).

In addition, Yuan and coworkers have studied a group of 18 pediatric epilepsy patients as well as a normal age, gender, and handedness-matched control group of 18 individuals using a silent verb generation fMRI task (52). They found significant differences in laterality index between the two groups with a higher percentage of individuals displaying atypical (bilateral or right dominant activation) language representation in the epilepsy group as well as an association between language laterality index and duration of epilepsy (52). Furthermore,

they noted that while a trend toward increasing language lateralization with age was seen in normal controls, this association was not present in the epilepsy group (52).

Voets and coworkers have studied 12 right-handed patients with left temporal lobe epilepsy (LTLE) and 12 normal right-handed controls with a verbal fluency fMRI task (53). During a phonemic fluency task, while LTLE patients demonstrated activation in a significantly more posterior region of the right insula and frontal operculum than the controls, left inferior frontal gyral activation did not differ significantly (in both groups, the pars opercularis was primarily activated) (53). In both the groups, the areas activated in the right inferior frontal gyrus were not homologous to those involving the left inferior frontal gyrus (53). Furthermore, a patient with Rasmussen's encephalitis, fMRI studies using both phonemic and semantic tasks were performed both before and after left hemispherectomy (53). Both increased activation intensity and posterior shift of location of activation were seen in the right inferior frontal gyrus after the hemispherectomy (53). The authors conclude that left temporal lobe injury is associated with adaptive changes in the right inferior frontal gyrus related to expressive language function (53).

Liegeois and colleagues have reported their work with a series of 10 children and adolescents with intractable epilepsy and early childhood damage to the left hemisphere from a variety of lesions; in five cases, the lesions were adjacent to or within Broca's or Wernicke's areas, and in the remaining five, the lesions were distant to these regions (54). Using an fMRI covert verb generation task, they noted that in four of the five patients with lesions in or near Broca's area, perilesional activation was present without interhemispheric language reorganization; however, in four of the five individuals with lesions distant to the classical language areas, absence of left-hemispheric lateralization was observed (54). Overall, 5 of the 10 patients demonstrated bilateral or right lateralization, but eight were left-handed (54). Thus, the patterns of reorganization seen in these patients were not predictable (54).

Furthermore, many studies have explored poststroke plasticity in adults. Saur and colleagues, on the basis of their study of 14 patients with left middle cerebral artery (MCA) infarction with an auditory comprehension task and event-related fMRI design, have noted a triphasic recovery pattern (55). Specifically, initially, a pattern of markedly reduced activation in viable left-hemispheric language cortex was observed in the acute phase. In the subacute phase, substantial increase in bilateral language cortex was seen with peak activation in the right-hemispheric homologue of Broca's area (right inferior frontal gyrus) and the right supplementary motor area (SMA) that correlated with clinically improved language function (55). In the chronic phase, normalization of activation was noted with reshift of peak activation to

left-hemispheric areas (55). The authors suggested that these findings indicate a triphasic pattern of cortical reorganization, with initial upregulation and recruitment of contralateral hemispheric areas within a previously existing bilateral language network, followed by recruitment of ipsilateral perilesional areas within the same network during the chronic consolidation phase (55).

In a similar study, Fernandez and coworkers have described a case of a patient with conduction aphasia during the first year of stroke recovery (56). This group also studied a group of 10 healthy right-handed volunteers with repeated scanning to evaluate both intersubject robustness and intrasubject reproducibility (56). While the controls did not demonstrate any significant changes (good reproducibility of activation was noted at both the intersubject and intrasubject levels), the patient did display dynamic changes in activation that were most prominently seen during performance of a phonological language task: one month following the stroke, homotopic right-hemispheric activation was noted, but 12 months poststroke, substantial left-hemispheric perilesional activation was seen (56). These findings are consistent with those of Saur's group described above.

Heller and coworkers have also described a case of a 44-year-old man with a history of a left-hemispheric perinatal infarct and chronic epilepsy who underwent fMRI (57). The fMRI results demonstrated excessive right-hemispheric language activation with only mild left-hemispheric activation; the authors suggested that this finding is indicative of neonatal neuronal reorganization (57).

Additional types of brain language plasticity have also been described. For example, some of our own yet unpublished work in postsurgical motor and language plasticity utilizing fMRI has demonstrated atypical examples of patients ($n = 2$) with left hemispheric lesions who have demonstrated new right-hemispheric (frontal lobe) activation on semantic noun-verb association and phonological (rhyming) tasks in the postoperative setting that was maintained on follow-up postoperative scanning (58,59). This may be representative of (homotopic or interhemispheric) language cortical reorganization or unmasking of previously latent contralateral hemispheric neural networks. These changes in activation were also accompanied by clinical improvement of language function following initial postoperative aphasia. A similar finding of contralateral ipsilateral (to the hand used in the motor task) new activation was seen postoperatively in additional patients following cortical resection of tumors or epileptogenic tissue (58,59). In our series, in normal control subjects, no such substantial changes (and certainly no interhemispheric shifts) in activation were observed on repeated scanning using identical paradigms; this suggests that the changes in BOLD activation represent real adaptive changes and not simply apparent changes due to systematic error (58,59). Thus, language

fMRI may be able to demonstrate cortical functional adaptive changes occurring in response to a variety of brain insults. In the future, hopefully, fMRI will be able to serve as a useful method for not only documenting CNS plasticity, but also monitoring therapy, such as speech rehabilitation in patients recovering from a variety of neurological conditions.

REFERENCES

1. Ogawa S, Lee TM, Kay AR, et al. Brain magnetic resonance imaging with contrast dependent on blood oxygenation. *Proc Natl Acad Sci U S A*. 1990; 87(24):9868–9872.
2. Huettel SA, Song AW, McCarthy G. Statistical analysis. In: Huettel SA, Song AW, McCarthy G, eds. *Functional Magnetic Resonance Imaging*. Sunderland, MA: Sinauer Associates, Inc., 2004:159–184.
3. Friston KJ. Testing for anatomically specified regional effects. *Hum Brain Mapp* 1997; 5(2):133–136.
4. Huettel SA, Song AW, McCarthy G. Statistical analysis. In: Huettel SA, Song AW, McCarthy G, eds. *Functional Magnetic Resonance Imaging*. Sunderland, MA: Sinauer Associates, Inc., 2004:321–357.
5. Pillai JJ, Araque JM, Allison JD, et al. Functional MRI study of semantic and phonological language processing in bilingual subjects: preliminary findings. *Neuro Image* 2003; 19(3):565–576.
6. GE Brainwave software package, General Electric Medical Systems (GE Healthcare), Waukesha, Wisconsin, USA.
7. Loring DW, Meador KJ, Allison JD, et al. Now you see it, now you don't: statistical and methodological considerations in fMRI. *Epilepsy Behav* 2002; 3:539–547.
8. Powell HWR, Duncan JS. Functional magnetic resonance imaging for assessment of language and memory in clinical practice: review. *Curr Opin Neurol* 2005; 18(2):161–166.
9. Binder JR, Swanson SJ, Hammeke TA, et al. Determination of language dominance using functional MRI: a comparison with the Wada test. *Neurology* 1996; 46(4):978–984.
10. Lehericy S, Cohen L, Bazin B, et al. Functional MR evaluation of temporal and frontal language dominance compared with the Wada test. *Neurology* 2000; 54(8):1625–1633.
11. Brannen JH, Badie B, Moritz CH, et al. Reliability of functional MR imaging with word-generation tasks for mapping Broca's area. *AJNR* 2001; 22(9):1711–1718.
12. Ruge MI, Victor J, Hosain S, et al. Concordance between functional magnetic resonance imaging and intraoperative language mapping. *Stereotact Funct Neurosurg* 1999; 72(2–4):95–102.
13. Woermann FG, Jokeit H, Luerding R, et al. Language lateralization by Wada test and fMRI in 100 patients with epilepsy. *Neurology* 2003; 61(5):699–701.
14. Meneses MS, Rocha SF, Blood MR, et al. Functional magnetic resonance imaging in the determination of dominant language cerebral area. *Arquivos de Neuro-Psiquiatria Arq Neuropsiquiatr* 2004; 62(1):61–67. (Epub 2004 Apr 28, Portuguese).
15. Sabbah P, Chassoux F, Leveque C, et al. Functional MR imaging in assessment of language dominance in epileptic patients. *Neuroimage* 2003; 18(2):460–467.
16. Hertz-Pannier L, Gaillard WD, Mott SH, et al. Noninvasive assessment of language dominance in children and adolescents with functional MRI: a preliminary study. *Neurology* 1997; 48(4):1003–1012.
17. Bahn MM, Lin W, Silbergeld DL, et al. Localization of language cortices by functional MR imaging compared with intracarotid amobarbital hemispheric sedation. *AJR* 1997; 169(2):575–579.
18. Benson RR, FitzGerald DB, LeSueur LL, et al. Language dominance determined by whole brain functional MRI in patients with brain lesions. *Neurology* 1999; 52(4):798–809.
19. Rutten GJ, Ramsey NF, van Rijen PC, et al. Development of a functional magnetic resonance imaging protocol for intraoperative localization of critical temporoparietal language areas. *Ann Neurol* 2002; 51(3):350–360.
20. Hirsch J, Ruge MI, Kim KH, et al. An integrated functional magnetic resonance imaging procedure for preoperative mapping of cortical areas associated with tactile, motor, language, and visual functions. *Neurosurgery* 2000; 47(3):711–721.
21. Yetkin FZ, Mueller WM, Morris GL, et al. Functional MR activation correlated with intraoperative cortical mapping. *AJNR* 1997; 18(7):1311–1315.
22. FitzGerald DB, Cosgrove GR, Ronner S, et al. Location of language in the cortex: a comparison between functional MR imaging and electrocortical stimulation. *AJNR* 1997; 18(8):1529–1539.
23. Roux FE, Boulanouar K, Lotterie JA, et al. Language functional magnetic resonance imaging in preoperative assessment of language areas: correlation with direct cortical stimulation. *Neurosurgery*. 2003; 52(6):1335–1345; discussion 1345–1347.
24. Desmond JE, Annabel Chen SH. Ethical issues in the clinical application of fMRI: factors affecting the validity and interpretation of activations. *Brain Cogn* 2002; 50(3):482–497.
25. Stippich C, Heiland S, Tronnier V, et al. Functional magnetic resonance imaging: physiological background, technical aspects and prerequisites for clinical use. (German) *Rofo: Fortschritte auf dem Gebiete der Rontgenstrahlen und der Nuklearmedizin* 2002; 174(1):43–49.
26. Detre JA, Floyd TF. Functional MRI and its applications to the clinical neurosciences. *Neuroscientist* 2001; 7(1):64–79.
27. Roux FE, Boulanouar K, Ranjeva JP, et al. Cortical intraoperative stimulation in brain tumors as a tool to evaluate spatial data from motor functional MRI. *Invest Radiol* 1999; 34(3):225–229.
28. Shinoura N, Yamada R, Kodama T, et al. Intraoperative cortical mapping has low sensitivity for the detection of motor function in proximity to a tumor in the primary motor area. *Stereotact Funct Neurosurg* 2005; 83(4):135–141. (Epub 2005 Sep 6).
29. Bittar RG, Olivier A, Sadikot A, et al. False negatives with intraoperative cortical stimulation: elucidation with PET and fMRI. *Neurology* 1998; 50(4) (suppl 4): A193–A194.

30. Janszky J, Jokeit H, Kontopoulou K, et al. Functional MRI predicts memory performance after right mesiotemporal epilepsy surgery. *Epilepsia* 2005; 46:244–250.
31. Rabin ML, Narayan VM, Kimberg DY, et al. Functional MRI predicts post-surgical memory following temporal lobectomy. *Brain* 2004; 127(pt 10):2286–2298.
32. Richardson MP, Strange BA, Thompson PJ, et al. Pre-operative verbal memory fMRI predicts post-operative memory decline after left temporal lobe resection. *Brain* 2004; 127(pt 11):2419–2426.
33. Kloppel S, Buchel C Alternatives to the Wada test: a critical view of functional magnetic resonance imaging in preoperative use. *Curr Opin Neurol* 2005; 18(4):418–423.
34. Ulmer JL, Krouwer HG, Mueller WM, et al. AJNR Am J Pseudo-reorganization of language cortical function at fMRI imaging: a consequence of tumor-induced neurovascular uncoupling. *Neuroradiol* 2003; 24(2):213–217.
35. Ulmer JL, Hacein-Bey L, Mathews VP, et al. Lesion-induced pseudo-dominance at functional magnetic resonance imaging: implications for preoperative assessments. *Neurosurgery* 2004; 55(3):569–579. (discussion 580–581).
36. Lehericy S, Biondi A, Sourour N, et al. Arteriovenous brain malformations: is functional MR imaging reliable for studying language reorganization in patients? Initial observations. *Radiology* 2002; 223(3):672–682.
37. Sorensen AG. Advancements in MRI scanner technology lead to improved functional imaging. *Electromedica* 2000; 68:112–115.
38. Port JD, Pomper MG. Quantification and minimization of magnetic susceptibility artifacts on GRE images. *J Comput Assist Tomogr* 2000; 24(6):958–964.
39. Glover GH, Law CS. Spiral-in/out BOLD fMRI for increased SNR and reduced susceptibility artifacts. *Magn Res Med* 2001; 46:515–522.
40. Menon RS, Thomas CG, Gati JS. Investigation of BOLD contrast in fMRI using multi-shot EPI. *NMR Biomed* 1997; 10:179–182.
41. Hesselmann V, Zaro Weber O, Wedekind C, et al. Age related signal decrease in functional magnetic resonance imaging during motor stimulation in humans. *Neurosci Lett* 2001; 308(3):141–144.
42. Konrad F, Nennig E, Ochmann H, et al. Does the individual adaptation of standardized speech paradigms for clinical functional magnetic resonance imaging (fMRI) affect the localization of the language-dominant hemisphere and of Broca's and Wernicke's areas. (German) *Fortschritte auf dem Gebiete der Rontgenstrahlen und der Nuklearmedizin* 2005; 177(3):381–385.
43. Dehaene S, Dupoux E, Mehler J, et al. Anatomical variability in the cortical representation of first and second language. *Neuro Report*; 1997; 8:3809–3815.
44. Calabrese P, Neufeld H, Falk A, et al. Word generation in bilinguals—fMRI study with implications for language and memory processes (German). *Fortschritte der Neurologie-Psychiatrie* 2001; 69(1):42–49.
45. Chee MW, Hon N, Lee HL, et al. Relative language proficiency modulates BOLD signal change when bilinguals perform semantic judgments. *Neuroimage* 2001; 13(6 pt 1): 1155–1163.
46. Yokoyama S, Okamoto H, Miyamoto T, et al. Cortical activation in the processing of passive sentences in L1 and L2: an fMRI study. *Neuroimage* 2006; 30(2):570–579.
47. Pillai JJ, Allison JD, Sethuraman S, et al. Functional MR imaging study of language-related differences in bilingual cerebellar activation. *AJNR Am J Neuroradiol* 2004; 25(4): 523–532.
48. Holodny AI, Schulder M, Ybasco A, et al. Translocation of Broca's area to the contralateral hemisphere as the result of the growth of a left inferior frontal glioma. *J Comput Assist Tomogr* 2002; 26(6):941–943.
49. Vikingstad EM, Cao Y, Thomas AJ, et al. Language hemispheric dominance in patients with congenital lesions of eloquent brain. *Neurosurgery* 2000; 47(3):562–570.
50. Lazar RM, Marshall RS, Pile-Spellman J, et al. Interhemispheric transfer of language in patients with left frontal cerebral arteriovenous malformation. *Neuropsychologia* 2000; 38(10):1325–1332.
51. Hertz-Pannier L, Chiron C, Jambaque I, et al. Late plasticity for language in a child's non-dominant hemisphere: a pre- and post-surgery fMRI study. *Brain* 2002; 125(pt 2): 361–372.
52. Yuan W, Szaflarski JP, Schmithorst VJ, et al. fMRI shows atypical language lateralization in pediatric epilepsy patients. *Epilepsia* 2006; 47(3):593–600.
53. Voets NL, Adcock JE, Flitney DE, et al. Distinct right frontal lobe activation in language processing following left hemisphere injury. *Brain* 2006; 129(pt 3):754–766. (Epub 2005 Nov 9).
54. Liegeois F, Connelly A, Cross JH, et al. Language reorganization in children with early-onset lesions of the left hemisphere: an fMRI study. *Brain* 2004; 127(pt 6):1217–1218.
55. Saur D, Lange R, Baumgaertner A, et al. Dynamics of language reorganization after stroke. *Brain* 2006; 129(pt 6): 1371–1384.
56. Fernandez B, Cardebat D, Demonet JF, et al. Functional MRI follow-up study of language processes in healthy subjects and during recovery in a case of aphasia. *Stroke* 2004; 35(9):2171–2176.
57. Heller SL, Heier LA, Watts R, et al. Evidence of cerebral reorganization following perinatal stroke demonstrated with fMRI and DTI tractography. *Clin Imaging* 2005; 29(4): 283–287.
58. Pillai JJ, Allison JD, Fick JR, et al. Functional MR Imaging of Postsurgical Language Plasticity Following Brain Tumor Resection. Paper 217, p.166. Proceedings, American Society of Neuroradiology 42nd Annual Meeting, Seattle, WA, 2004, June 9, (abstract). [Supported in part by grant support from the Radiological Society of North America (RSNA/Philips Medical Systems 2000 Seed Grant)].
59. Pillai JJ, Allison JD, Fick JR, et al. Functional MR Imaging Evaluation of Postsurgical Motor Plasticity. Paper 218, pp.166–167. Proceedings, American Society of Neuroradiology 42nd Annual Meeting, Seattle, WA, 2004, June 9, (abstract). (Supported in part by a RSNA/Philips Medical Systems 2000 Seed Grant).

6

Vision and Higher Cortical Function

SONIA GILL, JOHN ULMER, and EDGAR A. DEYOE

Department of Radiology, Medical College of Wisconsin, Milwaukee, Wisconsin, U.S.A.

INTRODUCTION

Vision is the ability to infer the attributes of objects in the visual scene from an analysis of the light patterns imaged in the eyes. From relatively simple visual cues such as luminance and spectral contrast, orientation, motion, and binocular disparity, the visual system infers complex three-dimensional attributes such as shape, texture, location, and trajectory. Ultimately, vision is an active process in which particular details of the visual scene are selected and passed into our awareness and memory as needed for the visual task at hand or as dictated by their novelty and salience. The advent of advanced neuroimaging techniques has made it possible to visualize various aspects of both the anatomy and function of visual system pathways and, more recently, to use this information in a clinical context to aid the diagnosis and treatment of patients with pathologies affecting the visual system. However, optimal use of such detailed information depends on a more advanced awareness of the functional principles of visual system organization and the effect of those principles on neuroimaging results. For example, neuroimaging in humans has revealed the existence of well over a dozen visual areas extending throughout the entire occipital lobe and into adjacent portions of the parietal and temporal lobes. Clinically, this means that visual function once thought to be confined to a small portion of the medial occipital lobe is far more widely distributed than previ-

ously thought. Accordingly, we now know that vision is not unitary. In a sense, there are multiple visual systems existing as subcomponents of the overall network of areas and pathways. The purpose of this chapter, then, is to review select principles of visual system organization that are particularly relevant for obtaining and interpreting modern neuroimaging data in a clinical context. We will discuss the application of these principles to the imaging of patients who suffer from focal brain pathology or who will undergo treatment that impacts central visual system function. We also provide practical recommendations concerning tasks and methods that can optimize imaging results and aid their interpretation in a clinical context.

PRINCIPLES OF VISUAL SYSTEM ORGANIZATION RELEVANT TO CLINICAL NEUROIMAGING

Visual Field Maps (retinotopy)

The “visual field” is that portion of the world that, at any instant, is imaged onto the retina by the optics of the eye. Since each eye has a slightly different view of the world, the visual field consists of a binocular portion that is viewed simultaneously by both eyes and supports stereoscopic vision, plus two monocular portions at the lateral periphery of the field that are only seen by each eye alone. Because of the optics of the eye, there is a direct

correspondence between points in the visual field and points in the image on the retina (albeit upside down and backwards due to the optical properties of the cornea and lens). The regular geometric array of photoreceptors in the eye(s) then converts the retinal light pattern into neural signals that preserve the spatial arrangements of points in the visual field. This retinotopic organization of the photoreceptor cells and their signals is then preserved at subsequent stages of neural processing within the visual system thus producing a neuroanatomical map of the visual field at each level. Clinically, damage to a part of the neuronal map in, say, the optic radiations or primary visual cortex will result in blindness in the corresponding portion of the visual field (Fig. 1). Conversely, visual stimulation of a specific location in the visual field will cause activation of the corresponding location within the neuronal maps. In this way, functional neuroimaging (e.g., fMRI) can be used to visualize the neuronal maps at different anatomical levels in the brain. Clinically, this can be used to identify brain maps that are critical for vision and that may be at risk if surgery is required to remove a nearby tumor or other focal pathology.

The general principle of retinotopic organization leads to a variety of more detailed corollary principles. Traditionally, careful neurological examination of a patient's visual field deficits (scotomata) combined with detailed knowledge of the functional anatomy have been used to infer the location and extent of visual system lesions. Since lesions of both gray matter and white matter can cause field defects, knowledge of both is helpful. Today functional neuroimaging techniques can provide additional patient-specific information about both gray matter

function (functional MRI, fMRI) and white matter integrity (diffusion tensor imaging, DTI). For neuroimaging purposes, important details of retinotopic organization are as follows.

1. There are both cortical and subcortical sites that are visually responsive and retinotopically organized. The basic anatomy of the primary pathways for conscious visual perception is outlined in Figure 1. Approximately 90% of axons from each retina pass through the optic nerves and optic chiasm to ultimately terminate in the lateral geniculate nucleus (LGN) of the thalamus, while the remaining 10% of axons transmit information to other brain systems that control the pupil of the eye, regulate circadian rhythms, and mediate subcortical control of eye movements (1).
2. The entire visual field of each eye is mapped within the fibers of its corresponding optic nerve, but at the optic chiasm, these fibers split so that each half of the visual field (left and right) is mapped to the opposite (contralateral) side of the brain. The visual maps in each half of the brain thus represent the contralateral half of the visual field, not the contralateral eye. Fibers representing the corresponding hemifield from each eye then pass through the optic tract to the LGN. From there, they pass through the optic radiations to the primary visual cortex of the occipital lobe.
3. In the optic radiations, superior fibers representing the inferior field tend to project directly posterior to the occipital lobe. However, inferior fibers representing

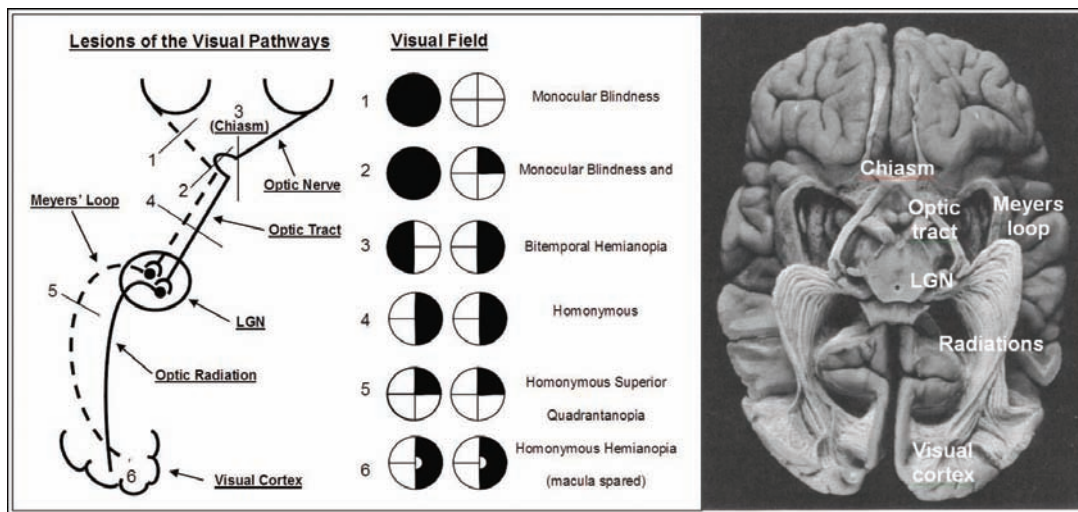


Figure 1 Visual field deficits associated with lesions of subcortical and early cortical visual pathways responsible for visual perception. Right: Anatomical dissection of visual pathways showing key subcortical structures especially the optic radiations with Meyer's "loop" that curves into the temporal lobe in the intact brain. Abbreviation: LGN, lateral geniculate nucleus. Source: From Ref. 55 and 5.

the superior field tend to swing anteriorly into the temporal lobe as “Meyer’s loop” before turning sharply posterior to the occipital lobe (2) (Fig. 1). (Meyer’s “loop” is actually a sharp bend in the more inferior portions of the continuous sheet of fibers that make up the radiations, not a loop with a hole in the middle.) This odd anatomical arrangement explains the upper visual field defect commonly associated with temporal lobe lesions or resections that transect “loop” fibers (3,4). Also the sharp bend in “loop” fibers tends to make them resistant to being accurately imaged with DTI and DTI-based fiber tracking. Sweeping posteriorly, radiation fibers representing both upper and lower visual field condense to form the lateral walls of the posterior ventricles. In contrast to Meyer’s loop, the fibers at this point can be readily visualized with DTI (Fig. 2).

4. In the occipital lobe, the radiations fan out across the calcarine fissure to form the first of several cortical maps of the visual field. This first map within primary visual cortex (a.k.a. V1, striate cortex) is characteristically “upside down and backwards” with the left visual field in the right hemisphere and the upper visual field in the lower banks of the sulcus (and vice versa).
5. The center of gaze (fovea) is represented at or near the posterior tip of the occipital lobe with the far peripheral field represented anteriorly near the junction of the calcarine and parieto-occipital sulci. However, there is a major distortion in this map in that portions of the field increasingly close to the center of

gaze are increasingly “magnified.” For example, the foveal region ($\sim 0^\circ$ – 5°), which occupies less than 1% of the retinal surface area, encompasses the posterior 40% of the primary visual cortex, reflecting the critical importance of foveal vision (5). In contrast, the most anterior 10% of primary visual cortex represents the entire monocular field (temporal crescent) extending from about 55° – 60° eccentricity to the edge of the field at roughly 90° – 100° . The clinical significance of “cortical magnification” is that large lesions of the posterior visual cortex can cause relatively small field defects that can be hard to demonstrate on confrontational neurological testing but can significantly impair visual functions such as reading that require high acuity vision. However, fMRI-based mapping of central versus peripheral field representations in the cortex can be readily accomplished and can help determine if a planned resection will impact central vision. Losses of large portions of the peripheral field are often well tolerated or can even go unnoticed unless the patient’s activities rely heavily on peripheral vision (e.g., truck driver).

Multiple Visual Areas and Pathways—Functional Specialization

As outlined in Figures 3 and 4, the visual system does not end in the calcarine sulcus. Beyond V1, there are multiple additional vision-related areas (numbering more than a

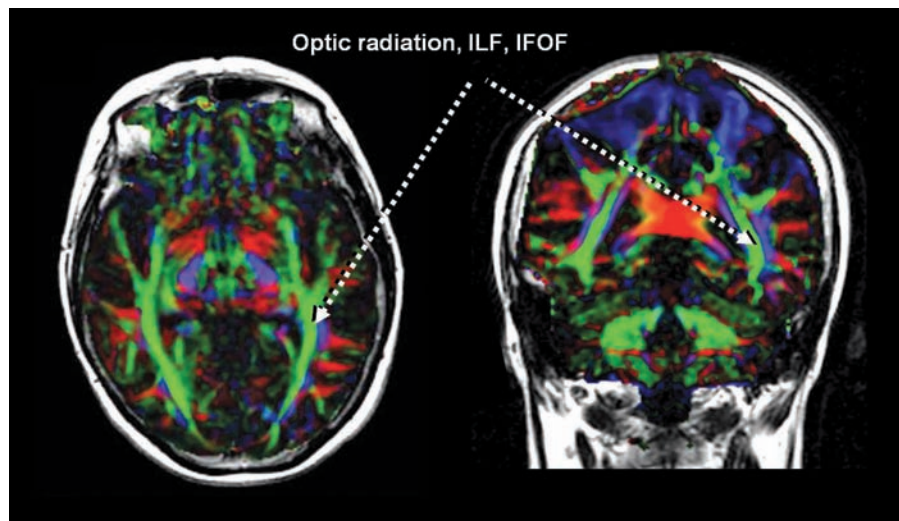


Figure 2 Optic radiations in color-coded orientation DTI maps. The fibers form a broad sheet, part of which sweeps directly backward from the LGN toward primary visual cortex in the occipital lobe (green fibers) and part of which loops into the temporal lobe before turning backwards (Meyer’s loop, not shown. See Fig. 1). This latter portion tends to be imaged poorly on DTI directional maps. Posteriorly, the optic radiations merge with the ILF and IFOF to form a compact bundle near the ventricular trigone. (Fiber orientation: green—rostral/caudal, red—left/right, blue—dorso/ventral.) Abbreviations: DTI, diffusion tensor imaging; LGN, lateral geniculate nucleus; ILF, inferior lateral fasciculus; IFOF, inferior fronto-occipital fasciculus.

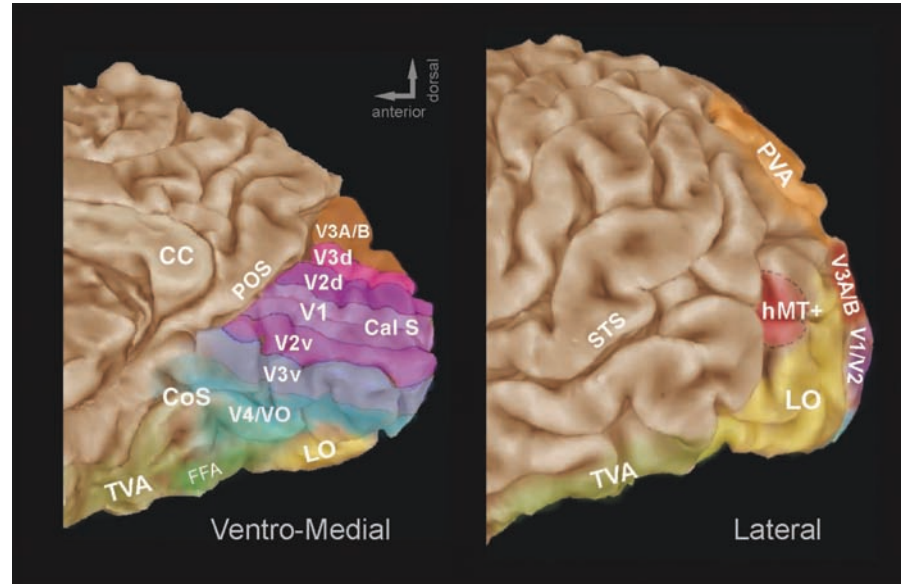


Figure 3 Schematic representation of human vision-related cortical areas. Left: ventro-medial view. Right: lateral view. These functionally defined visual areas do not correspond well to classical Brodmann areas or gyral anatomy with the exception of primary visual cortex, V1, which is identical to Brodmann's area 17 (striate cortex) located directly adjacent to the calcarine sulcus. Most cortical visual areas each contain a retinotopic map of the visual field though with decreasing precision at later stages of processing. Several of the individual areas designated here are known or suspected to contain multiple visual areas including V3A/B, V4/VO, LO, hMT+, TVA, and PVA. Nomenclature for different human visual areas is derived in part from monkeys (6) and *de novo* (56). Note that positions and sizes of each area can vary significantly from patient to patient. Abbreviations: V1, primary visual cortex; V2d and V2v, dorsal and ventral halves of the second visual area which together constitute a single retinotopic map; V3d and V3v, dorsal and ventral halves of the third visual area, though in macaques V3v is sometimes designated VP. V3A/B is distinct from V3 and probably contains two retinotopic maps. The region labeled here as V4/VO likely contains at least two retinotopic maps; FFA, fusiform face area is defined functionally and may be included within areas defined differently by some investigators; LO, lateral occipital complex, likely contains multiple maps, hMT+, middle temporal visual complex, a.k.a. V5 plus MST and possibly other small areas; MST, medial superior temporal area; PVA, parietal visual areas; TVA, temporal visual areas—Both of the latter zones likely contain multiple functional subdivisions but are only weakly retinotopic; Cal. S., calcarine sulcus; CC corpus callosum; CoS, collateral sulcus; POS, parieto-occipito sulcus; STS, superior temporal sulcus.

dozen, not all shown in Fig. 3) that, collectively, extend throughout the entire occipital lobe and into adjoining portions of parietal and temporal cortex (and even into frontal lobe “eye fields”). Most areas contain a more or less complete map of the visual field, albeit represented more coarsely at each successive level. Beyond medial occipital cortex (V1/V2), however, lesions may not produce localized blindness but rather a selective loss of some vision-related functions while sparing others depending on which areas and anatomical interconnections are affected.

The nomenclature for different areas of human visual cortex has been partly derived from the nomenclature used in macaque monkeys (6) and partly created *de novo* in the absence of clues to potential homology. This nomenclature largely ignores the traditional Brodmann classification of cortical areas because the anatomical distinctions used in that system largely fail to correspond to functional distinctions revealed by fMRI and other techniques

(though see Eickhoff, 2007 (7) for a modern approach to “functional histology”).

Conceptually, the different visual areas are interconnected “hierarchically” in that different groups represent successively higher stages of visual processing. But, they are also connected “in parallel” in that different areas within a hierarchical stage represent alternate concurrent, processing pathways (8) (Fig. 4). As one progresses hierarchically from “early” stages to “later” stages, the neurons explicitly encode progressively more complex and global features that begin to correspond more and more closely to the properties of objects and surfaces we consciously perceive. At the same time, different types of information contained within the patterns of light on the retina begin to be processed in different pathways that, beyond V1/V2, lead to a large-scale physical separation of cortical areas representing different visual properties such as color, shape, position, and movement. Consequently, lesions of visual areas at stages beyond medial occipital

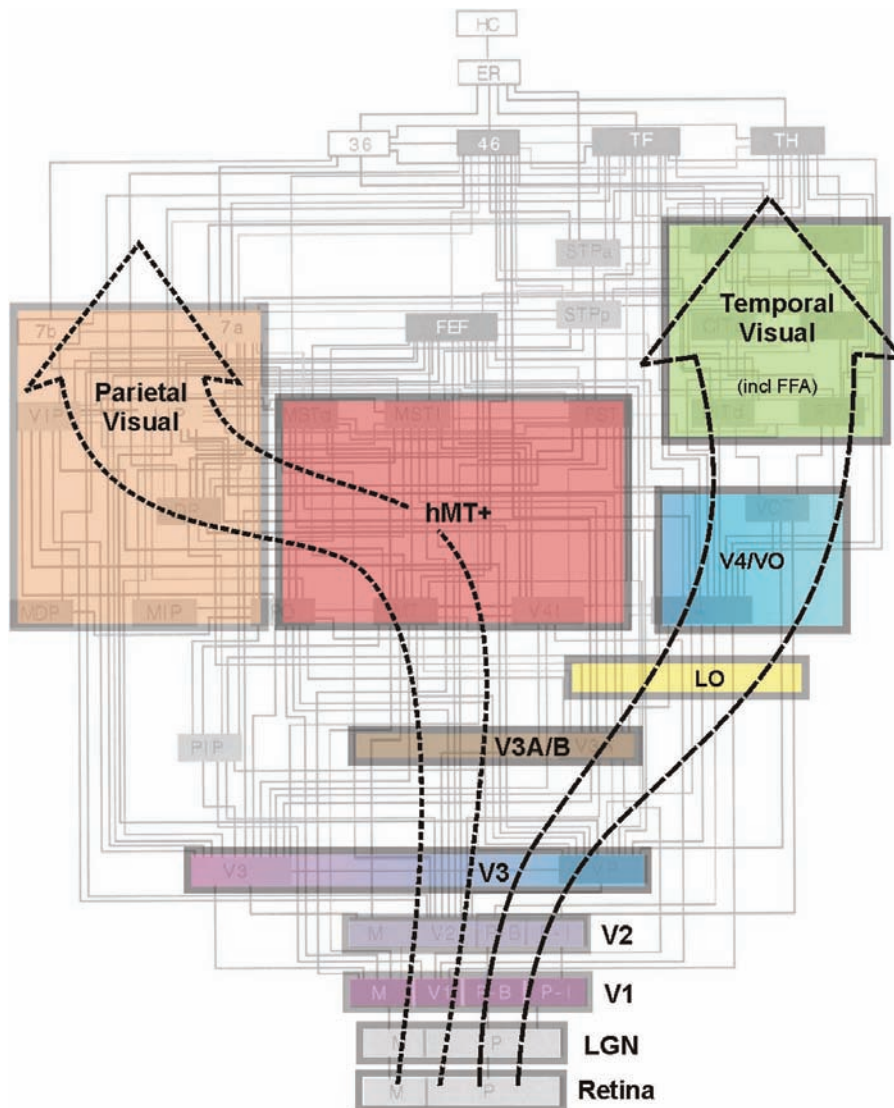


Figure 4 Simplified diagram of presumed visual processing streams in human cerebral cortex. Colored boxes indicate individual visual areas or groups of visual areas that have been identified in humans and correspond to those shown in Figure 3. (Sizes of boxes do not indicate relative physical size or functional importance.) Large dashed arrows indicate groups of areas that, by analogy with nonhuman primates, are likely to be interconnected to form two major visual processing streams feeding into parietal cortex (dorsal “what/how” stream) and temporal cortex (ventral “what” stream). Visual area boxes are overlaid on roughly corresponding portions of a connectional diagram of macaque monkey visual areas based on Felleman and Van Essen, 1991 (6) that provides an estimate of the two dozen+ visual areas and interconnecting pathways that eventually may be identified in humans, though departures from the macaque pattern are anticipated. Hierarchical positions of some human areas (e.g., V3A/B, LO) may differ from those shown. Each major stream has multiple functional substreams and the two streams have many cross-connections, so can interact heavily. Additional/alternate human areas have been proposed and the nomenclature of some areas can vary (see Fig. 3 for nomenclature used here). Abbreviation: LO, lateral occipital complex.

cortex can lead to selective deficits or visual agnosias such as prosopagnosia (inability to recognize faces), cerebral achromatopsia (brain-related color blindness), alexia (inability to read or understand written words), or akinetopsia (inability to perceive movement). Such selective deficits can lead to the misleading impression that there is a one-to-one relationship between individual visual areas

and the perception of individual visual properties (9,10). Hence, phrases such as “the face area,” “the color area,” the “movement area,” or the “word form area” have come into common parlance. While it is true that lesions of such areas can produce a selective deficit, this does not mean that fMRI with, say, a “visual motion” stimulus will only reveal activation of area hMT+, the human “movement

area". Rather, it will typically show activation of a group of areas representing many components of the extended network that extracts the three-dimensional trajectory of an object from the changing pattern of light falling on the retina. In this respect, it may be helpful to think of these cortical areas not as "centers" for particular functions but as critical processing stages that happen to be vulnerable to insult due to the particular hierarchical level and processing "stream" in which they are located. The perception of each visual property thus depends on a subnetwork involving more than one visual area, but not all of them. So, functions are at once both distributed and localized.

At the coarsest anatomical scale, occipital visual areas and pathways can be grouped rather loosely into two major streams, the dorsal stream extending from V1 into parietal cortex and the ventral stream extending from V1 into inferotemporal cortex (Fig. 4). There is a tendency for lesions of the dorsal stream to disrupt visual tasks involving guidance of actions directed toward objects within the visual field, whereas lesions of the ventral stream tend to disrupt identification tasks (11–13). Consequently, the two paths have been dubbed the "where" versus "what" systems, though this by no means captures their true functional complexity. Indeed, it has been proposed that operation of the dorsal stream to guide actions can occur without eliciting visual awareness whereas operation of the ventral stream may itself lead to visual awareness and memory (13). At a finer scale, individual visual areas in the human have been defined in part by retinotopy (see above) and in part by functional distinctions established by lesion effects or neuroimaging. The exact boundaries of many visual areas are difficult to identify precisely and in many instances remain open to future modification.

V1 is the first major stage of cortical visual processing. Virtually, all types of visual information are initially processed there and in the second visual area, V2, to which it is intimately connected. Within V1 and V2, different processing streams are intercalated on a microscopic scale, so that macroscopic lesions of V1/V2 produce virtually complete blindness in the affected portions of the visual field (scotomata). Beyond V1/V2, the processing of different types of information begins to segregate on a larger scale. A dorsally directed system consisting of V3A, hMT+, and other visual areas is heavily associated with the processing of visual motion. In humans, hMT+ may consist of a complex of subareas including medial superior temporal area (MST) and is located laterally near the temporoparieto-occipital junction at about the same dorsoventral level as the calcarine sulcus medially (14). (In macaques, area MT a.k.a. V5 is in the middle temporal lobe, hence its acronym.) Functionally it is one of the better defined extrastriate visual areas and can be activated by a wide variety of temporally dynamic visual stimuli but also responds to complex

relative motions (15) [but see Seiffert et al., 2003 (16)]. Lesions in hMT+ can cause a rare inability to perceive movement (17–19), a failure of ocular pursuit, and inaccurate saccades to moving targets (20). In monkeys, lesions of other components of the dorsal stream can cause optic ataxia or visually guided misreaching (21).

The ventrally directed stream extends from the occipital lobe into inferotemporal cortex (Fig. 4). At mid-level stages of this stream, there is a complex of visual areas whose boundaries and homology with monkey areas have been controversial (22). The areas labeled here as V4/VO are associated with color and form processing and are located in the posterior fusiform gyrus or anterior lingual gyrus in humans (23,24). Damage to this region can cause cerebral achromatopsia characterized by a loss of color vision with sparing of visual acuity (23,24). Just anterior to V4/VO is the "fusiform face area." Complex patterns, especially faces are analyzed here (25), and damage to this region can cause face agnosia (prosopagnosia). More generally, lesions near this same region, potentially involving the lateral occipital (LO) complex or other inferotemporal visual areas, produce visual object agnosias (26,27). Injury to this region in the dominant hemisphere can result in the inability to recognize words (alexia) (28,29), which is the written word analogue to visual object agnosia.

From a clinical neuroimaging perspective, functional mapping of individual components of these various systems has not been routine, in part because functional losses are typically less devastating than frank blindness, though still can be severe. Also, selective activation of these components [e.g., hMT+, fusiform face area (FFA)] require additional fMRI paradigms that, while effective, can be time consuming. Equally important, though, has been a general lack of awareness in the clinical community of the extent and functional complexity of visual cortex beyond V1/V2, but this can be expected to change as techniques for more detailed functional mapping become widely available and case reports demonstrating clinical utility become more prevalent.

Role of Visual Attention

Recent evidence shows quite dramatically that visual awareness can depend critically on visual attention (30,31). Without at least a brief (often unnoticed) shift of attention to an object, our awareness and memory of things and events in our world is highly generalized and fleeting. Moment by moment our attention jumps from place to place, typically following our incessant shifts of gaze. However, attention can be voluntarily directed toward objects in the periphery without moving the eyes, thus demonstrating that it can be controlled independently of eye movements. (To experience this, stare at

one word on this page while attempting to recognize other words or objects in the near and far periphery.) A network of areas involving parietal and frontal cortex as well as key subcortical structures (e.g., pulvinar of the thalamus) is thought to control both the reflexive and intentional allocation of attention (32,33). Projections from parietal cortex and the pulvinar to occipital visual areas provide a likely substrate for mediating the effects of attention on visual processing and perception (34). Indeed, damage to parietal cortex, typically on the right, can cause an impairment of attentional function, attentional neglect, that is often spatially localized to the left half of the visual world or to the left half of attended objects (35). Clinically, such attentional neglect can appear as a simple hemianopsia on automated visual field testing (e.g., Humphrey perimetry), and lesions of parieto-occipital cortex can lead to a complex mix of both attentional neglect and visual field scotomata that can be difficult to dissociate behaviorally. However, neuroimaging can distinguish between cortical signals that are driven by the visual properties of a stimulus and those that are driven by voluntary shifts of attention (36). In some patients, this can help unravel deficits that reflect a combination of both sensory and attentional effects. Neuroimaging has revealed spatially selective attentional modulation of virtually all areas of visual cortex (37). Surprisingly, the magnitude of attentional signals in some extrastriate visual areas can rival those evoked by a visual stimulus itself (36). Imaging has also shown that directing attention to a particular type of visual feature (e.g., blue objects) produces appropriate modulation of the corresponding cortical representations throughout the visual field (38,39). Visual memory for object features is probably stored in temporal lobe areas that are the ultimate targets of the ventral processing stream and that likely mediate complex pattern recognition (40) through a comparison of incoming visual information with visual memories stored there. Thus, attentional signals originating in the parieto-frontal network and its subcortical connections appear to both “select” visual information and “gate” its access to visual memory, thereby constituting a critical component of the object recognition process. Practically, this means that the control of visual attention during clinical imaging is an important factor in obtaining robust, reliable imaging results and that impairment of attention must be considered in conjunction with impairments of visual sensation and perception to correctly interpret imaging results.

CLINICAL APPLICATION OF VISION fMRI

Today, advanced neuroimaging is changing the way brain surgery is performed. Functional MRI (fMRI) mapping of eloquent cortex in and near a pathology site has been

established as a useful technique for assessing the risk of neurological impairment caused by surgical resection or endovascular treatment and can help guide a surgical approach (41). The proximity of eloquent cortex to a site of operable pathology can affect the selection of a surgical approach and can impact the placement of resection margins in order to preserve vital functions or to permit more aggressive extirpation in noneloquent areas. fMRI can also permit better preoperative counseling of patients for whom surgery-induced visual deficits may be unavoidable.

Practical Methodology for Clinical Imaging of Visual Cortex

From the forgoing discussion, it is obvious that lesions at different locations within the visual system can produce field defects and/or selective functional losses, depending on the pathways and visual areas affected and the portions of the constituent retinotopic maps damaged. Since vision-related structures extend throughout the entire occipital lobe and into adjoining portions of the parietal and temporal lobes, pathology- or treatment-induced vision deficits can be a consideration in a broader range of patients than just those with lesions of medial calcarine cortex. Mapping the extended network of multiple visual areas and distinguishing the representations of central versus peripheral vision cannot be accomplished by simply turning the lights on and off or by flashing a large checkerboard. Fortunately, detailed visual field mapping can be obtained very efficiently (<15 minutes) using a sequenced presentation of an expanding checkered annulus and a rotating wedge as outlined in Figure 5 (42,43). This figure also illustrates typical patterns of fMRI activation that are color coded to show which portions of the visual field maximally activate each cortical location (voxel). As described below, mapping both visual field eccentricity and angular position (clock angle) permits detailed comparison of the fMRI with behavioral perimetry and allows identification of multiple distinct visual areas. If appropriate for a particular patient, additional functionally specific tests using faces, words, complex motion fields, or volitional shifts of attention can be added to provide a more comprehensive mapping, albeit at the expense of additional imaging time.

Other practical considerations include control of gaze position through the use of a fixation marker at the center of the display, and use of a visual task requiring spatially controlled engagement of attention, the latter helps to ensure robust, reliable results. Use of a visual task is also mandatory for documenting patient compliance with the testing procedures, even if the task consists only of detecting brief dimming of the fixation marker and pressing a button in response. Such a record of task performance

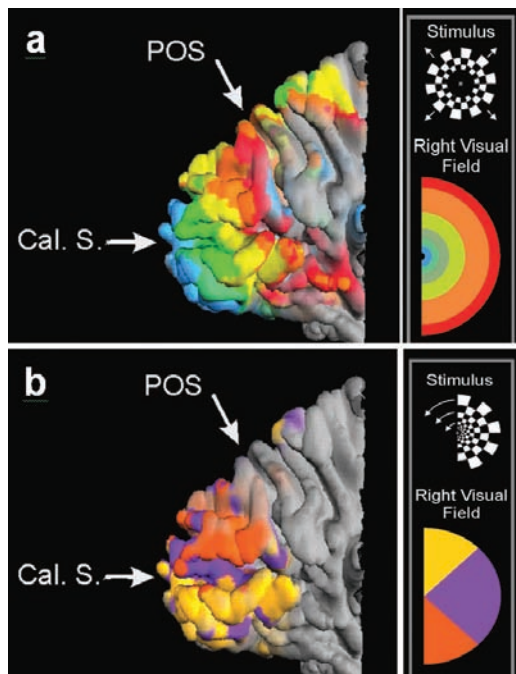


Figure 5 fMRI mapping of visually responsive cortex and its retinotopic organization. Right panels show annulus and wedge stimuli used to reveal brain maps (*left*) of visual field (**a**) eccentricity—distance from center of gaze (here to ~25° eccentricity) and (**b**) polar angle—clock position. Brain maps are shown displayed on surface maps of occipital lobe and neighboring portions of parietal and temporal lobes. Color codes indicate relative eccentricity of annulus or angle of wedge that maximally activated each voxel in cortex. In “a”, macular (*central*) vision is mapped to occipital pole (blue) with peripheral portions of visual field represented more anteriorly (orange/red). Note magnified representation of central vision in brain (*left*) compared with visual field (*right*). Polar angle mapping “b” shows superior visual field (yellow) represented ventrally and inferior visual field represented dorsally in V1. But note multiple representations of horizontal meridian (purple) indicating multiple visual field maps. Detailed analysis of such maps provides key evidence for the various visual areas indicated in Figure 3. Abbreviations: Cal. S., calcarine sulcus; POS, parieto-occipital sulcus.

can help assess changes in the patient’s alertness and can be used in conjunction with a self-rating of alertness by the patient following each MRI scan (scale: 1 asleep—5 most alert). Ultimately, video tracking of eye position can be used to further document task compliance and to identify changes in visual stimulation due to closure or drooping of the eyelids or due to losses of fixation.

Pretreatment Planning

Focal pathology or treatment-induced damage to the visual system can produce visual field scotomata that significantly impact a patient’s ability to use vision in

their daily activities. Vision deficits can prohibit the individual from reading or driving and may prevent employment, thereby significantly impacting the individual’s quality of life. The severity of this impact can vary with the portion of the visual field that is damaged. Involvement of the central 5°, especially in the right field, can be particularly devastating for reading and activities requiring high acuity (44–46). Deficits in more peripheral portions of the field, however, can go largely unnoticed or may be interpreted incorrectly by the patient as a nonvisual disorder [e.g., “I’m getting clumsier since I keep bumping into things” (that are not seen in the peripheral field.)] The actual impact for each individual will depend on his or her particular lifestyle and occupation (librarian—central vision, truck driver—central + peripheral vision). Consequently, some patients may tolerate peripheral field loss better than others. In such case, mapping the peripheral versus central field may allow a more aggressive, rather than less aggressive, resection. In addition to scotomata, functionally selective visual deficits due to damage of extrastriate or parietal areas also can impact quality of life. Prosopagnosia or word-form agnosia can be challenging for patients and their families, while severe deficits in visual attention (neglect) can be debilitating (35), with loss of both employment and overall independence.

While fMRI-based retinotopic- and function-specific mapping provide powerful tools for identifying viable gray matter that may be at risk from a planned treatment, damage to white matter connections can also induce functional deficits. In the visual system, this may involve damage to the incoming optic radiations, forward projecting corticocortical connections or “feedback” pathways from higher areas. DTI can permit visualization of these white matter tracts and should be performed routinely in conjunction with fMRI to provide a comprehensive risk assessment for pretreatment planning. Figure 6 illustrates DTI of a case in which resection of a left temporal glioblastoma multiforme (GBM) could have impacted vision by disruption of the optic radiations that, as seen in the figure, were compressed medially by the tumor margin.

Combining fMRI and DTI with other imaging data can provide an exceptionally detailed picture for treatment planning. Moreover, emerging evidence indicates that routine use of advanced neuroimaging techniques can significantly reduce the incidence of permanent neurological side effects (47,48). Figure 7 illustrates an example of a multiparameter imaging workup in which five types of data have been layered into a composite view of a grade II astrocytoma in the right occipital lobe of a 44-year-old female patient. The tumor bed has been highlighted by thresholding of a fluid attenuated inversion recovery (FLAIR) image superimposed upon a slightly transparent DTI image that, in turn, is overlaid on a standard TI-weighted spoiled, gradient-recalled (SPGR) anatomical

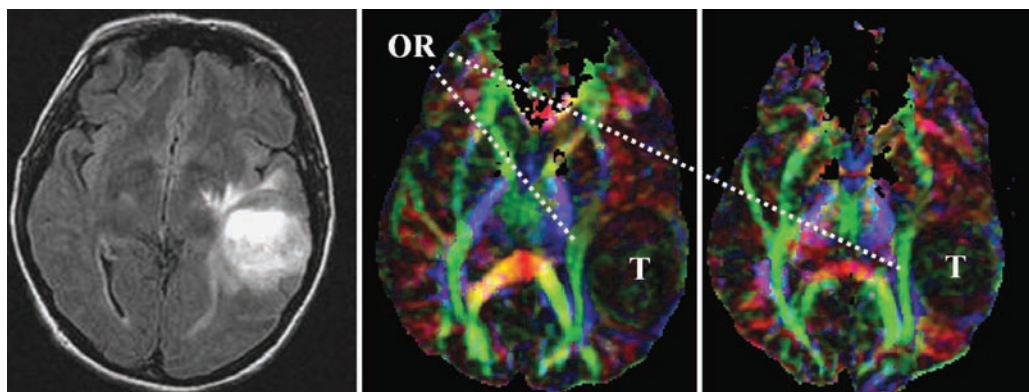


Figure 6 FLAIR image (*left*) and DTI directional maps (*right*) show a left temporal GBM in a 53-year-old female, contacting and medially displacing optic radiation (green in DTI). Despite the lack of proximity of the lesion to striate or extrastriate visual cortex, resection along the medial border of the tumor puts elementary visual function at risk. Abbreviations: GBM, glioblastoma multiforme; DTI, diffusion tensor imaging; FLAIR, fluid attenuated inversion recovery; OR, optic radiation; T, tumor.

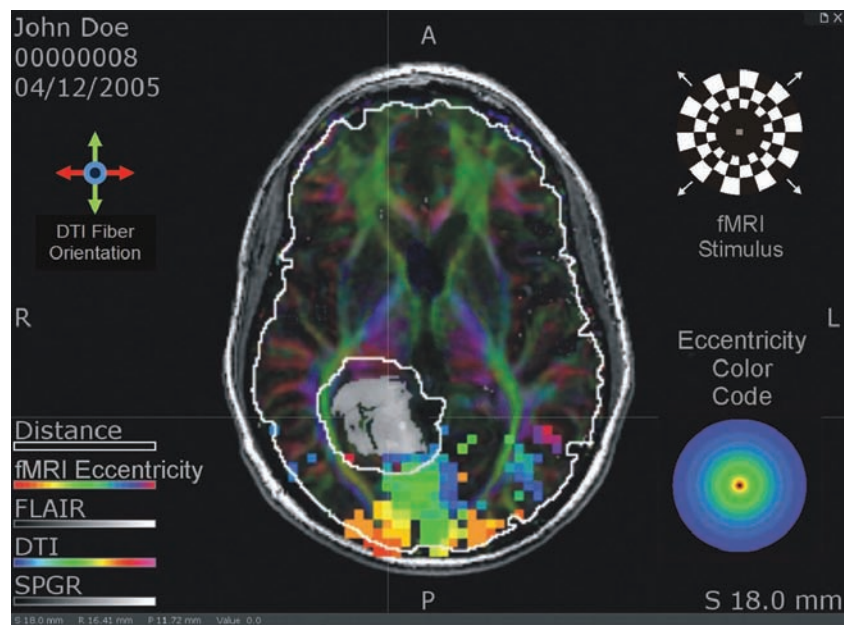


Figure 7 Grade II astrocytoma in the right occipital lobe of a 44-year-old female. Eccentricity fMRI map shows proximity of the posterior tumor border to eloquent cortex representing the peripheral visual field (blue and blue-green voxels). However, proximity of the optic radiations to lateral tumor border (green fibers in DTI) is of greater concern for surgery-induced vision deficit. White outline around tumor shows critical 5-mm distance within which structures have high probability of permanent damage from complete tumor resection. Upper right: schematic representation of stimulus for fMRI mapping. Lower right: fMRI color code indicating mean eccentricity of annulus that maximally activated each colored voxel. Note magnified cortical representation of fovea (red/orange voxels). Upper left: color code for DTI fiber orientation. Abbreviations: fMRI, functional magnetic resonance imaging; DTI, diffusion tensor imaging.

image. Optic radiation fibers shown in green pass laterally close to the tumor. fMRI mapping of visual field eccentricity using an expanding checkered annulus (upper right) reveals a map of blood oxygen-level dependent (BOLD) activation that is color coded to show the stimulus location that maximally activated each voxel (color code at bottom right). Voxels representing central vision are shown in red

with intermediate eccentricities in yellow/green and the periphery marked in blue. Finally, a distance algorithm was used to compute a three-dimensional “shell” around the tumor (indicated by white boundary) to help identify structures that were maximally at risk from resection of the tumor. Though the peripheral visual field represented near the posterior border of the tumor is clearly at risk

(blue fMRI voxels), the proximity of the optic radiations along the lateral border is probably of greater concern since a lesion there might interrupt fibers supporting foveal vision, thereby causing a severe vision deficit.

NEUROVASCULAR UNCOUPLING, DTI DROPOUT, AND REORGANIZATION

While advanced multiparameter neuroimaging can now provide an unprecedented level of information for the physician, a word of caution is necessary. BOLD fMRI contrast is based on changes in blood flow, volume, and oxygenation that are triggered by stimulus or task-induced changes in neuronal activity. However, focal pathology can itself alter vasoactivity, angiogenesis, arteriovenous shunting, and blood flow. Through chemical mediators and direct effects, lesion-induced alterations in oxygen extraction and cerebrovascular response can thus directly alter or destroy BOLD contrast while leaving the underlying neurons intact. This effect has been referred to generically as “neurovascular uncoupling” (NVU) to encompass virtually any disruption of the cascade of events that link neuronal activity to the BOLD vascular response. In the visual system, the presence of NVU can be detected by comparing the fMRI visual field mapping data with a conventional behavioral vision test (Humphrey perimetry) using a unique computational transform of the

fMRI data termed a “Functional Field Map” (FFMap). The construction of the FFMap from the fMRI data is outlined in Figure 8. Practically, the FFMap allows instant assessment of which parts of the visual field are capable of evoking an fMRI response in remaining eloquent cortex. In the absence of NVU, there should be a robust fMRI response in the FFMap (i.e., multiple circles) associated with all locations in the visual field that are associated with normal vision sensitivity. Figure 9, however, illustrates an example where an arteriovenous malformation in occipital visual cortex caused NVU (Fig. 9A). The FFMap shown in Figure 9B is a chart of the central 10° degrees of the patient’s visual field populated by circle symbols that each correspond to a single visually responsive voxel in the fMRI brain map. The position of each symbol indicates the visual field location that, when visually stimulated, maximally activated the corresponding voxel. The color of the circle encodes the magnitude of the fMRI response, and its size is a measure of the potential error in placing the symbol at a given location on the FFMap. Together, all the circles show which parts of the visual field evoked fMRI responses in visual cortex. In this case, stimulation of the right visual field produced activation in hundreds of voxels in the left hemisphere, but barely a dozen voxels were activated by stimulation of the left visual field. However, the Humphrey perimetry charts (Fig. 9C) show a left field deficit confined to the upper left quadrant (dark shading in Fig. 9C), but intact visual

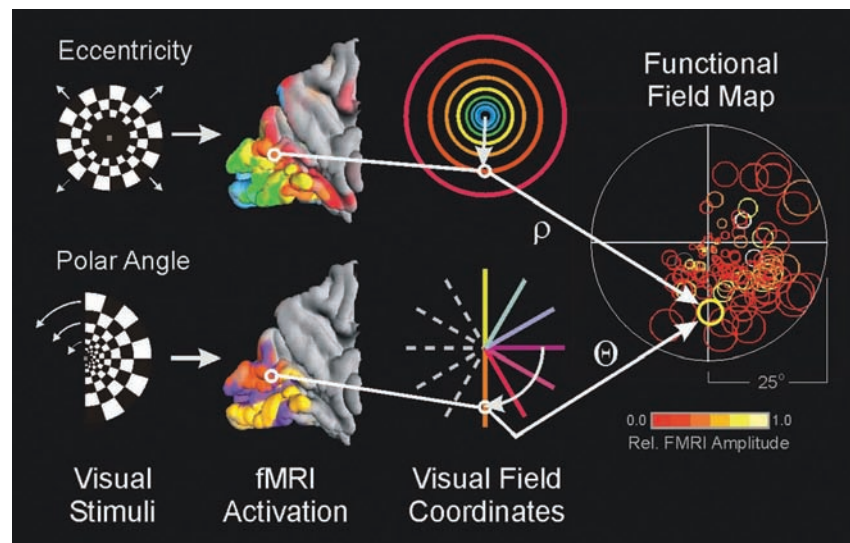


Figure 8 Creation of an FFMap. Left: Retinotopic organization of the occipital lobe is mapped using highly time-efficient stimulus paradigms. fMRI activation identifies the visual field location (eccentricity, polar angle) that maximally activates each brain voxel (brain map color code as in Fig. 5). This information is then used to construct a FFMap representing the visual field. Each circle symbol on the FFMap corresponds to a single brain voxel and shows the stimulus location that maximally activated it. The circle’s color encodes the relative fMRI amplitude, and its size is a measure of the potential error in placement. The FFMap allows the physician to instantly assess which portions of the visual field are associated with eloquent brain activation. FFMap locations lacking symbols are typically associated with scotomata—zones of blindness (e.g., upper left quadrant in figure). Abbreviations: FFMap, functional field map; fMRI, functional magnetic resonance imaging.

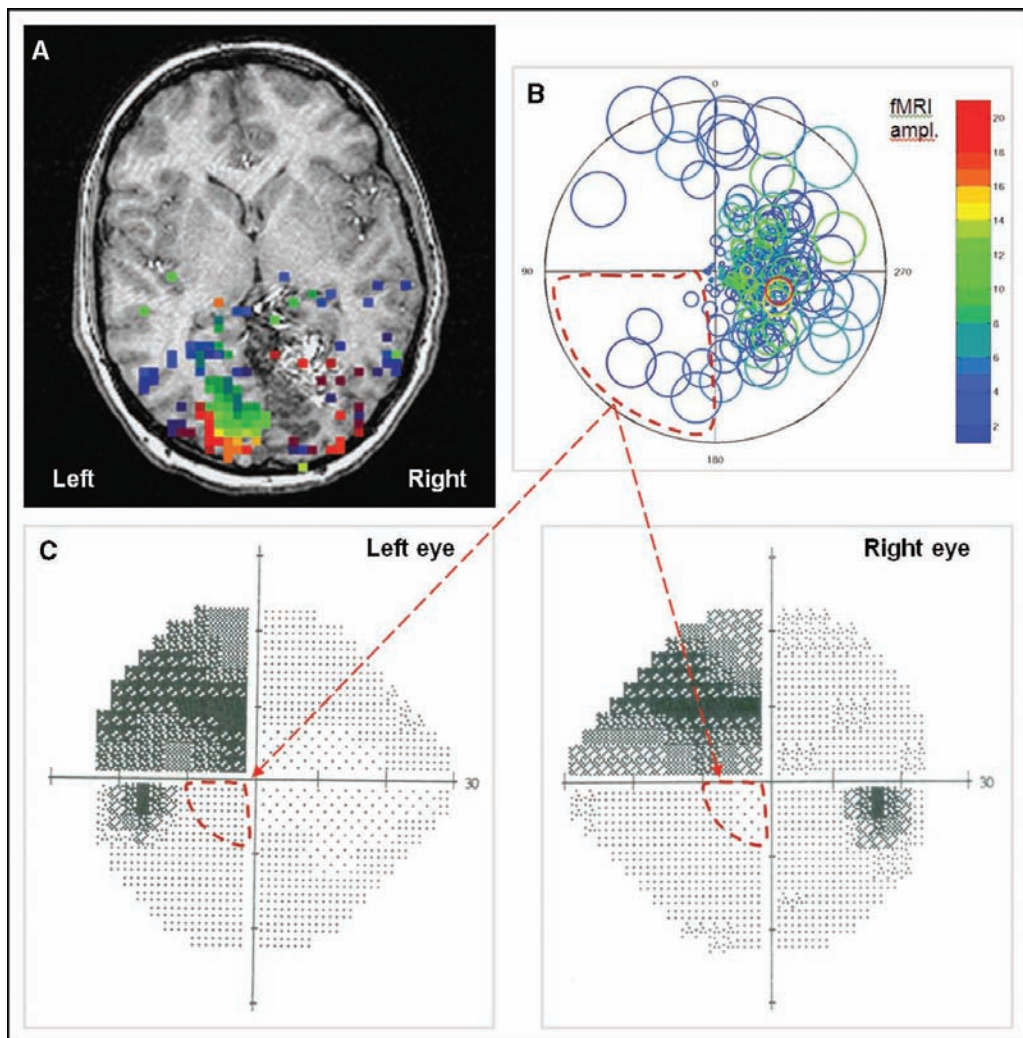


Figure 9 AVM-induced neurovascular uncoupling of the visual cortex. (A) fMRI eccentricity map overlaid on an SPGR image showing an AVM in right occipital lobe. (B) FFMap showing the central 10° of visual field that, when stimulated, evoked response in the visual cortex (see text and Fig. 8 for details). Note that the color code for fMRI amplitude is different from that used in Figure 8. (C) Behavior-based Humphrey perimetry of the central 30° of the visual field demonstrated a scotoma (dark shading) in upper left quadrant. Comparing FFMap to the perimetry revealed a poor fMRI response to lower left quadrant despite preserved vision (light stipple in perimetry chart) thereby identifying a zone of neurovascular uncoupling (red dashed lines). Note that for this patient the FFMap only encompasses the central 10° of the perimetry chart. Failure to appreciate the effect of neurovascular uncoupling could lead to the erroneous interpretation that right occipital cortex is largely unresponsive and could be surgically resected without risk to vision. Abbreviations: AVM, arteriovenous malformation; fMRI, functional magnetic resonance imaging; FFMap, functional field map; SPGR, spoiled gradient echo.

sensitivity in the lower left quadrant (except for the blind spot). Thus, the relative absence of fMRI activity in the intact lower left quadrant provides presumptive evidence for NVU. Clearly, this is important for surgical planning since the lack of an fMRI response in right occipital cortex could lead to the erroneous expectation that surgical resection of the arteriovenous malformation (AVM) would have little impact on the patient's vision.

An analogous type of error can occur with DTI. Current DTI techniques can fail to reveal individual white matter tracts in their entirety, even in healthy patients (49). For example, DTI of the optic radiations can be incomplete, especially within Meyer's loop where the fibers curve sharply into the temporal lobe. Temporal lobectomies for treatment of epilepsy often damage Meyer's loop, thereby causing a characteristic contralateral

“pie-in-the-sky” upper, quadrantanopsia (4,50) with variable invasion of the fovea. Reliably predicting the extent of such defects can be hampered by the vagaries of current DTI methods. Additionally, some pathologies may directly compromise water diffusion and/or the anisotropy on which DTI is based. At this juncture, it is not clear if this can cause a situation analogous to NVU in which there is a “dropout” of the DTI signal despite functional preservation of the white matter axons, though this seems plausible.

A final concern is the potential for lesion-induced reorganization of visual function. Lesion-induced reorganization with transfer of function to homologous regions of the opposite hemisphere has been reported for language and motor systems (51,52). However, there is little evidence that elementary visual function has the capacity for major reorganization, though the potential for some minor reorganization remains controversial (53). The potential for reorganization of higher visual functions is, as yet, poorly studied, and surgeons at the present time usually concentrate on preserving elementary visual function. In this context, the physician should be aware of the potential for “pseudoreorganization” in which there may appear to be a shift in the dominance of fMRI activation from one hemisphere to the other when, in fact, no actual shift in neural function has occurred. In some cases, this has been shown to reflect the effects of NVU causing a partial loss of fMRI activation in one hemisphere (54). Again, the use of visual field mapping in conjunction with behavioral perimetry can identify potential instances of such pseudoreorganization in the visual system.

CONCLUSION

fMRI of the visual cortex is a viable, noninvasive technique that can establish regional correlates of vision function within the human cortex. In combination with DTI and other types of medical imaging data, a detailed, comprehensive view of both the pathology and surrounding eloquent cortex can be provided. Additional postprocessing techniques can provide FFMaps that permit instant interpretation of the fMRI in terms of visual function and can permit detection of NVU. Use of these techniques, especially when optimally integrated into the clinical workflow, can provide better treatment outcomes with modest or minimal impact on patient throughput for the majority of cases. Though such refined techniques may seem moot for some patients with rapidly advancing, life-threatening tumors, it is important to recognize that this advanced technology can facilitate aggressive treatment while simultaneously preserving quality of life as much as possible for the patient. Certainly, it is likely that as

advanced imaging techniques and their potential benefits become more widely recognized, their use will be demanded both by patients and insurance companies seeking to minimize rehabilitation and maintenance costs.

ACKNOWLEDGMENT

This work was supported by NIH grants CA113186, EB00843 to E. DeYoe and NS052725 to J. Ulmer.

REFERENCES

1. Kline L. Anatomy and physiology of the optic tracts and lateral geniculate nucleus. In: Miller N, Newman N, eds. Walsh and Hoyt's Clinical Neuroophthalmology. 5th ed. Baltimore, MD: Williams & Wilkins, 1998.
2. Meyer A. The connections of the occipital lobes and the present status of the cerebral visual affections. *Trans Assoc Am Physicians* 1907; 22:7–15.
3. Hughes TS, Abou-Khalil B, Lavin PJ, et al. Visual field defects after temporal lobe resection: a prospective quantitative analysis. *Neurology* 1999; 53(1):167–172.
4. Tecoma ES, Laxer KD, Barbaro NM, et al. Frequency and characteristics of visual field deficits after surgery for mesial temporal sclerosis. *Neurology* 1993; 43(6): 1235–1238.
5. Horton JC. The central visual pathways. In: Hart WH, eds. Adler's Physiology of the Eye. St. Louis, MO: Mosby Year book, 1992:728–772.
6. Felleman DJ, Van Essen DC. Distributed hierarchical processing in the primate cerebral cortex. *Cereb Cortex* 1991; 1:1–47.
7. Eickhoff SB, Schleicher A, Scheperjans F, et al. Analysis of neurotransmitter receptor distribution patterns in the cerebral cortex. *Neuroimage* 2007; 34(4):1317–1330.
8. DeYoe EA, Van Essen DC. Concurrent processing streams in monkey visual cortex. *Trends Neurosci* 1988; 11(5):219–226.
9. Price CJ, Devlin JT. The myth of the visual word form area. *Neuroimage* 2003; 19(3):473–481.
10. O'Toole AJ, Jiang F, Abdi H, et al. Partially distributed representations of objects and faces in ventral temporal cortex. *J Cogn Neurosci* 2005; 17(4):580–590.
11. Ungerleider LG, Mishkin M, Goodale MA, et al. Two cortical visual systems. In: Ingle DJ, ed. *Analysis of Visual Behavior*. Cambridge, MA: MIT Press, 1982:549–586.
12. Pietrini P, Furey ML, Ricciardi E, et al. Beyond sensory images: object-based representation in the human ventral pathway. *Proc Natl Acad Sci U S A* 2004; 101(15): 5658–5663.
13. Goodale MA, Milner AD. Separate visual pathways for perception and action. *Trends Neurosci* 1992; 15(1): 20–125.
14. Zeki S, Watson JDG, Lueck CJ, et al. A direct demonstration of functional specialization in human visual cortex. *J Neurosci* 1991; 11(3):641–649.

15. Orban GA, Fize D, Peuskens H, et al. Similarities and differences in motion processing between the human and macaque brain: evidence from fMRI. *Neuropsychologia* 2003; 41(13):1757–1768.
16. Seiffert AE, Somers DC, Dale AM, et al. Functional MRI studies of human visual motion perception: texture, luminance, attention and after-effects. *Cereb Cortex* 2003; 13(4): 340–349.
17. Zihl J, Von Cramon D, Mai N. Selective disturbance of movement vision after bilateral brain damage. *Brain* 1983; 106:313–340.
18. Newsome WT, Pare EB. A selective impairment of motion perception following lesions of the middle temporal visual area (MT). *J Neurosci* 1988; 8(6):2201–2211.
19. Vaina LM, Cowey A, Eskew RT Jr., et al. Regional cerebral correlates of global motion perception: evidence from unilateral cerebral brain damage. *Brain* 2001; 124 (pt 2):310–321.
20. Newsome WT, Wurtz RH, Dursteler MR, et al. Deficits in visual motion processing following ibotenic acid lesions of the middle temporal visual area of the macaque monkey. *J Neurosci* 1985; 5(3):825–840.
21. Perenin MT, Vighetto A. Optic ataxia: a specific disruption in visuomotor mechanisms. I. Different aspects of the deficit in reaching for objects. *Brain* 1988; 111 (pt 3):643–674.
22. Wandell BA, Brewer AA, Dougherty RF. Visual field map clusters in human cortex. *Philos Trans R Soc Lond B Biol Sci* 2005; 360(1456):693–707.
23. McKeefry DJ, Zeki S. The position and topography of the human colour centre as revealed by functional magnetic resonance imaging. *Brain* 1997; 120(pt 12): 2229–2242.
24. Zeki S. A century of cerebral achromatopsia. *Brain* 1990; 113:1721–1777.
25. Kanwisher N, McDermott J, Chun MM. The fusiform face area: a module in human extrastriate cortex specialized for face perception. *J Neurosci* 1997; 17(11):4302–4311.
26. Feinberg TE, Schindler RJ, Ochoa E, et al. Associative visual agnosia and alexia without prosopagnosia. *Cortex* 1994; 30(3):395–411.
27. Salvan CV, Ulmer JL, DeYoe EA, et al. Visual object agnosia and pure word alexia: correlation of functional magnetic resonance imaging and lesion localization. *J Comput Assist Tomogr* 2004; 28(1):63–67.
28. Damasio AR, Damasio H. The anatomic basis of pure alexia. *Neurology* 1983; 33(12):1573–1583.
29. Binder JR, Mohr JP. The topography of callosal reading pathways. A case-control analysis. *Brain* 1992; 115 (pt 6):1807–1826.
30. Rensink RA, O'Regan JK, Clark JJ. To see or not to see: the need for attention to perceive changes in scenes. *Psychol Sci* 1997; 8:368–373.
31. Srinivasan N. Interdependence of attention and consciousness. *Prog Brain Res* 2007; 168:65–75.
32. Mesulam MM. A cortical network for directed attention and unilateral neglect. *Ann Neurol* 1981; 10(4):309–325.
33. Gitelman DR, Nobre AC, Parrish TB, et al. A large-scale distributed network for covert spatial attention: further anatomical delineation based on stringent behavioural and cognitive controls. *Brain* 1999; 122(pt 6):1093–1106.
34. Saalmann YB, Pigarev IN, Vidyasagar TR. Neural mechanisms of visual attention: how top-down feedback highlights relevant locations. *Science* 2007; 316(5831): 1612–1615.
35. Heilman KM, Valenstein E, Watson RT. Neglect and related disorders. *Semin Neurol* 2000; 20(4):463–470.
36. Brefczynski JA, DeYoe EA. A physiological correlate of the ‘spotlight’ of visual attention. *Nat Neurosci* 1999; 2(4): 370–374.
37. Liu T, Larsson J, Carrasco M. Feature-based attention modulates orientation-selective responses in human visual cortex. *Neuron* 2007; 55(2):313–323.
38. Saenz M, Buracas GT, Boynton GM. Global effects of feature-based attention in human visual cortex. *Nat Neurosci* 2002; 5(7):631–632.
39. Saenz M, Buracas GT, Boynton GM. Global feature-based attention for motion and color. *Vision Res* 2003; 43(6): 629–637.
40. Ungerleider LG. Functional brain imaging studies of cortical mechanisms for memory. *Science* 1995; 270: 769–775.
41. Roberts T. Is fMRI useful for pre-surgical mapping of tumors and other brain lesions. In: U Segall ed. Non-invasive Functional Localization in Patients with Brain Neoplasms. Internet Educational Lecture Series; 2001. Available at: <http://members.asnr.org/webcast/index.html>.
42. DeYoe EA, Carman G, Bandettini P, et al. Mapping striate and extrastriate visual areas in human cerebral cortex. *Proc Natl Acad Sci U S A* 1996; 93(6):2382–2386.
43. Engel SA, Glover GH, Wandell BA. Retinotopic organization in human visual cortex and the spatial precision of functional MRI. *Cereb Cortex* 1997; 7:181–192.
44. O'Regan JK. Eye movements and reading. *Rev Oculomot Res* 1990; 4:395–453.
45. Legge GE, Ahn SJ, Klitz TS, et al. Psychophysics of reading—XVI. The visual span in normal and low vision. *Vision Res* 1997; 37(14):1999–2010.
46. Legge GE, Mansfield JS, Chung ST. Psychophysics of reading. XX. Linking letter recognition to reading speed in central and peripheral vision. *Vision Res* 2001; 41(6): 725–743.
47. Ulmer JL, Salvan CV, Mueller WM, et al. The role of diffusion tensor imaging in establishing the proximity of tumor borders to functional brain systems: implications for preoperative risk assessments and postoperative outcomes. *Technol Cancer Res Treat* 2004; 3(6):567–576.
48. Maruyama K, Kamada K, Shin M, et al. Optic radiation tractography integrated into simulated treatment planning for Gamma Knife surgery. *J Neurosurg* 2007; 107(4): 721–726.
49. Dougherty RF, Ben-Shachar M, Bammer R, et al. Functional organization of human occipital-callosal fiber tracts. *Proc Natl Acad Sci U S A* 2005; 102(20):7350–7355.
50. Guenot M, Krolak-Salmon P, Mertens P, et al. MRI assessment of the anatomy of optic radiations after temporal lobe epilepsy surgery. *Stereotact Funct Neurosurg* 1999; 73(1–4):84–87.

51. Nudo RJ, Friel KM. Cortical plasticity after stroke: implications for rehabilitation. *Rev Neurol* 1999; 155(9): 713–717.
52. Roricht S, Meyer BU, Niehaus L, et al. Long-term reorganization of motor cortex outputs after arm amputation. *Neurology* 1999; 53(1):106–111.
53. Smirnakis SM, Brewer AA, Schmid MC, et al. Lack of long-term cortical reorganization after macaque retinal lesions. *Nature* 2005; 435(7040):300–307.
54. Ulmer JL, Hacein-Bey L, Mathews VP, et al. Lesion-induced pseudo-dominance at functional magnetic resonance imaging: implications for preoperative assessments. *Neurosurgery* 2004; 55(3):569–579 (discussion 580–581).
55. Gluhbegovic N, Williams TH. *The Human Brain: A Photographic Guide*. Hagerstown, MD: Harper and Row, 1980:176.
56. Wandell BA, Dumoulin SO, Brewer AA. Visual field maps in human cortex. *Neuron* 2007; 56(2):366–383.

7

Cortical Plasticity

ANDREI I. HOLODNY

*The Neuroradiology Section and the Functional MRI Laboratory, Department of Radiology,
Memorial Sloan-Kettering Cancer Center, New York, New York, U.S.A.*

INTRODUCTION

Brain plasticity or cortical reorganization can be defined as follows: when a pathological process affects the function of one part of the brain, another part of the brain attempts to take over that function and succeeds at least partially. Until rather recently, it was thought that cortical reorganization essentially never occurred in the adult brain. It was believed that once the adult brain was formed, the number of neurons could only diminish and that once a part of the brain became damaged, the function supplanted by that part could never be restored.

However, recent work, for example in the field of stem cells in the central nervous system, has altered this opinion. Functional brain imaging has also been instrumental in demonstrating that cortical reorganization actually does occur. Imaging is essential in revealing brain plasticity because of its ability to show changes in brain function over time. A number of different techniques have shown brain plasticity in both animals and humans. These include experimental techniques, such as stem cell tracking, most of which lie outside everyday clinical practice and are therefore outside the purview of this book. We will concentrate on a technique which is readily available—namely blood oxygen level-dependent (BOLD) functional magnetic resonance imaging (fMRI).

UNEXPECTED RESULTS

As we have already seen in other chapters, BOLD fMRI is becoming an indispensable technique in preoperative (as well as intraoperative) mapping of eloquent cortices adjacent to a tumor to be resected. If preoperative BOLD fMRI is available, neurosurgeons quickly become most appreciative of this technique and averse to operate without it (1). Therefore, one of the most frustrating and puzzling dilemmas that the radiologist is faced with is when BOLD fMRI data sets do not match the expected results.

An example is seen in Figure 1. The patients presented with a low-grade glioma, which involved a large part of the left hemisphere. Since the patient was right-handed, one could be approximately 95% to 98% sure that he/she would be left-side dominant for language. Therefore, after review of the anatomical magnetic resonance (MR) images, one may conclude that the tumor probably involved the expected locations of Broca's area and Wernicke's area.

However, the BOLD fMRI language paradigm demonstrated right language activation for both Broca's area and Wernicke's area—opposite of what was expected! Figure 1A and B shows the fMRI results for two different language paradigms. How does one interpret such results—especially with a neurosurgeon standing over one's shoulder awaiting guidance? How confident can I be? Should the neurosurgeon forego intraoperative

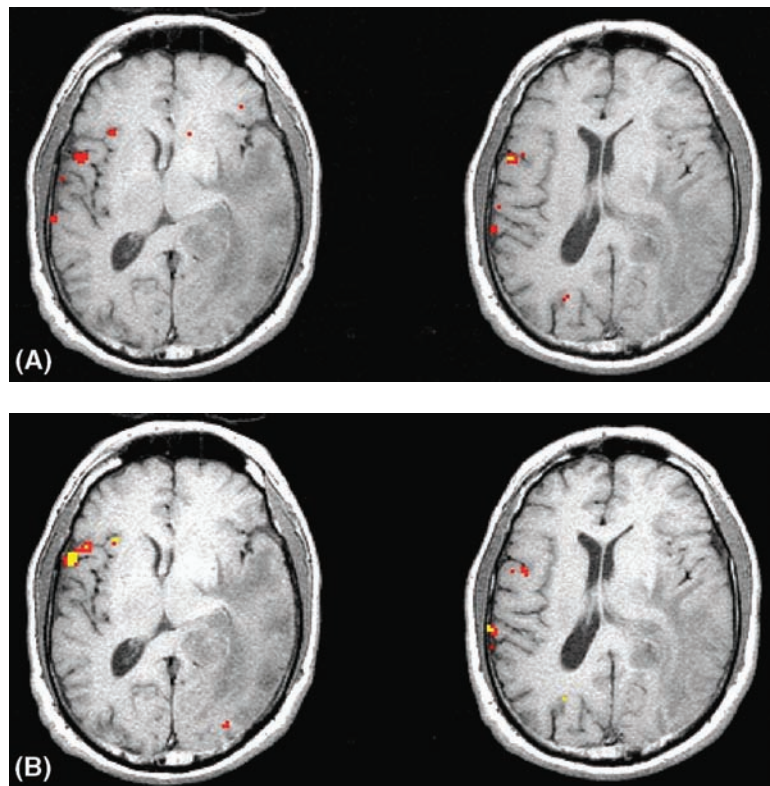


Figure 1 Unexpected results. Preoperative BOLD fMRI performed in a right-handed patient with a right-hemispheric tumor. One would expect that the language areas in a right-handed patient would be located on the left; however, the fMRI study shows both language areas to be on the right side. This result was unexpected. (A) and (B) show results of two different language paradigms.
Abbreviations: BOLD, blood oxygen level-dependent; fMRI, functional magnetic resonance imaging.

language mapping—a long and burdensome technique? Has the fMRI examination uncovered a true (but unexpected) result or is the test itself in error?

Clearly, the difference is crucial. If one could confidently conclude that language function actually was on the opposite side of the expected result, the neurosurgeon could contemplate a much more extensive resection, without fear of compromising the patient's essential language areas. How is one to practically approach such a dilemma?

GENERAL CONSIDERATIONS

A way to approach the aforementioned dilemma is to consider all of the possible sources of BOLD fMRI signal, whether accurate or not. In such situations, an appreciation of the physics and physiology of BOLD fMRI as a method becomes critical to arriving at the correct clinical interpretation.

The sources of BOLD fMRI signal can be summarized in the following (rather simplified) equation:

$$S = S_{\text{True}} + A + T \quad (1)$$

where

S = BOLD fMRI signal that one actually sees on the images,

S_{True} = true BOLD fMRI signal (including cortical reorganization),

A = technical artifacts (susceptibility), and

T = artifactual effects of the tumor (neurovascular uncoupling).

In this equation, S_{True} can be defined as the result of a functional imaging study had it been performed by an omnipotent being who could actually see things as they really are. Unfortunately, BOLD fMRI as a technique (as well as our own capacities) falls somewhat short of omnipotence. Specifically, and from the above formula, there are two factors that can affect the BOLD fMRI signal: technical artifacts (especially susceptibility) and the artifactual effect of the tumor itself on the BOLD fMRI signal (including neurovascular uncoupling). Consequently, in order to interpret the images correctly, one must attempt to eliminate, minimize, or at least appreciate “ A ” and “ T ”. The subject of artifacts is dealt with extensively in a separate chapter by Maldjian entitled “Fact or Artifact”.

NEUROVASCULAR UNCOUPLING

In interpreting BOLD fMRI studies, it is imperative to keep in mind that the BOLD signal is a measure of a vascular response rather than a measure of neuronal activity [as is magnetoencephalography (MEG)—see the chapter by Roberts]. Therefore, any alteration of the normal vascular bed, which supplies the part of the brain being studied, can potentially affect the BOLD fMRI signal. For example, if the blood vessels lose their ability to contract or dilate and hence are not able to respond to changes in neuronal activity, the BOLD response itself can become muted or even totally absent.

Unfortunately, a number of pathologies have been shown to affect the vasculature and consequently the resultant BOLD fMRI response. This phenomenon was first demonstrated by our group in a patient with a glioblastoma involving the left precentral gyrus—the expected location of the motor homunculus (2). The patient exhibited normal hand strength and was able to perform the finger tapping paradigm adequately; however, the BOLD fMRI images demonstrated a marked difference in the volume of activation between the side with the tumor and the contralateral side (Fig. 2).

We hypothesized that the muted BOLD fMRI response on the side with the tumor was due to the presence of abnormal tumor neovasculature, which lost (or at least partially lost) the ability to increase the flow of blood to the motor cortex in response to an increase in neuronal activity. This hypothesis has been supported by continued work by our group (3,4) as well as other investigators (1). Further support for the idea of

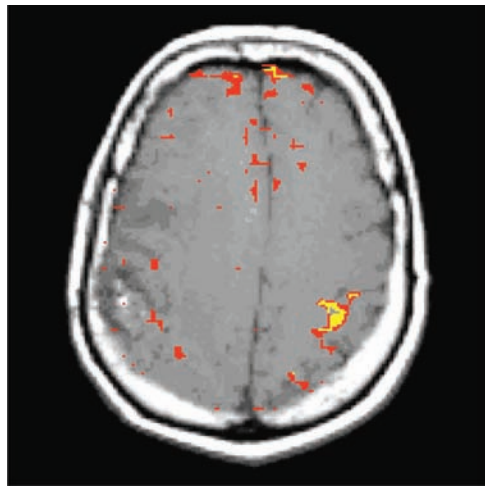


Figure 2 Preoperative BOLD fMRI in a patient with a right-side glioblastoma multiforme. The patient had normal hand strength and performed a bilateral finger tapping paradigm. However, there was significantly less BOLD fMRI signal on this side compared with the tumor on the contralateral side. It is thought that this phenomenon is due to neurovascular uncoupling. Abbreviations: BOLD, blood oxygen level-dependent; fMRI, functional magnetic resonance imaging. Source: From Ref. 2.

the presence of abnormal neovasculature was garnered from the paper by Hou et al. (4). The results from 57 brain tumor cases demonstrated that for grade IV gliomas only, decreases in the BOLD fMRI activation volumes within the primary motor cortex ipsilateral to the tumor, when compared to the contralateral side, correlated with increases in the relative regional cerebral blood volume (rCBV) (Fig. 3). These findings lend support to the hypothesis that decreases in the

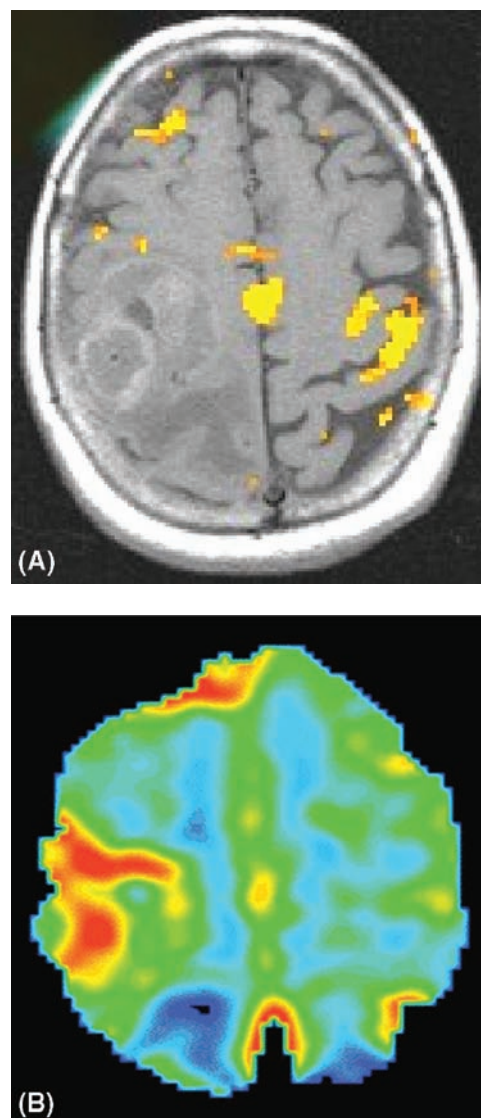


Figure 3 (A) Preoperative BOLD fMRI in a patient with a left-side glioblastoma multiforme shows a markedly diminished ipsilateral BOLD fMRI activation volume in the primary motor cortex (ratio = 0.1). This corresponds to an area of increased relative cerebral blood volume (ratio = 4.1) in (B). These images support the notion that the BOLD response is muted in areas of abnormal tumor neovasculature due to neurovascular uncoupling. Abbreviations: BOLD, blood oxygen level-dependent; fMRI, functional magnetic resonance imaging. Source: From Ref. 4.

fMRI activation volumes adjacent to a glioblastoma multiforme (GBM) may, in part, be due to the increased contribution of aberrant tumor neovascularity, with the resultant decoupling of blood flow from neuronal activity.

The effect of abnormal vasculature on the BOLD signal has also been reported in other pathologies such as arteriovenous malformations (AVMs) (1). A muted BOLD response has also been noted in older adults and has been hypothesized to result from the changes that normally occur in the vessels of the brain as one ages (5).

It is interesting to note that other factors such as the presence of edema in the eloquent gyrus of interest, the volume of peritumoral edema, or the volume of the tumor itself have not been shown to significantly affect the BOLD fMRI response (3).

Therefore, interpreting the BOLD fMRI images would behoove one to evaluate the patient for the possible presence of abnormal neovasculation. This can be accomplished with rather standard techniques such as rCBV measurements. More advanced measurements of cerebrovascular reactivity (6) have recently been proposed for the specific task of evaluating the BOLD response. We believe that such methods hold great promise.

In terms of the practical issue of interpreting BOLD fMRI images, it is important to acknowledge the presence of abnormal vasculature or abnormal vascular reactivity, since BOLD fMRI may become less reliable adjacent to such areas. In our clinical practice, this effect has limited consequences in terms of identifying the primary motor and sensory areas, since these areas can be identified in the overwhelming majority of cases.

Where the effect of abnormal vasculature may be more pronounced is in establishing language laterality. The dominance of one side of the brain for language function is usually established by the laterality index, using the formula $LI = (L - R)/(L + R)$, where L and R stand for the volume of BOLD fMRI activation in the region of interest of a specific language area (for example, Broca's area) on left and right, respectively. An artifactual decrease in the volume of BOLD fMRI activation on the side with the tumor, caused by abnormal vasculature, may influence the calculation of the laterality index and may lead to an underestimation of the presence of language function on the side with the tumor. Therefore, the operating neurosurgeon should be warned about the presence of abnormal vasculature and its possible effect on the BOLD fMRI signal by the person interpreting the BOLD fMRI images to ward off a possible false sense of security on the part of the operating neurosurgeon.

CORTICAL REORGANIZATION DUE TO TUMOR GROWTH

Notwithstanding the cautions expounded on in the prior section regarding the care one must take in misinterpreting

artifacts or neurovascular uncoupling as true cortical reorganization, this phenomenon has been shown to exist in patients with brain tumors. This possibility also has to be kept in mind when one interprets fMRI images since if brain plasticity is discounted, the optimal treatment may not be performed (7). In our clinical practice, we first came across this in the following case (8).

Example 1

A 34-year-old, right-handed man was first diagnosed with an astrocytoma involving the left inferior frontal cortex seven years prior. A stereotactic biopsy at that time demonstrated a grade II/IV astrocytoma. Surgical resection was not performed because of involvement of the presumed dominant Broca's area. Instead, the patient was treated with fractionated external radiation therapy and chemotherapy. He was followed with serial magnetic resonance imaging (MRI) scans, which demonstrated slow progression of the tumor.

The current admission was prompted by the presence of uncal herniation as detected on a follow-up MR imaging. A routine, anatomical, Gd-DTPA-enhanced MRI demonstrated a large-mass lesion involving the left inferior frontal lobe, including the expected location of Broca's area, and extending into the basal ganglia and anterior temporal lobe. A language fMRI study demonstrated Wernicke's area to be on the left side and Broca's area on the right (Fig. 4). During the operation, the patient did not tolerate conscious sedation. Therefore, intraoperative localization of Broca's area by direct brain stimulation with identification of the area of speech cessation could not be performed, again emphasizing the importance of preoperative fMRI. After gross total resection, the patient's mild dysarthria and right hemiparesis resolved.

To our knowledge, the location of Broca's area and Wernicke's area on opposite sides of the brain has never been described in normal individuals. What appears to have occurred in the current case is that the growth of the brain tumor in the left inferior frontal lobe led to an inability of this area to function properly. This led to the apparent transfer of the functional Broca's area to the contralateral side.

This case can serve to emphasize another important issue regarding the preoperative assessment of eloquent cortices adjacent to brain tumors. Surgical resection is the mainstay of the treatment of astrocytomas (9). Assumptions regarding language dominance that are based solely on handedness may be misleading, at least in part. This may result in an unnecessarily conservative treatment approach for certain patients with brain tumors in whom surgery is in fact safe and clinically desirable (8).

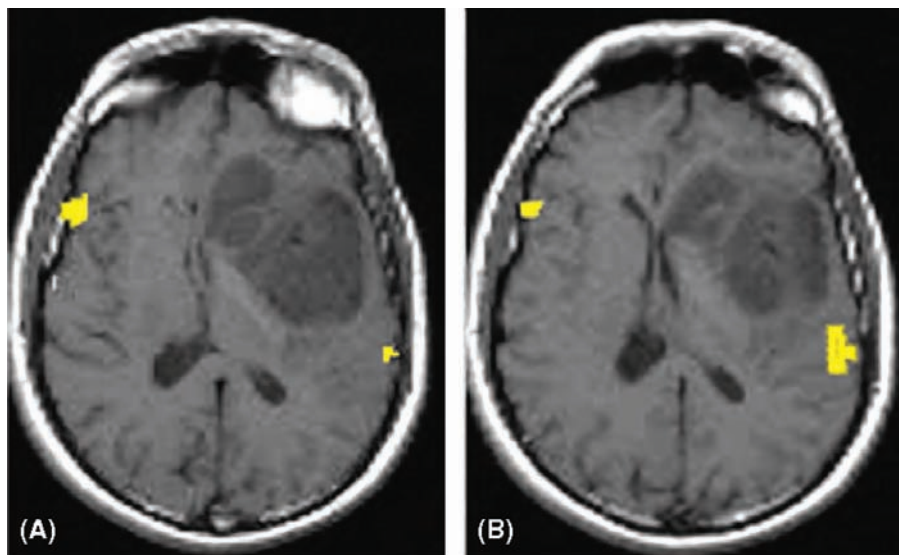


Figure 4 Functional magnetic resonance study identifying the language centers co-registered to an axial T1-weighted image in a right-handed 34-year-old man with a left inferior frontal glioma. A large tumor involves the left inferior frontal lobe including the expected location of the Broca's area. However, BOLD fMRI demonstrated activation of Broca's area on the right and Wernicke's area on the left. Abbreviations: BOLD, blood oxygen level-dependent; fMRI, functional magnetic resonance imaging. Source: From Ref. 8.

Example 2

In our second example (7), an MRI in a 62-year-old right-handed man revealed a left temporoparietal lesion measuring $3.1 \text{ cm} \times 2.8 \text{ cm}$ involving the expected location of Wernicke's area. Specifically, the lesion involved the

superior temporal gyrus, portions of the supramarginal and angular gyri, and subcortical white matter (Fig. 5A). Laterality indices generated from BOLD fMRI with multiple language paradigms revealed a left-hemispheric dominance for Broca's area and right-hemispheric dominance for Wernicke's area for all correlation coefficients tested (Fig. 5B).

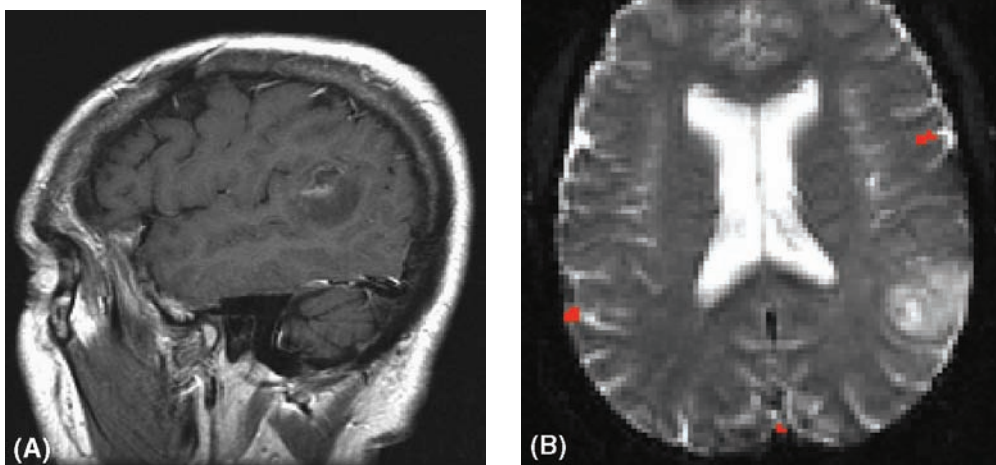


Figure 5 (A) Post-contrast left sagittal image from a 62-year-old right-handed man showing a mostly non-enhancing temporoparietal neoplasm involving the superior temporal gyrus and portions of the supramarginal and angular gyri and underlying white matter. This would be the expected location of Wernicke's area. (B) However, axial fMRI results show Broca's area on the left and activity most consistent with Wernicke's area on the right. Correlation coefficient is 0.46 ($p = 4.0 \times 10^{-6}$). This fMRI finding was confirmed by surgical resection. Abbreviation: fMRI, functional magnetic resonance imaging. Source: From Ref. 7.

The patient underwent awake craniotomy for language mapping and resection. Broca's area was then unambiguously identified in the left hemisphere by direct cortical stimulation, confirming the fMRI findings. However, the patient's language function remained intact during stimulation of the presumed left-sided Wernicke's area. He underwent gross total resection that included the expected location of Wernicke's area, namely the superior temporal, supramarginal, and angular gyri as well as portions of underlying white matter. The patient suffered no postoperative language dysfunction. Postoperative neuropsychological testing for language actually showed an improvement in scores compared to preoperative testing.

This case shows that fMRI should be routinely done preoperatively in patients with lesions in language cortex, particularly when brain tumors are deemed inoperable because of their proximity to essential language centers. Many surgeons would not offer surgery for a lesion in dominant temporoparietal cortex in a right-handed patient in the absence of techniques like fMRI. Even if an exploratory awake craniotomy were done, the finding of Broca's function in the left hemisphere would have suggested left language dominance and therefore a high risk to surgery. Further, direct cortical stimulation would not have provided any information about the functional capacity of right hemisphere. The current case exemplifies the need for functional imaging in presurgical planning as it demonstrated a translocation of Wernicke's area to the contralateral hemisphere, and correctly suggested that the lesion was safe to resect (7).

Prospective Study

The above two cases were acquired at a single point in time and demonstrated reorganization that had already occurred. Thus, in these studies, fMRI activation patterns represent the reorganized language network rather than the dynamics of reorganization. However, recent work by our group (10) has demonstrated actual translocation of language function over time in patients with brain tumors.

Five right-handed brain tumor patients with low-grade gliomas directly adjacent to the frontal language areas (Broca's areas) were prospectively studied. Four of five patients qualitatively demonstrated increased right-hemispheric compensation in either Broca's area, Wernicke's area, or both (Fig. 6). Whether or not this pattern of fMRI indicated functional compensation in the right-hemispheric language homologues is clinically meaningful (i.e., enables the surgeon to be more aggressive in the left assumed dominant hemisphere) is yet unknown. However, there is evidence using transcranial magnetic stimulation (TMS) to suggest that codominance or right dominance on fMRI does predict the extent of disruption of speech in the right hemisphere with TMS (11). Whether or not tumor invasion

of primary language centers can potentially alter functional assessments made at these sites is an important question that could impact presurgical planning efforts and needs to be further investigated.

These findings provide evidence of broader network underlying language function and support the notion that the right hemisphere may have a limited role in expressive language (12). The presence of some degree of language function on the right side in the area corresponding to Broca's area on the left probably allows for limited reorganization of language function to the contralateral side (13).

ARTERIOVENOUS MALFORMATIONS

AVMs in the brain are at a significant risk for bleeding and are therefore often treated by either surgical resection or neurovascular embolization. Consequently, as with brain tumors, the need arises to accurately identify eloquent cortices adjacent to the AVM to be avoided during the procedure. Functional MRI has been shown to be able to accomplish this goal (13,14).

Nevertheless, AVMs, by definition, are lesions essentially composed of abnormal vasculature. The presence of high-flow, dilated vessels can clearly affect the BOLD fMRI signal. Therefore, one must be wary of neurovascular uncoupling possibly even to a greater extent than in malignant brain tumors (1).

CORTICAL REORGANIZATION FOLLOWING STROKE

Functional MRI studies have allowed one to assess in much greater detail the processes that occur following an ischemic insult. Contrary to previously held beliefs, functional studies have demonstrated rather dramatic attempts of the brain to heal the injury. Clearly, in a large percentage of patients, such attempts are ultimately futile since the end result is a permanent deficit, nevertheless, functional imaging studies have increased our understanding of these processes. Currently the ability of the brain to reorganize (or at least attempt to reorganize) following an ischemic insult is generally acknowledged.

Language

Functional MRI studies of language areas have shown results similar to those described above in brain tumor patients in that there is an apparent transfer of function from the side of the insult to the contralateral (mirror) side (15–19). It appears that recovery of language function following an infarct (or for that matter any pathology,

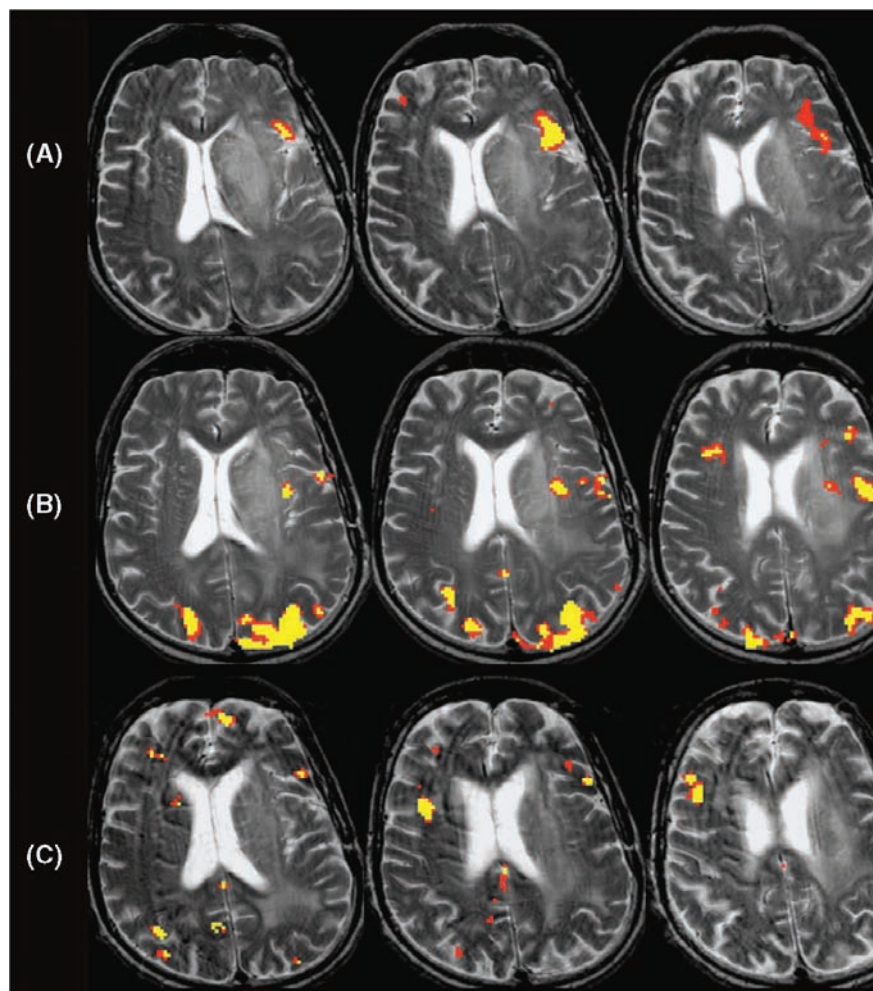


Figure 6 Language BOLD fMRI results at three different points in time in a patient with a left-hemispheric glioma: (A) before surgery (baseline fMRI scan), (B) three months post-surgery, and (C) six months post-surgery. The two postoperative follow-up fMRI scans (B) and (C) demonstrated progressively increasing fMRI activation in Broca's area in the right hemisphere (contralateral to the tumor). Presurgical fMRI indicated the expected left-hemispheric dominance for language. This finding was supported by intraoperative electrocorticography. Abbreviation: fMRI, functional magnetic resonance imaging. Source: From Ref. 10.

including brain tumors) is aided by the presence of homologous language areas in mirror locations on the contralateral side of the brain. It appears, therefore, that in recovery from stroke, there is recruitment and apparent strengthening of these mirror language areas, which take on more functions leading to clinical improvement. This concept is supported by imaging studies, which correlated changes on fMRI with actual clinical recovery from strokes. Imaging studies have occasionally demonstrated crossed language dominance with one primary language area translocating to the contralateral side (15).

The timing of language reorganization described in the literature has varied widely from three days (15) to years following the insult (16) and is currently incompletely understood. A recent publication suggested a triphasic recovery (17).

A number of recent studies have reported that rehabilitation methods can lead to clinical recovery from strokes even years after the initial insult (16,18). Such results have led to improved (and apparently successful) rehabilitation strategies in which functional imaging studies have played a key role (19).

Motor

Recovery from strokes involving the primary motor cortex is somewhat different from language since the presence of motor homologues in the contralateral hemisphere is more limited. Nevertheless, recovery from motor insults is possible in certain settings. Functional MRI studies have demonstrated that partial motor recovery is accompanied by BOLD fMRI activation in both intrahemispheric as

well as interhemispheric recruitment. Intrahemispheric reorganization is aided by the existence of a considerable overlap between adjacent motor areas in precentral gyrus (20). In addition, a number of studies have demonstrated that following an infarct of the primary motor cortex or of the corticospinal tract exiting from the primary motor cortex, the ipsilateral dorsal premotor cortex reorganizes to take on some of the functions of the affected area (21,22). Likewise, there are limited motor areas in the contralateral precentral gyrus (23) apparently to a lesser extent than homologous language areas.

As with language, functional imaging studies have not only facilitated elucidation of the mechanisms of clinical recovery of function, they have also guided the development of successful rehabilitation strategies in patients with primary motor cortex strokes (24). Partial rehabilitation, which correlated with fMRI results, has even been reported in patients with chronic motor strokes of greater than one year duration, who underwent the modified constraint-induced movement therapy (mCIMT) program (25). A recent study (26) demonstrated that the initial fMRI results in the acute post-infarct period can be used to predict future recovery. Consequently, this study also suggested basing and modifying the rehabilitation efforts on the initial post-infarct fMRI results.

Cortical reorganization of motor function has been reported following insults to the subcortical white matter tracts (21) as well as following spinal cord injury (27,28).

Pitfalls in Interpretation

In evaluating fMRI studies and contemplating the presence of cortical reorganization following an infarct, one must always keep in mind the physical principles that form the basis of fMRI. First, BOLD fMRI is based on a measure of changes in blood flow and oxygenation. An ischemic infarct, by definition, affects the vasculature, and consequently, the BOLD signal. Therefore, the absence of BOLD fMRI activation in an area of damaged brain may be due to a redistribution of blood flow rather than an actual change in neuronal activity. Second, hemorrhage or calcification often leads to magnetic field inhomogeneities, which lead to drop-off in the T2* signal intensity and a loss in the sensitivity of the sequence to the BOLD signal.

CONCLUSION

In conclusion, we can confidently aver that BOLD fMRI is an exceptionally powerful and useful technique, which has increased our understanding of the brain and has proven useful in the clinical arena. Specifically, BOLD fMRI has led to an increased awareness of the presence of cortical reorganization and brain plasticity.

However, in interpreting BOLD fMRI images, one must also be careful in acknowledging the possibility that the results may be affected by either technical artifacts or the presence of abnormal vasculature. In the context of a preoperative BOLD fMRI study, these concerns as well as the possibility of cortical reorganization should be communicated to a neurosurgeon.

It appears axiomatic that we have only begun to understand the complexities of the human brain, including the possibility of recovery of brain function after an insult. It is my sincere hope that these techniques as well as the development of newer and better techniques will further our understanding of brain plasticity and will indicate new avenues in the treatment of brain pathology.

REFERENCES

- Ulmer JL, Hacein-Bey L, Mathews VP, et al. Lesion-induced pseudo-dominance at functional magnetic resonance imaging: implications for preoperative assessments. *Neurosurgery* 2004; 55(3):569–579.
- Holodny AI, Schulder M, Liu WC, et al. Deceased BOLD functional MR activation of the motor and sensory cortices adjacent to a glioblastoma multiforme: implications for fMRI guided neurosurgery. *AJNR Am J Neuroradiol* 1999; 20:609–612.
- Holodny AI, Schulder M, Liu WC, et al. The effect of brain tumors on BOLD fMRI activation in the adjacent motor cortex: implications for image-guided neurosurgery. *AJNR Am J Neuroradiol* 2000; 21:1415–1422.
- Hou BL, Bradbury M, Peck KK, et al. Effect of brain tumor neovasculature defined by rCBV on BOLD fMRI activation volume in the primary motor cortex. *Neuroimage* 2006; 32:489–497.
- Chen C, Hou BL, Holodny AI. Effect of age and tumor grade on BOLD fMRI in preoperative assessment of glioma patients. *Radiology* (in press).
- Prisman E, Slessarev M, Han J, et al. Comparison of the effects of independently-controlled end-tidal PCO(2) and PO(2) on blood oxygen level-dependent (BOLD) MRI. *J Magn Reson Imaging* 2008; 27(1):185–191.
- Petrovich NM, Holodny AI, Brennan CW, et al. Isolated translocation of Wernicke's area to the right hemisphere in a 62 year old man with a temporo-parietal glioma. *AJNR Am J Neuroradiol* 2004; 25:130–133.
- Holodny AI, Schulder M, Ybasco A, et al. Translocation of Broca's area to the contralateral hemisphere due to the growth of a left inferior frontal glioma. *J Comput Assist Tomogr* 2002; 26:941–943.
- DeAngelis LM. Brain tumors. *N Engl J Med* 2001; 344:114–123.
- Peck KK, Brennan N, Hou BL, et al. A longitudinal study of the cortical reorganization of language function in brain tumor patients. Annual Meeting of the ISMRM, May 2008; Toronto, Canada.
- Knecht S, Flöel A, Dräger B, et al. Degree of language lateralization determines susceptibility to unilateral brain lesions. *Nat Neurosci* 2002; 5(7):695–699.

12. Springer JA, Binder JR, Hammeke TA, et al. Language dominance in neurologically normal and epilepsy subjects: a functional MRI study. *Brain* 1999; 122:2033–2046.
13. Lazar RM, Marshall RS, Pile-Spellman J, et al. Interhemispheric transfer of language in patients with left frontal cerebral arteriovenous malformation. *Neuropsychologia* 2000; 38(10):1325–1332.
14. Maldjian J, Atlas SW, Howard RS 2nd, et al. Functional magnetic resonance imaging of regional brain activity in patients with intracerebral arteriovenous malformations before surgical or endovascular therapy. *J Neurosurg* 1996; 84(3):477–483.
15. Thulborn KR, Carpenter PA, Just MA. Plasticity of language-related brain function during recovery from stroke. *Stroke* 1999; 30(4):749–754.
16. Meinzer M, Flaisch T, Breiteneck C, et al. Functional recruitment of dysfunctional brain areas predicts language recovery in chronic aphasia. *Neuroimage* 2008; 39(4): 2038–2046 [Epub October 18, 2007].
17. Saur D, Lange R, Baumgaertner A, et al. Dynamics of language reorganization after stroke. *Brain* 2006; 129(Pt 6): 1371–1384 [Epub April 25, 2006].
18. Vitali P, Abutalebi J, Tettamanti M, et al. Training-induced brain remapping in chronic aphasia: a pilot study. *Neurorehabil Neural Repair* 2007; 21(2):152–160.
19. Rijntjes M, Weiller C. Recovery of motor and language abilities after stroke: the contribution of functional imaging. *Prog Neurobiol* 2002; 66(2):109–122.
20. Kleinschmidt A, Nitschke MF, Frahm J. Somatotopy in the human motor cortex hand area: a high-resolution functional MRI study. *Eur J Neurosci* 1997; 9:2178–2186.
21. Fridman EA, Hanakawa T, Chung M, et al. Reorganization of the human ipsilesional premotor cortex after stroke. *Brain* 2004; 127(pt 4):747–758 [Epub January 28, 2004].
22. O’Shea J, Johansen-Berg H, Trief D, et al. Functionally specific reorganization in human premotor cortex. *Neuron* 2007; 54(3):479–490.
23. Nirkko AC, Ozdoba C, Redmond SM, et al. Different ipsilateral representations for distal and proximal movements in the sensorimotor cortex: activation and deactivation patterns. *Neuroimage* 2001; 13(5):825–835.
24. Dong Y, Winstein CJ, Albistegui-DuBois R, et al. Evolution of fMRI activation in the perilesional primary motor cortex and cerebellum with rehabilitation training-related motor gains after stroke: a pilot study. *Neurorehabil Neural Repair* 2007; 21(5):412–428 [Epub March 16, 2007].
25. Szaflarski JP, Page SJ, Kissela BM, et al. Cortical reorganization following modified constraint-induced movement therapy: a study of 4 patients with chronic stroke. *Arch Phys Med Rehabil* 2006; 87(8):1052–1058.
26. Loubinoux I, Dechaumont-Palacin S, Castel-Lacanal E, et al. Prognostic value of fMRI in recovery of hand function in subcortical stroke patients. *Cereb Cortex* 2007; 17(12):2980–2987 [Epub March 26, 2007].
27. Mikulis DJ, Jurkiewicz MT, McIlroy WE, et al. Adaptation in the motor cortex following cervical spinal cord injury. *Neurology* 2002; 58(5):794–801.
28. Jurkiewicz MT, Mikulis DJ, McIlroy WE, et al. Sensorimotor cortical plasticity during recovery following spinal cord injury: a longitudinal fMRI study. *Neurorehabil Neural Repair* 2007; 21(6):527–538 [Epub May 16, 2007].

8

Functional Image-Guided Neurosurgery

CAMERON W. BRENNAN

Department of Neurosurgery, Memorial Sloan-Kettering Cancer Center, New York, New York, U.S.A.

NICOLE M. PETROVICH BRENNAN

Department of Radiology, Memorial Sloan-Kettering Cancer Center, New York, New York, U.S.A.

INTRODUCTION

Imaging Revolution in Neurosurgery

Neurosurgical practice underwent a revolution in the 1970s with the advent of detailed anatomical imaging by CT, further improved by MRI in the 1980s. Prior to CT nervous system pathology (tumors, bleeds, strokes, etc.) were localized indirectly by neurological findings and by the shifts of shadows on X-ray studies such as angiograms and pneumoencephalograms. It is easy to imagine the relief felt by surgeons when they first saw preoperative images, which revealed tumor and brain anatomy in sufficient detail to guide a direct approach through the skull and brain.

Sometimes the safest approach is not the most direct one, and this depends partly on the location of pathology in relation to functional cortex and white matter tracts. Understanding of this functional anatomy and how it might vary from patient to patient has been central to neurosurgical practice from its inception, preceding refined brain imaging. Among the techniques historically developed to map function in neurosurgical patients, it is intraoperative electrical stimulation and recording that has become the mainstay in clinical practice. These intraoperative techniques play a key role in avoiding misadventure during surgery but cannot help in the preoperative

planning of an operation or in the assessment of risk, which is conveyed to the patient beforehand.

Functional imaging technologies offer the possibility of an enhanced roadmap for safe surgical approach. These techniques either extend the anatomical image to previously invisible anatomy, such as with diffusion tensor imaging, or annotate the cortex with specific functional roles as with positron emission tomography (PET) or functional MRI (fMRI). MRI-based techniques in particular are now increasingly available and readily integrated with presurgical planning software. Yet despite the substantial literature showing successful application of functional imaging in presurgical planning, there has yet been no equivalent revolution in neurosurgical practice with the advent of these techniques. This chapter will explore the circumstances where preoperative functional imaging can significantly guide surgery, and examine the unique constraints imposed by the surgical setting, where false-negative test results are of paramount concern.

THE ORIGINS OF FUNCTIONAL MAPPING IN NEUROSURGERY

The increase of cortical blood flow associated with functional “work” had been documented in animal models and inferred in humans by 1930 (1). It was the neurosurgeon

Wilder Penfield who first noted that the increase in blood flow over epileptic cortex during seizure was associated with decreased oxygen saturation in the draining venules (2). This observation was made by noting a red shift in the color of draining veins overlying and radiating from epileptic cortex during seizure. Penfield is especially noted for having performed extensive mappings of cortical function using direct cortical electrical stimulation in awake patients undergoing brain operations. Through meticulous notation of positive and negative responses elicited by stimulation, Penfield and colleagues were eventually able to produce a detailed map of cortical function, including the classical sensory and motor homunculi, which is still used as a reference for anatomical functional mapping (3,4). The essence of electrical stimulation and recording for intraoperative cortical mapping has changed little in practice in the intervening 70 years, and remains the “gold standard” for functional mapping in the context of surgery (5).

INVASIVE MAPPING TECHNIQUES

Electrocorticography and Electrocortical Stimulation in Practice

Electrocorticography (ECoG) and electrocortical stimulation (ECS) are commonly used intraoperative techniques for mapping and monitoring neurological function during surgery. ECoG can be used to map epileptic activity by recording voltage potentials on the cortical surface or through deep needle electrodes. Another common application of ECoG is as an initial means during surgery to identify the central sulcus dividing motor cortex and sensory cortex in the precentral and postcentral gyri, respectively. For this purpose, electrical current is delivered to the median nerve by surface electrodes on the patient's wrist. This stimulation induces action potentials in the median nerve, which are conveyed to somatosensory and motor cortex, eliciting a series of electrical potentials. These somatosensory evoked potentials (SSEP) are detected by an array (or strip) of multiple-recording electrodes placed over the cortical surface. The central sulcus is identified by the two electrodes across which the sign of the wave is inverted (Fig. 1). The presence of underlying tumor can distort the central sulcus anatomy and alter the SSEP distribution leading to ambiguous or misleading phase reversals. Central sulcus location can be confirmed by direct cortical stimulation (ECS, Fig. 1). Conversely, for patients under general anesthesia, ECS may fail to elicit motor responses at safe currents and SSEP may be the only usable technique.

ECS is an invasive mapping technique wherein an alternating current is applied directly to the cortex in either an awake or minimally sedated patient under local

anesthesia. Stimulation is most often performed with a dual-tipped (bipolar) electrode, which minimizes current spread to roughly the intertip distance of 5 mm. The specific effects of stimulation depend on the current and frequency parameters used, how the balance of excitatory and inhibitory neurons are affected, and ultimately whether pulsed stimulation of excitatory cells activates or disrupts normal cortical function. An example of excitatory (positive) activation would be stimulation of primary motor cortex, which induces muscular contraction through direct stimulation of the pyramidal neurons mediating volitional motor movement. During ECS mapping of primary sensory and motor cortex, patients are monitored for positive effects (e.g., tingling sensation or muscular contraction). Secondary motor cortex such as pre-motor and supplementary motor areas (SMAs) can show variable responses to cortical stimulation, reflecting the fact that their primary efferent projections are to other cortical areas rather than to descending corticospinal tracts (CST).

Inhibition responses to ECS are typically seen during mapping of language function. In Broca's area, for example, electrical stimulation most often causes abrupt loss of speech (speech arrest) and/or paraphasic errors. In Wernicke's area, electrical stimulation often imparts word-finding difficulty, semantic errors, and telegraphic speech. Figure 2 shows the typical layout of an operating room during awake language-mapping procedure. The cortex is stimulated with a bipolar stimulator in synchrony with language tasks administered by a neuropsychologist or neurologist to the patient under the drapes. Detailed functional mapping demands significant time and stamina of the patient and staff alike. The environment is often cramped and it can be difficult to get repeatable responses, especially in posterior language areas.

In practice, ECS mapping begins at low current amplitudes while continuously monitoring for potential seizures induced by the stimulation. Some centers also monitor ECoG to identify subclinical seizure activity or stimulation-induced afterdischarges. If no responses and no afterdischarges are seen at low current, the mapping is repeated at stepwise higher currents up to a maximum safe limit. When ECS identifies a site of repeatable behavior, a sterile label is placed on the cortical surface and mapping continues at that current level (shown in Fig. 1).

Although ECS current is locally applied by the electrode, the neurophysiological effects of ECS are both local and distant since the effects are conveyed away from stimulated cortex by axonal conduction. When ECS identifies a site, which inhibits a behavior, one may conservatively interpret that site as necessary for that function. Conversely, excitatory sites might be considered “sufficient” to drive a behavior, though not necessary. An inherent limitation of ECS is that only exposed surfaces can be stimulated; the large extent of cortex lining the sulci cannot be assessed without

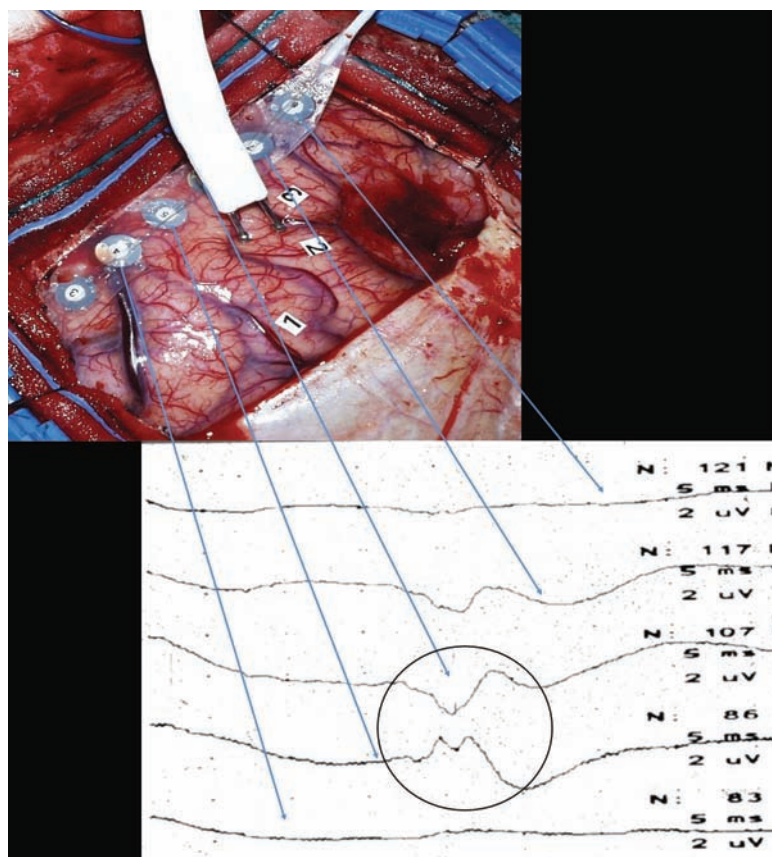


Figure 1 Intraoperative mapping by SSEP and direct ECS. A strip of eight recording electrodes is positioned on the cortical surface of the frontoparietal border crossing the gyral orientation at close to 90°. Electrical stimulation is applied to the median nerve at the wrist causing nerve action potentials. Arrival of these action potentials at the cortical surface induces an evoked potential, which is measured on the recording electrode. An electrographic phase reversal in the evoked potential tracings can be seen (*circled*) and marks the boundary between motor and sensory cortex—the central sulcus. Cortical mapping by ECS using a bipolar electrode (shown) can provide detailed information about somatotopic organization and can map a diversity of cortical functions such as expressive and receptive language. Abbreviations: SSEP, somatosensory evoked potentials; ECS, electrocortical stimulation.

special exposure. As a general rule, a margin of 1 cm from the stimulation point is generally respected in order to minimize functional deficit. It should be noted that even when these margins are respected, patients may emerge with functional deficits. These cases point in part to limitations of cortical mapping—unexposed cortex, variable stimulation thresholds, and diffuse networks subtending functions not amenable to focal stimulation. They also point to the critical importance of white matter in conveying cortical signals. These limitations are directly addressed by functional imaging techniques like fMRI and DTI.

ECS and ECoG are most commonly used intraoperatively but there are circumstances where an array of electrodes may be implanted such that lead wires tunneled to an exit through the skin. The patient may then be mapped by ECS and ECoG for several days by stimulating and recording during extensive tests. A typical application of this sort of staged invasive mapping would be for localization of epileptic foci with fine mapping of

language function. The electrodes are then removed prior to or during a later-staged therapeutic procedure.

Intracarotid Amobarbital Injection (Wada) Test

The intracarotid amobarbital test (IAT), or Wada test, is a technique originally designed to determine laterality of language function (6,7). Through angiographic catheterization of the internal carotid artery, a short-acting barbiturate is injected to provide transient unihemispheric anesthesia during which language testing can be performed. Prior to functional imaging, this test was the only preoperative means for determining hemispheric dominance for language. The testing has been extended to include assessment of temporal lobe dominance for memory; an important predictor of severe memory impairment following temporal lobectomy (8). In practice, IAT is challenging to perform and interpret. Patients under unihemispheric sedation may experience distress or show



Figure 2 Intraoperative assessment of the awake patient during functional mapping by ECS. Neuropsychological language tests are presented by computer screen to the patient under the drapes. Cortical sites showing stimulus-induced interference or activation are confirmed with retesting and then marked by sterile paper numbers, as shown in Figure 1. Successful mapping depends upon patient comfort and sustained attention during the procedure. Abbreviations: ECS, electrocortical stimulation.

complex behavior, which impedes detailed language and memory assessment. Testing is limited to the brief duration of short-acting drugs. Interpretation of IAT is somewhat subjective as there is no consensus standard for neuropsychological testing nor criteria for test failure across centers (9). Intacarotid injection may not perfuse brain regions supplied by the posterior circulation, including portions of the medial temporal lobe. Finally, angiography is an invasive procedure, which carries a small but worrisome risk of stroke or vascular injury.

NEUROSURGICAL APPLICATIONS OF FUNCTIONAL IMAGING

PET was the first practical technique for noninvasive functional brain mapping (10,11). Validation studies showed activity-dependent regional cerebral blood flow (rCBF) and glucose uptake could be imaged during sensory, motor, language, and memory tasks and this led to limited application in neurosurgical planning (12–14). Widespread use of PET for presurgical functional mapping has been limited by cost and complexity as well as inherent technical limits of spatial and temporal resolution, though applications remain in functional and epilepsy surgery (15).

Nearly two decades after the advent of PET imaging, it was shown that MRI could also measure brain activity through changes in the magnetic susceptibility that accompany

fluctuations in blood oxygenation during brain activity (16). Measurement of this blood oxygen level-dependent (BOLD) signal during specific functional tasks is the basis of BOLD fMRI. It has several important advantages over PET for presurgical mapping: it is less invasive and can be combined with anatomical imaging, has better spatial and temporal resolution, and can be used to test multiple functions serially in one study. For these main reasons, in addition to cost and availability, fMRI has entered mainstream use and is the most common technique of functional brain mapping for neurosurgical planning.

One of the most important steps in making functional data useful for neurosurgery is integration and visualization with anatomy. Neurosurgical navigation systems are a convenient way to visualize functional data in relation to brain anatomy and pathology. These systems maintain a 3-D map of anatomical images (CT or MRI), which can be annotated with co-registered functional data, such as PET, perfusion, magnetoencephalography (MEG), fMRI, and DTI. During an operation, the 3D volume is stereotactically registered to the patient's head position on the operating room (OR) table by optical or radiofrequency (RF) localization systems. A pointer instrument is dynamically tracked, allowing a cutaway view of the MRI or CT with functional data matching the position of the pointer on the brain. Figure 3 illustrates the registration procedure and navigation in the operating room using a camera-based navigational system. Registration may be accomplished by

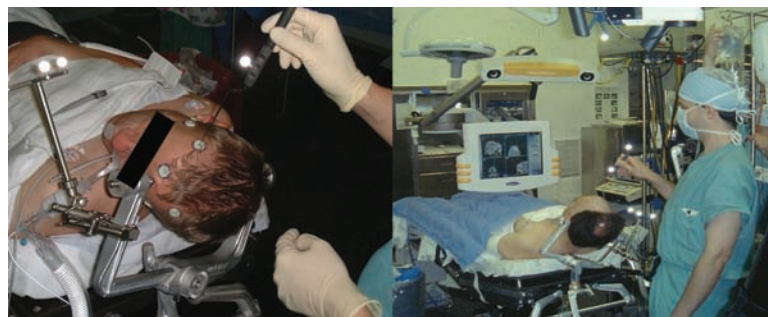


Figure 3 Intraoperative navigation by frameless stereotaxy. The patient is registered to a 3-D MRI or CT volume by touching a pointer to fiducial markers. The physical location of the pointer is tracked to millimeter accuracy by a binocular camera system, and calculated in relation to a reference star affixed to the head holder. The system can then dynamically recut and display MRI, CT, and functional data matching the location of the pointer or any tracked instrument. Abbreviations: fMRI, functional MRI.

surface matching using laser scan or by pointing to MRI/CT-visible fiducial markers placed on the patient's head prior to preoperative scan. An essential limitation of these systems is that they cannot account for shifting of the brain surface during retraction or tumor removal. Thus in many cases the anatomical and functional map becomes increasingly inaccurate as the procedure continues. Intraoperative MRI is particularly useful for updating this map during the case, localizing residual tumor and shifted brain anatomy to millimeter accuracy.

fMRI and other noninvasive functional techniques serve many practical needs in surgical planning, either alone or as an adjunct to invasive techniques. The next sections will review imaging applications in the context of common questions that arise before, during, and after surgery.

Operations in the Rolandic Region: Language Function not at Risk

Localizing the central sulcus is critical for resections near the frontoparietal border, whether for tumor, arteriovenous malformation, hemorrhage, or other pathology. First, we will consider cases where language function is determined not to be at risk either by tumor location or hemispheric dominance. In these cases the principal concern is paralysis from injury to the motor cortex of the precentral gyrus or descending CST. Central sulcus can be identified intraoperatively by ECoG and ECS, but preoperative mapping provides additional information that can help determine how an operation is done, or whether it is attempted at all. Surgical resections within or through the sensory cortex of the postcentral gyrus are far less likely to cause debilitating symptoms than those within the precentral gyrus. One might decide against surgery for the latter, particularly if the pathology is diffuse or the risk of paralysis is high. On the other hand, discrete lesions

within the precentral gyrus may be amenable to resection, in which case functional imaging can confirm the relationship of the lesion to motor cortex and descending CST. These decisions are best made prior to surgery, when the risks can be discussed together with the patient. Localizing central sulcus preoperatively also helps guide the extent of bone removal for surgical exposure and indicates where to begin ECS mapping on the cortical surface. Figure 4 shows a fMRI co-registered with an intraoperative MRI. fMRI activations during a finger-tapping task (pink) are co-registered to a high-resolution T1-postcontrast image. The central sulcus is indicated in green, the lesion is segmented in yellow and the veins are marked in purple. A picture of the cortical surface reveals the results of intraoperative ECG. fMRI was concordant with the location of hand motor intraoperatively (tag 2). After identifying motor cortex, this patient underwent awake speech mapping for this lesion.

Mapping motor and somatosensory function is among the most reliable and useful of fMRI applications for neurosurgical planning. Compared to speech and other higher cognitive functions, primary sensory and motor functions are relatively invariant in their cortical somatotopic organization, though anatomy alone can fail to clearly identify the central sulcus. This is a particular risk when tumor distorts or obscures the usual landmarks. Even in normal volunteers, interobserver agreement on central sulcus location by MRI has been reported as low as 76% (17). Motor and sensory tasks elicit strong BOLD signals from corresponding precentral and postcentral gyri. Sensorimotor BOLD activation is relatively robust to common problems, which can reduce the signal-to-noise ratio (SNR) in neurosurgical patients, like head motion, functional deficit, anxiety, abnormal vasculature, and edema. Our institution has shown the fMRI localization of rolandic cortex was more reliable than direct cortical SSEP recording (18,19), particularly when tumors distorted rolandic anatomy. Common motor and sensory

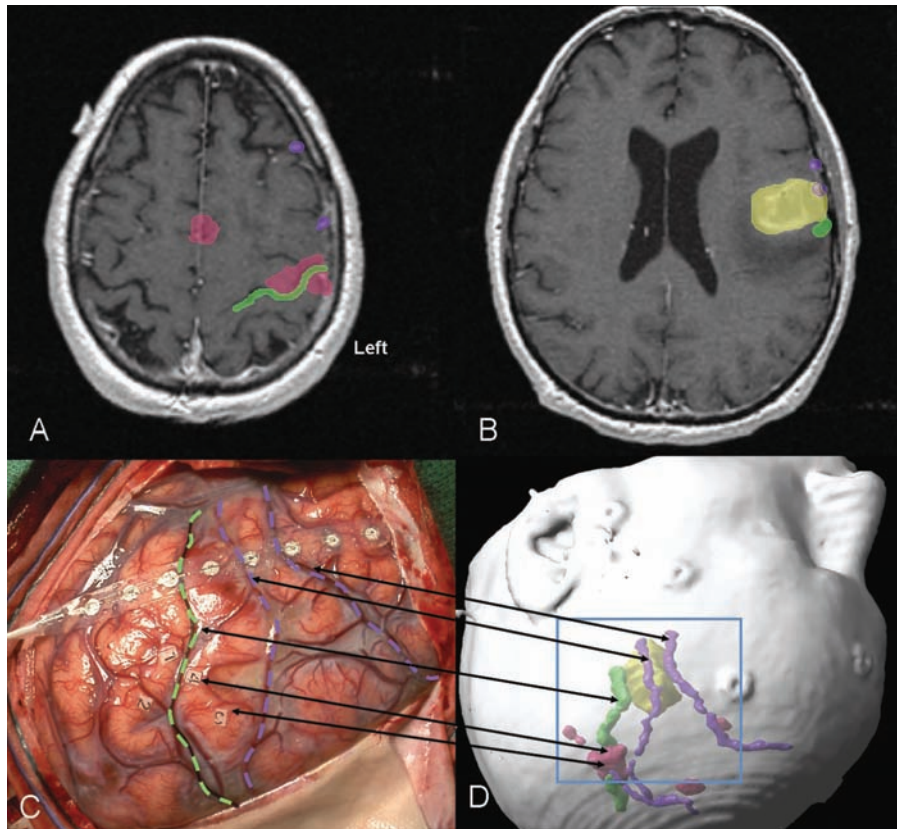


Figure 4 Motor fMRI integrated into the neuronavigational system for guidance during the neurosurgical procedure. **(A)** Pink indicates the location of right-hand motor on fMRI. Green line marks the central sulcus and purple marks veins. **(B)** Tumor is segmented in yellow. **(C)** and **(D)** show how segmented objects correlate with an intraoperative cortical surface photograph. Tag numbers 3 and 4 on the cortical surface are concordant with fMRI predictions of hand-motor localization. Abbreviations: fMRI, functional MRI.

fMRI paradigms (covered more completely in chapter 2) include finger-thumb tapping or passive sensory stimulation where the patient's hand is scrubbed with a rough object. Because of the reciprocity of connections between sensory and motor cortex, the precentral gyrus activates reliably with either task.

Distinguishing the postcentral gyrus from the precentral gyrus is, of course, one of the main goals of fMRI mapping for rolandic lesion. A surgical trajectory through motor cortex, or a resection carried into this region, risks a fixed postoperative paralysis. Debilitating deficits from injury to somatosensory cortex are rare and so a postcentral approach is the preferred trajectory to lesions deep to the central sulcus. Even with good BOLD response, it can be difficult to discern motor from sensory cortex in patients with brain tumors because of coactivation of pre- and postcentral cortex during most tasks. To interpret the activation patterns, it is useful to note that it is principally the posterior bank of grey matter in both the motor and sensory gyri that activate during fMRI tasks. Figure 5

demonstrates a widespread distribution of activation in finger-thumb tapping. As seen in this example, it is not uncommon to find BOLD activation in pre-motor areas anterior to the precentral gyrus as well. One must be cautious interpreting BOLD activation in cases where tumor invades the primary motor areas, potentially causing either false negative measurement of function in the motor gyrus itself or a relatively increased magnitude of activation in pre-motor or postcentral gyri. In our institution we first test fMRI localization of the central sulcus against anatomical prediction. Often the central sulcus is indicated by anatomical landmarks such as the "omega" curl representing cortical expansion of the hand representation of the precentral gyrus. Anatomical evidence of central sulcus location is balanced against fMRI evidence and further attention directed to discordances. When interpreting both sensory and motor task activation patterns, one would expect the sensory activation to be biased toward the postcentral gyrus and motor to be biased toward the precentral gyrus. However, there are cases where the

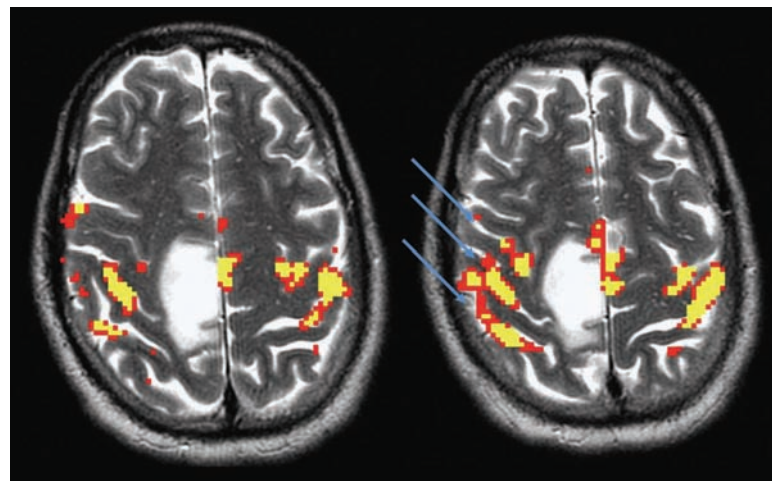


Figure 5 fMRI activation during bilateral finger tapping overlaid on two contiguous T2-weighted images in a patient with a glioma in the leg/foot portion of the motor gyrus. A simple task like finger tapping can produce ambiguous results in a patient without an obvious anatomical landmark like the reverse omega. In this case the premotor, motor, and sensory gyri all activate in comparable magnitude obscuring the location of the central sulcus (and motor gyrus). Central sulcus is the middle sulcus and the medial fMRI activation area is the supplementary motor area. Abbreviations: fMRI, functional MRI.

motor gyrus activates predominantly or equally regardless of the specific sensory/motor paradigm.

Preoperative functional localization of foot and leg motor cortex is of particular utility for surgery in the medial frontoparietal border. The motor cortex subtending foot and leg function abuts the interhemispheric fissure and can be difficult to expose during surgery because of cortical veins bridging over to the midline sagittal sinus. Injury to this area risks loss of ambulation yet poor access limits mapping by direct cortical stimulation. As a result, it is useful to have a functional map of foot and leg motor activation co-registered to the intraoperative navigation system during resection. Furthermore, the location of the foot/leg portion of the motor homunculus in relation to SMA can be difficult to delineate without an fMRI map of function. Figure 6 shows an example of the spatial distribution of SMA and foot motor. Speech SMA is not included in the fMRI map but its location is indicated in the anterior position in the mock figure below. Notice that it would be difficult to know the extent of localization of these structures without functional imaging.

As a practical consideration, every institution has different standards of scanning alignment for functional imaging. Common landmarks include the hard palate, AC/PC line or straight axial acquisition for import into format-constrained neuronavigational systems. fMRI should ideally be obtained on standardized alignment (AC/PC in our institution), which places the central sulcus near the y-axis center of the upper axial cuts, and thus

gives a complete picture of precentral, central, and postcentral activation in one plane.

Lesions located in the deep white matter (corona radiata) of the frontoparietal junction are especially challenging for safe resection because of the risk of injury to descending CST. As with ECS, bipolar electrical stimulation of white matter tracts can be done, and positive motor responses are somewhat predictive of postoperative deficits (20,21). A central problem with subcortical stimulation is that the edge of resection must closely approach CST or other functional tracts before stimulation can be effective. Compared to cortical stimulation, white matter ECS requires higher currents and is less reliable: false negative findings are a real danger.

Diffusion tractography, in conjunction with fMRI, can be especially useful in giving some indication where the CST resides in relation to the cavity and thereby guide more careful assessment by direct stimulation as the tracts are approached (22,23). Preoperative evaluation of DTI can help plan the approach to lesion in deep white matter. During resection, integration of DTI into neurosurgical navigation may increase confidence of resection and protect against inadvertent neurological injury (24). As previously discussed, brain shift during tumor resection often reduces the accuracy of intraoperative navigation when it is needed most: as the resection nears completion and white matter is approached. DTI can be reacquired intraoperatively in centers where intraop MRI is available (25). Even a static preoperative DTI map can be valuable in directing the surgeon to perform focussed white matter stimulation

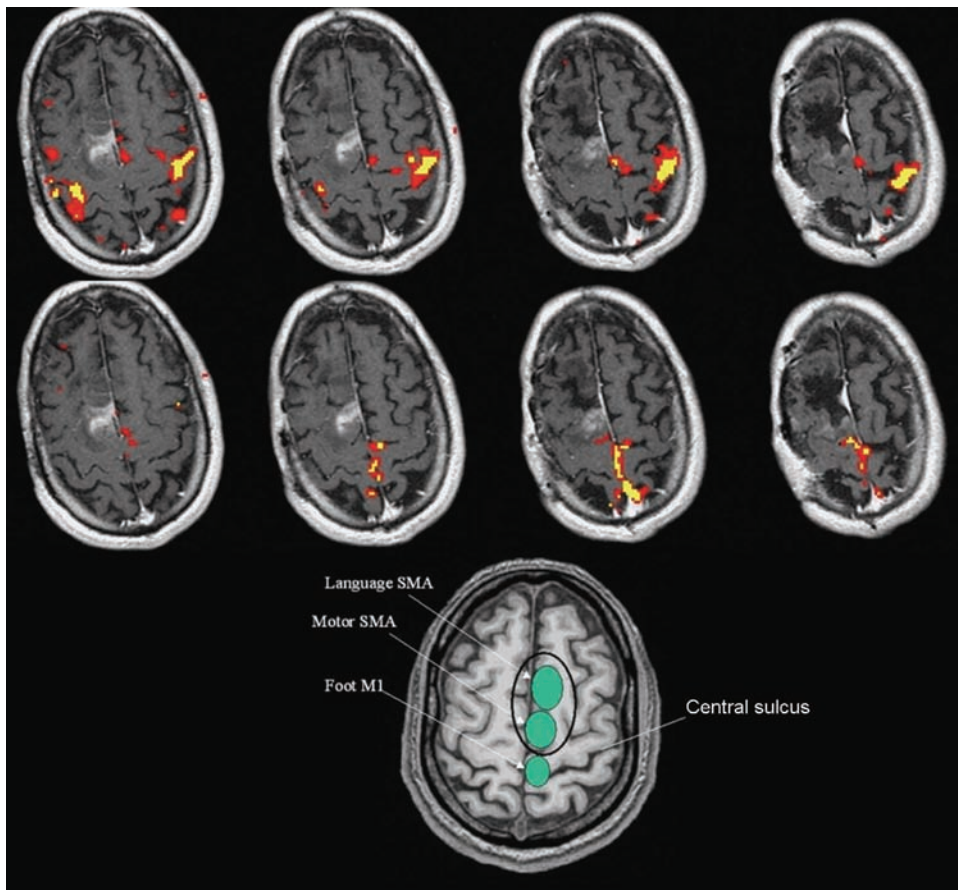


Figure 6 Anatomical boundaries of dorso-medial functional regions are poorly defined. The fMRI activated locations of the supplementary motor area and the foot portion of the M1 motor homunculus in a patient with a glioma is overlaid on a T1-post contrast. Bilateral finger tapping primarily results in pre-central and SMA activations whereas toe tapping primarily activates the medial aspects of the motor gyrus. Schematic represents the approximate organization of the SMA and medial aspect of the pre-central gyrus on the anterior/posterior axis. Language SMA (also referred to as pre-SMA) is anterior to the motor component of the SMA. The foot portion of the motor homunculus resides just posterior to the motor portion of the SMA. Similar organization exists in the non-dominant hemisphere, though the extent to which the language SMA activates is variable. Abbreviations: fMRI, functional MRI.

mapping as white matter is approached. Figure 7 shows how integration of DTI with intraoperative navigation system allows the surgeon to perform subcortical stimulation in the expected direction of the CST. In this case, leg paresthesias indicated sensory fibers lying posterior to the CST, and resection of the infiltrating tumor edge was halted on this border. This example also illustrates how the full complexity of the fractional anisotropy color map may be reduced to segmented tracts for presentation on the intraoperative navigation screen. This reduction of information can bring clarity to the display or can obscure important details. Figure 8 shows how a single DTI dataset can be represented in navigational software. Model-based fiber tracking is particularly apt to de-emphasize small fiber tracts or misrepresent crossing tracts. The starting point for understanding white matter anatomy should be the full FA map, and the neurosurgeon should initially work

together with a neuroradiologist to develop a reliable methodology for integrating DTI into navigational display.

Operations Risking Frontal Language Function

In contrast to sensory and motor function, language function is broadly distributed throughout the temporal, parietal, and frontal lobes, and may also be distributed across both cerebral hemispheres. Whether language is considered “at risk” for a surgical resection depends on the lesion location but also on the patient’s hemispheric dominance for language and their specific functional organization.

A wide range of techniques have been investigated to evaluate language distribution in the presurgical setting (9,26). Some techniques measure laterality only, such as

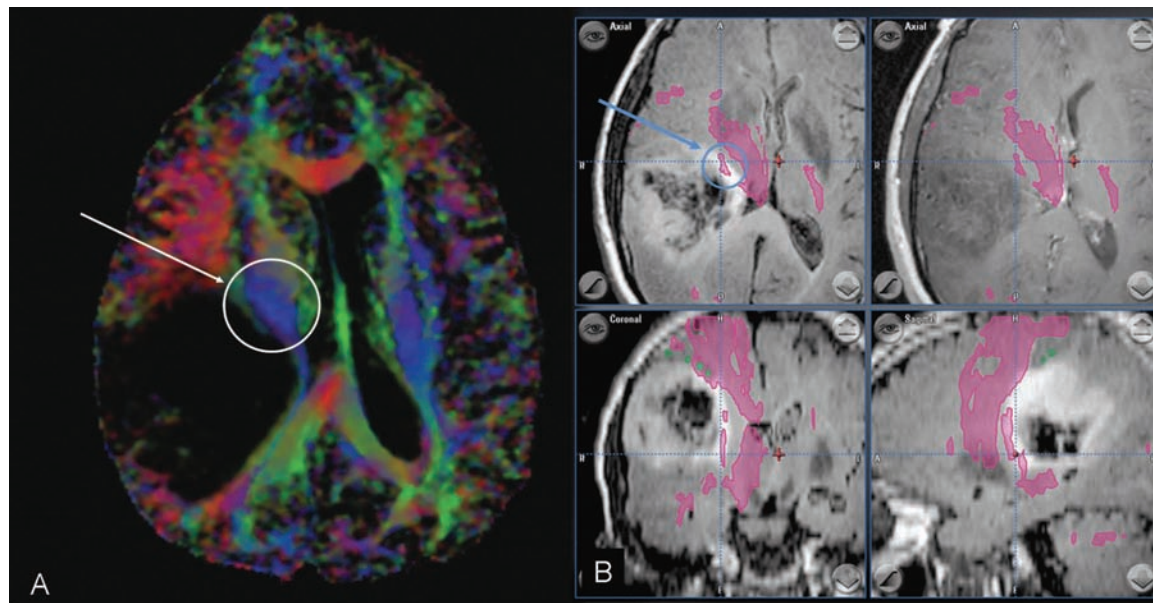


Figure 7 Color fractional anisotropy map (**A**) and intraoperative neuronavigational image (**B**) in a patient with a glioblastoma multiforme. White arrow on fractional anisotropy map indicates the expected anatomical location of the descending CST. Blue arrow in the neuronavigational image indicates the location that produced leg paresthesia upon subcortical electrical stimulation intraoperatively confirming DTI predictions by marking descending somatosensory fibers posterior to CST. Abbreviations: CST, corticospinal tract; DTI, diffusion tensor imaging.

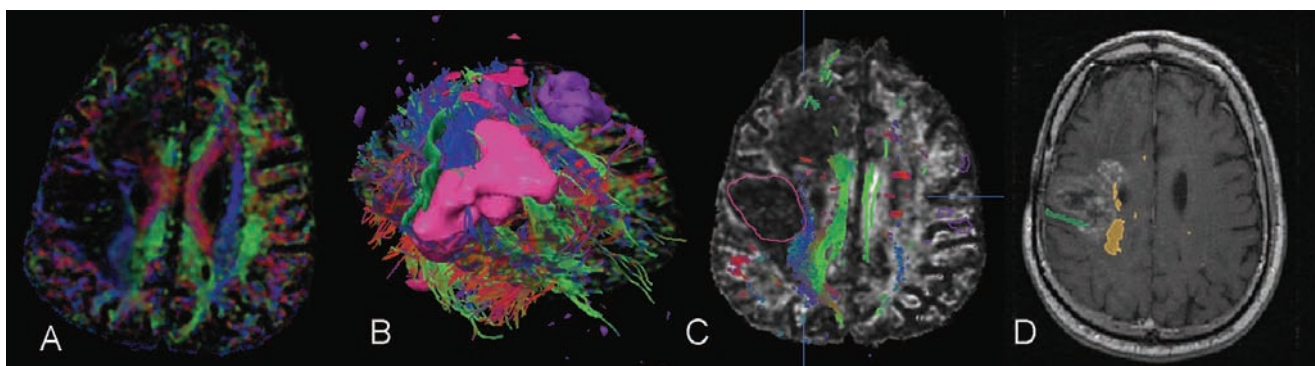


Figure 8 Different methods of summarizing a DTI dataset for surgical planning. (**A**) FA color map shows weak anisotropy for descending tracts medial to tumor. (**B**) Model-based fiber tracks, seeded from central sulcus, are plotted in relation to tumor (*pink*) and central sulcus (*drawn in green*). (**C**) Axial cut through 3-D model shows relation of medial tumor border to descending tracts. (**D**) Further reduction of data to highlight just the descending tracts determined by fiber tracking, overlayed on T1 contrast image. Note that by now the most prominent descending tracts are actually posterior to the central sulcus (*green*) and to the expected location of corticospinal tracts, confirmed in this case by intraoperative white-matter stimulation. The true location of the CST is better appreciated on the FA map (**A**). Abbreviations: DTI, diffusion tensor imaging; FA, fractional anisotropy.

IAT, transcranial doppler ultrasound, or tachistoscopic naming tests. Other techniques provide a degree of localization as well: transcranial magnetic stimulation (TMS), near-infrared spectroscopy (NIRS), magnetoencephalography (MEG), PET, and fMRI. At present, fMRI is the most widely used technology for presurgical language assessment and will be the focus of this section.

fMRI mapping of language activation is used for two main purposes in neurosurgical planning: language lateralization and localization. For tumor surgery, preoperative determination of laterality may be used to confirm expected hemispheric dominance or suggest atypical hemispheric dominance, either of which are important for risk assessment. Localization allows the surgeon to

assess preoperatively to what degree risk to language is suspected and either tailor the approach to avoid those areas or decide that a safe approach is not possible.

Laterality

Hemispheric language dominance is related to both the side and degree of handedness. Left hemispheric language dominance is often considered the general rule for both right- and left-handed patients, but atypical dominance (right- or bi-hemispheric) has been reported in 4% of strongly right-handed, 15% of ambidextrous, and 27% of strongly left-handed normal individuals by transcranial doppler ultrasound (27). Patients with longstanding tumor or epilepsy may have a higher incidence of atypical dominance presumably as a result of development or remodeling (28). A recent study of epileptic patients by IAT found atypical dominance in 9%, 46% and 69% of strongly right-handed, ambidextrous, and strongly left-handed individuals, respectively (29). Variability in the reported incidence of atypical dominance is attributable in part to the variety of techniques used to investigate laterality (26). From a practical standpoint, preoperative determination of laterality is most important for planning frontal resections when symptoms suggest atypical dominance. For example, a left-sided lesion in Broca's area presenting without speech disturbance suggests possible right-hemispheric dominance, which would reduce the risk of surgery. Similarly, a right-handed patient presenting with dysphasia and a right frontal lesion would also suggest right dominance. In both cases, awake craniotomy and ECS mapping should be considered regardless of laterality results. In our institution, awake mapping is standard for patients with language dysfunction or for left-sided lesions in locations close to functional language or motor cortex.

When analyzed for hemispheric lateralization of language, fMRI has achieved significant concordance with Wada results (30–33). One study of 100 patients reported 91% concordance between Wada and fMRI (32). Benke et al. found that fMRI and Wada results in patients with epilepsy was 89% concordant in patients with right-hemispheric temporal lobe epilepsy versus 73% in patients with left temporal lobe epilepsy, possibly highlighting differences in sensitivity to cortical remodeling (33).

There are as yet no standardized paradigms or analysis methods for determining laterality from fMRI. One may be able to bolster concordance with Wada by statistically combining the results of four separate language tasks (termed combined-task analysis) (30,31,34). In this approach, the resultant map is theoretically more indicative of essential speech across tasks rather than representative of those areas preferentially engaged in one task or another.

It should be noted that studies comparing fMRI and Wada are generally performed in patients with temporal lobe epilepsy or tumor. It is unclear yet whether the performance of fMRI will hold when assessing patients with frontal tumors or arteriovenous malformations. As acquisition parameters and paradigms are validated and standardized, fMRI may supplant the Wada test for determining hemispheric lateralization of language, at least in some cases.

Localization

For frontal lobe surgery, locations of most obvious concern for expressive language are the lateral precentral gyrus (motor cortex for face and tongue) and inferior frontal gyrus (Broca's area) in the dominant hemisphere. While these regions may be anatomically defined, the specific distribution of language function across this anatomy varies widely between individuals (35). Secondary language centers like the middle frontal gyrus and SMA may also harbor critical function, though the degree probably varies individually. The distributed nature of language makes language mapping more nuanced, whether done by ECS or functional imaging.

In fMRI mapping of primary sensory and motor tasks, there are two main gyri that are responsible for essential function. In contrast, language tasks may activate many locations (e.g., inferior frontal, middle frontal, superior frontal, superior temporal, middle temporal, and occasionally supramarginal and angular gyri). Furthermore, the patterns of activation may be task specific. However, only a subset of areas activated by speech tasks must be avoided during surgical resection to preserve essential speech function. As a result, fMRI localizations of speech function are often tested with intraoperative ECoG (18,36,37). An interruption of speech upon stimulation of a particular area (or fMRI activation) is taken to mean that that cortical space is essential for that function (5,38). Often fMRI activation sites do not exhibit language disruption with electrical stimulation (30,31), and these locations may be amenable to surgery in the service of removing tumor without leaving a gross deficit. These areas are thought to be secondary or supportive of speech function in a complicated functional network including perception, attention, and association and not critical to basic speech output. In testing concordance of fMRI with intraoperative direct cortical stimulation, Roux et al. found poor sensitivity for picture naming and verb-generation tasks (22% and 36%, respectively) but excellent specificity for both tasks (97% picture and 98% verb) (36). Combining two-language tasks improved both specificity and sensitivity to 97% and 59%, respectively. Another study by Rutten et al. found 100% sensitivity and 61% specificity when using a combined-task analysis (30,31). Interestingly, this study also suggested that fMRI had a

better negative predictive value (the absence of critical language areas) than positive predictive value (presence of activations at critical language sites).

In order to compare fMRI activation with intraoperative cortical stimulation, it is useful to use matching paradigms for both the fMRI task and the intraoperative language assessment. Historically, fMRI speech paradigms utilize silent tasks (e.g., think of the name of the picture) in order to avoid head motion during vocalization (39). Comparing fMRI activation from silent speech paradigms with intraoperative speech arrest, we have noted systematic discordance especially prominent over the inferior precentral gyrus. We have demonstrated that silent speech paradigms bias the fMRI map toward anterior aspects of the frontal language system (inferior frontal gyrus) (19). This, in turn, has consequences for intraoperative speech mapping where one of the most salient indicators of frontal speech localization is speech arrest. Figure 9 illustrates typically disparate findings between intraoperative mapping and fMRI activation based on silent speech paradigms. Numbers 1 to 5 indicate the location of speech errors and arrest with ECS, while the pink region represents the area of fMRI activation during a silent speech paradigm. When a tongue movement paradigm was included, the centroid of fMRI activation shifted to include the most common area of speech arrest. Where possible, vocalized speech paradigms be included in order to fully represent the speech network and provide

maximal positive predictive value for intraoperative mapping.

Dominant Posterior Temporal: Wernicke's Area

Lesions in the posterior portion of the superior or middle temporal gyri should be assessed for proximity to receptive language function, including the canonical Wernicke's area (38,40). As with expressive language, location of receptive function varies widely among individuals (35). Here too, ECS plays a primary role in mapping intraoperatively. Subcortical stimulation of white matter, aided by DTI delineation of major tracts, may be of utility in stopping resection before injury to functional tracts (41).

Hemispheric dominance for language and memory are of paramount concern when planning resection of the mesial temporal lobe for epilepsy, or rarely, for tumor. In this surgical approach, the boundaries of the resection encompass the anatomical mesial temporal structures, or their anterior portions. Postoperative deficits in verbal and other memory functions are predicted in part by preoperative dominance. Functional localization of cortical regions subtending receptive language by fMRI or ECS can help tailor the resection of the lateral temporal lobe. In some cases, it is possible to image an epileptic focus noninvasively either by ictal hyperperfusion (fMRI) and hypermetabolism (PET), or conversely by the relative hypoperfusion and hypometabolism of the focus between seizures.

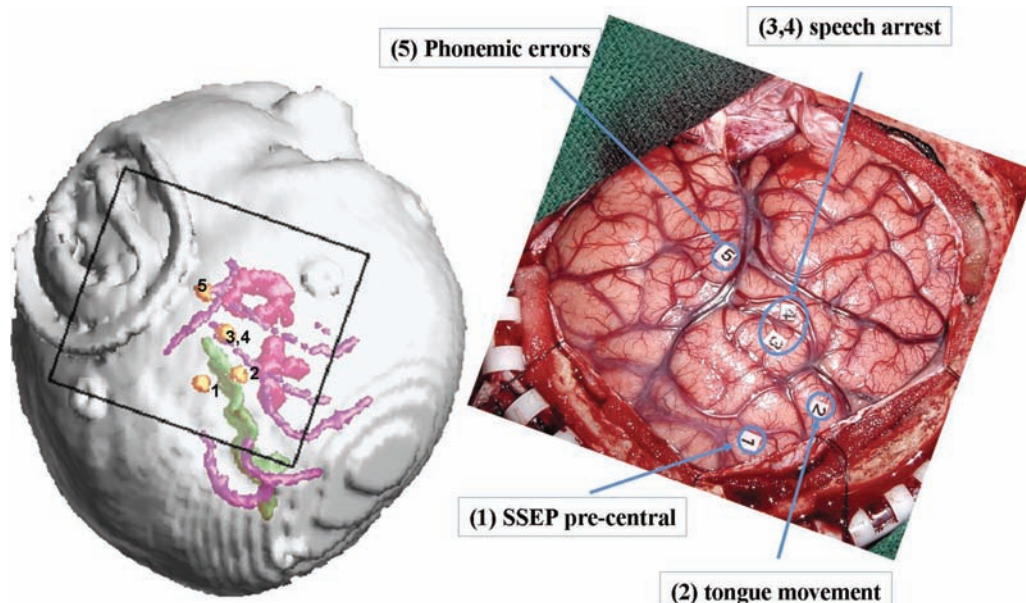


Figure 9 Speech fMRI integrated for navigation. Silent speech generated fMRI maps commonly used to avoid head motion, localized speech anterior to the site causing speech arrest (tag numbers 3 and 4) in this patient. Silent speech fMRI paradigms may not be the most indicative of where cortical stimulation will elicit intraoperative speech arrest, the most declarative language finding in and around Broca's area. *Source:* Adapted from Ref. 19. *Abbreviations:* fMRI, functional MRI.

Mapping posterior temporal speech areas requires special attention. Using ECoG during an awake craniotomy to assess speech function is difficult. This is particularly true when attempting to measure and assess posterior temporal speech areas (Wernicke's Area). It requires an experienced clinician to detect what are often subtle speech paraphasias in this area. Unlike speech mapping in the frontal region where patients often exhibit halting speech arrest, cortical mapping is more difficult in temporal areas, especially given patients' variable performance and lucidity emerging from anesthesia. For this reason, it is helpful to have a co-registered fMRI map of posterior temporal language function to guide stimulation. This can reduce the time of a fishing expedition that often results from mapping this area *de novo*.

Accordingly, temporoparietal speech areas can be elusive on fMRI as well. While many speech fMRI paradigms that are tailored to activate Wernicke's area also activate Broca's area as well, the converse is not true. That is, tasks designed to elicit productive Broca's area activations will not necessarily activate Wernicke's area. Tasks designed to tax the receptive language system like reading, auditory responsive naming (e.g., what do you write with?) and sentence comprehension and sentence completion are commonly used tasks for this purpose. Auditory responsive naming has the advantage of being easily performed in the operating room and during awake craniotomy. In this way the fMRI scanning procedures can parallel the intraoperative procedures and this may lead to better concordance of these very different functional techniques.

Secondary Speech Areas

Secondary speech areas are not a well-defined group: the extent to which one considers an area secondary and not essential for speech is directly dependent upon the sensitivity of the neuropsychological test. For example, the supramarginal and angular gyri may be considered secondary in a task like confrontation naming but are of primary concern in reading, writing, and judgment of quantity (42–44). Most fMRI speech paradigms for neurosurgical planning are designed with a general goal of localization of major language areas in mind. However, damage to a secondary area like dominant SMA can result in paucity of speech and in extreme cases mutism (45–47). Insult to middle frontal gyrus can cause deficits in verbal working memory (48). Though, it should be noted that deficits imparted by damage to these so-called secondary or nonessential speech areas do resolve more often than would similar damage in Broca's and Wernicke's areas. Fine mapping of secondary language areas may provide a more complete picture of a patient's speech network, but it may not translate to neurosurgical utility in most cases.

Risk of a transient or tolerable deficit has to be balanced against the medical benefit of surgery. One way in which fMRI may contribute to neurosurgical practice in this respect is by making predictions about deficit following surgical resection. Studies of patients with tumors in the dominant SMA have suggested that the degree to which the SMA lateralizes during speech fMRI paradigms may correlate with the risk of postoperative aphasia following surgical resection (47,49). Figure 10 shows two patient cases where low-grade gliomas invaded the left SMA. fMRI of speech (verb generation in both cases) in Patient 1 suggested right lateralized SMA activation. Patient 2 did not show significant lateralization. The extent of the resection was similar in both cases. Patient 2 developed a transient postoperative dysphasia while Patient 1 did not. fMRI may have untapped utility in helping predict expected postoperative deficits and allow counseling of patients prior to surgery.

Medial Temporal Resection or Lobectomy Memory Paradigms

Using fMRI to lateralize memory is currently not well established. Part of the difficulty stems from a lack of consensus for which of the various stages of processing (encoding, retrieval, recognition) provide the best predictive value in terms of postoperative outcomes. In temporal lobe memory lateralization, Avila et al. (50) suggested a differential response for encoding versus retrieval and cautioned against using one or the other to predict clinically significant memory lateralization. This study also noted a significant variability both across tasks (intra-subject) and across patients (inter-subject) in the pattern of lateralization for complex scenes versus a spatial recall task. Studies have also suggested memory lateralization based not only on the stage of processing but material specificity. For example, Golby et al. found that the ability of a stimulus to be verbalized affects the hemisphere to which it lateralizes with easily verbalizable stimuli lateralizing to the language-dominant hemisphere (usually the left) and stimuli not easily verbalizable lateralizing memory to the nonlanguage-dominant hemisphere (51). Consequently, it is not surprising that there is evidence of a correlation between language lateralization and verbal encoding (52). Specifically, strong leftward lateralization for language in this study was correlated with strong leftward dominance of verbal but not face encoding. (Interestingly, Golby et al. also found bilateral representation of faces and scenes during encoding in the MTL.) Thus, it may be that hemispheric dominance for verbal encoding may be inferred from hemispheric dominance for language, a measure better established using fMRI. Of course, while these correlations are helpful clinically

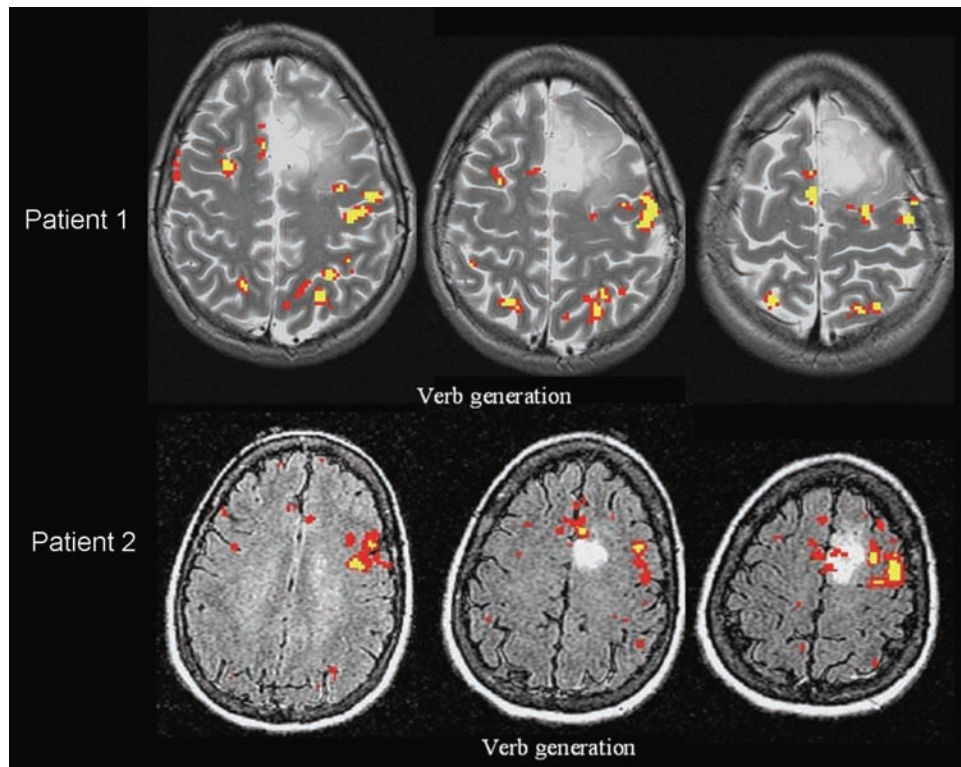


Figure 10 SMA activation on fMRI may predict risk for post-operative deficit. Two patients with low-grade gliomas in the superior frontal gyrus. During a covert verb-generation task, Patient 1 lateralized fMRI activation to the right hemisphere and patient 2 did not. Both had a similar extent of resection on the posterior margin of the lesions. Patient 2 developed a post-operative dysphasia. Patient 1 (showing lateralized SMA to the right hemisphere) did not develop dysphasia or an SMA syndrome in the postoperative period. Abbreviations: SMA, fMRI, functional MRI.

where memory cannot be explicitly measured, it is likely that there exists enough variability in functional organization in both normal and patient populations to warrant the development of techniques that measure memory function directly.

fMRI paradigms used for clinical memory localization can target both the encoding and retrieval aspects of memory. Some of the simpler encoding paradigms display either novel or repeated blocks of faces, patterns, complex scenes, and words and ask the patient to perform a distractor task like indicating outdoor scenes with a button box. Analysis finds activation during the novel conditions where the stimuli were encoded (51). Straightforward retrieval paradigms ask the patient to indicate whether a stimulus is novel or repeated (53). The “n-back” task has also been used in patients and is a more robust assay of frontal systems. Patients are presented with a series of stimuli (often numbers) and are asked whether the current stimulus occurred n stimuli back in the series (54). The task at higher numbers of n also measures executive function and can be a robust activator of working memory particularly in the dorsolateral prefrontal cortex.

Little is known yet about functional significance of injury to specific sites activated in these complex paradigms. A correlation has been shown between fMRI activation during a verbal working memory task and ECS of the dorsolateral prefrontal cortex (48). The authors removed the fMRI/ESM site as a necessary resection of an epileptogenic focus. The patient demonstrated a selective impairment in working memory tasks that persisted for over two years. Further, Richardson (55) showed a correlation between fMRI activation and postsurgical verbal memory decline. These studies illustrate the feasibility of using fMRI and ESM together to aid neurosurgeons in complex cognitive measures like memory function.

OTHER FUNCTIONAL TECHNIQUES

We have focussed on fMRI in this chapter as a practical acknowledgment of its increasing prevalence in neurosurgical planning. Techniques such as MEG and PET have established niche uses as well. Arguably, the technique with the most promise alongside fMRI in the near future is

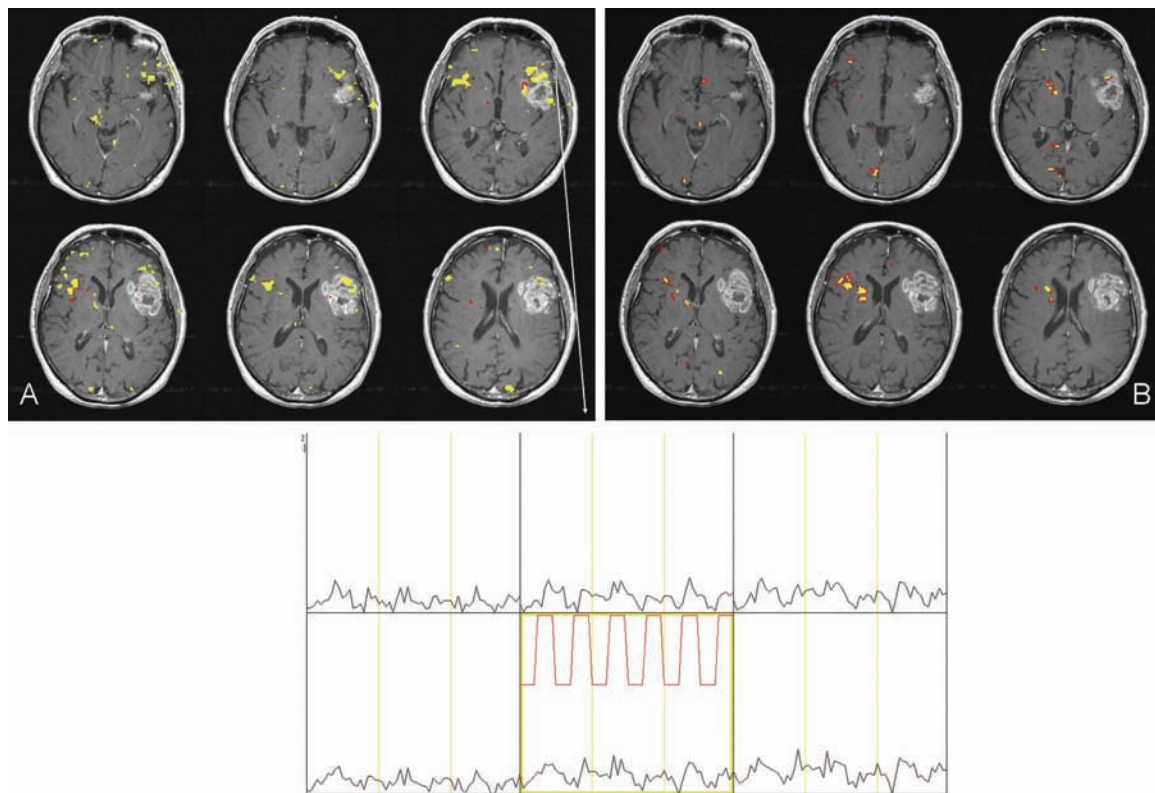


Figure 11 fMRI variability and task specificity. fMRI result in a 75-year-old man with a glioblastoma multiforme. (A) fMRI map during a phonemic fluency task suggests that there is functional activity within the contrast-enhancing lesion. (B) fMRI result in the same patient during a semantic fluency task did not suggest the same functional localization but instead suggests right dominance for Broca's area. While intraoperative direct cortical stimulation results were inconclusive, gross total resection of the lesion (in the anatomical location of Broca's area) did not impart aphasia postoperatively. The graph represents the fMRI signal time-course over the entire 60-image acquisition in six adjacent voxels; red boxcar function represents the stimulus presentation. Abbreviations: fMRI, functional MRI.

TMS. TMS is being used clinically with limited experience (56,57,58) and may be used to validate fMRI findings or to distinguish essential from nonessential activation sites. For example, Figure 11 shows a right-handed patient with a glioblastoma multiforme in the left hemisphere. fMRI using a phonemic-fluency task suggests bilateral representation of speech while a semantic-fluency task indicates right-hemisphere dominance for speech in Broca's area. Direct cortical stimulation was not possible for technical reasons. However, with the patient awake and functioning without deficit, gross-total resection of this lesion was possible without postoperative speech deficit. This suggests that the patient had translocated his Broca's area function to the right hemisphere as suggested by the semantic-fluency fMRI task. In a case like this, TMS could have validated or refuted the suggestion of right-hemispheric reorganization by significantly interrupting speech in the right hemisphere or not. In this way, not only is information gained in the interpretation of atypical speech dominance using fMRI, but preoperative surgical planning also benefits.

CONCLUSION

While functional imaging has progressed remarkably in the last 15 years, there has been no abrupt revolution in neurosurgical practice. Instead, we have seen the gradual improvement in functional paradigms and statistical analyses, and the accrual of validation results comparing new modalities against “gold standard” methods like ECS and IAT as well as against neurological outcomes. This quiet growth in the foundation of knowledge is leading surgeons, neurologists, and neuroradiologists to interpret functional mapping and confidently apply results to the assessment of risk and the planning of surgery. The gradual impact of functional imaging is tangible in practice for those who have used it—one can simply look back over the last 15 years and find that there are now fewer cases of surprise results in the OR, fewer aborted surgeries because of unanticipated function, and greater efficiency in conducting intraoperative mapping. The history of neurosurgery suggests that outcomes improve when more information is available to plan and guide surgery, and when procedures are made more efficient.

REFERENCES

1. Fulton JF. Observations upon vascularity of human occipital lobe during visual activity. *Brain* 1928; 51:310–320.
2. Penfield W. The evidence for a cerebral vascular mechanism in epilepsy. *Ann Intern Med* 1933; 7:303–310.
3. Penfield W, Boldrey E. Somatic motor and sensory representation in the cerebral cortex of man as studies by electrical stimulation. *Brain* 1937; 60(4):389–443.
4. Penfield W, Jasper H. Epilepsy and the Functional Anatomy of the Human Brain. Boston Little Brown and Company, 1954.
5. Ojemann G, Ojemann J, Lettich E, et al. Cortical language localization in left, dominant hemisphere. An electrical stimulation mapping investigation in 117 patients. *J Neurosurg* 1989; 71(3):316–326.
6. Wada J, Rasmussen T. Intracarotid injection of sodium amytal for the lateralization of cerebral speech dominance. *J Neurosurg* 1960; 17:266–282.
7. Branch C, Milner B, Rasmussen T, et al. Intracarotid sodium amytal for the lateralization of cerebral speech dominance; observations in 123 patients. *J Neurosurg* 1964; 21:399–405.
8. Milner B, Branch C, Rasmussen T, et al. Study of short-term memory after intracarotid injection of sodium Amytal. *Trans Am Neurological Association* 1962; 87:224–226.
9. Pelletier I, Sauerwein HC, Lepore F, et al. Non-invasive alternatives to the Wada test in the presurgical evaluation of language and memory functions in epilepsy patients. *Epileptic Disord* 2007; 9(2):111–126.
10. Phelps ME, Mazziotta JC. Positron emission tomography: human brain function and biochemistry. *Science* 1985; 228 (4701):799–809.
11. Fox PT, Mintun MA. Noninvasive functional brain mapping by change-distribution analysis of averaged PET images of H₂15O tissue activity. *J Nucl Med* 1989; 30(2): 141–149.
12. Leblanc R, Meyer E, Bub D, et al. Language localization with activation positron emission tomography scanning. *Neurosurgery* 1992; 31(2):369–373.
13. Fried I, Nenov VI, Ojemann SG, et al. Functional MR and PET imaging of rolandic and visual cortices for neurosurgical planning. *J Neurosurg* 1995; 83(5):854–861.
14. Polin RS, Lilien DL, et al. Applications of positron emission tomography in neurosurgery: past, present, and future. *Neurosurg Focus* 2000; 8(2):1–5.
15. Xiong J, Nickerson LD, Downs JH III, et al. Basic principles and neurosurgical applications of positron emission tomography. *Neurosurg Clin N Am* 1997; 8(3): 293–306.
16. Ogawa S, Lee TM, Kay AR, et al. Brain magnetic resonance imaging with contrast dependent on blood oxygenation. *Proc Natl Acad Sci U S A* 1990; 87(24): 9868–9872.
17. Sobel DF, Gallen CC, Schwartz BJ, et al. Locating the central sulcus: comparison of MR anatomic and magnetoencephalographic functional methods. *AJNR Am J Neuroradiol* 1993; 14(4):915–925.
18. Ruge MI, Victor J, Hosain S, et al. Concordance between functional magnetic resonance imaging and intraoperative language mapping. *Stereotact Funct Neurosurg* 1999; 72(2–4):95–102.
19. Petrovich N, Holodny AI, Tabar V, et al. Discordance between functional magnetic resonance imaging during silent speech tasks and intraoperative speech arrest. *J Neurosurg* 2005; 103(2):267–274.
20. Keles GE, Lundin DA, Lamborn KR, et al. Intraoperative subcortical stimulation mapping for hemispherical perirolandic gliomas located within or adjacent to the descending motor pathways: evaluation of morbidity and assessment of functional outcome in 294 patients. *J Neurosurg* 2004; 100(3): 369–375.
21. Carrabba G, Fava E, Giussani C, et al. Cortical and subcortical motor mapping in rolandic and perirolandic glioma surgery: impact on postoperative morbidity and extent of resection. *J Neurosurg Sci* 2007; 51(2):45–51.
22. Kamada K, Todo T, Masutani Y, et al. Combined use of tractography-integrated functional neuronavigation and direct fiber stimulation. *J Neurosurg* 2005; 102(4):664–672.
23. Berman JI, Berger MS, Chung SW, et al. Accuracy of diffusion tensor magnetic resonance imaging tractography assessed using intraoperative subcortical stimulation mapping and magnetic source imaging. *J Neurosurg* 2007; 107(3):488–494.
24. Wu JS, Zhou LF, Tang WJ, et al. Clinical evaluation and follow-up outcome of diffusion tensor imaging-based functional neuronavigation: a prospective, controlled study in patients with gliomas involving pyramidal tracts. *Neurosurgery* 2007; 61(5):935–948; discussion 948–949.
25. Nimsky C, Ganslandt O, Merhof D, et al. Intraoperative visualization of the pyramidal tract by diffusion-tensor-imaging-based fiber tracking. *Neuroimage* 2006; 30(4): 1219–1229.
26. Abou-Khalil B. An update on determination of language dominance in screening for epilepsy surgery: the Wada test and newer noninvasive alternatives. *Epilepsia* 2007; 48(3): 442–455.
27. Knecht S, Drager B, Deppe M, et al. Handedness and hemispheric language dominance in healthy humans. *Brain* 2000; 123(pt 12):2512–2518.
28. Seitz RJ, Huang Y, Knorr U, et al. Large-scale plasticity of the human motor cortex. *Neuroreport* 1995; 6(5):742–744.
29. Isaacs KL, Barr WB, Nelson PK, et al. Degree of handedness and cerebral dominance. *Neurology* 2006; 66(12): 1855–1858.
30. Rutten GJ, Ramsey NF, van Rijen PC, et al. FMRI-determined language lateralization in patients with unilateral or mixed language dominance according to the Wada test. *Neuroimage* 2002; 17(1):447–460.
31. Rutten GJ, Ramsey NF, van Rijen PC, et al. Development of a functional magnetic resonance imaging protocol for intraoperative localization of critical temporoparietal language areas. *Ann Neurol* 2002; 51(3):350–360.
32. Woermann FG, Jokeit H, Luerding R, et al. Language lateralization by Wada test and fMRI in 100 patients with epilepsy. *Neurology* 2003; 61(5):699–701.

33. Benke T, Köylü B, Visani P, et al. Language lateralization in temporal lobe epilepsy: a comparison between fMRI and the Wada Test. *Epilepsia* 2006; 47(8):1308–1319.
34. Ramsey NF, Sommer IE, Rutten GJ, et al. Combined analysis of language tasks in fMRI improves assessment of hemispheric dominance for language functions in individual subjects. *Neuroimage* 2001; 13(4):719–733.
35. Ojemann GA. Individual variability in cortical localization of language. *J Neurosurg* 1979; 50(2):164–169.
36. Roux FE, Boulanouar K, Lotterie JA, et al. Language functional magnetic resonance imaging in preoperative assessment of language areas: correlation with direct cortical stimulation. *Neurosurgery* 2003; 52(6):1335–1345; discussion 1345–1347.
37. Petrovich Brennan NM, Whalen S, de Morales Branco D, et al. Object naming is a more sensitive measure of speech localization than number counting: Converging evidence from direct cortical stimulation and fMRI. *Neuroimage* 2007; 37(Suppl 1):S100–108.
38. Haglund MM, Berger MS, Shamseldin M, et al. Cortical localization of temporal lobe language sites in patients with gliomas. *Neurosurgery* 1994; 34(4):567–576; discussion 576.
39. Hirsch J, Ruge MI, Kim KH, et al. An integrated functional magnetic resonance imaging procedure for preoperative mapping of cortical areas associated with tactile, motor, language, and visual functions. *Neurosurgery* 2000; 47(3):711–721; discussion 721–722.
40. Sanai N, Mirzadeh Z, Berger MS. Functional outcome after language mapping for glioma resection. *N Engl J Med* 2008; 358(1):18–27.
41. Bello L, Gallucci M, Fava M, et al. Intraoperative subcortical language tract mapping guides surgical removal of gliomas involving speech areas. *Neurosurgery* 2007; 60(1):67–80; discussion 80–82.
42. Horwitz B, Rumsey JM, Donohue BC, et al. Functional connectivity of the angular gyrus in normal reading and dyslexia. *Proc Natl Acad Sci U S A* 1998; 95(15):8939–8944.
43. Stanescu-Cosson R, Pinel P, van De Moortele PF, et al. Understanding dissociations in dyscalculia: a brain imaging study of the impact of number size on the cerebral networks for exact and approximate calculation. *Brain* 2000; 123(pt 11):2240–2255.
44. van Harskamp NJ, Rudge P, Cipolotti L. Are multiplication facts implemented by the left supramarginal and angular gyri? *Neuropsychologia* 2002; 40(11):1786–1793.
45. Peled R, Harnes B, Borovich B, et al. Speech arrest and supplementary motor area seizures. *Neurology* 1984; 34(1):110–111.
46. Wober C, Holzner F, Wessely P, et al. Speech arrest as first symptom of a tumour in the supplementary motor area. *Wien Klin Wochenschr* 1992; 104(3):73–75.
47. Krainik A, Lehericy S, Duffau H, et al. Postoperative speech disorder after medial frontal surgery: role of the supplementary motor area. *Neurology* 2003; 60(4):587–594.
48. Kho KH, Rutten GJ, Leijten FS, et al. Working memory deficits after resection of the dorsolateral prefrontal cortex predicted by functional magnetic resonance imaging and electrocortical stimulation mapping. Case report. *J Neurosurg* 2007; 106(6 suppl):501–505.
49. Nelson L, Lapsiwala S, Haughton VM, et al. Preoperative mapping of the supplementary motor area in patients harboring tumors in the medial frontal lobe. *J Neurosurg* 2002; 97(5):1108–1114.
50. Avila C, Barros-Loscertales A, Forn C, et al. Memory lateralization with 2 functional MR imaging tasks in patients with lesions in the temporal lobe. *AJNR Am J Neuroradiol* 2006; 27(3):498–503.
51. Golby AJ, Poldrack RA, Brewer JB, et al. Material-specific lateralization in the medial temporal lobe and prefrontal cortex during memory encoding. *Brain* 2001; 124(pt 9):1841–1854.
52. Weber B, Fliessbach K, Lange N, et al. Material-specific memory processing is related to language dominance. *Neuroimage* 2007; 37(2):611–617.
53. Preston AR, Gabrieli JD. Dissociation between explicit memory and configural memory in the human medial temporal lobe. *Cereb Cortex* 2008.
54. Barch DM, Sheline YI, Csemansky JG, et al. Working memory and prefrontal cortex dysfunction: specificity to schizophrenia compared with major depression. *Biol Psychiatry* 2003; 53(5):376–384.
55. Richardson MP, Strange BA, Thompson PJ, et al. Pre-operative verbal memory fMRI predicts post-operative memory decline after left temporal lobe resection. *Brain* 2004; 127(pt 11):2419–2426.
56. Rohde V, Mayfrank L, Weinzierl M, et al. Focused high frequency repetitive transcranial magnetic stimulation for localisation of the unexposed primary motor cortex during brain tumour surgery. *J Neurol Neurosurg Psychiatry* 2003; 74(9):1283–1287.
57. Hargreaves SJ, Watt JW. Intravenous anaesthesia and repetitive transcranial magnetic stimulation monitoring in spinal column surgery. *Br J Anaesth* 2005; 94(1):70–73.
58. Machii K, Cohen D, Ramos-Estebanez C, et al. Safety of rTMS to non-motor cortical areas in healthy participants and patients. *Clin Neurophysiol* 2006; 117(2):455–471.

9

Development and Developmental Disorders

ADAM P. WALLACH

Department of Radiology, Neuroradiology Division, Memorial Sloan Kettering Cancer Center, New York, New York, U.S.A.

CHALLENGES IN PEDIATRIC BOLD IMAGING

Blood oxygenation level-dependent (BOLD) functional magnetic resonance imaging (fMRI) is an important and useful tool in the study of mature human brain function. Its use in evaluation of the developing brain has lagged for several reasons. This chapter aims to describe some unique challenges faced by those conducting fMRI studies in the pediatric population and also to detail practical solutions to these problems.

Compliance

The most obvious challenge in tailoring fMRI imaging to children is compliance. There are two important components to noncompliance in children. The first is the crippling anxiety children often experience when confronted with the prospect of entering an MRI bore. The second is head motion.

Anxiety

While in traditional MRI a child can be sedated, doing so for an fMRI protocol is in many cases contraindicated, since target brain functions may be influenced by psychoactive compounds. Particularly in those cases where alertness or patient interaction is required, other means of achieving a calm state must be employed.

The method of pretraining with the best-demonstrated effectiveness is use of a simulated MRI unit (Fig. 1). According to the work of Rosenberg et al. (1), children who underwent desensitization in a simulator prior to scanning reported lower subjective levels of distress and lower heart rates compared with those who did not. A trend toward better signal-to-noise ratio was also reported, although this difference was not statistically significant (2).

Obviously, however, use of an MR simulator is not an option in most clinical and even research settings. Role-playing activities, with the child instructed to pretend he or she is in a scanner bore while being stimulated with scanner sounds is effective (3). Other methods of desensitization training include exposure to videos of or even just pictures of the scanner environment. These are effective in certain patients, particularly when an introduction to scanner sounds is also provided (3).

It is of utmost importance that the technical staff performing the procedure is comfortable and experienced in interacting with children and parents (2). On the day preceding the examination, there is demonstrated utility in having the child and parent/guardian meet with the staff members who will perform the study. On this day, the medical nature of the meeting should be minimized. This can be achieved, for example, by elimination of lab coats and experiences with medical equipment, to allow the child to become comfortable with the people he or she will again encounter on the day of the examination (3).



On the day of the examination, efforts should be made to keep the child as relaxed as possible. In older children, progressive relaxation techniques are useful when employed before entry into the bore and may be continued once the child is in the scanning position (2). For all age groups, external stimulation beginning as soon as possible when the child enters the bore is useful. For example, in a bore fitted with both an auditory apparatus and visual display, the child can be entertained with a movie immediately upon entering the unit (2).

In some cases, it may be necessary and appropriate to sedate the child. The most commonly employed fMRI presurgical planning protocols for brain lesion resection require active subject cooperation (i.e., finger tapping, object clenching, word repetition), and therefore an alert child is prerequisite. These protocols are usually limited to those aged seven years and older because of the need for cooperation. However, limited presurgical mapping for lesion resection can be performed in infants and young children with the subject asleep or sedated (4). In this age group, an alert child may prove to be an encumbrance, because of his or her inability to verbally or visually follow commands.

Souweidane et al., in 1999, (4) described an fMRI protocol for presurgical planning that can be performed with a sedated infant. Propofol was used for sedation, and children were stimulated with a battery of passive stimuli. These included photic stimulation via goggles equipped with light-emitting diode (LED) bulbs for identification of the visual cortices, tactile stimulation of the hand and other body parts for somatosensory mapping, and playback of the mother's recorded voice for localization of the auditory cortex. These limited techniques were found effective, with the understanding that mapping of cortex involved with voluntary action or patient responses is not possible in this setting (2).

Head Motion

It may seem like common sense that children undergoing fMRI examinations will exhibit more noise related to head motion than their adult counterparts. Poldrack et al.

Figure 1 (A) One way to prepare a child for an fMRI examination is to desensitize him/her by encouraging play in a toy tunnel (B and C). Further desensitization of a pediatric patient can be achieved by the use of a mock MRI, which can imitate the projection system, loud sounds, and closed-in feeling that a child may experience in an MRI. Allowing the child to watch a familiar movie or cartoons will also serve to prepare him/her for the fMRI examination. Abbreviations: MRI, magnetic resonance imaging; fMRI, functional magnetic resonance imaging. Source: Photos by Michael Weinstein, courtesy of Sackler Institute.

confirmed this and also demonstrated an additional significant increase in head motion among dyslexic children compared with those with normal reading skills (2).

In order to reduce noise related to head motion in children, two techniques are frequently employed: restraint and conditioning. Restraint is by far the most commonly used method.

The most commonly used form of restraint in children is the “bite bar” (2). This device is mounted within the head coil and contains a bite plate coated with dental thermoplastic. Dental thermoplastic molds to the subject’s dental impression, thereby restricting head motion. Other commonly used restraints include disposable head restraints, such as those typically used in the emergency department (i.e., Laerdal Head Bed) (2).

Other more restrictive forms of head restraint, such as stereotactic head frames, are available. However, as the effectiveness of the restraint increases, so typically does the degree of discomfort. Those methods which provide the greatest restraint to motion become uncomfortable almost immediately and are therefore not useful in pediatric fMRI scanning protocols (2). This is particularly true in the older child in whom alertness and active participation are required.

A highly cost-effective method useful in relatively cooperative children is the application of cloth tape across the subject’s forehead (2). This simply provides somatosensory feedback, without marked restraint, primarily to remind the patient not to move.

Training-based methods of head motion reduction use concepts of conditioning and biofeedback to make the child more aware of and better able to control head motion (2). One effective method uses a mock MRI scanner equipped with a movie screen and auditory input. When the subject’s head moves greater than allowed, the film is stopped and does not resume until the child’s head has returned to the proper position. The allowable degree of motion is reduced on subsequent sessions, until head motion is minimized. Silfer et al. (5) demonstrated that following training, this method resulted in decreased head motion during actual scanning.

Neonates and young infants typically have fMRI sequences performed as part of a standard MRI session. fMRI in these patients is nearly always passive, and as in standard MRI sessions, patients are placed into the bore after feeding and tight swaddling within a blanket (2).

Despite the best efforts of all involved, however, some head motion is inevitable, and it is therefore important that motion correction software be used to further improve precision. Motion related to tasks performed by the subject within an fMRI sequence protocol, however, is difficult to correct for even after motion correction software is used (2).

Anatomical and Functional Differences

fMRI is a powerful method for demonstrating evolution, development, and consolidation of neural networks (6). Comparison with adults has demonstrated that fMRI activation maps in children aged five years and older are consistently similar to those of adults (2,6). Nevertheless, important physiological differences are present, and awareness of these improves the effectiveness of fMRI, especially in young children (6).

Pediatric fMRI is plagued by the same problems that affect standard pediatric MRI. Children have smaller heads, which are not centered as readily within head coils designed for adults (6). Transmission of motion from jaw movements to the head is greater than in adults. The faster cardiorespiratory cycle results in greater inherent head motion than in adults. There is also increased pulsatility and possibly increased parenchymal compliance, which combine to result in a more plastic brain, further decreasing the signal-to-noise ratio. These changes are most pronounced in the basal ganglia, but do involve the cortex as well (6).

Differences in thickness of the gray mantle exist between children and adults and can contribute to differences in results between these groups (6). Children have a larger gray matter–white matter ratio than adults. This results in decreased volume averaging with subcortical white matter compared with that seen in adults. In children younger than two years, differentiation between gray and white matter becomes challenging because of the relative lack of myelinated white matter tracts. These differences affect warping onto a standardized brain atlas and also affect the choice of a motion correction algorithm, both of which are generally geared toward the adult brain (7).

Differences in the BOLD response itself may exist between children (especially infants and young children) and adults. When a stimulus is applied and results in cortical activation, the activated portion of brain experiences an increase in perfusion within two-to-four seconds. After the stimulus has abated, cortical perfusion returns to baseline levels after a mild but relatively prolonged undershoot period. This expected response can be plotted as a function of blood flow over time and is most commonly represented by the hemodynamic response function (Fig. 2).

Hemoglobin becomes strongly paramagnetic when in its deoxygenated state (deoxyhemoglobin). This is in contradistinction to oxyhemoglobin, which is diamagnetic. The resulting signal change related to an abundance of oxyhemoglobin flowing into an activated region of cortex is best observed using a T2*-weighted sequence with echo-planar imaging technique. The ensuing contrast between normally perfused brain, with a relative abundance of paramagnetic deoxyhemoglobin, and the

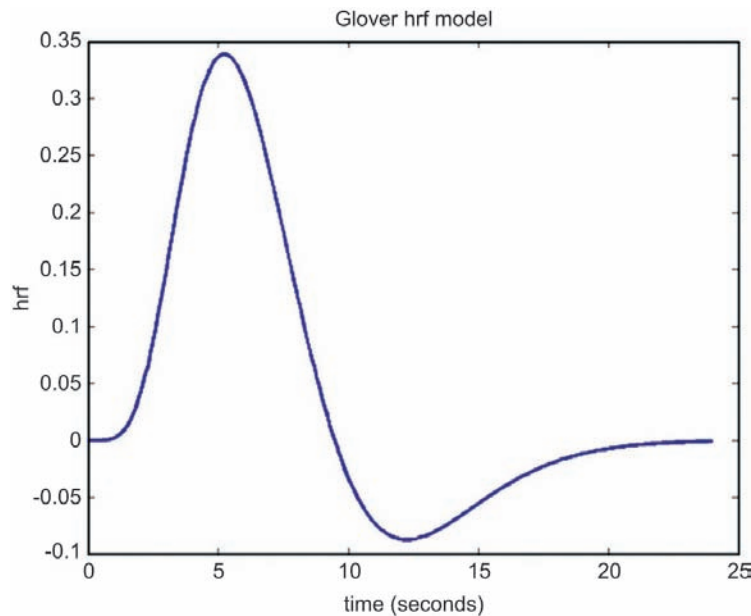


Figure 2 The hemodynamic response curve is characterized by an abrupt increase in local cerebral blood flow two to three seconds after stimulus onset. Flow remains elevated during the stimulus, then returns to baseline after a mild but relatively prolonged undershoot. *Source:* Courtesy of Keith J. Worsley, Department of Mathematics and Statistics, McGill University, Montreal, Quebec, Canada.

activated portion of brain with a relatively greater proportion of oxyhemoglobin is the basis for the BOLD contrast technique employed by fMRI. Thus, unlike with fluoro-deoxy-glucose positron emission tomography (FDG-PET), increases in cellular metabolism are not directly assessed. Instead, the associated secondary effect of increased local metabolism, increased blood flow, is measured.

In order to determine whether a voxel's change in signal over time within an fMRI sequence corresponds to a stimulus-onset-related change in local cerebral perfusion, statistical analysis is employed to compare a voxel's change in signal with that of a reference standard. As mentioned above, this is typically the hemodynamic response function, which occurs in a positive direction.

However, many studies have now documented the presence of a “negative BOLD response” within the occipital lobes of infants and young children presented with visual stimuli (7–11). This phenomenon appears to occur only in infants older than eight weeks of age and reverses between three and five years of age (12). Theories to explain the phenomenon center around the idea of deoxyhemoglobin accumulation and insufficient washout. Considering that the reversal from a positive to a negative BOLD response correlates with the period of heightened synaptogenesis in the occipital region (9,13), it is now thought to be related to increased metabolic activity causing increased production of deoxyhemoglobin in association with an immature vascular response limiting ability for washout.

FUNCTIONAL BRAIN DEVELOPMENT AS WITNESSED ON BOLD fMRI

While there is an abundance of information available on structural brain development from both cadaveric studies and *in vivo* imaging, this is in contradistinction to the relative poverty of information related to functional brain development (14). Many modalities, including PET, single-photon emission computed tomography (SPECT), magnetoencephalography (MEG), and optical tomography are now available to suit this purpose. However, considering the relative noninvasiveness of fMRI in comparison with many others and its real-time capabilities, fMRI is considered the leading technique for functional exploration of the developing brain (7,14).

The most dynamic period of brain development occurs while in utero, but continues at a fast rate for the first two years after birth. At two years of age, a child's brain mass is approximately 80% of the expected adult weight (14). Synapse formation follows a similar curve, with an overabundance of synaptic connections in the young child relative to the older child and adult. The process of synaptogenesis occurs in a region-specific fashion in humans. For example, in the auditory cortex, synaptic density peaks at three months of age, whereas in the middle frontal cortex, this occurs at 15 months of age (14).

The subsequent process of synaptic pruning, a systematic reduction in the number of synapses, increases the functional maturity of specific brain regions. The more effective and important connections are maintained, while superfluous

connections are eliminated. This process takes place rapidly in certain cortical regions (i.e., visual cortex), but is much more prolonged in others (i.e., prefrontal cortex, where logical processing and key elements of personality develop), extending into adolescence (14).

Structural MRI studies, the most informative being those based on volumetric measurements of brain tissue (e.g., work by Giedd et al. published in 1996), demonstrate certain consistent findings with respect to gross anatomical changes through childhood (14). These include the lack of significant change in cerebral volume after five years of age (15,16), a decrease in volume of gray matter nuclei (i.e., basal ganglia) during childhood (15–17), a decrease in cortical gray matter volume after 12 years of age (18), and an increase in cerebral white matter volume throughout childhood and early adulthood (14).

However, functional maturation is much more complex. A few studies have successfully evaluated the utility of fMRI in the fetal population (19–22), demonstrating that an external stimulus is capable of cortical activation within the unborn child (7). The first report was published in 1999 by Hykin et al. (19) who used a transabdominal auditory stimulus, while Fulford et al. (21) subsequently published results of fetal fMRI series on patients challenged with visual and vibroacoustic stimuli. All patients were near term (36 weeks gestational age). All studies demonstrated significant stimulus-related cortical activation. However, the visual stimulus (a light source intermittently projected onto the maternal abdomen) resulted in activation within the frontal cortex, not as would be expected within the occipital lobe. All studies were hampered to some degree by motion as well as susceptibility artifact related to maternal bowel. A practical future goal for fMRI in the fetal period is to evaluate for changes in the hemodynamic response to assess for fetal distress (7).

In 1996, Born et al. (23) were the first to perform fMRI on the newborn using a visual stimulus. Since then, more than 20 studies have been performed with fMRI on the newborn and infant (7).

Visual System

As mentioned above, in a single study targeting the late third trimester fetus with intermittent visual stimuli via the maternal abdomen (21), there was a significant positive BOLD fMRI response localized to the frontal lobes. No significant activation of the visual cortex was visualized.

In the newborn period, several studies have examined the fMRI response to photic stimulation (7,10,24–26). Results demonstrated two findings, which differ from that seen in adults. There is reversal of the normal positive BOLD response seen in adults, which was detailed above. There is also anterior localization of cortical activation

within the visual cortex of the medial occipital lobe relative to the adult. This difference in localization may be due to a lack of spatial contrast to the visual stimulus, stimulation of sensitive lateral retinal fields via closed eyelids, or incomplete maturation of the visual cortex (7).

In 2000, Born et al. published a series evaluating the effects of photic stimulation under fMRI with 37 children (12). After motion correction, 31 children produced at least one acceptable dataset for analysis. These children ranged in age from premature infancy (as young as 29 weeks postmenstrual age) to early childhood (as old as 6 years).

Infants with a postmenstrual age of less than 41 weeks generally showed no consistent focus of activation. Those greater than 41 weeks postmenstrual age demonstrated consistent occipital lobe activation. The characteristic reversal of BOLD signal typically occurred by 48 weeks postmenstrual age (about 8 weeks after a full-term birth) and had occurred in all children by 56 weeks postmenstrual age. In the infants, the activated region of visual cortex corresponded only to the anteromedial and antero-lateral portions of the visual cortex, whereas no consistent activation of the posterior portion of the occipital cortex was present. This is compatible with a long-suggested theory that in very young infants, response to visual stimuli is predominantly a subcortical phenomenon, involving such structures as the thalamic pulvinar and the superior colliculus, which are inconsistently visualized with fMRI in the neonate at 1.5T (12). The volume of activated visual cortex increases linearly with age from 41 to 90 weeks postmenstrual age, reaching an adult-like pattern with reversal of the negative BOLD response between three and five years of age (12).

Auditory System

In 2001, Anderson et al. published a series of infants presented with an auditory stimulus under fMRI to evaluate maturation of the infant auditory cortex (27). Unlike the visual cortex of the late third trimester fetus, premature baby, and very young infant, activation of the temporal cortex is typically seen very early, and there is evidence that the fetus can hear by 27 weeks postmenstrual age. The study examined 14 infants and four adults (as controls). It revealed bilateral superior temporal activation in all 14 infants. However, as seen in the visual cortex, a reversal of BOLD signal was present in infants older than 50 weeks gestational age (Fig. 3) (27). This is further confirmation that the vascular response to cortical activation is different in infants than it is in adults, be it secondary to an immature capillary bed, heightened synaptogenesis with increased oxygen consumption relative to the adult, or a combination of these factors. It should

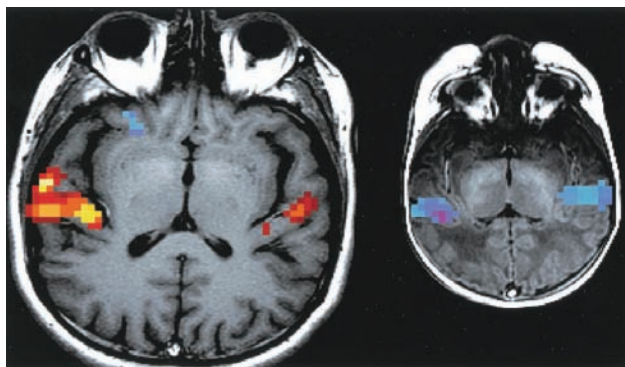


Figure 3 BOLD fMRI signal response in to auditory stimulation in an adult (*left*) and newborn (*right*). BOLD fMRI results are overlaid onto high-resolution T1-weighted images. Increased BOLD signal is depicted in red, whereas decreased signal is blue. Anderson et al. (27) demonstrated increased BOLD signal in the auditory cortex of all four adult subjects, but decreased BOLD signal in six of eight newborns. Abbreviations: BOLD, blood oxygenation level-dependent; fMRI, functional magnetic resonance imaging. Source: From Ref. 27 with permission from Elsevier.

also be noted that the infants scanned in this study were nonsedated during the examination, ruling out sedative drugs as the cause of the negative BOLD response in the auditory cortex.

Language

There is little published data evaluating fMRI activation differences between reception of generic auditory stimuli and language in the infant and young child. Altman and Bernal demonstrated in a study published in 2001, which sampled 31 patients aged two months to nine years, that younger children tend to activate temporal foci, while older children also activate frontal lobe foci when presented with a prerecorded sample of their mother's voice (24).

Most studies evaluating development of language have focused on language generation, with less of an emphasis on reception. These studies evaluate cortical activation related to thought process during a requested task. For example, a typical task is orthographic lexical retrieval (OLR). In this task, a single letter is projected onto a screen directly above the patient's eyes, so that no eye motion or strain is required to see the screen. The child is instructed to think of as many words that start with the projected letter as possible during the allotted time, omitting proper nouns. The child is instructed not to say or mouth the words he or she is thinking.

Another typical task is verb generation (VG), in which the subject is shown a word and is asked to think of as many "doing words" appropriate to the given noun within the allotted time. For example, when the word "rabbit" is

projected, the child would think of as many corresponding verbs, such as hop, jump, eat, and run during the allotted time (28).

These tasks are chosen for their ability to activate sites important for language generation and have been commonly employed in adults for presurgical planning. In 2004, Wood et al. published a paper (28) testing 48 children aged 6 to 15 years (median 11), using the above two protocols. Seventeen adults (median age 28) were used as control. They found little overall difference in cortical activation patterns between the children and the adults. Both the adult and child data, which included both right- and left-handed individuals, demonstrated approximately 85% left-sided language dominance. Specifically, activation of certain cortical regions was essentially ubiquitous (i.e., 96% showed significant activation within the mesial surface of the superior frontal gyrus), while other regions were more variable (i.e., 50% showed significant activation of the insular cortex). Within individuals with left language dominance, activated cerebral cortical structures were left sided, although cerebellar activity, when present, was usually right sided. Insular and posterior parietal activity was, however, variable in sidedness (Table 1).

Overall, there were only minimal differences in activation pattern between children and adults: Adults more commonly had activation of the cerebellum and the posterior parietal region. Also, children had better lateralization of activity on the VG task than on the orthographic lexical recall task. No such difference existed in adults. Therefore, it has been suggested that in the clinical setting, when scanner time issues are of concern, VG should be used over OLR because of its improved specificity for activation of the dominant hemisphere (28). Otherwise, no appreciable differences existed. Thus, from age range six to adult, cortical language representation appears to be stable, and although differences may exist in younger

Table 1 Areas Frequently Activated in 48 Child Subjects During VG and OLR Protocols (Results Combined)

Anterior mesial frontal lobe, mainly superior frontal gyrus (46/48 or 96%)
Inferior frontal gyrus (45/48; 94%)
Middle frontal gyrus (44/48; 92%)
Inferior temporal cortex (41/48; 85%)
Cerebellum (32/48; 67%)
Superior temporal gyrus (31/48; 65%)
Insular cortex (24/48; 50%)
Posterior parietal cortex—angular gyrus or superior parietal region (23/48; 48%)
Anterior cingulate region (not commonly activated—14/48; 30%)

Abbreviations: VG, verb generation; OLR, orthographic lexical retrieval. Source: Using data from Ref. 28.

children, this remains difficult to evaluate because of the need for cooperation.

Gaillard et al. (29) demonstrated, in a VG paradigm focused on evaluating differences in frontal lobe activation between adult and child subjects (age range 8–13), similar findings. However, in this more focused evaluation targeting the frontal lobe only, it was demonstrated that activation of language cortex was more intense and more widespread in children than in adults. Similar findings have been demonstrated using PET, which directly assesses neuronal metabolic activity. The peak increase in activation intensity is thought to reflect increased synaptic density in the frontal lobes of children and adolescents, correlating with increased cerebral blood flow and metabolic activity throughout childhood and well into adolescence, tapering as a function of synaptic pruning. Also demonstrated was a greater volume of activated pixels in children compared with adults, reflecting a greater volume of activated brain for a given VG task in children than in adults (29). This finding has also been demonstrated with PET and is thought to reflect maturational differences in functional cortical consolidation. Children recruit a greater number of neurons to complete a given task in comparison with adults, and age-related functional improvement for a given task parallels the consolidation of task-related brain activity into a smaller region of cortex with advancing age.

During the time period in which this process remains incomplete, children are thought to retain a degree of synaptic plasticity: Other regions of cortex retain the ability to assume the function originally destined for a given cortical locus damaged by disease or surgical resection. In adults, damage to the inferolateral frontal area of cortical language representation within the dominant hemisphere (including Broca's area) leaves the patient with persistent expressive aphasia. Damage to the posterior parietotemporal concentration of cortical language representation within the dominant hemisphere (including Wernicke's area) results in persistent receptive aphasia. Yet young children who undergo resection of the entire dominant hemisphere can expect to recover function to near normal levels. Wada testing in children with resection or disease involving cortical language regions demonstrates migration of functionality to the right hemisphere, which has been corroborated by PET and fMRI studies.

If such an insult does occur within the developing brain, function migrates to areas of brain homotopic to those seen in normal controls. For example, language-related activation, normally occurring within a damaged inferomesial left frontal lobe, will generally relocate to the equivalent site in the right hemisphere (Fig. 4). In fact, it has been suggested that on language-related tasks, foci of apparent cortical activation in the right hemisphere

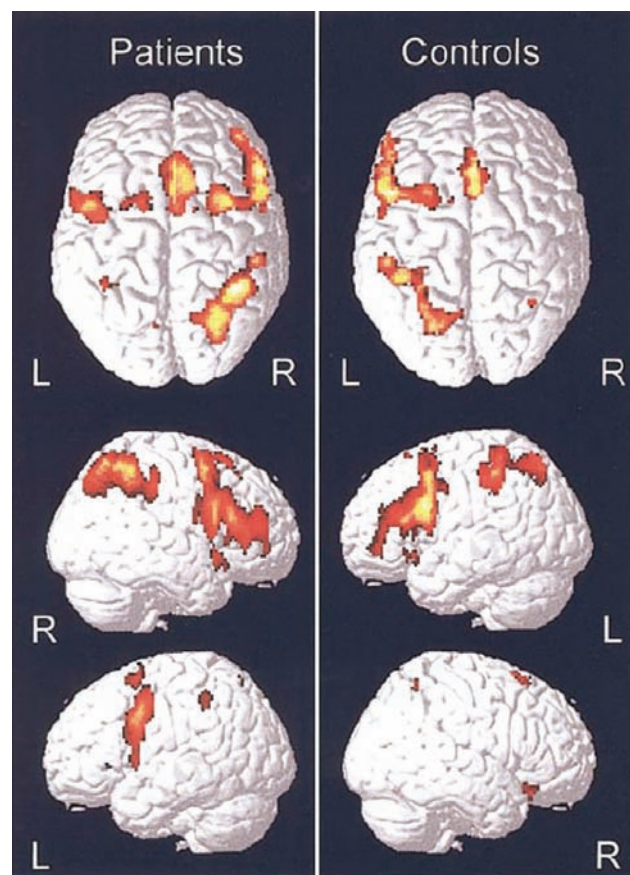


Figure 4 Organization of language on the right side in children following early left-side brain lesions. Functional MRI study by Staudt et al. (30) demonstrated normal expected language organization on the left side. However, in patients with left-brain lesions early on in life, language function was predominantly right side. Abbreviation: MRI, magnetic resonance imaging. Source: From Ref. 30 with permission from Elsevier.

occurring in locations nonhomologous to left hemispheric loci typically subserving language function should be interpreted with caution, as they may be artifactual (30).

The right hemisphere retains the plasticity to assume the responsibility of processing and generating verbal and written language until a certain age. However, in such cases of reorganization, there is typically a significant discrepancy in verbal versus performance intelligence quotient (IQ), as assessed by the Wechsler Intelligence Scale. Verbal IQ in patients with early left hemispheric lesions is generally comparable with that seen in normal age-matched counterparts. However, performance IQ in these patients, which deals with visuospatial processing, is consistently and significantly lower than the verbal IQ within the same child, even when both verbal and performance IQ remain within the normal range (31). The “crowding hypothesis” has long been suggested to explain these differences, theorizing that visuospatial functionality

destined to be subserved by the right hemisphere has been “crowded out” by the reorganization and reassignment of language processing to the right hemisphere (31).

In 2006, Lidzba et al. (31) demonstrated conclusively that in children with right-sided spastic hemiparesis (cerebral palsy) related to early left hemispheric lesions, the degree of visuospatial impairment (as assessed by performance IQ) correlated positively with lesion size, but only if reorganization of language activity to the right hemisphere (as demonstrated by fMRI) had occurred. This suggests prioritization of language function over others during human brain development (31).

Reading

Like language generation, reading is a left-dominant activity in most people. The perisylvian areas are most important for reading function, with additional input from occipital and occipitotemporal sites for visual word form processing (Fig. 5).

Reading comprehension is a complex activity, which occurs as a result of multiple interwoven processes (32) (Fig. 6). The initial process is word form (character) recognition, the process of recognizing characters composing a given written language as different from other shapes. This is a relatively automatic process once a set of characters is mastered, but an initial amount of memorization and processing is required.

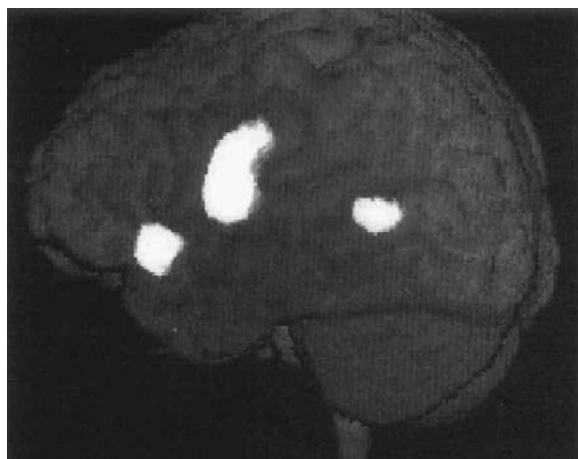


Figure 5 Functional loci associated with a single-word reading paradigm in a 12-year-old child. The most anterior region of activation is in the inferior frontal gyrus and frontal operculum (traditionally known as Broca's area). The middle region of activation is in the precentral gyrus, in the area of the motor cortex responsible for movement of the tongue and face. The posterior region of activation is in the posterior aspect of the middle and superior temporal gyri (traditionally known as Wernicke's area). Source: From Ref. 32 with permission from The Hammill Institute on Disabilities.

The next process is lexical orthography (32), which entails recognition of a sequence of characters as representative of a word. This process does not, however, entail extraction of the meaning of a word, which is a separate process.

Lexical and sublexical phonology encompass the internalized understanding of word sounds, including rules related to exceptions in word pronunciation. For example, “break” and “brake” both have the same pronunciation despite different appearances, and the word “gone” has a silent “e” (32). However, this stage of processing still does not require understanding of word meaning—just the understanding of rules that govern the sounds of words.

Semantic processing is the step where word meaning is assigned. This includes categorization of a word (i.e., does the word “bear” fit best into the category of animal or tool?) and understanding the relationship to other adjacent words to extract a greater amount of content (i.e., does the word “bear” refer to an animal or to the process of putting up with an undesirable situation).

Finally, although not necessary for comprehension, the phonological representation of a visualized word can be overtly articulated. Otherwise, all of the above processes are used to some degree in normal reading and subsequent comprehension, and all can become individually or more globally disordered.

Word form recognition is essentially localized to the left occipitotemporal sulcus (33). Separation of lexical orthography from other components of reading activity,

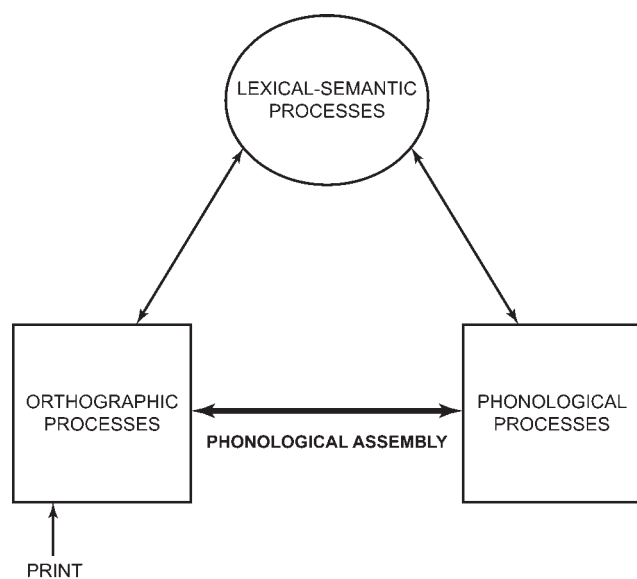


Figure 6 Component processes for word identification in reading. Evidence suggests that word identification problems in reading disability reflect core deficits at the level of orthographico-phonological mapping (shown in bold lines) Source: From Ref. 47 with permission from John Wiley and Sons.

such as phonological processing, is difficult. However, two forms of testing for localization of lexical orthography, which can be performed using PET or fMRI, include OLR and spelling judgment tasks. OLR was discussed earlier and consists of generating words that begin with a given letter. The subject is presented with a single letter and then asked to think of as many words as possible, which begin with that letter in a given amount of time. Overlap with phonological processing is an inevitable consequence, however, as the subject will hear the word internally (34). A spelling judgment task does a better job of separating lexical orthography from phonology (35,36). Two words are displayed, and the subject must choose the one that represents an actual word. For example, the word “third” and the pseudoword “thurd” are presented (33). This results in better isolation of lexical orthography from phonology since the spoken equivalent of both the words is the same (33). Testing performed for isolation of lexical orthography consistently shows activation of left posterior superior temporal cortex (Wernicke’s area) (34,37,38), left inferior frontal cortex (Broca’s area) (34,37–39), and left inferior parietal cortex (33).

Isolation of lexical phonology can be performed using the phonological lexical decision task (35). Instead of deciding which presented word is real and which is the pseudoword, two pseudowords are presented and the subject must decide which one would sound like a real word if spoken. For example, the subject might have to choose between the pseudowords “jope” and “joak” (33). Consistent activation was demonstrated in the left posterior superior temporal gyrus (Wernicke’s area), Broca’s area, and the left insula (33,35).

Isolation of sublexical phonology can be performed auditorily (33). The subject is asked to respond when he or she hears a particular phoneme, for example, the phoneme “bee” (i.e., beagle) (40–42). The subject can be further trained to respond only when the phoneme comes at the beginning of a word, at the end of a word, or is embedded within a word (33). An even more complex version is response only when the target phoneme is preceded by another given phoneme, for example, “dee.” These tasks force the subject to attend to sublexical word sounds, which lack semantic content. Activation of Broca’s area again occurs. Otherwise, however, regions of activation differ from those taking place in lexical phonology (33). Left insular activation does not occur, as it does in lexical phonology. Left temporal activation does occur, however, to a greater extent in the middle temporal cortex than in the superior temporal cortex (Wernicke’s area). There is also consistent activation of the occipitotemporal cortical junction (33).

Evaluation of semantic processing can be performed with both categorical and semantic generation tasks. In categorical assessment tasks, the subject is presented with

two words from different parts of speech (i.e., apple, eat) and is asked to determine whether these two words are related (43,44). In a semantic generation protocol, the subject is presented with a noun and then asked to think of a verb appropriate to that noun. For example, if presented with the word “chair,” the subject could respond with the word “sit” (33,44,45). Both types of tasks result in widespread frontal and temporal lobe activation; however, the categorical testing results in increased temporal lobe activation compared with the semantic generation protocol (46).

BOLD fMRI IMAGING OF COMMON DISORDERS OF THE PEDIATRIC AGE GROUP

BOLD fMRI as it relates to three common disorders typically identified in childhood—developmental dyslexia, attention deficit hyperactivity disorder (ADHD), and autism spectrum disorders (ASD)—is discussed below.

Developmental Dyslexia

Reading disability (developmental dyslexia) is defined as failure to attain age-appropriate reading skill despite normal intelligence and adequate instruction in reading technique. It cannot be related to problems with motivation, sensory acuity, or structural brain lesion (47,48). It is a common problem, affecting approximately 5% of the world population, although estimates as high as 17.5% have been reported (49,50). Dyslexia is a chronic persistent problem; it does not regress with age (50) (Fig. 7). It

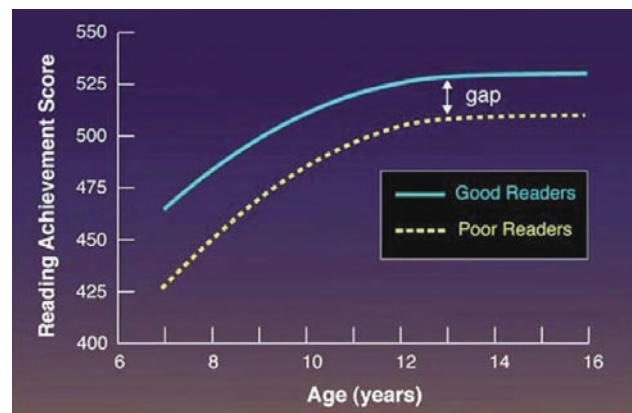


Figure 7 Trajectory of reading skills over time in nonimpaired and dyslexic readers. The ordinate is in Rasch scores (W scores) and the abscissa is in age in years. Both dyslexic and non-impaired readers improve their reading scores as they get older, but the gap between the dyslexic and nonimpaired readers remains. Thus, dyslexia is a deficit and not a developmental lag. *Source:* From Ref. 54 with permission from Elsevier.

is familial and heritable, with family history being one of the strongest risk factors—23% to 65% of those with an afflicted parent also develop the condition (50).

Multiple functional imaging studies have been performed for evaluation of the area(s) of deficiency, and while results have been varied, there is support for a temporoparietal deficiency as a culprit for the abnormalities seen in developmental dyslexia. While the temporoparietal cortex may be an offending focus for developmental dyslexia, there also appear to be abnormal inputs to this region from the magnocellular visual pathway (51).

Magnocellular Visual Pathway Theory of Developmental Dyslexia

The human visual pathway contains both magnocellular and parvocellular components. The magnocellular component of the visual pathway system (M pathway) is geared toward identification of object movement and luminance contrast, whereas the parvocellular system is geared for detailed static and color imagery.

After passing through the lateral geniculate nucleus of the thalamus, projections of the magnocellular visual pathway channel back to V1 (the medialmost portion of the retinotopically organized area of the occipital lobe) and then on to an extrastriate portion of the visual cortex (V5/MT, located laterally, near the temporooccipitoparietal junction). Postmortem evaluation of the lateral geniculate nuclei of dyslexics has demonstrated decreased magnocellular neuronal size compared with controls, without abnormalities in the parvocellular layer (52). Considering this postmortem study by Galaburda, the possibility of magnocellular pathway abnormalities resulting in abnormal reading ability was studied using fMRI.

Eden et al. (53) studied six male dyslexic subjects and eight age- and intelligence-matched male controls. A task geared toward isolation and activation of the magnocellular visual pathway was created. The subject was shown two low-contrast moving dots presented sequentially and asked to determine whether the first or second dot was moving faster. Dyslexics performed significantly more poorly than did control subjects ($p < 0.03$). Additionally, no significant activation occurred within the dyslexics' V5/MT visual cortices, while normal activation was seen bilaterally in control subjects. No activational differences were seen during a separate protocol with presentation of a nonmoving pattern (Fig. 8).

Demb et al. (48) used a different fMRI task geared toward M-pathway activation. Results also demonstrated lesser activation of V5/MT visual cortex in dyslexics and found that performance on tests of reading was directly correlated to the level of V5/MT fMRI activation. They concluded that the findings are supportive of an M-pathway-related reading deficiency.

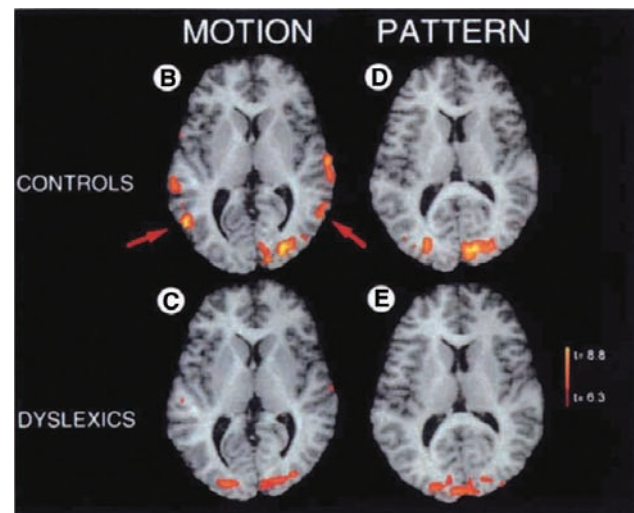


Figure 8 fMRI activation in control subjects (B,D) and dyslexics (C,E). The paradigms presented were of a moving object (B,C) and a high-contrast static pattern (D,E). Both control (D) and dyslexic (E) groups show similar responses in area V1/V2 to the stationary, high-contrast, patterned stimulus. However, during stimulation with a moving object, activation of V5/MT is clearly seen in the control group (B, arrows) but not in the dyslexic group (C). All images are presented in the neurological convention (subject left, image left). Abbreviation: fMRI, functional magnetic resonance imaging. Source: From Ref. 53 with permission from Macmillan Publishers Ltd.

Phonological Theory of Developmental Dyslexia

Despite the convincing findings given above, the phonological theory of dyslexia is now dominant in the field (50). It is based on the knowledge that speech is innate, but reading must be taught and is not innately understood (50). In order for reading to progress effectively, a child must be able understand that the words on a page are equivalent to the spoken word and, moreover, that spoken words can be separated into individual sounds (phonemes). It is a lack of understanding of these concepts despite a normal intellect, which defines developmental dyslexia (50).

Multiple interrelated neurological systems are used during normal reading. The two dominant systems are posteriorly located within the brain. Less dominant but nevertheless distinct systems are present anteriorly (50). One of the posterior systems performs word and phoneme analysis, requires significant amounts of attention, and works at a relatively slow rate. This system is located in the parietotemporal region (50). The other works much faster, does not require significant attentional resources, and can process entire words globally, without breaking them into individual phonemes (50). This system is located in the occipitotemporal region and is important

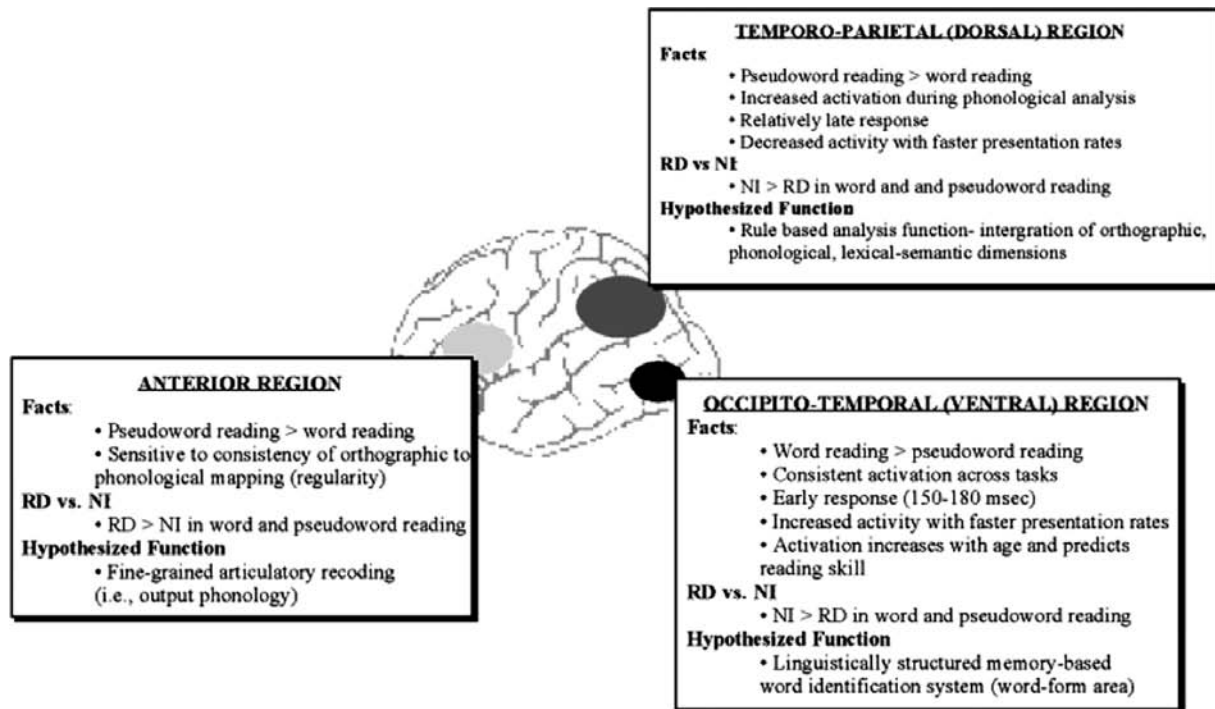


Figure 9 A general overview of the three major reading circuits. *Source:* From Ref. 47 with permission from John Wiley and Sons.

for rapid reading skills (Fig. 9). On fMRI, dyslexics consistently demonstrate decreased activation within these regions.

In 2003, Shaywitz et al. published work (54) using a cohort of young adults who had been tracked with regards to reading ability from age five years into high school. Three different groups emerged. The first had normal reading skills throughout the course of the cohort. The second was classified as reading disabled in grade 2 or 4, and demonstrated persistent poor reading (PPR) skills when reassessed at grade 9 or 10. The third group was classified as reading disabled in grade 2 or 4, but no longer met criteria for poor reading in grade 9 or 10 [accuracy improved readers (AIR)].

Seventy of these students were challenged with pseudoword and real-word rhyming as a part of an fMRI protocol. During pseudoword rhyming, both groups demonstrated findings similar to dyslexics studied previously, with hypoactivation involving both of the posterior neural systems located in the parietotemporal and parietooccipital regions. During real-word rhyming, however, the PPR group demonstrated normalization of activation of posterior neural systems, while the AIR group demonstrated persistently decreased activation (Fig. 10). The AIR group was representative of true developmental dyslexia, with functional improvement over time likely related to compensatory use of anterior neural systems to improve reading accuracy (fluency had not progressed into the normal

range) (50,54). The PPR group is probably representative of poor readings skill related to environmental factors, such as poor schooling, and not true developmental dyslexia (50,54).

However, even in patients with true developmental dyslexia, imaging abnormalities are not entirely resistant to improvement after appropriate intervention. Dyslexic children examined with fMRI before and then again after behavioral training showed improvement in activation of the superior parietotemporal cortex as well as other areas of cortex related to reading skill (55). Behavioral training consisted of seven different computerized training activities encoded on a software program (*Fast ForWord Language*—Scientific Learning Corporation, Oakland, California, U.S.). These activities are designed to improve auditory and language processing and use nonlinguistic and acoustically modified linguistic speech (55). fMRI activation improvement paralleled improvement in reading performance, and in fact, the magnitude of signal change in the left parietotemporal cortex between pre- and post-treatment scanning correlated with the degree of improvement in oral language ability (Fig. 11).

In summary, there is universal agreement that the (left) parietotemporal cortex plays an important role in developmental dyslexia. Lending further support to this is the observation that dyslexic children treated with behavioral modification demonstrate improved activation of the left parietotemporal cortex and that the degree of clinical

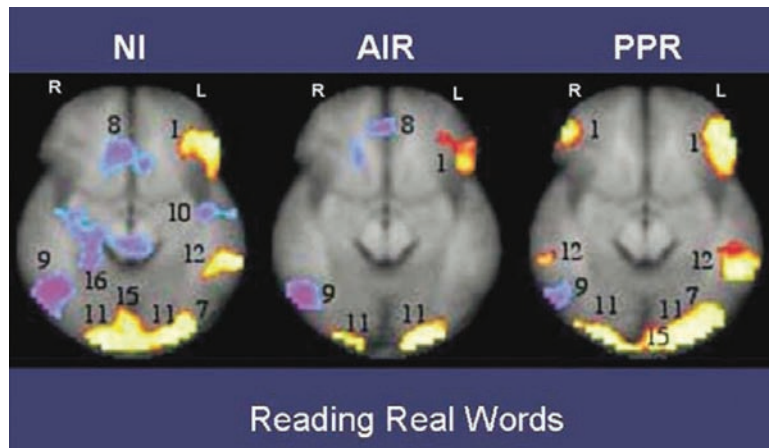


Figure 10 BOLD fMRI activation during a nonword rhyming paradigm in NI, AI, and PPR. The PPR group demonstrated normalization of activation of posterior neural systems, while the AIR group demonstrated persistently decreased activation. The AIR group was representative of true developmental dyslexia, with functional improvement over time likely related to compensatory use of anterior neural systems to improve reading accuracy. The PPR group is probably representative of poor reading skill related to environmental factors, such as poor schooling, and not true developmental dyslexia. Red-yellow indicates areas that had significantly greater activation ($p \leq 0.05$) in the reading task compared with the line task. Blue-purple indicates areas that had significantly greater activation ($p \leq 0.05$) in the line task compared with the reading task. The legend for regional brain activation is as follows: (1) inferior frontal gyrus, (2) precentral gyrus, (3) insula, (4) superior temporal gyrus and superior temporal sulcus, (5) middle temporal gyrus and superior sulcus, (6) cuneus, (7) middle occipital gyrus, (8) anterior cingulated sulcus and adjacent aspects of the cingulate gyrus and superior frontal gyrus, (9) posterior middle temporal gyrus and anterior middle occipital gyrus, (10) anterior aspect of the superior temporal gyrus, (11) inferior occipital gyrus, (12) middle temporal gyrus, (13) superior frontal gyrus, (14) posterior cingulate gyrus, (15) lingula gyrus, (16) medial occipital temporal gyrus (parahippocampal region), and (17) basal ganglia. Abbreviations: NI, nonimpaired; AI, accuracy improved; PPR, persistently poor readers; AIR, accuracy improved readers. Source: From Ref. 54 with permission from Elsevier.

improvement after treatment correlates directly to the change in fMRI signal in this region between pre- and posttreatment scans. As there is consistent abnormally low activation of this region on fMRI in untreated dyslexics, fMRI may eventually be considered a supplemental tool in the diagnosis of true developmental dyslexia. At the present time, however, such a statement cannot be made.

Although the magnocellular pathway theory is not presently dominant in developmental dyslexia, further research may continue to support the notion that abnormalities in this pathway are nevertheless contributory, especially toward processing deficits within the occipito-temporally based posterior neural reading system.

ADHD

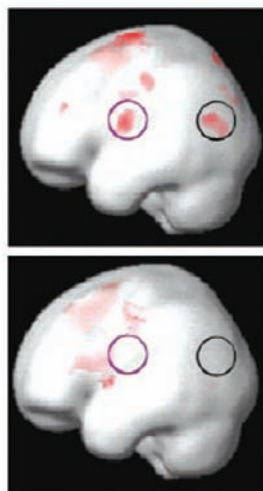
According to the DSM-IV-TR, ADHD is characterized by developmentally inappropriate inattention, motor restlessness, and impulsivity. The neuropsychological literature on ADHD is diverse, and as such many brain regions have been implicated. In general, based on the symptomatology of the condition and known function of certain brain regions, the imaging literature has focused on loci that are normally involved in attention/cognition, executive function, working memory, motivation, and response inhibition.

Early neuropsychological literature implicated the frontal lobe, theorizing that frontal lobe dysfunction led to decreased internal inhibitory control and thus decreased attentiveness with increased impulsivity (56–59). These theories were supported by identification of similarities in symptomatology between ADHD patients and those with frontal lobe injury. Eventually, research was expanded theorizing that frontal lobe dysfunction was due to insufficient inhibitory control by the frontolimbic system (56,60,61). With time, the dorsolateral prefrontal cortices (DLPFCs) and ventrolateral prefrontal cortices (VLPFCs) came to receive the most attention, with the neuropsychological literature suggesting that these regions are important for selective attention, attention shifting, planning, and executive control (56,62,63).

The dorsal anterior cingulate cortex (dACC), also known as the “cognitive division” (56) of the cingulate cortex, has received a great deal of attention in the functional imaging literature (Fig. 12). It is believed to modulate motivation, effortful cognitive processing, and inhibition, (56,63–66) and has been demonstrated in animal studies to be responsible for reward-based motivation (67). Abnormalities in this region have been noted in children and adolescents with ADHD on fMRI and PET as well as in a morphometric MRI study of normal adolescents by Casey et al. in 1997 showing right anterior

A Children with no remediation

Normal reading children while rhyming



Dyslexic reading children while rhyming before remediation

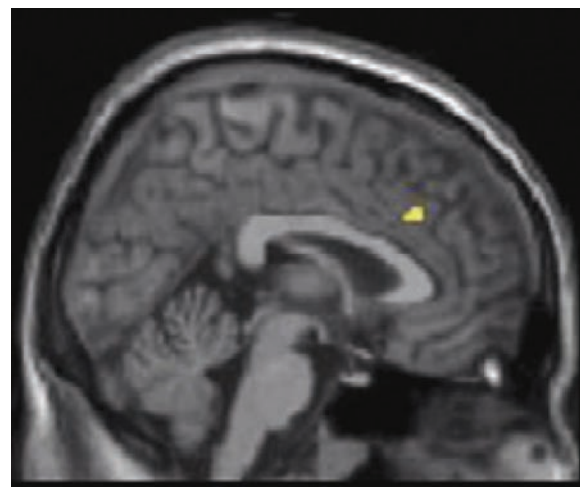
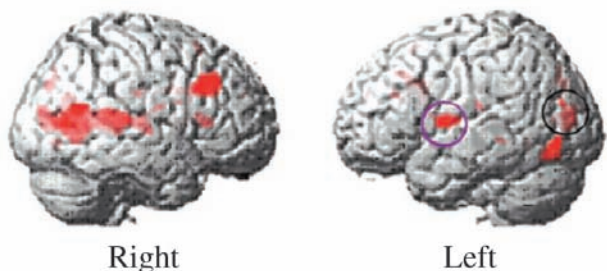
**B Dyslexic children increases after remediation**

Figure 11 Neural effects of remediation in children with developmental dyslexia. (A) Left hemisphere activations of control children and children with dyslexia are shown during rhyming (as compared with matching) letters. (B) Brain areas that showed increased activity during phonological processing in the dyslexic group after remediation. Black circles highlight left temporoparietal region, which is disrupted in children with dyslexia and affected by remediation. Purple circles highlight the left frontal region that is active in control children and is affected by remediation in children with dyslexia. Source: From Ref. 55 with permission from The National Academy of Sciences.

cingulate cortical volume to correlate with task performance (68).

The striatum (caudate and putamen), responsible for proper executive functioning, is also implicated in ADHD, particularly as it relates to abnormal dopaminergic activity (56). Other brain regions, including the thalamus, reticular activating system of the brainstem, and cerebellum have not yet received a great deal of attention, especially in the imaging literature (56). However, all may have a contributory role in pathogenesis of ADHD.

The earliest well-designed functional imaging study in ADHD was an FDG-PET study published in 1990 by

Figure 12 Location of the ACC, also known as the “cognitive division” of the cingulate cortex, has received a great deal of attention in the functional imaging literature. It is believed to modulate motivation, effortful cognitive processing, and inhibition and has been demonstrated in animal studies to be responsible for reward-based motivation. Abnormalities in this region have been noted in children and adolescents with ADHD. Abbreviations: ACC, anterior cingulate cortex; ADHD, attention deficit hyperactivity disorder. Source: From Ref. 89 with permission from Elsevier.

Zametkin et al. (69), demonstrating decreased global cerebral metabolism in untreated ADHD patients relative to control subjects. fMRI study of ADHD began in the late 1990s, and a wealth of data is now available.

The most consistent abnormality detected on fMRI is decreased activation within the dACC (56). Bush et al. in 1999 (70) used a counting Stroop test (Table 2) in a series of eight ADHD and eight normal controls, which demonstrated inactivation of the dACC in ADHD patients, while normal controls showed robust activation. The ADHD patients showed activation along an alternative pathway

Table 2 Stroop Test

The Stroop test creates cognitive interference and aims to activate brain function related to cognitive task switching. The subject is presented with a stimulus consisting of an arrow on the left side of the screen pointing leftward or an arrow on the right side of the screen pointing rightward and is instructed to press the thumb button on the corresponding side. In a small percentage of cases (20–25%), the subject is presented with an arrow on the left side of the screen pointing rightward or on the right side of the screen pointing leftward and has been instructed to press the thumb button corresponding to the direction the arrow is pointing, not the side of the screen on which it appears.

Table 3 Stop Signal Test

Purpose is to test the subject's ability to inhibit an impending action to determine which brain structures are activated in this process.

On "go" trials (75%), the letters "A" or "B" (a "go" stimulus) appear for 150 milliseconds. The subject is instructed to press a button with the left thumb for the letter "A" or a second button with the right thumb for the letter "B."

On "stop" trials (25%, selected at random), the "go" stimulus is followed by a "stop" signal (the letter "S"). On these trials, the subject is instructed not to press the button.

The length of time between onset of the "go" stimulus and onset of the "stop" stimulus is varied from 250 to 550 milliseconds. It is expected that in cases where there is a short interval between "go" and "stop" stimuli, subjects will have an easier time inhibiting the "go" response. However, especially with longer intervals between "go" and "stop" stimuli, there will be instances where the subject, whether ADHD or normal control, will be unsuccessful at inhibiting a "go" response already in progress. It is the unsuccessful "stop" trial (unsuccessful inhibition), which is of the greatest interest on fMRI, as it is presumed that the unsuppressed "go" response has occurred despite the brain's full-fledged, but nevertheless failed, attempt at response inhibition.

Abbreviations: ADHD, attention deficit hyperactivity disorder; fMRI, functional magnetic resonance imaging.

Source: As executed in Pliszka et al. (74) (2006).

Table 4 Go/No-Go Test

The subject is presented with a stimulus consisting of an arrow pointing to the left or right and is instructed to press a button with the left thumb for an arrow pointing left and to press a button with the right thumb for an arrow pointing right. In a small percentage of cases (20–25%), the subject is presented with an arrow pointing upward. In these cases, the subject has been instructed not to respond.

(frontostriatal insular), which was not seen in controls and may have represented a compensatory mechanism.

In 1999, Rubia et al. (71) published findings of hypo-function in the vicinity of the dACC, using stop-signal (Table 3) and motor-timing tasks, while Durston et al. (2003) (72) and Tamm et al. (2004) (73) used Go/No-Go (Table 4) tasks in children and adolescents. They found normal activation of the dACC among controls, while the ADHD subjects did not activate this structure.

Pliszka et al. (2006) (74) found lack of activation of the anterior cingulate cortex relative to control on unsuccessful inhibitions using a stop-signal task, implying that subjects with ADHD lack the activation of this important structure when attempting to "brake" an impending action before it is manifested. Some differences were seen in the left VLPFC as well; however, these were less profound

(Figs. 13, 14). These fMRI findings are consistent with the Zametkin et al. (1990) PET findings of decreased dACC activity in ADHD adults (69,74).

Abnormalities of striatal activation are fairly consistent in the fMRI literature. However, fMRI findings have been inconsistent with respect to abnormal activations in the DLPFCs and VLPFCs.

Thus, the dACC appears to be the most consistently abnormal structure in fMRI study of ADHD patients. Convergent data from neuroanatomy, structural imaging, electrophysiology, and lesion manifestation correlation all support the important role this structure plays in higher-level cognitive processes, and dysfunction of this structure may be able to explain the cardinal signs of ADHD (56). Nevertheless, the absence of consistent abnormality in other brain areas, including the DLPFC and VLPFC on fMRI studies, does not imply that these regions are not important contributors to the condition, and many other brain regions (i.e., brainstem, cerebellum) are still to be evaluated with fMRI protocols.

ASD

Autism is a complex, pervasive, and severe neurodevelopmental disorder. In DSM-IV, autism is defined by the presence of social deficits, abnormalities in communication, stereotyped, repetitive behaviors, and a characteristic course (75).

ASD range from individuals with little-to-no interest in interaction with others to those with only moderate impairment in interaction and includes autistic disorder and Asperger's syndrome (in which patients typically demonstrate milder symptomatology). The majority of autistic disorder patients have IQs in the mentally retarded range; however, IQs range from severely profoundly retarded to markedly above average (75). The prevalence of autism is estimated at one to two per 1000 individuals.

Structural imaging (76) and postmortem (77) studies have suggested an increase in total brain volume in ASD (75). In the face of modest overall brain enlargement, however, there appears to be a consistent modest decrease in the volume of the corpus callosum (78). This combination of findings is one of many in support of a general theory of cortical underconnectivity in ASD (75). As autism affects a multitude of cognitive functions, fMRI study of autism is more complicated than in the previously covered topics of dyslexia and ADHD. It is best to consider fMRI findings related to component problems faced by autistics.

Abnormalities of Socialization

One of the realms most affected in autism is social cognition. Autistics are generally poor at processing of

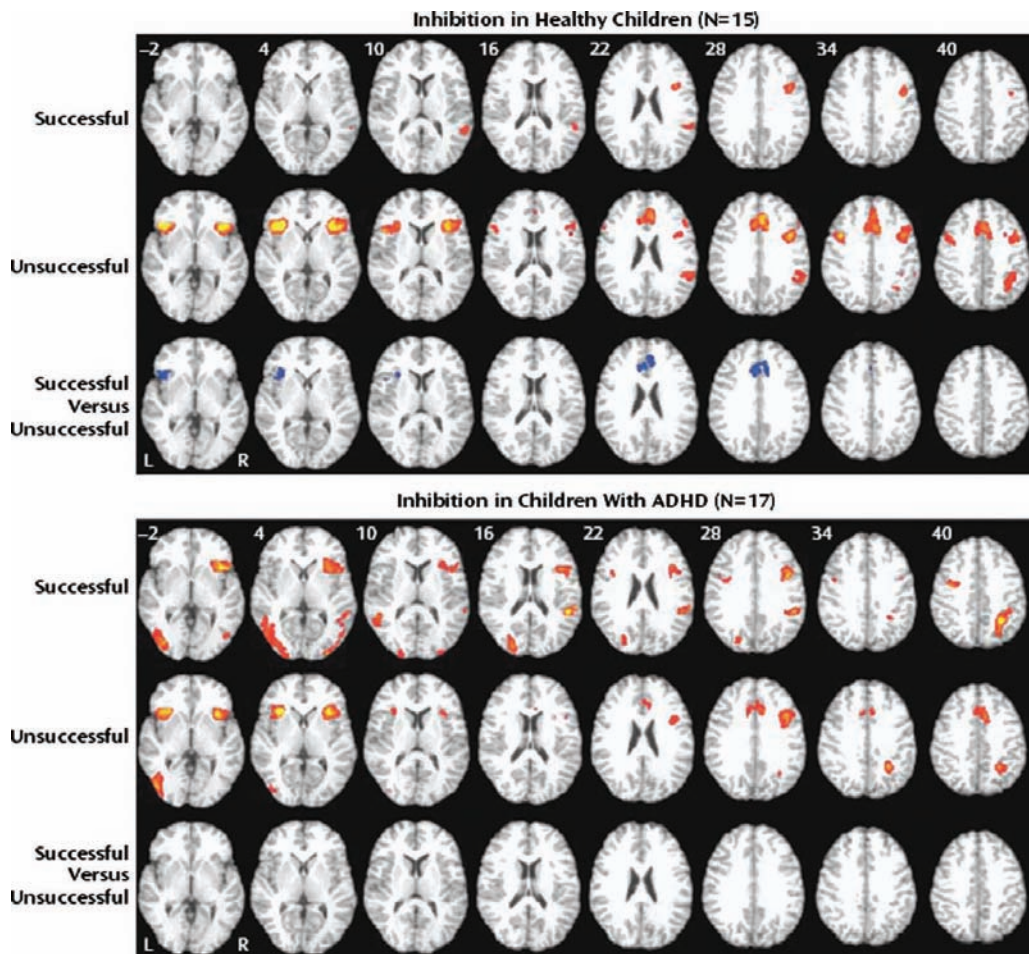


Figure 13 Activation patterns associated with successful and unsuccessful inhibition on the stop signal task in healthy children and in children with ADHD. Although healthy children showed relatively more activity in the left VLPFC for unsuccessful relative to successful inhibition, the children with ADHD did not. Slices were spaced 4 mm apart, beginning 2 mm below the anterior commissure-posterior commissure plane and were presented according to neurological conventions (right = right). Abbreviations: ADHD, attention deficit hyperactivity disorder; VLPFC, ventrolateral prefrontal cortex. Source: From Ref. 74 with permission from The American Psychiatric Association.

information normally gathered during social interaction, even while they may be high functioning and relatively unimpaired in other cognitive arenas (75). In addition to poor processing of socially acquired data, information appears to be inappropriately and ineffectively gathered, with research suggesting that autistics do not actively attend to portions of the human face (i.e., eyes, mouth) that confer the most information regarding another's state of mind (79).

Baron-Cohen et al. published, in 1997, a study comparing high-functioning autistics to normal-matched controls (80). They employed a task requiring subjects to infer a person's gender as well as information regarding their state of mind from a picture of the person's eyes only. Autistics performed more poorly on the task, did not activate the amygdala on fMRI, demonstrated relatively lower activation of frontal lobe foci, and demonstrated increased activation of the superior temporal gyrus (75).

Patients with ASD are also well known to have difficulty with face processing. This has been suggested observationally, but also by direct self reports from high-functioning individuals with ASD (75). In 2000, Schultz et al. published a study in which autistic spectrum patients were paired with age-, gender-, and IQ-matched controls (81). Subjects were presented with image pairs and asked to determine whether they were the same or different. Some image pairs were of objects (i.e., cars, chairs), others were human faces. In normal control subjects, a strong pattern of activation in the inferior frontal gyri for object pairing and of activation in the fusiform gyri (predominantly right sided) for facial pairing was noted. In contrast, however, autistic subjects demonstrated significantly less activation of the right fusiform gyrus, and instead activated the right inferior temporal gyrus in response to face pairing. These findings support the theory that autistic patients use feature-based strategies more typical of object perception for facial

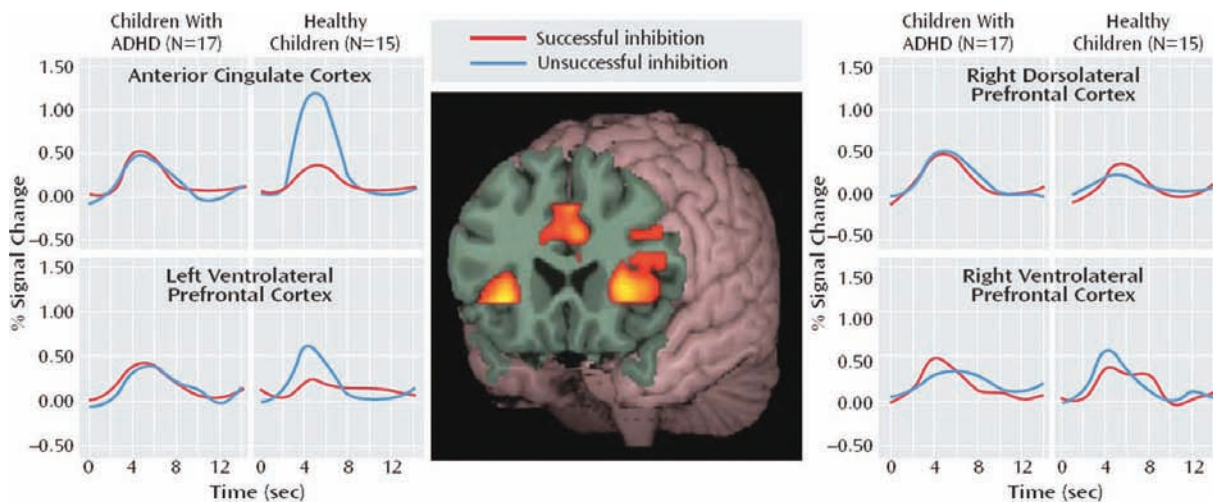


Figure 14 Time series plots of BOLD fMRI changes in various regions of interest in healthy children and in children with ADHD. Although the healthy children showed relatively more activity for unsuccessful “stop” trials within the anterior cingulate cortex and the left VLPFC than successful “stop” trials, the children with ADHD did not show differential activation patterns with unsuccessful inhibition in any region. The groups did not differ in the number of successful “stop” trials. Abbreviations: BOLD, blood oxygenation level-dependent; fMRI, functional magnetic resonance imaging; ADHD, attention deficit hyperactivity disorder; VLPFC, ventrolateral prefrontal cortex. Source: From Ref. 74 with permission from The American Psychiatric Association.

recognition (75,81). In theory, this may also explain the lack of emotional content gained from facial evaluation, since facial information is processed in inappropriate locations with expectedly different connectivities than those of the fusiform gyrus (Fig. 15).

Similar findings of absent activation of the fusiform gyrus were made by Critchley et al. (2000) (82) and Pierce et al. (2001) (83) (Fig. 16). Hubl et al. (2003) (84) (Fig. 17) also made similar findings regarding lack of fusiform gyral activation in response to face image presentation, but additionally demonstrated abnormally increased activation in regions of the brain related to effortful visual search tactics. This finding is consistent with self reports from high-functioning patients with ASD who have stated, for example, that they have learned to scan the corners of a person’s mouth and check if they are upturned to assess whether an individual is happy (75). Such a statement underscores another important aspect of abnormal cognition in those with ASD, namely, poor executive function secondary to piecemeal, rather than holistic (“big picture”), processing of information (75).

Executive Function

In the work by Just et al. (2006) (85), fMRI results from a group of high-functioning autistic spectrum individuals were compared with those of age-, gender-, and IQ-matched normal subjects using a Tower of London test modified to fMRI for assessment of executive functioning. Results demonstrated activation of similar brain areas between the two groups, but decreased functional con-

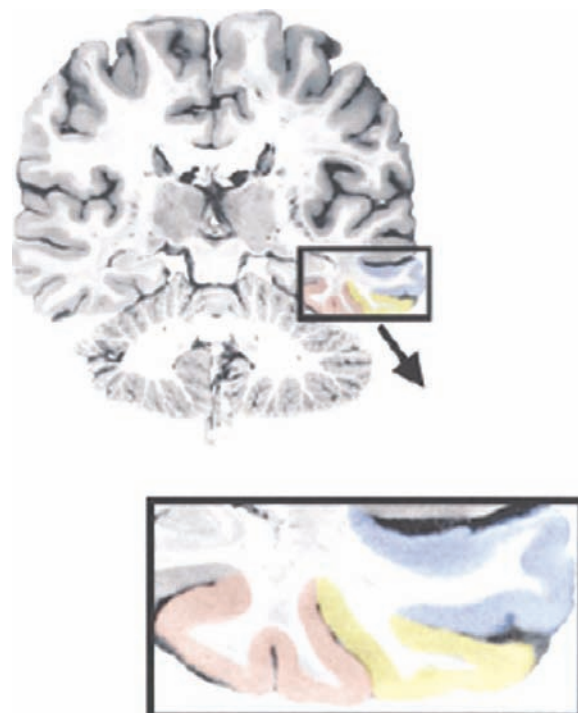


Figure 15 Face processing in autism. (A) The location of the middle (blue) and inferior (yellow) temporal gyri as well as of the fusiform gyrus (red). Source: From Ref. 83 with permission from Oxford University Press.

nnectivity between frontal and parietal regions. Functional connectivity was assessed by time course of activation in 15 regions of interest (ROIs)—seven paired brain ROIs

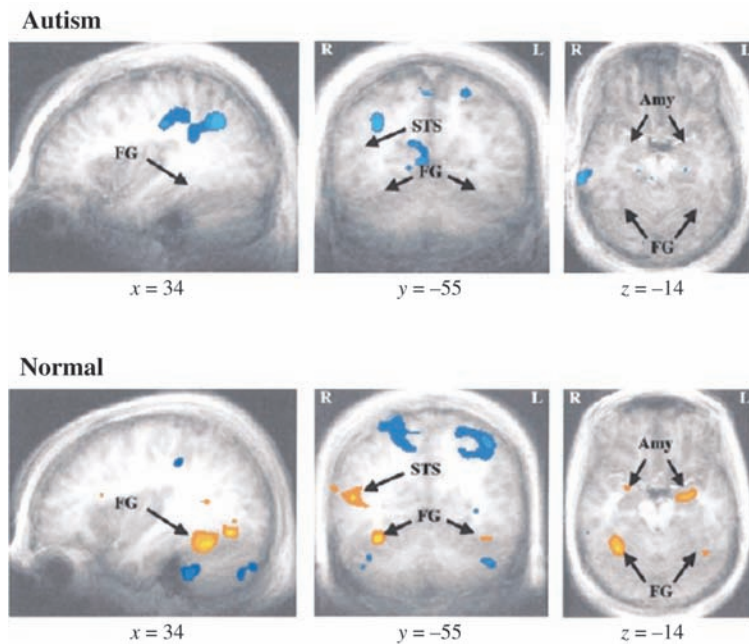


Figure 16 “Face” processing in autism. In autism, face processing occurs outside the “face area” normally located in the fusiform gyrus. Both autism and normal groups showing significant regions of activation (statistically significant positive activation noted by yellow and orange, deactivation noted by blue). Note FG, STS, and Amy activation in normals, in comparison with a lack of positive activation in the autism group. Decreased functional activity in the autism group is likely due to the inconsistent patterns of activation noted across individual autism subjects, which would fail to be seen when results are averaged. Abbreviations: FG, fusiform gyrus; STS, superior temporal sulcus; Amy, amygdala. Source: From Ref. 83 with permission from Oxford University Press.

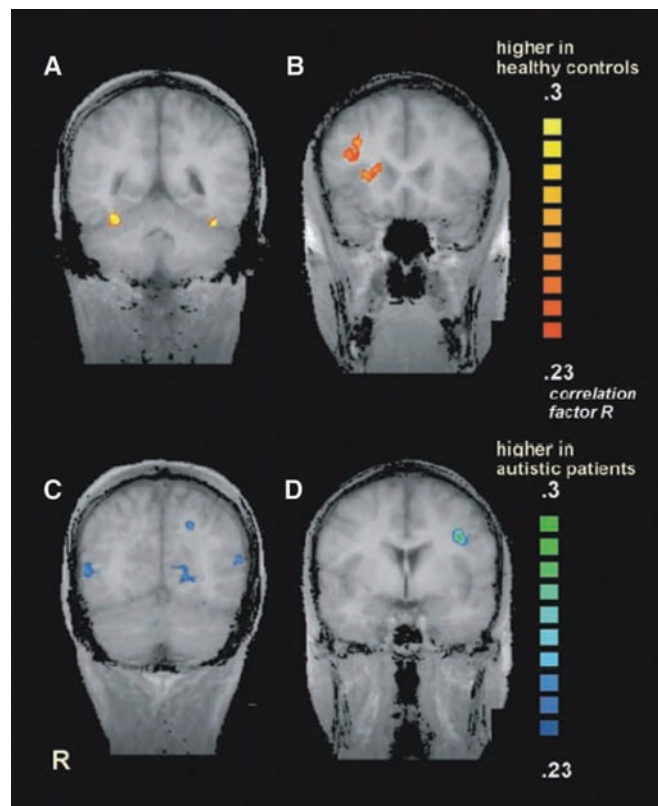


Figure 17 Differences in BOLD activation between healthy controls and autistic patients during face processing are shown in coronal slices. (A) Fusiform gyrus, (B) medial frontal gyrus and insular region show increased activation in healthy controls, while (C) the medial occipital gyrus and superior parietal lobule and (D) the precentral gyrus show increased activation in autistics. Abbreviations: BOLD, blood oxygenation level-dependent. Source: From Ref. 84 with permission from Wolters Kluwer/Lippincott Williams and Wilkins.

and the medial frontal gyrus. This study further supports the theory of underconnectivity in autistic spectrum patients and helps to explain piecemeal processing of data (85).

However, autistic patients are known to have preservation of visuospatial skills. In Silk et al. (2006) (86), seven high-functioning adolescents with autistic disorder or Asperger's syndrome as well as nine age- and IQ-matched controls were tested using a mental object rotation task during fMRI scanning. Results of testing showed no significant difference in performance between the autism and control groups. fMRI activation was significantly decreased in prefrontal brain regions, including the DLPFC and anterior cingulate gyrus similar to that seen in ADHD. There was also decreased activation in the caudate head. These areas are known to be important to executive functioning. Parietal cortical regions showed similar activation in both autistic and control subjects, consistent with the preserved visuospatial abilities typical of ASD (Fig. 18). It is interesting to note that while patients with ADHD and autism both have difficulty with executive functioning and demonstrate abnormal activation of prefrontal brain regions, autistic patients

demonstrate preserved ability to perform the mental object rotation task, while ADHD subjects perform significantly worse than matched controls (86,87).

Language Processing

The degree of language processing impairment in ASD tends to be directly related to individual patient IQ. However, in high-functioning autistic spectrum patients with normal IQ, certain abnormalities still remain. These include poor understanding of idioms and poor ability to extract the semantic content of words in context, (88) again consistent with impairment in processing multiple streams of information simultaneously (i.e., piecemeal processing). In a study of 14 high-functioning male patients with ASD and age-matched controls (88), decreased activation was noted in Broca's area and increased activation was noted in Wernicke's area among ASD patients when presented with words of "deep" semantic content (i.e., justice), while the difference was not seen for words of "shallow" semantic content (i.e., table). These findings may relate to the semantic processing difficulties seen in patients with ASD.

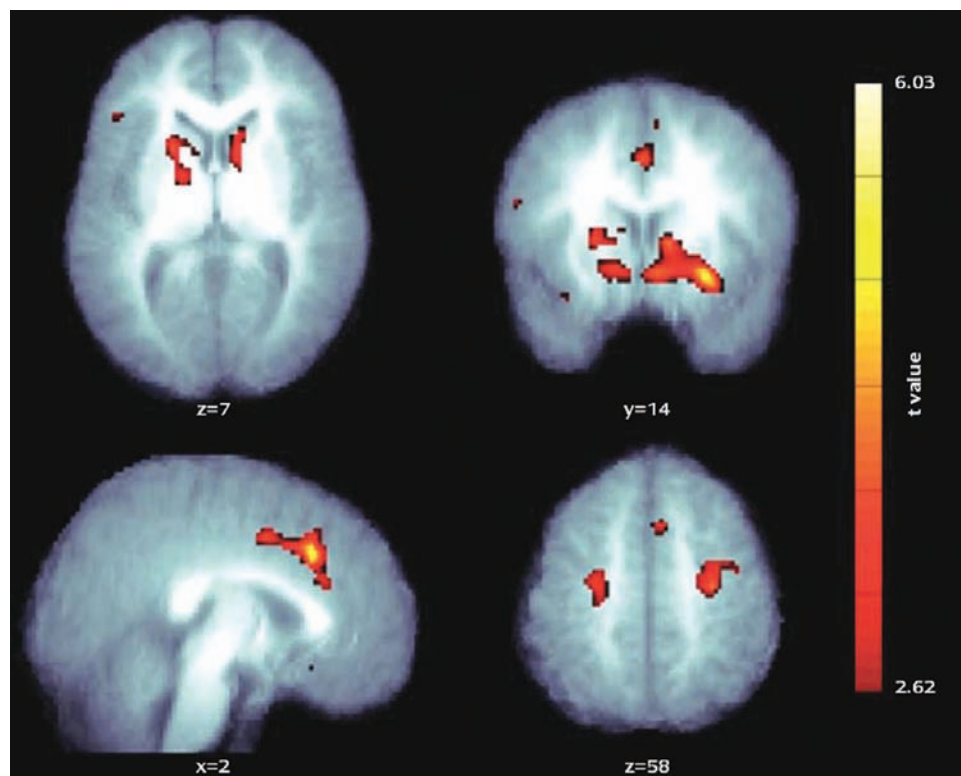


Figure 18 BOLD activation maps show greater activation (seen in red and yellow) in the comparison group than in the ASD group during performance of a mental rotation task. Abbreviations: BOLD, blood oxygenation level-dependent; ASD, autism spectrum disorders. Source: From Ref. 86 with permission from The American Psychiatric Association.

REFERENCES

1. Rosenberg DR, Sweeney JA, Gillen JS, et al. Magnetic resonance imaging of children without sedation: preparation with simulation. *J Am Acad Child Adolesc Psychiatry* 1997; 36(6):853–859.
2. Poldrack RA, Paré-Blagoev EJ, Grant PE. Pediatric functional magnetic resonance imaging: progress and challenges. *Top Magn Reson Imaging* 2002; 13(1):61–70.
3. Kotsoni E, Byrd D, Casey BJ. Special considerations for functional magnetic resonance imaging of pediatric populations. *J Magn Reson Imaging* 2006; 23(6):877–886.
4. Souweidane MM, Kim KH, McDowell R, et al. Brain mapping in sedated infants and young children with passive-functional magnetic resonance imaging. *Pediatr Neurosurg* 1999; 30(2):86–92.
5. Slifer KJ, Cataldo MF, Cataldo MD, et al. Behavior analysis of motion control for pediatric neuroimaging. *J Appl Behav Anal* 1993; 26(4):469–470.
6. Gaillard WD, Grandin CB, Xu B. Developmental aspects of pediatric fMRI: considerations for image acquisition, analysis, and interpretation. *Neuroimage* 2001; 13(2):239–249.
7. Seghier ML, Lazeyras F, Huppi PS. Functional MRI of the newborn. *Semin Fetal Neonatal Med* 2006; 11(6):479–488. (Epub 2006 Sep 25).
8. Yamada H, Sadato N, Konishi Y, et al. A milestone for normal development of the infantile brain detected by functional MRI. *Neurology* 2000; 55(2):218–223.
9. Yamada H, Sadato N, Konishi Y, et al. A rapid brain metabolic change in infants detected by fMRI. *Neuroreport* 1997; 8(17):3775–3778.
10. Morita T, Kochiyama T, Yamada H, et al. Difference in the metabolic response to photic stimulation of the lateral geniculate nucleus and the primary visual cortex of infants: a fMRI study. *Neurosci Res* 2000; 38(1):63–70.
11. Konishi Y, Taga G, Yamada H, et al. Functional brain imaging using fMRI and optical topography in infancy. *Sleep Med* 2002; 3(suppl 2):S41–S43.
12. Born AP, Miranda MJ, Rostrup E, et al. Functional magnetic resonance imaging of the normal and abnormal visual system in early life. *Neuropediatrics* 2000; 31(1):24–32.
13. Muramoto S, Yamada H, Sadato N, et al. Age-dependent change in metabolic response to photic stimulation of the primary visual cortex in infants: functional magnetic resonance imaging study. *J Comput Assist Tomogr* 2002; 26(6):894–901.
14. Casey BJ, Giedd JN, Thomas KM. Structural and functional brain development and its relation to cognitive development. *Biol Psychol* 2000; 54(1–3):241–257.
15. Giedd JN, Snell JW, Lange N, et al. Quantitative magnetic resonance imaging of human brain development: ages 4–18. *Cereb Cortex* 1996; 6(4):551–560.
16. Reiss AL, Abrams MT, Singer HS, et al. Brain development, gender and IQ in children. A volumetric imaging study. *Brain* 1996; 119(pt 5):1763–1774.
17. Frazier JA, Giedd JN, Hamburger SD, et al. Brain anatomic magnetic resonance imaging in childhood-onset schizophrenia. *Arch Gen Psychiatry* 1996; 53(7):617–624.
18. Giedd JN, Blumenthal J, Jeffries NO, et al. Brain development during childhood and adolescence: a longitudinal MRI study. *Nat Neurosci* 1999; 2(10):861–863.
19. Hykin J, Moore R, Duncan K, et al. Fetal brain activity demonstrated by functional magnetic resonance imaging. *Lancet* 1999; 354(9179):645–646.
20. Moore RJ, Vadeyer S, Fulford J, et al. Antenatal determination of fetal brain activity in response to an acoustic stimulus using functional magnetic resonance imaging. *Hum Brain Mapp* 2001; 12(2):94–99.
21. Fulford J, Vadeyer SH, Dodampahala SH, et al. Fetal brain activity in response to a visual stimulus. *Hum Brain Mapp* 2003; 20(4):239–245.
22. Fulford J, Vadeyer SH, Dodampahala SH, et al. Fetal brain activity and hemodynamic response to a vibroacoustic stimulus. *Hum Brain Mapp* 2004; 22(2):116–121.
23. Born P, Rostrup E, Leth H, et al. Change of visually induced cortical activation patterns during development. *Lancet* 1996; 347(9000):543.
24. Altman NR, Bernal B. Brain activation in sedated children: auditory and visual functional MR imaging. *Radiology* 2001; 221(1):56–63.
25. Born P, Leth H, Miranda MJ, et al. Visual activation in infants and young children studied by functional magnetic resonance imaging. *Pediatr Res* 1998; 44(4):578–583.
26. Martin E, Joeri P, Loenneker T, et al. Visual processing in infants and children studied using functional MRI. *Pediatr Res* 1999; 46(2):135–140.
27. Anderson AW, Marois R, Colson ER, et al. Neonatal auditory activation detected by functional magnetic resonance imaging. *Magn Reson Imaging* 2001; 19(1):1–5.
28. Wood AG, Harvey AS, Wellard RM, et al. Language cortex activation in normal children. *Neurology* 2004; 63(6):1035–1044.
29. Gaillard WD, Hertz-Pannier L, Mott SH, et al. Functional anatomy of cognitive development: fMRI of verbal fluency in children and adults. *Neurology* 2000; 54(1):180–185.
30. Staudt M, Lidzba K, Grodd W, et al. Right-hemispheric organization of language following early left-sided brain lesions: functional MRI topography. *Neuroimage* 2002; 16(4):954–967.
31. Lidzba K, Staudt M, Wilke M, et al. Visuospatial deficits in patients with early left-hemispheric lesions and functional reorganization of language: consequence of lesion or reorganization? *Neuropsychologia* 2006; 44(7):1088–1094. (Epub 2005 Nov 28).
32. Joseph J, Noble K, Eden G. The neurobiological basis of reading. *J Learn Disabil* 2001; 34(6):566–579.
33. Cohen L, Martinaud O, Lemer C, et al. Visual word recognition in the left and right hemispheres: anatomical and functional correlates of peripheral alexias. *Cereb Cortex* 2003; 13(12):1313–1333.
34. Friedman L, Kenny JT, Wise AL, et al. Brain activation during silent word generation evaluated with functional MRI. *Brain Lang* 1998; 64(2):231–256.
35. Rumsey JM, Horwitz B, Donohue BC, et al. Phonological and orthographic components of word recognition. A PET-rCBF study. *Brain* 1997; 120(pt 5):739–759.

36. Rumsey JM, Nace K, Donohue B, et al. A positron emission tomographic study of impaired word recognition and phonological processing in dyslexic men. *Arch Neurol* 1997; 54(5):562–573.
37. Benson RR, Logan WJ, Cosgrove GR, et al. Functional MRI localization of language in a 9-year-old child. *Can J Neurol Sci* 1996; 23(3):213–219.
38. Rueckert L, Appollonio I, Grafman J, et al. Magnetic resonance imaging functional activation of left frontal cortex during covert word production. *J Neuroimaging* 1994; 4(2):67–70.
39. Paulesu E, Goldacre B, Scifo P, et al. Functional heterogeneity of left inferior frontal cortex as revealed by fMRI. *Neuroreport* 1997; 8(8):2011–2017.
40. Démonet JF, Chollet F, Ramsay S, et al. The anatomy of phonological and semantic processing in normal subjects. *Brain* 1992; 115(pt 6):1753–1768.
41. Démonet JF, Price C, Wise R, et al. A PET study of cognitive strategies in normal subjects during language tasks. Influence of phonetic ambiguity and sequence processing on phoneme monitoring. *Brain* 1994; 117(pt 4):671–682.
42. Démonet JF, Price C, Wise R, et al. Differential activation of right and left posterior sylvian regions by semantic and phonological tasks: a positron-emission tomography study in normal human subjects. *Neurosci Lett* 1994; 182(1):25–28.
43. Warburton E, Wise RJ, Price CJ, et al. Noun and verb retrieval by normal subjects. Studies with PET. *Brain* 1996; 119(pt 1):159–179.
44. Wise R, Chollet F, Hadar U, et al. Distribution of cortical neural networks involved in word comprehension and word retrieval. *Brain* 1991; 114(pt 4):1803–1817.
45. Fitzgerald DB, Cosgrove GR, Ronner S, et al. Location of language in the cortex: a comparison between functional MR imaging and electrocortical stimulation. *AJNR Am J Neuroradiol* 1997; 18(8):1529–1539.
46. Peterson MS, Kramer AF, Wang RF, et al. Visual search has memory. *Psychol Sci* 2001; 12(4):287–292.
47. Pugh KR, Mencl WE, Jenner AR, et al. Functional neuroimaging studies of reading and reading disability (developmental dyslexia). *Ment Retard Dev Disabil Res Rev* 2000; 6(3):207–213.
48. Demb JB, Boynton GM, Heeger DJ. Functional magnetic resonance imaging of early visual pathways in dyslexia. *J Neurosci* 1998; 18(17):6939–6951.
49. Burdette JH. Functional MR imaging to evaluate sensory processing in dyslexia. *Acad Radiol* 2002; 9(9):1062–1063.
50. Shaywitz SE, Shaywitz BA. Dyslexia (specific reading disability). *Biol Psychiatry* 2005; 57(11):1301–1309.
51. Eden GF, Zeffiro TA. Neural systems affected in developmental dyslexia revealed by functional neuroimaging. *Neuron* 1998; 21(2):279–282.
52. Livingstone MS, Rosen GD, Drislane FW, et al. Physiological and anatomical evidence for a magnocellular defect in developmental dyslexia. *Proc Natl Acad Sci USA* 1991; 88(18):7943–7947.
53. Eden GF, VanMeter JW, Rumsey JM, et al. Abnormal processing of visual motion in dyslexia revealed by functional brain imaging. *Nature* 1996; 382(6586):66–69.
54. Shaywitz SE, Shaywitz BA, Fulbright RK, et al. Neural systems for compensation and persistence: young adult outcome of childhood reading disability. *Biol Psychiatry* 2003; 54(1):25–33.
55. Temple E, Deutsch GK, Poldrack RA, et al. Neural deficits in children with dyslexia ameliorated by behavioral remediation: evidence from functional MRI. *Proc Natl Acad Sci USA* 2003; 100(5):2860–2865. (Epub 2003 Feb 25).
56. Bush G, Valera EM, Seidman LJ. Functional neuroimaging of attention-deficit/hyperactivity disorder: a review and suggested future directions. *Biol Psychiatry* 2005; 57(11):1273–1284.
57. Barkley RA. Behavioral inhibition, sustained attention, and executive functions: constructing a unifying theory of ADHD. *Psychol Bull* 1997; 121(1):65–94.
58. Barkley RA, Grodzinsky G, DuPaul GJ. Frontal lobe functions in attention deficit disorder with and without hyperactivity: a review and research report. *J Abnorm Child Psychol* 1992; 20(2):163–188.
59. Mattes JA. The role of frontal lobe dysfunction in childhood hyperkinesia. *Compr Psychiatry* 1980; 21(5):358–369.
60. Casey BJ, Castellanos FX, Giedd JN, et al. Implication of right frontostriatal circuitry in response inhibition and attention-deficit/hyperactivity disorder. *J Am Acad Child Adolesc Psychiatry* 1997; 36(3):374–383.
61. Satterfield JH, Dawson ME. Electrodermal correlates of hyperactivity in children. *Psychophysiology* 1971; 8(2):191–197.
62. Duncan J, Owen AM. Common regions of the human frontal lobe recruited by diverse cognitive demands. *Trends Neurosci* 2000; 23(10):475–483.
63. Posner MI, Petersen SE. The attention system of the human brain. *Annu Rev Neurosci* 1990; 13:25–42.
64. Bush G, Vogt BA, Holmes J, et al. Dorsal anterior cingulate cortex: a role in reward-based decision making. *Proc Natl Acad Sci USA* 2002; 99(1):523–528. (Epub 2001 Dec 26).
65. Bush G, Luu P, Posner MI. Cognitive and emotional influences in anterior cingulate cortex. *Trends Cogn Sci* 2000; 4(6):215–222.
66. Vogt BA, Finch DM, Olson CR. Functional heterogeneity in cingulate cortex: the anterior executive and posterior evaluative regions. *Cereb Cortex* 1992; 2(6):435–443.
67. Barbelivien A, Ruotsalainen S, Sirviö J. Metabolic alterations in the prefrontal and cingulate cortices are related to behavioral deficits in a rodent model of attention-deficit hyperactivity disorder. *Cereb Cortex* 2001; 11:1056–1063.
68. Casey BJ, Trainor R, Giedd J, et al. The role of the anterior cingulate in automatic and controlled processes: a developmental neuroanatomical study. *Dev Psychobiol* 1997; 30(1):61–69.
69. Zametkin AJ, Nordahl TE, Gross M, et al. Cerebral glucose metabolism in adults with hyperactivity of childhood onset. *N Engl J Med* 1990; 323(20):1361–1366.
70. Bush G, Frazier JA, Rauch SL, et al. Anterior cingulate cortex dysfunction in attention-deficit/hyperactivity disorder revealed by fMRI and the Counting Stroop. *Biol Psychiatry* 1999; 45(12):1542–1552.

71. Rubia K, Overmeyer S, Taylor E, et al. Hypofrontality in attention deficit hyperactivity disorder during higher-order motor control: a study with functional MRI. *Am J Psychiatry* 1999; 156(6):891–896.
72. Durston S, Tottenham NT, Thomas KM, et al. Differential patterns of striatal activation in young children with and without ADHD. *Biol Psychiatry* 2003; 53(10):871–878.
73. Tamm L, Menon V, Ringel J, et al. Event-related fMRI evidence of frontotemporal involvement in aberrant response inhibition and task switching in attention-deficit/hyperactivity disorder. *J Am Acad Child Adolesc Psychiatry* 2004; 43(11):1430–1440.
74. Pliszka SR, Glahn DC, Semrud-Clikeman M, et al. Neuroimaging of inhibitory control areas in children with attention deficit hyperactivity disorder who were treatment naive or in long-term treatment. *Am J Psychiatry* 2006; 163(6):1052–1060.
75. Cody H, Pelphrey K, Piven J. Structural and functional magnetic resonance imaging of autism. *Int J Dev Neurosci* 2002; 20(3–5):421–438.
76. Piven J, Arndt S, Bailey J, et al. Regional brain enlargement in autism: a magnetic resonance imaging study. *J Am Acad Child Adolesc Psychiatry* 1996; 35(4):530–536.
77. Bailey A, Luthert P, Bolton P, et al. Autism and megalecephaly. *Lancet* 1993; 341(8854):1225–1226.
78. Egaas B, Courchesne E, Saitoh O. Reduced size of corpus callosum in autism. *Arch Neurol* 1995; 52(8):794–801.
79. Pelphrey KA, Sasson NJ, Reznick JS, et al. Visual scanning of faces in autism. *J Autism Dev Disord* 2002; 32(4):249–261.
80. Baron-Cohen S, Ring HA, Wheelwright S, et al. Social intelligence in the normal and autistic brain: an fMRI study. *Eur J Neurosci* 1999; 11(6):1891–1898.
81. Schultz RT, Gauthier I, Klin A, et al. Abnormal ventral temporal cortical activity during face discrimination among individuals with autism and Asperger syndrome. *Arch Gen Psychiatry* 2000; 57(4):331–340.
82. Critchley H, Daly E, Phillips M, et al. Explicit and implicit neural mechanisms for processing of social information from facial expressions: a functional magnetic resonance imaging study. *Hum Brain Mapp* 2000; 9(2):93–105.
83. Pierce K, Müller RA, Ambrose J, et al. Face processing occurs outside the fusiform ‘face area’ in autism: evidence from functional MRI. *Brain* 2001; 124(pt 10):2059–2073.
84. Hubl D, Bölte S, Feineis-Matthews S, et al. Functional imbalance of visual pathways indicates alternative face processing strategies in autism. *Neurology* 2003; 61(9):1232–1237.
85. Just MA, Cherkassky VL, Keller TA, et al. Functional and anatomical cortical underconnectivity in autism: evidence from an fMRI study of an executive function task and corpus callosum morphometry. *Cereb Cortex* 2007; 17(4):951–961. (Epub 2006 Jun 13).
86. Silk TJ, Rinehart N, Bradshaw JL, et al. Visuospatial processing and the function of prefrontal-parietal networks in autism spectrum disorders: a functional MRI study. *Am J Psychiatry* 2006; 163(8):1440–1443.
87. Silk T, Vance A, Rinehart N, et al. Fronto-parietal activation in attention-deficit hyperactivity disorder, combined type: functional magnetic resonance imaging study. *Br J Psychiatry* 2005; 187:282–283.
88. Harris GJ, Chabris CF, Clark J, et al. Brain activation during semantic processing in autism spectrum disorders via functional magnetic resonance imaging. *Brain Cogn* 2006; 61(1):54–68. (Epub 2006 Feb 13).
89. Levesque J, Beauregard M, Mensour B. Effect of neurofeedback training on the neural substrates of selective attention in children with attention-deficit/hyperactivity disorder: a functional magnetic resonance imaging study. *Neurosci Lett* 2006; 394(1):216–221.

10

Neurodegenerative Disorders

LIHONG WANG

Brain Imaging and Analysis Center, Duke University Medical Center, Durham, North Carolina, U.S.A.

JEFFREY R. PETRELLA

Department of Radiology, Duke University, Durham, North Carolina, U.S.A.

INTRODUCTION

Neurodegenerative diseases are insidious in onset and gradual in progression. Most of them are difficult to diagnose until their typical symptoms are fully developed in the middle or late stage of disease. However, potential clinical treatments are most likely to be effective at the early stage of neural degeneration before functional decline occurs. Thus, biomarkers for neurodegenerative diseases are essential to predict onset of disease and improve early diagnosis as well as to monitor clinical intervention. Conventional structural neuroimaging (1) plays a limited (exclusionary) role in the evaluation of neurodegenerative disorders because anatomical manifestations are often nonspecific or occur late in the disease course. Functional neuroimaging techniques such as blood oxygen level-dependent (BOLD) functional MRI (fMRI), positron emission tomography (PET), single positron emission computerized tomography (SPECT), magnetic resonance spectroscopy (MRS), diffusion tensor imaging (DTI), and MR perfusion imaging have great potential to detect functional change before clinical or volumetric changes are apparent (2–4). Such techniques are increasingly used and may serve in the future as biomarkers for facilitating accurate and early diagnosis and monitoring disease progression.

In this chapter, we will discuss the methodological challenges of fMRI in neurodegenerative diseases, summarize recent progress of fMRI research in neurodegenerative diseases, and highlight its potential role in clinical diagnosis.

METHODOLOGICAL CHALLENGES IN PATIENTS WITH NEURODEGENERATIVE DISEASE

Brain Atrophy

Brain imaging studies comparing young and old adults provide a powerful tool for understanding the functional alterations of aging and aging associated with progressive neurodegeneration. Meanwhile, a common aim of current fMRI studies is to find group differences between neurodegenerative subjects and healthy elderly controls. This may yield insights into the origins of aging-associated cognitive change and provide functional biomarkers that predict early functional neural decline associated with diseases. The technique of spatial normalization has been developed to facilitate intersubject comparisons by placing all subjects into a standardized stereotactic template space (5). This technique served to increase signal-to-noise ratio for higher statistical power to detect

activated regions (6–8) by averaging data from multiple subjects. Another important reason for the use of spatial normalization in neuroimaging studies is the ability to report findings in an accurate and reproducible manner that can be easily compared among studies and interpreted by other investigators (9).

While the use of spatial normalization is becoming a common way of data analysis in fMRI, there are still concerns that significant individual variations in neuroanatomical structure may persist even after spatial normalization (8,10). Spatial normalization is assumed to sufficiently account for individual differences in size/shape of neural anatomy to allow for comparison of homologous regions across subjects (6,8,11). While spatial normalization is not intended to account for all anatomical variation, systematic anatomical variation indicative of specific subject populations can confound analyses employing spatial normalization in different groups (12,13).

It is well known that brain atrophy occurs with normal aging and is even more profound in neurodegenerative diseases with dementia. Recent studies have shown that the accuracy of the final registration process may be dependent on the age of the subject population (14), and the accuracy of the normalization process might decline further if employed in memory-impaired populations (12,15). Krishnan et al. (12) studied 20 clinically defined mild cognitive impairment (MCI) subjects and 20 elderly controls at 4T with structural and functional MRI during a memory encoding-retrieval task. Bilateral anterior/posterior hippocampal regions of interest (ROIs) were manually drawn to assess normalization accuracy to the Montreal Neurological Institute template. The percentage of each template-defined hippocampal ROI originating from true hippocampal tissue was determined for all subjects. To assess the ability of spatial normalization to equalize group differences in hippocampal volume, pre- and post-normalization hippocampal volumes were compared. They also compared fMRI measures from template and nontemplate analyses. The authors found that normalization accuracy in the left hippocampus and bilateral posterior hippocampi was significantly poorer in MCI subjects, and the difference persisted after covarying for age. A significant correlation of template-based and nontemplate-based ROI measures of fMRI activation in the hippocampus was found in controls but not in the MCI group. Thus, the poor spatial normalization accuracy of the hippocampus in memory-impaired subjects might represent an important potential confounder of template-based assessment of fMRI activation in the medial temporal lobe (MTL).

Considering this and other evidences, it has been recommended by some to control for the impact of local atrophy on brain-activation difference in studying aging and neurodegenerative diseases (13,16,17). ROI analysis based on individual subject's brain structure is a favorable approach in neurodegenerative populations.

Neurovascular Coupling and Hemodynamic Response Variance

Neurovascular factor can also influence the outcome of group comparisons among different populations. Since the BOLD mechanism of fMRI (18,19) critically depends on the properties of local vasculature (20,21), direct comparison of the BOLD response among groups could be confounded by age-related or disease-related alterations in cerebrovascular dynamics.

Age-related changes of the microvasculature may alter the responsiveness of cerebral arterioles to metabolic changes (vascular reactivity) or to neuronal activity (decoupling) (22,23). Analysis of hemodynamic response variance shows increased response variance in nondemented older adults as compared with young adults (24), and demented older adults have more variance than young or nondemented older adults (25). Chronic cerebral ischemia can lead to secondary chronic vasodilatation, which may reduce the difference in cerebral blood flow between resting and activated states, and thus decrease the magnitude of the BOLD response (26–28). The intake of nonsteroidal anti-inflammatory drugs, prevalent in the elderly, may significantly reduce vasodilatation by reducing the production and release of eicosanoids from astrocytes (29) and lead to an increase in regional cerebral blood flow. Vasoconstrictors such as cocaine increase the apparent BOLD effect. Decrease in the hematocrit leads to a decrease in the magnitude of the BOLD signal. Acute hemodilution by infusion of saline may result in a 6% decrease in hematocrit, leading to an 8% to 31% decrease in BOLD signal (30,31). With many potential confounding factors, it is difficult to determine whether differences in the BOLD response between young and old subjects or between healthy subjects and patients with neurodegenerative diseases are due to an altered neurovascular response or altered neuronal activity.

To control for the influence of potentially different hemodynamic response functions (HRFs) among groups in functional activation studies, it has been proposed to include performance of simple sensorimotor tasks in addition to cognitive tasks, or analyze group-by-task interactions rather than a main effect of group difference (22,23). However, activation differences in brain regions related to simple sensorimotor tasks due to neurovascular coupling might not necessarily apply to other brain regions (25), such as those subserving a cognitive task. Moreover, HRF differences could have a nonlinear relation to neuronal activities difference in different tasks. Therefore, such measures cannot completely solve the problem of different HRF response functions in different populations. It is important to carefully control for vascular risk factors (hypotension, diabetes) on functional activation studies on healthy, aging, or Alzheimer disease (AD) populations (22,23).

Even when controlling for the factors mentioned above, conflicting findings of BOLD changes (hypoactivation or hyperactivation) that have been reported in patients in fMRI literature still may not be explained. Factors that might contribute to discrepancies in the literature include (*i*) different tasks employed across different studies; (*ii*) different MRI scanners, analysis software, analysis methods, and statistic thresholds; (*iii*) less well-controlled individual variance and clinical status; and (*iv*) varying level of attention and task performance related to clinical studies. Variable load stimulus conditions and functional connectivity approaches for data analysis might reconcile these issues.

Data Interpretation of Altered Activation in Aging and Neurodegenerative Disease

Under normal conditions, when brain function is not altered by neurodegeneration or aging, increased or extended functional activation is often associated with successful task performance, enhanced attention effect, or greater cognitive load. These rules generally also account for altered functional activation responses in patients with declining brain function where task difficulty is influenced not only by the task itself but also by the level of neurodegeneration. The progression of neurodegeneration can either lead to increased or extended activation (accompanying unaffected or mildly impaired performance) or to activation deficits (often with severely impaired performance), sometimes leading to apparently conflicting reports.

There are several existing models (23) and hypotheses for the interpretation of functional activation in aging and dementia. “Under-recruitment” or the “nonselective” model proposed by Logan et al. (32) posits that extra activation found in an aging or dementia might be due to inability to sufficiently engage specific cortical regions during cognitive performance. Additional areas are recruited and activated to compensate for this failure. The recruitment-compensation theory has been supported by both animal and clinical studies (33,34).

The “Degenerate theory” (35,36) presumes that different brain structures can subserve the same function. When damage occurs to only one or a subset of those systems, task performance may not be impaired, but differences in the brain-activation pattern may be found. As what Prvulovic et al. (23) noted, this theory would explain why in functional MRI studies not all healthy individuals activate the exact same brain regions during the same task and why patients show a different pattern of brain activation across certain areas during a cognitive task but often have preserved performance. Task performance will only be impaired when a necessary neuronal system has been

damaged that cannot be compensated by another system or when the complete set of potential systems are affected. This concept works very well for circumscribed focal brain lesions. Yet, when neural damage is more global in nature, it is more likely that all subsystems will be impaired, leading to global activation deficits or non-specific aberrant activation patterns across the brain, associated with poor task performance (23).

Rapoport and Grady (37) introduced the model of a sigmoidal relation between regional cerebral blood flow (y-axis) and a function of task difficulty and individual task performance (x-axis) (23). In early stages of mild pathological damage, patients may show reduced brain activation during control tasks with very low processing demand and increased activation with highly demanding tasks. With increasing neuronal damage, the maximum activation capacity of the brain decreases, and patients reveal a decrease in activation compared with controls.

Prvulovic et al. (23) extended the sigmoidal model into an integrative model that takes into account modulation of the neural network. The central element of the model is a cortical region [processing unit(PU)] that is part of a cortical circuitry required for successful processing of the task at hand. Decreased processing efficiency of PU in combination with almost preserved processing capacity and input will lead to a compensatory recruitment of an increased number of subunits within the PU to compensate for the diminished processing efficiency (dashed functional activation curve in the PU, Fig. 1), leading to higher workload and increased brain activation. The limits of the processing capacity of the PU will be reached earlier with increasing task difficulty due to an impairment of processing capacity and thus lead to earlier decompensation of task performance (dashed red line in Fig. 1). A greater amount of damage in the PU with a significant decrease of processing capacity or disruptions of the input channel(s) to the PU (38) will lead to diminished activation in the PU (dotted black functional activation curve, Fig. 1) (39–41). In this scenario, only a small part of the PU can be recruited for task processing. While in very simple tasks performance might be preserved, even slight increases of task difficulty will lead to a fast decrease of task performance (dotted red line in Fig. 1). Impaired functional connectivity might be an indicator of disrupted input channels and has been demonstrated between frontal and temporal brain regions in AD patients (42).

DEMENTIA

Due to a rapid increase in the elderly population, a dramatic increase in the incidence of neurodegenerative and cerebrovascular disorders causing dementia is also expected. AD is the most common cause of dementia.

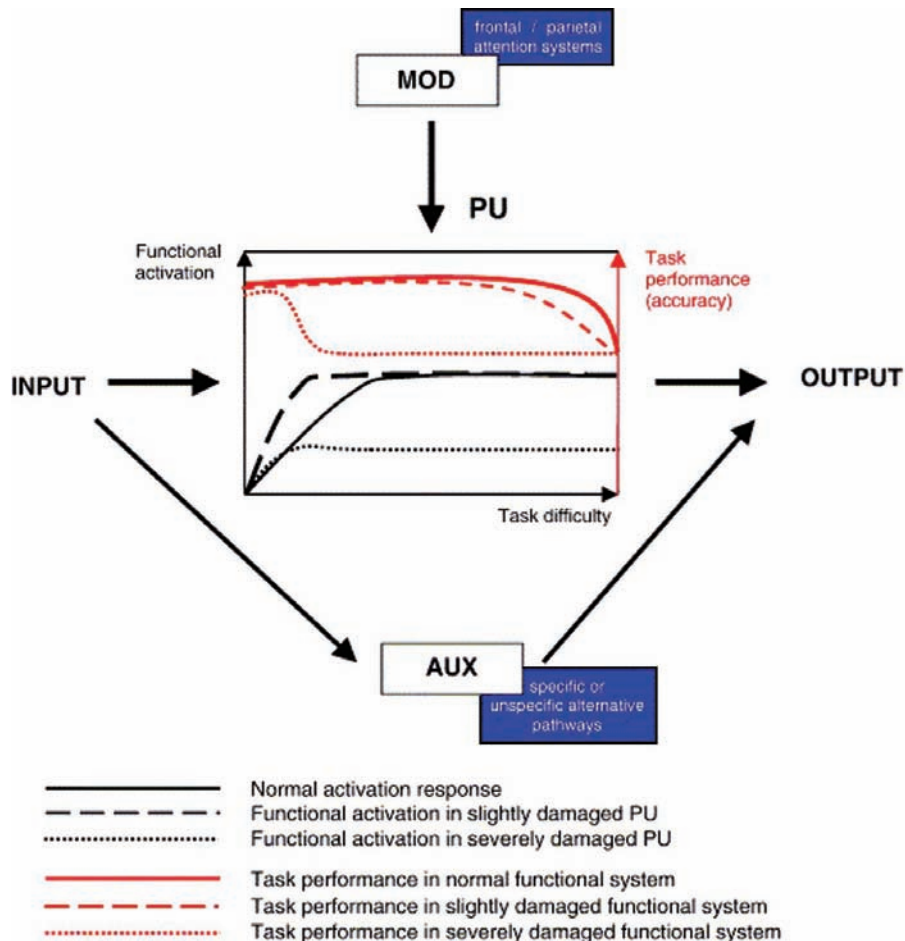


Figure 1 The integrated model proposed by Prvulovic et al. illustrating possible relations between damage to a PU, the dynamics of its activation response in relation to task difficulty, and the integrated network engaged during the processing of a cognitive task. Abbreviations: PU, processing unit; MOD, modulation unit; AUX, auxiliary unit. Source: From Ref. 23.

Vascular dementia, dementia with Lewy bodies, and frontotemporal dementia (FTD) are the most frequent causes for dementia after AD and need to be differentiated clinically. Accordingly, AD is the most extensively studied of the neurodegenerative diseases using fMRI. Given that neural dysfunction precedes neural death, fMRI offers considerable potential in early identification of patients with prodromal dementia.

AD and MCI

AD is a chronic neurodegenerative disease characterized by global cognitive decline including gradual loss of memory, reasoning, and language, preceded by progressive neuropathological damage to the brain (43,44). Episodic memory generally is the first and most severely affected (45–47). Progressive atrophy in the medial temporal, frontal, and parietal regions gives rise to clinical symptoms such as amnesia, agnosia, and aphasia (48,49).

The neuropathological hallmarks of AD are the presence of amyloid plaques broadly distributed in cerebral cortex, and neurofibrillary tangles (tau) initially prominent in the MTLs (hippocampus, entorhinal cortex, and association areas of the neocortex) early in the disease and progressively in the remaining neocortex (43,50–55) (Fig. 2).

In clinical practice, the diagnosis of AD is still largely based on consensus criteria combined with the exclusion of secondary causes of memory loss (56,57). The clinical progression from onset of mild AD to onset of severe AD, although variable, is about 10 years. Mini Mental State Examination (MMSE) scores correlate with the clinical course of AD. Greater diagnostic and predictive ability from progression to AD is obtained by combining measures of perfusion or metabolism with risk factors, tau protein levels, hippocampal N-acetyl aspartate concentrations, and/or hippocampal volume measures. A growing amount of research involved in fMRI suggests a promising role of fMRI in assisting diagnosis and prognosis. We will introduce the tasks employed during fMRI scans in AD,

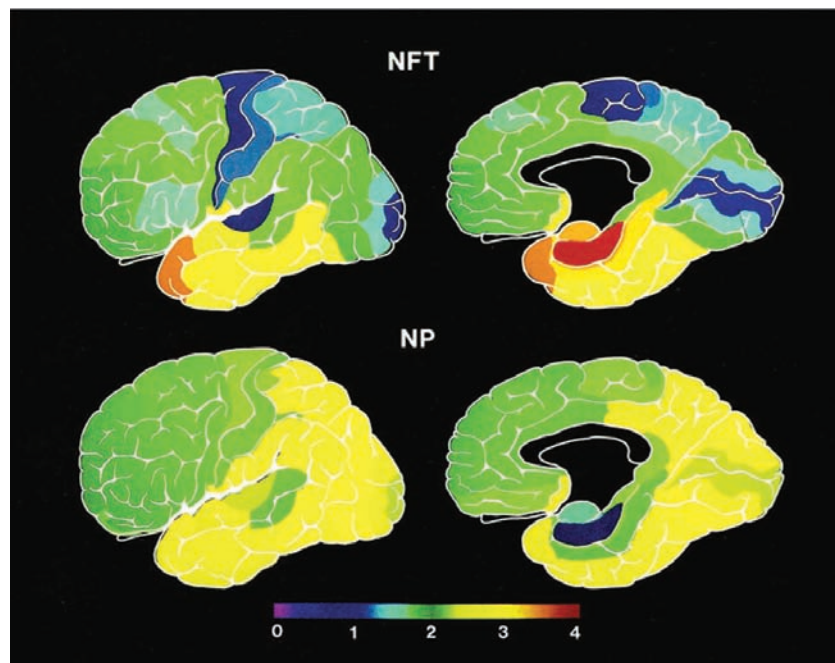


Figure 2 Topography of density rankings of neurofibrillary tangles (NFT) and neuritic plaques (NP) plotted onto Brodmann's lateral and medial views of the cerebral hemisphere. Abbreviations: NFT, neurofibrillary tangles; NP, neuritic plaques. Source: From Ref. 55.

followed by summaries of fMRI findings in AD, MCI, and at-risk populations.

Tasks and Methodological Considerations in AD

Because explicit memory loss is the most prominent clinical manifestation of the disease, most fMRI studies have employed memory-associated tasks (visual, visuospatial, or verbal), targeting on functional abnormalities in the MTL and prefrontal and parietal regions. Face-name association, episodic memory retrieval, digital span and n-back working memory tasks are most often used (Table 1). Novelty detection has been related to hippocampal and prefrontal activation (58–61). Novelty (new) relative to familiarity (old) or successfully remembered relative to forgotten items are often contrasted to investigate specific brain areas associated with novel or successfully remembered encoding and retrieval conditions. Successfully remembered and forgotten items during the encoding phase can be identified retrospectively in a later memory test (subsequent memory paradigm). Stimuli consciously experienced as novel are associated with anterior MTL activation, whereas posterior MTL activation is independent of participants' awareness (62). Tasks related to other symptoms of cognitive decline in AD, such as attention (63) and calculation, will not be discussed here.

Because cognitive impairment in AD prevents the adequate execution of complex tasks, an experimental design that puts only minor demands on the patients' cognitive

ability but engages disease-relevant brain structures is of benefit. Task performance is an important factor influencing results. In this regard, recent studies during the resting state offer an attractive alternative in this population.

Functional MRI Findings in AD

Consistent with the neuropathology in patients with manifest AD, a reduction of functional activation in the MTL and temporoparietal regions has been demonstrated when comparing AD to healthy controls on a variety of memory tasks (41,64–70). Conversely, lateral prefrontal activity has been shown to increase in AD patients relative to age-matched controls during verbal retrieval, suggesting the involvement of “under-recruitment” compensatory mechanisms (33,71–74). Table 1 summarizes the findings of fMRI in AD.

fMRI Findings in MCI

Accumulated research has demonstrated that there is likely a transitional period between normal aging and the diagnosis of clinically probable very early AD, and this transitional continuum has been described as MCI (75). Patients with MCI are at increased risk of developing AD, though clinical outcome may vary considerably (76). The typical length of the MCI phase remains undetermined. There are several subtypes of MCI. Amnestic mild cognitive impairment (AMCI), a subtype of MCI with an

Table 1 Summary of fMRI Studies in AD^a

Reference	Subjects	Task	Findings
Rombouts et al., 2000	10 elderly controls, 12 mild-to-moderate AD subjects	Color picture memory encoding task, and visual-paired associates (line drawings)	Decreased activation within the left hippocampus and parahippocampal gyrus bilaterally in AD subjects during color picture encoding but not visual paired-associates.
Johnson et al., 2000	8 mild AD, 16 controls with broad age and atrophy range	Semantic category-pair decision task	AD had significant correlation between activation in the left inferior frontal area and regional atrophy or total brain atrophy, but controls did not.
Kato et al., 2001	8 young, 8 elderly, 7 AD subjects	Encoding geometric shapes	AD had poor subsequent recall performance and did not show activation either in MTL nor frontal regions as young and old controls did.
Rombouts et al., 2002	11 subjects with AD pre- and post- ACHE Rx	Face encoding task plus n-back task (working memory)	ACHE inhibitor enhances brain activation in the fusiform and frontal cortices.
Pivulovic et al., 2002	14 probable AD, 14 controls	Angle discrimination task	Decreased activation in the superior parietal lobe and increased in left fusiform gyrus. The decreased SPL partially covaried with SPL atrophy.
Grossman et al., 2003	16 controls, 11 mild-to-moderate probable AD	Semantic memory task for animals and implements	Reduced activation in the left posterolateral temporal-inferior parietal cortex, increased activation in the left temporal cortex for both categories of knowledge. Category specifically, for animals in AD, the left ventral temporal cortex was activated, which was posterior to activation in controls. For implements in AD, frontal-striatal regions were activated, the same location as that in controls.
Sperling et al., 2003	10 young controls, 10 elderly controls, 7 subjects with mild probable AD	Face-name association encoding task	AD versus controls, decrease in hippocampal formation, and increase in medial parietal and posterior cingulate; elderly normals, less activation in superior and inferior prefrontal cortices, but greater activation in parietal than young controls.
Lipton et. al., 2003	Monzygotic twins discordant for AD (one twin affected with AD, the other twin unaffected with AD)	Visuospatial and verbal working memory tasks	The affected twin had greater parietal involvement bilaterally during both working memory tasks and reduced left dorsolateral prefrontal cortex activity on the visuospatial memory task.
Lustig et al., 2003	32 young controls, 27 elderly controls, 23 mild AD subjects	active semantic classification task and a passive fixation baseline	medial parietal/ posterior cingulate region showed differences in deactivation between young adults and older adults without dementia and an even more marked sustained activation in AD
Greicius et al., 2004	13 mild AD subjects, 13 controls	flashing checkerboard, resting-state (visual fixation) fMRI data	decreased resting-state activity in the posterior cingulate and hippocampus, suggesting that disrupted connectivity between these two regions accounts for the posterior cingulate hypometabolism
Gron et al., 2004	12 mild AD subjects, 24 controls	Episodic memory task	Recruitment of a posterior medio-temporal network was correlated with memory performance across the spectrum from high- and low-performing normal subjects to patients with early AD

Rémy et al., 2004	7 mild-to-moderate AD, 11 controls	Silent forward number counting + three-digit additions and subtractions	AD had poor performance in the arithmetic task and reduced activation associated with the contrast of calculating—counting in the inferior parietal and lateral prefrontal activations
Golby et al., 2005	7 AD subjects, 7 controls	Intentional encoding of scenes	Impaired explicit recognition memory, but intact implicit memory in AD. AD had a graded deficit in activation for novel versus repeated scenes in the ventral visual stream, with most impaired in the MTL and fusiform regions. Group-level correlations with behavioral measures of explicit memory were found in MTL, lingual and fusiform areas, whereas correlations with priming were found in lateral occipital, parietal, and frontal areas
Gould et al., 2005	12 mild AD subjects, 12 controls	Increasing difficulty of visuospatial-paired associate learning	As task difficulty increased, BOLD responses increased linearly in occipitoparietal regions during encoding and retrieval. By controlling for confounds of varying task difficulty and subsequent performance, remarkably similar brain activations were identified during successful paired associate learning in patients with AD and in controls.
Kircher et al., 2005	10 AD and 10 controls subject (pre-/postcholinesterase-inhibitor donepezil)	Face-name association task (encoding + retrieval, event-related design)	AD had reduced activation in the right fusiform gyrus, the activation was increased after cholinesterase-inhibitor treatment
Pariente et al., 2005	12 AD (early stage), 17 controls	Verbal episodic encoding and recognition tasks	AD had significant performance decline in accuracy and reaction time. Comparison of correctly versus incorrectly encoded and retrieval in the two groups, AD < controls in bilateral hippocampal and parts of the parietal and frontal lobes, both in encoding and retrieval.
Rémy et al., 2005	8 mild-to-moderate AD, 11 controls	(1) baseline task (recognizing a single digit, (2) SM, and (3) EWM task	AD patients had significant gray matter atrophy, reduced activations during encoding and recognition in the MTL and inferior parietal/superior temporal associative areas. The activation elicited by the recognition task was positively correlated with hippocampal gray matter volume. AD showed increased activation in the left prefrontal cortex during encoding and recognition, and the activation was positively correlated with task performance
Starr et al., 2005	9 AD, 10 HC	No activated brain regions in common for AD and HC for the EWM > SM contrast. HC subjects activated the right parahippocampal gyrus, subjects with AD activated the right superior frontal gyrus and left uncus. AD recruited brain regions for easier EWM tasks used by HCs for more difficult EWM tasks. AD subjects recruited brain regions for SM tasks used by HCs for more difficult EWM tasks suggesting a compensatory recruitment mechanism.	No activated brain regions in common for AD and HC for the EWM > SM contrast. HC subjects activated the right parahippocampal gyrus, subjects with AD activated the right superior frontal gyrus and left uncus. AD recruited brain regions for easier EWM tasks used by HCs for more difficult EWM tasks. AD subjects recruited brain regions for SM tasks used by HCs for more difficult EWM tasks suggesting a compensatory recruitment mechanism.

^aPubMed from 1995–2006.

Abbreviations: AD, Alzheimer's disease; MTL, medial temporal lobe; ACHE, Acetylcholinesterase; fMRI, functional MRI; BOLD, blood oxygen level-dependent; HC, healthy controls; SM, semantic memory task; EWM, episodic working memory.

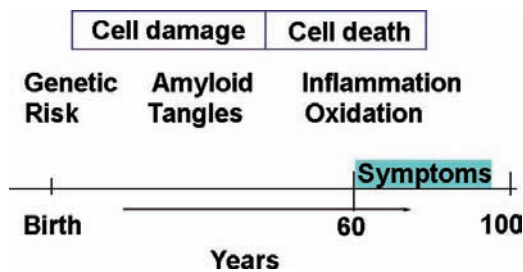


Figure 3 The figure demonstrates the protracted time course of the pathophysiology of Alzheimer's Disease. There are several known genetic risk factors that are present at birth, leading to amyloid overproduction. Gradually there is extracellular accumulation of amyloid plaques and intracellular accumulation of neurofibrillary tangles, occurring several decades prior to the onset of symptoms. Plaques and tangles incite an inflammatory, oxidative response, which first leads to cell damage and eventually to cell death. At this point atrophy may be seen on *in vivo* structural imaging studies. Eventually, accumulated cell damage leads to symptomatic clinical manifestations. The diagnosis is commonly made only after this point, despite the protracted time course of the underlying disease process.

emphasis on episodic memory impairment, represents a high-risk state for developing AD, with a 10% to 15% annual conversion rate compared with 1% to 2% in the normal elderly population (76,77). These patients exhibit gradual alterations in cognition, function, and behavior and mood with forgetfulness and repetitive questions as hallmarks. The onset of mild AD is suggested by MMSE scores of 20 to 23.

MCI is of great interest for studies on early diagnosis and intervention. Current research has revealed that the amyloid plaques and neurofibrillary tangles ultimately leading to AD are subtly present decades before symptoms of the disease (Fig. 3) (78–80). Preliminary data suggest that the earlier the treatments are introduced, the greater their benefit is (81). Novel treatments aimed at prevention are being developed to slow age-related cognitive decline and delay the onset of AD. Thus, identifying those who will ultimately develop AD is of paramount importance. Over the past several years, the search has intensified for reliable neuroimaging biomarkers that can serve as adjuncts to early diagnosis.

Table 2 summarizes fMRI studies in MCI. The MTL (including hippocampal formation, entorhinal cortex, and associated cortex) has been the principal focus of fMRI research in the MCI population. Activation of MTL appears to change with the clinical progression of MCI. At the early stage, when cognitive impairment is primarily subjective, activation in the MTL appears to increase (82,83) compared with controls with well-preserved task performance. With more advanced objective findings of

memory impairment, decreased MTL and impaired task performance may predominate (83,84). The need for recruiting additional neural resources to compensate for neuropathological damage or aberrant neuroplasticity (85) could be reasonable explanations for the increase in MTL activity in higher-functioning MCI subjects. Once the burden of pathology and neuronal loss accrues past a certain level and memory impairment becomes more pronounced prior to conversion, and certainly by the time AD is diagnosed clinically, memory-related MTL activation appears to be decreased. In a study (84) of 20 MCI individuals clinically defined on the basis of objective memory impairment and 20 healthy controls, our group has found decreased magnitude of activation in the left hippocampus during retrieval and in the bilateral inferior frontal cortex during both encoding and retrieval in the MCI group compared with the control group (Fig. 4). Lower hippocampal activation during retrieval was the most significant correlate of clinical severity of memory loss in MCI.

Through recent converging evidence, a key cortical region outside the MTL has emerged that may have a role in assessing disease progression: the posterior medial cortex (PMC), including posterior cingulate, retrosplenial, and precuneus region. The PMC region is believed to be a key component of a default network that normally shows higher levels of activation during periods of rest versus task, or low-level versus high-level tasks, a condition referred to as “deactivation” (86,87). Lustig et al. (67) demonstrated diminished deactivation in the PMC region in AD, and the subsequent studies have verified this finding (88,89). Our group has conducted a face-name associative encoding fMRI study in a population of AD, MCI, and elderly healthy controls (unpublished data). Increased activation associated with novel stimuli (both novel encoding vs. fixation and novel vs. familiar encoding) in the MTL was only found in AD, but not in MCI. Whereas, there was a linear transition from controls to MCI to AD with respect to the deactivation in the PMC region, with predominantly negative-activation magnitude in the PMC in controls, positive-activation magnitude in AD subjects, with MCI subjects falling in between (Fig. 5). The receiver-operating characteristic (ROC) curve with one-leave-out analysis revealed excellent sensitivity and specificity of this index for classification of AD versus controls (Fig. 6). Although the left hippocampus showed a significant difference among the three groups, the ROC curve did not support its diagnostic value over and above standard neuropsychological testing (Fig. 6). The PMC has also been found to be most predictive of cognitive decline in resting-state metabolic studies and is one of the first regions to show decreased fluorodeoxyglucose-positron emission tomography (FDG-PET) metabolism in MCI subjects (90–92).

Table 2 Summary of Studies in Mild Cognitive Impairments using fMRI^a

Reference	Subjects	Task	Findings
Machulda et al., 2003	11 elderly controls, 9 MCI subjects, 9 early AD subjects	Complex visual scene memory encoding + recall task	Significant decrease in activation found in MTL of MCI and AD subjects when compared to elderly controls; no significant differences found between MCI and AD subjects.
Daselaar et al., 2003	17 young normals, 19 elderly normals, 21 elderly subjects with reduced memory	Single word incidental encoding with emotional component + retrieval	Elderly with reduced memory have lower activation in MTL during encoding. Once corrected for performance, no difference during retrieval.
Goeckoep et al., 2004	30 MCI subjects, tested with no medications, then one dose ACHE inhibitor, then prolonged ACHE Rx.	Face-encoding plus n-back task (working memory)	Increases in activation after prolonged exposure only. Face encoding, left prefrontal, anterior cingulate, left occipital, L posterior hippocampus. WM task, R precuneus, R middle frontal gyrus.
Saykin et al., 2004	9 MCI subjects (pre- and post-ACHE Rx), 9 elderly normals	Auditory n-back task (working memory)	MCI < controls in frontoparietal regions at baseline. After Rx, MCIs increase frontal activity.
Dickerson et al., 2004	32 "MCI" subjects	Encoding of novel and repeated scenes	Subjects with greater clinical impairment activated larger area of right parahipp gyrus during encoding. Those who subsequently declined also activated greater extent of parahipp gyrus.
Dickerson et al., 2005	9 MCI (very mild), 10 probable AD, 10 controls; across all subjects, 13 APOE e4 and 16 APOE e3 carriers	Face-name associative encoding task	Increased hippocampal activation in MCI relative to controls, but decreased activation in both hippocampal and entorinal in AD coupled with atrophy in the two regions and poor task performance; across all subjects, APOE e4 > e3 carriers in mean entorhinal activation.
Johnson et al., 2005	14 MCI and 14 control subjects	Encoding of novel and repeated objects	The MCI patients exhibited reduced activity in the posterior cingulate during retrieval, and in the right hippocampus during novel encoding, despite comparable task performance to the controls.
Rombouts et al., 2005	28 MCI, 18 AD, 41 HC subjects	An n-letter back task and a face-encoding task	Deactivation was found in the default mode network (the anterior frontal, precuneus, and posterior cingulate cortex). MCI patients had less deactivation than HCs, but more than AD. The default mode network response in the anterior frontal cortex distinguished MCI from both HC (in the medial frontal) and AD (in the anterior cingulate). The response in the precuneus could only distinguish between patients and HC, not between MCI and AD.
Goeckoep et al., 2006	28 MCI subjects, 18 AD subjects (baseline, acute one dose, and prolong 5 days ACHE Rx)	Face recognition task	In MCI subjects, acute exposure increased activation in the posterior cingulate, left inferior parietal, and anterior temporal lobe. Prolonged exposure decreased activation in similar posterior cingulated and bilateral prefrontal areas. Effects were stronger for positive ("familiar") than for negative ("unfamiliar") decisions. In AD patients, acute exposure increased activation bilaterally in hippocampal areas, prolonged exposure decreased activation in these areas. Effects were stronger for negative than for positive decisions.

(Continued)

Table 2 Summary of Studies in Mild Cognitive Impairments using fMRI^a (*Continued*)

Reference	Subjects	Task	Findings
Ries et al., 2006	14 MCI, 14 control subjects	A visual episodic recognition task + an autobiographical self-appraisal task	PCC as the sole region commonly active during both tasks in controls, but activate only during self-appraisal, but not episodic retrieval in MCI.
Petrella et al., 2006	20 MCI, 20 controls	A face-name paired associative task	Both encoding and retrieval activated prefrontal, medial temporal, and parietal regions with larger areas activated during retrieval. MCI < controls in bilateral frontal cortex (encoding and retrieval), left HC (retrieval), and left cerebellum (encoding). MCI > controls in the posterior frontal lobes (retrieval). Lower hippocampal activation during retrieval was the most significant correlate of clinical severity of memory loss in MCI.
Yetkin et al., 2006	10 MCI, 11AD, 9 controls	A visual working memory task	MCI and AD groups > controls in right superior frontal, bilateral middle temporal, middle frontal, anterior cingulate, and fusiform gyri. AD < MCI in right parahippocampal, left inferior frontal, and supramarginal gyrus, bilateral cingulate and lingual gyri, right lentiform nucleus, and right fusiform gyrus
Vandenbulcke et al., 2006	13 amnestic MCI and 13 controls	Associative semantic versus visuoperceptive judgment; pictures versus printed words	MCI patients reduced the word-specific activation in the lower bank of the posterior third of the left superior temporal sulcus; patients performed significantly worse than control subjects on all measures of episodic memory performance but not in other cognitive domains

^aPubMed from 1995 to 2006.

Abbreviations: WM, working memory; HC, healthy control; MCI, mild cognitive impairment; AD, MTL, medial temporal lobe; Alzheimer's disease; APOE, Apolipoprotein E; PCC, posterior cingulate cortex.

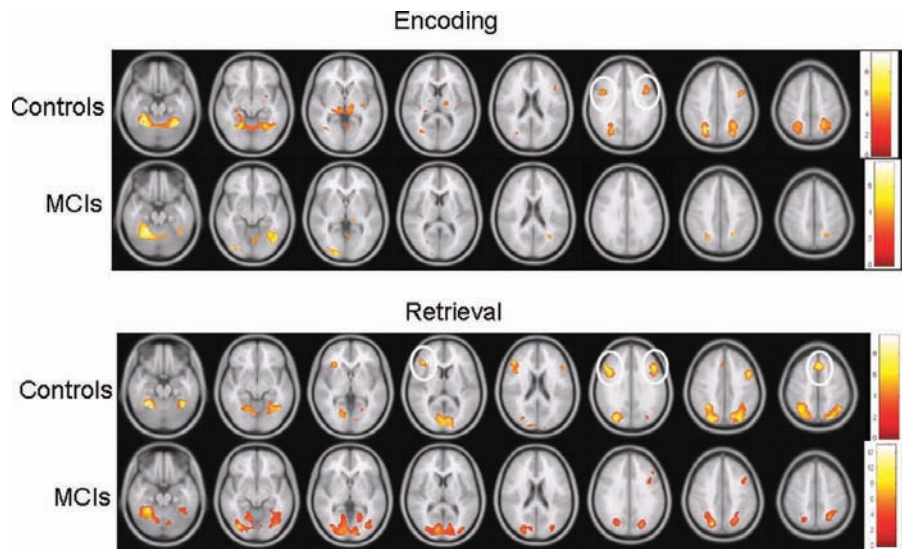


Figure 4 Task-related activation in control subjects and MCI patients. Upper panel, activation maps obtained with transverse functional MR imaging during encoding (upper panel) and retrieval created (lower panel). The controls revealed significantly greater activation than MCI patients in specific brain regions, especially in the prefrontal cortex (circles), parietal lobe, and in the mesial temporal lobe ($p > 0.001$). Data acquired using Statistical Parametric Mapping 2 software with an analysis of variance ($p = .001$, uncorrected threshold level for statistical significance; minimal cluster size, 10 voxels). Abbreviation: MCI, mild cognitive impairment. Source: From Ref. 84.

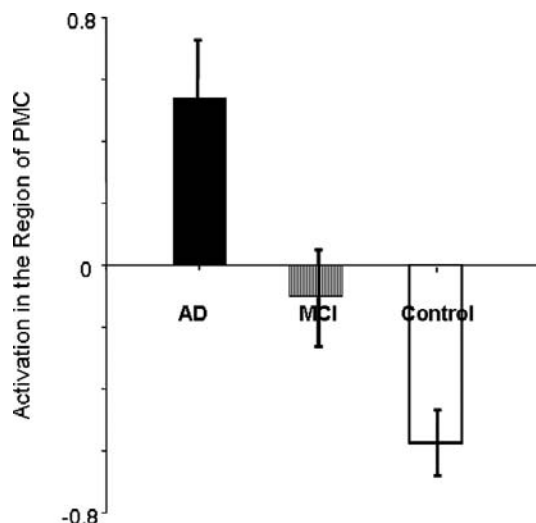


Figure 5 Bold signal under contrast of novel versus familiar encoding in the PMC in AD, MCI, and controls. The controls revealed a negative activation in the PMC in contrasting novel and familiar encoding, the default negativity was diminished in MCI and reversed in AD. Abbreviations: PMC, posterior medial cortex; AD, Alzheimer's disease; MCI, mild cognitive impairment.

The default network has been implicated in attending to environmental stimuli (87,93), planning future behaviors (94), self-awareness (95), conscious processes (96–101), and episodic memory retrieval (102–104). Bilateral posterior cingulate metabolism has been positively correlated with episodic memory retrieval (90). Our group has found a

negative correlation between magnitude of activation in the PMC and verbal memory test score, suggesting a possible role related to memory (105). We have also found distinct functional connectivity of the PMC with the MTL and inferior frontal gyrus in five healthy subjects (unpublished data). It is possible that default activation in the PMC reflects self-conscious or self-mentoring processes where memory retrieval is part of that operation. Growing knowledge regarding the posterior cingulate's reciprocal anatomical connectivity with mesial temporal, thalamic, and prefrontal regions further supports the posterior cingulate's role in mnemonic processing (106–108). Along similar lines, Buckner et al. (104) has noted that regions showing default activity in young adults are highly similar to those showing amyloid deposition in older adults with AD as revealed by amyloid-binding PET ligands. In addition, atrophy and metabolism disruption in AD prominently affect the posterior cortical regions also affected by amyloid deposition; moreover, the regions affected in AD and those active in default states in young adults overlap with memory networks showing retrieval success effects during recognition in young adults (Fig. 7). These authors have further proposed one possible configuration of lifelong events that lead to AD: vascular factors or other metabolic conditions that result in decreased default activity may lead to regionally specific amyloid deposition. In turn, atrophy and dementia may then result (Fig. 8). Although there are many aspects that need to be further clarified, particularly default activity in an asymptomatic genetically at-risk population, the alteration of default activity in the PMC

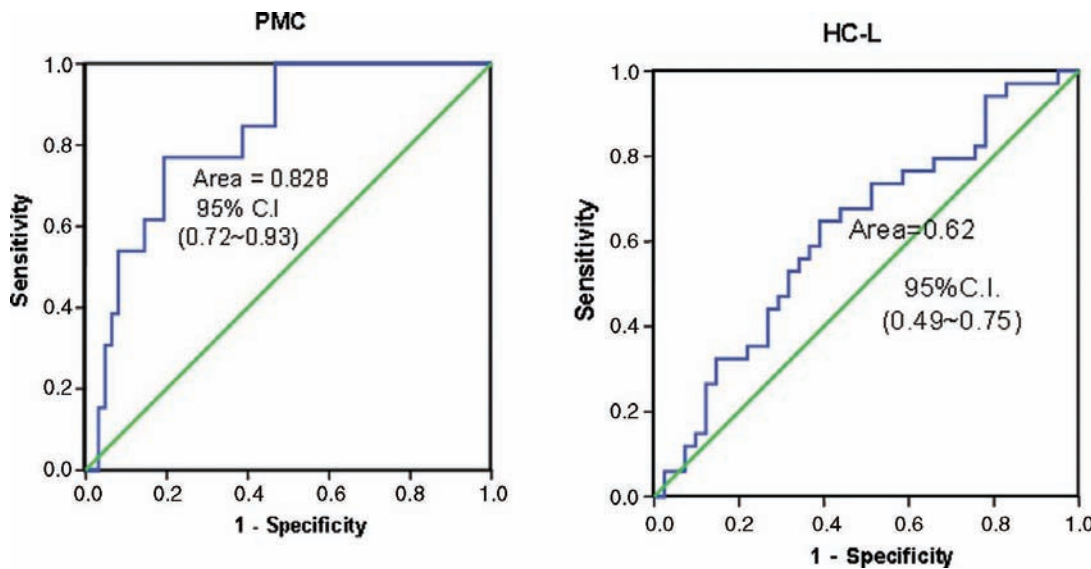


Figure 6 The ROC curve for assessment of potential diagnostic accuracy of AD (differentiating AD from MCI and controls) using activation in the PMC and HC. The negative activity in the PMC revealed a high accuracy than the activation in the HC. Abbreviations: ROC, receiver-operating characteristic; AD, Alzheimer's disease; MCI, mild cognitive impairment; PMC, posterior medial cortex; HC, hippocampus

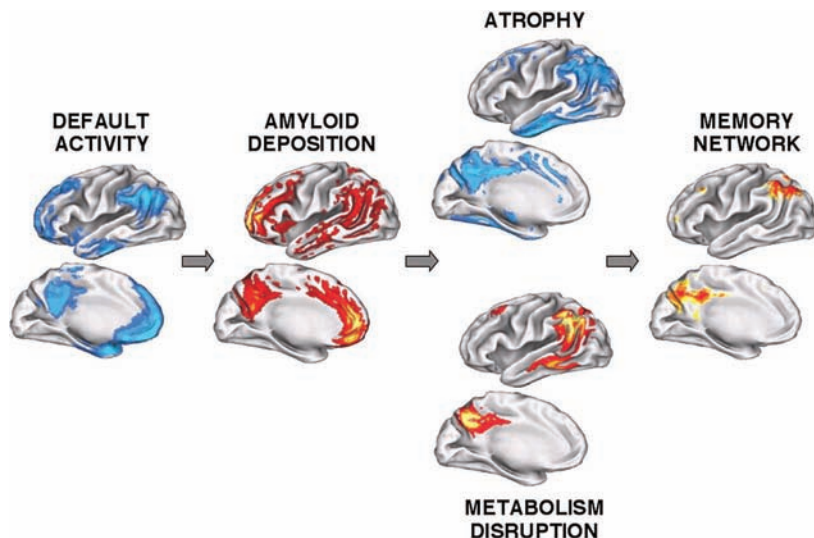


Figure 7 Convergence and hypothetical relationships across molecular, structural, and functional measures proposed by Buckner et al. Three patterns emerge. First, regions showing default activity in young adults are highly similar to those showing amyloid deposition in older adults with AD, including both posterior cortical regions and anterior regions. Second, atrophy and metabolism disruption in AD prominently affect the posterior cortical regions also affected by amyloid deposition. Third, the regions affected in AD and those active in default states in young adults overlap memory networks showing retrieval success effects during recognition in young adults. Abbreviation: AD, Alzheimer's disease. Source: From Ref. 104.

could represent a promising neuroimaging marker for disease progression in AD. Measurement of default activation in the resting state is independent of a significantly effortful task and thus maybe less affected by variance of task performance. Moreover, connectivity measurements may be obtained in the resting state without performing any cognitive task.

Functional MRI Findings in Asymptomatic At-Risk Subjects

The apolipoprotein E type 4 allele (APOE-epsilon 4) has been consistently associated with the common late-onset familial and sporadic forms of AD (109). Although some recent studies have questioned its positive predictive value

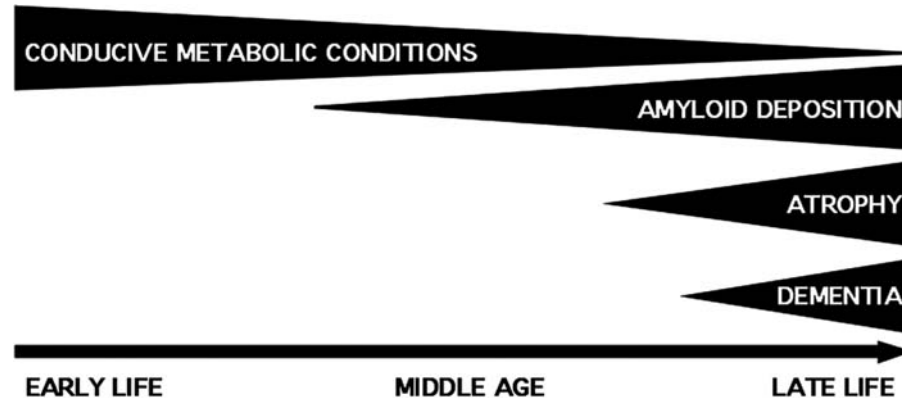


Figure 8 A schematic illustration of one possible configuration of lifelong events that lead to AD proposed by Bucker et al. Conducive metabolic conditions, associated with default mode activity patterns, may lead to regionally specific amyloid deposition. In turn, atrophy and dementia may then result. This metabolism cascade promising fMRI as a potential powerful biomarker in identifying high-AD risk individuals. Abbreviations: AD, Alzheimer's disease; fMRI, functional magnetic resonance imaging. Source: From Ref. 104.

for the diagnosis of AD (110–114), increasing numbers of neuroimaging studies have identified functional alteration in homozygous compared with heterozygous carriers. Reiman et al. (80) were the first to report on the prognostic value of cortical metabolism studied with PET in healthy elderly subjects with an increased risk of having AD. In 11 APOE 4 homozygotes and 22 controls without the ε 4 allele, cortical metabolism in subjects with risk of AD was reduced in the posterior cingulate, parietal, temporal, and prefrontal regions. Thereafter, several fMRI studies have revealed altered activation in subjects at increased risk of AD (41,115) (Table 3). Subjects at risk by virtue of family history of AD and APOE status (at least one apolipoprotein 4 allele) had reduced activation in mid- and posterior inferotemporal areas during the recall of items from both working and long-term memory (41). Whereas some studies have found that increased risk is accompanied by reduced functional brain activity in parietal, temporal, and frontal areas (41,116), some studies have found increased activity in the same general areas (115,117–119), and others have found no difference (120).

Frontotemporal Disease

Frontotemporal lobar degeneration (FTLD) is a heterogeneous disease condition both clinically and pathologically, consisting of mainly FTD, nonfluent progressive aphasia (NFPA), and semantic dementia. In FTD, changes in social behavior and personality predominate, reflecting the orbitobasal frontal lobe focus of the pathology with relative preservation of memory and visuospatial skills (121–125). NFPA affects the phonologic and syntactic components of language. Semantic dementia shows deficits both in language production and comprehension. A

variant of this syndrome affecting the right temporal lobe presents with progressive prosopagnosia, a symptom with difficulty in recognizing people by faces in spite of normal eyesight. FTLD has been characterized by frontal and temporal atrophy, with NFPA having increased rates of atrophy in the left perisylvian area and semantic dementia having increased rates of atrophy in posterior left temporal and inferior frontal regions (126). PET studies in FTLD have shown hypometabolism in frontal, anterior temporal, and mesiotemporal areas even in early stage. The lateral temporal and parietal cortices are affected only in later stages. Thus, differentiation between AD and FTLD is relatively straightforward in late-stage disease. The deficits in AD are temporal-parietal dominant and the deficits in FTLD are frontal-temporal dominant (127). However, clinical differentiation between AD and FTLD is difficult early in the disease when results on MRI are normal and clinical signs inconspicuous.

Gregory et al. (128) followed two FTD patients over the course of five to six years and initially found little abnormality on neuropsychological testing, or MRI and hexamethyl propylene amine oxime single photon emission computed tomography (HMPAO-SPECT). Over time, however, tracer uptake abnormalities on SPECT, frontal atrophy on MRI, and a neuropsychological profile typical of FTD developed in both patients. Standard neuropsychological tests and conventional brain-imaging techniques (MRI and SPECT) may not be sensitive to the early changes in FTD that occur in the ventromedial frontal cortex. Better methods for accurate early detection are required. Although fMRI could potentially reveal early changes in the disease, to date, there is only one study that compared brain activation in FTD ($n = 7$) and AD ($n = 7$) during a verbal working memory task (n-back) using fMRI (129). This study found that brain activation associated with working memory was

Table 3 Studies in High-Risk Population Using fMRI^a

Reference	Subjects	Task	Findings
Smith et al., 1999	14 high-risk (family history, APOE e4 carriers), 12 low-risk subjects	Visual, letter fluency and object naming	Decreased activation in high-risk group in middle and posterior inferior temporal regions.
Bookheimer et al., 2000	16 elderly APOE e4 carriers, 14 elderly APOE e3 carriers (all cognitively normal)	Word pairs memory encoding + retrieval task	Increased activation in left parahippocampal region, left dorsal prefrontal cortex, inferior and superior parietal lobes, and anterior cingulate gyrus of APOE e4 carriers versus e3 carriers. During recall, APOE4 > APOE3 in hippocampus.
Burggren et al., 2002	13 elderly APOE e4 carriers, 12 elderly APOE e3 carriers (all cognitively normal)	Digit span memory encoding task	Task not sensitive for hippocampal activation, no significant differences found between APOE e4 and APOE e3 groups.
Smith et al., 2002	21 high-risk (familial history of AD and APOE e4 carriers), 17 low-risk (no familial history) subjects	Letter fluency task (subjects covertly generated as many words as they could, beginning with a randomly selected uppercase cue letter)	The regional patterns of brain activation were similar between groups and similar to patterns observed by other investigators. However, the high-risk group showed significantly increased activation in the left parietal region despite identical letter fluency performance between the two groups.
Bondi et al., 2005	10 APOE 4 versus 10 APOE 3, all cog normal	Complex color picture encoding	APOE 4 > controls during encoding in bilateral fusiform gyri, medial frontal gyri, L inferior and middle frontal, R superior parietal, and R hippocampal and parahippocampal cortices. APOE 4 < controls L hippocampus.
Fleisher et al., 2005	10 elderly high-risk APOE (9 e3/e4, 1e4/e4) carriers, 10 elderly low-risk APOE e3/e3 carriers	Verbal paired associative encoding task	Increased activation in the high-risk group in the left MTL and many other regions associated with novel encoding versus fixation. In low-risk group, CVLT and cued recall performance after scan were positively correlated with the activation in the left MTL.
Lind et al., 2006	10 APOE (e4/e4) and 20 APOE (e3/e4), 30 APOE (e3/e3)	Semantic categorization task (abstract or concrete), subsequent recognition after scan	No significant between-group difference in the behavioral performance. APOE 4 carriers showed reduced task-related responses in the left inferior parietal cortex, and bilateral anterior cingulate. A dose-related response was observed in the parietal area such that diminution was most pronounced in homozygous compared with heterozygous carriers. In addition, APOE 4 carriers had reduced activation in novel versus neutral contrast in the right hippocampus.
Trivedi et al., 2006	23 e3/4 heterozygotes and 17 e3/3 homozygotes	An episodic encoding task	e3/4 heterozygotes displayed reduced activation in response to novel versus familiar pictures in the hippocampus and MTL compared with e3/3 homozygotes.
Bassett et al., 2006	95 at-risk (family history), 90 controls	An auditory word-pair-associative learning task	At-risk individuals showed more intense and extensive activation in the frontal and temporal lobes including the hippocampus during memory encoding, an increase unrelated to the APOE 4 allele. There are also decreased activation particularly in the cingulum and thalamus during both the encoding and recall phases of the task in the risk group.

^aPubMed from 1995 to 2006.
Abbreviations: APOE, Apolipoprotein E; MTL, medial temporal lobe; CVLT, California verbal learning test.

significantly decreased in FTD compared with AD in frontal and parietal cortex. Frontal regions in patients with FTD showed a less linear activation increase with working memory load than in AD. The cerebellum in FTD showed a stronger increasing response than in AD, possibly as a compensation mechanism.

One study had examined semantic processing in NFPA (130). In patients with NFPA, different components of the semantic network, i.e., inferior frontal sulcus, superior temporal sulcus and anterior temporal pole, show less activity than in healthy controls. The activity levels correlated with performance on off-line picture naming tasks. Interestingly, the right MTL, classically implicated in episodic memory functions, showed higher activity in primary progressive aphasics than in healthy controls, suggesting that patients may make use of nonverbal episodic memory strategies to compensate for their semantic deficit. In contrast, patients with MCI, who clinically have an isolated episodic memory deficit and perform within the normal range on semantic tasks, showed profound alterations, including decreased activity in Wernicke's area (posterior middle temporal gyrus) on the left compared with age-matched controls, suggesting that semantic strategies are not used to compensate for their episodic memory deficit.

MOVEMENT DISORDERS

Movement disorders are a group of neurological diseases characterized by an impairment of the regulation of voluntary motor activity, including hypokinetic disorders associated with a slowing of movements such as parkinsonian syndromes as well as hyperkinetic disorders characterized by involuntary abnormal movements such as Huntington's disease (HD), torsion dystonia, and tic disorders. Generally, the clinical manifestations of movement disorders result from dysfunction of the basal ganglia. Parkinsonism is most often caused by Parkinson's disease (PD), but can also be caused by other disorders, including progressive supranuclear palsy (PSP), cortico-basal degeneration (CBD), multiple-system atrophy (MSA), cerebrovascular disease, and other neurodegenerative disorders. In addition to motor deficits, cognitive impairments are not rare in parkinsonian syndromes. The differential diagnosis is difficult among these diseases at their early stage. PET imaging techniques has been widely used to evaluate and quantify changes in dopaminergic neurons and specific neurochemical systems. Research using fMRI has also been underway given its superior spatial and temporal resolution. In this section, we focus on addressing fMRI applications mainly on PD, since PD is the most common and broadly studied disease among movement disorders.

The application of fMRI in PD is primarily focused on understanding the neuropathological circuits associated with clinical symptoms, facilitating accurate diagnosis, elucidating functional roles of basal ganglia, and evaluating and monitoring therapeutic interventions for movement disorders. The identification of presymptomatic cases remains problematic but is motivated by the hope for treatment before symptoms appear. In addition, since PD involves both motor and cognitive impairments that have been associated with different corticostriatal loops with predominant dopamine depletion (131), fMRI research in PD greatly benefits the understanding of the functional role of dopamine in humans.

PD

Idiopathic PD is a common movement disorder with characteristic clinical symptoms of akinesia, bradykinesia, rigidity, resting tremor, and impaired postural reflexes or gait with asymmetric onset. Nonmotor-related cognitive, perceptual, and neuropsychiatric deficits also exist. In particular, subtle cognitive impairments early in the disease have been shown to be predictive to quality of life (132,133). The core pathological feature of PD is degeneration of the dopaminergic cells in the midbrain [primarily the substantia nigra pars compacta (SNc)], which leads to depletion of dopamine in the striatum and subsequently results in the disruption of striatal-thalamocortical loops (Fig. 9) (134). The disruption of striatal-thalamocortical loops with progressive loss of motor control leads to characteristic symptoms of the disease. Serotonergic cells in the median raphe, noradrenergic cells in the locus ceruleus, and cholinergic cells in the nucleus basalis are also involved to a lesser extent as are other pigmented and brainstem nuclei. Lewy bodies are also found in neurons of the anterior cingulate and frontal, parietal, and temporal association cortex of most nondemented PD cases at postmortem.

The majority of fMRI research has been related to the basal ganglia-thalamocortical circuits (135) with four major areas of focus: (*i*) understanding the pathophysiological basis of the core motor symptoms, (*ii*) understanding the pathophysiological basis of cognitive and emotional impairment, (*iii*) clarifying the effect of dopaminergic treatment on cognitive function, and (*iv*) monitoring surgical intervention.

Neural Pathways Contributing to Motor Deficits in Nondemented PD

Akinesia, bradykinesia, and tremor are essential motor symptoms in PD. Akinesia refers to a poverty of spontaneous movement (facial expression) or associated movement (arm swing during walking) and impaired initiation

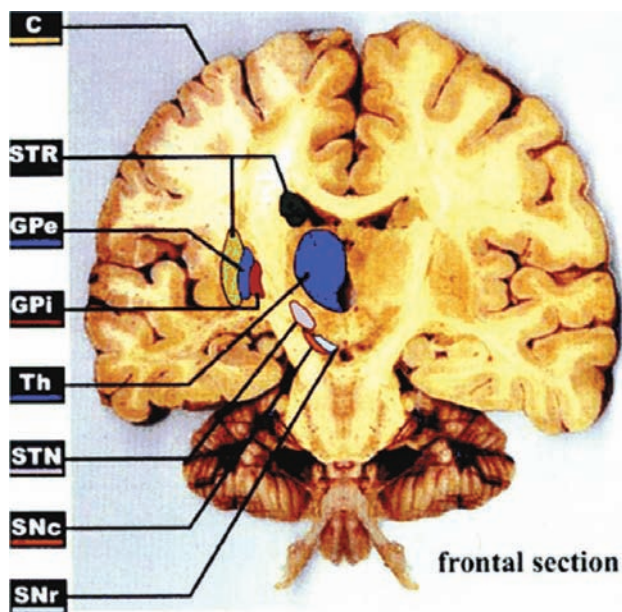


Figure 9 Illustration of the main basal ganglia nuclei from a coronal view of the brain. The section is angled rostrocaudally to encounter most of the BG nuclei in a single section. Abbreviations: BG, basal ganglia; C, cortex; STR, striatum (Note STR consisted of caudate-green arrow and putamen-red arrow); GPe, globus pallidus pars externa; GPi, globus pallidus pars interna; Th, thalamus; STN, subthalamic nucleus; SNC, substantia nigra pars compacta; SNr, substantia nigra pars reticulata. Source: From Ref. 134.

of sequences of movement (136). Bradykinesia refers to slowness of free limb movement. Intensive studies have been conducted using PET to determine correlates of brain glucose metabolism. Functional MRI studies have focused on akinesia (or mixed akinesia and bradykinesia), rather than bradykinesia or tremor.

Akinesia is thought to result from functional deafferentation of the supplementary motor area (SMA), i.e., excessive inhibition of thalamo-SMA/premotor projection due to the striatal dopamine depletion in PD (137–141). SMA, in particular its rostral part, which connects to the prefrontal cortex, has been shown to be important in movement selection and preparation, sequentially structured action, or performance of complex movements (142–146). Therefore, tasks (such as paced joystick movement task) that require motor selection and initiation normally activate SMA. PD patients “off” medication revealed reduced movement-related activation in rostral SMA but increased activation in the lateral premotor cortex bilaterally during performing sequential hand movement task (140) or a paced joystick movement task (147) (Table 4). Parallel to the improvement in akinesia, levodopa increased the activation in the SMA and decreased the activation in lateral premotor cortex and

superior parietal cortex, although it did not completely normalize (147). These results are consistent with the early PET studies (138,139,148). Overactivation in the lateral premotor cortex has been suggested to compensate for the SMA deficit via the cerebello-parieto-lateral premotor loops, similar to the clinical phenomenon of improved movement performance under guidance of external visual or auditory cues (149).

Bradykinesia and rigidity are thought to result from deafferentation of the motor cortex (150,151). Studies of patients on medications show a significant correlation between the severity of bradykinesia and bilateral putamen and globus pallidus metabolism (152). However, there are no fMRI studies so far to differentiate the pathways that are specific to akinesia and bradykinesia.

Multiple mechanisms have been recognized to be responsible for the resting tremor in PD. To date, there is no definitive evidence for a specific pattern of striatal dopamine deficiency or postsynaptic dopamine receptor density reduction corresponding to this phenotype. Probably due to technical difficulty and task design, there are no studies related to resting tremor in fMRI.

Neural Pathways Contributing to Cognitive Deficits in Nondemented PD

The pattern of cognitive impairments seen in the early stages of PD resembles that produced by frontal lobe damage, namely, deficits in executive function, including difficulties in attentional set-shifting and perseverative behavior, poor spatial working memory, difficulties with response suppression, increased distractibility, poor executive strategies, and temporal sequencing (153–155). However, the cognitive deficits in PD are not only restricted to frontal lobe function, there are other characteristic impairments such as probabilistic classification learning (156), simple digital span, procedural learning (157), and memory (158). Studies suggest that the level of cognitive dysfunction in PD varies depending on task demands, disease stages, and medication (159,160).

There are two major dopaminergic pathways proposed for the neurobiological basis of the cognitive impairment in PD: (i) an alteration in outflow of the caudate nuclei to frontal cortex via the thalamus (nigrostriatal pathway) and (ii) diminished dopamine activity in the frontal lobes consequent to degeneration of the frontal projections of the ventral tegmental area (VTA) and other nigral cell groups (161) (mesocortical pathway). A number of studies have been designed to test these hypotheses, some of them favor the nigrostriatal theory (162–165), some favor the mesocortical theory (166–169), and others support both pathways (165,170).

Cools (160) proposed a model based on the spatiotemporal progression of dopamine cell degeneration: the core

Table 4 Summary of Studies in Parkinson's Disease Using fMRI^a

Study domain	Reference	Subjects	Hoehn and Yahr Stage	Task	Findings
	Sabatini et al., 2000	6 PD patients, 6 healthy subjects	2.7 +/- s.5	Sequential movement	PD patients showed a decreased fMRI signal in the rostral SMA and right dlPFC, but increased signal in bilateral primary sensorimotor cortex, lateral premotor cortex, inferior parietal cortex, caudal SMA, and anterior cingulate cortex.
Motor	Haslinger et al., 2001	8 patients with early state akinetic PD, 8 healthy subjects	1-2	A single joystick movement in response to each tone, performed with the right hand; tested levodopa-off and levodopa-on state	Aknesia improved after oral levodopa. PD with both off and on levodopa showed movement-related decreased activation in the rostral SMA and increased activation in the primary motor cortex (M1) and lateral premotor cortex; levodopa relatively normalized the impaired activation in the mesial premotor cortex, and decreased signal in M1, lateral premotor and superior parietal cortex.
	Elsinger et al., 2003	10 mild PD, 13 healthy controls; tested drug-off and drug-on states	Did not exceed stage II	A PFT, either tapping in synchrony with isochronous tones (ISI, 0.6 second), or tapping in a continuous manner after discontinued tones (ISI, 30 seconds)	PD had a reduction in IRI during the continuation condition and an increase in variability during both task conditions, the medication did not make an improvement despite improved motor symptoms in UPDRS. PD with drug off showed decreased activation in the sensorimotor area (SMA), cerebellum, and medial premotor regions during both task conditions. Dopamine replacement partially normalized brain activation during explicit timing (increase in SMA, thalamus, and putamen). The hypoactivation in contralateral M1 and bilateral SMA (contralateral predominant) in levodopa-off state was reversed by levodopa intake. The signal changes were correlated with motor performance.
	Buhmann et al., 2003	8 drug naive PD patients, 10 healthy subjects	1-1.5	Auditory-paced random finger-opposition task; tested at L-dopa off and on states	Apomorphine reduced activation in the contralateral precentral gyrus affecting both clinically affected and unaffected sides.
	Peters et al., 2003	7 PD patients tested before and after apomorphine injection	unknown	Internally generated, noncued index finger-to-thumb opposition movements at subjects' fastest possible speed;	For both groups, sequential movements activated similar brain regions before and after automaticity; In normal subjects, many areas had reduced activity at the automatic stage, whereas, in PD patients, only the bilateral superior parietal lobe and left insular cortex were less activated. PD patients can achieve motor automaticity after proper training, but with more difficulty.
	Wu and Hallett, 2005	12 PD patients (drug off), 14 healthy subjects	mean 2.04	Two self-initiated, self-paced sequences of finger movement tasks with different complexity until participants could perform the tasks automatically	(Continued)

Table 4 Summary of Studies in Parkinson's Disease Using fMRI^a (*Continued*)

Study domain	Reference	Subjects	Hoehn and Yahr Stage	Task	Findings
	Macri, et al., 2006	8 PD patients treated apomorphine with an infusion pump and 6 controls	2.5–3	A thumb-index opposition finger tapping task; The levodopa treatment was interrupted 48 hours prescan, the infusion pump was deactivated and removed immediately before the first session	Both patients and controls had activation in the contralateral primary sensorimotor cortex and SMA. With the drug concentration gradually decreased during subsequent sessions, PD revealed a decreased activation in the SMA.
Visual	Stebbins et al., 2006	12 PD with hallucination, 12 PD without hallucinations (control)	Mean = 3	Stroboscopic and kinematic tasks	PD patients with chronic visual hallucinations respond to visual stimuli with greater frontal and subcortical activation and less visual cortical activation than nonhallucinating PD subjects.
Cognitive	Mattay et al., 2002	10 PD patients (mean age 55) tested drug off and on states	UPDRS: drug off, 8.8 +/– 2.6; drug on, 5 +/– 1.9	An n-back working memory task and a visually paced motor task	Cortical motor regions activated during the motor task showed greater activation during the dopamine-replete state; however the cortical regions (PFC, insular, parietal, and precuneus cortex) subserving working memory displayed greater activation during the hypodopaminergic state; the worse the patients perform, the more cortical tissue they activate in the drug-off state.
	Rowe et al., 2002	12 PD patients, 12 healthy subjects	2–3	5 motor and cognitive tasks, (1) MOVE task (over learned sequence) (2) SEARCH task (red letter 'r') (3) DUAL task (a and b) (4) ATTEND task (task 'a' but thinking about the next move) (5) REST	In control subjects, but not patients, attention to action was associated with activation of prefrontal, parietal, paracingulate, and SMA. Motor abnormalities in PD are due, at least partly, to a reduction in effective connectivity; tasks that require attentional selection of motor representations are associated with lesser activation of SMA in PD.
	Tessitore et al., 2002	10 PD patients, 10 healthy subjects; tested drug off and on states	2 in stage I and 8 in stage II	A fearful emotional task and a control task	A robust bilateral amygdala response in normal controls was absent in PD patients during the hypodopaminergic state; dopamine repletion partially restored this response in PD patients.

Cognitive	Lewis et al., 2003	10 cognitively unimpaired PD, 11 executive impaired PD, 10 healthy subjects	2	A work memory task that has two conditions: retrieval, to retrieve a pre-presented letter sequence; manipulation, to reorder the pre-presented letter sequence in a simple or complex way	The cognitively impaired PD group had significant signal reduction in bilateral caudate in relative to cognitively unimpaired PD group and healthy controls during both retrieval and manipulation. The cognitively impaired PD group also had underactivity in the dlPFC and vIPFC during the manipulation, but not during retrieval condition.
	Grossman et al., 2003	7 PD patients, 9 healthy seniors	1	A sentence comprehension task: answer a simple probe about written sentences that vary in their grammatical and cognitive resource properties	Direct activation contrasts showed that striatal, anteromedial prefrontal, and right temporal regions are recruited to a significantly lesser degree in PD, but these patients have increased activation of right inferior frontal and left posterolateral temporal parietal areas during sentence comprehension.
	Mood et al., 2004	8 PD patients, 8 healthy subjects	mean = 1.9	The probabilistic classification task	Patients with PD showed less activation in the caudate nucleus and greater activation in a region of prefrontal cortex and MTL that has been associated with explicit memory.
	Werheid et al., 2004	7 PD patients, 7 healthy subjects	mean = 1.5	The SRT task with prelearned sequences of stimuli (rule learning) and random stimuli (novel)	PD revealed intact rule learning performance during fMRI scan. Highly similar frontomedian and posterior cingulate activations was found in the patients and controls in sequence versus random blocks. Patients had absent activation in the striatal and inferior frontal activations that did not correlate with the behavioral index for rule learning.

^aPubMed from 1995 to 2006.

Abbreviations: fMRI, functional MRI; PD, Parkinson's disease; PFT, paced finger tapping task; ISI, interstimuli interval; UPDRS, Unified Parkinson Disease Rating Scale; SRT, serial reaction time; SMA, supplementary motor area; dlPFC, dorsolateral prefrontal cortex; IRI, interresponse interval; MTL, medial temporal lobe; vIPFC, ventrolateral prefrontal cortex.

pathology of dopamine cell degeneration progressed from the ventral tier (SNc) to the dorsal tier of the midbrain including the VTA. The severely degenerated ventral tier sends dopamine projections primarily to the dorsal striatum (dorsal putamen and dorsal caudate nucleus), which projects to dorsolateral prefrontal cortex (dlPFC). The relatively intact dorsal tier of the midbrain including VTA sends its dopamine projections primarily to the ventral striatum (ventral putamen, ventral caudate, and the nucleus accumbens), which projects strongly via the output nuclei of the basal ganglia and the thalamus to ventrolateral prefrontal cortex (vlPFC) and orbitofrontal cortex (Fig. 10) (160). Thus, at the early stage, PD performs poorly in tasks that depend on the function of dorsal striatum and dlPFC, whereas tasks that critically depend on the ventral stratum and orbitofrontal and vlPFC are left unaffected.

Cools' model can explain why some aspects of cognitive function are affected and other aspects are not. She also proposed that the prefrontal cortex (PFC) functions are critical in tasks with high demands for cognitive stability, whereas striatum is important in tasks with high demands for cognitive flexibility. The dlPFC has been proposed to be critical in manipulation, strategies, and planning (for example, the reorder), whereas the vlPFC is more important in basic mnemonic functions such as maintenance and recall (for example, the retrieval task) (171–174). Most of the studies on cognitive deficits in PD employed tasks that were preferentially dependent on functional roles of striatum and prefrontal cortex. Some studies (175,176) support this model and some do not (165). Table 4 summarizes previous fMRI studies in PD. Tasks that can clearly differentiate the dorsal and ventral function of striatum and PFC are needed to test and refine this model.

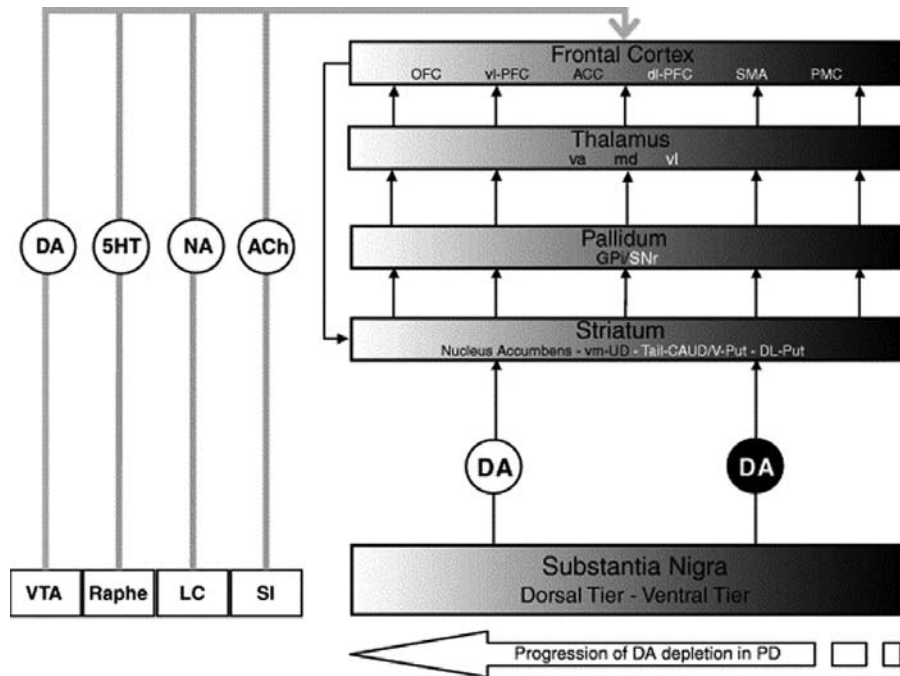


Figure 10 The neuropathological progressive model responsible for the motor and cognitive deficits in PD proposed by Cools. The black-to-white shading gradient represents the spatiotemporal progression of pathology from dorsal to ventral frontostriatal circuitries over the course of the disease. The severely degenerated ventral tier sends dopamine projections primarily to the dorsal striatum, which projects to relatively restricted portions of the more dorsal and lateral parts of the PFC. The relatively intact dorsal tier sends its dopamine projections primarily to the ventral striatum, which projects strongly via the output nuclei of the basal ganglia and the thalamus to medial and lateral orbitofrontal cortex (ventrolateral and ventromedial PFC). Thus, at the early stage, PD preferential performs poorly in tasks that depend on the function of dorsal striatum and dlPFC, whereas preserves function in tasks that depends on the ventral stratum and orbitofrontal and vlPFC. Abbreviations: PD, Parkinson's disease; PFC, prefrontal cortex; VTA, ventral tegmental area; Raphé, dorsal and medial raphé nuclei; 5-HT, serotonin; LC, locus coeruleus; NA, noradrenaline; SI, substantia innominata; ACh, acetylcholine; vm-CAUD, ventromedial caudate nucleus; Tail-CAUD, tail of the caudate nucleus; V-Put, ventral putamen; DL-Put, dorsolateral putamen; GPi, internal segment of the globus pallidus; SNr, substantia nigra pars reticulata; va, ventral anterior nucleus; md, dorsomedial nucleus; vl, ventrolateral nucleus; OFC, orbitofrontal cortex; vl-PFC, ventrolateral PFC; ACC, anterior cingulate nucleus; dl-PFC, dorsolateral PFC; SMA, supplementary motor area; PMC, premotor cortex. Source: From Refs. 135 and 160.

As an example, Lewis et al. (164) designed a working memory paradigm that required subjects to retrieve a prepresented letter sequence (retrieval) or to reorder the prepresented letter sequence in a simple or complex way (manipulation). Authors (164) compared brain activation elicited by retrieval and manipulation among early PD patients with cognitive impairment and nonimpairment as well as healthy controls. The cognitively impaired group showed decreased activation in bilateral caudate nuclei during both retrieval and manipulation conditions as well as underactivity in the dlPFC and vIPFC during manipulation but not during retrieval relative to unimpaired group and healthy controls (Fig. 11). The results demonstrate that early PD preferentially affects processes involved in the manipulation of information within working memory, and fMRI could be used to identify the neural locus of selective executive and mnemonic deficit in a subgroup of patients with early PD. Monchi et al. (165) studied the activation pattern of PFC and striatum during Wisconsin Card Sorting Task (WCST) in early PD. WCST is a set-shifting task that requires mental shifting after a negative feedback and requires maintenance of the rule of classification after a positive feedback. Monchi et al. (165) found decreased activation in PD in the vIPFC when receiving negative feedback and in the posterior prefrontal cortex when matching after-negative feedback. Moreover, these PFC regions were coactivated with the striatum in the control group, but not in PD. In contrast, PD had

increased activation in the posterior PFC and dlPFC when receiving positive or negative feedback. The results suggested that the pattern of activity in a specific area of the PFC depends on its specific relationship with the striatum for the task at hand. The increased activation could reflect a compensatory mechanism or result from intracortical dopamine regulated by the mesocortical system to help focus activity in the PFC.

Moody et al. (175) found less activation in the caudate nucleus and greater activation in the right anterior dlPFC (BA10) and MTL in early PD relative to controls during performing a probabilistic classification task. The probabilistic classification task requires a category learning (“weather prediction”) with probabilistic cue-outcome relations based on trial-by-trial feedback. This type of task, which involves online learning of stimulus-response associations, is thought to engage nondeclarative (implicit) memory and has been proved to largely depend on the function of caudate nucleus (177). The dlPFC and MTL have been associated with explicit memory. Moody et al.’s study suggests that patients with PD might rely on the explicit memory system for tasks that can be learned implicitly in controls using neostriatal circuitry.

Werheid et al. (176) found intact performance on pretrained sequence learning in early PD and preserved anterior medial prefrontal cortex activation using a serial reaction time (SRT) task, but reduced activation in the putamen. The SRT task requires subjects to

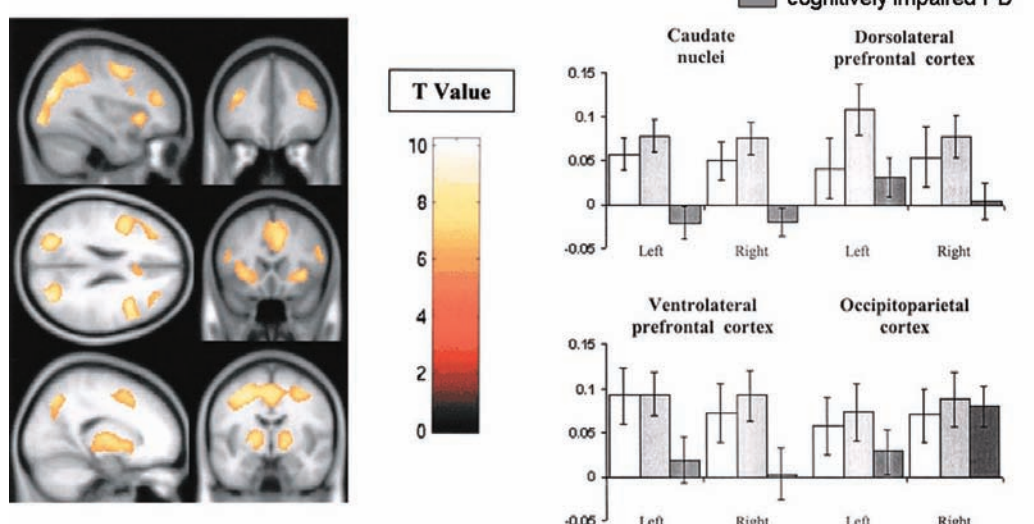


Figure 11 fMRI of PD. Left, pattern of fMRI activity during the working memory paradigm contrast the retrieving/manipulating working memory period with the retention and task maintenance period. Right, Regional mean fMRI signal during manipulation and retrieval in cognitively impaired, unimpaired PD groups and the control group. The mean fMRI signal (parameter estimates) reflects the mean of the ROI contrast values \pm SEM. Abbreviations: fMRI, functional MRI; PD, Parkinson’s disease; ROI, regions of interest; SEM, standard error of the mean. Source: From Ref. 164.

respond to a pretrained sequence of visual stimuli that have been previously learned at regular sequences. Werheid et al.'s study supports Cools' model in that performance in tasks that depend on maintenance or stability is preserved in PD.

The Effect of Dopaminergic Treatment in Cognitive Function in PD

It has long been found that L-dopa treatment benefits certain cognitive functions and impairs other functions at the early stage of disease. The dopaminergic treatment effect can also be explained by the model proposed by Cools to some extent. Review of behavioral studies (160) reveals that never-treated PD patients or patients with controlled L-dopa withdrawal appear to have significant impairments (beneficial effects of L-dopa) on tasks requiring high demands for cognitive flexibility that are critically dependent on the dorsal frontostriatal circuits; such as attentional set-shifting or task-switching (170, 178–180), working memory, cognitive sequencing or feedback sequence learning (181–183), spatial delayed memory or n-back working memory (184,185), dual-tasking (186), and complex spatial search task (187). By contrast, never-treated or controlled L-dopa withdrawal patients have been observed to perform better (detrimental effect of L-dopa) on tasks requiring high demands for cognitive stability that are critically dependent on the ventral frontostriatal circuits, such as probabilistic and concurrent reversal learning tasks (170,185), verbal memory, recognition memory and visuospatial skills (181,188), and betting strategies in a gambling task (179).

Given the fact that it is difficult to tease apart completely the striatal and prefrontal origin of cognitive deficits in PD, the role of some of the tasks mentioned above were confirmed with fMRI, and some of them revealed more complicated results (169). The n-back task that requires participants to respond to the stimulus that was presented n trials before is a task requiring cognitive stability. On the basis of the model of Cools, a beneficial effect of L-dopa administration should be expected. Mattay et al. (169) studied 10 PD at the early stage during L-dopa Off and On state using an n-back working memory task and a cued sensorimotor task. The authors found greater activation in the SMA and primary motor and parietal cortices in the "drug-on" state during the sensorimotor task. The increased activity in motor cortex was associated with improvement in motor symptoms as determined by the motor subscale of Unified Parkinson Disease Rating Scale (UPDRS) and a decrease in reaction time (RT) during the motor task. Whereas more extensive activation in the lateral PFC and anterior cingulate regions during the working memory task was found in the "drug-off" relative to "drug-on" state. The

extensive activation correlated with error performance in the "drug-off" state. The authors proposed a compensatory mechanism to explain the extensive activation during the hypodopaminergic state that was focalized by dopamine treatment. Although less brain activation during "drug-on" state does not support a drug beneficial effect, correlation of poorly focused, more extensive activation with poor task performance suggests a positive effect of medication.

The dopaminergic system has also been implicated as participating in internal timekeeping, reward, and emotional processing. Dopamine improved brain activation associated with explicit timing (189) and fearful emotional processing (190) in PD. Intact use of reward feedback was found in PD patients (191); however, dopamine treatment enhanced pathological gambling (192) and drug-seeking behavior (193), which supports Cools' model.

In addition to dopaminergic alteration, cortical cholinergic (194), adrenergic (195), and serotonergic (196) deficits have also been reported in PD, which may also play a role in cognitive impairment in PD. However, fMRI studies of these systems are scant.

Monitoring Surgical Intervention

Surgical lesions and deep brain stimulation (DBS) of pallidum, subthalamic nucleus (STN) and Fields of Forel/zona incerta (FF/zi) not only successfully alleviate PD motor symptoms but also alter certain cognitive functions (197–201) such as attention (202) and mood (203,204). Surgical intervention within the basal ganglia for PD provides the opportunity to better characterize the pathophysiological mechanisms related to these putative motor, cognitive, and limbic pathways. PET has been widely used in studies dealing with DBS in PD, whereas fMRI has entered this field only recently. Potential risk of brain damage by possible displacement or heating of the implanted electrode postponed the application of fMRI in this field. A pilot study of DBS by Jech et al. (205) in four PD patients confirmed that fMRI during DBS is a safe method. A local (ipsilateral thalamus and globus pallidus) increase of BOLD signal was found during DBS (205,206). To minimize the risk of heating damage, the guidewire has to be placed parallel to the z-direction through the isocenter of the magnet, where the B-field has its lowest value. This also reduces the length of the conductor inside the scanner bore. In addition to this setup, using MR sequences with low-specific absorption rates is another technique to ensure no temperature increase at the tip of the electrode (207).

Application of fMRI to study the effect of DBS needs to be explored further. The fMRI scan timing relative to electrode implantation, i.e., acute versus chronic DBS may affect the results of fMRI (208,209). Neural plasticity or change over time in functional circuits with chronic

DBS may mediate delayed improvement (210). Stefurak et al. (208) scanned an acute implantation case who had early-onset PD with history of depression. The left electrode was within inferior STN and right electrode was marginally superior and lateral to the intended STN target within the FF/zi. fMRI-contrasting stimulation OFF versus ON (30 seconds each) revealed increased BOLD signal in premotor and motor cortices, ventrolateral thalamus, putamen, and cerebellum associated with movement improvement during left DBS. Decreased activation was also found in the SMA. Right DBS induced a dysphoric mood and little change in motor symptoms. Increased activation in dlPFC, ipsilateral medial superior frontal cortex, anterior cingulate, anterior thalamus, caudate, and pons as well as marked decreased activation in contralateral medial prefrontal cortex was found during right DBS. This case supports cortical segregation of motor and nonmotor corticostriatal circuits that may converge in close proximity at the level of the STN and the FF/zi. Monitoring DBS intervention using fMRI has only been possible in recent years and results are variable (211). A better technique to improve signal-to-noise ratio is needed to reduce artifacts caused by the electrode itself.

Conclusion Regarding fMRI Findings in PD

Despite evidence for the role of dopamine and cortico-striato-pallidal-thalamocortical loops in cognition, the specific contributions of mesocortical dopamine depletion and striatal dysfunction with downstream consequences on the loops remain to be separated. Additionally, more research is needed into the role of nondopaminergic pathology in cognitive decline in PD. Meanwhile, current unresolved issues around the clinical role of neuroimaging in monitoring patients over time and validation of quantitative imaging measures of dopaminergic function are immediate issues for the field.

CBD

CBD is a neurodegenerative disease with asymmetric parkinsonism, dystonia or focal myoclonus, and specific cognitive-behavioral changes (212), including ideomotor apraxia, cortical sensory loss or alien hand phenomenon (213,214), frontal executive deficits (215,216), and less often, dementia. CBD is now recognized as part of the spectrum of FTLD (213). Frontal deficits may include psychomotor slowing, a dysexecutive syndrome, and impaired memory retrieval. Patients with CBD often have constructional and visuospatial difficulties, acalculia, elements of Gerstmann syndrome, and nonfluent aphasia. The alien limb phenomenon is a dramatic manifestation of CBD. A definitive diagnosis requires neuro-

pathological confirmation: the presence of intraneuronal tau-immunoreactive inclusions (CBD inclusions) in the substantia nigra and cortical layer II. Astrocytic plaques and coiled bodies in oligodendroglia are characteristic. The clinical diagnosis of CBD is challenging. It may be difficult to differentiate CBD in its early course from PD or other parkinsonian disorders, such as PSP or MSA. Functional imaging studies may be very helpful in demonstrating asymmetrical abnormalities in frontoparietal regions, basal ganglia, and thalamus contralateral to clinical symptoms, particularly in the early stages (217,218).

Only one group has used fMRI to probe cortical function in patients with CBD (219,220). Simple and complex finger-opposition tasks with varying difficulty were used. The affected hand revealed decreased activation of the contralateral sensorimotor and parietal cortices and SMA during performance of the simple task, whereas there was preserved activation in the bilateral sensorimotor cortex and SMA and less activation of the parietal cortex bilaterally during performance of the complex task. These results suggest parietal lobe dysfunction contralateral to the affected hand. Thus, fMRI provides evidence of asymmetrical disorganization of the hierarchical cortical motor program, before structural and even SPECT changes become evident. Studies in comparing early PD and PSP are needed to better assess the specificity of these findings in CBD.

HD

HD is an autosomal dominant neurodegenerative disorder clinically characterized by progressive involuntary choreiform movements, cognitive impairment, and neuropsychiatric disturbances. This inherited disease is caused by an unstable extension of the trinucleotide (CAG) repeat on the Huntington gene on chromosome 4, which leads to widespread degeneration of GABAergic neurones preferentially in the caudate and putamen with projections to the globus pallidus and substantia nigra. Other regions such as the frontal and temporal lobes are also involved as the disease progresses. Cognitive dysfunction has always been considered an intrinsic feature of HD, which is believed to be due to impairment of function of the striatum and frontostriatal circuits. There is evidence that cognitive symptoms and psychiatric disturbance may precede the presentation of motor symptoms by several years. In the early stage of the disorder, cognitive dysfunctions in attention, executive function, visuospatial skills, implicit memory, and emotional processing are common (221–223).

Imaging data are largely PET-based; there are only a few fMRI studies using cognitively challenging tasks.

Tasks involved in procedural learning or implicit memory, which critically depend on striatal function (224–226) are of interest to investigate functional striatal alteration in HD (227). With the SRT, a typical task to evaluate implicit memory, Kim et al. (227) reported reduced activation in bilateral dlPFC, left precuneus, and left middle occipital regions in early HD relative to healthy controls. However, no between-group difference in activation was found in the basal ganglia. The Porteus Maze task was designed to examine the individual's ability to use planning, patience, and mental alertness in a novel, concrete performance task. Using this task, Clark et al. (228) acquired fMRI data from three HD patients and three controls. Reduced BOLD signal was observed in patients relative to the controls in the occipital, parietal and somatomotor cortex and in the caudate, while increased signal was also found in the left postcentral and right middle frontal gyri.

With the availability of a specific gene test, a growing population of individuals is identified as HD mutation carrier without clinical symptoms, in whom we can investigate the earliest manifestations of the illness. Cognitive dysfunction is an important aspect in the early-onset variants and in presymptomatic gene carriers. Longitudinal neuropsychological studies of asymptomatic mutation carriers have found subtle cognitive deficits in psychomotor, attentional, and executive functions (222,229), as well as deficits in semantic verbal fluency and visual working memory. Thus, fMRI studies (230–232) recently focused on exploring biomarker in presymptomatic gene carriers.

Abnormal performance on the Stroop interference task, a test of mental and attentional vitality and flexibility, which is known to be mediated in part by corticostriatal circuitry, has been repeatedly found in presymptomatic individuals (233,234). Reading et al. (230) found significantly reduced activation in the left anterior cingulate cortex (BA 24,32) in carriers compared with matched controls during an interference protocol, which likely represents a specific functional abnormality of the anterior cingulate circuit of the corticostriatal pathway in these individuals. Paulsen et al. (232) further separated subjects with presymptomatic HD into two groups based on estimated years to diagnosis of manifest disease: close to onset (<12 years) and far to onset (≥ 12 years). Age at disease onset was estimated using a regression equation based on the number of CAG repeats. Functional images were acquired during a time-discrimination task (T task), which requires participants to determine whether a specified interval was shorter or longer than a standard interval of 1200 milliseconds, and a pitch-discrimination (P) task as well as a sensorimotor control (C) task. The close-to-onset gene carrier group had smaller caudate nuclei, worse behavioral performance, and reduced activation in the

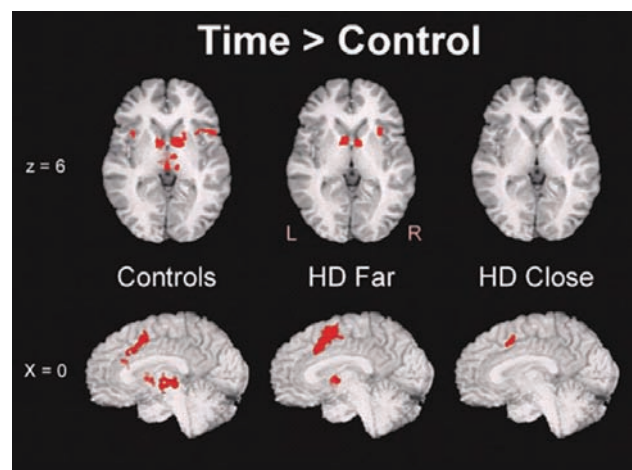


Figure 12 fMRI of (HD). Activation foci ($p < 0.01$) derived from the time-discrimination (T) task versus a sensorimotor control (C) task (T-minus-C comparison) for the control, far, and close groups. Subjects with presymptomatic HD were separated into two groups based on estimated years to clinical manifestation of disease: close to onset (<12 years) and far to onset (>12 years). Abbreviations: HD, Huntington's disease; fMRI, functional MRI. Source: From Ref: 232.

caudate, thalamus, and putamen relative to healthy controls in the T-minus-C task comparison. Reduced activation in the same areas was also found in the group of far-to-onset gene carrier group but without any volumetric or behavioral differences relative to controls. The far-to-onset participants also had hyperactivation in the anterior cingulate and pre-SMA area relative to the close-to-onset and control groups, suggesting a compensatory mechanism (Fig. 12) (232). Thus, fMRI may be a very useful measurement for tracking the evolution of changes in neural function during the earliest presymptomatic stages of HD. By working to understand the timing of these changes in HD and the relationship of caudate volume loss to specific functional losses, the hope is that treatment interventions (as they become available) can be timed appropriately to delay onset or slow progression of this devastating illness.

FUTURE DIRECTIONS

Direct *in vivo* imaging of dynamic cognitive systems at different disease stages offers an unprecedented opportunity to gain insight into evolving cognitive dysfunctions and corresponding changing brain systems. Theoretically, fMRI is a powerful and promising tool for early disease detection and progress monitoring. However, due to the heterogeneity of neurodegenerative diseases, variance in neurovascular properties among subjects, diverse cognitive tasks, and differences in task performance, the results

of fMRI are unstable across individuals and across studies. Thus, consistency of fMRI study results is an immediate issue that must be resolved to move the field forward.

Considerable efforts will be needed for increasing the diagnostic utility of fMRI in individual subjects, examining the incremental diagnostic value of fMRI over current methods, and assessing its impact on therapeutic decision making and outcomes. This will not only involve careful characterization of functional alterations for a task or combination of tasks in a given diseased population but will also require discrimination among two or more diseased populations. Correlating and covarying functional activation with task performance, clinical and neuropsychological measurements, and/or functional connectivity analysis may help reduce intraindividual variance, minimize baseline differences, and better understand alteration of activation in neurodegenerative disease. Large-scale longitudinal studies to track functional alteration across time is a powerful way for pursuing reliable biomarkers of neurodegenerative diseases. Simple, reproducible tasks (or use of the resting state) are ideal for the purpose of exploring feasible biomarkers of disease.

One should keep in mind that there is no single imaging technique or biomarker likely to become a stand-alone method of diagnosing and/or monitoring neurodegenerative diseases. Instead, combining different neuroimaging techniques will likely complement existing clinical tests. Ideally, the use of functional imaging in the clinical arena will need to be targeted to a specific question. The clinician or imaging specialist should understand the limitations of the technique, know whether the designed task is capable of answering the question posed and whether the results from fMRI are specific to the diseased population.

Currently, we are only beginning to assess the diagnostic efficacy of fMRI over more conventional methods in a number of disease processes. Regardless of whether the diagnostic utility is proven, further fMRI studies may give us greater insight in closing the gap between our molecular understanding of neurodegenerative disease and its functional, anatomical, and clinical manifestations.

REFERENCES

- Scheltens P. Early diagnosis of dementia: neuroimaging. *J Neurol* 1999; 246(1):16–20.
- Coleman RE. Positron emission tomography diagnosis of Alzheimer's disease. *Neuroimaging Clin N Am* 2005; 15(4):837–846, x.
- Krishnan S, Talley BD, Slavin MJ, et al. Current status of functional MR imaging, perfusion-weighted imaging, and diffusion-tensor imaging in Alzheimer's disease diagnosis and research. *Neuroimaging Clin N Am* 2005; 15(4):853–868, xi.
- Soher BJ, Doraiswamy PM, Charles HC. A review of 1H MR spectroscopy findings in Alzheimer's disease. *Neuroimaging Clin N Am* 2005; 15(4):847–852, xi.
- Friston KJ. Commentary and opinion: II. Statistical parametric mapping: ontology and current issues. *J Cereb Blood Flow Metab* 1995; 15(3):361–370.
- Brett M, Johnsrude IS, Owen AM. The problem of functional localization in the human brain. *Nat Rev Neurosci* 2002; 3(3):243–249.
- Swallow KM, Braver TS, Snyder AZ, et al. Reliability of functional localization using fMRI. *Neuroimage* 2003; 20(3):1561–1577.
- Toga AW, Thompson PM. Maps of the brain. *Anat Rec* 2001; 265(2):37–53.
- Fox PT, Laird AR, Lancaster JL. Coordinate-based voxel-wise meta-analysis: dividends of spatial normalization. Report of a virtual workshop. *Hum Brain Mapp* 2005; 25(1):1–5.
- Juch H, Zimine I, Seghier ML, et al. Anatomical variability of the lateral frontal lobe surface: implication for intersubject variability in language neuroimaging. *Neuroimage* 2005; 24(2):504–514.
- Ashburner JA, Friston KJ. Spatial normalization using basis functions. In: Frackowiak RSJ, Friston KJ, Frith C, et al. eds. *Human Brain Function*. 2nd ed. Academic Press, 2003.
- Krishnan S, Slavin MJ, Tran TT, et al. Accuracy of spatial normalization of the hippocampus: implications for fMRI research in memory disorders. *Neuroimage* 2006; 31(2):560–571.
- Sandstrom C, Krishnan S, Slavin MJ, et al. Hippocampal atrophy confounds template-based fMRI measures of hippocampal activation in patients with mild cognitive impairment. *AJNR Am J Neuroradiol* 2006; 27(8):1622–1627.
- Hoeksma MR, Kenemans JL, Kemner C, et al. Variability in spatial normalization of pediatric and adult brain images. *Clin Neurophysiol* 2005; 116(5):1188–1194.
- Vandenbroucke MW, Goekoop R, Dusche EJ, et al. Interindividual differences of medial temporal lobe activation during encoding in an elderly population studied by fMRI. *Neuroimage* 2004; 21(1):173–180.
- Dickerson BC, Salat DH, Bates JF, et al. Medial temporal lobe function and structure in mild cognitive impairment. *Ann Neurol* 2004; 56(1):27–35.
- Prvulovic D, Hubl D, Sack AT, et al. Functional imaging of visuospatial processing in Alzheimer's disease. *Neuroimage* 2002; 17(3):1403–1414.
- Ogawa S, Tank DW, Menon R, et al. Intrinsic signal changes accompanying sensory stimulation: functional brain mapping with magnetic resonance imaging. *Proc Natl Acad Sci U S A* 1992; 89(13):5951–5955.
- Kwong KK, Belliveau JW, Chesler DA, et al. Dynamic magnetic resonance imaging of human brain activity during primary sensory stimulation. *Proc Natl Acad Sci U S A* 1992; 89(12):5675–5679.
- Kuschinsky W. *Regulation of Cerebral Blood Flow*. New York: Springer 1999.

21. Villringer A. Physiological Changes During Brain Activation. New York: Springer, 1999.
22. D'Esposito M, Deouell LY, Gazzaley A. Alterations in the BOLD fMRI signal with ageing and disease: a challenge for neuroimaging. *Nat Rev Neurosci* 2003; 4(11): 863–872.
23. Prvulovic D, Van de Ven V, Sack AT, et al. Functional activation imaging in aging and dementia. *Psychiatry Res* 2005; 140(2):97–113.
24. D'Esposito M, Zarahn E, Aguirre GK, et al. The effect of normal aging on the coupling of neural activity to the bold hemodynamic response. *Neuroimage* 1999; 10(1):6–14.
25. Buckner RL, Snyder AZ, Sanders AL, et al. Functional brain imaging of young, nondemented, and demented older adults. *J Cogn Neurosci* 2000; 12(suppl 2):24–34.
26. Derdeyn CP, Videen TO, Fritsch SM, et al. Compensatory mechanisms for chronic cerebral hypoperfusion in patients with carotid occlusion. *Stroke* 1999; 30(5):1019–1024.
27. Pineiro R, Pendlebury S, Johansen-Berg H, et al. Altered hemodynamic responses in patients after subcortical stroke measured by functional MRI. *Stroke* 2002; 33(1): 103–109.
28. Rother J, Knab R, Hamzei F, et al. Negative dip in BOLD fMRI is caused by blood flow–oxygen consumption uncoupling in humans. *Neuroimage* 2002; 15(1):98–102.
29. Zonta M, Angulo MC, Gobbo S, et al. Neuron-to-astrocyte signaling is central to the dynamic control of brain microcirculation. *Nat Neurosci* 2003; 6(1):43–50.
30. Levin JM, Frederick Bde B, Ross MH, et al. Influence of baseline hematocrit and hemodilution on BOLD fMRI activation. *Magn Reson Imaging* 2001; 19(8):1055–1062.
31. Levin JM, Ross MH, Mendelson JH, et al. Reduction in BOLD fMRI response to primary visual stimulation following alcohol ingestion. *Psychiatry Res* 1998; 82(3): 135–146.
32. Logan JM, Sanders AL, Snyder AZ, et al. Under-recruitment and nonselective recruitment: dissociable neural mechanisms associated with aging. *Neuron* 2002; 33(5): 827–840.
33. Grady CL, McIntosh AR, Beig S, et al. Evidence from functional neuroimaging of a compensatory prefrontal network in Alzheimer's disease. *J Neurosci* 2003; 23(3): 986–993.
34. Stern E, Silbersweig DA. Advances in functional neuroimaging methodology for the study of brain systems underlying human neuropsychological function and dysfunction. *J Clin Exp Neuropsychol* 2001; 23(1):3–18.
35. Tononi G, Sporns O, Edelman GM. Measures of degeneracy and redundancy in biological networks. *Proc Natl Acad Sci U S A* 1999; 96(6):3257–3262.
36. Price CJ, Friston KJ. Degeneracy and cognitive anatomy. *Trends Cogn Sci* 2002; 6(10):416–421.
37. Rapoport SI, Grady CL. Parametric in vivo brain imaging during activation to examine pathological mechanisms of functional failure in Alzheimer disease. *Int J Neurosci* 1993; 70(1–2):39–56.
38. Morrison JH, Hof PR, Bouras C. An anatomic substrate for visual disconnection in Alzheimer's disease. *Ann N Y Acad Sci* 1991; 640:36–43.
39. Schroder J, Buchsbaum MS, Shihabuddin L, et al. Patterns of cortical activity and memory performance in Alzheimer's disease. *Biol Psychiatry* 2001; 49(5): 426–436.
40. Small SA, Perera GM, DeLaPaz R, et al. Differential regional dysfunction of the hippocampal formation among elderly with memory decline and Alzheimer's disease. *Ann Neurol* 1999; 45(4):466–472.
41. Smith CD, Andersen AH, Kryscio RJ, et al. Altered brain activation in cognitively intact individuals at high risk for Alzheimer's disease. *Neurology* 1999; 53(7):1391–1396.
42. Grady CL, Furey ML, Pietrini P, et al. Altered brain functional connectivity and impaired short-term memory in Alzheimer's disease. *Brain* 2001; 124(pt 4):739–756.
43. Braak H, Braak E. Staging of Alzheimer-related cortical destruction. *Int Psychogeriatr* 1997; 9(suppl 1):257–261 (discussion 269–272).
44. Price JL, Morris JC. Tangles and plaques in nondemented aging and “preclinical” Alzheimer's disease. *Ann Neurol* 1999; 45(3):358–368.
45. Desgranges B, Eustache F, Rioux P, et al. Memory disorders in Alzheimer's disease and the organization of human memory. *Cortex* 1996; 32(3):387–412.
46. Gainotti G, Marra C, Villa G, et al. Sensitivity and specificity of some neuropsychological markers of Alzheimer dementia. *Alzheimer Dis Assoc Disord* 1998; 12(3): 152–162.
47. Petersen RC, Smith GE, Ivnik RJ, et al. Memory function in very early Alzheimer's disease. *Neurology* 1994; 44(5): 867–872.
48. Braak E, Griffing K, Arai K, et al. Neuropathology of Alzheimer's disease: what is new since A. Alzheimer? *Eur Arch Psychiatry Clin Neurosci* 1999; 249(suppl 3):14–22.
49. Geula C. Abnormalities of neural circuitry in Alzheimer's disease: hippocampus and cortical cholinergic innervation. *Neurology* 1998; 51(1 suppl 1):S18–S29 (discussion S65–S17).
50. Khachaturian ZS. Diagnosis of Alzheimer's disease. *Arch Neurol* 1985; 42(11):1097–1105.
51. Mirra SS, Heyman A, McKeel D, et al. The Consortium to Establish a Registry for Alzheimer's Disease (CERAD). Part II. Standardization of the neuropathologic assessment of Alzheimer's disease. *Neurology* 1991; 41(4):479–486.
52. Consensus recommendations for the postmortem diagnosis of Alzheimer's disease. The National Institute on Aging, and Reagan Institute Working Group on Diagnostic Criteria for the Neuropathological Assessment of Alzheimer's Disease. *Neurobiol Aging* 1997; 18(suppl 4): S1–S2.
53. Braak H, Braak E. Neuropathological staging of Alzheimer-related changes. *Acta Neuropathol (Berl)* 1991; 82(4):239–259.
54. Price JL, Davis PB, Morris JC, et al. The distribution of tangles, plaques and related immunohistochemical markers in healthy aging and Alzheimer's disease. *Neurobiol Aging* 1991; 12(4):295–312.
55. Clark CM, Karlawish JH. Alzheimer disease: current concepts and emerging diagnostic and therapeutic strategies. *Ann Intern Med* 2003; 138(5):400–410.

56. Knopman D. Cerebrospinal fluid beta-amyloid and tau proteins for the diagnosis of Alzheimer disease. *Arch Neurol* 2001; 58(3):349–350.
57. McKhann G, Drachman D, Folstein M, et al. Clinical diagnosis of Alzheimer's disease: report of the NINCDS-ADRDA Work Group under the auspices of Department of Health and Human Services Task Force on Alzheimer's Disease. *Neurology* 1984; 34(7):939–944.
58. Gabrieli JD. Cognitive neuroscience of human memory. *Annu Rev Psychol* 1998; 49:87–115.
59. Gabrieli JD, Brewer JB, Desmond JE, et al. Separate neural bases of two fundamental memory processes in the human medial temporal lobe. *Science* 1997; 276 (5310):264–266.
60. Golby AJ, Poldrack RA, Brewer JB, et al. Material-specific lateralization in the medial temporal lobe and prefrontal cortex during memory encoding. *Brain* 2001; 124(pt 9): 1841–1854.
61. Saykin AJ, Johnson SC, Flashman LA, et al. Functional differentiation of medial temporal and frontal regions involved in processing novel and familiar words: an fMRI study. *Brain* 1999; 122(pt 10):1963–1971.
62. Daselaar SM, Fleck MS, Prince SE, et al. The medial temporal lobe distinguishes old from new independently of consciousness. *J Neurosci* 2006; 26(21):5835–5839.
63. Perry RJ, Hodges JR. Attention and executive deficits in Alzheimer's disease. A critical review. *Brain* 1999; 122 (pt 3): 383–404.
64. Gron G, Bittner D, Schmitz B, et al. Subjective memory complaints, objective neural markers in patients with Alzheimer's disease and major depressive disorder. *Ann Neurol* 2002; 51(4):491–498.
65. Grossman M, Koenig P, DeVita C, et al. Neural basis for verb processing in Alzheimer's disease: an fMRI study. *Neuropsychology* 2003; 17(4):658–674.
66. Kato T, Knopman D, Liu H. Dissociation of regional activation in mild AD during visual encoding: a functional MRI study. *Neurology* 2001; 57(5):812–816.
67. Lustig C, Snyder AZ, Bhakta M, et al. Functional deactivations: change with age and dementia of the Alzheimer type. *Proc Natl Acad Sci U S A* 2003; 100(24): 14504–14509.
68. Rombouts SA, Barkhof F, Veltman DJ, et al. Functional MR imaging in Alzheimer's disease during memory encoding. *AJNR Am J Neuroradiol* 2000; 21(10): 1869–1875.
69. Saykin AJ, Flashman LA, Frutiger SA, et al. Neuroanatomic substrates of semantic memory impairment in Alzheimer's disease: patterns of functional MRI activation. *J Int Neuropsychol Soc* 1999; 5(5):377–392.
70. Sperling RA, Bates JF, Chua EF, et al. fMRI studies of associative encoding in young and elderly controls and mild Alzheimer's disease. *J Neurol Neurosurg Psychiatry* 2003; 74(1):44–50.
71. Backman L, Andersson JL, Nyberg L, et al. Brain regions associated with episodic retrieval in normal aging and Alzheimer's disease. *Neurology* 1999; 52(9):1861–1870.
72. Becker JT, Mintun MA, Aleva K, et al. Compensatory reallocation of brain resources supporting verbal episodic memory in Alzheimer's disease. *Neurology* 1996; 46(3): 692–700.
73. Herbster AN, Nichols T, Wiseman MB, et al. Functional connectivity in auditory-verbal short-term memory in Alzheimer's disease. *Neuroimage* 1996; 4(2):67–77.
74. Woodard JL, Grafton ST, Votaw JR, et al. Compensatory recruitment of neural resources during overt rehearsals of word lists in Alzheimer's disease. *Neuropsychology* 1998; 12(4):491–504.
75. Petersen RC. Mild cognitive impairment as a diagnostic entity. *J Intern Med* 2004; 256(3):183–194.
76. Petersen RC, Doody R, Kurz A, et al. Current concepts in mild cognitive impairment. *Arch Neurol* 2001; 58(12): 1985–1992.
77. Petersen RC, Smith GE, Waring SC, et al. Mild cognitive impairment: clinical characterization and outcome. *Arch Neurol* 1999; 56(3):303–308.
78. Morris JC, Storandt M, McKeel DW Jr., et al. Cerebral amyloid deposition and diffuse plaques in "normal" aging: evidence for presymptomatic and very mild Alzheimer's disease. *Neurology* 1996; 46(3):707–719.
79. Small GW, La Rue A, Komo S, et al. Predictors of cognitive change in middle-aged and older adults with memory loss. *Am J Psychiatry* 1995; 152(12):1757–1764.
80. Reiman EM, Caselli RJ, Yun LS, et al. Preclinical evidence of Alzheimer's disease in persons homozygous for the epsilon 4 allele for apolipoprotein E. *N Engl J Med* 1996; 334(12):752–758.
81. Tariot PN, Federoff HJ. Current treatment for Alzheimer disease and future prospects. *Alzheimer Dis Assoc Disord* 2003; 17(suppl 4):S105–S113.
82. Machulda MM, Ward HA, Borowski B, et al. Comparison of memory fMRI response among normal, MCI, and Alzheimer's patients. *Neurology* 2003; 61(4):500–506.
83. Dickerson BC, Salat DH, Greve DN, et al. Increased hippocampal activation in mild cognitive impairment compared to normal aging and AD. *Neurology* 2005; 65(3):404–411.
84. Petrella JR, Krishnan S, Slavin MJ, et al. Mild cognitive impairment: evaluation with 4-T functional MR Imaging. *Radiology* 2006; 240(1):177–186.
85. Mesulam MM. Neuroplasticity failure in Alzheimer's disease: bridging the gap between plaques and tangles. *Neuron* 1999; 24(3):521–529.
86. Greicius MD, Krasnow B, Reiss AL, et al. Functional connectivity in the resting brain: a network analysis of the default mode hypothesis. *Proc Natl Acad Sci U S A* 2003; 100(1):253–258.
87. Raichle ME, MacLeod AM, Snyder AZ, et al. A default mode of brain function. *Proc Natl Acad Sci U S A* 2001; 98(2):676–682.
88. Greicius MD, Srivastava G, Reiss AL, et al. Default-mode network activity distinguishes Alzheimer's disease from healthy aging: evidence from functional MRI. *Proc Natl Acad Sci U S A* 2004; 101(13):4637–4642.
89. Rombouts S, Scheltens P. Functional connectivity in elderly controls and AD patients using resting state fMRI: a pilot study. *Curr Alzheimer Res* 2005; 2(2): 115–116.

90. Chetelat G, Desgranges B, de la Sayette V, et al. Dissociating atrophy and hypometabolism impact on episodic memory in mild cognitive impairment. *Brain* 2003; 126(pt 9): 1955–1967.
91. Huang C, Wahlund LO, Svensson L, et al. Cingulate cortex hypoperfusion predicts Alzheimer's disease in mild cognitive impairment. *BMC Neurol* 2002; 2:9.
92. Kogure D, Matsuda H, Ohnishi T, et al. Longitudinal evaluation of early Alzheimer's disease using brain perfusion SPECT. *J Nucl Med* 2000; 41(7):1155–1162.
93. Gusnard DA, Akbudak E, Shulman GL, et al. Medial prefrontal cortex and self-referential mental activity: relation to a default mode of brain function. *Proc Natl Acad Sci U S A* 2001; 98(7):4259–4264.
94. Binder JR, Frost JA, Hammeke TA, et al. Conceptual processing during the conscious resting state. A functional MRI study. *J Cogn Neurosci* 1999; 11(1):80–95.
95. Kjaer TW, Lou HC. Interaction between precuneus and dorsolateral prefrontal cortex may play a unitary role in consciousness—a principal component analysis of rCBF. *Conscious Cognition* 2000; 9:S59.
96. Maquet P. Brain mechanisms of sleep: contribution of neuroimaging techniques. *J Psychopharmacol* 1999; 13(4 suppl 1):S25–S28.
97. Laureys S, Lemaire C, Maquet P, et al. Cerebral metabolism during vegetative state and after recovery to consciousness. *J Neurol Neurosurg Psychiatry* 1999; 67(1):121.
98. Cavanna AE, Trimble MR. The precuneus: a review of its functional anatomy and behavioural correlates. *Brain* 2006; 129(pt 3):564–583.
99. Laureys S, Owen AM, Schiff ND. Brain function in coma, vegetative state, and related disorders. *Lancet Neurol* 2004; 3(9):537–546.
100. Lou HC, Kjaer TW, Friberg L, et al. A ¹⁵O-H₂O PET study of meditation and the resting state of normal consciousness. *Hum Brain Mapp* 1999; 7(2):98–105.
101. Lou HC, Luber B, Crupain M, et al. Parietal cortex and representation of the mental Self. *Proc Natl Acad Sci U S A* 2004; 101(17):6827–6832.
102. Buckner RL, Petersen SE, Ojemann JG, et al. Functional anatomical studies of explicit and implicit memory retrieval tasks. *J Neurosci* 1995; 15(1 pt 1):12–29.
103. Tulving E, Kapur S, Markowitsch HJ, et al. Neuroanatomical correlates of retrieval in episodic memory: auditory sentence recognition. *Proc Natl Acad Sci U S A* 1994; 91(6):2012–2015.
104. Buckner RL, Snyder AZ, Shannon BJ, et al. Molecular, structural, and functional characterization of Alzheimer's disease: evidence for a relationship between default activity, amyloid, and memory. *J Neurosci* 2005; 25(34): 7709–7717.
105. Petrella JRK, S. Wang, L. Slavin, et al. Functional Deactivation in Midline Posterior Cortical Regions Correlates with Severity of Memory Dysfunction in MCI and Mild Alzheimer Disease. In 10th International Conference on Alzheimer's Disease and related Disorders. Madrid, Spain, 2006.
106. Kobayashi Y, Amaral DG. Macaque monkey retrosplenial cortex: II. Cortical afferents. *J Comp Neurol* 2003; 466 (1):48–79.
107. Morris R, Paxinos G, Petrides M. Architectonic analysis of the human retrosplenial cortex. *J Comp Neurol* 2000; 421(1):14–28.
108. Morris R, Petrides M, Pandya DN. Architecture and connections of retrosplenial area 30 in the rhesus monkey (*Macaca mulatta*). *Eur J Neurosci* 1999; 11(7):2506–2518.
109. Corder EH, Saunders AM, Strittmatter WJ, et al. Gene dose of apolipoprotein E type 4 allele and the risk of Alzheimer's disease in late onset families. *Science* 1993; 261(5123):921–923.
110. Devanand DP, Pelton GH, Zamora D, et al. Predictive utility of apolipoprotein E genotype for Alzheimer disease in outpatients with mild cognitive impairment. *Arch Neurol* 2005; 62(6):975–980.
111. Khachaturian AS, Corcoran CD, Mayer LS, et al. Apolipoprotein E epsilon4 count affects age at onset of Alzheimer disease, but not lifetime susceptibility, The Cache County Study. *Arch Gen Psychiatry* 2004; 61(5):518–524.
112. Marquis S, Moore MM, Howieson DB, et al. Independent predictors of cognitive decline in healthy elderly persons. *Arch Neurol* 2002; 59(4):601–606.
113. Slooter AJ, Breteler MB, Ott A, et al. APOE genotyping in differential diagnosis of Alzheimer's disease. *Lancet* 1996; 348(9023):334.
114. Wang PN, Liu HC, Liu TY, et al. Estrogen-metabolizing gene COMT polymorphism synergistic APOE epsilon4 allele increases the risk of Alzheimer disease. *Dement Geriatr Cogn Disord* 2005; 19(2–3):120–125.
115. Bookheimer SY, Strojwas MH, Cohen MS, et al. Patterns of brain activation in people at risk for Alzheimer's disease. *N Engl J Med* 2000; 343(7):450–456.
116. Fleisher AS, Houston WS, Eyler LT, et al. Identification of Alzheimer disease risk by functional magnetic resonance imaging. *Arch Neurol* 2005; 62(12):1881–1888.
117. Smith CD, Andersen AH, Kryscio RJ, et al. Women at risk for AD show increased parietal activation during a fluency task. *Neurology* 2002; 58(8):1197–1202.
118. Lind J, Persson J, Ingvar M, et al. Reduced functional brain activity response in cognitively intact apolipoprotein E epsilon4 carriers. *Brain* 2006; 129(pt 5):1240–1248.
119. Trivedi MA, Schmitz TW, Ries ML, et al. Reduced hippocampal activation during episodic encoding in middle-aged individuals at genetic risk of Alzheimer's disease: a cross-sectional study. *BMC Med* 2006; 4:1.
120. Burggren AC, Small GW, Sabb FW, et al. Specificity of brain activation patterns in people at genetic risk for Alzheimer disease. *Am J Geriatr Psychiatry* 2002; 10(1): 44–51.
121. Lindau M, Almkvist O, Johansson SE, et al. Cognitive and behavioral differentiation of frontal lobe degeneration of the non-Alzheimer type and Alzheimer's disease. *Dement Geriatr Cogn Disord* 1998; 9(4):205–213.
122. Neary D, Snowden JS, Gustafson L, et al. Frontotemporal lobar degeneration: a consensus on clinical diagnostic criteria. *Neurology* 1998; 51(6):1546–1554.

123. Rascovsky K, Salmon DP, Ho GJ, et al. Cognitive profiles differ in autopsy-confirmed frontotemporal dementia and AD. *Neurology* 2002; 58(12):1801–1808.
124. Mendez MF, Perryman KM. Neuropsychiatric features of frontotemporal dementia: evaluation of consensus criteria and review. *J Neuropsychiatry Clin Neurosci* 2002; 14(4): 424–429.
125. Rosen HJ, Gorno-Tempini ML, Goldman WP, et al. Patterns of brain atrophy in frontotemporal dementia and semantic dementia. *Neurology* 2002; 58(2):198–208.
126. Whitwell JL, Anderson VM, Scahill RI, et al. Longitudinal patterns of regional change on volumetric MRI in frontotemporal lobar degeneration. *Dement Geriatr Cogn Disord* 2004; 17(4):307–310.
127. Ishii K, Sasaki M, Sakamoto S, et al. Tc-99m ethyl cysteinate dimer SPECT and 2-[F-18]fluoro-2-deoxy-D-glucose PET in Alzheimer's disease. Comparison of perfusion and metabolic patterns. *Clin Nucl Med* 1999; 24(8):572–575.
128. Gregory CA, Serra-Mestres J, Hodges JR. Early diagnosis of the frontal variant of frontotemporal dementia: how sensitive are standard neuroimaging and neuropsychologic tests? *Neuropsychiatry Neuropsychol Behav Neurol* 1999; 12(2):128–135.
129. Rombouts SA, van Swieten JC, Pijnenburg YA, et al. Loss of frontal fMRI activation in early frontotemporal dementia compared to early AD. *Neurology* 2003; 60(12): 1904–1908.
130. Vandenberghe R. Language, ageing and neurodegenerative disease. *Bull Mem Acad R Med Belg* 2004; 159(pt 2): 161–166.
131. DeLong MR, Alexander GE, Mitchell SJ, et al. The contribution of basal ganglia to limb control. *Prog Brain Res* 1986; 64:161–174.
132. Karlsen KH, Larsen JP, Tandberg E, et al. Quality of life measurements in patients with Parkinson's disease: a community-based study. *Eur J Neurol* 1998; 5(5): 443–450.
133. Schrag A, Jahanshahi M, Quinn N. What contributes to quality of life in patients with Parkinson's disease? *J Neurol Neurosurg Psychiatry* 2000; 69(3):308–312.
134. Obeso JA, Rodriguez-Oroz MC, Rodriguez M, et al. The basal ganglia and disorders of movement: pathophysiological mechanisms. *News Physiol Sci* 2002; 17:51–55.
135. Alexander GE, DeLong MR, Strick PL. Parallel organization of functionally segregated circuits linking basal ganglia and cortex. *Annu Rev Neurosci* 1986; 9:357–381.
136. Berardelli A, Rothwell JC, Thompson PD, et al. Pathophysiology of bradykinesia in Parkinson's disease. *Brain* 2001; 124(pt 11):2131–2146.
137. DeLong MR. Primate models of movement disorders of basal ganglia origin. *Trends Neurosci* 1990; 13(7): 281–285.
138. Jenkins IH, Fernandez W, Playford ED, et al. Impaired activation of the supplementary motor area in Parkinson's disease is reversed when akinesia is treated with apomorphine. *Ann Neurol* 1992; 32(6):749–757.
139. Rascol O, Sabatini U, Chollet F, et al. Normal activation of the supplementary motor area in patients with Parkinson's disease undergoing long-term treatment with levodopa. *J Neurol Neurosurg Psychiatry* 1994; 57(5): 567–571.
140. Sabatini U, Boulanouar K, Fabre N, et al. Cortical motor reorganization in akinetic patients with Parkinson's disease: a functional MRI study. *Brain* 2000; 123(pt 2): 394–403.
141. Grafton ST. Contributions of functional imaging to understanding parkinsonian symptoms. *Curr Opin Neurobiol* 2004; 14(6):715–719.
142. Goldberg G. Supplementary motor area structure and function: review and hypotheses. *Behav Brain Sci* 1985; 8:567–615.
143. Boecker H, Weindl A, Leenders K, et al. Secondary parkinsonism due to focal substantia nigra lesions: a PET study with [18F]FDG and [18F]fluorodopa. *Acta Neurol Scand* 1996; 93(6):387–392.
144. Deiber MP, Passingham RE, Colebatch JG, et al. Cortical areas and the selection of movement: a study with positron emission tomography. *Exp Brain Res* 1991; 84(2): 393–402.
145. Halsband U, Ito N, Tanji J, et al. The role of premotor cortex and the supplementary motor area in the temporal control of movement in man. *Brain* 1993; 116(pt 1): 243–266.
146. Picard N, Strick PL. Motor areas of the medial wall: a review of their location and functional activation. *Cereb Cortex* 1996; 6(3):342–353.
147. Haslinger B, Erhard P, Kampfe N, et al. Event-related functional magnetic resonance imaging in Parkinson's disease before and after levodopa. *Brain* 2001; 124(pt 3):558–570.
148. Rascol O, Sabatini U, Chollet F, et al. Supplementary and primary sensory motor area activity in Parkinson's disease. Regional cerebral blood flow changes during finger movements and effects of apomorphine. *Arch Neurol* 1992; 49(2):144–148.
149. Georgiou N, Bradshaw JL, Iansek R, et al. Reduction in external cues and movement sequencing in Parkinson's disease. *J Neurol Neurosurg Psychiatry* 1994; 57(3): 368–370.
150. Hoover JE, Strick PL. Multiple output channels in the basal ganglia. *Science* 1993; 259(5096):819–821.
151. Parr-Brownlie LC, Hyland BI. Bradykinesia induced by dopamine D2 receptor blockade is associated with reduced motor cortex activity in the rat. *J Neurosci* 2005; 25(24): 5700–5709.
152. Lozza C, Marie RM, Baron JC. The metabolic substrates of bradykinesia and tremor in uncomplicated Parkinson's disease. *Neuroimage* 2002; 17(2):688–699.
153. Rogers RD, Sahakian BJ, Hodges JR, et al. Dissociating executive mechanisms of task control following frontal lobe damage and Parkinson's disease. *Brain* 1998; 121(pt 5): 815–842.
154. Dubois B, Pillon B, Sternic N, et al. Age-induced cognitive disturbances in Parkinson's disease. *Neurology* 1990; 40(1):38–41.

155. Sagar HJ, Sullivan EV, Gabrieli JD, et al. Temporal ordering and short-term memory deficits in Parkinson's disease. *Brain* 1988; 111(pt 3):525–539.
156. Knowlton BJ, Mangels JA, Squire LR. A neostratal habit learning system in humans. *Science* 1996; 273(5280): 1399–1402.
157. Jackson GM, Jackson SR, Harrison J, et al. Serial reaction time learning and Parkinson's disease: evidence for a procedural learning deficit. *Neuropsychologia* 1995; 33(5): 577–593.
158. Wilson RS, Kaszniak AW, Klawans HL, et al. High speed memory scanning in parkinsonism. *Cortex* 1980; 16(1): 67–72.
159. Owen AM. Cognitive dysfunction in Parkinson's disease: the role of frontostriatal circuitry. *Neuroscientist* 2004; 10(6): 525–537.
160. Cools R. Dopaminergic modulation of cognitive function—implications for L-DOPA treatment in Parkinson's disease. *Neurosci Biobehav Rev* 2006; 30(1):1–23.
161. Jellinger KA. The pathology of Parkinson's disease. *Adv Neurol* 2001; 86:55–72.
162. Owen AM, Stern CE, Look RB, Tracey I, Rosen BR, Petrides M. Functional organization of spatial and non-spatial working memory processing within the human lateral frontal cortex. *Proc Natl Acad Sci U S A* 1998; 95(13):7721–7726.
163. Dagher A. Functional imaging in Parkinson's disease. *Semin Neurol* 2001; 21(1):23–32.
164. Lewis SJ, Dove A, Robbins TW, et al. Cognitive impairments in early Parkinson's disease are accompanied by reductions in activity in frontostriatal neural circuitry. *J Neurosci* 2003; 23(15):6351–6356.
165. Monchi O, Petrides M, Doyon J, et al. Neural bases of set-shifting deficits in Parkinson's disease. *J Neurosci* 2004; 24(3):702–710.
166. Cools R, Stefanova E, Barker RA, et al. Dopaminergic modulation of high-level cognition in Parkinson's disease: the role of the prefrontal cortex revealed by PET. *Brain* 2002; 125(pt 3):584–594.
167. Leenders KL, Salmon EP, Tyrrell P, et al. The nigrostriatal dopaminergic system assessed in vivo by positron emission tomography in healthy volunteer subjects and patients with Parkinson's disease. *Arch Neurol* 1990; 47(12): 1290–1298.
168. Rinne JO, Portin R, Ruottinen H, et al. Cognitive impairment and the brain dopaminergic system in Parkinson disease: [¹⁸F]fluorodopa positron emission tomographic study. *Arch Neurol* 2000; 57(4):470–475.
169. Mattay VS, Tessitore A, Callicott JH, et al. Dopaminergic modulation of cortical function in patients with Parkinson's disease. *Ann Neurol* 2002; 51(2):156–164.
170. Cools R, Barker RA, Sahakian BJ, et al. Enhanced or impaired cognitive function in Parkinson's disease as a function of dopaminergic medication and task demands. *Cereb Cortex* 2001; 11(12):1136–1143.
171. Owen AM. The role of the lateral frontal cortex in mnemonic processing: the contribution of functional neuroimaging. *Exp Brain Res* 2000; 133(1):33–43.
172. Owen AM, Evans AC, Petrides M. Evidence for a two-stage model of spatial working memory processing within the lateral frontal cortex: a positron emission tomography study. *Cereb Cortex* 1996; 6(1):31–38.
173. Petrides M. Frontal Lobes and Working Memory: evidence from Investigations of the Effects of Cortical Excisions in Nonhuman Primates. Amsterdam: Elsevier, 1994.
174. Bor D, Duncan J, Wiseman RJ, et al. Encoding strategies dissociate prefrontal activity from working memory demand. *Neuron* 2003; 37(2):361–367.
175. Moody TD, Bookheimer SY, Vanek Z, et al. An implicit learning task activates medial temporal lobe in patients with Parkinson's disease. *Behav Neurosci* 2004; 118(2): 438–442.
176. Werheid K, Zysset S, Muller A, et al. Rule learning in a serial reaction time task: an fMRI study on patients with early Parkinson's disease. *Brain Res Cogn Brain Res* 2003; 16(2):273–284.
177. Poldrack RA, Clark J, Pare-Blairev EJ, et al. Interactive memory systems in the human brain. *Nature* 2001; 414(6863):546–550.
178. Bowen FP, Kamienny RS, Burns MM, et al. Parkinsonism: effects of levodopa treatment on concept formation. *Neurology* 1975; 25(8):701–704.
179. Cools R, Barker RA, Sahakian BJ, et al. L-Dopa medication remediates cognitive inflexibility, but increases impulsivity in patients with Parkinson's disease. *Neuropsychologia* 2003; 41(11):1431–1441.
180. Downes JJ, Roberts AC, Sahakian BJ, et al. Impaired extra-dimensional shift performance in medicated and unmedicated Parkinson's disease: evidence for a specific attentional dysfunction. *Neuropsychologia* 1989; 27(11–12): 1329–1343.
181. Cooper JA, Sagar HJ, Doherty SM, et al. Different effects of dopaminergic and anticholinergic therapies on cognitive and motor function in Parkinson's disease. A follow-up study of untreated patients. *Brain* 1992; 115(pt 6): 1701–1725.
182. Gowdon JH, Kieburtz K, McDermott MP, et al. Levodopa improves motor function without impairing cognition in mild non-demented Parkinson's disease patients. *Parkinson Study Group. Neurology* 1998; 50(5):1327–1331.
183. Shohamy D, Myers CE, Grossman S, et al. The role of dopamine in cognitive sequence learning: evidence from Parkinson's disease. *Behav Brain Res* 2005; 156(2): 191–199.
184. Gotham AM, Brown RG, Marsden CD. 'Frontal' cognitive function in patients with Parkinson's disease 'on' and 'off' levodopa. *Brain* 1988; 111(pt 2):299–321.
185. Swainson R, Rogers RD, Sahakian BJ, et al. Probabilistic learning and reversal deficits in patients with Parkinson's disease or frontal or temporal lobe lesions: possible adverse effects of dopaminergic medication. *Neuropsychologia* 2000; 38(5):596–612.
186. Fournet N, Moreaud O, Roulin JL, et al. Working memory functioning in medicated Parkinson's disease patients and

- the effect of withdrawal of dopaminergic medication. *Neuropsychology* 2000; 14(2):247–253.
187. Owen AM, James M, Leigh PN, et al. Fronto-striatal cognitive deficits at different stages of Parkinson's disease. *Brain* 1992; 115(pt 6):1727–1751.
188. Whittington CJ, Podd J, Kan MM. Recognition memory impairment in Parkinson's disease: power and meta-analyses. *Neuropsychology* 2000; 14(2):233–246.
189. Elsinger CL, Rao SM, Zimbelman JL, et al. Neural basis for impaired time reproduction in Parkinson's disease: an fMRI study. *J Int Neuropsychol Soc* 2003; 9(7): 1088–1098.
190. Tessitore A, Hariri AR, Fera F, et al. Dopamine modulates the response of the human amygdala: a study in Parkinson's disease. *J Neurosci* 2002; 22(20):9099–9103.
191. Swainson R, Sengupta D, Shetty T, et al. Impaired dimensional selection but intact use of reward feedback during visual discrimination learning in Parkinson's disease. *Neuropsychologia* 2006; 44(8):1290–1304.
192. Gschwandtner U, Aston J, Renaud S, et al. Pathologic gambling in patients with Parkinson's disease. *Clin Neuropharmacol* 2001; 24(3):170–172.
193. Bonci A, Singh V. Dopamine dysregulation syndrome in Parkinson's disease patients: from reward to penalty. *Ann Neurol* 2006; 59(5):733–734.
194. Mattila PM, Roytta M, Lonnberg P, et al. Choline acetyltransferase activity and striatal dopamine receptors in Parkinson's disease in relation to cognitive impairment. *Acta Neuropathol (Berl)* 2001; 102(2):160–166.
195. Javoy-Agid F, Scatton B, Ruberg M, et al. Distribution of monoaminergic, cholinergic, and GABAergic markers in the human cerebral cortex. *Neuroscience* 1989; 29(2): 251–259.
196. Scatton B, Javoy-Agid F, Rouquier L, et al. Reduction of cortical dopamine, noradrenaline, serotonin and their metabolites in Parkinson's disease. *Brain Res* 1983; 275(2):321–328.
197. Alegret M, Junque C, Valldeoriola F, et al. Effects of bilateral subthalamic stimulation on cognitive function in Parkinson disease. *Arch Neurol* 2001; 58(8):1223–1227.
198. Dujardin K, Defebvre L, Krystkowiak P, et al. Influence of chronic bilateral stimulation of the subthalamic nucleus on cognitive function in Parkinson's disease. *J Neurol* 2001; 248(7):603–611.
199. Jahanshahi M, Ardouin CM, Brown RG, et al. The impact of deep brain stimulation on executive function in Parkinson's disease. *Brain* 2000; 123(pt 6):1142–1154.
200. Pillon B, Ardouin C, Damier P, et al. Neuropsychological changes between "off" and "on" STN or GPi stimulation in Parkinson's disease. *Neurology* 2000; 55(3):411–418.
201. Trepanier LL, Kumar R, Lozano AM, et al. Neuropsychological outcome of GPi pallidotomy and GPi or STN deep brain stimulation in Parkinson's disease. *Brain Cogn* 2000; 42(3):324–347.
202. Giovannoni G, O'Sullivan JD, Turner K, et al. Hedonistic homeostatic dysregulation in patients with Parkinson's disease on dopamine replacement therapies. *J Neurol Neurosurg Psychiatry* 2000; 68(4):423–428.
203. Bejjani BP, Damier P, Arnulf I, et al. Transient acute depression induced by high-frequency deep-brain stimulation. *N Engl J Med* 1999; 340(19):1476–1480.
204. Berney A, Vingerhoets F, Perrin A, et al. Effect on mood of subthalamic DBS for Parkinson's disease: a consecutive series of 24 patients. *Neurology* 2002; 59(9):1427–1429.
205. Jech R, Urgosik D, Tintera J, et al. Functional magnetic resonance imaging during deep brain stimulation: a pilot study in four patients with Parkinson's disease. *Mov Disord* 2001; 16(6):1126–1132.
206. Rezai AR, Lozano AM, Crawley AP, et al. Thalamic stimulation and functional magnetic resonance imaging: localization of cortical and subcortical activation with implanted electrodes. Technical note. *J Neurosurg* 1999; 90(3):583–590.
207. Girnus R, GessekabbV , Luyken KJ, et al. Interventional MRI in patients with implanted deep brain stimulation electrodes: safety aspects. *Proc Int Sic Magn Reson Med* 2002; 10:2242.
208. Stefurak T, Mikulis D, Mayberg H, et al. Deep brain stimulation for Parkinson's disease dissociates mood and motor circuits: a functional MRI case study. *Mov Disord* 2003; 18(12):1508–1516.
209. Hesselmann V, Sorger B, Girnus R, et al. Intraoperative functional MRI as a new approach to monitor deep brain stimulation in Parkinson's disease. *Eur Radiol* 2004; 14(4): 686–690.
210. Mayberg HS, Lozano AM. Penfield revisited? Understanding and modifying behavior by deep brain stimulation for PD. *Neurology* 2002; 59(9):1298–1299.
211. Phillips MD, Baker KB, Lowe MJ, et al. Parkinson disease: pattern of functional MR imaging activation during deep brain stimulation of subthalamic nucleus—initial experience. *Radiology* 2006; 239(1):209–216.
212. Wenning GK, Granata R. Multiple system atrophy: more on the nature of the beast. *Neurologia* 1998; 13(3):105–110.
213. Mendez M, Cummings JL. *Dementia: A Clinical Approach*. Philadelphia: Butterworth Heinemann, 2003.
214. Cummings J. *The Neuropsychiatry of Alzheimer's Disease and Related Dementias*. London: Martin Dunitz, 2003.
215. Frasson E, Moretto G, Beltramello A, et al. Neuropsychological and neuroimaging correlates in corticobasal degeneration. *Ital J Neurol Sci* 1998; 19(5):321–328.
216. Soliveri P, Monza D, Paridi D, et al. Cognitive and magnetic resonance imaging aspects of corticobasal degeneration and progressive supranuclear palsy. *Neurology* 1999; 53(3):502–507.
217. Coulier IM, de Vries JJ, Leenders KL. Is FDG-PET a useful tool in clinical practice for diagnosing corticobasal ganglionic degeneration? *Mov Disord* 2003; 18(10):1175–1178.
218. Seritan AL, Mendez MF, Silverman DH, et al. Functional imaging as a window to dementia, corticobasal degeneration. *J Neuropsychiatry Clin Neurosci* 2004; 16(4):393–399.
219. Moretti R, Ukmor M, Torre P, et al. Cortical-basal ganglionic degeneration: a clinical, functional and cognitive evaluation (1-year follow-up). *J Neurol Sci* 2000; 182(1):29–35.
220. Ukmor M, Moretti R, Torre P, et al. Corticobasal degeneration: structural and functional MRI and single-photon

- emission computed tomography. *Neuroradiology* 2003; 45(10):708–712.
221. Lemiere J, Decruyenaere M, Evers-Kiebooms G, et al. Cognitive changes in patients with Huntington's disease (HD) and asymptomatic carriers of the HD mutation—a longitudinal follow-up study. *J Neurol* 2004; 251(8):935–942.
 222. Snowden J, Craufurd D, Griffiths H, et al. Longitudinal evaluation of cognitive disorder in Huntington's disease. *J Int Neuropsychol Soc* 2001; 7(1):33–44.
 223. Ho AK, Sahakian BJ, Brown RG, et al. Profile of cognitive progression in early Huntington's disease. *Neurology* 2003; 61(12):1702–1706.
 224. Rauch SL, Savage CR. Neuroimaging and neuropsychology of the striatum. Bridging basic science and clinical practice. *Psychiatr Clin North Am* 1997; 20(4):741–768.
 225. Rauch SL, Whalen PJ, Curran T, et al. Thalamic deactivation during early implicit sequence learning: a functional MRI study. *Neuroreport* 1998; 9(5):865–870.
 226. Willingham D, Koroshetz WJ. Evidence for dissociable motor skills in Huntington's disease patients. *Psychobiology* 1993; 21:173–182.
 227. Kim JS, Reading SA, Brashers-Krug T, et al. Functional MRI study of a serial reaction time task in Huntington's disease. *Psychiatry Res* 2004; 131(1):23–30.
 228. Clark VP, Lai S, Deckel AW. Altered functional MRI responses in Huntington's disease. *Neuroreport* 2002; 13(5): 703–706.
 229. Kirkwood SC, Siemers E, Bond C, et al. Confirmation of subtle motor changes among presymptomatic carriers of the Huntington disease gene. *Arch Neurol* 2000; 57(7):1040–1044.
 230. Reading SA, Dziorny AC, Peroutka LA, et al. Functional brain changes in presymptomatic Huntington's disease. *Ann Neurol* 2004; 55(6):879–883.
 231. Hennenlotter A, Schroeder U, Erhard P, et al. Neural correlates associated with impaired disgust processing in pre-symptomatic Huntington's disease. *Brain* 2004; 127 (pt 6):1446–1453.
 232. Paulsen JS, Zimbelman JL, Hinton SC, et al. fMRI biomarker of early neuronal dysfunction in presymptomatic Huntington's Disease. *AJNR Am J Neuroradiol* 2004; 25(10):1715–1721.
 233. Brandt J, Shpritz B, Codori AM, et al. Neuropsychological manifestations of the genetic mutation for Huntington's disease in presymptomatic individuals. *J Int Neuropsychol Soc* 2002; 8(7):918–924.
 234. Paulsen JS, Zhao H, Stout JC, et al. Clinical markers of early disease in persons near onset of Huntington's disease. *Neurology* 2001; 57(4):658–662.

11

Diffusion Imaging and Tensor Physics for the Clinician

RICHARD WATTS

Department of Physics and Astronomy, University of Canterbury, Christchurch, New Zealand

AN INTRODUCTION TO DIFFUSION

Diffusion MRI is a noninvasive, clinically important technique that is uniquely sensitive to tissue microstructure, including development and damage. The MRI signal is made sensitive to the motion of water molecules, which in turn depends on their microscopic environment. Diffusion MRI allows quantitative measurements of both the magnitude of motion of water and its directional variation. The degree of directional variation is most pronounced in white matter and allows fiber tracts to be followed from one part of the brain to another (tractography). This chapter introduces the physics underlying diffusion MRI and how the data obtained can be processed to yield clinically relevant information.

Historical Background

In 1827, the Scottish botanist Robert Brown observed that tiny grains of pollen suspended in water moved around randomly, and no matter how long he waited for them to settle, they remained in this constant state of motion. This apparent perpetual motion was a puzzle to 19th century scientists, and a full explanation had to wait until Albert Einstein's ground-breaking work of 1905 (1). We now understand that the motion of the pollen grains is caused by collisions with molecules of water, which themselves move around because of their thermal energy at room temperature. It is this random (Brownian) motion of water

molecules that is measured in diffusion MRI, and we shall see that this motion is uniquely sensitive to the microscopic environment in which the water molecules exist.

The Drunkard's Walk

Imagine that we have a microscope that is capable of watching the motion of a single molecule of water. At room (or body) temperature the molecule will have thermal energy and thus it will be moving rather fast (several hundred meters per second). However, before the water molecule can travel very far, it will collide with one of its neighbors. The collision is similar to that between two billiard balls inexpertly struck at one another, with the result that each molecule is deflected into another, random direction. This process is repeated, with both the distance that the water molecule travels between collisions and the direction it is deflected to, being random. Figure 1 shows an example of such a random path.

This motion is sometimes referred to as a drunkard's walk, the random path that an inebriated person might take as he (or she) bounces off obstacles such as lamp-posts and walls on the way home. However, the drunkard's walk is not a perfect analogy for Brownian motion. In general the objects that he bounces off are stationary (despite appearances to the contrary), and on the whole he will usually make it home—he has some preferred direction that he tries to move in.

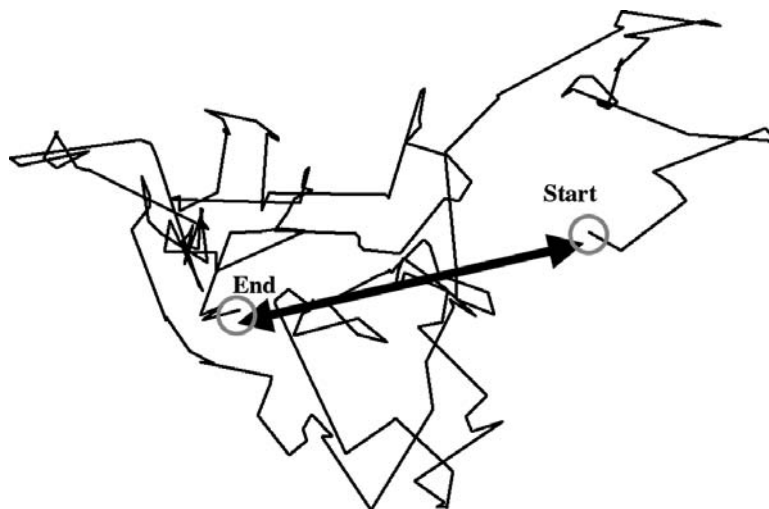


Figure 1 Simulation of a water molecule undergoing a random walk. The molecule travels a random distance between one collision and the next. Note that the total path length is much longer than the straight-line distance between the start and endpoints. This is why diffusion occurs over small distances (a few tens of micrometers in 100 milliseconds), despite molecular velocities being very large (several hundred m/sec).

How do we quantify this random motion? At any point in time, each water molecule is moving very fast, but because it keeps changing direction, it does not actually get very far. The average displacement of molecules from their starting locations is an obvious measure, but because this displacement is equally likely to be positive as negative, the average is always zero. A better measure is the average value of the *squared* displacement, which is always positive, so does not suffer from the same cancellation problem. Einstein calculated that the mean-square displacement of a molecule varied linearly with its diffusion constant and time.

$$\langle r^2 \rangle = 6Dt$$

Where the term in angled brackets indicates the mean of the squared displacement, r^2 , D is the diffusion constant (with units of mm^2/sec), and t is time. A more intuitive measure is obtained by taking the square root of both sides of this equation. The root-mean-square (RMS) displacement is a measure of the “typical” distance a molecule would travel, and is proportional to the square root of the product of D and t . This dependence means that for the molecules to spread out twice as far, we would have to wait four times as long.

Diffusion and Brownian Motion

The term “diffusion” is often used to describe the intermingling of one substance into another, driven by a concentration gradient. This process can be described mathematically with Fick’s law, in which the flux of molecules across a boundary is proportional to the con-

centration gradient across it. The constant of proportionality is the diffusion constant D , the same constant as in Einstein’s equation for the mean-squared displacement. It is the random motion of the molecules that allows this diffusive intermingling, so it is perhaps not surprising that the same constant appears in both equations. The term “self-diffusion” is used to describe water molecules spreading out among other water molecules. It is worth emphasizing that unlike tracer methods, diffusion MRI simply follows the movement of water molecules, without the need to introduce a foreign contrast agent.

WHY MEASURE DIFFUSION WITH MRI?

The other chapters of this book amply illustrate the importance of diffusion MRI to clinical radiology. However, from a physical perspective, diffusion MRI is clinically useful because the distance over which water molecules travel during the MRI measurement time (which is limited by T_2 decay to a few hundred milliseconds or so) is comparable to the sizes of microscopic structures such as cells. This compatibility means that their motion will depend strongly on their immediate environment. Diffusion MRI of the brain is wonderfully sensitive to neuronal density and integrity. The sensitivity of diffusion MRI decreases rapidly with increasing structure size because the fraction of water molecules that are close enough to the structures for their motion to be affected by them falls rapidly.

The diffusion constant of freely diffusing water at 37°C is approximately $3.2 \times 10^{-3} \text{ mm}^2/\text{sec}$. Using Einstein’s

equation for diffusion, we can calculate that in 100 milliseconds, the water molecules will spread out a distance of about 40 micrometers. For this reason, diffusion MRI is sensitive to structures on a scale of a few 10s of micrometers or less.

HOW DO WE MEASURE DIFFUSION WITH MRI?

The MRI signal can be made sensitive to the diffusive motion of water molecules by the addition of diffusion-weighting magnetic field gradients. The images produced are referred to as diffusion-weighted images, and from these images various parameters relating to diffusion can be calculated. A common method for obtaining diffusion-weighted images is based on a spin-echo acquisition. In such a “Stejskal-Tanner” pulse sequence (2), two equal magnetic field gradient pulses are added, one on either side of the 180° radiofrequency (RF) refocusing pulse (Fig. 2) (3).

The spin-echo acquisition is often explained by analogy with runners racing around a track, and this can be extended to include the effects of diffusion. The position of the runners on the track represents the precession phase

of the hydrogen nucleus and their speed is the Larmor frequency. The 90° RF pulse acts as the starting gun, with all the runners starting together. Over time, the faster runners get ahead and the slower runners fall behind. At a later point in time, the 180° RF pulse turns the runners around such that the slower runners are now in front of the faster runners (a closer analogy would be if the runners were instantly teleported to the opposite side of the track—Star Trek style—and continued running in the same direction). An equal amount of time after the 180° RF pulse, as the 90° RF pulse was before, all the runners will catch up with each other at the start/finish line. Their positions are now an “echo” of their original starting location, and because they are all together (in phase), a strong signal is measured.

However, such a perfect echo is only produced if the speed of the runners is the same for both the outgoing and incoming legs of the run. If this is not the case then they will not all arrive back at the start/finish line at the same time (their phases will be spread out), and the signal measured will be weaker. In a standard spin-echo sequence, this loss of signal can be caused by motion and random

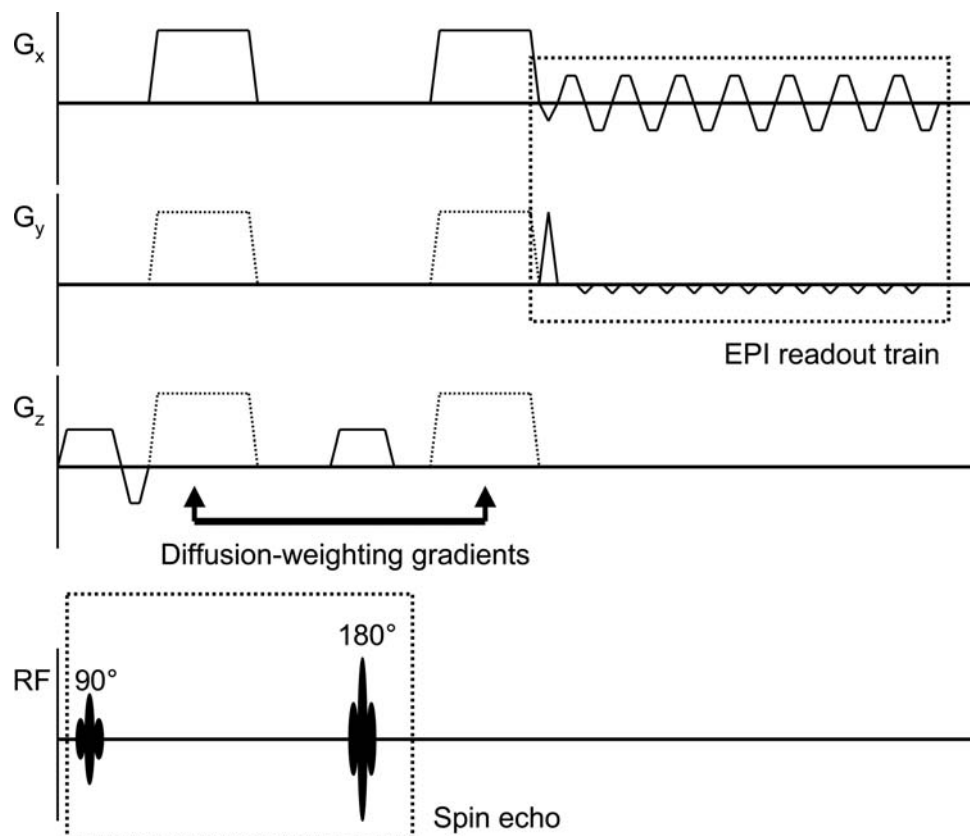


Figure 2 Schematic of a Stejskal-Tanner diffusion-weighted imaging sequence, based on a single shot spin-echo EPI acquisition. The diffusion-weighting gradients are added on the x-axis, making the acquisition sensitive to motion in that direction. The sequence may be made sensitive to motion in any other direction by changing the axis on which the diffusion gradients are applied (*dashed lines*) or through a combination of the three axes. Abbreviation: EPI, echo-planar imaging.

variations in the local magnetic field that the hydrogen atom experiences, and is responsible for T_2 decay.

In diffusion-weighted imaging, the additional magnetic field gradients serve to deliberately spread out the speeds of the runners, based on their location. If their location does not change, then the equal gradient pulses before and after the 180° RF pulse will have no effect—the runners will speed up or slow down an equal amount during both legs of their run. However, if the hydrogen atoms have moved between one gradient pulse and the other, then this cancellation is not perfect, and the phase of each hydrogen atom at the spin-echo acquisition will depend on how far it has moved, and in what direction.

The diffusion-weighting gradient shown in Figure 2 (solid line) is along the x-axis, and makes the acquisition sensitive to motion in the x-direction. If the hydrogen atoms move in the y- or z-directions then the magnetic field that they experience and hence their phase are unchanged. The diffusion-weighting gradient can be applied in any of the three axes (dashed lines in Fig. 2), or in combination to allow us to examine the directional variation of the motion and to calculate a quantity known as the diffusion tensor.

Coherent and Incoherent Motion

The result of the diffusion-weighting gradients is that the phase of the signal from each hydrogen nucleus depends on its motion. This is exactly the same principle that is used in phase-contrast imaging, in which the signal phase varies in proportion to the velocity of the motion (3). The difference between these two techniques is that in diffusion-weighted imaging we are interested in the very small, random (incoherent) motions of water molecules, whereas in phase-contrast imaging we are usually interested in much larger motions, for example, motion of blood or cerebrospinal fluid (CSF), in which the material is all moving in the same direction at the same velocity (coherent motion).

For diffusion-weighted imaging, the incoherent water motion leads to a spreading out in the phases of the hydrogen nuclei and a reduction in the signal magnitude that is measured. This signal loss depends on how much the nuclei move [related to the diffusion coefficient] and the strength and timing of the diffusion-weighting gradients.

In most practical clinical imaging situations, there are both coherent (blood and CSF flow, patient movement) and incoherent (diffusion) motions present. To measure the small displacements caused by diffusion, the acquisition must be made extremely motion sensitive using strong diffusion-weighting gradients. Fortunately, coherent motion results in phase changes in the resultant images (as in phase-contrast techniques), while incoherent motion results in magnitude changes. Simply ignoring the phase information

removes the effects of coherent motion. However, coherent motion is a problem for sequences in which the data are acquired over multiple acquisitions (multishot sequences) because the coherent motion will not be the same for each acquisition. The resultant phase errors cause unacceptable ghosting artifacts. For this reason, single-shot echo-planar imaging (EPI) techniques are usually used for diffusion-weighted imaging, although the resolution that can be attained is quite limited. Recent developments and alternative techniques for measuring diffusion are discussed later.

There is an apparent paradox in diffusion-weighted imaging in that the images are sensitive to microscopic structures, and yet the resolution of the images obtained is often quite poor (typically greater than 1mm). This can be resolved by noting that the image that we obtain represents the average motion of all the water molecules within the voxel. A significant limitation of diffusion imaging is that it is usually assumed that all molecules within a voxel exist in a similar microstructural environment.

WHAT IS THE DIFFUSION TENSOR?

The diffusion tensor is a mathematical model that describes both the degree and directional variation of water motion. Before including this directional variation, we begin with the simpler case in which the water motion is the same in all directions (isotropic diffusion).

Isotropic Diffusion and the ADC

The motion of the molecules in a glass of water is isotropic; on average it is the same in all directions. There is no direction that the molecules would prefer to move in. This can be demonstrated by carefully injecting a drop of ink into the water; over time, the ink will spread out as a sphere. In this situation the degree of diffusion can be represented by a single numerical value, the apparent diffusion coefficient (ADC). The ADC is a measure of how much a water molecule moves because of its environment and temperature. At higher temperatures the water molecules have more energy, move faster, and have a higher ADC. If the water molecules are restricted in their motion, for example, because of surrounding cell membranes, then the ADC will be reduced. It is called the *apparent* diffusion coefficient because strictly speaking the diffusion coefficient of water is a physical constant that depends only on temperature, and not on its environment. However, it is a good approximation to say that the diffusion coefficient *appears* to be reduced by restrictions.

For isotropic diffusion, the signal measured in diffusion-weighted MRI decays exponentially with the ADC such that

$$S = S_0 e^{-bD}$$

Where S is the measured signal, S_0 is the signal measured without diffusion-weighting gradients, b is a constant related to the strength and timing of the diffusion-weighting gradients, and D is the ADC.

The b value is a critical parameter in the acquisition of diffusion-weighted images. In general, we want the signal to be as sensitive as possible to the effects of diffusion (to make b large). This is achieved by making the diffusion-weighting gradients very strong (usually the maximum allowed by the gradient amplifiers) and maximizing their duration and separation. The use of such strong gradients, along with the EPI readout typically used, causes such acquisitions to be acoustically extremely noisy and

demanding on the gradient system. The duration and separation of the diffusion-weighting gradients is limited by T_2 decay. While high b values increase the sensitivity to diffusion, they also cause the measured signal strength to decrease. A compromise must be found in which there is sufficient sensitivity to diffusion while retaining reasonable signal strength. b values of around 1000 sec/mm^2 are typically used for clinical imaging. Diffusion constants in brain tissue are usually less than $1 \times 10^{-3} \text{ mm}^2/\text{sec}$, giving a reduction of signal strength by a factor of between two and three.

The distinction between a diffusion-weighted image and a calculated ADC map is important (Fig. 3). A larger

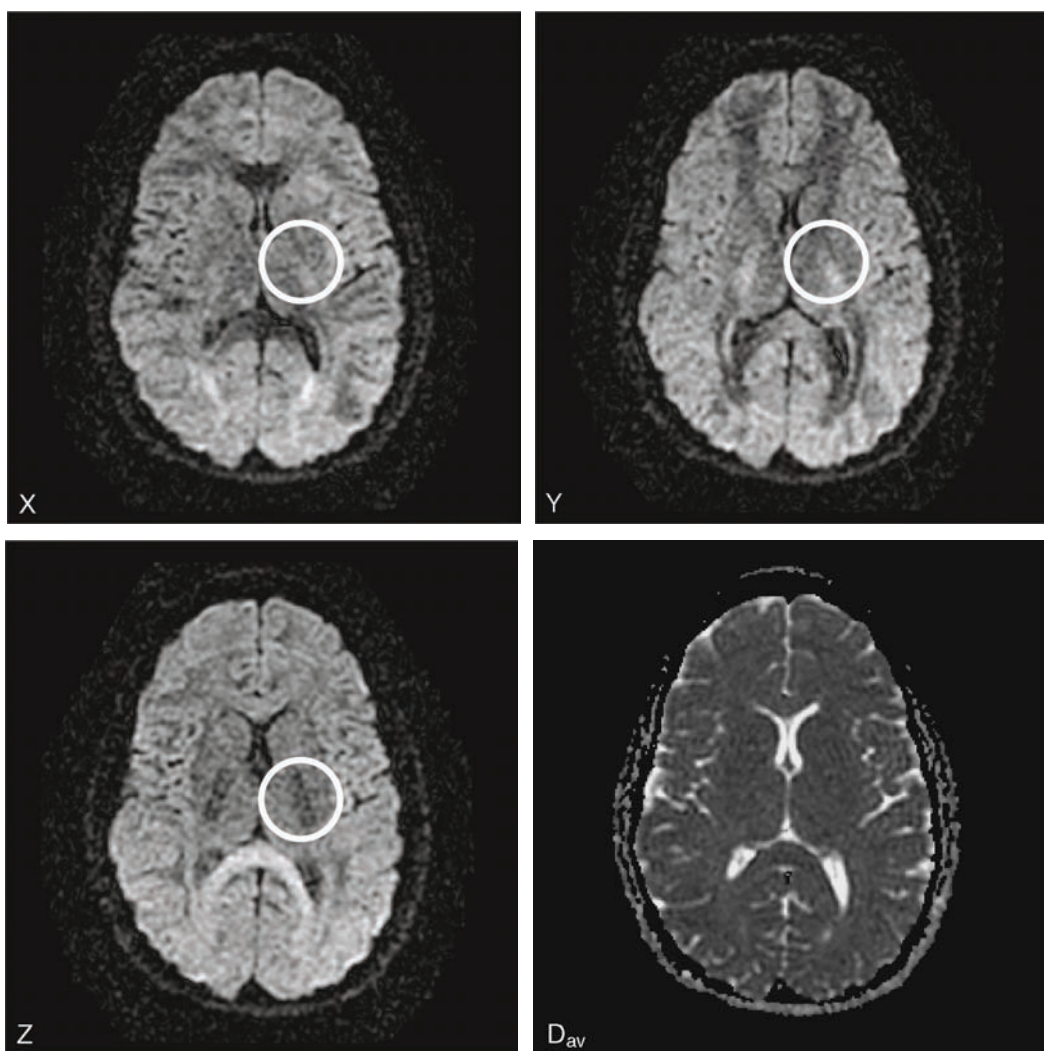


Figure 3 Diffusion-weighted images obtained with diffusion gradients applied along the X- (right-left), Y- (anterior-posterior), and Z- (superior-inferior) axes, and the corresponding map of the average apparent diffusion coefficient (D_{av} , ADC). In the diffusion-weighted images, regions with high diffusion appear dark (signal loss), whereas in the ADC map they appear bright. Circles indicate a region of the brain in which the diffusion is different in the three directions, corresponding to highly anisotropic white matter. The corticospinal tract runs superior-inferior through this section, and displays high diffusion (low signal) in the Z-image and low diffusion (high signal) in the X- and Y-images. Abbreviation: ADC, apparent diffusion coefficient.

value of ADC produces a greater signal loss in the diffusion-weighted image. For example, CSF appears bright on an ADC map (the water molecules can move freely) and dark on a diffusion-weighted image (this motion causes a large drop in signal). The ADC map also isolates the diffusion from other factors that affect the signal strength. The diffusion-weighted image signal strength depends on factors such as T_2 and proton density that enter the signal equation by the S_0 term.

Anisotropic Diffusion and the Diffusion Tensor

Water molecules in the brain do not exist in such a uniform environment as those in a glass of water. They are instead surrounded by barriers such as cell membranes and myelin that restrict their movement. If these restricting structures themselves have some preferred orientation then the motion of the water will also vary with direction—it will be anisotropic. We can no longer describe diffusion with a single parameter because we now need to include its directional dependence. The mathematical model that is most commonly used to describe this directional dependence is called the diffusion tensor. In this model, the spreading out of a tracer injected into the brain would be described by the surface of an ellipsoid. Figure 4 illustrates how an imaginary blob of ink would spread out if it were injected into white matter. The spreading is greatest when parallel to the fibers and smallest when perpendicular to them.

While it sounds complicated, the diffusion tensor is just a mathematical description of the angular variation of

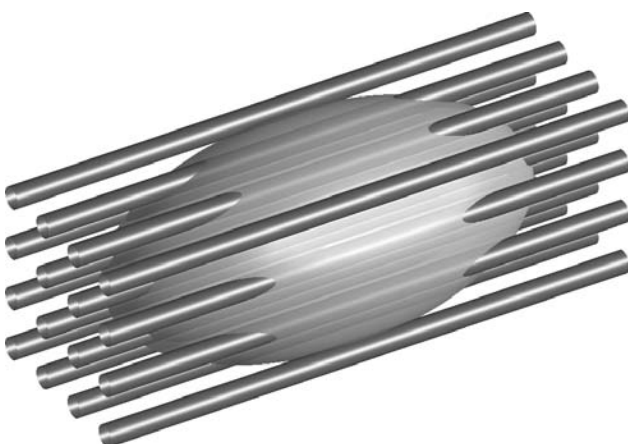


Figure 4 Diffusion (represented by an ellipsoid) in the presence of oriented fibers (cylinders) may be highly anisotropic (varies strongly with direction). It is usually assumed that the axis of maximum diffusion corresponds to the predominant fiber orientation in each voxel.

diffusion (4). It can be written as a 3×3 symmetric matrix as shown below.

$$\bar{\bar{D}} = \begin{pmatrix} D_{xx} & D_{xy} & D_{xz} \\ D_{xy} & D_{yy} & D_{yz} \\ D_{xz} & D_{yz} & D_{zz} \end{pmatrix}$$

Given the diffusion tensor, we can calculate the diffusion constant in any direction. If we represent the direction as a column vector of unit length \underline{g} , then the ADC in the direction of \underline{g} can be written as

$$D(\underline{g}) = \underline{g}^T \bar{\bar{D}} \underline{g} \\ = (g_x \ g_y \ g_z) \begin{pmatrix} D_{xx} & D_{xy} & D_{xz} \\ D_{xy} & D_{yy} & D_{yz} \\ D_{xz} & D_{yz} & D_{zz} \end{pmatrix} \begin{pmatrix} g_x \\ g_y \\ g_z \end{pmatrix}$$

For example, if we measure diffusion in the x-direction ($g_x = 1, g_y = g_z = 0$), then the diffusion constant simplifies to D_{xx} . For directions not aligned to the x-, y-, or z-axes, the calculation involves the off-diagonal terms of the tensor. For isotropic diffusion, the diagonal terms D_{xx}, D_{yy} , and D_{zz} are equal and nonzero, while the off-diagonal terms D_{xy}, D_{xz} , and D_{yz} are all zero. As we would expect, the tensor model then simplifies to the isotropic model.

The signal that we measure can now be written as a function of the diffusion tensor and the direction \underline{g}

$$S = S_0 e^{-bg^T \bar{\bar{D}} \underline{g}}$$

As with diffusion-weighted imaging, we have a choice of b value, but now we can also select the directions (\underline{g}) along which we measure diffusion.

The diffusion tensor can be visualized in different ways. One option is to generate a surface in which the distance from the center is given by the ADC in each direction, $D(\underline{g})$. In this representation, shapes that look like peanuts or pumpkins can be produced. See, for example, Jones et al. (5).

A more intuitive view of diffusion is to generate an ellipsoid, which represents how a blob of ink would spread out if it was injected into that voxel in the brain. Figure 5 shows some examples of diffusion ellipsoids with different degrees of anisotropy.

Calculation of the Diffusion Tensor

The diffusion tensor models the variation in the ADC with direction. To calculate the components of the tensor, we must make measurements of diffusion in different directions. Since the diffusion tensor has six independent components (remembering that the 3×3 matrix is symmetric about its diagonal), we must measure diffusion in a minimum of six directions to unambiguously determine the tensor, although more measurements are often obtained to improve the accuracy of the derived tensor components (6). An additional measurement without

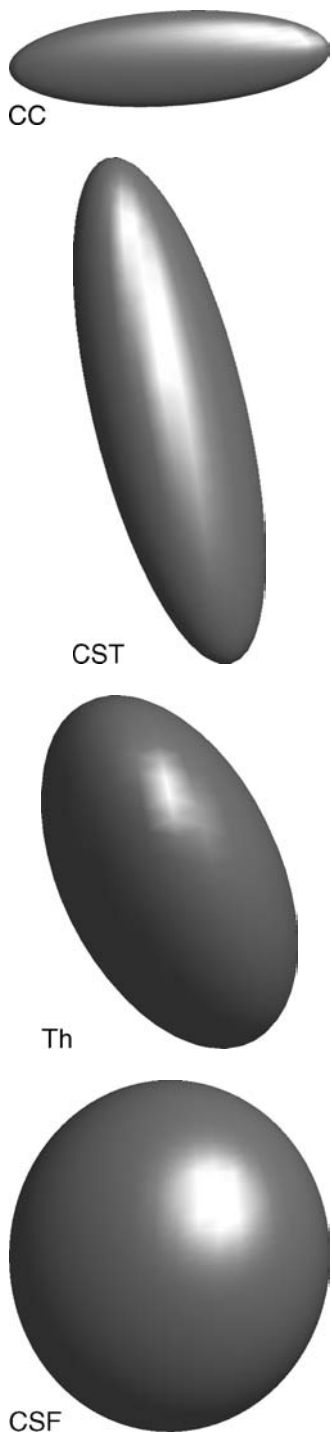


Figure 5 Diffusion ellipsoids corresponding to the regions indicated in Figure 7, displayed in a coronal view. CC, FA = 0.761; CST (right), FA = 0.681; Th (right), FA = 0.300; CSF, FA < 0.200. Abbreviations: CC, genu of corpus callosum; FA, fractional anisotropy; CST, corticospinal tract; Th, thalamus; CSF, cerebrospinal fluid.

diffusion weighting is also required to eliminate the S_0 term in the signal equation.

Measuring diffusion in different directions is quite straightforward. Varying the axes on which the diffusion-weighting gradients are applied changes the component of the water molecules' motion to which we are sensitive. With suitable combinations of these gradients on the three axes, we can measure motion in any arbitrary direction. The range of directions should be evenly distributed to minimize any possible angular bias in the results obtained. Much work has been done to optimize the choice of directions, although there is still significant debate over the best choice (7).

Standard mathematical techniques are used to calculate the components of the diffusion tensor at every voxel within the imaging volume (8,9). This computation is substantial, given that a high-resolution diffusion tensor imaging (DTI) data set can contain several million voxels. Fortunately modern computers are capable of handling such calculations quite rapidly. It is important that the processing takes into account the strength of the signal and noise in each measurement when fitting the tensor to the data (5,10).

Quantities Derived from the Diffusion Tensor

The diffusion tensor includes information about both the magnitude of diffusion and its directional dependence. Initial processing usually involves separating the parts of the tensor that depend on the patient orientation within the MRI scanner from the more intrinsic properties, which are independent. The latter are referred to as "frame-independent" quantities or "invariants."

Figure 6 illustrates the diffusion tensor as an ellipsoid. The quantities λ_1 , λ_2 , and λ_3 represent the major and minor

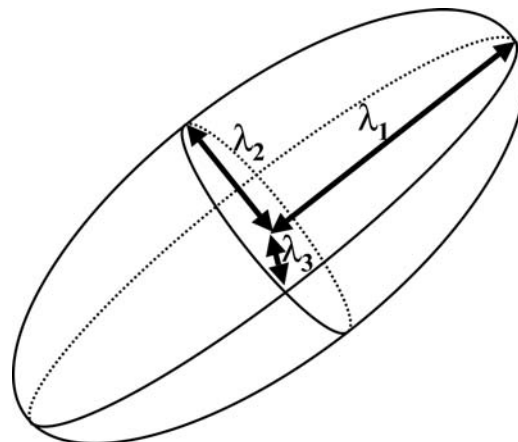


Figure 6 Illustration of the diffusion ellipsoid. λ_1 , λ_2 , and λ_3 are the major and minor axes of the ellipsoid and correspond to the eigenvalues of the diffusion tensor. The direction of each axis is the corresponding eigenvector. The principal eigenvector (the long axis, λ_1) is of particular interest because it represents the predominant fiber orientation within each voxel and is the basis of diffusion tractography.

axes of the ellipsoid, and do not depend on its orientation. Hence, these quantities and any other values that can be derived from them must also be frame invariant.

Mathematically, λ_1 , λ_2 , and λ_3 are the eigenvalues of the diffusion tensor, and their directions (which are of course frame-dependent) are the corresponding eigenvectors. The eigenvalues and eigenvectors may be readily calculated from the diffusion tensor using a standard mathematical technique called “matrix diagonalization.”

The most common parameter that is calculated is a measure of the average diffusion over all directions. This is often referred to as the ADC. However, to indicate explicitly that this is the average value over all directions, we use the symbol D_{av} .

$$D_{av} = \frac{D_{xx} + D_{yy} + D_{zz}}{3} = \frac{\lambda_1 + \lambda_2 + \lambda_3}{3}$$

A related property is the trace of the diffusion tensor, which is the sum of D_{xx} , D_{yy} , and D_{zz} (and equal to $3D_{av}$). In fact we do not need to calculate the entire tensor to derive D_{av} —only the diagonal elements are required. Calculation of D_{av} requires measurements along the three axes and an additional measurement without diffusion weighting. The term “diffusion-weighted imaging” is commonly used to describe the acquisition of this limited data set. The distinction between diffusion-weighted imaging and DTI is only in the number of directions that are required, with a minimum of six for DTI. The data acquisition is otherwise identical.

Another important frame-independent parameter that may be obtained from the diffusion tensor is the degree of angular variation (anisotropy). A commonly used measure is the fractional anisotropy (FA), although other related measures such as relative anisotropy (RA) and volume ratio (VR) are sometimes used (11). The FA is defined as

$$FA = \sqrt{\frac{3}{2}} \cdot \sqrt{\frac{(\lambda_1 - D_{av})^2 + (\lambda_2 - D_{av})^2 + (\lambda_3 - D_{av})^2}{(\lambda_1^2 + \lambda_2^2 + \lambda_3^2)}}$$

FA values can vary between zero and one, where zero represents isotropic diffusion ($\lambda_1 = \lambda_2 = \lambda_3 = D_{av}$ and the diffusion ellipsoid is a sphere) and one represents diffusion in a single direction only ($\lambda_1 > 0$, $\lambda_2 = \lambda_3 = 0$, and the diffusion ellipsoid is a thin cigar-like shape).

Visualization of Diffusion Tensor Data

Diffusion tensor data suffer from an embarrassment of riches. There is too much information at each voxel to be visualized in a single grayscale image. Most of the important information in the tensor can be summarized in three quantities:

- The average diffusion constant, D_{av} .
- The fractional anisotropy, FA.

- The direction of maximum diffusion (principal eigenvector).

Worse, the direction of maximum diffusion is a vector quantity and requires three numbers to be specified to uniquely identify it in three dimensions.

A common method of visualization uses color to denote the direction and the brightness to represent the anisotropy. The three primary colors red, green, and blue correspond to the right-left, anterior-posterior, and superior-inferior directions, respectively. Combinations of these colors represent directions not aligned with the axes of our coordinate system. For example, yellow is a combination of red and green, so corresponds to a direction from right anterior to left posterior (although this is ambiguous because left-anterior to right-posterior is represented by the same color).

Figure 7 shows an example of a color map showing both the degree and direction of anisotropy at each voxel. The use of color allows tracts that pass close to each other but in different directions to be easily distinguished. An alternative visualization is shown in Figure 8, with the entire diffusion ellipsoid represented. This technique does not require the reader to interpret colors as directions, but due to the large number of ellipsoids displayed, each must be small, and the use of a high-resolution display is essential.

DIFFUSION TRACTOGRAPHY

While most quantitative analysis is based primarily on the frame-invariant properties of the tensor, the remaining directional information is also extremely useful, and provides the only noninvasive method to follow white matter fiber tracts, a technique known as diffusion tractography.

The principal eigenvector of the diffusion tensor represents the long axis of the diffusion ellipsoid and is assumed to correspond to the predominant fiber orientation. Since this direction can be calculated at each voxel, this allows us to follow white matter pathways from one part of the brain to another.

One of the simplest methods for tractography is “fiber assignment by continuous tracking” (FACT), and is illustrated in Figure 9. In this method, a seed point is first chosen within the white matter tract to be followed. The tracking algorithm then starts traveling in the direction of the principal eigenvector of the current voxel until the edge of the voxel is met. At that point, the line abruptly changes direction to that of the new voxel. This process repeats until the current voxel is no longer sufficiently anisotropic that the fiber orientation can be confidently determined. A threshold anisotropy is often defined, such that when the tracking leaves the white matter, the

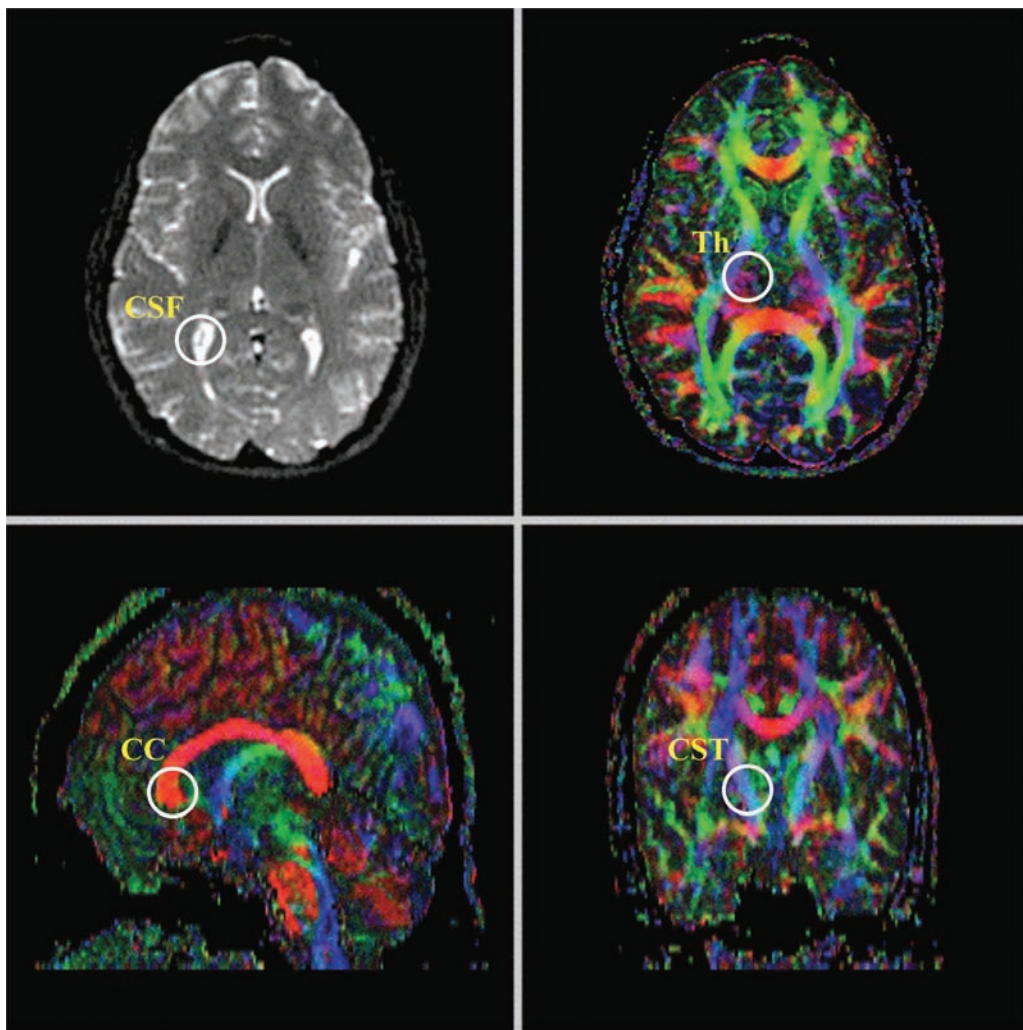


Figure 7 Axial, sagittal, and coronal color DTI maps. The color corresponds to the direction of maximum diffusion (white matter fiber orientation) and the brightness to the FA. (top-left) T₂-weighted image for comparison. The CSTs (blue, superior-inferior) can be clearly distinguished from CC (red, right-left) and optical radiations (green, anterior-posterior) by the addition of the directional information. Circles indicate regions of the genu of CC, CST, and thalamus used to generate the diffusion ellipsoids shown in Figure 5. Abbreviations: FA, fractional anisotropy; DTI, diffusion tensor imaging; CC, corpus callosum; CST, corticospinal tracts

anisotropy drops below this value and the tracking stops. A flowchart of a simplified FACT algorithm is shown in Figure 10.

It should be noted that the diffusion tensor only provides an axis of maximum diffusion, rather than a direction. Diffusion is symmetric, such that (for example) high diffusion in the +x-direction implies an equally high diffusion in the -x-direction. In practice, this ambiguity is not problematic because we can assume that as the tracking algorithm moves from one voxel to the next, the fiber does not change direction by more than 90°, resolving this degeneracy. From the seed point, two tracks are followed, starting from the same location, but traveling in opposite directions. These tracks may be combined

to give a single pathway that passes through the seed point.

The choice of seed point location, the density of seed points, and the threshold anisotropy determine the pathways that are visualized. Selecting seed points uniformly throughout the entire brain shows all the major fiber tracts (Fig. 11, top row), although it is difficult to distinguish one tract from another. To limit the computational cost of calculating and displaying such a large number of pathways, the density of seed points may be quite low and some of the less major fiber tracts may be missed.

To be more selective, seed point regions can be defined through which the fibers of interest are known to pass. For example, since corpus callosum is one of few structures

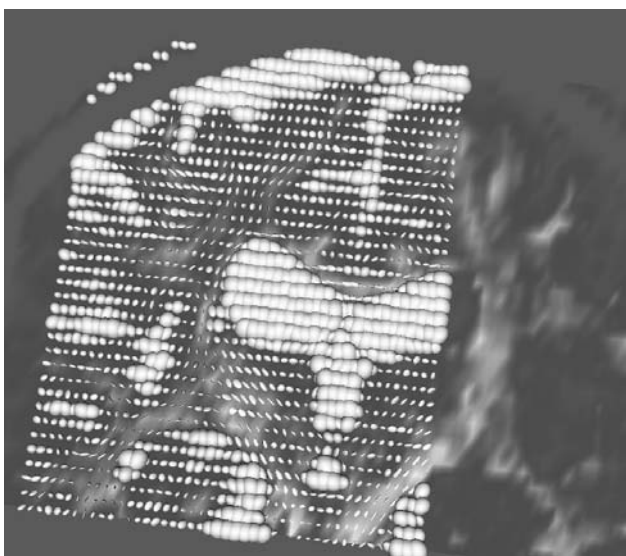


Figure 8 Representation of the diffusion tensor in the brain by ellipsoids. The ellipsoids in the corticospinal tract show a high degree of diffusion anisotropy (*prolate ellipsoids*), with their axis corresponding to the direction of the fibers. Cerebrospinal fluid (*shown as large spheres*) displays a high degree of diffusion, which is almost isotropic because there are few restrictions on motion. *Source:* Image courtesy P.R. Smale, University of Auckland, New Zealand.

that cross between the cerebral hemispheres, it can be tracked by simply defining a rectangular region of seed points on a midsagittal view. Similarly, fiber tracking of the corticospinal tracts can be performed by defining seed regions encompassing the posterior limb of the internal capsule on an axial view (12,13). Since these regions are small, it is appropriate to use a high density of seed points. It should be noted that seed points which start in the same voxel may later diverge, allowing us to follow branching fibers (illustrated in Fig. 9, tracks 1 and 2). Figure 11 (middle) shows an example of tracking corpus callosum and the corticospinal tracts.

In situations where the seed region contains multiple fiber bundles, of which only some are of interest, it may also be useful to define destination volumes. In this case, only those pathways that start at the seed points and pass through the destination volumes are displayed. A natural extension of this is to use the Boolean operators (such as *AND*, *OR*, and *NOT*) to define which tracts are to be displayed. For example, a particular fiber may be identified by noting that it starts from region **A** *AND* passes through region **B**, but *NOT* through region **C**. This has been used by Wakana et al. to define an atlas of white matter tractography (14). Figure 12 shows examples of the use of seed and destination volumes to define various tracts.

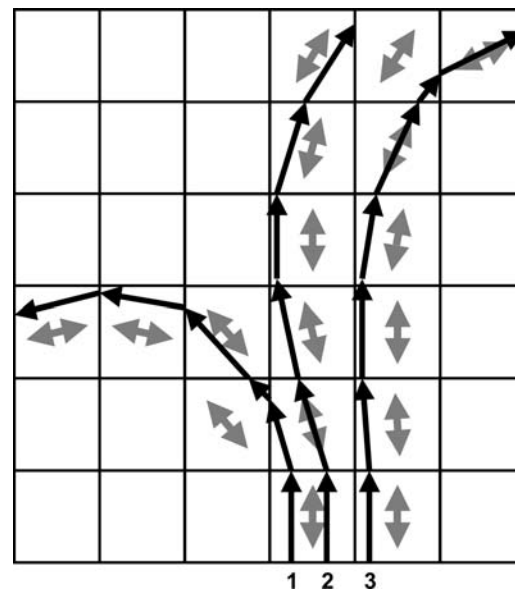


Figure 9 An illustration of the FACT-tracking algorithm (43). The double-headed gray arrows indicate the axis of maximum diffusion in each voxel, which is assumed to correspond to the fiber orientation. Each track follows the direction of maximum diffusion in each voxel and abruptly changes direction when it enters the next voxel. Seed points starting from the same voxel (for example, **1** and **2**) can diverge, allowing branching fibers to be visualized. A high density of seed points may be required to ensure that as many paths as possible are generated by the algorithm. *Abbreviation:* FACT, fiber assignment by continuous tracking.

Incorporating additional anatomical information into the fiber tracking may improve the reliability of the results obtained. For instance, it may be assumed that fibers within the human brain do not abruptly (on the voxel scale) change direction. This allows us to define a minimum radius of curvature of the pathways and to reject sudden directional changes from one voxel to the next. Tractography algorithms that are based on continuous trajectories through the diffusion tensor data set may be less susceptible to the effects of noise and uncertainty in the direction of the principal eigenvector (15).

LOOKING TO THE FUTURE

Many techniques that are currently used in research centers are likely to be used in routine clinical practice in the future. General improvements in MRI technology such as higher magnetic field scanners, stronger gradients, and more use of parallel imaging are likely to increase both image resolution and signal-to-noise ratio. However, there are other improvements, which may more specifically improve diffusion imaging.

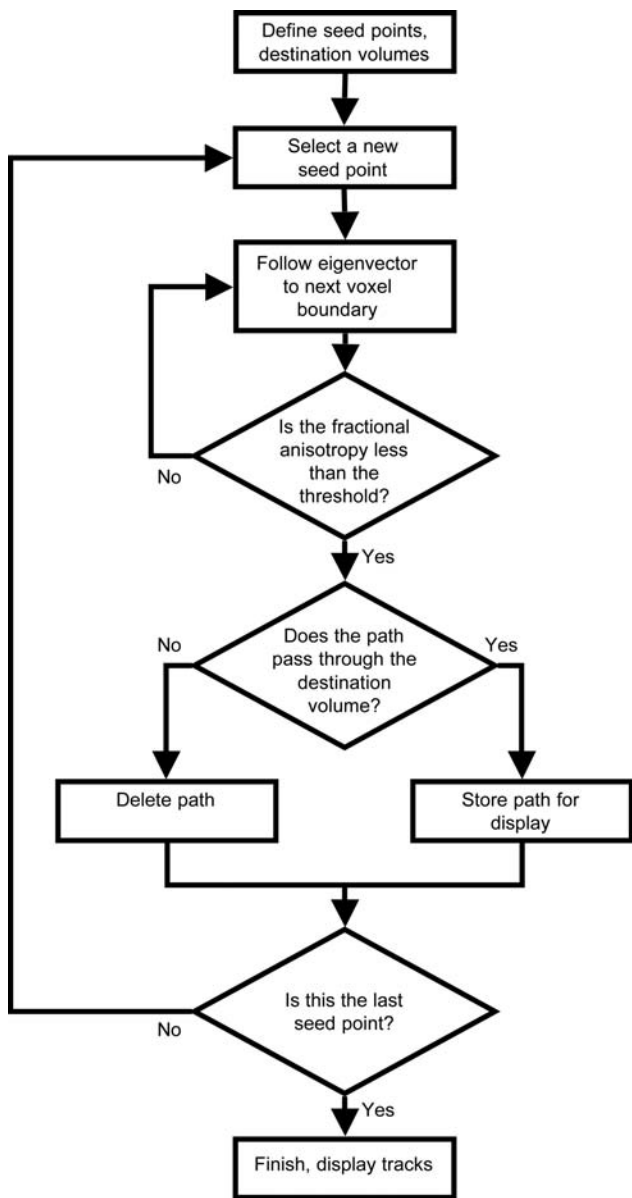


Figure 10 Flowchart for diffusion tractography. Additional options such as limiting the radius of curvature of the path and tracking in both directions from the seed point may be incorporated.

Data Acquisition

Most diffusion-weighted images are currently acquired using single-shot EPI-based techniques. These methods have the advantage that the (magnitude) signal is unaffected by coherent motion such as small-scale patient movement. However, single-shot EPI is limited in the resolution that can be attained because all the data for a single image must be acquired before T_2 and T_{2^*} losses destroy the MR signal. Additionally, magnetic field inhomogeneities cause EPI distortion and may be particularly severe near air-tissue interfaces such as the sinuses. These distortions may cause substantial problems, particularly in tractography of the brain stem and spinal cord.

EPI may be corrected for distortion using various techniques, including field mapping (16) and reversed-gradient acquisitions (17). The length of the EPI readout can also be reduced using parallel-imaging techniques such as SENSE (SENSitivity Encoding) (18). This has the dual advantage that both the signal dropout due to T_2 and T_{2^*} and the distortion are reduced, but it comes at a cost of decreased signal-to-noise ratio (19,20). Single-shot spiral acquisitions may be more efficient and introduce less obvious artifacts than conventional EPI, but are still limited in their resolution.

Multishot techniques require a combination of navigator data and cardiac gating to correct for motion. New techniques based on Periodically Rotated Overlapping Parallel Lines with Enhanced Reconstruction (PROPELLER) (21,22) and spiral-EPI [Self-Navigated Interleaved Spirals (SNAILS)] (23,24) use oversampling of the center of k space to determine and correct for the effects of coherent motion and may allow high-resolution diffusion imaging in a clinically acceptable time.

Beyond the Diffusion Tensor

The diffusion tensor model does not provide a perfect description of water diffusion in the brain. In particular, it is assumed that all the water molecules in a particular voxel exist in a similar physical and chemical environment. In practice, water exists in a variety of environments, notably intracellular and extracellular; what we measure in DTI is an average of these compartments (25). A variety of techniques have been developed to better model these more complicated (and more realistic) situations. A particularly elegant approach is that of q-space imaging (26), in which the probability distribution of the water displacements can be directly calculated. This allows estimates of the sizes and contributions of these multiple compartments to be determined with few assumptions.

Additionally, some voxels may contain several bundles of fibers that are oriented in different directions, particularly in those parts of the brain where fibers cross (27), as illustrated in Figure 13. Diffusion within such voxels cannot be accurately modeled using a single ellipsoid (tensor). To determine the more complicated angular variation in such cases requires a substantial increase in the number of diffusion directions that must be measured—high-angular resolution diffusion (HARD) imaging (27–29). More complicated models must then be used to fit the measured angular distribution.

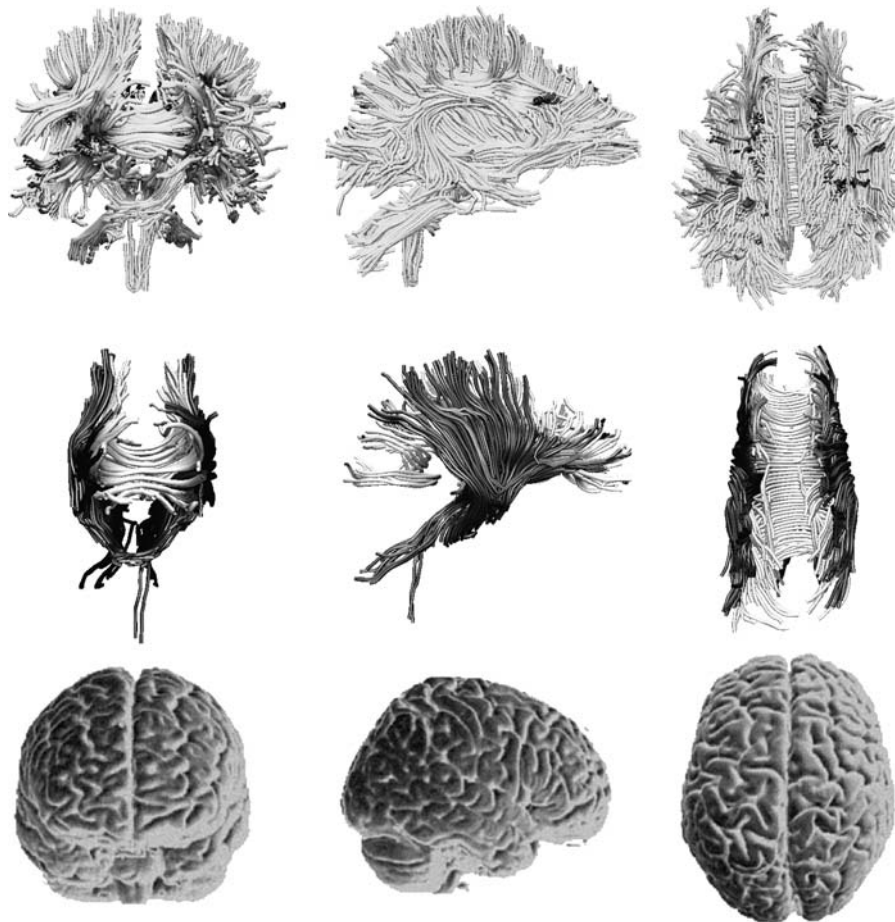


Figure 11 Examples of fiber tracking, viewed in coronal, sagittal, and axial projections. (*top*) Fiber tracking of the entire brain, (*middle*) selective tracking of CC (*light*) and the CSTs (*dark*), and (*bottom*) corresponding surface rendered views indicating the orientation of each tractogram. Abbreviations; CC, corpus callosum; CST, corticospinal tract.

However, all of these more complicated, more realistic models have one feature in common: they have more parameters that need to be determined and require more measurements to be made. The increased acquisition time has limited their application to clinical imaging. While it is far from perfect, the diffusion tensor model represents a good compromise between accuracy and measurement time.

Quantitative DTI

Unlike most MRI techniques used for clinical imaging, DTI produces parameters at each voxel that have physical meaning and may be compared across subjects and (to a lesser extent) across MRI scanners. The reason why DTI is quantitative is that in the calculation of the tensor, it is the *ratio* of the signal strengths that is important, not the absolute values. All the additional parameters such as proton density, T_2 , and the scanner settings are the same

for each measurement (these form the S_0 term in the signal equation), so do not affect this ratio.

The quantitative nature of DTI allows us to determine normative values for average diffusion and FA to compare to individuals' parameters. The analysis of DTI data can be performed on a global (whole brain), regional, or voxel-by-voxel basis. The most appropriate method depends upon the disease pathology and whether we have *a priori* knowledge of the disease distribution.

Global analysis of diffusion changes over the entire brain is straightforward and can be automated. Segmentation of tissue and CSF can be achieved by histogram analysis because of their very different diffusion values. The diffusion constant at each voxel is assigned a bin based on its value, and the number of voxels in each bin is plotted as a histogram. Ulug has shown that the histogram is usually well fitted as a sum of three Gaussian distributions that represent tissue, CSF, and voxels containing a mixture of the two (partial voluming) (30). The position and width of the Gaussian corresponding to the tissue

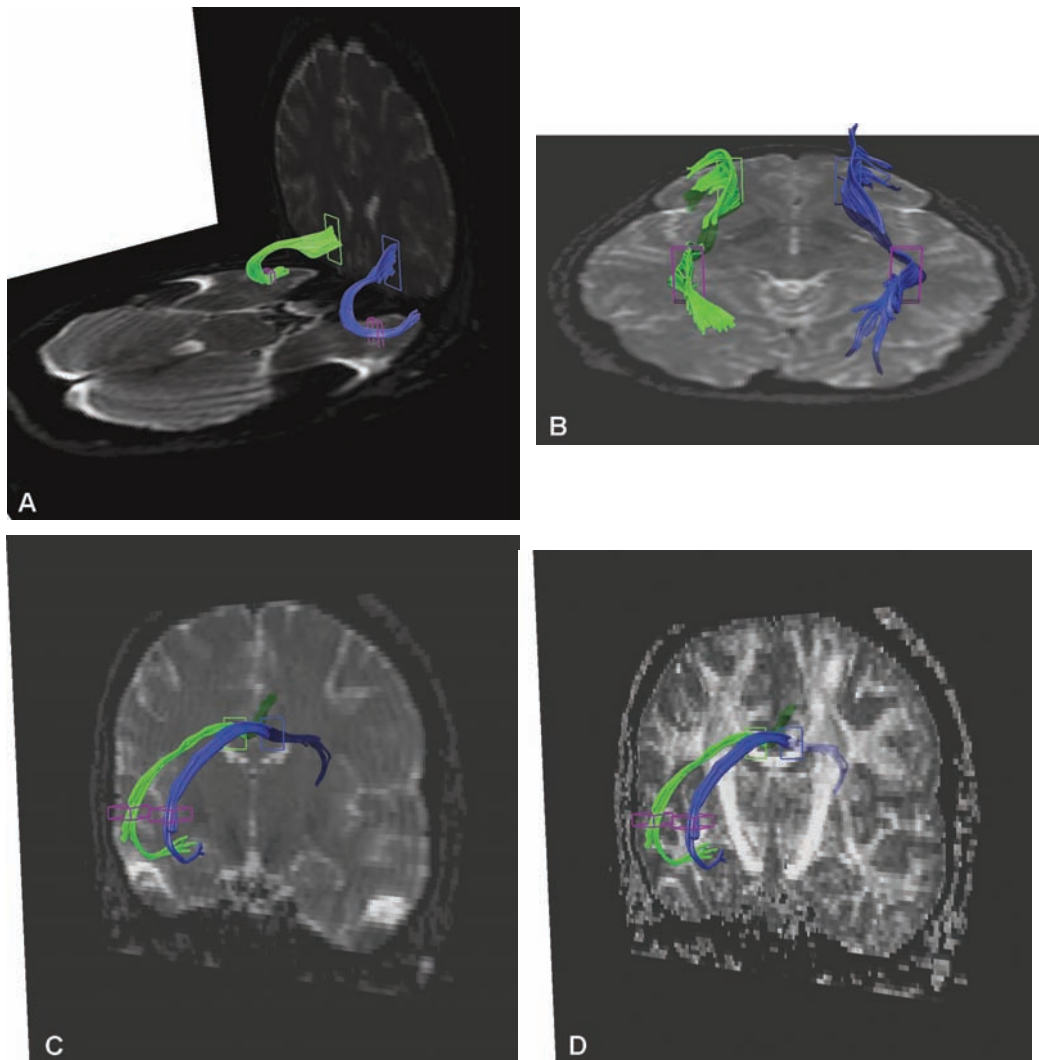


Figure 12 Examples of fiber tracking. (A) uncinate fasciculus, (B) inferior fronto-occipital fasciculus, (C, D) cingulum bundles overlaid onto coronal T₂ and FA slices, respectively, with the latter showing the fibers passing over the top of CC. In each image the seed regions are shown as boxes in the same color as the tracts, while the destination volumes are shown in purple. Abbreviations: FA, fractional anisotropy; CC, corpus callosum.

contribution is a sensitive measure and has been successfully applied to the diagnosis of hydrocephalus (31) and head injuries (32).

Region-of-interest (ROI) analysis considers the distribution of measures within preselected regions of the brain. These regions can be defined manually based on anatomical knowledge or automatically based on comparison of the individual with a segmented template brain. The accuracy of ROI-based techniques relies on consistent definitions of the anatomical areas by experienced observers and prior knowledge of the regions that are likely to be affected. ROI analysis is most sensitive where changes are expected to be limited to well-defined anatomical regions.

Voxel-based analysis (VBA) methods use computational techniques to deform (warp) an individual brain to match a standard template (33,34). Automated tests can then be performed on every voxel within the data set or within a predefined region. VBA has the advantages of allowing a fully automated objective spatial analysis without requiring prior knowledge of the likely distribution of disease. The reliability of the imaging warping procedure is open to question. An important weakness in VBA is the problem of multiple comparisons when the number of voxels that are tested is large (which is normally the case). The simplest way to account for this is using a Bonferroni correction in which the threshold significance is reduced

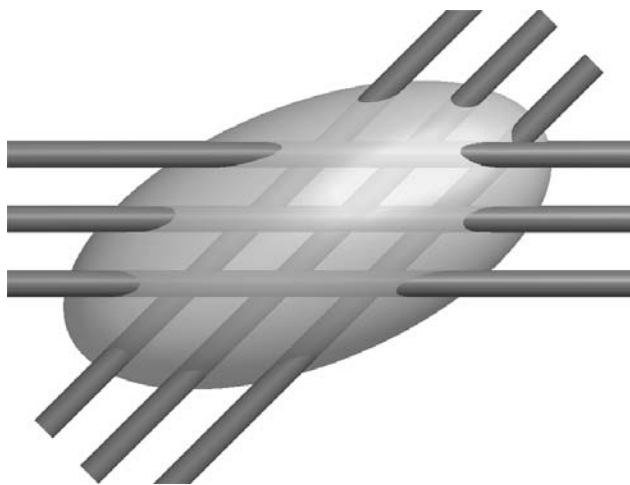


Figure 13 Illustration of crossing fibers. In this case the diffusion ellipsoid cannot accurately represent both the fiber orientations, but instead a combination the two fiber groups within the voxel. The long axis of the ellipsoid may not correspond to either of the individual tract orientations. This represents a significant limitation on, although more complex models have been proposed for such situations. Abbreviation: DTI, diffusion tensor imaging.

by the number of tests performed. However, this test is very strict, and more complex corrections based on the statistics of clusters of voxels may be more appropriate.

Tractography Techniques

While diffusion tractography has produced spectacular images, with generally good agreement with anatomical studies (12,13), quantification of connectivity remains difficult. For example, if a tract cannot be followed then it is unclear whether this is due to damage to the fiber concerned or simply inadequate data or poor tractography. There is a temptation to regard tractograms as representing individual fibers. This is emphatically not the case—and there is little prospect of MRI attaining the resolution required to image a single axon. The streamlines shown in Figure 10 and 11 represent pathways through the diffusion tensor data set, which may (or may not) correspond to bundles of fibers. While generating a large number of pathways between two regions may suggest that the tracking is robust, it is a rather large leap to suggest that more pathways necessarily correspond to more axons.

However, attempts have been made to quantify the results of diffusion tractography. In particular, models have been developed that can yield a probability of two regions being connected. This has been successfully applied to mapping connections from the thalamus to the cortex (35).

Combining Diffusion Tractography and Functional MRI

Functional MRI (fMRI) and diffusion tensor MRI form a powerful combination, which has yet to be fully exploited. fMRI is capable of identifying the functionally eloquent parts of the brain, while diffusion tractography allows connections between brain regions to be determined. Areas determined by fMRI can then be used as seed regions for subsequent tractography (36–38). This combination of function and structure allows both the white and the gray matter to be examined as a complete system in a single examination.

CONCLUSION

Diffusion tensor MRI provides new diagnostic information on the basis of the microscopic motion of water molecules. This has found applications to a wide range of neurological problems, including monitoring age-related changes in both children (39,40) and the elderly (30), stroke (41), hydrocephalus (31), ALS (42), and head injuries (32). The determination of quantitative parameters such as the average diffusion constant and the FA provide sensitive information about microscopic structure, while diffusion tractography provides unique *in vivo* information about brain connectivity.

REFERENCES

1. Einstein A. The motion of elements suspended in static liquids as claimed in the molecular kinetic theory of heat. Annalen Der Physik 1905; 17:549–560.
2. Stejskal EO, Tanner JE. Spin Diffusion Measurements—Spin echoes in presence of a time-dependent field gradient. J Chem Phys 1965; 42:288.
3. Bernstein MA, King KF, Zhou XJ. Handbook of MRI pulse sequences. New York: Elsevier Academic Press, 2004.
4. Le Bihan D. Diffusion and perfusion magnetic resonance imaging: Applications to functional MRI. New York: Raven Press, 1995.
5. Jones DK, Basser PJ. “Squashing peanuts and smashing pumpkins”: how noise distorts diffusion-weighted MR data. Magn Reson Med 2004; 52:979–993.
6. Jones DK, Williams SC, Gasston D, et al. Isotropic resolution diffusion tensor imaging with whole brain acquisition in a clinically acceptable time. Hum Brain Mapp 2002; 15:216–230.
7. Jones DK. The effect of gradient sampling schemes on measures derived from diffusion tensor MRI: a Monte Carlo study. Magn Reson Med 2004; 51:807–815.
8. Basser PJ, Mattiello J, LeBihan D. Estimation of the effective self-diffusion tensor from the NMR spin echo. J Magn Reson B 1994; 103:247–254.

9. Basser PJ, Mattiello J, LeBihan D. MR diffusion tensor spectroscopy and imaging. *Biophys J* 1994; 66:259–267.
10. Chang LC, Jones DK, Pierpaoli C. RESTORE: robust estimation of tensors by outlier rejection. *Magn Reson Med* 2005; 53:1088–1095.
11. Ulug AM, van Zijl PC. Orientation-independent diffusion imaging without tensor diagonalization: anisotropy definitions based on physical attributes of the diffusion ellipsoid. *J Magn Reson Imaging* 1999; 9:804–813.
12. Holodny AI, Gor DM, Watts R, et al. Diffusion-tensor MR tractography of somatotopic organization of corticospinal tracts in the internal capsule: initial anatomic results in contradistinction to prior reports. *Radiology* 2005; 234:649–653.
13. Holodny AI, Watts R, Korneinko VN, et al. Diffusion tensor tractography of the motor white matter tracts in man: current controversies and future directions. *White Matter in Cognitive Neuroscience: advances in Diffusion Tensor Imaging and its applications*. Ann N Y Acad Sci 2005; 1064:88–97.
14. Wakana S, Jiang H, Nagae-Poetscher LM, et al. Fiber tract-based atlas of human white matter anatomy. *Radiology* 2004; 230:77–87.
15. Lazar M, Weinstein DM, Tsuruda JS, et al. White matter tractography using diffusion tensor deflection. *Hum Brain Mapp* 2003; 18:306–321.
16. Jezzard P, Balaban RS. Correction for geometric distortion in echo planar images from B0 field variations. *Magn Reson Med* 1995; 34:65–73.
17. Voss HU, Watts R, Ulug AM, et al. Fiber tracking in the cervical spine and inferior brain regions with reversed gradient diffusion tensor imaging. *Magn Reson Imaging* 2006; 24:231–239.
18. Pruessmann KP, Weiger M, Scheidegger MB, et al. SENSE: sensitivity encoding for fast MRI. *Magn Reson Med* 1999; 42:952–962.
19. Jaermann T, Crelier G, Pruessmann KP, et al. SENSE-DTI at 3 T. *Magn Reson Med* 2004; 51:230–236.
20. Jaermann T, Pruessmann KP, Valavanis A, et al. Influence of SENSE on image properties in high-resolution single-shot echo-planar DTI. *Magn Reson Med* 2006; 55:335–342.
21. Pipe JG, Farthing VG, Forbes KP. Multishot diffusion-weighted FSE using PROPELLER MRI. *Magn Reson Med* 2002; 47:42–52.
22. Pipe JG. Motion correction with PROPELLER MRI: application to head motion and free-breathing cardiac imaging. *Magn Reson Med* 1999; 42:963–969.
23. Li TQ, Kim DH, Moseley ME. High-resolution diffusion-weighted imaging with interleaved variable-density spiral acquisitions. *J Magn Reson Imaging* 2005; 21:468–475.
24. Liu C, Bammer R, Kim DH, et al. Self-navigated interleaved spiral (SNAILS): application to high-resolution diffusion tensor imaging. *Magn Reson Med* 2004; 52:1388–1396.
25. Clark CA, Hedenus M, Moseley ME. In vivo mapping of the fast and slow diffusion tensors in human brain. *Magn Reson Med* 2002; 47:623–628.
26. Callaghan PT. Principles of NMR microscopy. Oxford: Oxford University Press, 1993.
27. Hirsch JG, Schwenk S, Rossmanith C, et al. Identification of regions with a high proportion of crossing fibres in the human white matter with high angular resolution diffusion-weighted imaging. *Rivista Di Neuroradiologia* 2003; 16:1076–1078.
28. Frank LR. Anisotropy in high angular resolution diffusion-weighted MRI. *Magn Reson Med* 2001; 45:935–939.
29. Zhan W, Gu H, Xu S, et al. Circular spectrum mapping for intravoxel fiber structures based on high angular resolution apparent diffusion coefficients. *Magn Reson Med* 2003; 49:1077–1088.
30. Chun T, Filippi CG, Zimmerman RD, et al. Diffusion changes in the aging human brain. *AJNR Am J Neuroradiol* 2000; 21:1078–1083.
31. Ulug AM, Truong TN, Filippi CG, et al. Diffusion imaging in obstructive hydrocephalus. *AJNR Am J Neuroradiol* 2003; 24:1171–1176.
32. Zhang L, Ravdin LD, Relkin N, et al. Increased diffusion in the brain of professional boxers: a preclinical sign of traumatic brain injury? *AJNR Am J Neuroradiol* 2003; 24:52–57.
33. Ashburner J, Friston KJ. Nonlinear spatial normalization using basis functions. *Hum Brain Mapp* 1999; 7:254–266.
34. Jones DK, Griffin LD, Alexander DC, et al. Spatial normalization and averaging of diffusion tensor MRI data sets. *Neuroimage* 2002; 17:592–617.
35. Behrens TE, Woolrich MW, Jenkinson M, et al. Characterization and propagation of uncertainty in diffusion-weighted MR imaging. *Magn Reson Med* 2003; 50: 1077–1088.
36. Holodny AI, Ollenschleger MD, Liu WC, et al. Identification of the corticospinal tracts achieved using blood-oxygen-level-dependent and diffusion functional MR imaging in patients with brain tumors. *AJNR Am J Neuroradiol* 2001; 22:83–88.
37. Parmar H, Sitoh YY, Yeo TT. Combined magnetic resonance tractography and functional magnetic resonance imaging in evaluation of brain tumors involving the motor system. *J Comput Assist Tomogr* 2004; 28:551–556.
38. Watts R, Holodny AI, Filippi CG, et al. Somatotopic organization of motor fibers in the corticospinal tract: a combined fMRI and DTI study. *Proceedings, International Society for Magnetic Resonance in Medicine*, 2003.
39. Casey BJ. Neuroscience. Windows into the human brain. *Science* 2002; 296:1408–1409.
40. Filippi CG, Lin DDM, Tsioris AJ, et al. Diffusion-tensor MR imaging in children with developmental delay: preliminary findings. *Radiology* 2003; 229:44–50.
41. Heller SL, Heier LA, Watts R, et al. Evidence of cerebral reorganization following perinatal stroke demonstrated with fMRI and DTI tractography. *Clin Imaging* 2005; 29:283–287.
42. Ulug AM, Watts R, Hays AP. Magnetic resonance (MR) diffusion tensor imaging (DTI) detects widespread frontal lobe involvement in ALS. *Neurology* 2005; 64: A140–A141.
43. Mori S, Crain BJ, Chacko VP, et al. Three-dimensional tracking of axonal projections in the brain by magnetic resonance imaging. *Ann Neurol* 1999; 45:265–269.

12

Diffusion-Weighted Imaging in Stroke

PAMELA W. SCHAEFER and WILLIAM A. COPEN

*Department of Radiology, Division of Neuroradiology, Massachusetts General Hospital,
Boston, Massachusetts, U.S.A.*

INTRODUCTION

Diffusion magnetic resonance imaging provides image contrast that is dependent on the molecular motion of water and therefore provides unique information on the state of brain parenchyma as it responds to acute ischemia. Because it employs ultrafast, echo planar MRI scanning, with imaging times ranging from a few seconds to two minutes, it is generally forgiving of patient motion. The characteristic changes in diffusion that occur in acute infarctions often enable diffusion-weighted images (DWI) to detect lesions that would not be detected by any other imaging technique. Diffusion MRI has therefore assumed an essential role in the detection of acute ischemic brain infarction and in differentiating acute infarction from other disease processes.

This chapter begins with a brief review of the biophysical basis for the changes in diffusion associated with acute stroke followed by a description of the appearance of ischemic lesions as they evolve on diffusion MR images. Subsequently, the reliability of diffusion MR imaging, the concept of the DWI lesion as representing the infarct core, the rare recovery of DWI hyperintense ischemic tissue, the use of diffusion imaging to predict hemorrhagic transformation, the potential of diffusion tensor imaging, and the correlation of the DWI lesion with clinical stroke scales are discussed. Finally, we

address the utility of DWI in differentiating acute ischemic stroke from diseases that mimic stroke clinically and on CT and conventional MR images.

THEORY FOR RESTRICTED DIFFUSION IN ACUTE STROKE

The biophysical basis for the rapid decrease in diffusion coefficients in acutely ischemic brain tissue is complex (Table 1) (1–4). Approximately 80% of the volume of gray matter is occupied by cells, with the remaining 20% composed of the interstitial and intraluminal spaces. The intracellular space and the interstitial space differ with respect to their concentrations of various ionic species, and these differences are maintained by energy-dependent membrane ion pumps, of which the best known is the sodium-potassium ATPase pump. The operation of membrane ion pumps is dependent on cellular synthesis of adenosine triphosphate (ATP) and other high-energy phosphate compounds, which in turn requires delivery of oxygen and metabolic fuel. The collective effect of energy-dependent ion pumps is to extrude ions from the intracellular space and deposit them in the extracellular interstitial space.

With acute ischemia, ATP concentrations fall and Na^+/K^+ ATPase and other ionic pumps fail (4–6). There is a net transfer of ions from the extracellular

Table 1 Theories for Decreased Diffusion in Acute Stroke

Number	Theory
1.	Failure of Na^+/K^+ ATPase and other ionic pumps with loss of ionic gradients and net transfer of water from the extracellular to the intracellular compartment, where cellular organelles, cytoskeletal macromolecules, and other structures are barriers to the random motion of water molecules.
2.	Reduced extracellular space volume and increased extracellular space pathway tortuosity due to cell swelling.
3.	Increased intracellular space viscosity and tortuosity from fragmentation of cellular components such as microtubules.
4.	Decreased cytoplasmic mobility.
5.	Increased cell membrane permeability.
6.	Temperature decrease.

space to the intracellular space. Water follows the ions by osmosis, resulting in cellular swelling or cytotoxic edema. Several reasons have been proposed to explain the restriction of diffusion [decrease in the apparent diffusion coefficient (ADC)] that is observed in cytotoxic edema. The first is related to the difference in ADC that exists between the intracellular and extracellular spaces. In the intracellular space, cellular organelles, cytoskeletal

macromolecules, and other subcellular structures serve as barriers to the random motion of water molecules. In an acute gray matter infarct, cytotoxic edema increases the fraction of water molecules that are in the intracellular space, where diffusion is relatively restricted, from approximately 80% to approximately 95%. Furthermore, cellular swelling leads to a reduction in the extracellular space volume and a consequential increase in the tortuosity of extracellular space pathways (7,8). In addition, ischemic rat brains demonstrate significant reductions in intracellular metabolite ADCs (8–11). Proposed explanations include an increased intracellular viscosity due to dissociation of microtubules and fragmentation of other cellular components due to collapse of the energy-dependent cytoskeleton, increased tortuosity of the intracellular space, and decreased cytoplasmic mobility. Temperature decreases and cell membrane permeability may also play a minor role in explaining ADC reduction in acutely ischemic tissue (11–13).

DIFFUSION MR IMAGES

Chapter 11 outlines the physical principles of diffusion imaging. When evaluating a patient for acute stroke, DWI images and exponential images or ADC maps should be available for review (Fig. 1, Table 2). It is important to understand that the DWI image has T2 contrast as well as

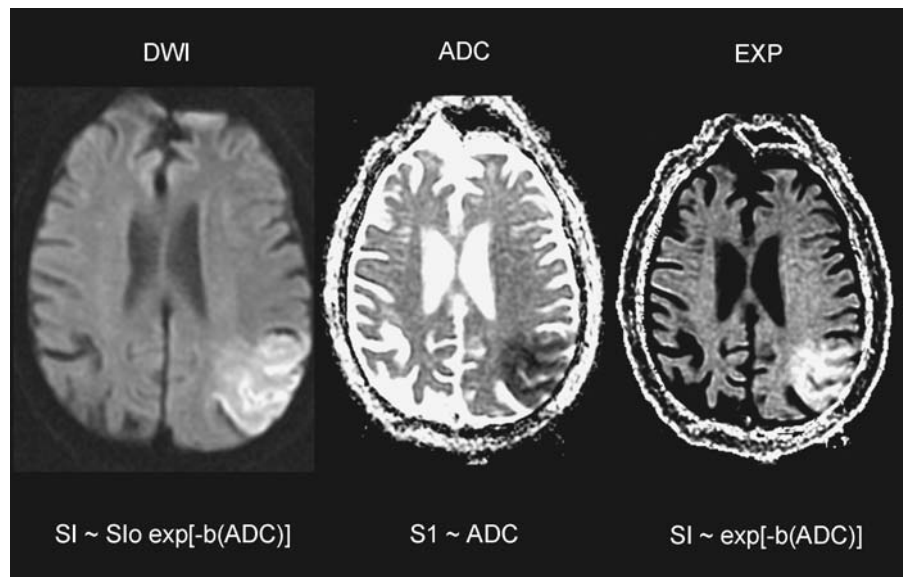


Figure 1 Typical diffusion MR image maps. DWI, ADC map, and EXP images along with the corresponding mathematical expressions for their signal intensities are shown. Image parameters are $b = 1000 \text{ sec/mm}^2$; effective gradient, 25 mT/m; repetition time, 7500 milliseconds; minimum echo time; matrix, 128×128 ; field of view, $200 \times 200 \text{ mm}$; section thickness, 5 mm with 1 mm gap. The acute left parietal stroke has restricted diffusion characterized by hyperintensity on the DWI and EXP images and hypointensity on the ADC maps. Abbreviations: DWI, diffusion-weighted image; ADC, apparent diffusion coefficient; EXP, exponential; SI, signal intensity, S_{Io}, signal intensity on echo planar T2-weighted image.

Table 2 Diffusion MR Image Findings in Stroke

	Hyperacute (0–6 hr)	Acute (6–24 hr)	Early subacute (1–7 days)	Late subacute (7–14 days)	Chronic
Reason for ADC changes	Cytotoxic edema	Cytotoxic edema	Cytotoxic edema with small amount of vasogenic edema	Cytotoxic and vasogenic edema	Gliosis and neuronal loss
DWI	Hyperintense	Hyperintense	Hyperintense, gyral hypointensity from petechial hemorrhage	Hyperintense (due to T2 component)	Isointense to hypointense
ADC EXP	Hypointense	Hypointense	Hypointense	Isointense	Hyperintense
Low b T2	Hyperintense	Hyperintense	Hyperintense	Isointense	Hypointense
FA	Isointense	Hyperintense to hypointense	Hyperintense, gyral hypointensity from petechial hemorrhage	Hyperintense	Hyperintense
			Hypointense	Hypointense	Hypointense

Abbreviations: ADC, apparent diffusion coefficient; DWI, diffusion-weighted images; EXP, exponential; FA, fractional anisotropy.

contrast due to differences in diffusion. To remove the T2 contrast, the DWI can be divided by the echo planar spin-echo (SE) T2 image (or $b = 0$ image), which does not have a diffusion component, to give an exponential image whose signal intensity is exponentially related to the ADC. Alternatively, an ADC map, whose signal intensity is linearly related to the ADC, can be created by taking a logarithm of the exponential image. On DWI images, regions with decreased diffusion are relatively hyperintense. Regions with elevated diffusion [such as the cerebrospinal fluid (CSF) spaces] are usually hypointense but may be isointense, or slightly hyperintense, depending on the strength of the diffusion and T2 components. On ADC maps, regions with decreased diffusion are relatively hypointense, while regions with elevated diffusion are relatively hyperintense. On exponential images, regions with decreased diffusion are relatively hyperintense while lesions with elevated diffusion are relatively hypointense. For lesions with decreased diffusion, the DWI images have superior lesion contrast. However, since hyperintense signal abnormality on DWI images could result from the T2 component rather than from abnormal diffusion, review of the ADC maps or the exponential images is important. The exponential image and ADC map are also useful for detecting areas of increased diffusion that may be masked by T2 effects on the DWI images.

TIME COURSE OF DIFFUSION CHANGES

In animals, following middle cerebral artery (MCA) occlusion, the ADC of ischemic tissue decreases to 16% to 68% below that of normal tissue at 10 minutes to two hours (2,3,14–18). In animals, diffusion coefficients

pseudonormalize (the ADCs are similar to those of normal brain tissue but the tissue is not viable) at approximately 48 hours and are elevated thereafter. In humans, the time course is longer (Fig. 2, Table 2). In humans, restricted diffusion (decreased ADC) in ischemic brain tissue is observed as early as 30 minutes after vascular occlusion (19–22). The ADC continues to decrease with peak signal reduction at one to four days. This restricted diffusion is markedly hyperintense on DWI (a combination of T2 and diffusion weighting), less hyperintense on exponential images, and hypointense on ADC images. Several hours after stroke onset, release of inflammatory mediators from ischemic brain tissue begins to result in increasing extracellular edema. Over time, the ongoing extravasation of water molecules newly delivered via blood vessels expands the interstitial space and results in an increasing number of water molecules whose diffusion is unrestricted. Consequently, after one to four days, the ADC begins to rise and returns to baseline (or pseudonormalizes) at one to two weeks. At this point, a stroke is usually mildly hyperintense on the DWI images due to the T2 component and isointense on the ADC and exponential images. Thereafter, the ADC continues to rise due to continuing increased extracellular water and over months to years, tissue cavitation, and gliosis. There is slight hypointensity, isointensity, or hyperintensity on the DWI images (depending on the strength of the T2 and diffusion components), increased signal intensity on ADC maps, and decreased signal on exponential images.

The time course is influenced by a number of factors including infarct type and patient age (23). Minimum ADC is reached later and transition from decreasing to increasing ADC takes more time in lacunes versus other

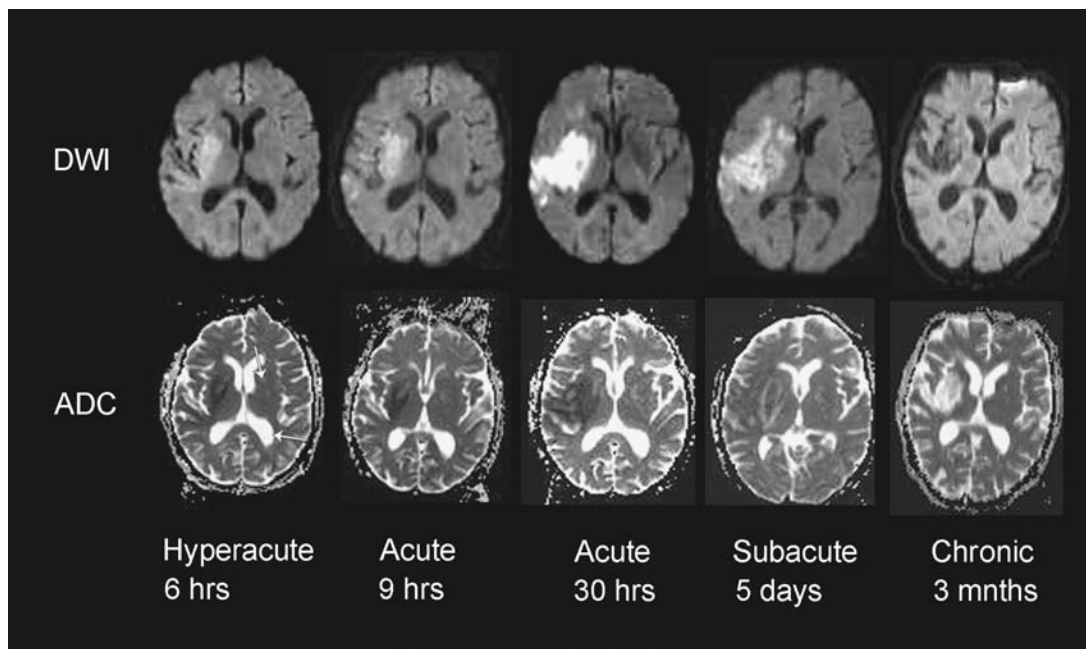


Figure 2 DWI and ADC time course of stroke evolution. Seventy-two-year-old female with atrial fibrillation and acute left hemiparesis. At six and nine hours, the right MCA infarction is mildly hyperintense on DWI and mildly hypointense on ADC images secondary to early cytotoxic edema. By 30 hours, the DWI hyperintensity and ADC hypointensity are pronounced secondary to increased cytotoxic edema. At five days, the infarction is mildly hypointense on ADC images because the ADC has nearly pseudonormalized, secondary to cell lysis and the development of vasogenic edema. The lesion remains markedly hyperintense on the DWI images because the T2 and diffusion components are combined. At three months, the infarction is hypointense on DWI and hyperintense on ADC images, secondary to gliosis and tissue cavitation. Abbreviations: DWI, diffusion-weighted images; ADC, apparent diffusion coefficient; MCA, middle cerebral artery.

stroke types (nonlacunes). In nonlacunes, the subsequent rate of ADC increase is more rapid in younger versus older patients. Early reperfusion may also alter the time course. Early reperfusion causes pseudonormalization as early as one to two days in humans who receive intravenous recombinant tissue plasminogen activator (rtPA) within three hours after stroke onset (24). Furthermore, there are different temporal rates of tissue evolution toward infarction within a single ischemic lesion. Nagesh et al. demonstrated that while the average ADC of an ischemic lesion is depressed within 10 hours, different zones within an ischemic lesion may demonstrate low, pseudonormal, or elevated ADCs (25). Such differences could conceivably reflect different windows of efficacy for thrombolytic or neuroprotective agents. In the absence of thrombolysis, in spite of these variations, tissue with reduced ADC nearly always progresses to infarction.

Although there is great variation in the time course of these ADC changes, it is generally true that infarcts with lower-than-normal ADC are less than approximately two weeks of age and those with low ADC and little or no associated abnormality on T2-weighted images are less than approximately six hours of age.

RELIABILITY OF DIFFUSION MR IMAGES

Conventional CT and MR imaging cannot reliably detect infarction at early time points (less than six hours). Detection of hypoattenuation on CT and hyperintensity on T2-weighted and fluid-attenuated inversion recovery (FLAIR) MR images requires a substantial increase in tissue water due to extracellular edema. However, because there is little extracellular edema present during the first six hours after stroke onset, conventional CT and MR images are not reliable at early time points (Table 3). For infarctions imaged within six hours after stroke onset, reported sensitivities are 38% to 45% for CT and 18% to 46% for MRI (26,27). For infarctions imaged within 24 hours, one study reported a sensitivity of 58% for CT and 82% for MRI (28).

Regardless of the mechanism, DW images are highly sensitive and specific in the detection of hyperacute and acute infarctions (29–31). Reported sensitivities range from 88% to 100% and reported specificities range from 86% to 100%. The rare infarcts not identified on DWI are typically very small lacunar brain stem or deep gray nuclei infarctions (Fig. 3). False-negative DW images also occur

Table 3 Reliability of DWI for the Detection of Acute Ischemic Infarction up to Six Hours

Imaging	Sensitivity	Specificity
CT	38–45%	82–96%
Conventional MR	18–46%	70–94%
DWI	88–100%	88–100%
DWI—false-negative lesions	Brain stem or deep gray nuclei lacunes	
DWI—false-positive lesions	1. T2 shine through 2. Other entities with decreased diffusion—usually demyelinative lesion or nonenhancing tumor	

Abbreviations: CT, computer tomography; MR, magnetic resonance; DWI, diffusion-weighted images.

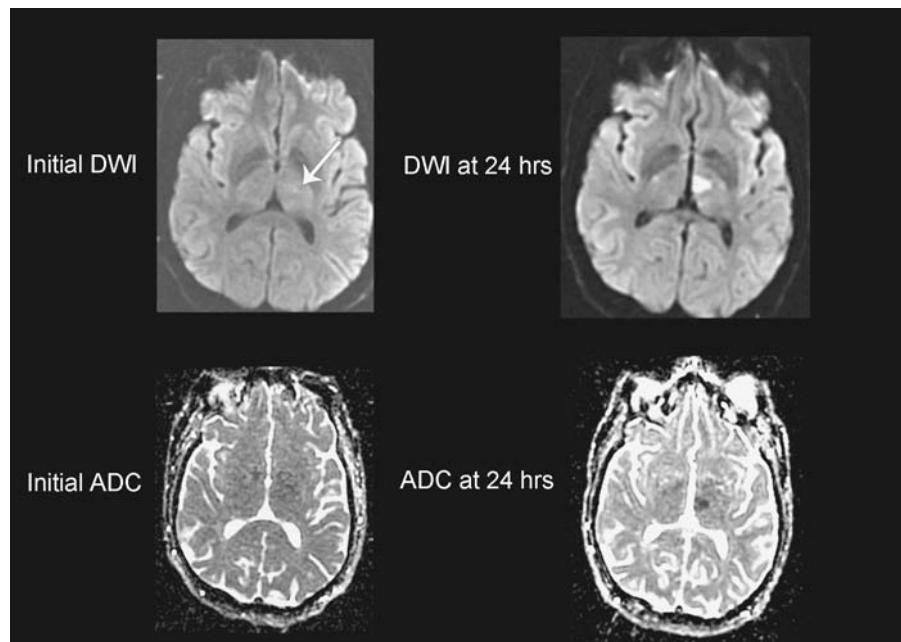


Figure 3 Thalamic lacune “without an acute DWI abnormality.” Forty-seven-year-old male with sensory loss, imaged at 1.5 hours after symptom onset. Initial DWI and ADC images were interpreted as demonstrating no definite acute infarction. In retrospect, there is a punctate left thalamic DWI hyperintense lesion (*arrow*). Follow-up DWI and ADC images clearly demonstrate a left thalamic lacunar infarction. Abbreviations: DWI, diffusion-weighted images; ADC, apparent diffusion coefficient.

in patients with regions of decreased perfusion (increased mean transit time and decreased relative cerebral blood flow) that are hyperintense on follow-up DWI; that is, brain regions with initial ischemic but viable tissue that eventually infarcted (Fig. 4). These findings stress the importance of obtaining perfusion in combination with DW images in patients with normal DW images and persistent strokelike deficits so that appropriate treatment is initiated as early as possible.

False-positive DW images may occur in patients with a subacute or chronic infarction with “T2 shine through” (Fig. 5). In these patients, a lesion appears hyperintense on the DW images because of an increase in the T2 signal. This error is easily avoided by interpreting the DW images

in combination with ADC maps. All acute lesions should demonstrate a hypointense signal on ADC maps because of restricted diffusion. False-positive DW images can also occur with restricted diffusion due to a number of other entities that are delineated in the subsequent section on stroke mimics.

Although after 24 hours, CT, FLAIR, and T2-weighted images are reliable in detecting acute infarctions, diffusion imaging continues to improve stroke diagnosis in the subacute setting. Older patients commonly have FLAIR and T2 hyperintense white matter abnormalities that are indistinguishable from acute lesions (Fig. 6). However, the acute infarctions are hyperintense on DWI and hypointense on ADC maps while the chronic foci are usually

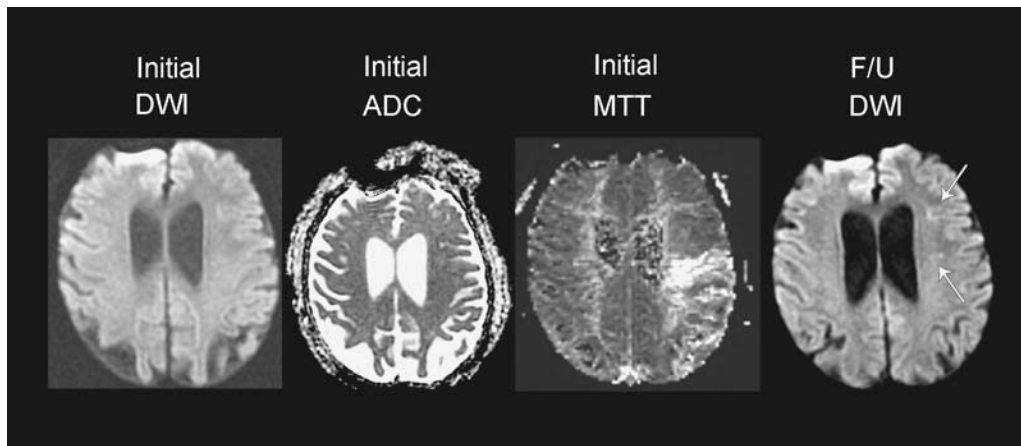


Figure 4 Acute stroke with normal DWI but abnormal perfusion (MTT) images. Seventy-two-year-old male with right-sided weakness imaged at five hours after symptom onset. Initial DWI image demonstrates no acute infarction. The MTT map demonstrates delayed MTT in the left posterior frontal and parietal lobes. The follow-up DWI image demonstrates punctate infarctions in the left corona radiata (arrows). Abbreviations: DWI, diffusion-weighted images; MTT, mean transit time.

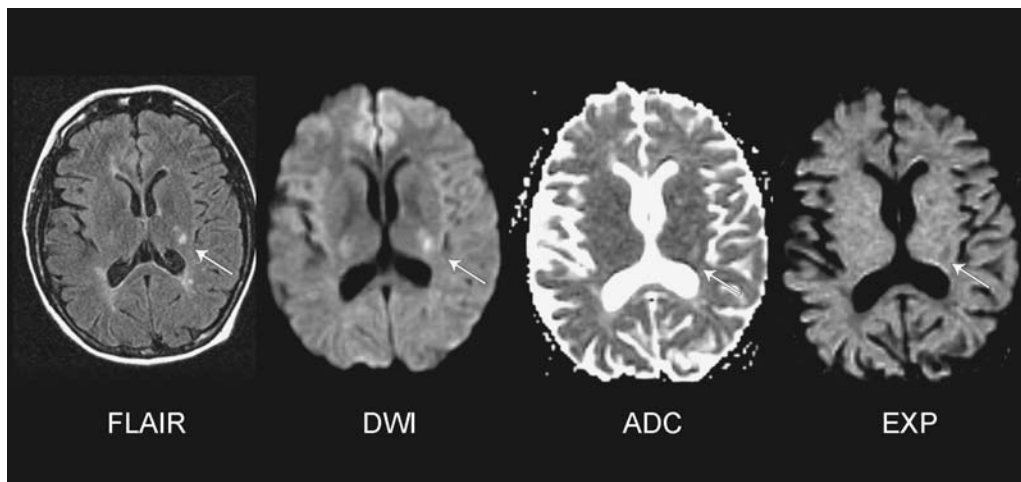


Figure 5 T2 shine through. Sixty-five-year-old female with mental status changes. DWI hyperintense lesion in the posterior limb of the left internal capsule is hyperintense on FLAIR images and ADC maps and hypointense on exponential images (arrow). These findings are consistent with elevated diffusion secondary to microangiopathic change rather than acute infarction suggested by the DWI images alone. Abbreviations: DWI, diffusion-weighted images; ADC, apparent diffusion coefficient; FLAIR, fluid-attenuated inversion recovery.

isointense on DWI and hyperintense on ADC maps due to elevated diffusion. In one study of indistinguishable acute and chronic white matter lesions on T2-weighted images, the sensitivity and specificity of DWI for detecting the acute subcortical infarction were 94.9% and 94.1%, respectively (32).

REVERSIBILITY OF DIFFUSION ABNORMALITIES

The DWI lesion is thought to represent the infarction core, or tissue that is destined to infarct. In most cases, the ultimate volume of an infarct is larger than that seen on initial DW images (30,33–38) encompassing both initial

DWI abnormal tissue and other tissue into which the infarct extends. Indeed, reversibility (abnormal on initial DWI but normal on follow-up images) of DWI hyperintense lesions is very rare and is usually only seen with nonischemic etiologies exhibiting restricted diffusion or with very early reperfusion following intravenous and/or intra-arterial thrombolysis (Fig. 7, Table 4). Grant et al. could identify only 21 of thousands of DWI hyperintense lesions that demonstrated reversibility and most of these did not represent acute ischemic infarction. The etiologies were acute stroke or transient ischemic attack (TIA) (three patients), transient global amnesia (TGA) (seven patients), status epilepticus (four patients), hemiplegic migraine

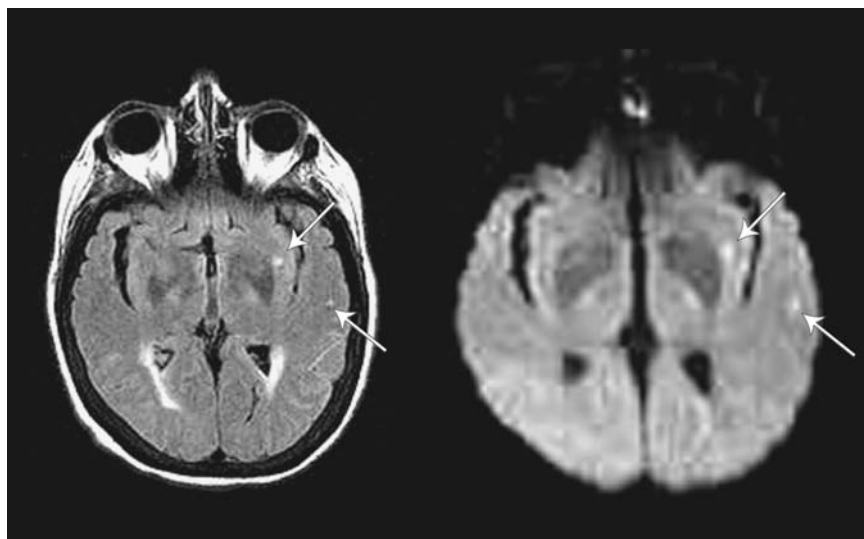


Figure 6 Nonspecific white matter changes versus acute ischemic infarction. Sixty-one-year-old female with hypertension. FLAIR-weighted images demonstrate multiple hyperintense white matter foci of unclear chronicity. DWIs demonstrate that lesions in the left external capsule and left temporal subcortical white matter (arrows) are acute. Abbreviations: DWI, Diffusion-weighted image; FLAIR, fluid-attenuated inversion recovery.

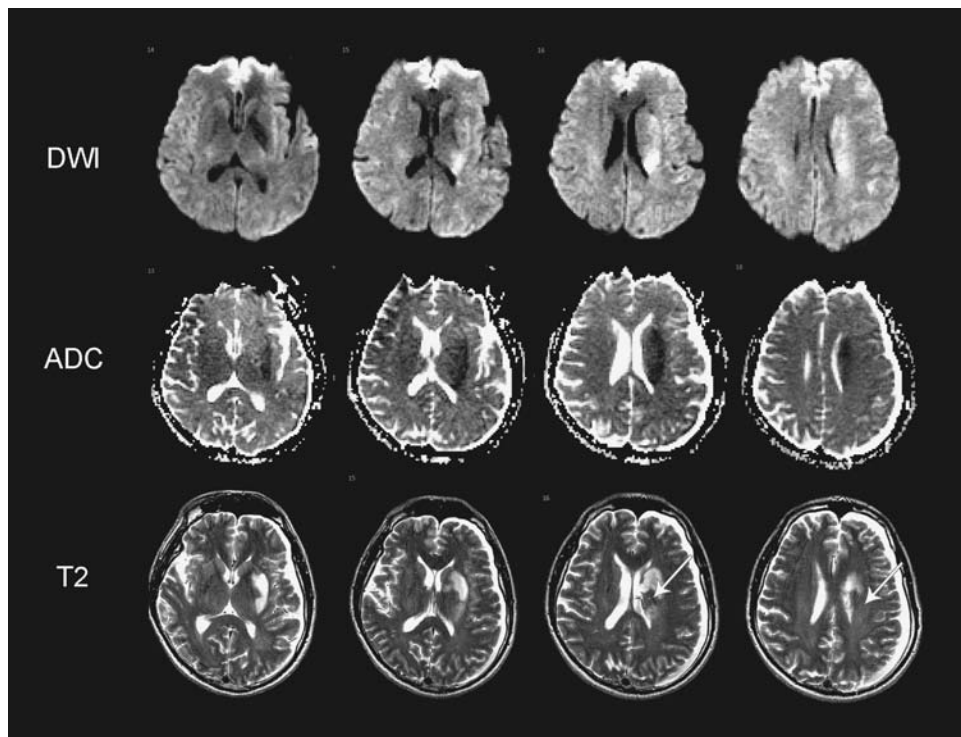


Figure 7 Acute ischemic stroke with DWI reversibility. Sixty-five-year-old male with sudden onset of right-sided weakness and slurred speech. CTA (not shown) demonstrated left M1 occlusion. He was treated with IA rtPA with near complete recanalization. DWI images and ADC maps demonstrate acute ischemia involving the left external capsule, caudate body, corona radiata, and parietal subcortical white matter. Follow-up T2-weighted images demonstrate hyperintensity, consistent with infarction in the putamen, external capsule and part of the caudate body, and corona radiata. However, part of the corona radiata and caudate body appear normal on the follow-up T2-weighted images (arrows). In addition, the left parietal lesion is not seen. Abbreviations: DWI, diffusion-weighted images; ADC, apparent diffusion coefficient; rtPA, recombinant tissue plasminogen activator; CTA, computer tomography angiography.

Table 4 DWI Stroke Lesion Reversibility

Definition	DWI abnormal tissue that appears normal at follow-up imaging
Entities with DWI reversibility	Acute stroke—usually following thrombolysis Venous infarction Hemiplegic migraine Transient global amnesia Seizure Hypoglycemia
Lesion location	White matter more often than gray matter
Amount of DWI reversible tissue in arterial strokes following tPA	12–33%
ADC values	Higher in DWI reversible versus DWI nonreversible tissue 663 to 732×10^{-6} mm 2 /sec in DWI reversible regions 608 to 650×10^{-6} mm 2 /sec in DWI abnormal regions that progress to infarction

Abbreviations: DWI, diffusion-weighted images; tPA, tissue plasminogen activator; ADC, apparent diffusion coefficient.

(three patients), and venous sinus thrombosis (four patients). ADC ratios (ipsilateral over contralateral normal appearing brain) were similar to those in patients with acute stroke. Gray matter ADC ratios were 0.64 to 0.79. White matter ADC ratios were 0.20 to 0.87 (39).

Even with thrombolysis, the volume of DWI abnormal tissue that recovers is usually relatively small and typically involves white matter more often than gray matter. Furthermore, judging whether tissue with a diffusion abnormality is normal at follow-up is complicated. Kidwell et al. reported a decrease in size from the initial DWI abnormality when compared with the follow-up DWI abnormality immediately after IA thrombolysis in 8 of 18 patients (40). However, despite the initial apparent recovery, a subsequent increase in the volume of the DWI lesion was observed in five patients. Furthermore, a number of studies have demonstrated that ADC values are significantly higher in DWI reversible tissue compared with DWI abnormal tissue that progresses to infarction. Mean ADC values range from 663 to 732×10^{-6} mm 2 /sec in DWI reversible regions compared with 608 to 650×10^{-6} mm 2 /sec in DWI abnormal regions that progress to infarction (40,41). Animal models have also shown high correlation between threshold ADC values of 550×10^{-6} mm 2 /sec and tissue volume with histologic infarction.

Other studies suggest that an absolute ADC threshold does not exist. In one study, more than 50% of the tissue volume with an initial ADC of less than 60% of normal tissue appeared unremarkable on T2-weighted images obtained seven days after stroke onset in two patients with early reperfusion (42). This is well below the threshold ADCs of approximately 80% of those of normal tissue, as discussed above. It is likely that duration and degree of ischemia rather than absolute ADC value determine tissue recovery and DWI reversibility. This concept is supported by the fact that the degree of ADC decrease correlates strongly with severity of cerebral blood flow

reduction, and the cerebral blood flow threshold for tissue infarction increases with the prolongation of occlusion time (43). For example, Jones et al. demonstrated that cerebral blood flow threshold for tissue infarction was 10 to 12 mL/100 g/min for two to three hours of occlusion but 17 to 18 mL/100 g/min for permanent occlusion of the MCA in monkeys (44).

HEMORRHAGIC TRANSFORMATION

Hemorrhagic transformation is a major complication of acute stroke with a natural incidence of 15% to 26% during the first two weeks and up to 43% over the first month after cerebral infarction (Table 5) (45–48). It is commonly thought that reperfusion into severely ischemic tissue leads to hemorrhagic transformation. However, some investigators have shown that hemorrhagic transformation can occur distal to permanently occluded vessels and suggest that collateral flow into ischemic tissue can lead to hemorrhage (45,49). Furthermore, thrombolytic agents increase the risk of hemorrhage. They are thought to aggravate microvascular damage by activation of the plasminogen-plasmin system with release of metalloproteinases that cause degradation of the basal lamina (50,51).

ADC values are thought to signify the severity and extent of ischemia and may be useful in predicting hemorrhagic transformation (Fig. 8). Oppenheim et al. demonstrated 100% sensitivity and 71% specificity for predicting hemorrhage into ischemic tissue when they divided infarcts into those with a mean ADC core of less than 300×10^{-6} mm 2 /sec versus those with a mean ADC core of greater than 300×10^{-6} mm 2 /sec (52). Selim et al. demonstrated that the volume of the initial DWI lesion and the absolute number of voxels with ADC value of 550×10^{-6} mm 2 /sec or less correlated with hemorrhagic transformation of infarctions treated with intravenous tPA (53). Tong et al. demonstrated that the

Table 5 Factors Associated with Hemorrhagic Transformation of Arterial Stroke

Clinical	Low platelets High glucose Hypertension High NIHSS
Vascular	Embolic stroke Good collateral vessels Early reperfusion
Treatment	Thrombolytic therapy Anticoagulation
Imaging parameters	Larger volume of the initial DWI abnormality Higher percentage of pixels with ADC $<550 \times 10^{-6} \text{ mm}^2/\text{sec}$ CT hypodensity in $>1/3$ rd of the MCA territory Early parenchymal enhancement Larger volume of the initial DWI abnormality Severe decreases in CBV and CBF on SPECT and MRP Increased T1 permeability. Prior microbleeds detected on T2* gradient echo do not signify risk for hemorrhagic transformation

Abbreviations: CT, computer tomography; NIHSS, National Institutes of Health Stroke Scale; DWI, diffusion-weighted images; ADC, apparent diffusion coefficient; MCA, middle cerebral artery; CBV, cerebral blood volume; CBF, cerebral blood flow; SPECT, single photon emission computed tomography; MRP, magnetic resonance perfusion.

mean ADC of ischemic regions that developed hemorrhage was significantly lower than the overall mean ADC of all ischemic areas analyzed ($510 +/ - 140 \times 10^{-6} \text{ mm}^2/\text{sec}$ vs. $623 +/ - 113 \times 10^{-6} \text{ mm}^2/\text{sec}$) (54). Other imaging parameters predictive of hemorrhagic transformation include (i) hypodensity in greater than one-third of the MCA territory on CT (55), (ii) early parenchymal enhancement on T1-weighted images (56), (iii) larger volume of the initial DWI abnormality (53), (iv) a more severe decrease in cerebral blood volume and cerebral blood flow versus the entire perfusion abnormality (57), (v) at least 126 voxels with cerebral blood volume less than 5% of contralateral normal gray matter in patients who received intravenous tPA (58), and (vi) increased T1 permeability (59). Prior microbleeds detected on T2* gradient echo do not signify risk for hemorrhagic transformation following thrombolytic therapy (60,61).

DIFFUSION TENSOR IMAGING

The physical principles of diffusion tensor imaging (DTI) are addressed in chapter 11. DTI allows the calculation of three basic parameters (Table 6).

1. The trace of the diffusion tensor [Tr(ADC)] or the average diffusivity, $\langle D \rangle$ ($\langle D \rangle = (\lambda_1 + \lambda_2 + \lambda_3)/3$, where λ_1 , λ_2 , and λ_3 are the eigenvalues of the

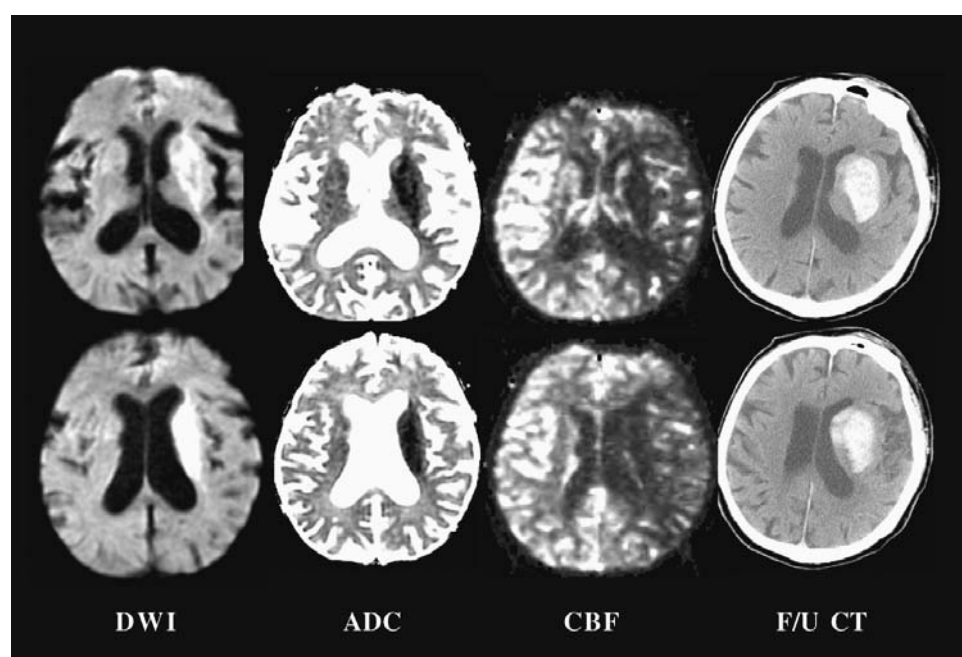


Figure 8 Acute ischemic stroke with hemorrhagic transformation. Seventy-three-year-old male with right hemiplegia, treated with IA tPA. There is an acute stroke (DWI hyperintense, ADC hypointense) involving the left basal ganglia, anterior limb of internal capsule, and corona radiata. Note the profound reduction in ADC and CBF in these regions where there is hemorrhagic transformation on follow-up CT. CBF images also demonstrate less severely reduced CBF in most of the left MCA territory. *Abbreviations:* tPA, tissue plasminogen activator; DWI, diffusion-weighted images; ADC, apparent diffusion coefficient; CBF, cerebral blood flow; MCA, middle cerebral artery.

Table 6 Diffusion Tensor Imaging

Parameters measured
1. Trace of the diffusion tensor [Tr(ADC)] or the average diffusivity ($\langle D \rangle$) calculates overall diffusion in a tissue region, independent of direction
2. Indices of diffusion anisotropy, FA and LI, calculate the degree of differences in diffusion in different directions
3. Fiber orientation mapping provides information on WM tract structure, integrity, and connectivity
Tr(ADC)
Discriminates differences in GM versus WM diffusion
$\langle D \rangle$ decreases greater in WM versus GM in acute and subacute periods
$\langle D \rangle$ increases much higher in WM versus GM in the chronic period
FA
Correlates with stroke-onset time
Elevated for up to 12 hr and then decreases over time
Correlates inversely with T2 change
Three temporal stages in stroke evolution
Increased FA and reduced ADC
Decreased FA and decreased ADC
Decreased FA and elevated ADC
Fiber orientation mapping
Can detect Wallerian degeneration prior to conventional images
May be useful in predicting motor function at outcome

Abbreviations: ADC, apparent diffusion coefficient; FA, fractional anisotropy; L, lattice index; WM, white matter; GM, gray matter.

- tensor). This is a calculation of the diffusion in a tissue region, independent of direction (62).
- Indices of diffusion anisotropy such as fractional anisotropy (FA) that calculate the degree of differences in diffusion in different directions (63,64).
 - Fiber orientation mapping that provides information on white matter tract structure and integrity (65–67).

Measurement of average diffusivity ($\langle D \rangle$) using DTI has demonstrated differences between gray and white matter diffusion that were not appreciable with measurement of diffusion along three orthogonal directions using DWI (68,69). These differences are likely detected with DTI because of the much higher signal-to-noise ratio. $\langle D \rangle$ decreases are greater in white matter versus gray matter in the acute and subacute periods and $\langle D \rangle$ increases are much higher in white matter versus gray matter in the chronic period. Furthermore, $\langle D \rangle$ images may detect regions of reduced white matter diffusion that appeared normal on DW images. While gray matter is thought to be more vulnerable to ischemia than white matter, animal experiments have demonstrated histopathologic changes in white matter as early as 30 minutes after acute stroke onset. Also, reduced bulk water motion from cytoskeletal collapse and disruption of fast axonal transport may explain the $\langle D \rangle$ changes in white matter.

Diffusion anisotropy refers to the principle that the degree of water diffusion is different in different directions due to tissue structure (70,71). White matter has relatively high FA because white matter has highly

organized tract bundles and diffusion is much greater parallel than perpendicular to white matter tracts (16,62,70,72). Oligodendrocyte concentration and fast axonal transport may also contribute to white matter diffusion anisotropy. Gray matter has relatively low FA. Furthermore, it is also thought that the intracellular compartment is more anisotropic than the extracellular compartment due to the presence of microtubules, organelles, and intact membranes (73,74).

In general, FA is elevated in the hyperacute and early acute phases of acute stroke, becomes reduced at 12 to 24 hours, and progressively decreases over time. However, the rate of FA evolution varies between lesions and within lesions, likely due to different temporal rates of stroke progression and different tissue composition (75,76). For example, the FA decreases associated with acute ischemia are significantly greater in white matter compared with gray matter (69,76). In the white matter extracellular space, there are dense arrays of parallel white matter tracts, where the diffusion decrease is much greater in λ_1 (the eigenvalue that coincides with the long axis of white matter fiber tracts) compared with the other eigenvalues. In the gray matter extracellular space there is a meshwork, where the diffusion decrease is more similar between eigenvalues.

Yang et al. described three different phases in the relationship between FA and ADC: (i) increased FA and reduced ADC in the initial phase, (ii) reduced FA and reduced ADC in an intermediate phase, and (iii) reduced FA with elevated ADC in the later third

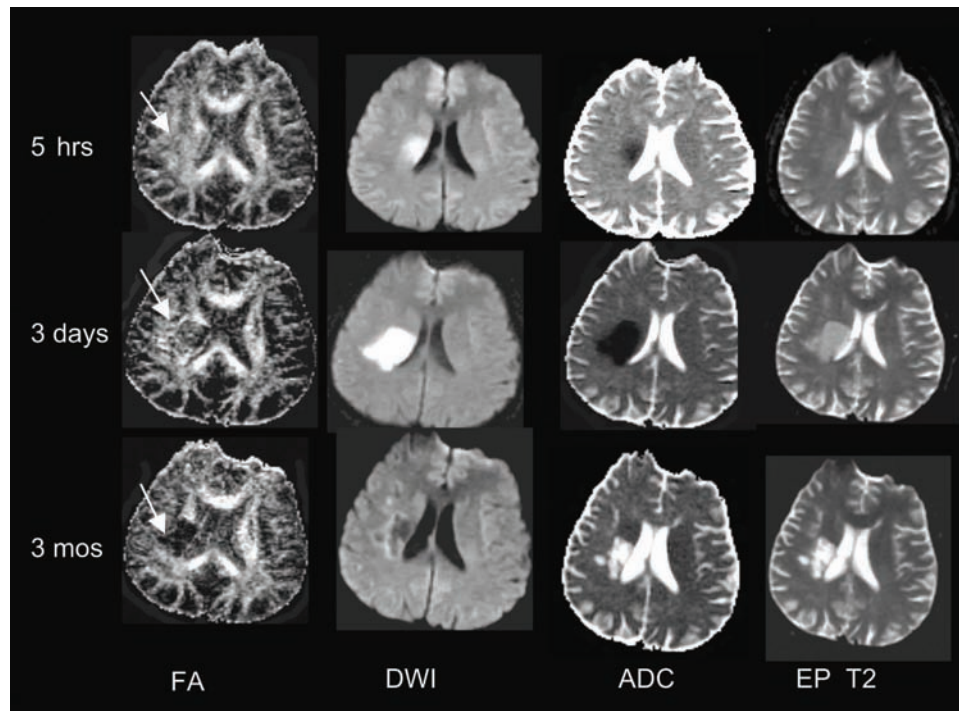


Figure 9 Temporal evolution of FA in acute ischemia. A 50-year-old male with left hemiparesis was imaged at five hours, three days, and three months following symptom onset. At five hours, the right corona radiata and caudate stroke are hyperintense on FA and DWI images (arrow), hypointense on ADC images, and not seen on echo planar T2-weighted images. These findings are consistent with the first stage of FA changes in stroke described by Yang et al. After three days, the lesion is hypointense on FA images, hyperintense on DWI images, hypointense on ADC images, and hyperintense on echo planar T2-weighted images. These findings are consistent with the second stage of FA changes in stroke. At three months, the lesion is hypointense on FA images, hypointense on DWI images, hyperintense on ADC images, and hyperintense on echo planar T2-weighted images. These findings are consistent with third stage of FA changes in stroke. Abbreviations: FA, fractional anisotropy; ADC, apparent diffusion coefficient; DWI, diffusion-weighted images.

phase (Fig. 9) (76). Furthermore, FA inversely correlates with T2 signal change (77). These changes may occur for the following reasons. As cytotoxic edema develops, there is a net shift of water from the extracellular to the intracellular space, but cell membranes remain intact and there is no significant overall increase in tissue water. This would explain the elevated FA, reduced ADC, and normal T2. As the ischemia progresses, cell membranes break down, an inflammatory response occurs, the blood-brain barrier degrades, and there is a substantial increase in tissue water, predominantly in the extracellular space. This scenario explains the observed reduced FA, elevated ADC, and elevated T2. Reduced FA, reduced ADC, and elevated T2 may occur when there is an overall increase in tissue water, but the intracellular fraction is still high enough to cause reduced ADC and the extracellular component is high enough to cause reduced FA. Loss of axonal transport and decreases in interstitial fluid flow may also contribute to decreases in FA over time.

DTI can detect Wallerian degeneration prior to conventional images and may be useful in predicting long-term motor function. One study demonstrated that FA is

significantly decreased in the ipsilateral corticospinal tracts in acute stroke patients with moderate-to-severe hemiparesis but not in patients with no or mild hemiparesis (78). Another study of subacute stroke patients demonstrated a significant reduction in the eigenvalues perpendicular to the axial imaging plane at two to three weeks in eight patients with poor recovery, but no reduction in eight patients with good recovery (Fig. 10) (79). DTI can also distinguish between a primary chronic stroke and a region of Wallerian degeneration. A primary chronic stroke has reduced FA and elevated mean diffusivity while Wallerian degeneration of the corticospinal tract has reduced FA but preserved or only slightly elevated mean diffusivity (80).

CORRELATION OF DIFFUSION MR IMAGES WITH CLINICAL OUTCOME

A number of studies have shown that DWI can be used to predict clinical outcome. Some studies have demonstrated statistically significant correlations between the acute anterior circulation DWI and/or ADC lesion volumes and both acute and chronic neurologic assessment tests

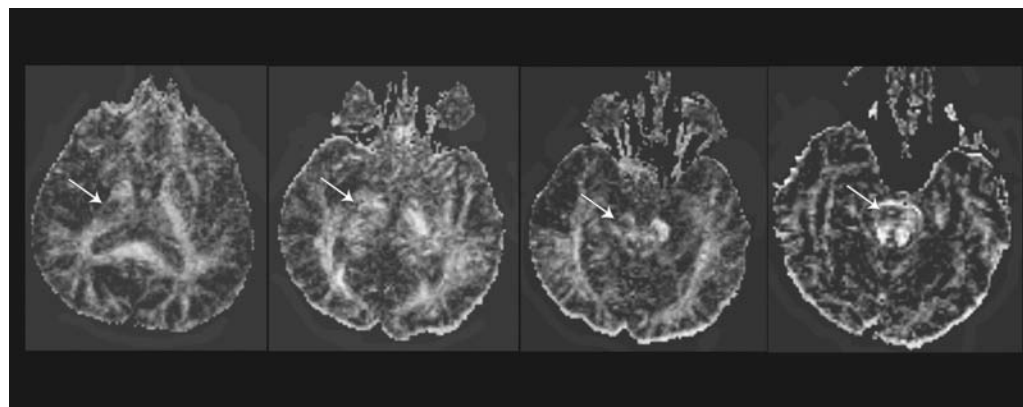


Figure 10 Wallerian degeneration in the right corticospinal tract three months after an infarction in the right MCA territory. FA images demonstrate reduced FA in the right corticospinal tract (arrow). Abbreviations: FA, fractional anisotropy; MCA, middle cerebral artery.

including the National Institutes of Health Stroke Scale (NIHSS), the Canadian Neurologic Scale, the Glasgow Outcome Score, the Barthel Index, and the Modified Rankin Scale (22,34,81–86). Correlations between DWI and ADC volumes and clinical outcome range from 0.65 to 0.78. In general, large initial DWI volumes are predictive of poor outcome. For example, one study demonstrated that for internal carotid artery and MCA strokes treated with various therapies including thrombolytic agents, a DWI volume greater than 89 cc was highly predictive of early neurologic deterioration (ROC curve with 85.7% sensitivity and 95.7% specificity) (87). Another study, performed in patients with proximal MCA emboli, who received intra-arterial and/or intravenous thrombolytic agents, demonstrated that patients with an initial DWI lesion volume of greater than 70 cc had a much worse outcome compared with patients with an initial DWI lesion volume of less than 70 cc (71.5% vs. 0% 90-day mortality, respectively) (88). Because patients with a large initial DWI stroke volume have poor outcomes in spite of aggressive therapy and have an increased risk of hemorrhage, those with an initial DWI lesion volume of greater than one-third of the MCA territory or greater than 100 cc are typically excluded from acute stroke trials (89,90).

In general, correlations are stronger for cortical strokes than for penetrating artery strokes (22,82). Lesion location likely explains this discrepancy since small ischemic lesions in the brain stem, in general, produce worse neurologic deficits compared with cortical lesions of the same size. In fact, one study of posterior circulation strokes showed no correlation between initial DWI lesion volume and NIHSS (91). Significant correlations have also been reported for absolute ADC values and ADC ratios (ADC of lesion/ADC of normal contralateral brain) versus chronic neurologic assessment scales (22,81). One study also demonstrated that patients with a mismatch

between the initial NIHSS score (>8) and the initial DWI lesion volume (<25 mL) had a higher probability of infarct growth and early neurologic deterioration (92).

SYNDROMES THAT MIMIC STROKE

Syndromes which clinically mimic strokes generally fall into four categories (Tables 7 and 8): (i) nonischemic lesions with no acute abnormality on routine or DW images; (ii) ischemic lesions with reversible clinical deficits which may have imaging abnormalities; (iii) vasogenic edema syndromes which may mimic acute infarction clinically and on conventional imaging; and (iv) other entities with decreased diffusion.

Nonischemic Lesions with no Acute Lesion on Conventional or Diffusion-Weighted Images

Nonischemic syndromes that present with signs and symptoms of acute stroke but have no acute abnormality identified on DWI or conventional MR images include dementia, functional disorders, metabolic disorders, peripheral vertigo, migraines, and seizures (Table 7). The clinical deficits associated with these syndromes usually resolve. If initial imaging is normal and a clinical deficit persists, repeat DW images should be obtained (30). False-negative DWI images can occur in patients with small brain stem or deep gray nuclei lacunar infarctions.

Ischemic Lesions with Reversible Clinical Deficits

Transient Ischemic Attacks (TIAs)

The classic definition of a TIA is an acute neurologic deficit resulting from brief interruption of the cerebral vascular supply that typically resolves within 10 to 15 minutes but

Table 7 Entities that Mimic Acute Ischemic Stroke

Nonischemic syndromes that present with signs and symptoms of acute stroke but usually have no acute abnormality identified on DWI or routine MR images

Peripheral vertigo

Migraines^a

Seizures^a

Dementia

Functional disorders

Metabolic disorders

Potentially ischemic syndromes with reversible clinical deficits that may have decreased diffusion

Transient ischemic attacks

Approximately 50% with DWI hyperintense lesions

DWI hyperintense lesions associated with increased stroke risk

DWI hyperintense lesions change the suspected localization of the ischemic lesion as well as the suspected etiologic mechanism in over one-third of patients

Transient global amnesia

Punctate lesions with decreased diffusion in the hippocampus, the parahippocampal gyrus, and the splenium of the corpus callosum

Some lesions appear at later time points

Some lesions resolve

Question of ischemic versus spreading depression mechanism

Hypoglycemia

Decreased diffusion in parietal/occipital lobes and splenium

Energy failure with failure of cell membrane ionic pumps, similar to ischemia

Hemiplegic migraine

Decreased diffusion in contralateral hemisphere

Primary neuronal versus ischemic etiology

May cover more than one vascular territory

May be associated with normal or elevated perfusion

Angiography—normal or vasospasm, but no proximal vessel cutoff

Lesions are reversible

Seizure

Decreased diffusion in nonvascular region

Increased glucose utilization leads to energy failure

Elevated perfusion

Lesions are reversible

Syndromes

Vasogenic edema/capillary leak syndromes

PRES

Hyperperfusion syndrome postcarotid endarterectomy

Conventional MR imaging findings

T2 hyperintensity in gray and/or white matter that may mimic acute stroke

DWI findings

Elevated diffusion secondary to vasogenic edema

May have peripheral cytotoxic edema due to mass effect and capillary compression

Occasionally have vasogenic edema followed by cytotoxic edema in the whole lesion

^aMay also have decreased diffusion.

Abbreviations: DWI, diffusion-weighted images; PRES, posterior reversible encephalopathy syndrome.

may persist for up to 24 hours. While patients' symptoms usually resolve by the time they are imaged, DWI has become integral in evaluating this patient population (Fig. 11).

Approximately 50% (range 1–67%) of patients with TIAs have DWI hyperintense lesions that are usually less than 20 mm in size (Fig. 11) (37,93–97). In one study, the

information obtained from DWI changed the suspected localization of the ischemic lesion as well as the suspected etiologic mechanism in over one-third of patients (93). Reported statistically significant independent predictors of these DWI hyperintense lesions are previous nonstereotypic TIA, cortical syndrome, an identified stroke mechanism,

Table 8 Other Entities that may show Decreased Diffusion

Disease	Possible pathophysiologic basis for decreased diffusion
Diffuse axonal injury	Cytotoxic edema, myelin vacuolization, or axonal retraction balls
Herpes virus encephalitis	Necrotizing meningoencephalitis with cytotoxic edema
Lymphoma, medulloblastoma	High tumor cellularity
Epidermoid tumors	Tumor cellularity
Bacterial and some fungal abscesses	Viscous pus
Hemorrhage—Oxyhemoglobin and extracellular methemoglobin	Oxyhemoglobin—cell membranes intact, Extracellular methemoglobin—viscosity from high protein content
Acute multiple sclerosis or acute disseminated encephalomyelitis	Myelin vacuolization, increased inflammatory infiltrate
Creutzfeldt-Jakob Disease	Myelin vacuolization
Heroin leukoencephalopathy	Myelin vacuolization

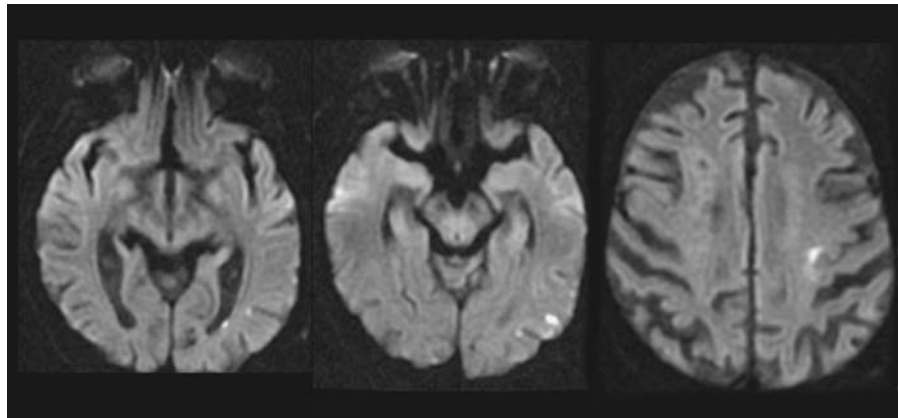


Figure 11 Transient ischemic attack. Sixty-one-year-old female with transient right hand, arm, and leg weakness. DWI images demonstrate punctate hyperintense lesions, consistent with acute infarctions, in the left occipital and frontal lobes. Abbreviation: DWI, diffusion-weighted images.

TIA duration greater than 30 minutes, aphasia, motor deficits, and disturbance of higher brain function (37,93,95,96,98,99). Moreover, patients with TIA and DWI hyperintense lesions have an increased risk of having a future stroke (94,100). In one study, the in-hospital stroke and recurrent TIA rate was 1.3% in TIA patients without DWI hyperintense lesions and 19.4% in patients with DWI hyperintense lesions (100). In another study, TIA patients with DWI hyperintense lesions and symptom duration greater than one hour had a higher risk of future vascular events (stroke, myocardial infarction, or peripheral vascular disease) (94). Because the TIAs in patients with DWI hyperintense lesions have unique features, some authors propose that they be classified as acute strokes and that TIA be redefined as “a brief episode of neurologic dysfunction presumptively caused by focal brain or retinal ischemia, with clinical symptoms typically lasting less than one hour and without neuroimaging evidence of acute infarction” (101). Approximately 20% to 50% of these small DWI hyperintense lesions are not seen on follow-up images. The lesions could be too small to see on follow-up conventional MRI due to atrophy or they could be reversible (93,101).

Transient Global Amnesia (TGA)

TGA is a syndrome characterized by sudden onset of severe memory impairment associated with both retrograde and anterograde amnesia without other neurologic deficits. The symptoms typically resolve in three to four hours. Many patients with TGA have no acute abnormality on conventional or DW images (102), but others have reported punctate lesions with decreased diffusion in the medial hippocampus, the parahippocampal gyrus, and the splenium of the corpus callosum (Fig. 12) (103–106). Follow-up T2-weighted sequences have shown persistence of some of these lesions, which, the authors concluded, were small infarctions. Another study, however, reported more diffuse and subtle DWI hyperintense lesions in the hippocampus that resolved on follow-up imaging, which were thought to be secondary to spreading depression rather than reversible ischemia (107). One more recent study demonstrated that the detection of DWI changes in TGA is delayed (108); the authors observed DWI abnormalities in only 2 of 31 patients with TGA in the acute phase, but at 48 hours, 26 of 31 patients had DWI hyperintense foci in the

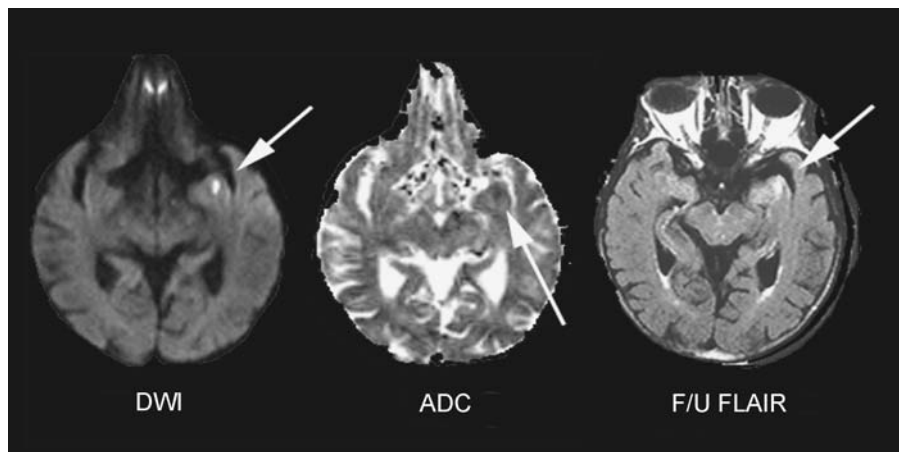


Figure 12 Transient global amnesia. Seventy-seven-year-old female with acute transient global amnesia that resolved within 24 hours. There is a punctate DWI hyperintense and ADC hypointense lesion in the left medial temporal lobe (*arrows*). The lesion persists on follow-up FLAIR images. Abbreviations: DWI, diffusion-weighted images; ADC, apparent diffusion coefficient; FLAIR, fluid-attenuated inversion recovery.

hippocampus. The authors speculate that this phenomenon may result from venous congestion. It is currently unclear whether the TGA patients with DWI abnormalities have a different prognosis or a different etiologic mechanism, or whether they should be managed differently compared with TGA patients without DWI abnormalities.

Seizures

Patients with prolonged seizures may have regions with decreased diffusion that should not be confused with acute ischemic stroke and can be differentiated from stroke by a number of factors (Fig. 13): (*i*) there is usually increased

perfusion, (*ii*) the lesions are not usually in a single vascular distribution, (*iii*) there is sulcal effacement and mass effect earlier than would be expected with acute stroke, and (*iv*) the lesions are usually reversible. The reason for the decreased diffusion in such cases is not clear but may result from the following mechanism: prolonged ictal activity increases glucose utilization, which is not adequately compensated by the increased blood flow, which results in a reduction in high-energy adenosine phosphates and tissue ischemia. Markedly increased release of excitatory amino acids (109,110) and increased membrane ion permeability (111) are other mechanisms that may cause cytotoxic edema during status epilepticus.

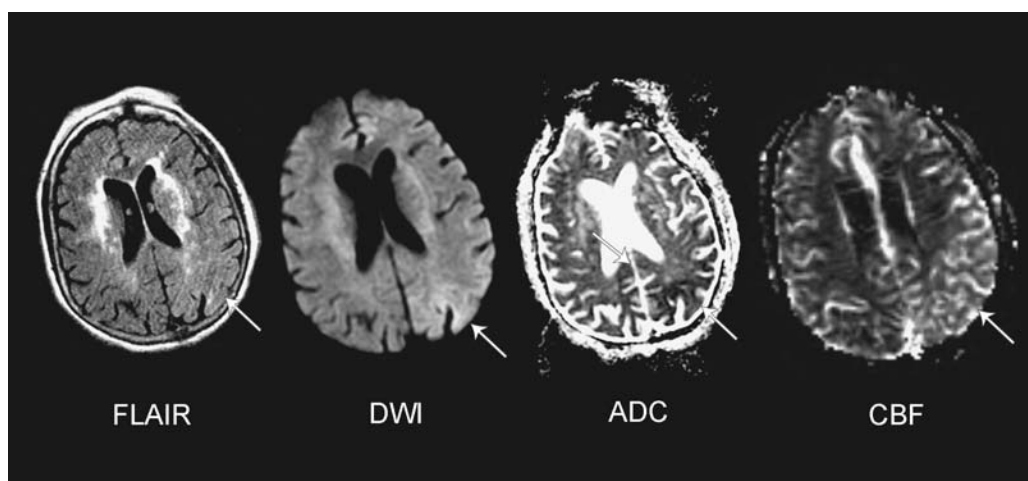


Figure 13 Eighty-five-year-old female with seizures. The FLAIR image demonstrates subtle hyperintensity in the left parietal lobe (*arrow*). The left parietal region is characterized by decreased diffusion with DWI hyperintensity and ADC hypointensity. In contradistinction to acute stroke, there is increased cerebral blood flow. Abbreviations: FLAIR, fluid-attenuated inversion recovery; DWI, diffusion-weighted images; ADC, apparent diffusion coefficient.

Hemiplegic Migraine

Some patients with prolonged hemiplegic migraine have regions with decreased diffusion involving cortex and subcortical white matter in the contralateral hemisphere that can be confused with acute stroke (112–115). The lesions are thought to result from primary neuronal dysfunction. A number of factors can distinguish these lesions from acute stroke: (i) the patients usually have a strong history of migraines, (ii) the lesions may cover multiple arterial vascular territories, (iii) perfusion is frequently elevated or normal, (iv) angiography may be normal or show vasospasm but vessel cut-offs are not identified, and (v) the lesions and clinical deficits are usually reversible.

Hypoglycemia

Patients with hypoglycemic coma or hypoglycemic encephalopathy may have T2 hyperintense regions with decreased diffusion in the cortex and the subcortical white matter (Fig. 14) (116–119). The lesions tend to have a posterior predominance with involvement of the occipital and parietal lobes and the splenium of the corpus callosum. In some patients, who are treated promptly and recover, the lesions completely resolve on conventional and DW images. In others, especially neonates, the lesions evolve similar to acute infarctions; in the chronic stage they have elevated diffusion with persistent T2 hyperintensity and tissue loss. It is thought that, similar to ischemia, severe hypoglycemia causes energy failure with failure of cell membrane ionic pumps and a net translocation of cerebral water from the extracellular to

the intracellular space. The reason for the posterior predominance is unclear but may be related to regional imbalances between energy supply and demand, spreading depression, or an excitotoxic mechanism.

Vasogenic Edema Syndromes

Patients with syndromes characterized predominantly by vasogenic edema may present with acute focal neurologic deficits that suggest acute ischemic stroke (Table 7). Diffusion MR imaging is essential in differentiating these syndromes from acute stroke because it can reliably distinguish vasogenic from cytotoxic edema. While cytotoxic edema results in decreased diffusion, vasogenic edema is characterized by elevated diffusion due to a relative increase in extracellular compared with intracellular water (120–122). Vasogenic edema is hypointense to slightly hyperintense on DWI images because these images have both T2 and diffusion weighting. Vasogenic edema is hyperintense on ADC maps and hypointense on exponential images. Conversely, cytotoxic edema is hypointense in ADC maps and hyperintense on DWI and exponential images.

Posterior Reversible Encephalopathy Syndrome

Posterior reversible encephalopathy syndrome (PRES) is a syndrome that results from loss of cerebral autoregulation and capillary leakage in association with a variety of clinical entities (Fig. 15) (123) including acute hypertension; treatment with chemotherapeutic agents such as intrathecal methotrexate, cisplatin, and interferon alpha;

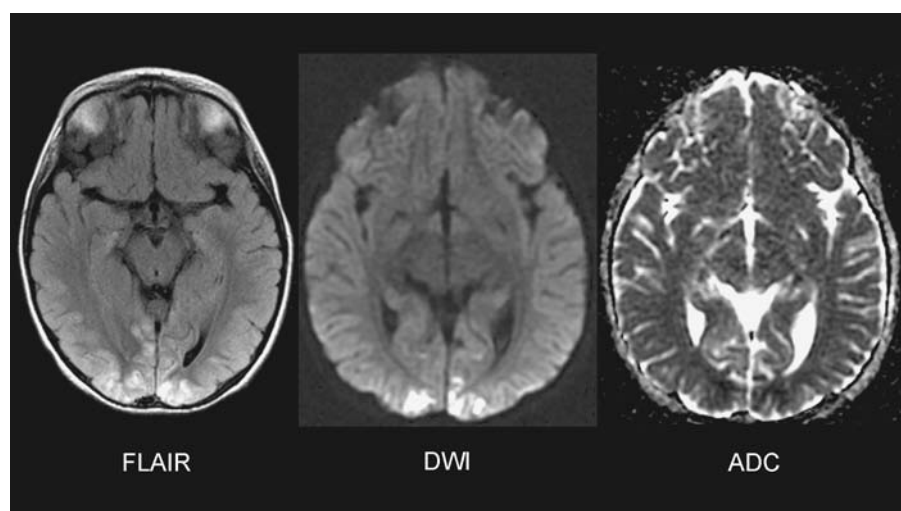


Figure 14 Thirty-five-year-old male with diabetes and hypoglycemia. There are bilateral occipital lobe lesions that are FLAIR and DWI hyperintense. The lesions are ADC hypointense, consistent with decreased diffusion due to low glucose. The MRA (not shown) showed a normal posterior circulation. Abbreviations: FLAIR; fluid-attenuated inversion recovery, DWI, diffusion-weighted images; ADC, apparent diffusion coefficient; MRA, magnetic resonance angiography.

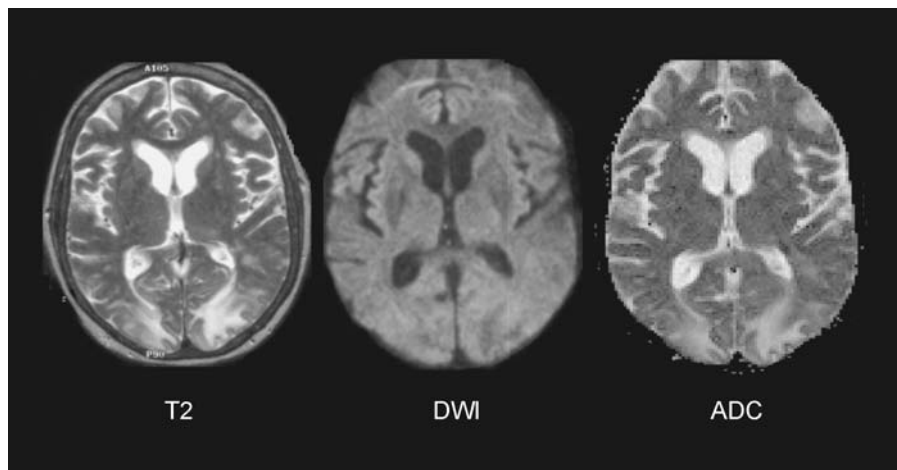


Figure 15 Posterior reversible encephalopathy syndrome (PRES). Fifty-six-year-old hypertensive female with visual changes and question of a basilar tip syndrome. T2-weighted images demonstrate hyperintense lesions in the occipital lobes bilaterally that suggest acute infarctions. The lesions are isointense on DWI images and hyperintense on ADC images. These diffusion MR characteristics are consistent with vasogenic edema. Abbreviations: DWI, diffusion-weighted images; ADC, apparent diffusion coefficient; MR, magnetic resonance.

treatment with immunosuppressive agents such as cyclosporin and tacrolimus; and hematologic disorders such as hemolytic uremic syndrome, thrombotic thrombocytopenia purpura, acute intermittent porphyria, and cryoglobulinemia (124–135). Typical acute neurologic symptoms are headaches, decreased alertness, altered mental status, seizures, and visual loss including cortical blindness.

The pathophysiology is not entirely understood (122,136). One hypothesis is that markedly increased pressure and/or toxins damage endothelial tight junctions. This results in extravasation of fluid with the development of vasogenic edema. Another, less-favored hypothesis, based on angiographic findings of narrowings in medium and large size vessels, is that the pathophysiology is due to vasospasm.

T2- and FLAIR-weighted sequences demonstrate bilateral, relatively symmetric hyperintensity and swelling in the subcortical white matter and overlying cortex in the occipital, parietal, and posterior temporal lobes as well as the posterior fossa. The posterior circulation predominance is thought to occur because, in the setting of acute hypertension, there is less sympathetic innervation to supply vasoconstrictive protection to the brain in the posterior compared with the anterior circulation. However, anterior circulation lesions are also seen and are frequently in a borderzone distribution.

Acutely, DW images of PRES usually show elevated diffusion. This is helpful since posterior distribution lesions can mimic basilar tip occlusion with arterial infarctions and borderzone anterior circulation lesions can mimic watershed infarctions both clinically and on T2-weighted sequences. Arterial and watershed infarctions are characterized by decreased diffusion. The clinical deficits and MR abnormalities are typically reversible. However, rare

small areas of decreased diffusion that progress to infarction have been observed, and in some cases, tissue initially characterized by elevated or normal diffusion progresses to infarction (137).

Hyperperfusion Syndrome Following Carotid Endarterectomy

In rare cases following carotid endarterectomy, patients develop a hyperperfusion syndrome (138). Patients usually present with seizures, but may have focal neurologic deficits. T2-weighted images demonstrate hyperintensity in the frontal and parietal cortex and subcortical white matter that may mimic arterial infarction. However, unlike acute infarctions, the lesions have increased diffusion. Also, there is typically increased rather than diminished flow-related enhancement in the ipsilateral MCA. It is thought that similar to PRES, increased pressure damages endothelial tight junctions, leading to a capillary leakage syndrome and the development of vasogenic edema.

Other Syndromes

Rarely, other disease entities such as viral encephalopathies, tumor, and acute demyelination can present with acute neurologic deficits and patterns of edema on conventional images suggestive of stroke. Similar to PRES and hyperperfusion syndrome following carotid endarterectomy, DW images show increased diffusion.

Other Entities with Decreased Diffusion

A number of other entities are characterized by restricted diffusion (increased signal on DWI and decreased signal

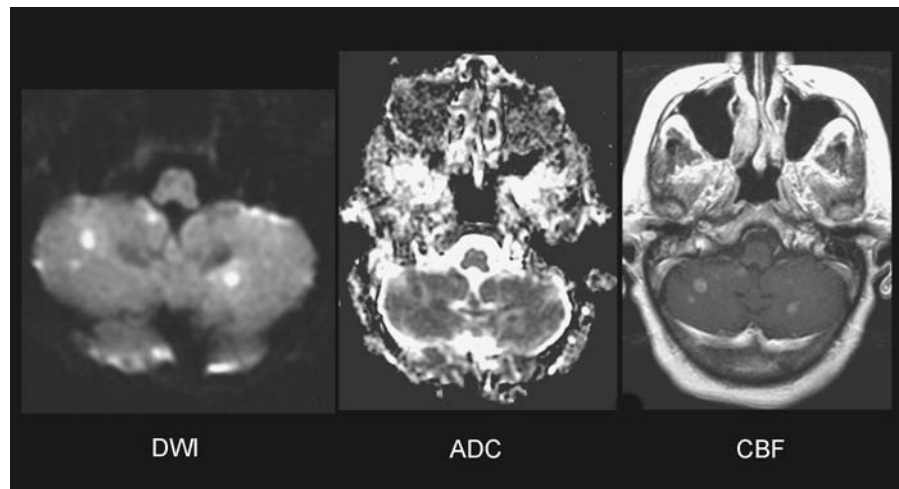


Figure 16 Small cell lung carcinoma metastases. There are multiple, bilateral cerebellar lesions that are DWI hyperintense and ADC hypointense, consistent with decreased diffusion, which mimic acute infarctions. On gadolinium-enhanced T1-weighted images, the lesions homogeneously enhance, which is most consistent with metastases. Abbreviations: DWI, diffusion-weighted images; ADC, apparent diffusion coefficient.

on ADC maps) (Table 8) (139). Abscess cavities have homogeneously restricted diffusion due to the high viscosity of pus. Some tumors such as lymphoma, small cell lung carcinoma metastases, and medulloblastoma have restricted diffusion due to dense cell packing (Fig. 16). A number of entities such as Creutzfeldt-Jakob Disease, acute demyelinating lesions, and heroin leukoencephalopathy demonstrate restricted diffusion due to myelin vacuolization. Creutzfeldt-Jakob Disease is characterized by lesions in the cortex and deep gray nuclei. Heroin leukoencephalopathy is characterized by diffusely restricted diffusion throughout the deep and subcortical white matter. Up to two-thirds of diffuse axonal injury lesions have restricted diffusion that may be secondary to myelin vacuolization or cytotoxic edema. When these lesions are reviewed in combination with routine T1, T2, and gadolinium-enhanced T1-weighted images and clinical history, they can usually be readily differentiated from acute ischemic infarctions. Occasionally, a single demyelinating lesion or a nonenhancing tumor cannot be distinguished from an acute ischemic event with diffusion or conventional imaging. In this case, spectroscopy and perfusion imaging may be helpful.

VENOUS INFARCTION

Cerebral venous sinus thrombosis (CVT) is a rare condition that affects less than 1 in 10,000 people (Fig. 17, Table 9). The most common presenting symptoms and signs are headache, vomiting, seizures, and papilledema. Other relatively frequent symptoms are visual changes, altered consciousness, cranial nerve palsies, nystagmus, and focal neurologic deficits. Predisposing factors are

protein C and S deficiencies; malignancies; pregnancy; oral contraceptives, steroids, and hormone replacement therapy; collagen vascular diseases; infection; trauma; surgery; and immobilization (140).

The pathophysiology of cerebral venous sinus thrombosis is complex (141–152). Venous obstruction results in increased venous pressure, increased intracranial pressure, decreased perfusion pressure, and decreased cerebral blood flow. Increased venous pressure may result in breakdown of the blood-brain barrier, capillary leakage, and extravasation of fluid and/or blood into the extracellular space. Severely decreased blood flow may also result in ischemia. Increases in CSF production and resorption have also been reported.

Parenchymal findings on imaging correlate with degree of venous pressure elevation (153). With mild-to-moderate pressure elevations, there is parenchymal swelling with sulcal effacement. With more severe pressure elevations, there is increasing edema and the development of intraparenchymal hemorrhage. Superior sagittal sinus thrombosis is characterized by bilateral parasagittal T2 hyperintense lesions involving the cortex and the subcortical white matter. Transverse sinus thrombosis results in T2 hyperintense signal abnormality involving the temporal cortex and the subcortical white matter. Deep venous thrombosis is characterized by T2 hyperintense signal abnormalities in the thalamus bilaterally and sometimes the basal ganglia. Up to 40% of patients with CVT (154,155) develop hemorrhage that is usually located at gray-white matter junctions or within the white matter.

DWI has proven helpful in the differentiation of venous from arterial infarction and in the prediction of tissue outcome (Figs. 11 and 12). T2 hyperintense lesions may

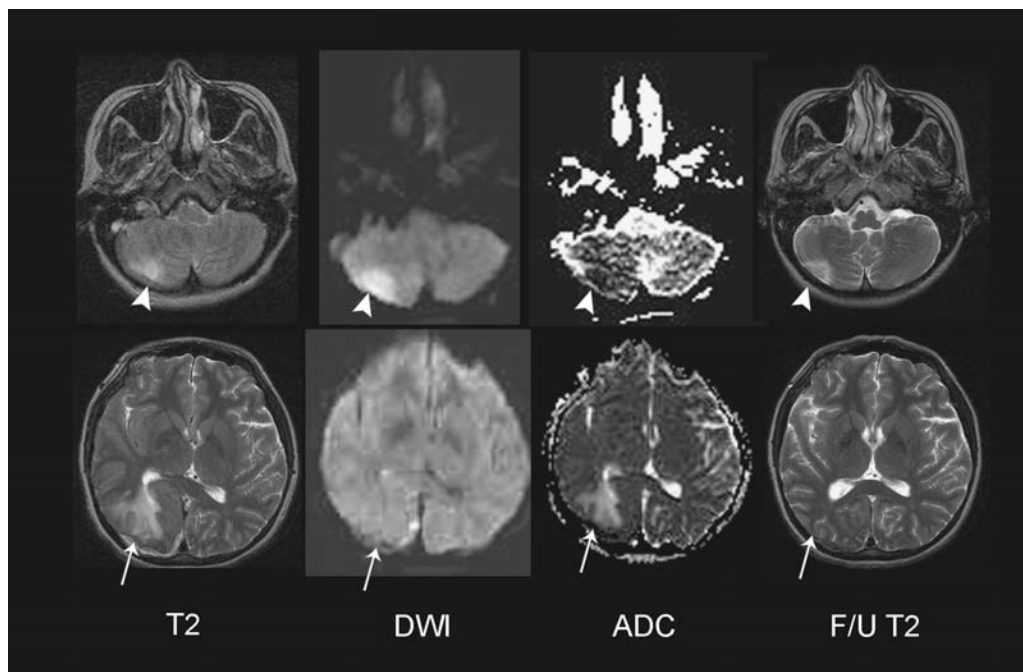


Figure 17 Cerebral venous sinus thrombosis with parenchymal lesions characterized by both vasogenic and cytotoxic edema. Thirty-one-year-old male with severe headache and vomiting. MR venogram (not shown) demonstrated thrombosis of the superior sagittal, right transverse, and right sigmoid sinuses. The T2 hyperintense right cerebellar lesion has decreased diffusion (DWI hyperintense and ADC hypointense), consistent with cytotoxic edema (arrowhead). The lesion is present at follow-up. The T2 hyperintense right parietal occipital lesion has elevated diffusion (DWI isointense, ADC hyperintense), consistent with vasogenic edema (white arrow). It is no longer present at follow-up. Abbreviations: DWI, diffusion-weighted images; ADC, apparent diffusion coefficient.

Table 9 Cerebral Venous Sinus Thrombosis

Pathophysiology

Increased venous pressure leads to vasogenic edema from blood-brain barrier breakdown and fluid extravasation into the extracellular space

Increased venous pressure leads to increased intracranial pressure, decreased perfusion pressure, decreased blood flow, and cytotoxic edema

Signs and symptoms

Headache

Seizure

Vomiting

Papilledema

Conventional MR imaging

Hydrocephalus

Parenchymal swelling with sulcal effacement

Intraparenchymal edema

Intraparenchymal hemorrhage

Venous clot

Diffusion MR Imaging of T2 hyperintense parenchymal lesions

Lesions with elevated diffusion c/w vasogenic edema resolve

Lesions with decreased diffusion c/w cytotoxic edema that resolve—resolution may be related to early drainage of blood through collateral pathways or to seizure activity

Lesions with decreased diffusion c/w cytotoxic edema that persist

Heterogeneous lesions c/w combination of vasogenic and cytotoxic edema

have decreased diffusion, elevated diffusion, or a mixed pattern. Lesions with elevated diffusion are thought to represent vasogenic edema and usually resolve. Lesions with decreased diffusion are thought to represent cytotoxic edema. Some of these lesions persist but many of these lesions resolve. Resolution of lesions with decreased diffusion may be related to better drainage of blood through collateral pathways in some patients. In one paper, lesions with decreased diffusion that resolved were seen only in patients with seizure activity (156).

CONCLUSION

DWI has greatly improved evaluation of patients with acute ischemic stroke because it is highly sensitive and specific in the detection of acute stroke at very early time points when CT and conventional MR sequences are unreliable. The initial DWI hyperintense lesion likely represents infarct core and usually infarcts except in the very rare cases, when early reperfusion occurs. The initial DWI and ADC lesion volumes correlate highly with final infarct volume and with acute and chronic neurologic assessment tests. ADC values may be useful in differentiating tissue likely to infarct from tissue that is ischemic but potentially salvageable with reperfusion therapy. ADC values may also be useful in determining tissue at risk of hemorrhaging following reperfusion therapy. DTI can delineate the differences in responses of gray versus white matter to ischemia. FA may be important in determining stroke-onset time and in providing early detection of Wallerian degeneration. Diffusion MR imaging can determine which TIA patients are at most risk for subsequent large vessel infarction and can usually differentiate stroke from conditions that mimic stroke. With improvements in MR magnets, diffusion MR will undoubtedly continue to improve our management and treatment of acute stroke patients.

REFERENCES

- Chien D, Kwong KK, Gress DR, et al. MR diffusion imaging of cerebral infarction in humans. *AJNR Am J Neuroradiol* 1992; 13:1097-102; (discussion 1103-1105).
- Kucharczyk J, Vexler ZS, Roberts TP, et al. Echo-planar perfusion-sensitive MR imaging of acute cerebral ischemia. *Radiology* 1993; 188:711-717.
- Matsumoto K, Lo EH, Pierce AR, et al. Role of vasogenic edema and tissue cavitation in ischemic evolution on diffusion-weighted imaging: comparison with multiparameter MR and immunohistochemistry. *AJNR Am J Neuroradiol* 1995; 16:1107-1115.
- Mintorovitch J, Yang GY, Shimizu H, et al. Diffusion-weighted magnetic resonance imaging of acute focal cerebral ischemia: comparison of signal intensity with changes in brain water and $\text{Na}^+, \text{K}(+)$ -ATPase activity. *J Cereb Blood Flow Metab* 1994; 14:332-336.
- Sevick RJ, Kanda F, Mintorovitch J, et al. Cytotoxic brain edema: assessment with diffusion-weighted MR imaging. *Radiology* 1992; 185:687-690.
- Benveniste H, Hedlund LW, Johnson GA. Mechanism of detection of acute cerebral ischemia in rats by diffusion-weighted magnetic resonance microscopy. *Stroke* 1992; 23:746-754.
- Sykova E, Svoboda J, Polak J, et al. Extracellular volume fraction and diffusion characteristics during progressive ischemia and terminal anoxia in the spinal cord of the rat. *J Cereb Blood Flow Metab* 1994; 14:301-311.
- Niendorf T, Dijkhuizen RM, Norris DG, et al. Biexponential diffusion attenuation in various states of brain tissue: implications for diffusion-weighted imaging. *Magn Reson Med* 1996; 36:847-857.
- van der Toorn A, Dijkhuizen RM, Tulleken CA, et al. Diffusion of metabolites in normal and ischemic rat brain measured by localized ^1H MRS. *Magn Reson Med* 1996; 36:914-922.
- Duong TQ, Ackerman JJ, Ying HS, et al. Evaluation of extra- and intracellular apparent diffusion in normal and globally ischemic rat brain via ^{19}F NMR. *Magn Reson Med* 1998; 40:1-13.
- Morikawa E, Ginsberg MD, Dietrich WD, et al. The significance of brain temperature in focal cerebral ischemia: histopathological consequences of middle cerebral artery occlusion in the rat. *J Cereb Blood Flow Metab* 1992; 12:380-389.
- Szafer A, Zhong J, Gore JC. Theoretical model for water diffusion in tissues. *Magn Reson Med* 1995; 33: 697-712.
- Le Bihan D, Delannoy J, Levin RL. Temperature mapping with MR imaging of molecular diffusion: application to hyperthermia. *Radiology* 1989; 171:853-857.
- Kucharczyk J, Mintorovitch J, Asgari HS, et al. Diffusion/perfusion MR imaging of acute cerebral ischemia. *Magn Reson Med* 1991; 19:311-315.
- Moseley ME, Cohen Y, Mintorovitch J, et al. Early detection of regional cerebral ischemia in cats: comparison of diffusion- and T2-weighted MRI and spectroscopy. *Magn Reson Med* 1990; 14:330-346.
- Moseley ME, Cohen Y, Kucharczyk J, et al. Diffusion-weighted MR imaging of anisotropic water diffusion in cat central nervous system. *Radiology* 1990; 176:439-445.
- Mintorovitch J, Moseley ME, Chileuitt L, et al. Comparison of diffusion- and T2-weighted MRI for the early detection of cerebral ischemia and reperfusion in rats. *Magn Reson Med* 1991; 18:39-50.
- Moonen CT, Pekar J, de Vleeschouwer MH, et al. Restricted and anisotropic displacement of water in healthy cat brain and in stroke studied by NMR diffusion imaging. *Magn Reson Med* 1991; 19:327-332.
- Warach S, Gaa J, Siewert B, et al. Acute human stroke studied by whole brain echo planar diffusion-weighted magnetic resonance imaging. *Ann Neurol* 1995; 37:231-241.
- Schlaug G, Siewert B, Benfield A, et al. Time course of the apparent diffusion coefficient (ADC) abnormality in human stroke. *Neurology* 1997; 49:113-119.
- Lutsep HL, Albers GW, DeCresigny A, et al. Clinical utility of diffusion-weighted magnetic resonance imaging

- in the assessment of ischemic stroke. *Ann Neurol* 1997; 41:574–580.
- 22. Schwamm LH, Koroshetz WJ, Sorensen AG, et al. Time course of lesion development in patients with acute stroke: serial diffusion- and hemodynamic-weighted magnetic resonance imaging. *Stroke* 1998; 29:2268–2276.
 - 23. Copen WA, Schwamm LH, Gonzalez RG, et al. Ischemic stroke: effects of etiology and patient age on the time course of the core apparent diffusion coefficient. *Radiology* 2001; 221:27–34.
 - 24. Marks MP, Tong DC, Beaulieu C, et al. Evaluation of early reperfusion and i.v. tPA therapy using diffusion- and perfusion-weighted MRI. *Neurology* 1999; 52:1792–1798.
 - 25. Nagesh V, Welch KM, Windham JP, et al. Time course of ADCw changes in ischemic stroke: beyond the human eye! *Stroke* 1998; 29:1778–1782.
 - 26. Gonzalez RG, Schaefer PW, Buonanno FS, et al. Diffusion-weighted MR imaging: diagnostic accuracy in patients imaged within 6 hours of stroke symptom onset. *Radiology* 1999; 210:155–162.
 - 27. Mohr J, Biller J, Hial S, et al. Magnetic resonance versus computed tomographic imaging in acute stroke. *Stroke* 1995; 26:807–812.
 - 28. Bryan R, Levy L, Whitlow W, et al. Diagnosis of acute cerebral infarction: comparison of CT and MR imaging. *AJNR Am J Neuroradiol* 1991; 12:611–620.
 - 29. Lovblad KO, Laubach HJ, Baird AE, et al. Clinical experience with diffusion-weighted MR in patients with acute stroke. *AJNR Am J Neuroradiol* 1998; 19:1061–1066.
 - 30. Ay H, Buonanno FS, Rordorf G, et al. Normal diffusion-weighted MRI during stroke-like deficits. *Neurology* 1999; 52:1784–1792.
 - 31. Mullins ME, Schaefer PW, Sorensen AG, et al. CT and conventional and diffusion-weighted MR imaging in acute stroke: study in 691 patients at presentation to the emergency department. *Radiology* 2002; 224:353–360.
 - 32. Singer MB, Chong J, Lu D, et al. Diffusion-weighted MRI in acute subcortical infarction. *Stroke* 1998; 29:133–136.
 - 33. Ostergaard L, Sorensen AG, Kwong KK, et al. High resolution measurement of cerebral blood flow using intravascular tracer bolus passages. Part II: Experimental comparison and preliminary results. *Magn Reson Med* 1996; 36:726–736.
 - 34. Tong DC, Yenari MA, Albers GW, et al. Correlation of perfusion- and diffusion-weighted MRI with NIHSS score in acute (<6.5 hour) ischemic stroke. *Neurology* 1998; 50:864–870.
 - 35. Beaulieu C, de Crespigny A, Tong DC, et al. Longitudinal magnetic resonance imaging study of perfusion and diffusion in stroke: evolution of lesion volume and correlation with clinical outcome. *Ann Neurol* 1999; 46:568–578.
 - 36. Karonen JO, Vanninen RL, Liu Y, et al. Combined diffusion and perfusion MRI with correlation to single-photon emission CT in acute ischemic stroke. Ischemic penumbra predicts infarct growth. *Stroke* 1999; 30:1583–1590.
 - 37. Ay H, Oliveira-Filho J, Buonanno FS, et al. ‘Footprints’ of transient ischemic attacks: a diffusion-weighted MRI study. *Cerebrovasc Dis* 2002; 14:177–186.
 - 38. Karonen JO, Liu Y, Vanninen RL, et al. Combined perfusion- and diffusion-weighted MR imaging in acute ischemic stroke during the 1st week: a longitudinal study. *Radiology* 2000; 217:886–894.
 - 39. Grant PE, He J, Halpern EF, et al. Frequency and clinical context of decreased apparent diffusion coefficient reversal in the human brain. *Radiology* 2001; 221:43–50.
 - 40. Kidwell CS, Saver JL, Starkman S, et al. Late secondary ischemic injury in patients receiving intraarterial thrombolysis. *Ann Neurol* 2002; 52:698–703.
 - 41. Schaefer PW, Hunter GJ, He J, et al. Predicting cerebral ischemic infarct volume with diffusion and perfusion MR imaging. *AJNR Am J Neuroradiol* 2002; 23:1785–1794.
 - 42. Fiehler J, Foth M, Kucinski T, et al. Severe ADC decreases do not predict irreversible tissue damage in humans. *Stroke* 2002; 33:79–86.
 - 43. Fiehler J, Knab R, Reichenbach JR, et al. Apparent diffusion coefficient decreases and magnetic resonance imaging perfusion parameters are associated in ischemic tissue of acute stroke patients. *J Cereb Blood Flow Metab* 2001; 21:577–584.
 - 44. Jones TH, Morawetz RB, Crowell RM, et al. Thresholds of focal cerebral ischemia in awake monkeys. *J Neurosurg* 1981; 54:773–782.
 - 45. Horowitz SH, Zito JL, Donnarumma R, et al. Computed tomographic-angiographic findings within the first five hours of cerebral infarction. *Stroke* 1991; 22:1245–1253.
 - 46. Hornig CR, Dorndorf W, Agnoli AL. Hemorrhagic cerebral infarction—a prospective study. *Stroke* 1986; 17:179–185.
 - 47. Hakim AM, Ryder-Cooke A, Melanson D. Sequential computerized tomographic appearance of strokes. *Stroke* 1983; 14:893–897.
 - 48. Calandre L, Ortega JF, Bermejo F. Anticoagulation and hemorrhagic infarction in cerebral embolism secondary to rheumatic heart disease. *Arch Neurol* 1984; 41: 1152–1154.
 - 49. Ogata J, Yutani C, Imakita M, et al. Hemorrhagic infarct of the brain without a reopening of the occluded arteries in cardioembolic stroke. *Stroke* 1989; 20:876–883.
 - 50. Liotta LA, Goldfarb RH, Brundage R, et al. Effect of plasminogen activator (urokinase), plasmin, and thrombin on glycoprotein and collagenous components of basement membrane. *Cancer Res* 1981; 41:4629–4636.
 - 51. Lijnen HR, Silence J, Lemmens G, et al. Regulation of gelatinase activity in mice with targeted inactivation of components of the plasminogen/plasmin system. *Thromb Haemost* 1998; 79:1171–1176.
 - 52. Oppenheim C, Samson Y, Dormont D, et al. DWI prediction of symptomatic hemorrhagic transformation in acute MCA infarct. *J Neuroradiol* 2002; 29:6–13.
 - 53. Selim M, Fink JN, Kumar S, et al. Predictors of hemorrhagic transformation after intravenous recombinant tissue plasminogen activator: prognostic value of the initial apparent diffusion coefficient and diffusion-weighted lesion volume. *Stroke* 2002; 33:2047–2052.
 - 54. Tong DC, Adami A, Moseley ME, et al. Prediction of hemorrhagic transformation following acute stroke: role of diffusion- and perfusion-weighted magnetic resonance imaging. *Arch Neurol* 2001; 58:587–593.
 - 55. von Kummer R, Allen KL, Holle R, et al. Acute stroke: usefulness of early CT findings before thrombolytic therapy. *Radiology* 1997; 205:327–333.

56. Vo KD, Santiago F, Lin W, et al. MR imaging enhancement patterns as predictors of hemorrhagic transformation in acute ischemic stroke. *AJNR Am J Neuroradiol* 2003; 24:674–679.
57. Fiehler J, Remmeli C, Kucinski T, et al. Reperfusion after severe local perfusion deficit precedes hemorrhagic transformation: an MRI study in acute stroke patients. *Cerebrovasc Dis* 2005; 19:117–124.
58. Alsop D, Makovetskaya E, Kumar S, et al. Markedly reduced apparent blood volume on bolus contrast magnetic resonance imaging as a predictor of hemorrhage after thrombolytic therapy for acute ischemic stroke. *Stroke* 2005; 36:746–750.
59. Kassner A, Roberts T, Taylor K, et al. Prediction of hemorrhage in acute ischemic stroke using permeability MR imaging. *AJNR Am J Neuroradiol* 2005; 26:2213–2217.
60. Kakuda W, Thijs VN, Lansberg MG, et al. Clinical importance of microbleeds in patients receiving IV thrombolysis. *Neurology* 2005; 65:1175–1178.
61. Kim HS, Lee DH, Ryu CW, et al. Multiple cerebral microbleeds in hyperacute ischemic stroke: impact on prevalence and severity of early hemorrhagic transformation after thrombolytic treatment. *AJR Am J Roentgenol* 2006; 186:1443–1449.
62. Le Bihan D, Mangin JF, Poupon C, et al. Diffusion tensor imaging: concepts and applications. *J Magn Reson Imaging* 2001; 13:534–546.
63. Basser PJ, Pierpaoli C. Microstructural and physiological features of tissues elucidated by quantitative-diffusion-tensor MRI. *J Magn Reson B* 1996; 111:209–219.
64. Shimony JS, McKinstry RC, Akbudak E, et al. Quantitative diffusion-tensor anisotropy brain MR imaging: normative human data and anatomic analysis. *Radiology* 1999; 212:770–784.
65. Bammer R, Acar B, Moseley ME. In vivo MR tractography using diffusion imaging. *Eur J Radiol* 2003; 45:223–234.
66. Conturo TE, Lori NF, Cull TS, et al. Tracking neuronal fiber pathways in the living human brain. *Proc Natl Acad Sci U S A* 1999; 96:10422–10427.
67. Makris N, Worth AJ, Sorensen AG, et al. Morphometry of in vivo human white matter association pathways with diffusion-weighted magnetic resonance imaging. *Ann Neurol* 1997; 42:951–962.
68. Mukherjee P, Bahn MM, McKinstry RC, et al. Differences between gray matter and white matter water diffusion in stroke: diffusion-tensor MR imaging in 12 patients. *Radiology* 2000; 215:211–220.
69. Sorensen AG, Wu O, Copen WA, et al. Human acute cerebral ischemia: detection of changes in water diffusion anisotropy by using MR imaging. *Radiology* 1999; 212:785–792.
70. Pierpaoli C, Jezzard P, Basser PJ, et al. Diffusion tensor MR imaging of the human brain. *Radiology* 1996; 201:637–648.
71. Reese TG, Weisskoff RM, Smith RN, et al. Imaging myocardial fiber architecture in vivo with magnetic resonance. *Magn Reson Med* 1995; 34:786–791.
72. Moseley ME, Kucharczyk J, Asgari HS, et al. Anisotropy in diffusion-weighted MRI. *Magn Reson Med* 1991; 19:321–326.
73. Beaulieu C. The basis of anisotropic water diffusion in the nervous system—a technical review. *NMR Biomed* 2002; 15:435–455.
74. Le Bihan D, van Zijl P. From the diffusion coefficient to the diffusion tensor. *NMR Biomed* 2002; 15:431–434.
75. Zelaya F, Flood N, Chalk JB, et al. An evaluation of the time dependence of the anisotropy of the water diffusion tensor in acute human ischemia. *Magn Reson Imaging* 1999; 17:331–348.
76. Yang Q, Tress BM, Barber PA, et al. Serial study of apparent diffusion coefficient and anisotropy in patients with acute stroke. *Stroke* 1999; 30:2382–2390.
77. Ozsunar Y, Grant P, Huisman T, et al. Evolution of water diffusion and anisotropy in hyperacute stroke: significant correlation between fractional anisotropy and T2. *AJNR Am J Neuroradiol* 2004; 25:699–705.
78. Higano S, Zhong J, Shrier DA, et al. Diffusion anisotropy of the internal capsule and the corona radiata in association with stroke and tumors as measured by diffusion-weighted MR imaging. *AJNR Am J Neuroradiol* 2001; 22:456–463.
79. Watanabe T, Honda Y, Fujii Y, et al. Three-dimensional anisotropy contrast magnetic resonance axonography to predict the prognosis for motor function in patients suffering from stroke. *J Neurosurg* 2001; 94:955–960.
80. Werring DJ, Toosy AT, Clark CA, et al. Diffusion tensor imaging can detect and quantify corticospinal tract degeneration after stroke. *J Neurol Neurosurg Psychiatry* 2000; 69:269–272.
81. van Everdingen KJ, van der Grond J, Kappelle LJ, et al. Diffusion-weighted magnetic resonance imaging in acute stroke. *Stroke* 1998; 29:1783–1790.
82. Lovblad KO, Baird AE, Schlaug G, et al. Ischemic lesion volumes in acute stroke by diffusion-weighted magnetic resonance imaging correlate with clinical outcome. *Ann Neurol* 1997; 42:164–170.
83. Engelter S, Provenzale JM, Petrella JR, et al. Infarct volume on apparent diffusion coefficient maps correlates with length of stay and outcome after middle cerebral artery stroke. *Cerebrovasc Dis* 2003; 15:188–191.
84. Nighoghossian N, Hermier M, Adeleine P, et al. Baseline magnetic resonance imaging parameters and stroke outcome in patients treated by intravenous tissue plasminogen activator. *Stroke* 2003; 34:458–463.
85. Rohl L, Geday J, Ostergaard L, et al. Correlation between diffusion- and perfusion-weighted MRI and neurological deficit measured by the Scandinavian Stroke Scale and Barthel Index in hyperacute subcortical stroke (< or = 6 hours). *Cerebrovasc Dis* 2001; 12:203–213.
86. Thijs V, Lansberg M, Beaulieu C, et al. Is early ischemic lesion volume on diffusion-weighted imaging an independent predictor of stroke outcome? A multivariable analysis. *Stroke* 2000; 31:2597–2602.
87. Arenillas J, Rovira A, Molina C, et al. Prediction of early neurologic deterioration using diffusion- and perfusion-weighted imaging in hyperacute middle cerebral artery stroke. *Stroke* 2002; 33:2197–2203.
88. Sanak D, Nosal V, Horak D, et al. Impact of diffusion-weighted MRI-measured initial cerebral infarction volume on clinical outcome in acute stroke patients with middle

- cerebral artery occlusion treated by thrombolysis. *Neuroradiology* 2006; 48:632–639.
89. Hacke W, Albers G, Al-Rawi Y, et al. The Desmoteplase in Acute Ischemic Stroke Trial (DIAS): a phase II MRI-based 9-hour window acute stroke thrombolysis trial with intravenous desmoteplase. *Stroke* 2005; 36:66–73.
 90. Furlan AJ, Eyding D, Albers GW, et al. Dose Escalation of Desmoteplase for Acute Ischemic Stroke (DEDAS): evidence of safety and efficacy 3 to 9 hours after stroke onset. *Stroke* 2006; 37:1227–1231.
 91. Engelter S, Wetzel S, Radue E, et al. The clinical significance of diffusion-weighted MR imaging in infratentorial strokes. *Neurology* 2004; 62:474–480.
 92. Davalos A, Blanco M, Pedraza S, et al. The clinical-DWI mismatch: a new diagnostic approach to the brain tissue at risk of infarction. *Neurology* 2004; 62:2187–192.
 93. Kidwell CS, Alger JR, Di Salle F, et al. Diffusion MRI in patients with transient ischemic attacks. *Stroke* 1999; 30:1174–1180.
 94. Purroy F, Montaner J, Rovira A, et al. Higher risk of further vascular events among transient ischemic attack patients with diffusion-weighted imaging acute ischemic lesions. *Stroke* 2004; 35:2313–2319.
 95. Crisostomo R, Garcia M, Tong D. Detection of diffusion-weighted MRI abnormalities in patients with transient ischemic attack: correlation with clinical characteristics. *Stroke* 2003; 34:932–937.
 96. Gass A, Ay H, Szabo K, et al. Diffusion-weighted MRI for the “small stuff”: the details of acute cerebral ischaemia. *Lancet Neurol* 2004; 3:39–45.
 97. Inatomi Y, Kimura K, Yonehara T, et al. Hyperacute diffusion-weighted imaging abnormalities in transient ischemic attack patients signify irreversible ischemic infarction. *Cerebrovasc Dis* 2005; 19:362–368.
 98. Inatomi Y, Kimura K, Yonehara T, et al. DWI abnormalities and clinical characteristics in TIA patients. *Neurology* 2004; 62:376–380.
 99. Lamy C, Oppenheim C, Calvet D, et al. Diffusion-weighted MR imaging in transient ischaemic attacks. *Eur Radiol* 2006; 16:1090–1095.
 100. Ay H, Koroshetz WJ, Benner T, et al. Transient ischemic attack with infarction: a unique syndrome? *Ann Neurol* 2005; 57:679–686.
 101. Oppenheim C, Lamy C, Touze E, et al. Do transient ischemic attacks with diffusion-weighted imaging abnormalities correspond to brain infarctions? *AJNR Am J Neuroradiol* 2006; 27:1782–1787.
 102. Huber R, Aschoff AJ, Ludolph AC, et al. Transient Global Amnesia. Evidence against vascular ischemic etiology from diffusion weighted imaging. *J Neurol* 2002; 249:1520–1524.
 103. Saito K, Kimura K, Minematsu K, et al. Transient global amnesia associated with an acute infarction in the retrosplenium of the corpus callosum. *J Neurol Sci* 2003; 210:95–97.
 104. Matsui M, Imamura T, Sakamoto S, et al. Transient global amnesia: increased signal intensity in the right hippocampus on diffusion-weighted magnetic resonance imaging. *Neuroradiology* 2002; 44:235–238.
 105. Ay H, Furie KL, Yamada K, et al. Diffusion-weighted MRI characterizes the ischemic lesion in transient global amnesia. *Neurology* 1998; 51:901–903.
 106. Greer DM, Schaefer PW, Schwamm LH. Unilateral temporal lobe stroke causing ischemic transient global amnesia: role for diffusion-weighted imaging in the initial evaluation. *J Neuroimaging* 2001; 11:317–319.
 107. Woolfenden AR, O’Brien MW, Schwartzberg RE, et al. Diffusion-weighted MRI in transient global amnesia precipitated by cerebral angiography. *Stroke* 1997; 28: 2311–2314.
 108. Sedlaczek O, Hirsch J, Grips E, et al. Detection of delayed focal MR changes in the lateral hippocampus in transient global amnesia. *Neurology* 2004; 62:2165–2170.
 109. Sloviter RS, Dempster DW. “Epileptic” brain damage is replicated qualitatively in the rat hippocampus by central injection of glutamate or aspartate but not by GABA or acetylcholine. *Brain Res Bull* 1985; 15:39–60.
 110. Olney JW. Excitatory transmitters and epilepsy-related brain damage. *Int Rev Neurobiol* 1985; 27:337–362.
 111. McNamara JO. Cellular and molecular basis of epilepsy. *J Neurosci* 1994; 14:3413–3425.
 112. Jacob A, Mahavish K, Bowden A, et al. Imaging abnormalities in sporadic hemiplegic migraine on conventional MRI, diffusion and perfusion MRI and MRS. *Cephalgia* 2006; 26:1004–1009.
 113. Butteriss DJ, Ramesh V, Birchall D. Serial MRI in a case of familial hemiplegic migraine. *Neuroradiology* 2003; 45:300–303.
 114. Gutschalk A, Kollmar R, Mohr A, et al. Multimodal functional imaging of prolonged neurological deficits in a patient suffering from familial hemiplegic migraine. *Neurosci Lett* 2002; 332:115–118.
 115. Chabriat H, Vahedi K, Clark CA, et al. Decreased hemispheric water mobility in hemiplegic migraine related to mutation of CACNA1A gene. *Neurology* 2000; 54:510–512.
 116. Kim JH, Choi JY, Koh SB, et al. Reversible splenial abnormality in hypoglycemic encephalopathy. *Neuroradiology* 2007; 49:217–222. (Epub 2006 Nov 30).
 117. Yanagawa Y, Isoi N, Tokumaru AM, et al. Diffusion-weighted MRI predicts prognosis in severe hypoglycemic encephalopathy. *J Clin Neurosci* 2006; 13:696–699.
 118. Kim SY, Goo HW, Lim KH, et al. Neonatal hypoglycaemic encephalopathy: diffusion-weighted imaging and proton MR spectroscopy. *Pediatr Radiol* 2006; 36: 144–148.
 119. Maekawa S, Aibiki M, Kikuchi K, et al. Time related changes in reversible MRI findings after prolonged hypoglycemia. *Clin Neurol Neurosurg* 2006; 108:511–513.
 120. Ebisu T, Naruse S, Horikawa Y, et al. Discrimination between different types of white matter edema with diffusion-weighted MR imaging. *JMRI* 1993;863–868.
 121. Schaefer PW, Buonanno FS, Gonzalez RG, et al. Diffusion-weighted imaging discriminates between cytotoxic and vasogenic edema in a patient with eclampsia. *Stroke* 1997; 28:1082–1085.
 122. Schwartz RB, Mulkern RV, Gudbjartsson H, et al. Diffusion-weighted MR imaging in hypertensive encephalopathy: clues to pathogenesis. *AJNR Am J Neuroradiol* 1998; 19:859–862.
 123. Hinckley J, Chaves C, Appignani B, et al. A reversible posterior leukoencephalopathy syndrome. *N Engl J Med* 1996; 334:494–500.

124. Nakazato T, Nagasaki A, Nakamura K, et al. Reversible posterior leukoencephalopathy syndrome associated with tacrolimus therapy. *Intern Med* 2003; 42:624–625.
125. Henderson RD, Rajah T, Nicol AJ, et al. Posterior leukoencephalopathy following intrathecal chemotherapy with MRA-documented vasospasm. *Neurology* 2003; 60:326–328.
126. Sylvester SL, Diaz LA Jr., Port JD, et al. Reversible posterior leukoencephalopathy in an HIV-infected patient with thrombotic thrombocytopenic purpura. *Scand J Infect Dis* 2002; 34:706–709.
127. Utz N, Kinkel B, Heddle JP, et al. MR imaging of acute intermittent porphyria mimicking reversible posterior leukoencephalopathy syndrome. *Neuroradiology* 2001; 43:1059–1062.
128. Edwards MJ, Walker R, Vinnicombe S, et al. Reversible posterior leukoencephalopathy syndrome following CHOP chemotherapy for diffuse large B-cell lymphoma. *Ann Oncol* 2001; 12:1327–1329.
129. Soylu A, Kavukcu S, Turkmen M, et al. Posterior leukoencephalopathy syndrome in poststreptococcal acute glomerulonephritis. *Pediatr Nephrol* 2001; 16:601–603.
130. Ikeda M, Ito S, Hataya H, et al. Reversible posterior leukoencephalopathy in a patient with minimal-change nephrotic syndrome. *Am J Kidney Dis* 2001; 37:E30.
131. Kamar N, Kany M, Bories P, et al. Reversible posterior leukoencephalopathy syndrome in hepatitis C virus-positive long-term hemodialysis patients. *Am J Kidney Dis* 2001; 37:E29.
132. Honkanen J, Kahara V, Dastidar P, et al. Reversible posterior leukoencephalopathy after combination chemotherapy. *Neuroradiology* 2000; 42:895–899.
133. Taylor MB, Jackson A, Weller JM. Dynamic susceptibility contrast enhanced MRI in reversible posterior leukoencephalopathy syndrome associated with haemolytic uraemic syndrome. *Br J Radiol* 2000; 73:438–442.
134. Lewis MB. Cyclosporin neurotoxicity after chemotherapy. Cyclosporin causes reversible posterior leukoencephalopathy syndrome. *BMJ* 1999; 319:54–55.
135. Ito Y, Arahata Y, Goto Y, et al. Cisplatin neurotoxicity presenting as reversible posterior leukoencephalopathy syndrome. *AJNR Am J Neuroradiol* 1998; 19:415–417.
136. Covarrubias DJ, Luetmer PH, Campeau NG. Posterior reversible encephalopathy syndrome: prognostic utility of quantitative diffusion-weighted MR images. *AJNR Am J Neuroradiol* 2002; 23:1038–1048.
137. Ay H, Buonanno FS, Schaefer PW, et al. Posterior leukoencephalopathy without severe hypertension: utility of diffusion-weighted MRI. *Neurology* 1998; 51: 1369–1376.
138. Breen JC, Caplan LR, DeWitt LD, et al. Brain edema after carotid surgery. *Neurology* 1996; 46:175–181.
139. Schaefer PW, Grant PE, Gonzalez RG. Diffusion-weighted MR imaging of the brain. *Radiology* 2000; 217:331–345.
140. Smith WH, Hauser SL, Easton JD. Cerebrovascular Disease. In: Braunwald E, Fauci AS, Kasper DL, et al. eds. *Harrison's Principles of Internal Medicine*. New York: McGraw-Hill, 2001:2369–2391.
141. Ameri A, Bousser MG. Cerebral venous thrombosis. *Neurol Clin* 1992; 10:87–111.
142. Daif A, Awada A, al-Rajeh S, et al. Cerebral venous thrombosis in adults. A study of 40 cases from Saudi Arabia. *Stroke* 1995; 26:1193–1195.
143. Hickey WF, Garnick MB, Henderson IC, et al. Primary cerebral venous thrombosis in patients with cancer—a rarely diagnosed paraneoplastic syndrome. Report of three cases and review of the literature. *Am J Med* 1982; 73:740–750.
144. Crawford SC, Digre KB, Palmer CA, et al. Thrombosis of the deep venous drainage of the brain in adults. Analysis of seven cases with review of the literature. *Arch Neurol* 1995; 52:1101–1108.
145. Villringer A, Einhaupl KM. Dural sinus and cerebral venous thrombosis. *New Horiz* 1997; 5:332–341.
146. Lefebvre P, Lierneux B, Lenaerts L, et al. Cerebral venous thrombosis and procoagulant factors—a case study. *Angiology* 1998; 49:563–571.
147. Ito K, Tsugane R, Ikeda A, et al. Cerebral hemodynamics and histological changes following acute cerebral venous occlusion in cats. *Tokai J Exp Clin Med* 1997; 22:83–93.
148. Nagai S, Horie Y, Akai T, et al. Superior sagittal sinus thrombosis associated with primary antiphospholipid syndrome—case report. *Neurol Med Chir (Tokyo)* 1998; 38:34–39.
149. Vielhaber H, Ehrenforth S, Koch HG, et al. Cerebral venous sinus thrombosis in infancy and childhood: role of genetic and acquired risk factors of thrombophilia. *Eur J Pediatr* 1998; 157:555–560.
150. van den Berg JS, Boerman RH, vd Stolpe A, et al. Cerebral venous thrombosis: recurrence with fatal course. *J Neurol* 1999; 246:144–146.
151. Forbes KP, Pipe JG, Heiserman JE. Evidence for cytotoxic edema in the pathogenesis of cerebral venous infarction. *AJNR Am J Neuroradiol* 2001; 22:450–455.
152. Allroggen H, Abbott RJ. Cerebral venous sinus thrombosis. *Postgrad Med J* 2000; 76:12–15.
153. Tsai FY, Wang AM, Matovich VB, et al. MR staging of acute dural sinus thrombosis: correlation with venous pressure measurements and implications for treatment and prognosis. *AJNR Am J Neuroradiol* 1995; 16:1021–1029.
154. Yuh WT, Simonson TM, Wang AM, et al. Venous sinus occlusive disease: MR findings. *AJNR Am J Neuroradiol* 1994; 15:309–316.
155. Dormont D, Anxionnat R, Evrard S, et al. MRI in cerebral venous thrombosis. *J Neuroradiol* 1994; 21:81–99.
156. Kassem-Moussa H, Provenzale JM, Petrella JR, et al. Early diffusion-weighted MR imaging abnormalities in sustained seizure activity. *AJR Am J Roentgenol* 2000; 174:1304–1306.

13

Diffusion Imaging in Brain Tumors and Treatment Response

SHAREEF RIAD

The Functional MRI Laboratory, Department of Radiology, Memorial Sloan-Kettering Cancer Center, New York, New York, U.S.A.

ANDREI I. HOLODNY

The Neuroradiology Section and the Functional MRI Laboratory, Department of Radiology, Memorial Sloan-Kettering Cancer Center, New York, New York, U.S.A.

SURESH K. MUKHERJI

Department of Radiology, University of Michigan, Ann Arbor, Michigan, U.S.A.

INTRODUCTION

Diffusion (or diffusion-weighted) MRI is a magnetic resonance imaging technique that visualizes the speed at which molecules of water diffuse through tissue. Diffusion MRI has found the greatest clinical utility in its ability to detect hyperacute stroke; however, the application of this modality is rapidly expanding to other clinical pathologies such as tumors. This chapter will briefly outline the physical principles whose understanding will allow the radiologist to properly interpret diffusion-based images and advanced applications of diffusion MRI. We will also discuss the most important clinical applications of diffusion imaging in the evaluation of tumor pathology. Finally, we will discuss the application of diffusion imaging to the assessment of solid tumor response to therapy.

PHYSICAL PRINCIPLES OF DIFFUSION MRI (FOR THE PHYSICIAN)

Diffusion

The key to understanding diffusion MRI is realizing that it is fundamentally different from routine MR sequences such as T1 and T2 and, in fact, conceptually easier to understand. T1- and T2-weighted images are generated from the time it takes for molecules to return to their original resting state after undergoing a series of excitations. Diffusion MRI is based on visualizing the relative speeds at which water molecules diffuse through tissue.

What does the term diffusion mean? Diffusion describes the random, or *Brownian*, motion of molecules. All molecules exhibit this kind of motion at temperatures greater than absolute zero. Diffusion exists in all states of

matter, and is very high in gases, intermediate in liquids, and very low in solids. A helpful analogy in understanding diffusion MRI is the glass of water: If one adds material to the water in the glass that will impede the motion of the water molecules, then the diffusion of the water molecules will decrease.

The diffusion of water in the human body is determined by the type and density of tissue through which it must pass. In the human brain, diffusion is highest in the ventricles, where there are no structures to impede the motion of water, as in a glass of water. In the brain parenchyma, the diffusion of water is significantly slower due to structures such as cell membranes and myelin sheaths, which impede the motion of water molecules. Tissues with greater impediments to water diffusion exhibit what is known as *restricted diffusion*.

Data derived from diffusion MRI can be presented in several ways: as diffusion-weighted images, T2-corrected diffusion-weighted images, apparent diffusion coefficient maps, and in other ways that will be described later. Increased diffusion may appear bright or dark, depending on how the data is presented. However, one can always tell where the maximal diffusion is by looking for the ventricles, which act as a sort of internal control. If the ventricles appear dark, the increased diffusion is dark. If the ventricles appear bright, the increased diffusion is bright.

Diffusion-Weighted Images and ADC Maps

In physics, diffusion is defined by a coefficient known as D . In clinical imaging, diffusion is defined by the apparent diffusion coefficient or ADC. This is because clinical imaging does not exist in the ideal universe often invoked by physics, and it is impossible to separate the translational displacement of water due to diffusion from other sources of water motion such as blood flow, head movement, and physiologic brain movement. To illustrate this difference, imagine a water molecule attached to the cell membrane of an erythrocyte that starts off in a voxel that is being scanned. Relative to the erythrocyte, the water molecule will not diffuse anywhere; however, the erythrocyte itself is coursing through an artery and out of the voxel being scanned. Strictly speaking, the attached water molecule has not diffused anywhere, but rather has been displaced by the gross motion of blood. This physical reality is not registered by an MRI scanner, which instead will “see” that the water molecule has “diffused” out of the voxel being scanned. Generally speaking, motion in the brain other than diffusion has only a minor contribution to the ADC, except in voxels containing large arteries, so that the ADC can be regarded as a good estimate of the true diffusion coefficient, D .

Diffusion weighting results from adding a pair of pulsed magnetic field gradients to standard MR sequences. For example, in a routine spin-echo sequence, the initial

90° pulse is followed by the application of a pulsed gradient. This pulsed gradient brings about a rapid de-phasing of the spins. A refocusing 180° pulse, normally employed in routine spin-echo sequences, is followed by the second pulsed gradient that has the opposite effect of the previously applied gradient. If there has not been significant diffusion of water molecules between the applications of the two gradients, the second gradient will effectively refocus the spins. If, however, significant diffusion has occurred, the re-phasing will be incomplete. This manifests as signal dropout in regions with high rates of water diffusion. This explains why the signal intensity of cerebrospinal fluid (CSF) in the ventricles is hypointense to signal intensity of the brain parenchyma.

The b value describes the sensitivity of a particular sequence to diffusion and depends on a number of factors including the magnitude and direction of the pulsed gradient pair. Higher b values denote stronger diffusion weighting.

DIFFUSION IN DIAGNOSTIC MRI (OR CLINICAL APPLICATION OF DTI)

Standard MRI sequences have greatly improved the clinician’s ability to accurately diagnose various mass lesions in the brain. Since diffusion MRI measures a different parameter than conventional MRI sequences, it seemed promising that diffusion MRI could enhance the sensitivity and specificity of standard MRI in characterizing tumors of the brain.

Dermoid and Epidermoid Tumors and Arachnoid Cysts

The area where diffusion imaging has been shown great efficacy is in differentiating arachnoid cysts from dermoid or epidermoid tumors. These tumors cannot readily be distinguished from one another on T1- and T2-weighted images nor can they be differentiated on proton density and fluid attenuated inversion recovery (FLAIR) images. However, on diffusion-weighted images, these entities have very different signal characteristics. Arachnoid cysts are hypointense to brain and isointense to CSF on diffusion-weighted images, whereas dermoids and epidermoids are hyperintense to brain (Fig. 1) (1,2).

The difference in signal characteristics between these tumors is conceptually straightforward from a physics point of view. In arachnoid cysts, there is a paucity of structures to impede the motion of water; therefore, arachnoid cysts have signal intensities that are equivalent to CSF (e.g., low signal on diffusion-weighted images). In contrast, dermoids and epidermoids are packed with cells and keratinous debris, which act as significant barriers to water diffusion (1,2). It follows that the ADC of epidermoids is similar to that of brain, but the reason why epidermoids have higher signal intensity on diffusion-weighted images is due to T2 shine through effect (3).

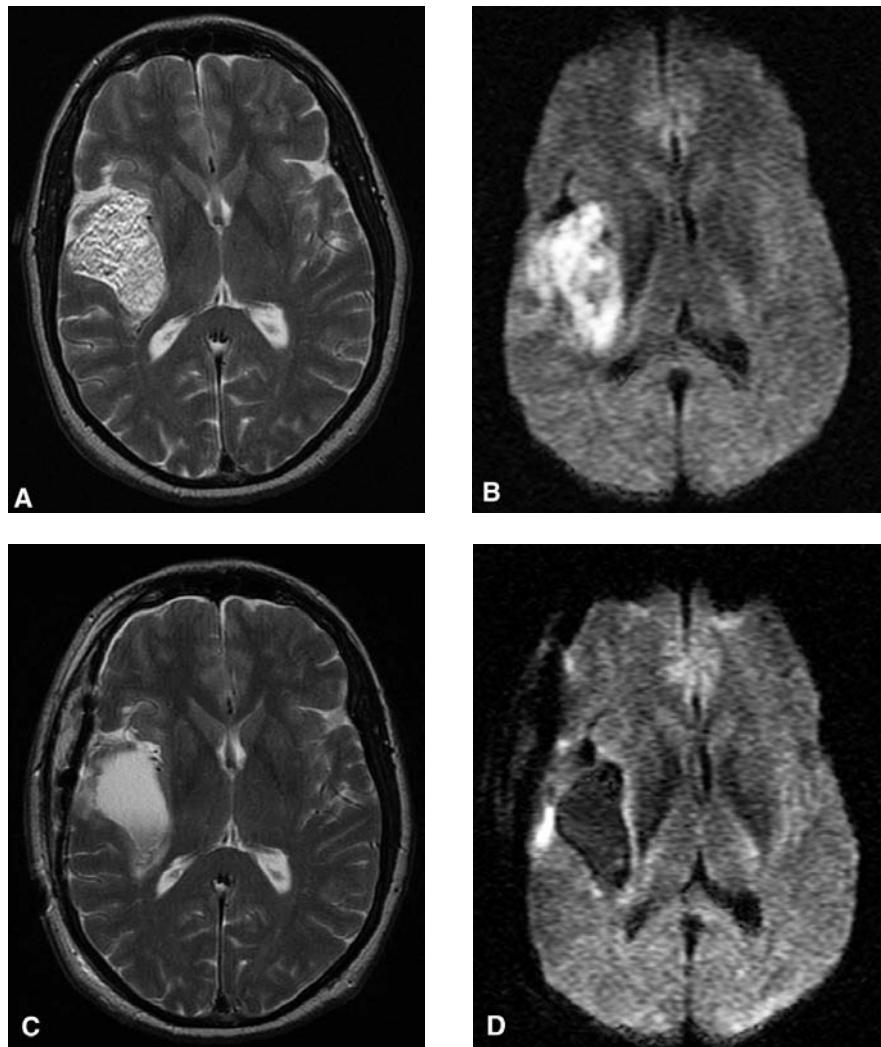


Figure 1 A 53-year-old woman with a dermoid tumor. (A) Axial T2-weighted image demonstrates a tumor in the right Sylvian fissure that is isointense to the CSF in the ventricles. (B) Axial DWI demonstrates the tumor to be hyperintense. This indicates restricted diffusion excluding an arachnoid cyst. Compare with the signal intensity of the CSF in the ventricles. (C) Postoperative T2-weighted image. The surgical cavity is again isointense to the CSF, except for a small area of hematocrit effect. This makes detection of residual tumor difficult. (D) Postoperative DWI demonstrates no residual tumor in the surgical cavity. However, there is a small focus of ischemia just lateral to the surgical cavity. Abbreviations: CSF; DWI, diffusion-weighted imaging. Source: Reprinted from Ref. 66 with permission from Elsevier.

The difference in signal characteristics between epidermoids and CSF on diffusion-weighted imaging (DWI) has clinical utility in the diagnosis of these tumors within the spine (4). Additionally, DWI is reported to be the optimal sequence to identify postoperative residual epidermoid tumors (5).

Primitive Neuroectodermal Tumors

Primitive neuroectodermal tumors (PNETs) comprise a heterogeneous group of embryonal, largely undifferentiated malignancies primarily affecting children. In the CNS,

these tumors can be broadly divided into supratentorial tumors, of which neuroblastoma is prototypical, and infratentorial tumors, most commonly medulloblastoma. The role of DWI in PNETs has been explored with promising results.

Medulloblastomas are the most common primary CNS tumor in children and, like other PNETs, are highly cellular (6). These tumors are generally isointense to cortex on T1- and T2-weighted imaging (7). Studies using DWI have shown decreased signal intensity on ADC maps of solid tumor, in contrast to other pediatric brain tumors that are generally hyperintense on T2 and show increased signal on ADC (7,8). The densely packed cells of medulloblastomas likely constitute a barrier to

water movement resulting in restricted diffusion, or decreased signal, on ADC (8). Unlike medulloblastomas, neuroblastomas and other supratentorial brain tumors are relatively rare, constituting less than 1% of all pediatric brain tumors. One small case series showed that these tumors are also characterized by restricted diffusion, suggesting a role for DWI in diagnosis; however, DWI was found to be no better than T1- and T2-weighted images in accurately defining the surrounding zones of neoplastic infiltration (9).

Tumor Infarction and Necrosis

DWI has been shown to be efficacious in demonstrating areas of acute infarction in the setting of brain tumors, edema, and postoperative changes. All of these areas will be hyperintense on T2-weighted images. However, the area of acute infarction will be hyperintense on diffusion-weighted images, whereas tumor, edema, and postoperative changes will remain isointense (Fig. 1D). DWI has also demonstrated efficacy in differentiating cerebral abscess from necrotic tumor. Both may appear as ring-enhancing lesions on CT and conventional MR sequences; however, abscess will have restricted diffusion and appear bright on DWI, while necrotic gliomas and necrotic metastases have less-restricted diffusion and far lower signal intensity on DWI (10–12).

Other Brain Tumors

DWI so far has demonstrated less efficacy in distinguishing between other tumor pathologies. Unfortunately,

tumors are nonuniform entities and present with a wide variability in ADC values. Consequently, there is significant overlap between different pathologies, rendering specific diagnoses difficult to make (13–15).

This is especially true for heterogeneous tumors such as glioblastoma multiforme (GBM). To better appreciate the diffusion images, let us consider what is physically occurring on a cellular level within the tumor. Within a high-grade glioma, or GBM, there are regions of high cellularity interspersed with regions of necrosis. The necrotic regions of tumor have less cell membranes than the viable cellular regions. Within areas of necrotic tumor, cells have died and their constituent parts, including myelin sheaths and cell membranes, are undergoing disintegration. This breakdown of structure leads to a decrease in the impedance to the diffusion of water molecules and an increase in the ADC. Therefore, necrotic areas of tumor will have signal intensities closer to that of the ventricles (the highest ADC values in the brain), while viable areas of tumor will have ADC values closer (but not equivalent) to healthy brain parenchyma.

Non-necrotic or viable regions of tumor are characterized by high cellularity. In other words, these regions will have more structure (e.g., more cell membranes) when compared with normal brain. This excess of structure leads to an increase in the impedance to the diffusion of water and a decrease in ADC values. Signal intensity in these regions will be less like that in the ventricles. Figure 2 illustrates this relationship. The diagnosis is GBM. The T1-weighted image clearly shows a necrotic region as well as an area of enhancing viable tumor. On the diffusion-weighted image, the area of necrosis has decreased signal intensity, corresponding to an increase in the ADC of

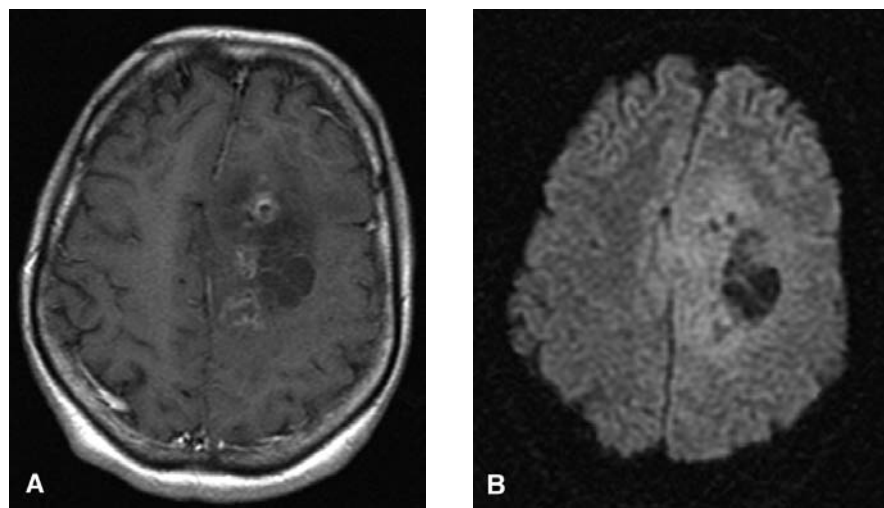


Figure 2 A 38-year-old woman with a glioblastoma multiforme. (A) Axial T1-weighted image demonstrates enhancing tumor and areas of necrosis. (B) Axial DWI shows focal areas of decreased diffusion corresponding to areas of high cellularity (contrast enhancement on the T1-weighted images) as well as increased diffusion that correspond to areas of tumor necrosis (low signal on the T1-weighted images). *Source:* Reprinted from Ref. 66 with permission from Elsevier.

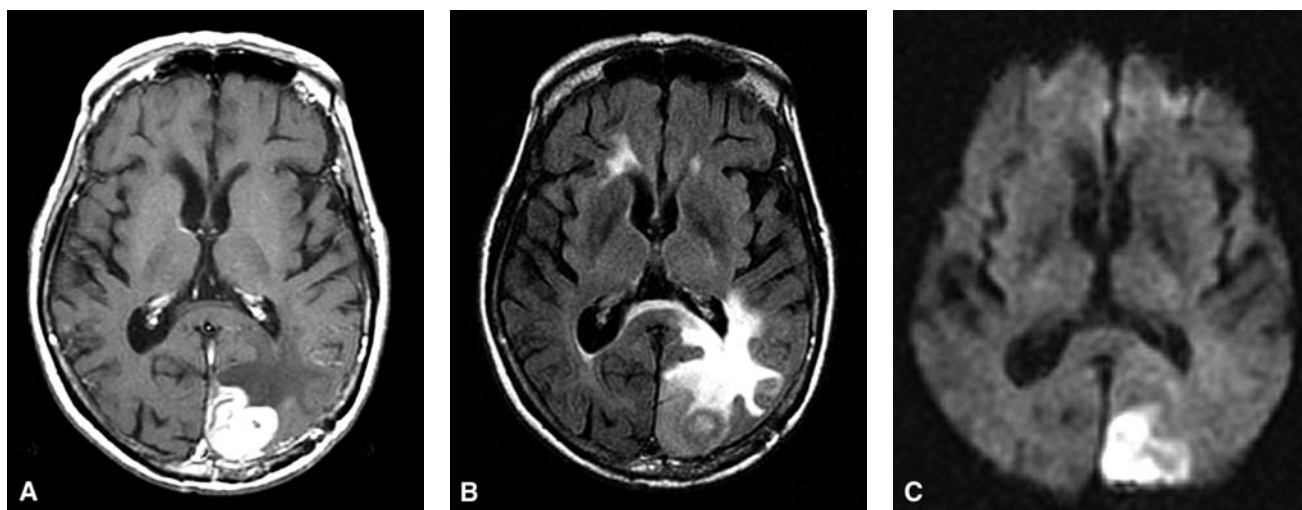


Figure 3 An 81-year-old female with CNS lymphoma. (A) Gadolinium-enhanced axial T1-weighted image of enhancing mass representing biopsy-proven lymphoma. (B) Axial FLAIR image shows peritumoral edema. (C) Axial DWI shows increased signal in the region of the tumor owing to restricted diffusion believed to be caused by increased cellularity. Note that the tumor was only mildly hyperintense on the FLAIR, $b = 0$, and T2-weighted images (not shown), indicating that the hyperintensity on DWI is not caused by T2 shine through. Abbreviations: FLAIR, fluid attenuated inversion recovery; DWI, diffusion-weighted imaging. Source: Reprinted from Ref. 66 with permission from Elsevier.

water molecules in that region. On the other hand, the areas on the diffusion-weighted image that correspond to more cellular portions of tumor have an increased signal intensity corresponding to a decrease in the ADC.

As the above discussion suggests, diffusion imaging has been successful in assessing the cellularity of tumors. First, tumors that tend to be highly cellular, such as lymphomas (Fig. 3), are likely to have higher ADC values than less cellular tumor pathologies, such as astrocytomas (10,16). Furthermore, more cellular astrocytomas, as determined on biopsy, have higher ADC values than less cellular astrocytomas (17,18). In general, this is not enough to be able to differentiate between different tumor pathologies since there tends to be a large overlap.

Another disappointment of DWI is the inability to reliably differentiate between tumor infiltration and peritumoral edema, an important distinction for tumors such as GBM, known to have distant infiltration of neoplastic cells (19). Studies have compared peritumoral regions of high-grade gliomas with peritumoral regions of noninfiltrating tumors such as meningiomas and metastases with the hope using ADC values to distinguish edema from infiltration. Because different tumor types infiltrate surrounding brain parenchyma to different degrees, some information on tumor pathology can be inferred from the ADC values of peritumoral regions. Several studies have demonstrated a significant difference between the peritumoral regions of gliomas and metastases (20–22), while another showed no significant difference between the peritumoral regions of gliomas and meningiomas (23); these conflicting results

may be attributable to differences in study design. However, another study of 22 patients with glioma who underwent biopsy found significant overlap in ADC values between tumor and peritumoral regions, suggesting DWI is not helpful in demarcating tumor margins (24). Recent work has cast doubt on the previously suggested role of ADC values in distinguishing pure edema from tumor-infiltrated edema when gliomas, meningiomas, and metastases were compared (25). There is some evidence that using high b values of up to 5000 and biexponential analysis of decay curves can differentiate tumor infiltration from peritumoral edema (26). At best it appears that ADC values of peritumoral regions can be informative—but not definitive—in distinguishing high-grade gliomas from metastases and meningiomas, though diffusion imaging at this time cannot directly depict neoplastic infiltration. Studies using combinations of MR spectroscopy, perfusion, and diffusion-weighted MRI, though demonstrating superiority to conventional MRI, have been marked by similar limitations (20,27,28).

FRACTIONAL ANISOTROPY MAPS

One promising application of diffusion MRI in the imaging of mass lesions in the brain is *diffusion tractography*. This application of diffusion MRI allows for the identification of specific white matter tracts running adjacent to mass lesions in the brain and is well suited for intraoperative guidance and neurosurgical planning.

Physical Principles

Briefly, let us review the physical principles involved in diffusion tractography. A term closely entwined with diffusion imaging is *anisotropy*. Simply put, anisotropy means that an object (or function) has different values in different directions. An object or function with a higher value in the x-direction than the y-direction is considered anisotropic. Imagine an American football or the Goodyear blimp. These objects are anisotropic because they achieve much greater values along the long axis than the short axis. On the other hand, a soccer ball or sphere achieves the same value in all directions and is considered isotropic.

The concept of anisotropy is relevant to diffusion imaging of the brain because in many areas of the brain the diffusion of water is anisotropic, or not the same in all directions. This property of diffusion is most prominent in the white matter tracts of the brain. What underlies this directionality of diffusion in white matter? Why should molecules of water diffuse more strongly in one direction than the other? The motion of water molecules is impeded by hydrophobic structures, such as myelin sheaths and cell membranes. Myelinated axons in the central nervous system are packed with hydrophobic elements, and water molecules are impeded from crossing or moving perpendicular to these elements. Instead, water molecules move (or diffuse) much more readily parallel to the long axis of these axons, minimizing interactions with hydrophobic elements. This phenomenon applies to both intracellular and extracellular water.

In order to better conceptualize this concept, let us return to our previous model for diffusion—the glass of water. In a normal glass of water, the water molecules diffuse in every direction equally. There are no structural elements present to hinder their Brownian motion. The diffusion of water molecules in this model is isotropic. However, if one puts a handful of thin glass rods into the glass, the motion of water molecules will be impeded in the direction perpendicular to the long axis of these rods. Water molecules will bump into the outer walls of these glass rods. Instead, water will move preferentially in parallel to the long axis of these rods, and the diffusion of water molecules in the glass will acquire directionality and become anisotropic.

Returning to the imaging of the brain, let us use the corticospinal tract in the internal capsule as an example. Most axons in this region are aligned in a particular direction. Within a particular voxel being scanned, so long as the axons in that voxel are aligned in a particular direction, there will be more net water diffusion parallel to the direction of the axons. Therefore, the voxel in question will have a net anisotropic diffusion in that direction.

In the previous discussion of the diagnosis of brain tumors with DWI, only the absolute value of diffusion in a voxel was considered; that is to say, the value being measured was how many water molecules moved out of the voxel, but not the directionality of this movement. The black and white images did not portray directionality of water diffusion. Instead, diffusion was defined by a scalar value:

$$D_{\text{average}} = \frac{D_x + D_y + D_z}{3}$$

We must now introduce a new concept—the tensor—to complete the discussion of the physical principles of diffusion. The tensor seems to generate the most consternation among radiologists. What is a tensor, and how is it different from a vector? Readers already familiar with tensor physics can pass over this section, but most physicians with some knowledge of physics and mathematics will (hopefully) find this next section enlightening.

A tensor is like a nine-dimensional vector. The familiar vector has three components (x, y, z), while a tensor has nine (xx, xy, xz, yx, yy, yz, zx, zy, zz). These can be arranged into the following matrix:

$$\begin{matrix} xx & xy & xz \\ yx & yy & yz \\ zx & zy & zz \end{matrix}$$

The component xx can be interpreted as motion in the x-direction with respect to the x-direction. Similarly, xz is motion in the x-direction with respect to the z-direction, and so forth. A vector is essentially a tensor in which six of the nine components (xy, xz, yx, yz, zx, zy) equal zero, leaving xx, yy, and zz, which become the x, y, and z components of a vector.

$$\begin{aligned} & xx, 0, 0 \\ & 0, yy, 0 = (x, y, z) \\ & 0, 0, zz \end{aligned}$$

Why are nine dimensions needed to describe motion, and why does a standard three-dimensional vector not suffice? What are the extra six dimensions? A vector describes motion along the three main Cartesian coordinates (x, y, z). In effect, a vector can describe all motion where the tip of a finger can be used to move something (e.g., pushing a paper clip across a table with the tip of your finger, or in three dimensions, moving a floating jar of olives in outer space at zero gravity with the tip of your finger).

A tensor is capable of describing more complicated motion. Imagine what is needed to unfold a paper clip. You can push a paper clip along with the tip of your finger, but you cannot undo its coiled form. In order to uncoil a paper clip, you need to move an end of the paper clip in one direction with respect to another. This is where

a tensor component such as xy becomes important, which describes motion in the x -direction with respect to the y -direction. In our paper clip example, this would be akin to one hand (uncoiling one end of the paper clip) with respect to another hand (holding the other end of the paper clip in place). A three-dimensional vector cannot be used to define the sort of “twisting” motion required to uncoil a paper clip. Instead, a nine-dimensional tensor is necessary. In physics, there is a distinction between “force” (which can be described by a three-dimensional vector) and “torque” (which can only be described by a nine-dimensional tensor).

A second example of complex motion can be found in the American game of baseball. A pitcher may choose to throw a “fast ball” in which the baseball travels along a linear trajectory because the pitcher does not place any “spin” on the ball. This straight-line motion can be described by a vector. However, if the pitcher throws a “curve ball” by placing spin on the ball, the ball will rotate on an internal axis unrelated to the direction the ball is flying. This spin will affect the overall trajectory of the ball, causing it to arc or curve toward the batter rather than fly directly at him. Changing the spin placed on the baseball will change the trajectory of the ball, but so long as the ball is spinning on an axis, its motion will be nonlinear. This complex motion can only be described by a tensor. A three-dimensional vector cannot account for the effect of spin on the trajectory of the ball. Therefore, a batter who can appreciate tensors will be able to understand the trajectory of a curve ball, anticipate its motion, and hit the pitch. On the other hand, a batter who cannot appreciate tensors, but only vectors, will not be able to predict the motion of the curve ball. Consequently, the pitcher will always be able to strike out such a batter. This same phenomenon can be seen in soccer in which a player, making a free kick, places spin on the ball to direct it around the wall of opponents blocking the goal—“bending it like Beckham.” This complex motion, which can only be described by a tensor, makes scoring a goal in this situation possible (Fig. 4).

Data Acquisition and Calculation of Diffusion Tensor

As described previously, a diffusion-weighted image or an ADC map is generated from water diffusion in each of the three directions (x , y , z) of the Cartesian coordinate system. These images show the amount of diffusion (a scalar value) in each voxel, but not the direction of diffusion.

To generate diffusion images based on a tensor, one needs a more sophisticated acquisition than that employed to generate standard diffusion-weighted images or ADC maps. At least six directions (xx , xy , xz , yy , yz , zz) need

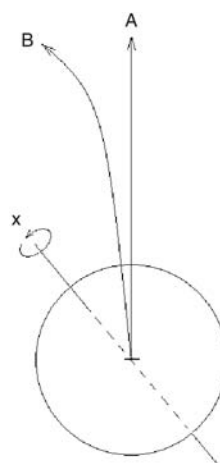


Figure 4 The baseball/soccer analogy that illustrates the difference between a vector and a tensor (see text). A vector (with 3 dimensions) can only define the path that the ball would take if thrown with no spin (**A**). More dimensions (a tensor) are needed to define the path that the ball would take if a spin were placed on it (**x**). The spin would cause the ball to take a different path (**B**). Therefore, if the batter is capable of understanding only a three-dimensional vector, he will not appreciate that the trajectory of the ball is changing and will strike out every time.
Source: Reprinted from Ref. 66 with permission from Elsevier.

to be acquired, along with the $b = 0$ images, to generate a diffusion tensor. Although a tensor, strictly speaking, has nine values, one can generally get away with acquiring six values and assuming $xy = yx$, $xz = zx$, and $yz = zy$ to complete the nine-dimensional tensor.

More accurate diffusion tensor imaging (DTI), based on the acquisition of even more directions, is also available with most MRI manufacturers. The issue is that more directions require longer scan times. In addition, the signal-to-noise ratio of these sequences is rather weak. Therefore, one may elect to scan with a number of acquisitions ($NEX > 1$). Currently, the optimal number of directions and NEXs is not established and is probably different for each scanner and each academic center or clinical practice. The “optimal” parameters may even change with individual patients, for example, if a patient is having difficulty holding still, one may elect to use less directions and NEXs. As scanner technology improves (faster acquisitions and greater gradient strengths), we suspect that the “optimal” number of acquisitions and NEXs will also increase.

Fractional Anisotropy Maps

The diffusion tensor (D) for each voxel (29–31) defines the complex motion of water molecules in that voxel.

From each diffusion tensor (D) defined for a voxel, three eigenvalues, ($\lambda_1, \lambda_2, \lambda_3$), can be derived (29,30). This is represented mathematically by the diffusion ellipsoid (31). If a particular voxel has a high degree of anisotropy, one of the eigenvalues will be much greater than the other two: $\lambda_1 >> \lambda_2 = \lambda_3$. Each eigenvalue has an associated eigenvector; the eigenvector corresponding to the largest eigenvalue is termed the “principal eigenvector.”

Simply put, the principle eigenvector is a mathematical description of the main direction of water diffusion. This direction is almost never along the primary Cartesian (x, y, z) axes. A voxel containing axons running predominantly in one direction will have a principal eigenvector pointing in the same direction. Diffusion of water molecules, then, describes the primary direction of white matter tracts in a voxel, and a fractional anisotropy (FA) value of the voxel is calculated from the eigenvalues.

FA values range between 0 and 1 and represent how strongly water diffuses in the direction of the principle eigenvector. In a region of the brain with white matter tracts predominantly aligned in one direction, water molecules will diffuse strongly in that direction and the FA value will approach 1 (Fig. 5A). In a region with more variation in axon alignment, the FA value will be between 0 and 1 (Fig. 5B). Very random alignment of axons will yield an FA value near 0 (Fig. 5C). Using FA values to generate an FA map allows the visualization not only of the amount of water diffusion in a particular voxel but also the direction of diffusion within that voxel (Fig. 5).

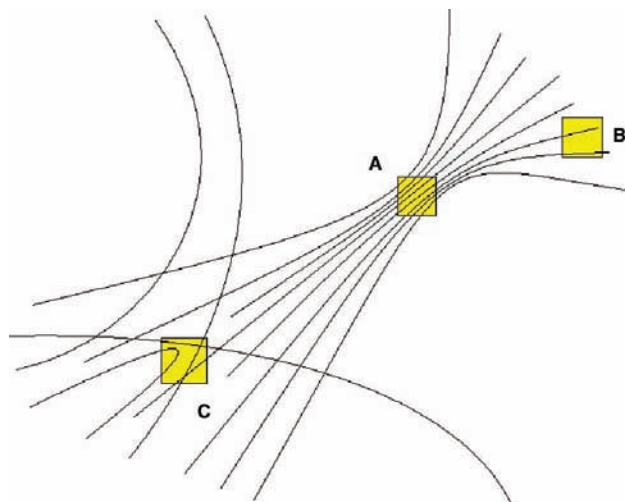


Figure 5 Fractional anisotropy (FA) is greatest when axons are aligned in parallel (voxel A) and least when axons are arranged randomly (voxel C). Voxel B captures axons with moderate organization corresponding to an intermediate FA value. *Source:* Reprinted from Ref. 66 with permission from Elsevier.

Clinical Application

Diffusion tensor images and FA maps are visually striking. They depict what conventional MRI sequences cannot: the directionality of white matter tracts. This permits the identification of different tracts that appeared as an amorphous mass of white matter before DTI.

In the images provided (Fig. 6), craniocaudad white matter tracts are shown in blue, anterior-posterior tracts in green, and right-to-left tracts in red. Clearly visible are tracts such as the internal capsule, optic radiations, and tracts of the superior frontal gyrus. Smaller tracts such as the external capsule and the corticospinal tract in the brainstem are also visible.

Notwithstanding the aesthetic considerations, the role of FA maps in differentiating tumor pathologies is uncertain. The basic limitation is the same as with diffusion-weighted images and ADC maps. The ability to visualize the directionality of the white matter tracts does not necessarily add to the ability to distinguish one pathology from another, although there is some evidence to suggest that tumor pathologies can be differentiated on the basis of decreased anisotropy in adjacent white matter tracts. It has been shown that the FA in normal appearing white matter adjacent to high-grade gliomas is significantly lower than the FA in white matter adjacent to meningiomas (23), or adjacent to low-grade gliomas or metastases (32) but these findings were not supported in a recent study showing no difference in FA or ADC in normal appearing white matter adjacent to gliomas, meningiomas, and metastases (25). As in DWI and ADC maps, there are differences in the diffusion characteristic of different tumors; however, there is also a large overlap.

The FA maps do demonstrate that there is a decrease in the diffusion anisotropy as one enters the tumor from normal white matter tracts. This is illustrated by the drawing in Figure 7 and is an expected finding when one considers the microscopic structure of the changes in white matter tracts with the infiltration of a tumor. Diffusion anisotropy decreases as a result of two processes that disturb the orderliness and directionality of axons. One process is the infiltration of free water, or edema, and tumor cells into the spaces between the axons. As a result, less axons are present per voxel, and fewer myelin sheaths and cell membranes are present within each voxel to restrict water diffusion in a particular direction. The second process is the phenomenon of tumor necrosis in which the resultant destruction of the cytoarchitecture reduces the FA to near zero.

While many investigations have successfully demonstrated white matter tracts near brain tumors using FA or ADC maps (33,34), these technologies have not adequately defined the precise limits of the tracts to be avoided during operations. Neither have they been able

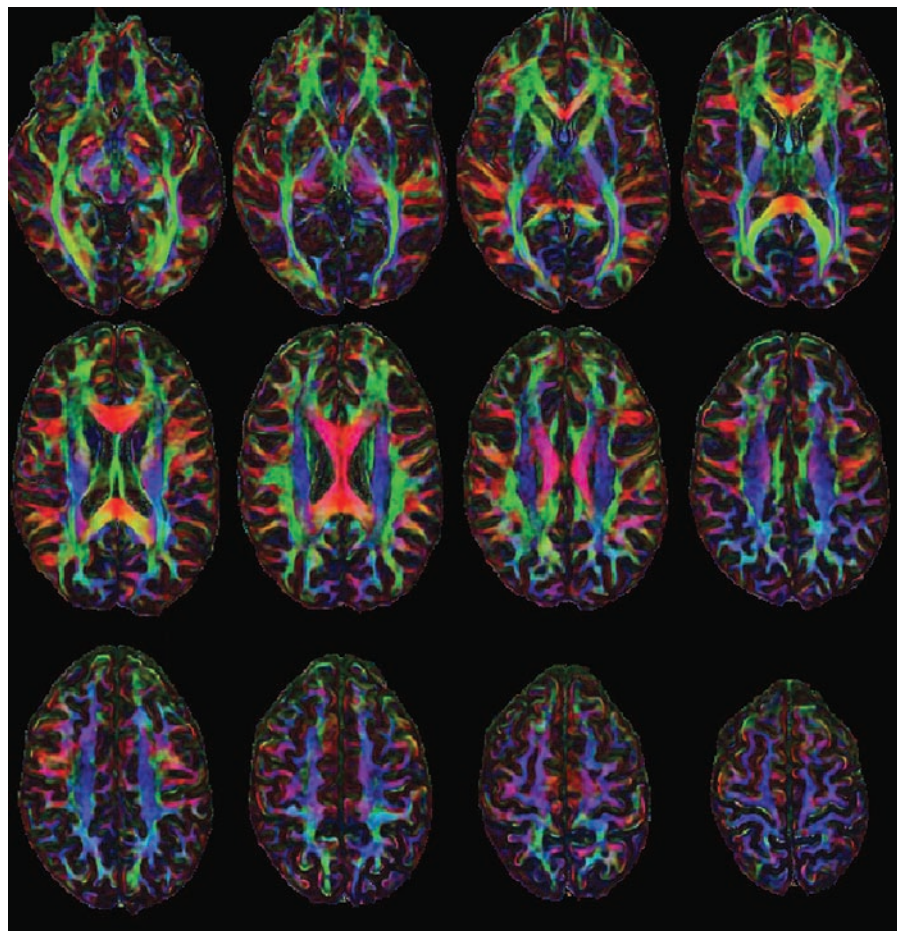


Figure 6 Fractional anisotropy (FA) map. Blue indicates a craniocaudad direction of the white matter tracts, green is anterior-posterior, and red is right-left. The internal capsules and even the external capsules are seen clearly in blue. The genu and the splenium of the corpus callosum and the optic radiations are seen in green. The white matter tracts of the motor strip and the sensory strip are clearly seen as they descend toward the posterior limb of the internal capsule (corticospinal tract) and the thalamus (thalamocortical tract), respectively.

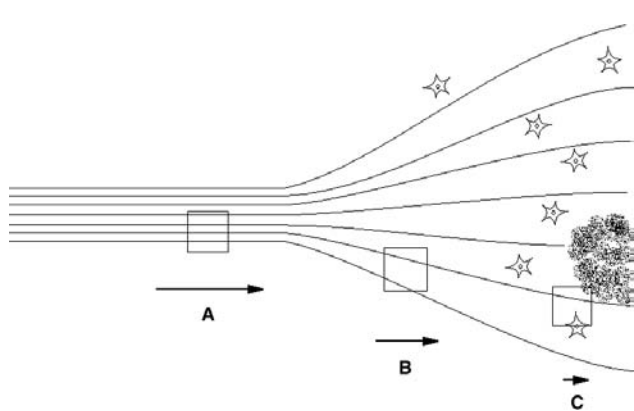


Figure 7 A decrease in diffusion anisotropy occurs as one moves from normal axons in parallel arrangement (**A**) to axons infiltrated by edema (**B**) or tumor and areas of necrosis (**C**).

to accurately depict patterns of infiltration and displacement of white matter by tumor.

Tumor Grade

Standard MR sequences with gadolinium contrast are incapable of accurately determining the grade of cerebral tumors because there does not exist a straightforward relationship between contrast enhancement and malignancy: low-grade gliomas may enhance while glioblastomas may not. This likely reflects the morphological character of gliomas, which infiltrate along vascular channels without necessarily disrupting them (35). MRI enhancement depicts focal disruptions in the blood-brain barrier rather than localizing exclusively to regions of vascular proliferation (36), which better correlate with histopathologic grade.

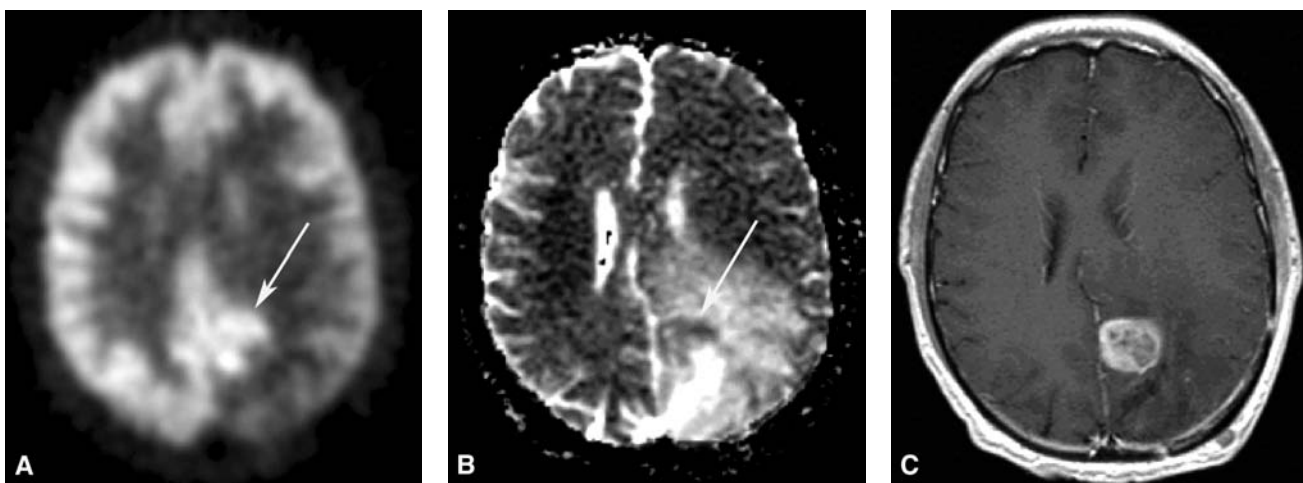


Figure 8 A 49-year-old man with an anaplastic astrocytoma. The PET scan (**A**) demonstrates a C-shaped area of increased radiopharmaceutical uptake, which exquisitely matches the area of restricted diffusion on the ADC map (**B**). The correspondence between the FDG-PET scan and the ADC map is better than the gadolinium-enhanced MRI (**C**). Abbreviations: ADC, apparent diffusion coefficient; PET, positron emission tomography; FDG-PET, 2-fluoro-2-deoxy-D-glucose positron emission tomography.

DWI has demonstrated some efficacy in depicting tumor grade, especially with respect to gliomas. ADC values are increased in low-grade gliomas and decreased in high-grade gliomas (17,27,28). Thus, high-grade gliomas demonstrate more restricted diffusion and will appear bright on DWI. The decreased water diffusion in higher-grade gliomas is often attributed to cellularity, but appears to also reflect the decreased expression of hydrophilic glycosaminoglycans in the extracellular matrix of high-grade gliomas (37). Though well established, the relationship between restricted diffusion and tumor grade is not absolute, and overlap of ADC values between grade II astrocytomas and glioblastomas has been documented (13,38). While a relationship between tumor grade and ADC holds across most studies, this association currently has more utility on the population level in broadly categorizing patients. On the individual level, the overlap in ADC values between tumor, edema, and normal brain calls into question the role of DWI in guiding clinical practice (13,24,38,39).

However, recent work suggests a role for DWI in characterizing tumor grade that is analogous to 2-fluoro-2-deoxy-D-glucose positron emission tomography (FDG-PET). In current practice, FDG-PET is used to identify regions suspicious for malignancy by using glucose uptake to depict areas of increased metabolic activity. Unlike routine gadolinium-enhanced MRI, which demonstrates defects in the blood-brain barrier and depicts structural information, FDG-PET is able to offer information on the physiology of gliomas (40). DWI also visualizes physiology in the form of the free movement of water within tissue, itself determined by other physiologic

conditions. In a retrospective review of 21 patients with gliomas imaged with FDG-PET, contrast-enhanced MRI, and DWI, the author's group found a striking co-localization of increased glucose uptake on FDG-PET and restricted diffusion as measured by ADC maps (Figs. 8 and 9) (41). Findings on FDG-PET and ADC maps correlated better with each other than either did with contrast-enhanced MRI, and though they visualize different physiologic parameters, they appear to provide similar information that is not available on routine gadolinium-enhanced MRI. Furthermore, in this set of 21 patients, findings on ADC maps were the most predictive of overall survival (41).

It may seem surprising that FDG-PET and DWI, which measure different physiologic parameters, would yield such strong overlap in the imaging of gliomas. There are two possible mechanisms that, alone or in combination, may underlie this finding.

First, increased uptake of glucose on FDG-PET indicates increased glycolysis, a consequence of increased metabolic activity known to occur in high-grade tumors. This phenomenon, known as the Warburg effect (42), corresponds to areas of rapid cell cycling and division that occur within actively growing tumor. As previously described, areas of high cellularity contain greater barriers to diffusion than normal brain, owing to increased density of cell membranes and decreased volume of extracellular space (43). DWI, by depicting areas of restricted diffusion, has been successful in assessing the cellularity of tumors. Tumors that tend to be highly cellular, such as lymphomas, are likely to have more restricted diffusion and decreased signal on ADC maps (16). The co-localization of increased

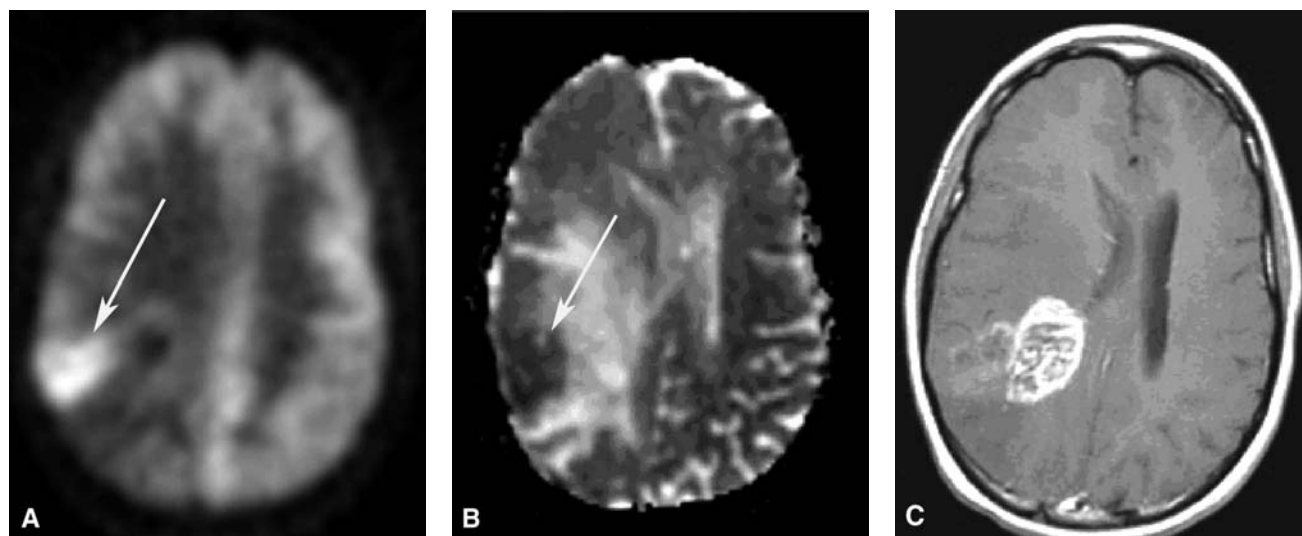


Figure 9 A 20-year-old woman with an anaplastic astrocytoma. The area of FDG-PET (A) uptake closely matches the area of restricted diffusion on the ADC map (B). This area shows only subtle enhancement (C). The area of bright enhancement does not correlate to either increased FDG-PET uptake or restricted diffusion. Abbreviations: PET, positron emission tomography; ADC, apparent diffusion coefficient; FDG-PET, 2-fluoro-2-deoxy-D-glucose positron emission tomography.

glucose uptake on FDG-PET and restricted diffusion on ADC maps suggests that the most metabolically active portions of tumor are also the most cellular.

Second, rapidly growing tumor is capable of outstripping its vascular supply, leading to areas of irreversible cellular ischemia. Studies have established that increased glucose uptake on FDG-PET can result from ischemia as cells switch from aerobic metabolism to glycolysis. As a tumor grows rapidly, cells toward the center of the tumor become removed from their blood supply, leading to focal ischemia and eventual cell death. Though restricted diffusion can result from increased cell density, it also manifests in the early stages of irreversible ischemia, a well-known finding from diffusion imaging of stroke (44–47). Ischemic cells within a brain tumor likely behave in a similar manner. As cells within a tumor lose their vascular supply, glycolysis increases and an increase in glucose uptake is reflected on FDG-PET. These same ischemic cells will appear as areas of restricted diffusion on ADC maps, owing to the same principles of irreversible ischemia seen in stroke. Thus, increased glucose uptake on FDG-PET would correspond to areas of restricted diffusion as measured on ADC maps.

Tumor grade is determined by the region of highest grade, and preoperative biopsies, guided by areas of contrast enhancement on standard MR sequences, are susceptible to substantial sampling error. The correlation between FDG-PET and ADC maps suggests a role for diffusion imaging in defining sites of high-grade tumor that could be

candidates for stereotactic biopsy. The findings on FDG-PET and ADC maps found in this study were never correlated with histology and cannot definitively be said to demonstrate areas of high-grade malignancy. More studies in both animals and humans correlating imaging and histology will need to be performed to further define the role of DWI. Preliminary data from glioma patients (48) supports the role of DWI in biopsy planning.

Tumor Response to Therapy

An emerging application of DWI is the assessment of solid tumor response to treatment. The method most commonly employed for assessing CNS tumor treatment response involves measuring overall change in tumor volume several weeks to months after the initiation of therapy. This method, which employs comparison of pre- and post-treatment CT or MRI images, is limited by the relatively slow rate at which tumor volume shrinks in response to therapy (49) and fails to allow rapid tailoring of therapy should tumor response be suboptimal. Recent work in animals (50–56) and humans (50,57–64) suggests an important role for DWI in allowing the assessment of solid tumor response to treatment earlier than ever before.

Preclinical studies on rodents with orthotopically implanted 9L glioma tumors demonstrated that elevations in mean tumor ADC values shortly after the initiation of chemotherapy were an early and sensitive predictor of response to treatment (55,56). Elevations in mean ADC

consistently preceded changes in tumor volume and corresponded histologically to decreases in tumor cellularity (50). These findings were recapitulated for a number of treatment strategies and tumor types, including gene therapy in gliomas (52–54) as well as treatment with radiation and tumor necrosis factor-related apoptosis-inducing ligand (TRAIL) in mouse breast cancer xenografts (51). Taken together, these animal studies argued that increases in water diffusivity as measured on DWI could be used as an early measure of cell death that occurs in successful treatment of solid tumors.

Studies with human subjects have also demonstrated the role of ADC values in the early quantification of treatment response in patients with brain tumors such as PNET and oligodendrogloma (50), high-grade glioma (59), and metastases (63). Studies using high *b*-value DWI further demonstrated that treatment outcome can be predicted prior to therapy initiation: tumors with low pretreatment ADC values, indicating increased cellularity, respond better than tumors with high ADC values (61,62). As in the earlier animal models, increases in ADC values soon after the initiation of treatment were predictive of subsequent tumor response. However, trials with convection-enhanced drug delivery (CEDD) in human patients demonstrated initial decreases in ADC values following the initiation of treatment (60,64). These seemingly inconsistent findings may reflect a peculiarity of CEDD; more likely, however, these findings reflect the heterogeneous composition of brain tumors and the dynamic changes that take place in the morphology and arrangement of dying cells (58). In response to antitumor therapies, tumor cells manifest a variety of fates (Fig. 10A,B). One involves transient cell swelling followed by cell lysis and necrosis. Alternatively, cells can also undergo shrinkage and blebbing during apoptosis. Cell swelling might be expected to cause a transient decrease in ADC values as the volume of extracellular space decreases while cell shrinkage and blebbing would have the opposite effect on ADC values. Furthermore, dying tumor cells likely bring about a dynamic reorganization of the tumor structure leading to greater overall heterogeneity. Likely these processes are occurring simultaneously throughout the tumor volume, and measures such as mean ADC fail to accurately depict the regional variations in tumor ADC values (58).

Future Directions

A solution to the problem of heterogeneous ADC values in tumors undergoing treatment comes in the form of the functional diffusion map (fDM). This approach involves coregistration of diffusion images before and during treatment to generate a three-color overlay conveying direction and magnitude of therapeutic-induced ADC change within the tumor (Fig. 10C). Tumor voxels are divided into

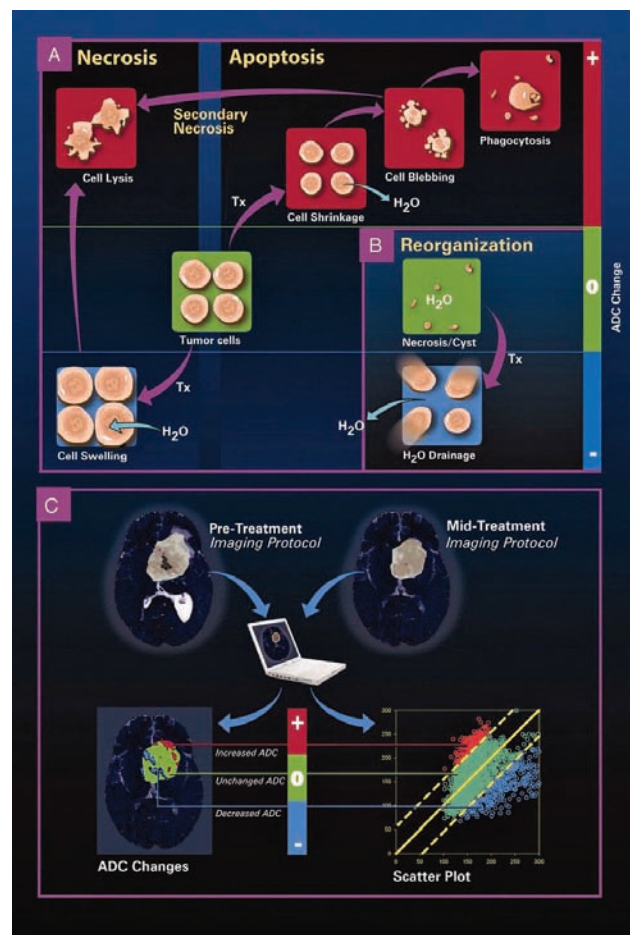


Figure 10 Biological processes proposed to be involved in therapeutic-induced changes in tumor ADC values along with a pictorial description of the fDM analytical process. (A) A schematic representation of the dynamic biological processes associated with changes (increase or decrease) in tumor water diffusion values. Tumor cells within an image voxel have several fates during treatment. Cells can be resistant to therapy (unaltered ADC, green) or can undergo necrosis initiated by a transient cell swelling (decreased ADC, blue). Cell enlargement (swelling) can also be associated with mitotic catastrophe or a reduction in tumor blood flow resulting in focal ischemia/hypoxia (decreased ADC, blue). These processes can eventually progress to cell lysis and necrosis (increased ADC, red). Cells can also undergo apoptosis involving cell shrinkage and blebbing followed by phagocytosis (increased ADC, red). (B) The concept that necrotic or cystic regions of a tumor can undergo drainage (displacement) of water as cells move into the region resulting in a drop in diffusion values (decreased ADC, blue) is summarized. (C) Diffusion MRI data undergo digital image postprocessing and analysis that involves coregistration of images before and during treatment. Data are used to generate a three-color overlay representing regions in which tumor ADC values are unchanged (green voxels), significantly increased (red voxels), or significantly decreased (blue voxels). This data can also be presented in a scatter plot and percentages assigned to the three defined ADC regions, allowing quantitative assessment of overall changes in tumor ADC values. Abbreviations: ADC, apparent diffusion coefficient; fDM, functional diffusion map. Source: From Ref. 58.

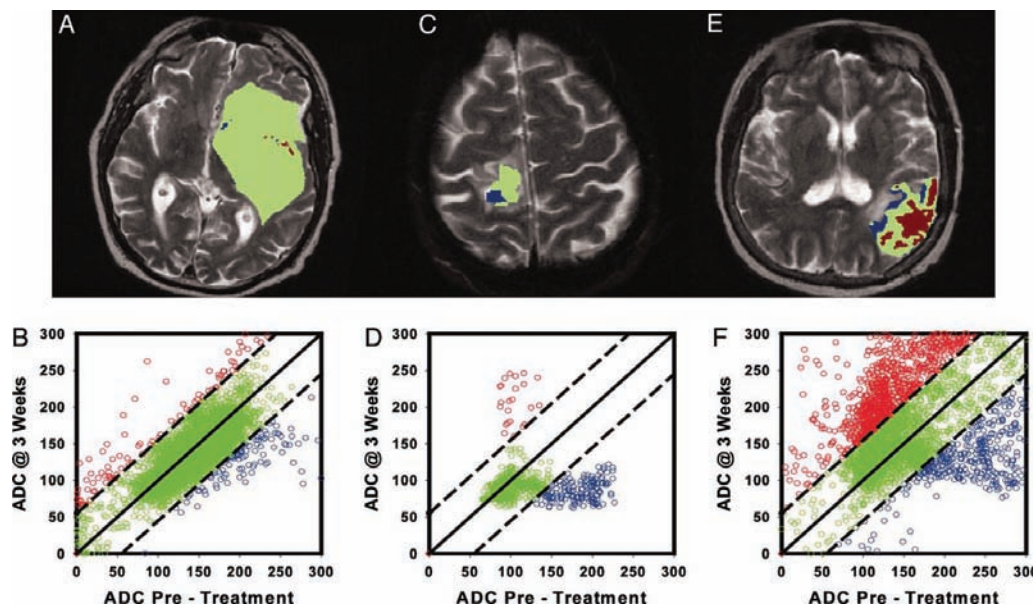


Figure 11 MRI of three patients with oligodendrogliomas. MR image datasets obtained from three different patients diagnosed with anaplastic oligodendroglomas. Images shown are at three weeks into a seven-week fractionated ionizing radiation regimen. Regions of interest were drawn for each tumor image by using anatomical images. (A, C, and E) The regional spatial distribution of ADC changes (fDMs) of a single slice through each tumor as color overlays for the PD, SD, and PR patients, respectively. The red pixels indicate areas of increased diffusion, whereas the blue and green pixels indicate regions of decreased and unchanged ADC, respectively. The scatter plots (B, D, and F) show quantitatively the distribution of ADC changes for the entire three-dimensional tumor volume for each corresponding patient (A, C, and E), respectively. Abbreviations: ADC, apparent diffusion coefficient; fDMs, functional diffusion map; PD, progressive disease; SD, stable disease; PR, partial response. Source: From Ref. 58.

three categories: (i) red voxels (V_R) for which the ADC increased, (ii) blue voxels (V_B) for which the ADC decreased, and (iii) green voxels (V_G) for which the ADC remained unchanged. These data can also be presented as a scatter plot allowing quantitation of overall changes in tumor ADC values (Fig. 10C). This approach was applied to a prospective study of 20 patients (57) with unresectable primary brain tumors who were imaged prior to treatment (radiation, chemotherapy, or a combination) and again at three weeks. Analysis with fDM was successful at identifying partial response (PR), stable disease (SD), and progressive disease (PD) patients with 100% sensitivity and specificity. Partial response patients, who experienced substantial decreases in tumor volume at least four weeks after the conclusion of therapy, had a significantly greater V_R than either the SD or PD groups. The SD group had a significantly greater V_{TOTAL} ($=V_R + V_B$) than the PD group. These results suggest that responders to treatment will have a significantly greater increase in ADC values than those with stable or progressive disease. Furthermore, patients with stable disease will have significantly greater overall change in ADC (areas of increased and decreased ADC) than patients with progressive disease, who will have the least change in ADC values from pretreatment levels. Figure 11 depicts fDM analysis of three patients who underwent therapy for oligodendrogioma. In a follow-up

study of 34 patients with malignant glioma, findings on fDM were predictive of treatment response and correlated with time to progression and overall survival (57). Animal studies have confirmed a correlation between findings on fDM and biologically relevant end points such as tumor growth, cell death, histopathology, and survival (65).

The approach in these studies avoids the oversimplification of using the mean ADC value of the entire tumor to represent a spatially heterogeneous treatment response. Furthermore, the color overlay and the scatter plot provide both a spatial and a quantitative display of regions responsive and resistant to treatment. These findings have implications for early assessment of therapeutic efficacy as well as individually tailored and regionally targeted therapies.

REFERENCES

1. Tsuruda JS, Chew WM, Moseley ME, et al. Diffusion-weighted MR imaging of the brain: value of differentiating between extraaxial cysts and epidermoid tumors. AJNR Am J Neuroradiol 1990; 11:925–931.
2. Tsuruda JS, Chew WM, Moseley ME, et al. Diffusion-weighted MR imaging of extraaxial tumors. Magn Reson Med 1991; 19:316–320.
3. Chen S, Ikawa F, Kurisu K, et al. Quantitative MR evaluation of intracranial epidermoid tumors by fast

- fluid-attenuated inversion recovery imaging and echo-planar diffusion-weighted imaging. *AJNR Am J Neuroradiol* 2001; 22:1089–1096.
4. Teksam M, Casey SO, Michel E, et al. Intraspinal epidermoid cyst: diffusion-weighted MRI. *Neuroradiology* 2001; 43:572–574.
 5. Dechambre S, Duprez T, Lecouvet F, et al. Diffusion-weighted MRI postoperative assessment of an epidermoid tumour in the cerebellopontine angle. *Neuroradiology* 2001; 43(10):891.
 6. Packer RJ. Childhood medulloblastoma: progress and future challenges. *Brain Dev* 1999; 21:75.
 7. Erdem E, Zimmerman RA, Haselgrave JC, et al. Diffusion-weighted imaging and fluid attenuated inversion recovery imaging in the evaluation of primitive neuroectodermal tumors. *Neuroradiology* 2001; 43:927–933.
 8. Wilke M, Eidenschink A, Müller-Wehrich S, et al. MR diffusion imaging and ^1H spectroscopy in a child with medulloblastoma. *Acta Radiol* 2001; 42:39–42.
 9. Klisch J, Husstedt H, Hennings S, et al. Supratentorial primitive neuroectodermal tumours: diffusion-weighted MRI. *Neuroradiology* 2001; 42:393–398.
 10. Stadnik TW, Chaskis C, Michotte A, et al. Diffusion-weighted MR imaging of intracerebral masses: comparison with conventional MR imaging and histologic findings. *AJNR Am J Neuroradiol* 2001; 22:969–976.
 11. Desprechins B, Stadnik T, Koerts G, et al. Use of diffusion-weighted MR imaging in differential diagnosis between intracerebral necrotic tumors and cerebral abscesses. *AJNR Am J Neuroradiol* 1999; 20:1252–1257.
 12. Ebisu C, Tanaka C, Umeda M, et al. Discrimination of brain abscess from necrotic or cystic tumors by diffusion-weighted echo planar imaging. *Magn Reson Imaging* 1996; 14(9):1113–1116.
 13. Kono K, Inoue Y, Nakayama K, et al. The role of diffusion-weighted imaging in patients with brain tumors. *AJNR Am J Neuroradiol* 2001; 22:1081–1088.
 14. Krabbe K, Gideon P, Wagn P, et al. MR diffusion imaging of human intracranial tumours. *Neuroradiology* 1997; 39:483–489.
 15. Le Bihan D, Douek P, Argyropoulou M, et al. Diffusion and perfusion magnetic resonance imaging in brain tumors. *Top Magn Reson Imaging* 1993; 5:25–31.
 16. Guo AC, Cummings TJ, Dash RC, et al. Lymphomas and high-grade astrocytomas: comparison of water diffusibility and histologic characteristics. *Radiology* 2002; 224(1):177–183.
 17. Sugahara T, Korogi Y, Kochi M, et al. Usefulness of diffusion-weighted MRI with echo-planar technique in the evaluation of cellularity in gliomas. *J Magn Reson Imaging* 1999; 9(1):53–60.
 18. Gupta RK, Sinha U, Cloughesy TF, et al. Inverse correlation between choline magnetic resonance spectroscopy signal intensity and the apparent diffusion coefficient in human glioma. *Magn Reson Med* 1999; 41(1):2–7.
 19. Johnson PC, Hunt SJ, Drayer BP. Human cerebral gliomas: correlation of postmortem imaging findings and neuropathologic findings. *Radiology* 1989; 170:211–217.
 20. Chiang IC, Kuo UT, Lu CY, et al. Distinction between high-grade gliomas and solitary metastases using peritumoral 3-T magnetic resonance spectroscopy, diffusion, and perfusion imagings. *Neuroradiology* 2004; 46:619–627.
 21. Lu S, Ahn D, Johnson G, et al. Diffusion-tensor MR imaging of intracranial neoplasia and associated peritumoral edema: introduction of the tumor infiltration index. *Radiology* 2004; 232(1):221–228.
 22. Lu S, Ahn D, Johnson G, et al. Peritumoral diffusion tensor imaging of high grade gliomas and metastatic brain tumors. *AJNR Am J Neuroradiol* 2003; 24:937–941.
 23. Provenzale JM, McGraw P, Mhatre P, et al. Peritumoral brain regions in gliomas and meningiomas: investigation with isotropic diffusion-weighted MR imaging and diffusion-tensor MR imaging. *Radiology* 2004; 232(2):451–460.
 24. Pauleit D, Langen KJ, Floeth F, et al. Can the apparent diffusion coefficient be used as a noninvasive parameter to distinguish tumor tissue from peritumoral tissue in cerebral gliomas? *J Magn Reson Imaging* 2004; 20(5):758–764.
 25. Van Westen D, Latt J, Englund E, et al. Tumor extension in high-grade gliomas assessed with diffusion magnetic resonance imaging: values and lesion-to-brain ratios of apparent diffusion coefficient and fractional anisotropy. *Acta Radiol* 2006; 47(3):311–319.
 26. Maier SE, Bogner P, Bajzik G, et al. Normal brain and brain tumor: multicomponent apparent diffusion coefficient line scan imaging. *Radiology* 2001; 219(3):842–849.
 27. Bulakbasi N, Kocaoglu M, Ors F, et al. Combination of single-voxel proton MR spectroscopy and apparent diffusion coefficient calculation in the evaluation of common brain tumors. *AJNR Am J Neuroradiol* 2003; 24(2):225–233.
 28. Yang D, Korogi Y, Sugahara T, et al. Cerebral gliomas: prospective comparison of multivoxel 2D chemical-shift imaging proton MR spectroscopy, echoplanar perfusion and diffusion-weighted MRI. *Neuroradiology* 2002; 44(8):656–666.
 29. Basser PJ, Mattiello J, Le Bihan D. MR diffusion tensor spectroscopy and imaging. *Biophysical J* 1994; 66: 259–267.
 30. Basser PJ, Mattiello J, Le Bihan D. Anisotropic diffusion: MR diffusion tensor imaging. In: Le Bihan D, ed. *Diffusion and Perfusion Magnetic Resonance Imaging*. New York, NY: Raven Press, 1995:140–149.
 31. Basser PJ, Pierpaoli C. Microstructural and physiological features of tissue elucidated by quantitative-diffusion-tensor MRI. *J Magn Reson B* 1996; 111:209–219.
 32. Price SJ, Burnet NG, Donovan T, et al. Diffusion tensor imaging of brain tumours at 3T: a potential tool for assessing white matter tract invasion? *Clin Radiol* 2003; 58(6):455–462.
 33. Inoue T, Shimizu H, Yoshimoto T. Imaging the pyramidal tract in patients with brain tumors. *Clin Neurol Neurosurg* 1999; 101:4–10.
 34. Nakada T, Nakayama N, Fujii Y, et al. Clinical application of three-dimensional anisotropy contrast magnetic resonance axonography. Technical note. *J Neurosurg* 1999; 90:791–795.
 35. Knopp EA, Cha S, Johnson G, et al. Glial neoplasms: dynamic contrast-enhanced T2*-weighted MR imaging. *Radiology* 1999; 211(3):791–798.

36. Brasch RC, Weinmann HJ, Wesbey GE. Contrast-enhanced NMR imaging: animal studies using gadolinium-DTPA complex. *AJR* 1984; 142:625–630.
37. Sadeghi N, Camby I, Goldman S, et al. Effect of hydrophilic components of the extracellular matrix on quantifiable diffusion-weighted imaging of human gliomas: preliminary results of correlating apparent diffusion coefficient values and hyaluronan expression level. *AJR Am J Roentgenol* 2003; 181(1):235–241.
38. Catalaa I, Henry R, Dillon WP, et al. Perfusion, diffusion and spectroscopy values in newly diagnosed cerebral gliomas. *NMR Biomed* 2006; 19(4):463–475.
39. Castillo M, Smith JK, Kwock L, et al. Apparent diffusion coefficients in the evaluation of high-grade cerebral gliomas. *AJNR Am J Neuroradiol* 2001; 22(1):60–64.
40. Di Chiro G, De La Paz RL, Brooks RA, et al. Glucose utilization of cerebral gliomas measured by [18F]fluoro-deoxyglucose and positron emission tomography. *Neurology* 1982; 32:1323–1329.
41. Holodny AI, Makeyev S, Beattie B, et al. Apparent Diffusion Coefficient (ADC) of Glial Neoplasms: Correlation with Fluorodeoxyglucose Positron Emission Tomography (FDG-PET) and Routine Gadolinium Enhanced MRI. Annual Meeting of the American Society of Neuroradiology, Washington, DC, May 2003.
42. Warburg O. On the origin of cancer cells. *Science* 1956; 123:309–314.
43. Van der Toorn A, Sykova E, Dijkhuizen RM, et al. Dynamic changes in water ADC, energy metabolism, extracellular space volume, and tortuosity in neonatal rat brain during global ischemia. *Magn Reson Med* 1996; 36(1):52–60.
44. Warach S, Gaa J, Siewert B, et al. Acute human stroke studied by whole brain echo planar diffusion-weighted magnetic resonance imaging. *Ann Neurol* 1995; 37:231–241.
45. Warach S, Chien D, Li W, et al. Fast magnetic resonance diffusion-weighted imaging of acute human stroke. *Neurology* 1992; 42:1717–1723. Erratum in: *Neurology* 1992; 42:2192.
46. Moseley ME, Wendland MF, Kucharczyk J. Magnetic resonance imaging of diffusion and perfusion. *Top Magn Reson Imaging* 1991; 3:50–67.
47. Mintorovitch J, Moseley ME, Chileuitt L, et al. Comparison of diffusion- and T2-weighted MRI for the early detection of cerebral ischemia and reperfusion in rats. *Magn Reson Med* 1991; 18:39–50.
48. Baehring JM, Bi WL, Bannykh S, et al. Diffusion MRI in the early diagnosis of malignant glioma. *J Neurooncol* 2007; 82:221–225.
49. Ross BD, Moffat BA, Lawrence TS, et al. Evaluation of cancer therapy using diffusion magnetic resonance imaging. *Mol Cancer Ther* 2003; 2:581–587.
50. Chenevert TL, Stegman LD, Taylor JMG, et al. Diffusion magnetic resonance imaging: an early surrogate marker of therapeutic efficacy in brain tumors. *J Natl Cancer Inst* 2000; 92(24):2029–2036.
51. Chinnaiyan AM, Prasad U, Shankar S, et al. Combined effect of tumor necrosis factor-related apoptosis-inducing ligand and ionizing radiation in breast cancer therapy. *Proc Natl Acad Sci U S A* 2000; 97(4):1754–1759.
52. Stegman LD, Rehemtulla A, Hamstra DA, et al. Diffusion MRI detects early events in the response of a glioma model to the yeast cytosine deaminase gene therapy strategy. *Gene Ther* 2000; 7(12):1005–1010.
53. Poptani H, Puusalainen AM, Grohn OH, et al. Monitoring thymidine kinase and ganciclovir-induced changes in rat malignant glioma in vivo by nuclear magnetic resonance imaging. *Cancer Gene Ther* 1998; 5(2):101–109.
54. Hakumaki JM, Poptani H, Puusalainen AM, et al. Quantitative 1H nuclear magnetic resonance diffusion spectroscopy of BT4C rat glioma during thymidine kinase-mediated gene therapy in vivo: identification of apoptotic response. *Cancer Res* 1998; 58(17):3791–3799.
55. Chenevert TL, McKeever PE, Ross BD. Monitoring early response of experimental brain tumors to therapy using diffusion magnetic resonance imaging. *Clin Cancer Res* 1997; 3(9):1457–1466.
56. Ross B, Chenevert T, Kim B, et al. Magnetic resonance imaging and spectroscopy: application to experimental neuro-oncology. *Quart Magn Reson Biol Med* 1994; 1:89–106.
57. Hamstra DA, Chenevert TL, Moffat BA, et al. Evaluation of the functional diffusion map as an early biomarker of time-to-progression and overall survival in high-grade glioma. *Proc Natl Acad Sci U S A* 2005; 102(46):16759–16764.
58. Moffat BA, Chenevert TL, Lawrence TS, et al. Functional diffusion map: a noninvasive MRI biomarker for early stratification of clinical brain tumor response. *Proc Natl Acad Sci U S A* 2005; 102(15):5524–5529.
59. Hein PA, Eskey CJ, Dunn JF, et al. Diffusion-weighted imaging in the follow-up of treated high-grade gliomas: tumor recurrence versus radiation injury. *AJNR Am J Neuroradiol* 2004; 25(2):201–209.
60. Lidar Z, Mardor Y, Jonas T. Convection-enhanced delivery of paclitaxel for the treatment of recurrent malignant glioma: a phase I/II clinical study. *J Neurosurg* 2004; 100(3):472–479.
61. Mardor Y, Roth Y, Ochershville A, et al. Pretreatment prediction of brain tumors' response to radiation therapy using high b-value diffusion-weighted MRI. *Neoplasia* 2004; 6(2):136–142.
62. Roth Y, Tichler T, Kostenich G, et al. High-b-value diffusion-weighted MR imaging for pretreatment prediction and early monitoring of tumor response to therapy in mice. *Radiology* 2004; 232(3):685–692.
63. Mardor Y, Pfeffer R, Spiegelmann R, et al. Early detection of response to radiation therapy in patients with brain malignancies using conventional and high b-value diffusion-weighted magnetic resonance imaging. *J Clin Oncol* 2003; 21(6):1094–1100.
64. Mardor Y, Roth Y, Lidar Z, et al. Monitoring response to convection-enhanced taxol delivery in brain tumor patients using diffusion-weighted magnetic resonance imaging. *Cancer Res* 2001; 61(13):4971–4973.
65. Moffat BA, Chenevert TL, Meyer CR, et al. The functional diffusion map: an imaging biomarker for the early prediction of cancer treatment outcome. *Neoplasia* 2006; 8(4):259–267.
66. Holodny AI, Ollenschleger, Liu WC. Diffusion imaging in brain tumors. *Neuroimaging Clin N Am* 2002; 12(1):107–124.

14

DTI of Developmental and Pediatric Disorders

MICHAEL J.J. KIM

Department of Radiology, Memorial Sloan-Kettering Cancer Center, New York, New York, U.S.A.

JAMES M. PROVENZALE

Department of Radiology, Duke University Medical Center, Durham, North Carolina, U.S.A.

INTRODUCTION

The central nervous system (CNS) undergoes profound and predictable developmental changes during the first few years of life that provide the structural and functional elements necessary for normal neurological development. The establishment and maturation of white matter pathways, which are heavily dependent on the process of myelination, are critical components of the developing nervous system. Myelin, which is produced by oligodendrocytes, is the phospholipid layer that surrounds axons and increases the impulse propagation speed by saltatory conduction. Myelination, which begins around the fourth month of gestation, predominantly occurs during the first few years of life and continues into early adulthood. Dysmyelination (failure of formation of normal myelin) and demyelination (destruction of myelin) are the common denominators in childhood leukodystrophies. In these disorders, the failure of myelination produces deficits in motor and cognitive function because of impairment of white matter pathways that link various gray matter regions.

Diffusion tensor imaging (DTI) has been shown to provide a noninvasive and quantitative means for the evaluation of brain maturation *in vivo*. DTI measures

both the magnitude and directionality of the diffusion of water molecules. In an unrestricted space, this movement reflects Brownian motion. However, in normal white matter tracts, the presence of axonal cell membranes and myelin sheaths restricts the motion of water molecules. This results in anisotropic diffusion, where movement is limited to a greater degree in the transverse direction than in the longitudinal direction.

Logically, if DTI detects anisotropic diffusion and the presence of myelin sheaths increases the degree of anisotropy, then DTI should be sensitive to changes in myelination and white matter tract maturation (1). In fact, DTI has been shown to identify microstructural changes in white matter before histological or conventional MR imaging signs are visible (2). However, the exact mechanisms underlying changes in anisotropy are not fully understood and likely include other factors.

In addition to monitoring normal brain maturation, DTI can be used to follow brain maturation in abnormal states, such as premature birth or early brain injury. DTI has also contributed to the evaluation of a number of childhood leukoencephalopathies. Furthermore, DTI has helped characterize the relation between white matter integrity and cognitive abilities. Finally, DTI has played a role in the diagnostic process of pediatric CNS malignancies. In

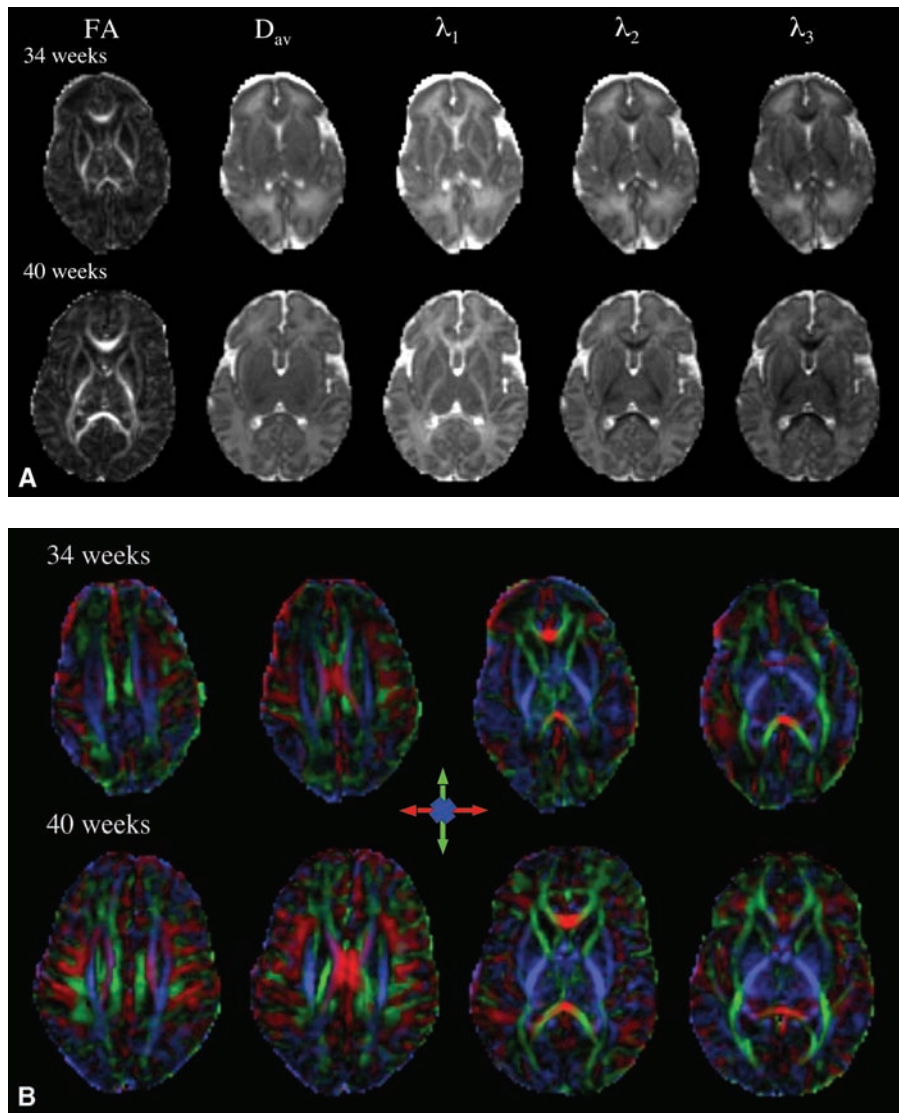


Figure 1 An infant born at 33 weeks was studied serially using DTI at 34 weeks and 40 weeks gestational age. (A) DTI parametric maps at a single slice location. (B) Directionally encoded anisotropy color maps from four slice locations. Subcortical tract development showed notable increases between earlier and later scans, particularly visible in (B). Abbreviation: DTI, diffusion tensor imaging.

short, DTI holds substantial potential for diagnosis, monitoring, and understanding the pathophysiology of a wide variety of pediatric diseases.

NORMAL NEURODEVELOPMENTAL MATURATION

Perinatal Period

In both preterm and term infants, apparent diffusion coefficient (ADC, which measures the mean of the diffusion tensor eigenvalues) and diffusion anisotropy measurements have been shown to correlate with gestational age (3). In one study, serial DTI scans were performed

to assess maturational changes in the white matter of premature newborns that showed no abnormalities on conventional MRI (Fig. 1) (4). In this study, earlier maturing of white matter tracts showed higher fractional anisotropy (FA, which measures the fraction of diffusion tensor magnitude due to anisotropic diffusion) values than later maturing pathways, which is the same pattern found in normal adults (5). This finding suggests that anisotropy is already seen in preterm unmyelinated white matter and that, even at this very early age, differences in anisotropy can be seen across WM structures of varying degrees of myelination. Also, the investigators found that diffusion anisotropy was the most sensitive measure for detecting differences between tracts. More specifically, FA was able

to detect smaller differences compared with relative anisotropy (RA, which measures the ratio of anisotropic to isotropic diffusion tensor magnitude), suggesting that FA is a superior measurement in patients with inherently low anisotropic values, such as premature infants.

A maturational pattern characterized by increasing anisotropy with increasing gestational age was seen in serial measurements of infants (6). These changes were more pronounced in the peripheral (i.e., subcortical) white matter, a similar finding to that seen during the first six years of life (7). In comparison to conventional MR images, on which discrete milestones in myelination are apparent (8), DTI showed only a gradual quantitative change from premyelination to myelination with no discrete increases.

Childhood Period

Myelination is believed to occur most rapidly during the first two years of life (9,10). In fact, by the age of two years, the pediatric brain appears similar to the adult brain on conventional MR images (7). However, histological studies have shown that the process of myelination continues well beyond this initial period and likely into early adulthood (11,12). To better understand the pathological processes involving myelination during childhood, DTI has been used to characterize the normal developmental trends of white matter in subjects without neurological deficits and deemed normal by conventional MRI.

One study, which compared the anisotropy values of children in the one- to three-year-old range and the four- to six-year-old range, showed a statistically significant increase in white matter anisotropy in the older group (6). In a separate retrospective analysis of 153 children between the ages of 1 day and 11 years, isotropic diffusion coefficient was found to be lower and diffusion anisotropy values higher in the white matter tracts of the older patients (13). These findings are consistent with the notion that myelination, as reflected by changes in the magnitude and directionality of water diffusion and similar to that seen during the perinatal period, continues into childhood.

Adolescence

Histological studies suggest that myelination and axonal growth continue into adolescence and young adulthood, which would be expected to produce increases in anisotropy with age (10,11). DTI studies have indeed shown anisotropy changes consistent with these histological features. One study demonstrated a significant increase in anisotropy values in the frontal white matter from late childhood (8–12-years old) to young adulthood (20–31-years old) (14). Another study compared diffusion parameters in 8- to 12-year olds and 21- to 27-year olds and found significant

increases in FA and decreases in ADC values in many white matter regions in the older age group (15).

ABNORMAL NEURODEVELOPMENTAL MATURATION

Short-Term Effects

Premature infants pose a major public health challenge for a multitude of reasons. At 12.5% of all live births or over half a million infants in the United States in 2004 (16), premature births are an extremely common occurrence. Also, the etiology of many disorders, ranging from autism to attention deficit hyperactivity disorder, is believed to have neurobiological origins (17,18). In addition, premature babies are particularly susceptible to developing neurological deficits, including cerebral palsy, developmental delay, and visual impairment, likely due to white matter injury and subsequent impairment of development (6,19). Because the white matter is substantially impaired in many of these disease states, one might expect that DTI would provide insights not available from conventional MR images.

DTI has been used to compare two groups of premature infants at term, those who exhibited conventional MR imaging findings of cerebral white matter injury and those who did not (Fig. 2) (20). In preterm neonates with perinatal white matter lesions, RA was reduced by 25% in the central white matter (i.e., the principal site of injury) and 20% in the internal capsule (i.e., descending fibers emanating from site of injury). RA measurements were not lowered in noninjured sites and ADC was unchanged in all areas. As this study measured DTI parameters only once at term, the question still remained whether early white matter damage would lead to progressively abnormal brain development and if the severity of damage would modulate these effects.

Miller et al. compared serial DTI scans in a control group of infants with no white matter injury to premature newborns who were classified into two groups, one with mild white matter injury and one with moderate white matter injury (21). In the control group, results were consistent with previous observations—that is, ADC decreased and diffusion anisotropy increased from 27 to 42 weeks postconception. However, in newborns with moderate white matter injury, both ADC and diffusion anisotropy did not change in most regions of the brain and ADC actually increased over time in the frontal white matter and visual association areas. Also, in newborns with mild white matter injury, RA failed to increase in the frontal white matter. These results show that early injury to white matter of preterm infants interferes with subsequent normal development in these areas. Furthermore, certain regions of the brain (e.g., frontal and visual

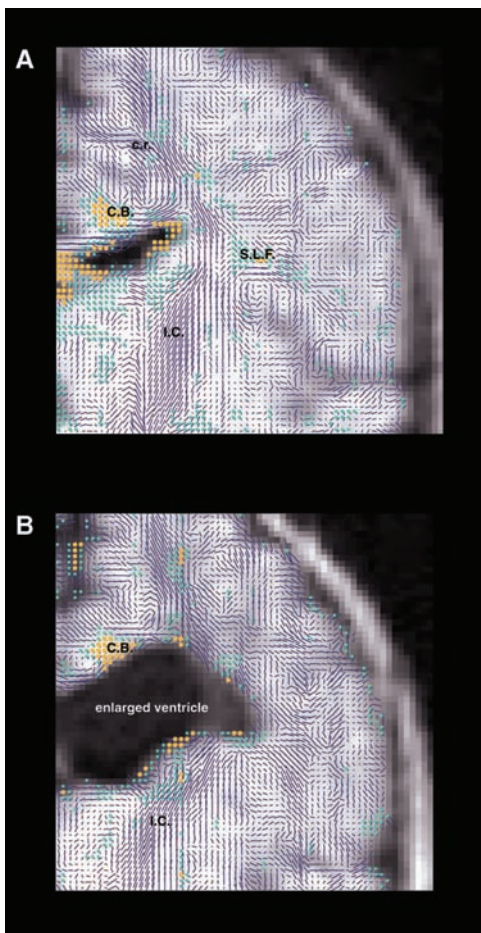


Figure 2 Diffusion vector maps were overlaid on coronal diffusion-weighted MRI scans; yellow dots represent higher relative anisotropy values than green dots. The images show a premature infant at term (A) without perinatal white matter injury in and (B) with perinatal white matter injury in. The posterior limb of the internal capsule in (A) shows more homologous-directed vectors that are longer and more densely packed than in the internal capsule of (B). Anteroposterior-oriented WM fibers in the area of the superior longitudinal fasciculus in (A) indicate the presence of fiber bundles that are missing or less prominent in (B). Fibers in the corona radiata appear better organized in (A) than in (B). Abbreviation: MRI, magnetic resonance imaging.

association areas) may have increased vulnerability to perinatal insults. Thus, DTI may be used as an early marker of injury in the developing brain.

Measuring Long-Term Effects of Perinatal Insults

The pediatric population has an enhanced capacity for neuroplasticity as compared with their adult counterparts. This feature is seen in the extraordinary aptitude for

language and their superior ability to recover from brain injuries (22). Conventional MRI studies have shown that adolescents born prematurely have reduced brain and white matter volumes (23,24). The question remained whether effects of early injury to the developing white matter persisted over time and whether these changes could be accurately assessed by DTI. In one study, DTI was used to compare white matter characteristics in 11-year-old children who were born preterm to age-matched peers born at the normal gestational age (25). FA was found to be significantly reduced in the posterior corpus callosum of the preterm group. Notably, in this study, the population of preterm children was recruited on the basis of having attentional deficits and hyperactivity. Therefore, due to this selection bias, the results may only be applicable to prematurely born children with inattention and hyperactivity.

LEUKOENCEPHALOPATHIES

Communication among various areas of the brain depends on intact and functioning white matter pathways. When myelinated tracts are compromised (either by dysmyelination or demyelination), axonal impulse propagation speed is dramatically delayed, ultimately impeding brain function.

In many pediatric neurological disorders, the white matter is disproportionately affected by genetic mutations that disrupt a wide variety of biochemical pathways. Some examples of these disorders include diseases of the lysosome, peroxisome, and mitochondria, and various acidopathies. Although each mutation has a different effect on brain function (and consequently a unique clinical presentation), they share the fact that abnormal white matter findings are seen on radiological imaging due to loss of myelin and failure to develop new myelin. The features of a number of such disorders have been characterized using DTI.

Krabbe Disease

Globoid cell leukodystrophy, also known as Krabbe disease, is an autosomal recessive white matter disorder caused by the deficiency of β -galactocerebrosidase (26). In the normal brain, galactolipids that are toxic to brain tissue are formed during white matter myelination but are quickly hydrolyzed by the enzyme β -galactocerebrosidase. However, in Krabbe disease, diminished levels of this enzyme allow galactolipids to accumulate and myelin-forming oligodendroglia are destroyed. In early-onset Krabbe disease, this leads to the failure of normal myelin production in infants and subsequent development

of severe neurological deficits (27). These children typically deteriorate neurologically until they reach a vegetative state and ultimately die within two to four years. Hematopoietic stem cell transplantation has been suggested as a treatment for asymptomatic infantile Krabbe disease (28). There are currently no proven therapeutic options for *symptomatic* patients with the infantile form of Krabbe disease. Therefore, early diagnosis of the disease is critical for any treatment to be effective.

The standard use of MR imaging to assess Krabbe disease has been to assess findings indicative of a lack of progression of myelination and development of frankly abnormal regions of white matter on conventional MR images (29). However, in the newborn brain, myelination milestones are relatively few and areas of abnormal signal intensity can be difficult to detect against the background of relatively unmyelinated white matter.

DTI anisotropy maps offer a quantitative and reproducible way of assessing white matter integrity. Guo et al. showed that diffusion anisotropy maps are more sensitive than T2-weighted MR images in detection of white matter abnormalities in patients with Krabbe disease (30). This finding, along with the fact that the white matter tracts correspond to known areas affected in Krabbe disease (31–35), suggests anisotropy indices may play a valuable role in assessment of this disease.

Serial DTI scans, including pre- and posttransplantation imaging, have also been performed to prospectively compare disease progress in two groups of patients with Krabbe disease: those treated with stem cell transplantation in the first month of life and those treated after the first month (usually by six months of age but typically after symptom onset) (Fig. 3) (32). Pretransplantation FA ratios were shown to be decreased in the late transplantation group only, suggesting Krabbe disease infants may have relatively normal white matter in the first month of life. At one-year follow-up in the early transplantation group, most white matter regions showed substantial increases in anisotropy values, with measurements of at least 85% of those in age-matched controls. On the other hand, the late transplantation group at one-year follow-up had generally showed no change or a decrease in anisotropy values in most sites. The DTI findings are consistent with clinical studies that show that treatment in the first month of life is critical for a substantial treatment effect to be seen (33). These preliminary results support stem cell transplantation as a possible viable treatment for Krabbe disease patients.

Adrenoleukodystrophy

X-linked adrenoleukodystrophy (ALD) is a peroxisomal disorder caused by a defect in ABCD1 gene, leading to the accumulation of saturated very long-chain fatty acids that

affect the CNS, adrenal cortex, and testes (34–41). The brain lesions are typically characterized by symmetrical inflammatory demyelination in the cerebral and cerebellar white matter (35). The childhood cerebral form of ALD most commonly presents in boys four- to eight-years old. The initial clinical manifestations are often learning disabilities and behavioral problems, rapidly deteriorating to blindness, quadriplegia, and ultimately death within ten years of diagnosis (36). Bone marrow transplantation during a limited time window is generally considered the most effective treatment.

Because the phenotypic ALD presentation varies widely and treatment decisions depend on both onset and extent of demyelination (37), noninvasive imaging plays a central role in the early detection of demyelination in ALD. A scoring method using routine MR imaging has been developed to measure disease severity by evaluating the signal intensity alterations on T2-weighted images, presence of atrophy, and contrast enhancement in white matter lesions (38). Proton MR spectroscopy has been shown to be a more sensitive indicator of neurological abnormalities than conventional MR imaging (39).

Comparison of DTI to conventional MRI in patients with ALD has shown that (as with many other white matter disease processes) mean diffusivity (MD) (essentially equivalent to ADC) was increased and FA was decreased in white matter areas that are hyperintense on T2-weighted images. More significantly, the same result was observed in areas without visible alterations on T2-weighted images. Another study showed a similar pattern of DTI findings (i.e., increased MD and decreased FA) in the normal appearing white matter in two of three patients with peroxisomal biogenesis disorders. Together, these results suggest DTI may be more sensitive in detecting early demyelination in patients with ALD than conventional MR imaging.

One study directly compared proton MR spectroscopy with DTI (which are both considered more sensitive for disease detection than conventional MR imaging) in the evaluation of X-linked ALD (40). Quantitative measures of *N*-acetylaspartate by MR spectroscopy, FA, and isotropic ADC were measured in the normal appearing white matter of asymptomatic ALD patients. *N*-acetylaspartate was found to be significantly reduced in regions where the DTI indices were normal. The DTI parameters showed changes similar to those found previously (i.e., decreased FA and increased ADC) only after significant decreases in *N*-acetylaspartate were apparent. These findings suggest proton MR spectroscopy has superior sensitivity for early detection of demyelination abnormalities in ALD patients.

Holoprosencephaly

The holoprosencephalies are a heterogeneous group of developmental disorders caused by both genetic and

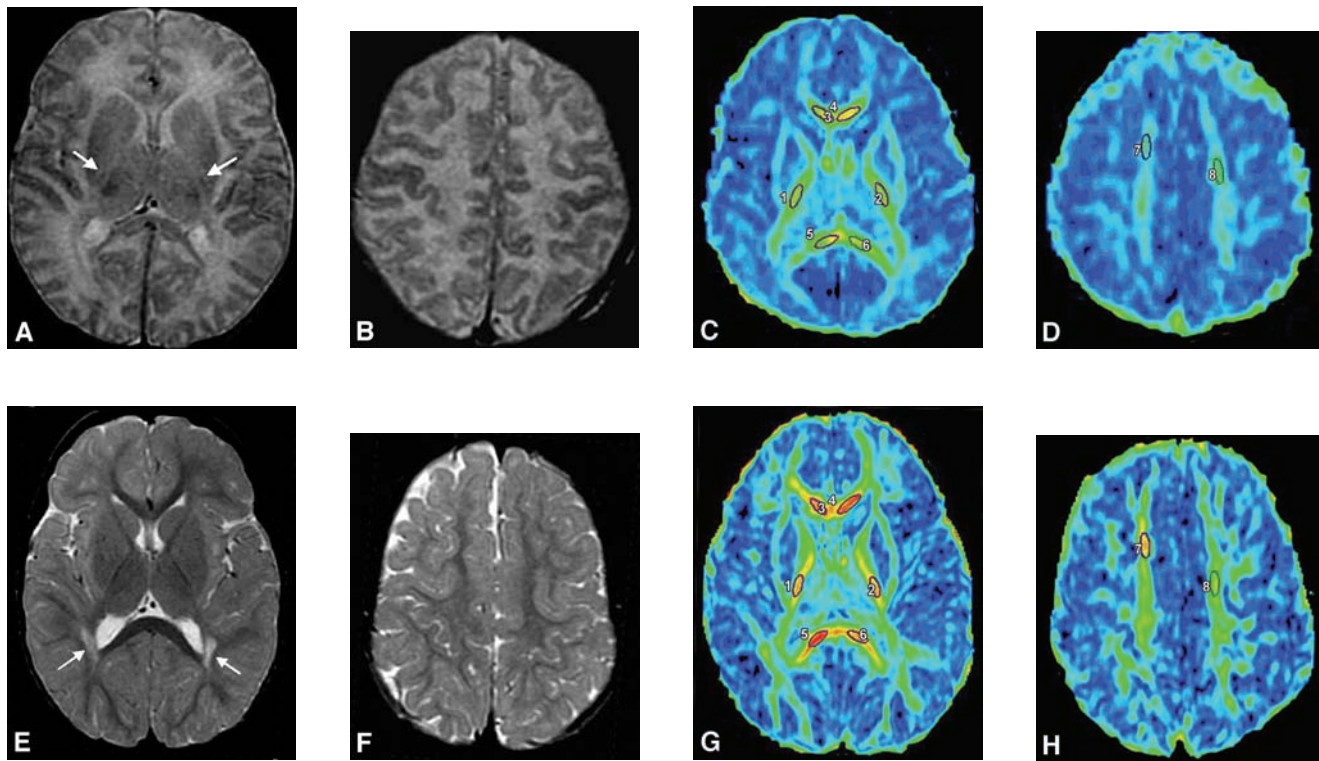


Figure 3 An asymptomatic boy with confirmed Krabbe disease was studied serially using DTI. (A) T2-weighted image obtained at the level of internal capsule two days before transplantation shows that the signal intensity in the posterior limb of the internal capsule (*arrows*) was slightly higher than expected for age, but no other abnormalities. (B) T2-weighted image just subjacent to the cerebral vertex shows no areas of abnormal signal intensity and normal myelination pattern for age. (C) FA map at the same level as (A) shows placement of ROIs in the internal capsule, genu of corpus callosum, and splenium of corpus callosum in sites in those structures that had the highest FA values. Mean FA ratios measured 131% of those in age-matched brains on normal MR images in the genu of corpus callosum, 116% of those in the splenium of corpus callosum, and 106% of those in the internal capsule. (D) FA map at the same level as (B) shows placement of ROI in frontal white matter. Mean FA ratio measured 113% of those in age-matched normal brain images. (E) T2-weighted image obtained 24 months after transplantation at the same level as (A) shows areas of hyperintense signal intensity (*arrows*) adjacent to the trigone of lateral ventricles. The myelination pattern is otherwise normal for age. (F) T2-weighted image at the same level as (B) shows no areas of abnormal signal intensity and normal myelination pattern for age. (G) FA map at the same level as (E) shows placement of ROIs in the internal capsule, genu of corpus callosum, and splenium of corpus callosum. Mean FA ratios in the genu of corpus callosum measured 102% of those in age-matched brains on normal MR images, 88% of those in the splenium of corpus callosum, and 88% of those in the internal capsule. (H) FA map at same level as (F) shows placement of ROI in frontal white matter. Mean FA ratio measured 89% of those in age-matched brains on normal MR images. Abbreviation: DTI, diffusion tensor imaging; FA, fractional anisotropy; ROI, region of interest; MR, magnetic resonance.

environmental insults resulting in incomplete development and septation of the midline structures during the first five weeks of embryonic development (41,42). The clinical severity depends on the degree of developmental inhibition, ranging from complete failure of division with cyclopia and rapid death to mild symptoms such as a single maxillary central incisor (43).

Albayram et al. used DTI to qualitatively evaluate white matter tract abnormalities in the brain stems of patients with holoprosencephaly (44). In this study, DTI was able to determine findings that were not appreciated on conventional MRI, such as the lack of extension of the pyramidal tract into the spinal cord and failure of separa-

tion of the medial lemniscal tracts. Further studies may provide insight into the wide clinical variability seen in the holoprosencephalies (45).

Malignant Phenylketonuria

Phenylketonuria (PKU) is an inborn error of amino acid metabolism classically caused by a deficiency of phenylalanine hydroxylase, which converts the essential amino acid phenylalanine to tyrosine (46). Without this enzyme, serum concentrations of phenylalanine and its metabolites rise to toxic levels. Malignant PKU is a rare variant caused by a deficiency of dihydropteridine reductase,

which produces a cofactor for phenylalanine hydroxylase and similarly blocks the conversion of phenylalanine to tyrosine. Additionally, the biosynthesis of dopamine, norepinephrine, and serotonin is interrupted (47). Elevated levels of phenylalanine are hypothesized to interfere with brain growth, neurotransmitter synthesis, and myelination (48,49). On neuropathological staining, myelin appears pale with splayed lamellae and vacuoles within the myelin sheath (50,51). If dietary phenylalanine is not restricted, most patients develop varying degrees of mental retardation.

In malignant PKU, conventional MRI can show subtle findings, such as subcortical cyst-like lesions and abnormal signal intensities (52,53). However, MR findings are often normal in patients with this disease (54). DTI has been compared with T2-weighted MR imaging in detecting abnormalities in normal-appearing white matter in patients with chronic malignant PKU (55). Significant increases were found in the second and third eigenvalues without any changes in the first eigenvalue within the parietooccipital white matter of the majority of patients older than three years. This finding, along with decreased FA in these patients, suggests an increase in the transverse diffusion of water molecules without any change in the longitudinal direction. Thus, individual eigenvalues (i.e., EV2 and EV3) and FA maps may provide more sensitive information than conventional MR images in patients with malignant PKU.

Progressive Multifocal Leukoencephalopathy

Progressive multifocal leukoencephalopathy (PML) is a demyelinating disease caused by John Cunningham (JC) virus infection of the oligodendrocytes, typically occurring in immunocompromised individuals. As white matter becomes damaged due to myelin breakdown, patients present with rapidly progressing focal neurological deficits (56). T2-weighted MR images typically show multifocal, bilateral, and asymmetrical areas of increased intensity (57,58). However, in a large multicenter cohort study, none of these characteristics correlated with prognosis (59).

A small number of cases using DTI to assess PML have been described. In one case, DTI was used to evaluate a 15-year-old girl with PML associated with congenital human immunodeficiency virus infection (60). On initial imaging, DTI detected white matter changes in the right internal capsule, whereas conventional T2-weighted MR imaging did not. Tissue injury became apparent on both modalities on follow-up imaging. In addition, there were differences in sensitivity within the DTI parameters. FA values were decreased on both initial and subsequent imaging, whereas the ADC measure was increased only on follow-up imaging. These results suggest that DTI, specifically FA values, can play a prognostic role in predicting future demyelination in patients with PML.

Maple Syrup Urine Disease

Maple syrup urine disease (MSUD) is a rare autosomal recessive disorder of amino acid metabolism caused by a deficiency of the branched-chain α -ketoacid dehydrogenase complex (61). As a result, the three branched-chain amino acids (leucine, isoleucine, and valine) accumulate to toxic levels in the serum, urine, and cerebrospinal fluid. The classical form of the disease is seen in newborns and presents with lethargy, dystonia, feeding difficulties, a maple syrup odor of the urine, and ultimately coma. T2-weighted MR imaging typically reveals hyperintense lesions (62,63). To prevent the development of symptoms, early diagnosis is critical since intake of branched-chain amino acids must be restricted as soon as possible, as in other amino acid metabolic disorders.

Parmar et al. described the DTI findings in areas of the brain that showed classic T2-weighted MR findings in a 10-day-old neonate with biochemically proved MSUD (64). ADC was reduced by 68%, while FA was also decreased by 57%. Due to these relatively large, quantitative changes, DTI has been suggested as a potentially more sensitive means of evaluating white matter lesions in MSUD than conventional MRI.

Mitochondrial Encephalomyopathy

Mitochondrial encephalomyopathies are a maternally inherited heterogeneous group of neurodegenerative disorders likely caused by mitochondrial or nuclear DNA mutations (65). There is a wide range of clinical presentations, including mitochondrial encephalomyopathies, lactic acidosis, stroke-like episodes, hearing loss, and diabetes mellitus. Demyelination has been postulated to occur secondary to oligodendrocyte degeneration (66). Also, it has been shown that these patients can develop white matter lesions, possibly attributable to small vessel ischemia and/or demyelination, although this is not well understood (67).

To further characterize these white matter abnormalities, DTI was used to evaluate a five-month-old male with mitochondrial encephalomyopathy. In this patient, FA maps revealed decreased anisotropy in the temporoparietal white matter. This finding supports the hypothesized role of oligodendrocytes and the potential diagnostic utility of DTI in mitochondrial encephalomyopathy.

NEUROCOGNITION AND WHITE MATTER STRUCTURE

Childhood is a period of dramatic development, both at the level of macroscopic behavioral changes and microstructural tissue changes. White matter structure, in

particular, has been shown to be associated with cognitive abilities in a wide patient population. In both adults and children, DTI has played a role characterizing this relationship. In one study, FA measurements of the centrum semiovale correlated with a battery of neuropsychological tests at age 83 and IQ at age 11 (68). In multiple sclerosis patients, white matter volume and diffusion properties were significantly correlated with cognitive performance, including verbal fluency and spatial recall (69,70). In Alzheimer's disease patients, MD was significantly correlated with executive function abilities (71). In reading-impaired and normal adults, diffusion anisotropy in the left temporoparietal region was significantly correlated with reading scores (72). Thus, there appears to be a clear connection between white matter structure and cognition.

Cognition in the Normal Population

Diffusion anisotropy and MD have been observed to change throughout the developmental period in the normal pediatric population (73,74). To unite the ideas of white matter changes and cognitive function in the normal pediatric population, DTI parameters were compared with IQ values in 47 normal children between the ages of 5 and 18 years (75). FA was found to positively correlate with IQ in many specific white matter association fibers bilaterally. MD, on the other hand, was only correlated in the right frontal lobe, which also overlapped with a FA-correlated region. Therefore, fiber organization, as reflected by the predominant increase in diffusion anisotropy, may play an important role in the cognitive development of normal children.

In a long-term study, DTI was used to examine the relationship between white matter integrity in old age and cognitive ability in both young age and old age (76). The study's participants included 40 nondemented, surviving participants of the 1932 Scottish Mental Survey. These subjects took an IQ test (Moray House Test) at age 11, a battery of psychometric tests again at age 83, and underwent an MRI also at age 83. The results showed that FA measurements of the centrum semiovale correlated with IQ at age 11 and four of five tests of cognition at age 83. In addition to supporting the applicability of DTI to assessing cognitive ability in old age, these findings suggest that future imaging studies of the elderly population should take into account prior mental ability when possible to account for the association between prior cognitive abilities (e.g., childhood IQ) and present anisotropy measurements.

Cognition in the Abnormal Population

In patients with PKU, the most common clinical finding is retarded intellectual development. Patient IQ scores and

conventional T2-weighted MR signal intensity changes in classic PKU have not shown any significant correlation (76). Certain DTI indices, however, have shown an association with clinical IQ scores in early chronic malignant PKU patients (63). Specifically, the third eigenvalue and ADC of the parietooccipital white matter were negatively correlated with verbal IQ and performance IQ, respectively. FA showed borderline positive correlation ($p = 0.05$) with full-scale IQ in the parietal and central white matter. These data suggest that IQ may be related to specific DT parameters in the white matter of patients with malignant PKU.

DTI has also been used to examine neurocognitive function in pediatric survivors of cancer. In childhood posttreatment medulloblastoma and acute lymphoblastic leukemia, FA has been significantly correlated with IQ measures, even after adjusting for age at treatment, irradiation dose, and time interval since treatment (77). Another study compared actual school performance to FA maps in medulloblastoma patients who were successfully treated with surgery, irradiation, and chemotherapy (78). The patients' performance was classified as mild, moderate, or severe, depending on whether they required special classes or were unable to attend school altogether. FA of the supratentorial white matter decreased in parallel with the severity of school performance deterioration. In addition, the degree of FA drop was correlated with younger treatment age and longer intervals since treatment, both known risk factors for poor neuropsychological outcome (79,80). These results suggest that FA values correlate with neurocognitive performance and may serve as a clinically useful biomarker for the assessment of treatment-related neurotoxicity.

Potential for Clinical Intervention

The aforementioned studies appear to establish a clear association between cognitive function and white matter structure as defined by DTI parameters. However, no studies had previously examined whether experimental intervention, rather than simple observation, could effect a change in white matter structure.

In a randomized clinical trial, DTI was used to investigate the effect of developmental intervention on brain structure in low-risk preterm infants in the newborn intensive care unit (NICU) (Fig. 4) (81). Infants are placed in the NICU after preterm births, where their immediate environment includes bright lights, loud sounds, and frequent interventions. The Newborn Individualized Developmental Care and Assessment Program (NIDCAP) was developed to minimize the effects of this potentially deleterious environment (82). The experimental group, who received the NIDCAP intervention, showed an

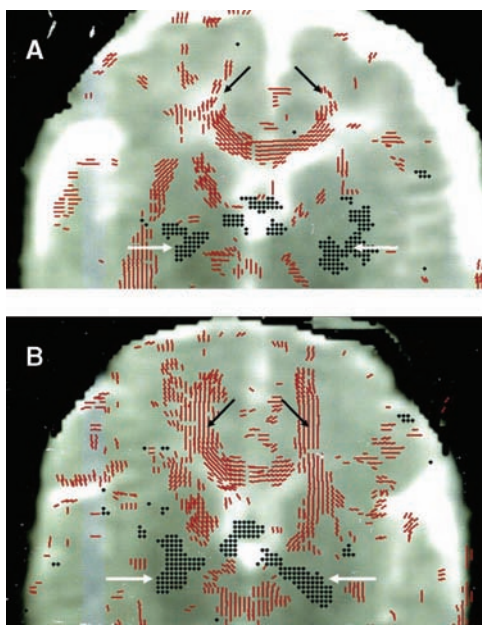


Figure 4 Infants from control (A) and experimental groups (B) were compared using diffusion tensor maps obtained from identical axial slices through the frontal lobes at two weeks age. Red lines denote eigenvectors located within the plane of the image, and the black dots indicate eigenvectors oriented mostly perpendicular to the image plane. Compared with the control infants, experimental infants showed greater anisotropy at the posterior limbs of the internal capsule (*white arrows*) and the frontal white matter adjacent to the corpus callosum (*black arrows*).

overall significant increase in RA and eigenvalue-1/eigenvalue-3 (E1/E3) ratio using multivariate analysis of variance. However, in the individual regions tested (frontal white matter, right internal capsule, and left internal capsule), the *p*-values for RA and E1/E3 ranged from 0.008 to 0.10. Since all values trended in the same direction, the small sample size may likely account for the lack of statistical significance. These results show an example where DTI can be used to assess white matter changes in an experimental design in preterm patients.

BRAIN TUMORS

CNS tumors represent 17% of all malignancies in children younger than 20 years, account for 2200 new cases annually in the United States, and have a five-year relative survival of less than 70% with substantial morbidity for survivors (83). Conventional MRI can characterize the general location and extent of brain neoplasms, but it is imprecise in delineating the exact margins of infiltrative tumors and white matter tract involvement. Prior studies performed mostly in adult populations have demonstrated the potential of DTI to further characterize CNS tumors

and assess involvement of surrounding tracts (84–95). In adult patients with high-grade gliomas, for example, subtle white matter changes were identified using diffusion anisotropy. These changes were not seen in low-grade gliomas or metastases, suggesting a method to detect white matter invasion in higher-grade tumors (85). Also, ADC has shown the ability to distinguish between the tumor core and other tumor components, the highest ADC values being within cystic or necrotic tumor areas (86,87).

Tumor Cellularity

The treatment and prognosis of pediatric CNS neoplasms depend on multiple variables, including tumor type, grade, and stage. Diagnostic imaging could play a key role in the workup and management of these tumors if it could reliably distinguish among the heterogeneous cell types (88). Conventional MRI is unable to definitively discriminate between these variables, leaving biopsy as the remaining procedure of choice.

Some studies have suggested that DTI parameters might correlate with tumor cellularity. In a mixed pediatric and adult population (aged 13 to 69 years), ADC of high-grade gliomas was found to be significantly higher than that of the low-grade gliomas (89). Also, a case report of a 12-year-old boy with medulloblastoma showed increased tumor signal on diffusion-weighted MR imaging, suggesting small-cell histology, and its high nuclear-to-cytoplasm ratio limited extracellular diffusion (90).

Another study supported these findings by comparing the tumor ADC to histopathological features and tumor types in 12 pediatric patients (aged 3 months to 17 years) (91). The most cellular tumors and those with the greatest total nuclear area were significantly correlated with reduced ADC values, consistent with decreased diffusion in areas of tumor tissue. Tumor classification (low-grade gliomas, embryonal tumors, and nonembryonal high-grade tumors) also correlated with ADC ratio (tumor to normal brain). Together, these findings suggest a potential role for DTI in determining the cellularity as well as the classification of tumors.

Pontine Tumors

Pontine tumors, which make up 15% of all pediatric brain tumors, can be classified as either diffuse or focal based on well-described conventional MRI findings (92,93). Diffuse pontine tumors, in particular, are known to infiltrate among normal axonal fibers (94). Conventional T2-weighted MR imaging has not been shown to reliably identify invasion of white matter tracts.

One study investigated whether invasion of white matter tracts could be demonstrated by changes in DTI parameters in children with pontine tumors (Fig. 5) (95). FA and ADC were shown to be significantly altered in all

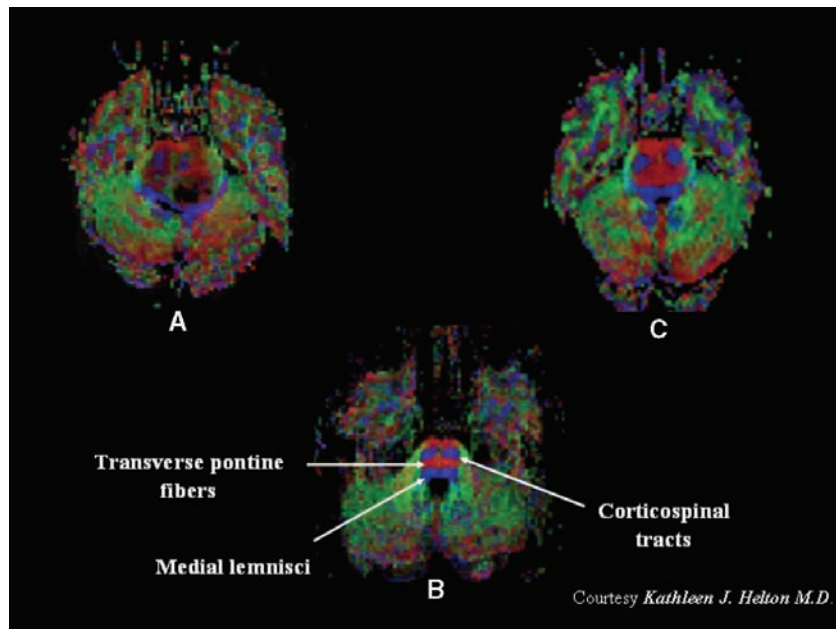


Figure 5 Axial diffusion tensor color maps at the level of the middle cerebellar peduncles are shown. Figure (A) shows a pontine tumor with destruction of the normal anisotropy of the corticospinal tracts and posterior displacement of the medial lemnisci. By comparison, Figure (B) shows a control image with normal corticospinal tracts, transverse pontine fibers, and medial lemnisci. Figure (C) shows a pontine tumor with a diffusely infiltrating pattern.

measured tracts (corticospinal, transverse pontine, and medial lemniscal) of the affected children. Differences in these tracts were not detectable by conventional MR. A marginally significant ($p = 0.057$) association was found between neurological deficit severity and decreased FA. These results suggest that DTI may be a sensitive measure of white matter tract invasion.

Tuberous Sclerosis

Tuberous sclerosis (TS) is an autosomal dominant neurocutaneous syndrome caused by inherited or sporadic mutations in specific tumor suppressor genes (96). Patients develop benign hamartomatous lesions, most commonly manifesting in the CNS as cortical tubers, subependymal nodules and astrocytomas, and white matter abnormalities (97). The classic symptomatic triad, which occurs in less than 50% of patients, includes seizures, mental retardation, and facial angiofibromas (98). Conventional MRI can demonstrate the CNS lesions but cannot characterize the microstructural changes within the white matter.

Karadag et al. used DTI to evaluate diffusivity and anisotropy properties within the cortical tubers and white matter abnormalities in seven children and adolescents (aged 2 to 20 years) with TS. Cortical tubers were shown to have higher ADC values only, while white matter lesions had higher ADCs and lower FA values (99). Thus, DTI has potential utility in describing lesions found in TS patients.

Treatment-Induced Injury

The treatment of medulloblastoma involves a combination of surgery, radiation, and chemotherapy and is associated with significant morbidity in children. Patients who survive treatment often develop significant cognitive and neuropsychological deficits (100,101). Radiation, in particular, is known to damage white matter in the brain (102). DTI has demonstrated its unique ability to quantitatively assess treatment-induced white matter injury in a study involving posttreatment medulloblastoma survivors (86). FA values were found to be significantly reduced in multiple regions that appeared normal on conventional MR images, defining a new role for DTI as a marker in treatment-induced white matter injury.

OTHER APPLICATIONS OF DTI

Disease Pathophysiology

In a number of cases, DTI has provided insight into the pathophysiology underlying the disease process itself. For example, the spasticity seen in periventricular leukomalacia has been traditionally believed to be related to descending pyramidal corticospinal tract injury. In one study that used DTI in two children with spastic quadriplegic cerebral palsy, prominent abnormalities were

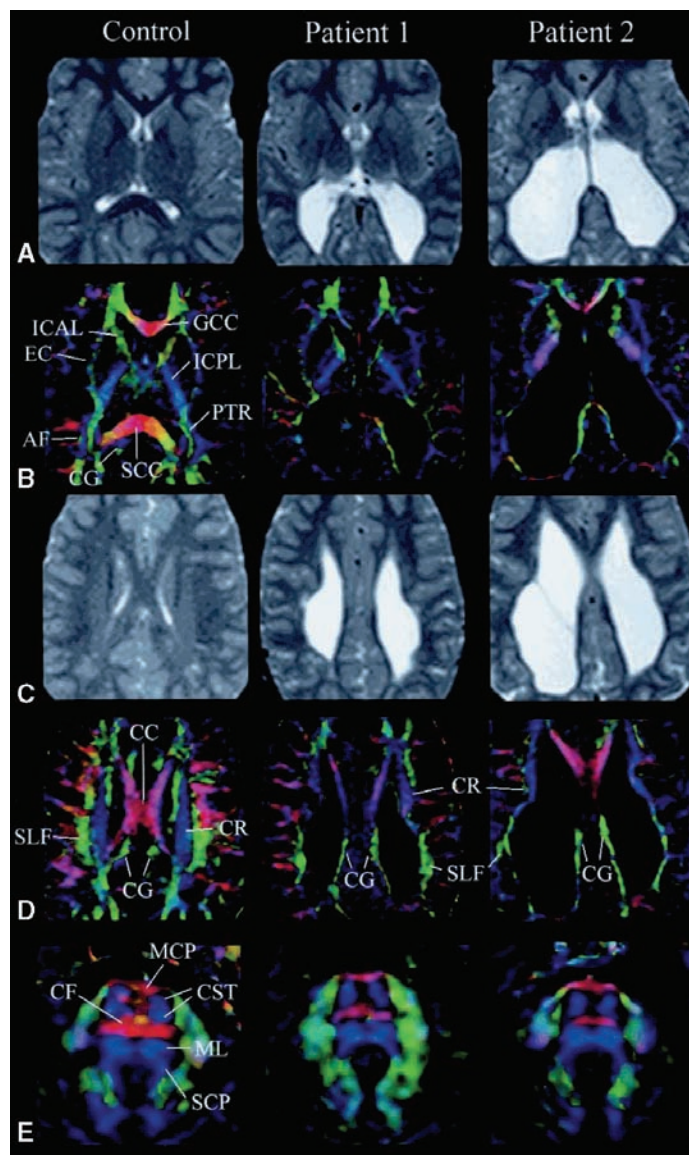


Figure 6 (A) and (C) T2-weighed images and (B), (D), and (E) diffusion tensor MRI (DTI)-based color maps at three axial slice levels of the eight-year-old control and patients 1 and 2. On the color maps, red color represents tracts oriented in the right-left direction, green anterior-posterior, and blue superior-inferior. (B) The ICAL was similar in controls and subjects, but posterior fibers in the ICPL, posterior CC, and PTR are decreased in size. (D) At the level of the CR, the posterior CR was not seen in subjects, but was clearly present in controls. The posterior CC was also severely affected. (E) The CST in the brain stem was similar in controls and subjects. Major identifiable structures are annotated. Abbreviations: CST, corticospinal tract; MCP, middle cerebellar peduncle; SCP, superior cerebellar peduncle; CF, crossing fiber; ML, medial lemniscus; ICAL/ICPL, anterior/posterior limb of internal capsule; EC, external capsule; AF, arcuate fasciculus; PTR, posterior thalamic radiation; CC, corpus callosum; GCC, genu of corpus callosum; SCC, splenium of corpus callosum; CR, corona radiata; CG, cingulum; SLF, superior longitudinal fasciculus.

found in the white matter fiber tracts of the occipital and parietal lobes, while the corticospinal tract appeared relatively normal (Fig. 6) (103). These findings suggest that in at least some patients with periventricular leukomalacia the white matter tracts of the sensory cortex (rather than the pyramidal motor cortex) may be implicated in the etiology of motor disability.

Neuroanatomical Structures

DTI can distinguish among some of these structural features of the brain, such as the compactness of white matter. On conventional MR images, compact and non-compact white matter structures differ in their onset and rate of myelination. Compact structures (e.g., corpus

callosum, cerebral peduncle) show changes consistent with myelination during the first year of life, while non-compact structures (e.g., frontal-parietal white matter, corona radiata) develop these features during the first few years following infancy. One study compared anisotropy measurements in compact and noncompact white matter structures in three age groups (0–12 months, 12–35 months, and 36–71 months) (6). Anisotropy values were found to be higher in compact white matter structures, but the increase in anisotropy was greater in the noncompact structures across all age groups. These findings suggest that myelination in noncompact white matter occurs more rapidly after the first year of life.

FUTURE DIRECTIONS

In the past decade, research has continued to define and expand the clinical and academic applications of DTI. As these investigations accelerate in the near future and as the underlying technology advances, DTI is expected to play an increasingly large role in defining developmental abnormalities at an early age and in assessment of therapies for pediatric disorders such as leukodystrophies.

REFERENCES

- Basser PJ. Inferring microstructural features and the physiological state of tissues from diffusion-weighted images. *NMR Biomed* 1995; 8(7–8):333–344.
- Wimberger DM, Roberts TP, Barkovich AJ, et al. Identification of “premyelination” by diffusion-weighted MRI. *J Comput Assist Tomogr* 1995; 19:28–33.
- Neil JJ, Shiran SI, McKinstry RC, et al. Normal brain in human newborns: apparent diffusion coefficient and diffusion anisotropy measured by using diffusion tensor MR imaging. *Radiology* 1998; 209(1):57–66.
- Partridge SC, Mukherjee P, Henry RG, et al. Diffusion tensor imaging: serial quantitation of white matter tract maturity in premature newborns. *Neuroimage* 2004; 22(3): 1302–1314.
- Shimony JS, McKinstry RC, Akbudak E, et al. Quantitative diffusion-tensor anisotropy brain MR imaging: normative human data and anatomic analysis. *Radiology* 1999; 212(3):770–784.
- Paus T, Collins DL, Evans AC, et al. Maturation of white matter in the human brain: a review of magnetic resonance studies. *Brain Res Bull* 2001 Feb; 54(3):255–266.
- McGraw P, Liang L, Provenzale JM. Evaluation of normal age-related changes in anisotropy during infancy and childhood as shown by diffusion tensor imaging. *AJR Am J Roentgenol* 2002; 179(6):1515–1522.
- Barkovich AJ, Kjos BO, Jackson DE Jr., et al. Normal maturation of the neonatal and infant brain: MR imaging at 1.5 T. *Radiology* 1988; 166(1 pt 1):173–180.
- Dobbing J, Sands J. Quantitative growth and development of human brain. *Arch Dis Child* 1973; (10):757–767.
- Hayakawa K, Konishi Y, Kuriyama M, et al. Normal brain maturation in MRI. *Eur J Radiol* 1991; 12(3):208–215.
- Richardson EP Jr. Myelination in the human central nervous system. In: Haymaker W, Adams RD, eds. *Histology and Histopathology of the Nervous System*. Springfield, Ill: Thomas, 1982: 146–173.
- van der Knaap MS, Valk J, Bakker CJ, et al. Myelination as an expression of the functional maturity of the brain. *Dev Med Child Neurol* 1991; 33(10):849–857.
- Mukherjee P, Miller JH, Shimony JS, et al. Normal brain maturation during childhood: developmental trends characterized with diffusion-tensor MR imaging. *Radiology* 2001; 221(2):349–358.
- Klingberg T, Vaidya CJ, Gabrieli JD, et al. Myelination and organization of the frontal white matter in children: a diffusion tensor MRI study. *Neuroreport* 1999; 10(13): 2817–2821.
- Snook L, Paulson LA, Roy D, et al. Diffusion tensor imaging of neurodevelopment in children and young adults. *Neuroimage* 2005; 26(4):1164–1173.
- Hamilton BE, Martin JA, Ventura SJ, et al. Births: preliminary data for 2004. *Natl Vital Stat Rep* 2005; 54(8): 1–17.
- Rapin I. Autism. *N Engl J Med* 1997; 337(2):97–104.
- Schonwald A, Lechner E. Attention deficit/hyperactivity disorder: complexities and controversies. *Curr Opin Pediatr* 2006; 18(2):189–195.
- Okumura A, Kato T, Kuno K, et al. MRI findings in patients with spastic cerebral palsy. II: correlation with type of cerebral palsy. *Dev Med Child Neurol* 1997; 39(6): 369–372.
- Huppi PS, Murphy B, Maier SE, et al. Microstructural brain development after perinatal cerebral white matter injury assessed by diffusion tensor magnetic resonance imaging. *Pediatrics* 2001; 107(3):455–460.
- Miller SP, Vigneron DB, Henry RG, et al. Serial quantitative diffusion tensor MRI of the premature brain: development in newborns with and without injury. *J Magn Reson Imaging* 2002; 16(6):621–632.
- Johnston MV. Clinical disorders of brain plasticity. *Brain Dev* 2004; 26(2):73–80.
- Nosarti C, Al-Asady MH, Frangou S, et al. Adolescents who were born very preterm have decreased brain volumes. *Brain*. 2002; 125(pt 7):1616–1623.
- Stewart AL, Rifkin L, Amess PN, et al. Brain structure and neurocognitive and behavioral function in adolescents who were born very preterm. *Lancet* 1999; 353(9165): 1653–1657.
- Nagy Z, Westerberg H, Skare S, et al. Preterm children have disturbances of white matter at 11 years of age as shown by diffusion tensor imaging. *Pediatr Res* 2003; 54 (5):672–679.
- Suzuki K. Globoid cell leukodystrophy (Krabbe's disease): update. *J Child Neurol* 2003; 18(9):595–603.
- Loes DJ, Peters C, Krivit W. Globoid cell leukodystrophy: distinguishing early-onset from late-onset disease using a

- brain MR imaging scoring method. *AJNR Am J Neuroradiol* 1999; 20(2):316–323.
- 28. Kravit W, Shapiro EG, Peters C, et al. Hematopoietic stem-cell transplantation in globoid-cell leukodystrophy. *N Engl J Med* 1998; 338:1119–1126.
 - 29. Barkovich AJ. Concepts of myelin and myelination in neuroradiology. *AJNR Am J Neuroradiol* 2000; 21: 1099–1109.
 - 30. Guo AC, Petrella JR, Kurtzberg J, Provenzale JM. Evaluation of white matter anisotropy in Krabbe disease with diffusion tensor MR imaging: initial experience. *Radiology* 2001; 218(3):809–815.
 - 31. Barone R, Bruhl K, Stoeter P, et al. Clinical and neuro-radiological findings in classic infantile and late-onset globoid-cell leukodystrophy (Krabbe disease). *Am J Med Genet* 1996; 63(1):209–217.
 - 32. McGraw P, Liang L, Escolar M, et al. Krabbe disease treated with hematopoietic stem cell transplantation: serial assessment of anisotropy measurements—initial experience. *Radiology* 2005; 236(1):221–230.
 - 33. Escolar ML, Poe MD, Provenzale JM, et al. Transplantation of umbilical-cord blood in babies with infantile Krabbe's disease. *N Engl J Med* 2005; 352(20): 2069–2081.
 - 34. Moser HW, Loes DJ, Melhem ER, et al. X-Linked adrenoleukodystrophy: overview and prognosis as a function of age and brain magnetic resonance imaging abnormality. A study involving 372 patients. *Neuropediatrics* 2000; 31(5):227–239.
 - 35. Powers JM. Adreno-leukodystrophy (adreno-testiculoleukomyelo-neuropathic-complex). *Clin Neuropathol* 1985; 4(5):181–199.
 - 36. Percy AK, Rutledge SL. Adrenoleukodystrophy and related disorders. *Ment Retard Dev Disabil Res Rev* 2001; 7(3):179–89.
 - 37. Suzuki Y, Isogai K, Teramoto T, et al. Bone marrow transplantation for the treatment of X-linked adrenoleukodystrophy. *J Inherit Metab Dis* 2000; 23(5):453–458.
 - 38. Loes DJ, Hite S, Moser H, et al. Adrenoleukodystrophy: a scoring method for brain MR observations. *AJNR Am J Neuroradiol* 1994; 15(9):1761–1766.
 - 39. Kruse B, Barker PB, van Zijl PC, et al. Multislice proton magnetic resonance spectroscopic imaging in X-linked adrenoleukodystrophy. *Ann Neurol* 1994; 36(4):595–608.
 - 40. Eichler FS, Itoh R, Barker PB, et al. Proton MR spectroscopic and diffusion tensor brain MR imaging in X-linked adrenoleukodystrophy: initial experience. *Radiology* 2002; 225(1):245–252.
 - 41. Simon EM, Barkovich AJ. Holoprosencephaly: new concepts. *Magn Reson Imaging Clin N Am* 2001; 9(1): 149–64, viii–ix.
 - 42. DeMeyer W, Zeman W, Palmer CG. The face predicts the brain: diagnostic significance of median facial anomalies for holoprosencephaly (arhinencephaly). *Pediatrics* 1964; 34:256–263.
 - 43. Roessler E, Belloni E, Gaudenz K, et al. Mutations in the human Sonic Hedgehog gene cause holoprosencephaly. *Nat Genet* 1996; 14(3):357–360.
 - 44. Albayram S, Melhem ER, Mori S, et al. Holoprosencephaly in children: diffusion tensor MR imaging of white matter tracts of the brainstem—initial experience. *Radiology* 2002; 223(3):645–651.
 - 45. Kinsman SL. White matter imaging in holoprosencephaly in children. *Curr Opin Neurol* 2004; 17(2):115–119.
 - 46. Scriver CR. Science, medicine and phenylketonuria. *Acta Paediatr Suppl* 1994; 407:11–18.
 - 47. Pietz J, Meyding-Lamade UK, Schmidt H. Magnetic resonance imaging of the brain in adolescents with phenylketonuria and in one case of 6-pyruvoyl tetrahydropteridine synthase deficiency. *Eur J Pediatr* 1996; 155(suppl 1): S69–S73.
 - 48. Ushakova GA, Gubkina HA, Kachur VA, et al. Effect of experimental hyperphenylalaninemia on the postnatal rat brain. *Int J Dev Neurosci* 1997; 15(1):29–36.
 - 49. Infante JP, Huszagh VA. Impaired arachidonic (20:4n-6) and docosahexaenoic (22:6n-3) acid synthesis by phenylalanine metabolites as etiological factors in the neuropathology of phenylketonuria. *Mol Genet Metab* 2001; 72(3):185–198.
 - 50. Malamud N. Neuropathology of phenylketonuria. *J Neuropathol Exp Neurol* 1966; 25(2):254–268.
 - 51. Poser CM, Van Bogaert L. Neuro-pathologic observations in phenylketonuria. *Brain* 1959; 82(1):1–9.
 - 52. Sugita R, Takahashi S, Ishii K, et al. Brain CT and MR findings in hyperphenylalaninemia due to dihydropteridine reductase deficiency (variant of phenylketonuria). *J Comput Assist Tomogr* 1990; 14(5):699–703.
 - 53. Gudinchet F, Maeder P, Meuli RA, et al. Cranial CT and MRI in malignant phenylketonuria. *Pediatr Radiol* 1992; 22(3):223–224.
 - 54. Brismar J, Aqeel A, Gascon G, et al. Malignant hyperphenylalaninemia: CT and MR of the brain. *AJNR Am J Neuroradiol* 1990; 11(1):135–138.
 - 55. Peng SS, Tseng WY, Chien YH, et al. Diffusion tensor images in children with early-treated, chronic, malignant phenylketonuric: correlation with intelligence assessment. *AJNR Am J Neuroradiol* 2004; 25(9):1569–1574.
 - 56. Mader I, Herrlinger U, Klose U, et al. Progressive multifocal leukoencephalopathy: analysis of lesion development with diffusion-weighted MRI. *Neuroradiology* 2003; 45(10):717–721. (Epub 2003 Aug 27).
 - 57. Skiest DJ. Focal neurological disease in patients with acquired immunodeficiency syndrome. *Clin Infect Dis* 2002; 34(1):103–115.
 - 58. Whiteman ML, Post MJ, Berger JR, et al. Progressive multifocal leukoencephalopathy in 47 HIV-seropositive patients: neuroimaging with clinical and pathologic correlation. *Radiology* 1993; 187(1):233–240.
 - 59. Post MJ, Yiannoutsos C, Simpson D, et al. Progressive multifocal leukoencephalopathy in AIDS: are there any MR findings useful to patient management and predictive of patient survival? AIDS Clinical Trials Group, 243 Team. *AJNR Am J Neuroradiol* 1999; 20(10):1896–1906.
 - 60. Huisman TA, Boltshauser E, Martin E, et al. Diffusion tensor imaging in progressive multifocal leukoencephalopathy: early predictor for demyelination? *AJNR Am J Neuroradiol* 2005; 26(8):2153–2156.

61. Morton DH, Strauss KA, Robinson DL, et al. Diagnosis and treatment of maple syrup disease: a study of 36 patients. *Pediatrics* 2002; 109(6):999–1008.
62. Brismar J, Aqeel A, Brismar G, et al. Maple syrup urine disease: findings on CT and MR scans of the brain in 10 infants. *AJNR Am J Neuroradiol* 1990; 11(6): 1219–1228.
63. Uziel G, Savoardo M, Nardocci N. CT and MRI in maple syrup urine disease. *Neurology* 1988; 38(3):486–488.
64. Parmar H, Sitoh YY, Ho L. Maple syrup urine disease: diffusion-weighted and diffusion-tensor magnetic resonance imaging findings. *J Comput Assist Tomogr* 2004; 28(1):93–97.
65. DiMauro S, Moraes CT. Mitochondrial encephalomyopathies. *Arch Neurol* 1993; 50(1):1197–1208.
66. Ohara S, Ohama E, Takahashi H, et al. Alterations of oligodendrocytes and demyelination in the spinal cord of patients with mitochondrial encephalomyopathy. *J Neurol Sci* 1988; 86(1):19–29.
67. Sandhu FS, Dillon WP. MR demonstration of leukoencephalopathy associated with mitochondrial encephalomyopathy: case report. *AJNR Am J Neuroradiol* 1991; 12(2): 375–379.
68. Deary IJ, Bastin ME, Pattie A, et al. White matter integrity and cognition in childhood and old age. *Neurology* 2006; 66(4):505–512.
69. Edwards SG, Liu C, Blumhardt LD. Cognitive correlates of supratentorial atrophy on MRI in multiple sclerosis. *Acta Neurol Scand* 2001; 104(4):214–223.
70. Rovaris M, Iannucci G, Falautano M, et al. Cognitive dysfunction in patients with mildly disabling relapsing-remitting multiple sclerosis: an exploratory study with diffusion tensor MR imaging. *J Neurol Sci* 2002; 195(2):103–109.
71. O'Sullivan M, Jones DK, Summers PE, et al. Evidence for cortical “disconnection” as a mechanism of age-related cognitive decline. *Neurology* 2001; 57(4):632–638.
72. Klingberg T, Hedeus M, Temple E, et al. Microstructure of temporo-parietal white matter as a basis for reading ability: evidence from diffusion tensor magnetic resonance imaging. *Neuron* 2000; 25(2):493–500.
73. Paus T, Collins DL, Evans AC, et al. Maturation of white matter in the human brain: a review of magnetic resonance studies. *Brain Res Bull* 2001; 54(3):255–266.
74. Huppi PS, Maier SE, Peled S, et al. Microstructural development of human newborn cerebral white matter assessed *in vivo* by diffusion tensor magnetic resonance imaging. *Pediatr Res* 1998; 44(4):584–590.
75. Schmithorst VJ, Wilke M, Dardzinski BJ, et al. Cognitive functions correlate with white matter architecture in a normal pediatric population: a diffusion tensor MRI study. *Hum Brain Mapp* 2005; 26(2):139–147.
76. Pearsen KD, Gean-Marton AD, Levy HL, et al. Phenylketonuria: MR imaging of the brain with clinical correlation. *Radiology* 1990; 177(2):437–440.
77. Khong PL, Leung LH, Fung AS, et al. White matter anisotropy in post-treatment childhood cancer survivors: preliminary evidence of association with neurocognitive function. *J Clin Oncol* 2006; 24(6):884–890.
78. Khong PL, Kwong DL, Chan GC, et al. Diffusion-tensor imaging for the detection and quantification of treatment-induced white matter injury in children with medulloblastoma: a pilot study. *AJNR Am J Neuroradiol* 2003; 24(4): 734–740.
79. Chin HW, Maruyama Y. Age at treatment and long-term performance results in medulloblastoma. *Cancer* 1984; 53(9):1952–1958.
80. Kimmings E, Kleinlugtebeld AT, Casey A, et al. Medulloblastoma: factors influencing the educational potential of surviving children. *Br J Neurosurg* 1995; 9(5):611–617.
81. Als H, Duffy FH, McAnulty GB, et al. Early experience alters brain function and structure. *Pediatrics* 2004; 113(4): 846–857.
82. Westrup B, Kleberg A, von Eichwald K, et al. A randomized, controlled trial to evaluate the effects of the newborn individualized developmental care and assessment program in a Swedish setting. *Pediatrics* 2000; 105(1 pt 1): 66–72.
83. Gurney JG, Smith MA, Bunin GR. CNS and miscellaneous intracranial and intraspinal neoplasms. In: Ries LAG, Smith MA, Gurney JG, et al., eds. *Cancer Incidence and Survival among Children and Adolescents: United States SEER Program 1975–1995*. Bethesda, MD: National Cancer Institute, SEER Program, 1999:51–64.
84. Tien RD, Felsberg GJ, Friedman H, et al. MR imaging of high-grade cerebral gliomas: value of diffusion-weighted echoplanar pulse sequences. *AJR Am J Roentgenol* 1994; 162(3):671–677.
85. Price SJ, Burnet NG, Donovan T, et al. Diffusion tensor imaging of brain tumours at 3T: a potential tool for assessing white matter tract invasion? *Clin Radiol* 2003; 58(6):455–462.
86. Le Bihan D, Turner R, Douek P, et al. Diffusion MR imaging: clinical applications. *AJR Am J Roentgenol* 1992; 159(3):591–599.
87. Krabbe K, Gideon P, Wagn P, et al. MR diffusion imaging of human intracranial tumours. *Neuroradiology* 1997; 39(7):483–489.
88. Becker LE. Pathology of pediatric brain tumors. *Neuroimaging Clin N Am* 1999; 9(4):671–690.
89. Sugahara T, Korogi Y, Kochi M, et al. Usefulness of diffusion-weighted MRI with echo-planar technique in the evaluation of cellularity in gliomas. *J Magn Reson Imaging* 1999; 9(1):53–60.
90. Kotzenas AL, Roth TC, Manness WK, et al. Abnormal diffusion-weighted MRI in medulloblastoma: does it reflect small cell histology? *Pediatr Radiol* 1999; 29(7): 524–526.
91. Gauvain KM, McKinstry RC, Mukherjee P, et al. Evaluating pediatric brain tumor cellularity with diffusion-tensor imaging. *AJR Am J Roentgenol* 2001; 177(2): 449–454.
92. Barkovich AJ, Krischer J, Kun LE, et al. Brain stem gliomas: a classification system based on magnetic resonance imaging. *Pediatr Neurosurg* 1990–91; 16(2):73–83.
93. Fischbein NJ, Prados MD, Wara W, et al. Radiologic classification of brain stem tumors: correlation of magnetic resonance imaging appearance with clinical outcome. *Pediatr Neurosurg* 1996; 24(1):9–23.

94. Lesniak MS, Klem JM, Weingart J, et al. Surgical outcome following resection of contrast-enhanced pediatric brain-stem gliomas. *Pediatr Neurosurg* 2003; 39(6):314–322.
95. Helton KJ, Phillips NS, Khan RB, et al. Diffusion tensor imaging of tract involvement in children with pontine tumors. *AJNR Am J Neuroradiol* 2006; 27(4):786–793.
96. Mukonoweshuro W, Wilkinson ID, Griffiths PD. Proton MR spectroscopy of cortical tubers in adults with tuberous sclerosis complex. *AJNR Am J Neuroradiol* 2001; 22(10):1920–1925.
97. Baron Y, Barkovich AJ. MR imaging of tuberous sclerosis in neonates and young infants. *AJNR Am J Neuroradiol* 1999; 20(5):907–916.
98. Roach ES, Gomez MR, Northrup H. Tuberous sclerosis complex consensus conference: revised clinical diagnostic criteria. *J Child Neurol* 1998; 13(12):624–628.
99. Karadag D, Mentzel HJ, Güllmar D, et al. Diffusion tensor imaging in children and adolescents with tuberous sclerosis. *Pediatr Radiol* 2005; 35(10):980–983.
100. Johnson DL, McCabe MA, Nicholson HS, et al. Quality of long-term survival in young children with medulloblastoma. *J Neurosurg* 1994; 80(6):1004–1010.
101. Packer RJ, Spoto R, Atkins TE, et al. Quality of life in children with primitive neuroectodermal tumors (medulloblastoma) of the posterior fossa. *Pediatr Neurosci* 1987; 13(4):169–175.
102. Valk PE, Dillon WP. Radiation injury of the brain. *AJNR Am J Neuroradiol* 1991; 12(1):45–62.
103. Hoon AH Jr., Lawrie WT Jr., Melhem ER, et al. Diffusion tensor imaging of periventricular leukomalacia shows affected sensory cortex white matter pathways. *Neurology* 2002; 59(5):752–756.

15

DTI of Neurodegenerative Disorders

SUMEI WANG, JOHN H. WOO, and ELIAS R. MELHEM

*Department of Radiology, Division of Neuroradiology, Hospital of the University of Pennsylvania,
Philadelphia, Pennsylvania, U.S.A.*

INTRODUCTION

Neurodegenerative disorders are conditions which result from gradual deterioration of certain neurons, leading to progressive brain dysfunction and eventually death (1). Generally, neurodegenerative disorders can be classified by their primary manifestations into two broad categories: those affecting movement [such as Parkinson's disease (PD)] and those affecting memory and cognitive function [such as Alzheimer's disease (AD)]. In practice, it refers to a large group of neurological disorders with heterogeneous clinical and pathological expressions affecting specific subsets of neurons in specific functional anatomical systems. Largely as a result of increased life expectancy, neurodegenerative dementias and neurodegenerative movement disorders are becoming more common (2,3). As they are prevalent with advancing age, improved understanding of these diseases will be vital to develop more effective therapies and combat the staggering personal, social, and economic costs.

Conventional magnetic resonance (MR) imaging is frequently insensitive to the underlying pathological processes in neurodegenerative diseases. Focal or global atrophy due to associated neuronal loss is usually subtle or absent, particularly in the early stages of the disease. Fortunately, several recently developed advanced MR techniques have shown promise in the study of neurodegenerative disorders.

One technique for exploring white matter (WM) pathways *in vivo* is diffusion tensor imaging (DTI), which can reveal the microstructural changes in neurodegenerative diseases (4,5).

This chapter will outline some of the most recent developments of DTI and its application to neurodegenerative disorders. Since neurodegenerative disorders represent a wide variety of diseases, we only focus on several common diseases.

METHODOLOGICAL BACKGROUND

DTI

DTI provides microscopic structural information about tissue *in vivo*. Diffusion is the molecular movement of bulk water. When unimpeded, water molecules move in a random manner (isotropic diffusion). However, the presence of obstacles to free motion, such as axonal membranes and myelin sheaths in WM fiber tracts, hinders molecular motion in a particular direction, resulting in anisotropic diffusion (5). Diffusivity is generally higher in directions along fiber tracts than perpendicular to them (6). This can be described mathematically by a tensor, which is characterized by its three eigenvectors and the corresponding eigenvalues. The eigenvector associated with the largest eigenvalue indicates the predominant orientation of fibers in the given voxel.

Two DTI-based indices are often used to characterize microstructure of the brain tissue: apparent diffusion coefficient (ADC) and fractional anisotropy (FA), which can be calculated according to Equations (1) and (2), respectively,

$$\text{ADC} = (\lambda_1 + \lambda_2 + \lambda_3)/3 \quad (1)$$

$$\text{FA} = \sqrt{\frac{3}{2}} \sqrt{\frac{(\lambda_1 - \bar{\lambda})^2 + (\lambda_2 - \bar{\lambda})^2 + (\lambda_3 - \bar{\lambda})^2}{\lambda_1^2 + \lambda_2^2 + \lambda_3^2}} \quad (2)$$

where λ_1 , λ_2 , and λ_3 are the three eigenvalues of the diffusion tensor and $\bar{\lambda}$ denotes the mean of the three eigenvalues, a measure of directionally averaged diffusivity.

ADC is a measure of the directionally averaged magnitude of diffusion and is related to the integrity of the local brain tissue. FA represents the degree of anisotropy in the diffusion and reflects the degree of alignment of cellular structure (4).

DTI also provides information about the direction of the principal eigenvector, which denotes the direction of maximum diffusivity. The principal eigenvector represents the major orientation of the interrogated WM tracts. Hence, DTI allows mapping of the WM tracts in the brain, where the orientation is coded using red, green, and blue color channels, and the brightness of the assigned color is modulated by the degree of anisotropy (FA). This display technique results in a convenient orientation-based color map in which both the degree of anisotropy and the local fiber orientation can be determined. Application of this technique to the brain has been demonstrated to be useful in showing WM architecture (7–10).

DTI produces numerous measures ranging in dimensions from scalars to tensor fields, calling for a wide variety of statistical techniques to perform group analyses. Specific methods remain under development (11–13). Currently, most commonly used three methods for the analysis of DTI data are histogram, region of interest (ROI), and voxel-based analysis.

Histogram approach enables quantitative analysis of the whole brain. Histogram-derived metrics including mean value, peak position, and peak height are used to quantify the global properties (14). It is possible to obtain histograms from the gray matter (GM) and WM, separately. However, the overall sensitivity may be low. It is suitable for a widespread disease like multiple sclerosis (MS) (15,16).

ROI analysis allows identification between group differences in a specific brain region, thus offering correlation between structure and function. Potential pitfalls include bias in ROI selection. Tract-specific measurements (17,18) (Fig. 1), which use fiber-tracking images as an unbiased guide to place ROIs, overcome some of the limitations of ROI analysis.

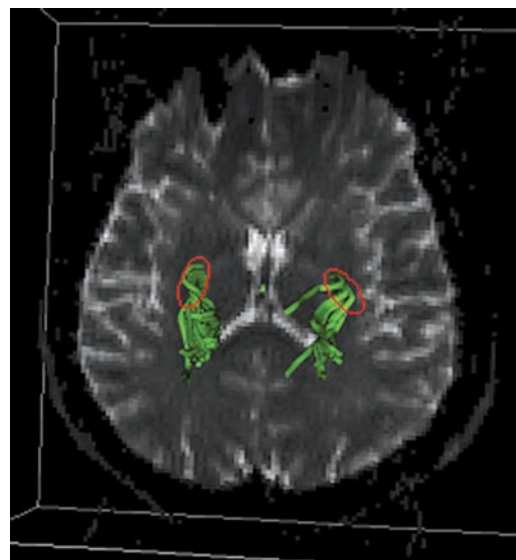


Figure 1 The CSTs (green) are reconstructed and overlaid on b0 images in a healthy subject. ROIs (red) are placed manually in the left and right side of the PLIC on the axial slice based on the location of CSTs. Abbreviations: CST, corticospinal tract; ROI, region of interest; PLIC, posterior limb of internal capsule.

Voxel-based analysis is an operator-independent approach that allows the analysis of the entire brain volumes without a prior hypothesis regarding the anatomical location (12,19,20). This approach can be very useful as an exploratory analysis, especially for the regions where WM changes are extensive. However, it can be done only after intersubject registration. Coregistration of low-resolution FA maps may generate significant misregistration and partial volume artifacts. Also, the accurate localization of differences to specific tracts is difficult since data are often heavily smoothed as part of the preprocessing (21).

Diffusion Tensor Tractography

DTI techniques also allow interregional fiber tracking, known as diffusion tensor tractography, which allows tracking of major WM tracts (9,22–24). This process could be carried out with a wide variety of algorithms. The streamline tractography is generally performed using a line propagation technique based on continuous number fields (22,23) and a multiple ROI approach (25,26). Tracking is launched from a “seed” voxel from which a line is propagated in both retrograde and antegrade directions according to the major eigenvector at each voxel. Tracking propagates on the basis of the orientation of the eigenvector that is associated with the largest eigenvalue. The propagation terminates when it reaches a voxel with FA lower than a specified FA threshold or when the angle between two principal eigenvectors is greater than an

angle threshold. Tract selection and seed placement are typically highly interactive and thus may have strong operator dependence.

Probabilistic tractography is a novel approach, which generates probabilistic maps of fiber connectivity among brain regions. The value of each voxel in a map is the likelihood that the voxel is included in the diffusion path between two ROIs (27,28). Tractography algorithms have been developed which propagate in the form of wavefront of varying sizes rather than a streamline, allowing fiber tracts to diverge and recombine (29–31). Probabilistic tracking allows tracing connectivity distributions all the way to the GM (28).

Although DTI carries important anatomical information about the WM, interpretation of the results is not always straightforward. An acknowledged limitation of DTI concerns crossing WM tracts (32). DTI reflects the averaged water diffusion property within a voxel. If a voxel has several bundles of fibers with different orientations, it may not be possible to separate these bundles. Furthermore, tractography could not differentiate between efferent and afferent fibers. The reliability of this technique depends on the quality of the data and on the robustness of the algorithms used (33). Also, the validation of tractography is harder to address because of lack of a gold standard (34).

Relationship Between Pathology and Diffusion in Neurodegenerative Disorders

Neurodegenerative diseases share one unifying pathological process—namely, progressive neuronal damage or death. The WM has close anatomical and functional connections to the overlying cortex. For example, the subcortical WM consists of either axons of neurons in the overlying cortex or axons originating from the other cerebral cortex that has synaptic connections with the cortical neurons. As a matter of fact, cortical degeneration results in the microstructural degradation of adjacent subcortical WM. Pathologically, the brain cortex undergoes different degree of atrophy in specific areas, the WM experiences degenerative alterations, such as axonal dissolution, loss of continuity of myelin sheaths, and reactive gliosis (35–37). Englund (38) studied subcortical and deep WM in the patients with AD and found that subcortical WM changes were consistent with findings of Wallerian degeneration and their distribution was well correlated with the extent of cortical degeneration. Furthermore, the study also revealed that changes in deep WM were more likely of vascular origin and their distribution did not match what was found in the cortical lesions. As the diffusion properties are directly related to the microstructure of the medium, they can be used to characterize tissue and to detect underlying histological changes due to physiological and pathological

states. Looking across studies, DTI can reflect the myelin status, axonal integrity, and the organization and alignment of group of axons and fibers in WM tissue (5,39). Thus, DTI is a promising tool for the identification of underlying tissue integrity and organization at multiple levels in neurodegenerative disorders.

NORMAL AGING

The aging brain exhibits varying micro- and macroscopic changes that ultimately cause some degree of cognitive and functional decline. Although the majority of studies of normal aging have focused on the cerebral cortex, it is obvious that cerebral WM also exhibits various types of age-related degenerative changes. Neuropathological studies have reported age-related deterioration in the microstructure of WM, including demyelination and axonal loss (40,41).

DTI has proved itself to be a suitable method for exploring age-related changes. Previous studies (42,43) using an ROI approach have demonstrated a significant decrease in FA and increase in ADC in different regions of the brain. Whole-brain ADC histograms (44) showed higher mean ADC and reduced peak height and skew in the older age group compared with the younger age group. Recently voxel-based analysis has been performed to identify age-related alterations at a voxel level (45–47). Ardekani et al. (45) reported a significant decline in FA with frontal predominance, covering frontal WM, genu, and anterior body of corpus callosum (CC), superior portions of splenium, posterior limb of internal capsule (PLIC), and anterior and posterior limbs of external capsule (Fig. 2). On the basis of these studies, frontal WM changes exhibit highly significant correlations with age, implying the vulnerability of frontal WM in aging. Salat et al. (48) found that ventromedial and deep prefrontal regions in prefrontal WM showed a somewhat greater reduction of FA compared with other areas. Therefore, quantitative DTI analysis correlates with normal aging and may be helpful in assessing normal age-related changes and serve as a standard for comparison with neurodegenerative disorders (49).

ALZHEIMER'S DISEASE

AD is the most common cause of dementia in the elderly. Mild cognitive impairment (MCI) is considered as the early stage of AD. The diagnosis is made on the basis of appearance of symptoms (50). The primary symptoms—loss of both memory and the ability to communicate—gradually become more pronounced over time. Sufferers initially have difficulty in completing daily tasks and appear disoriented. They may also encounter changes in

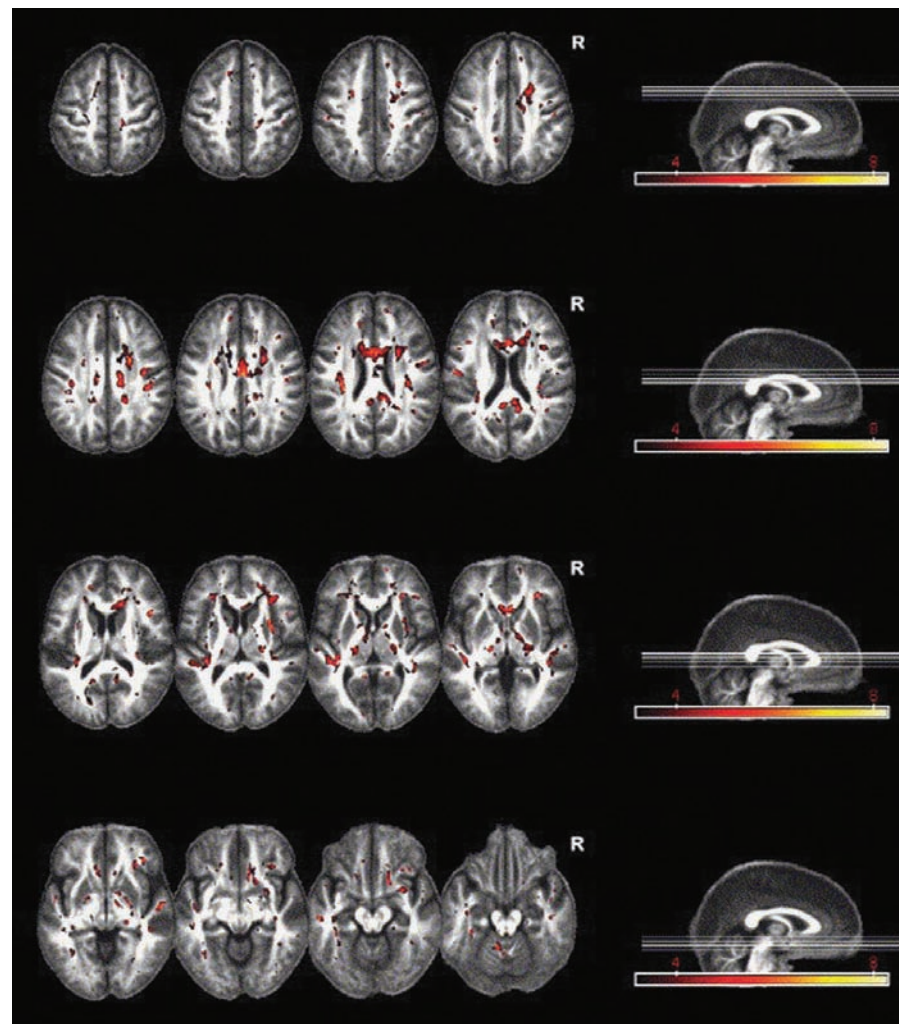


Figure 2 Map of the voxel-based significance of FA decline with normal aging. The map is generated by computing voxel-level *t* tests between the young-age group and the middle-age group. Maps are presented axially, with the corresponding location marked on sagittal view. In each row, the planes are separated by 4 mm. The color scale represents the significance of FA decline with age, as measured in *t* values, with yellow representing the most significant area. The beginning of the scale is marked with corrected threshold for multiple comparisons ($t = 3.23$ or $p = 0.025$). Abbreviation: FA, fractional anisotropy. Source: From Ref. 45.

personality. Depression, general unease, and paranoia may set in. Current consensus statements have emphasized the need for early recognition.

The two main pathological structures found within the AD brain are extracellular neuritic plaques, consisting largely of A β peptide, and intracellular neurofibrillary tangles, composed primarily of the cytoskeletal protein tau (51). The loss of the large cortical neurons (layer III and V) is the pathological substrate of the progressive dementing process in AD. AD initially affects medial temporal lobe structures, most noticeably the hippocampus and entorhinal cortex, with later involvement of temporal and parietal neocortex (52). Besides GM, several WM abnormalities have been observed: rarefaction, loss of axon and myelin and oligodendrocytes, and reactive astrocytosis (35).

DTI has been applied to the study of patients with AD to achieve in vivo estimates of WM alterations. An increase in ADC and a decrease in FA values have been reported in multiple WM regions (53–58). Voxel-based analysis of whole brain revealed widely distributed disintegration of WM in patients with mild AD, reflecting biophysical alterations early in the progression of AD (12). In one study (55), significant variability existed in ADC values, which overlapped between subject groups; this limited the reliable use of ADC values to help diagnose MCI or AD or predict the likelihood of progression from MCI to AD. Most of the studies (12,53,56,58) also reported strong correlations between Mini-Mental State Examination score (59) and average overall ADC and FA values in WM.

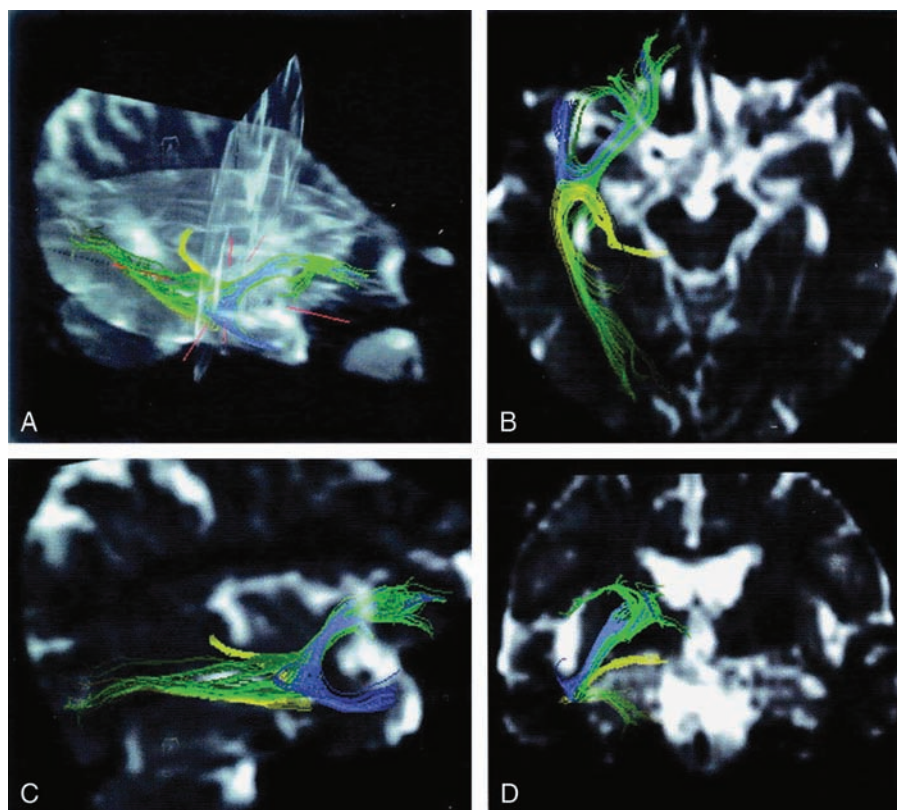


Figure 3 Changes in the WM tracts of the temporal stem in patients with AD. Impairment of the uncinate fasciculus and inferior occipitofrontal fasciculus has been reported in AD patients, while Meyer's loop, which was included as a control, was not affected. Tractographies are drawn by using diffusion-weighted images (EPI: TR/TE, 2300/122 msec; $b = 1000 \text{ sec/mm}^2$; 6-axis encoding; FOV, 230 mm; matrix, 128×128 ; section spacing, 3.3 mm; section thickness, 3 mm; averaging 6). Tractographies of the inferior occipitofrontal fasciculus (green), uncinate fasciculus (blue), and Meyer's loop (yellow) are shown. (A) 3D view from the right upper; (B) view from the bottom; (C) view from the right; and (D) view from the front. Mean FA and ADC values are measured along these tracts of interest separately. Abbreviations: WM, white matter; AD, Alzheimer's disease; EPI, echo-planar imaging; FOV, field of view; FA, fractional anisotropy; ADC, apparent diffusion coefficient. Source: From Ref. 62.

Another tensor index, lattice index, has also been used as a quantitative measure of anisotropy in DTI. Reduced lattice index, like FA, has been reported in the splenium of the CC, superior longitudinal fasciculus, and left cingulum in patients with AD (60).

The distribution of WM abnormalities was not homogeneous but involved selective regions connected with association cortices (temporal and frontal WM, CC). These findings supported the theory of “retrogenesis,” which suggests that the pathological processes in AD proceed in an opposite manner to normal developmental patterns (61). The frontal and temporal WM, which mature later in life may be affected first in pathological conditions such as AD.

WM tracts of the temporal stem can be evaluated independently by using diffusion tensor tractography. Impairment of the uncinate fasciculus and inferior occipitofrontal fasciculus has been reported in AD patients,

while Meyer's loop, which was included as a control, was not affected (Fig. 3) (62).

OTHER DEMENTIAS

Dementia With Lewy Bodies

Dementia with Lewy bodies (DLB) is the second most common form of dementia in the elderly after AD. Three major clinical features characterize DLB: fluctuations in cognition, visual hallucinations, and spontaneous parkinsonism (63).

Pathological studies have demonstrated widespread distribution of Lewy bodies in the neocortex, limbic structures, subcortical nuclei, and brain stem of patients with DLB (64). A confounding feature is that Lewy bodies are also found in the brains of patients with PD and AD, showing their association with these diseases.

DTI can provide indirect insights into the brain microstructural characteristics. In a study employing DTI in the patients with DLB, Bozzali et al. (65) found widespread WM abnormalities in CC, frontal, parietal, and occipital regions. The caudate nucleus and putamen were also involved. Increased ADC and decreased FA in the CC and pericallosal areas might suggest the presence of neurodegeneration involving associated cortices. The modest involvement of temporal lobe fits with the relative preservation of global neuropsychological measures and memory tasks in the early stage of DLB (65).

Frontotemporal Dementia

“Frontotemporal dementia (FTD)” is a term used to describe a family of neurodegenerative disorders characterized by degeneration of frontal and temporal lobes (66). The three most common FTD syndromes are Pick’s disease, frontal-lobe degeneration, and FTD with amyotrophic lateral sclerosis (ALS). FTD accounts for approximately 5% to 10% of cases of dementia. It is clinically characterized by behavior and language disturbances that may precede or overshadow memory deficits. Currently, there is no treatment for this condition.

At gross pathology, the brain in FTD demonstrates circumscribed atrophy of the frontal and temporal lobes. Histopathologically, the affected area demonstrated gliosis, loss of large cortical neurons, loss of myelin, and microvacuolation. Pick’s bodies are found in Pick’s disease.

DTI can evaluate the brain tissue damage in FTD. Larsson et al. (67) first applied DTI to the formalin-fixed brain of an FTD patient. Decreased diffusion anisotropy was observed in the bilateral frontal WM. Yoshiura et al. (68) demonstrated elevated ADC in the frontal and temporal WM using diffusion-weighted imaging (DWI). In a recent study, Borroni et al. (69), based on major clinical presentation, classified FTD into two types: frontal variant and temporal variant. The frontal variant group showed a selective WM reduction in the superior longitudinal fasciculus, while the temporal variant group demonstrated WM reductions in the inferior longitudinal fasciculus.

HUMAN PRION DISEASE

Creutzfeldt-Jakob Disease

Creutzfeldt-Jakob Disease (CJD) is a fatal neurodegenerative disease caused by accumulation of an abnormally shaped membrane-bound protein, the prion protein, in neurons (70). There are four forms: sporadic, iatrogenic, familial, and variant. CJD is clinically characterized by rapidly progressive dementia, myoclonus, and periodic sharp wave complexes (PSWCs) on electroencephalograms

(EFGs). However, this triad may be lacking in as many as 25% of the patients (71), especially in the early course of the disease.

The characteristic histopathological features of CJD are spongiform degeneration of the neurons and their processes, neuronal loss, intensively reactive astrocytic gliosis, and amyloid plaque formation. Spongiform degeneration is observed in the cerebral cortex, putamen, caudate nucleus, thalamus, and hippocampus. Under electron microscopy, the spongiform degeneration is typically observed in the form of vacuoles located in the neuropil among the nerve cell bodies. The vacuoles are round or oval in shape and vary in diameter from 5 to 25 μm. In the late stage of the disease (status spongiosus), the vacuoles become very large, up to 100 μm in diameter, and are surrounded by a dense meshwork of reactive astrocytosis (71).

T2-weighted and fluid-attenuated inversion recovery (FLAIR) images show hyperintense lesions in the cerebral cortex and bilateral basal ganglia in patients with CJD. But in the early stage of the disease, the appearance of the brain on T2-weighted images is often normal. DWI therefore has gained attention as a useful modality for the early diagnosis of CJD. DWI depicts areas of abnormal signal hyperintensity in the cortex, basal ganglia, or thalamus. These imaging abnormalities are accompanied by decreased ADC (Fig. 4). Signal changes in DWI are detected earlier than conventional MR images during the course of the disease (72–75). Using DWI, we can follow the disease’s progression by serial MR imaging (72,76). The reduced ADC may be due to the abnormal vacuoles in the cytoplasm (77,78). However, another study (79) reported there was no correlation between the degree of radiological and pathological abnormalities.

PARKINSON’S AND RELATED MOVEMENT DISORDERS

PD is characterized by progressive dementia, bradykinesia, shuffling gait, rigidity, and involuntary tremors. Usually it is considered to be associated with a deficiency of a neurotransmitter called dopamine, which breakdowns the communication among neurons. PD is the most common cause of parkinsonism, a group of similar symptoms. Other diseases causing parkinsonism include progressive supranuclear palsy (PSP), multiple system atrophy (MSA), and striatonigral degeneration (SND).

The pathological hallmark of PD is the selective loss of dopaminergic neurons projecting from the substantia nigra in the midbrain to the neostriatum. In MSA, pontine nuclei and middle cerebellar peduncles are severely involved, while, in PSP, the dentate nuclei and their outflow tracts, the superior cerebellar peduncles, are extensively damaged.

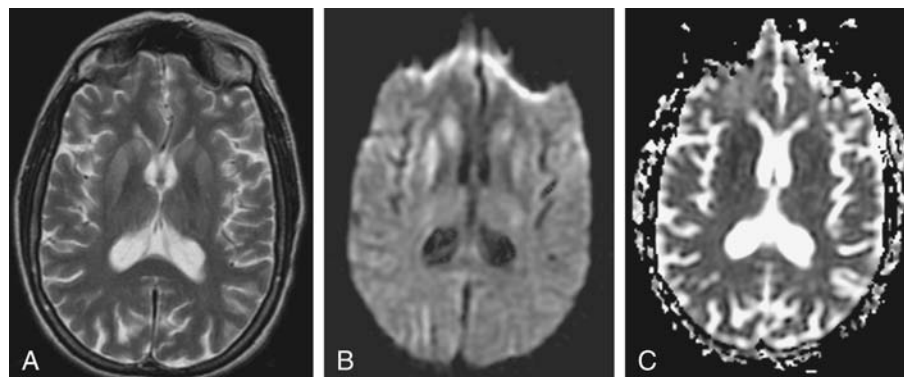


Figure 4 Sporadic Creutzfeldt-Jakob disease in a 34-year-old male, who presented with abnormal leg movement and slowness of thinking. (A) Axial T2-weighted MR image shows an area of subtle abnormal signal hyperintensity in the right putamen and caudate nuclei. (B) Axial diffusion-weighted images show bilateral areas of abnormal high signal intensity at the putamen and caudate nuclei, particularly in the right. (C) Axial ADC map from diffusion-weighted imaging demonstrates reduced ADC value. Abbreviations: MR, magnetic resonance; ADC, apparent diffusion coefficient.

A study of patients with early PD demonstrated decreased anisotropy in the nigrostriatal projection, in which most of the dopaminergic neurons are present. Loss of FA in this region was evident even during the early clinical stages of PD (80). Voxelwise analysis (81) revealed increased diffusivity in the region of both olfactory tracts in PD, which is in line with the well-established clinical finding of hyposmia in these patients. Recently Padovani et al. (82) reported a decrease in FA in the main association fibers, superior longitudinal fasciculus and arcuate fasciculus, and commissural fibers, CC in PSP patients, which indicates the WM degeneration in the early stage of PSP.

DTI and tractography could also be used to quantify neurodegenerative processes in different brain stem and cerebellar structures in parkinsonian disorders, such as MSA and PSP, and might have diagnostic significance (83–85). Patients with MSA demonstrated decreased FA and increased ADC in the middle cerebellar peduncles and pontine crossing tracts, while patients with PSP showed a selected degeneration of superior cerebellar peduncle. Tractography images of the whole brain demonstrated a reduction of cortical projection fibers in all patients with PSP (83).

HUNTINGTON'S DISEASE

Huntington's disease (HD) is an autosomal dominant neurodegenerative disorder caused by expansion of a CGA triplet in the gene IT15 of chromosome 4, which encodes a protein called huntingtin. Clinical manifestations include involuntary movements, psychiatric disturbance, and cognitive decline.

The pathological characteristics of brain damage in HD are neuronal loss and increased astroglia and

oligodendrocytes in the neostriatum. There is a growing body of evidence in the literature, suggesting that the degeneration in HD may be more widespread, with significant involvement of extrastriate structures including WM (86,87).

DTI can depict tissue damage associated with HD. Several studies demonstrated that ADC values in the caudate nucleus and putamen were elevated (88,89), whereas FA values in the internal capsule, CC, and frontal WM were reduced (Fig. 5) (9,90). WM alterations occur both in presymptomatic individuals known to carry the genetic mutation that causes HD and in very early stage of symptomatic HD patients (9,90).

MOTOR NEURON DISEASE

Amyotrophic Lateral Sclerosis

ALS, also called Lou Gehrig's disease, is a motor neuron disease characterized by progressive degeneration of upper motor neurons (UMN) and lower motor neurons (LMN). Patients with ALS experience a relentlessly progressive paralysis of the skeletal muscles, culminating in loss of mobility, loss of the ability to speak and eat, and eventual loss of respiratory function, making ALS one of the most devastating neurodegenerative diseases (91). The diagnosis of ALS is currently based on clinical features, electromyography (EMG), and exclusion of other diseases with similar symptoms. LMN dysfunction can be confirmed by EMG and muscle biopsy, whereas UMN involvement is more difficult to detect, particularly in the early phase (91,92). Objective and sensitive measures of UMN dysfunction are needed since delayed diagnosis may lead to loss of motor function, which might not be corrected by therapeutic interventions (93).

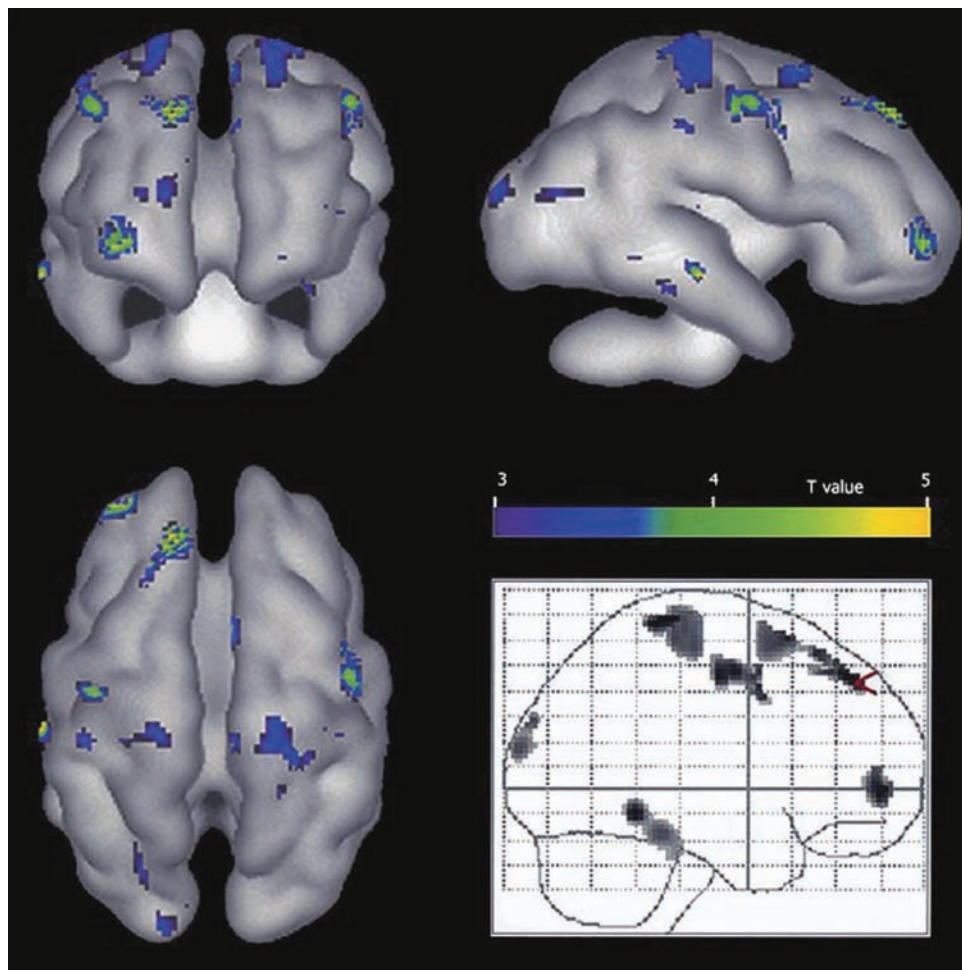


Figure 5 Regions of decreased FA in presymptomatic HD. Between-group differences of FA superimposed on an opaque white matter surface rendering. Areas of decreased FA in the presymptomatic HD group are marked in yellow/green. The area of maximal difference is noted by the arrow on the transparent “glass” brain (*bottom right*) and is in the superior frontal white matter. Abbreviations: FA, fractional anisotropy; HD, Huntington’s disease. Source: From Ref. 9.

The classical neuropathological features of ALS include loss and degeneration of the large motor neurons in the GM of the spinal cord, brain stem, and cortex, as well as degeneration of the corticospinal tracts (CST) that contain axons of the cortical UMN. Other extramotor systems are also involved to various degrees (94–96). Two percent to 3% of ALS cases are accompanied by FTD (95,97), while in approximately 50% of cases cognitive impairment can be observed (94,98).

DTI can provide important measures of UMN dysfunction. Changes in tissue structure can lead to alterations in the diffusion characteristics, which can be reflected by the changes in FA and ADC values. Previous DTI studies have demonstrated significant changes of diffusion parameters in the brain of ALS patients (99–103). Most of these studies focused on the measurements of FA and ADC values along the CST at different

levels using an ROI approach. The common finding is that there is a reduction of FA in the CST, which is thought to reflect the neuronal degeneration of UMN. Significant correlations of diffusion parameters with measures of disease severity and duration have been established in some of the studies (17,99,100). However, in other studies, these correlations could not be confirmed (101,102).

Voxel-based analysis has also been used to evaluate the WM integrity in ALS (104–106). Sage et al. (106) recently reported significant reduction in FA scattered throughout the brain, including the cranial CST, frontal and parietal WM, as well as the hippocampal formation and insula. Their study supports the view of ALS being a multisystem degenerative disease, in which abnormalities of extramotor areas play an important role in its pathophysiology.

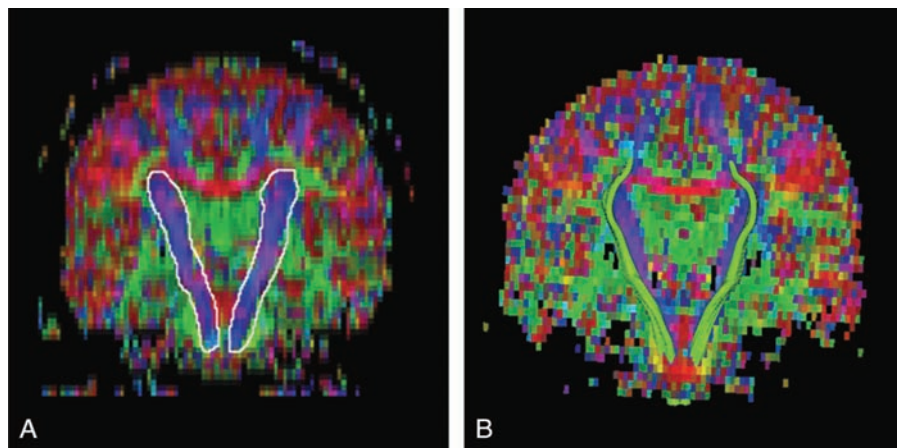


Figure 6 DTI-based color map of a healthy subject. Colors indicate directions as follows: red, left-right; green, anterior-posterior; blue, superior-inferior. (A) The white line delineates manually segmented CST. (B) Reconstructed CSTs (green) are overlaid on color maps. Abbreviations: DTI, diffusion tensor imaging; CST, corticospinal tract.

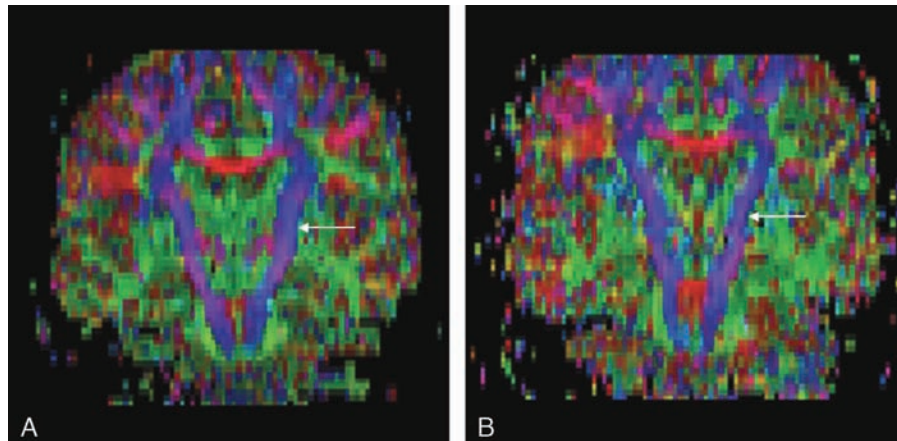


Figure 7 DTI-based color maps of (A) a healthy subject and (B) an ALS patient. The left CST (arrows) appears thinner in the ALS patient (B). Abbreviations: DTI, diffusion tensor imaging; ALS, amyotrophic lateral sclerosis; CST, corticospinal tract.

DTI-based color maps can be useful in showing brain WM architecture (7–10). CST can be readily identified in color on every cross-sectional slice along its course. This technique makes it feasible to segment the CST and quantify the volume in ALS patients (Figs. 6 and 7). According to the author's experience, ALS patients exhibit a decrease in CST volume compared with healthy subjects (107).

Several studies have reported depiction of the CST using diffusion tensor tractography (9,23,25). ALS patients with severe clinical deficits demonstrated decreased number of CST fibers compared with normal subjects (Fig. 8). A recent study by Ciccarelli et al. (27) developed a voxel-based summary connectivity measure along the CST using probabilistic tractography and found that such connectivity measures strongly correlated with disease progression.

MULTIPLE SCLEROSIS

MS is the most common demyelinating disorder. Although there are strong inflammatory components to MS, it is clear that the disease also has a strong neurodegenerative component (108–110). The clinical course of MS is quite variable, but most patients experience a relapsing-remitting course of exacerbations and remissions of multifocal neurological deficits (111).

MS is characterized by multiple well-defined lesions scattered throughout white and, less commonly, gray matter. Typically, these lesions go through the initial acute stage, subacute stage, and finally reach the gliotic stage. Different lesions in a brain are usually not in the same stage of disease progression. The histology of MS plaques is related to the disease stage and may include

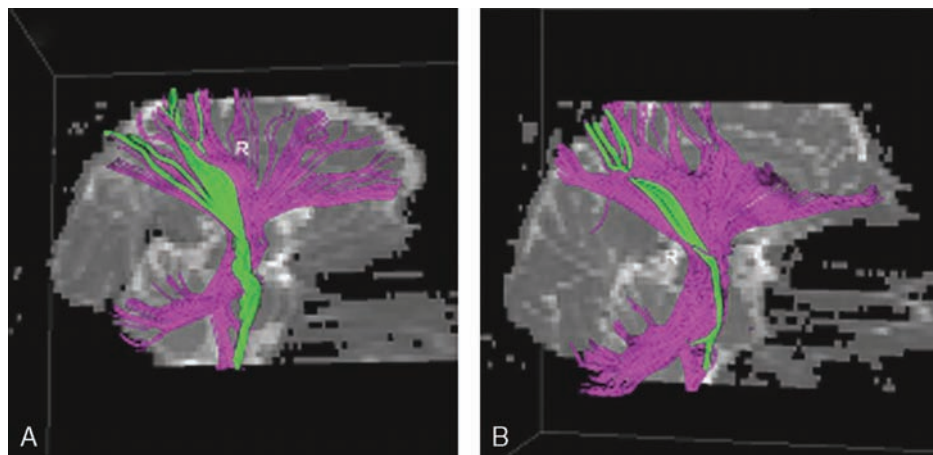


Figure 8 Fiber-tracking images of (A) a healthy subject and (B) an ALS patient. Descending fibers connecting the cortex and brain stem are shown in purple. CSTs are green. The CST fibers are diminished in ALS patients (B). Abbreviations: CST, corticospinal tract; ALS, amyotrophic lateral sclerosis

edema, demyelination, remyelination, inflammation, gliosis, and axonal loss. Axonal damage is a key feature in MS lesions and has a major impact on permanent neurological deficits (110). Axonal damage occurs within both acute and chronic plaques, as well as in the normal appearing WM, and it already presents in the early stage of the disease (112). Axonal damage may occur in parallel with myelin destruction or during a second phase when the axon is demyelinated and more susceptible to damage.

DTI is potentially useful for the study of MS, due to its ability to assess *in vivo* the presence of tissue damage within and outside T2-hyperintense lesions (15,113). In a recent postmortem study, Schmierer et al. (114) demonstrated a strong correlation of DTI parameters to myelin content and a lesser correlation to axonal count, suggesting that FA and ADC are useful indicators of demyelination in MS.

MR appearance of MS lesions is highly variable and certainly not specific. DTI studies have displayed higher ADC and lower FA values in MS lesions (Fig. 9). The highest ADC values appear to be found in nonenhancing T1 hypointense lesions compared with enhancing lesions and nonenhancing T1 isointense lesions. This may be due to the long-standing destructive damage in those T1 hypointense lesions or so-called black holes (115), in which water diffusion is most mobile. However, conflicting results have been achieved when comparing ADC values in enhancing versus nonenhancing lesions or between lesions with different patterns of enhancement (116–119). This discrepancy may be due to the variable degree of tissue damage during the active period of the lesion. Although DTI cannot differentiate enhancing from nonenhancing lesions by measuring their ADC, DTI studies have shown that FA is always lower in enhancing

than in nonenhancing lesions, indicating that FA is more sensitive in differentiating pathological substrates of MS lesions (116,120,121).

Numerous DTI studies have consistently shown increased ADC and reduced FA in the normal appearing WM (NAWM) from patients with MS when compared with the WM from healthy controls (117,122–126), suggesting the presence of tissue damage outside MRI-visible lesions. Although the DTI abnormalities seem to be quite widespread in NAWM, they tend to be more severe in the periplaque regions (125) and in sites where MRI-visible MS lesions are usually located (116,117,122,123). Anisotropy measurements seem to be potentially more sensitive than diffusivity measurements for the detection of MS pathology (125). Myelin and axonal loss in the NAWM are considered to contribute most to the DTI changes (111). DTI changes in the NAWM damage have been reported to be correlated with the clinical disability (127).

Previous studies (122,127–129) have pointed out that the average ADC of normal appearing GM (NAGM) from patients with primary or secondary progressive MS was higher than that of brain GM from relapsing-remitting MS or healthy controls. Two possible explanations for NAGM abnormalities might be the presence of a certain amount of discrete MS lesions, which might go undetected on conventional T2-weighted imaging (130), and the retrograde degeneration of GM neurons secondary to the damage of fibers traversing MS WM lesions (131).

Diffusion-based tractography has a potential role in quantifying the degree of axonal loss and demyelination within different types of lesions and NAWM. The difference in WM tract disruption can be directly visualized (Fig. 10) and may help better understand the association between lesion type and location with clinical signs as

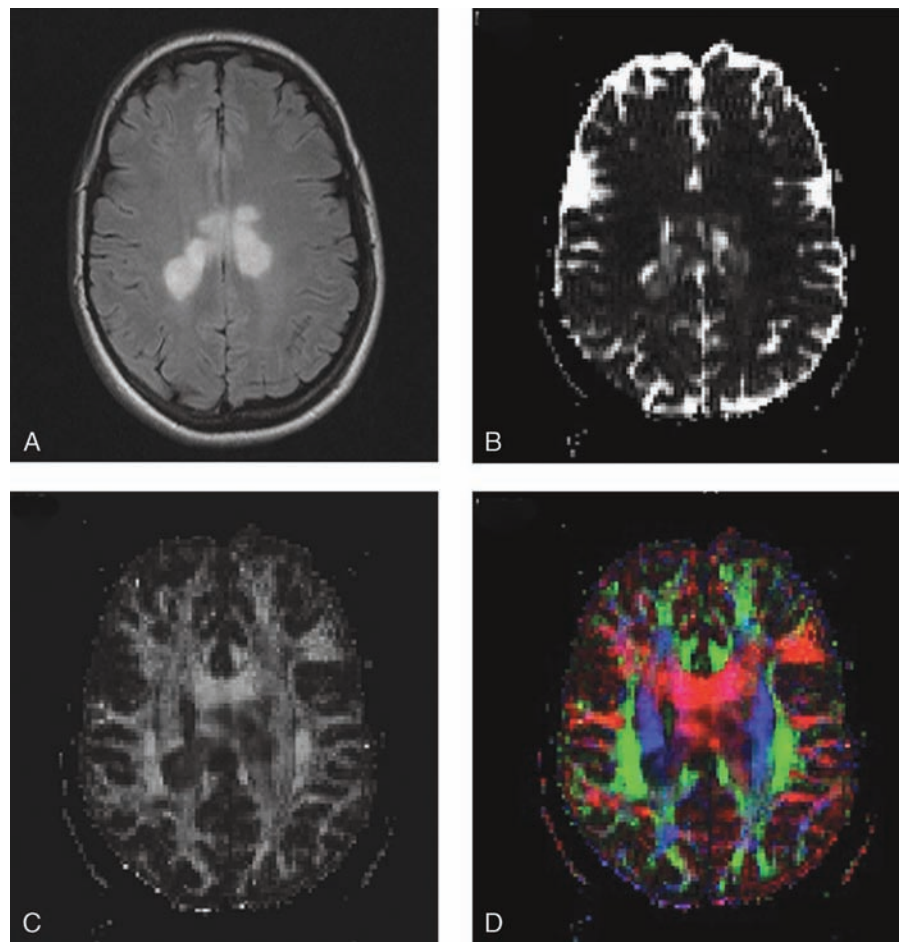


Figure 9 Multiple sclerosis. (A) FLAIR image, (B) ADC map, (C) FA map, and (D) DTI-based color map from the brain of a patient with MS. The lesions demonstrate increased ADC value and reduced FA value. Abbreviations: FLAIR, Axial fluid-attenuated inversion recovery; FA, fractional anisotropy; ADC, apparent diffusion coefficient; MS, multiple sclerosis.

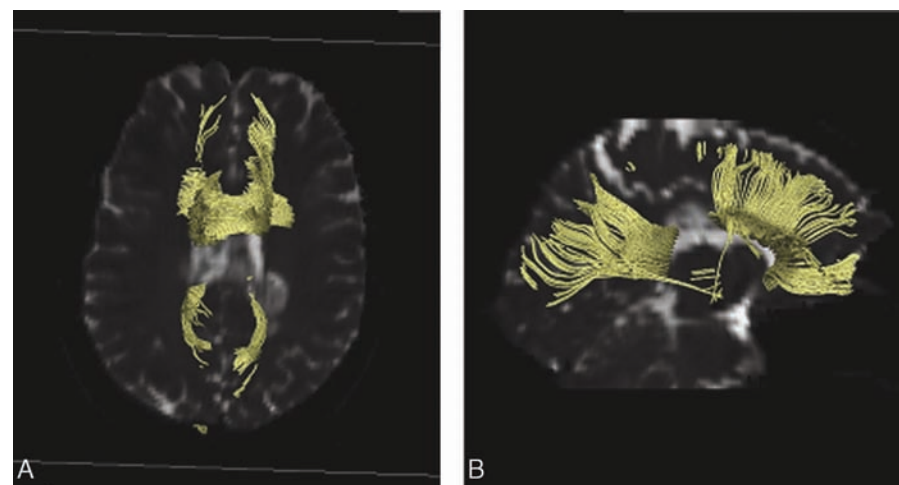


Figure 10 Diffusion tensor tractography of CC in the same patient as in Figure 9. ROIs are placed in midsagittal level. Note the fibers of CC are disrupted in the location of the lesions. Abbreviations: CC, corpus callosum; ROIs, regions of interest.

well as monitor disease progression. Ciccarelli et al. (132) have found reduced connectivity values in both left and right optic radiations compared with controls, suggesting mechanism of transsynaptic degeneration (133) secondary to optic nerve damage.

CONCLUSION

DTI have been successfully used to reveal the WM changes in various neurodegenerative disorders. The results are heterogeneous. Some of the findings are derived from analysis of relatively small cohorts. There is no doubt that with the deeper insights of investigations into larger groups of the patients, its clinical significance will be further acknowledged. Explorations to its basics will be emphasized on anatomical-pathological correlations to investigate disease mechanisms. While interpreting DTI data, it is important to keep in mind that diffusion measurements are often confounded by a variety of technical factors.

REFERENCES

- Przedborski S, Vila M, Jackson-Lewis V. Neurodegeneration: what is it and where are we? *J Clin Invest* 2003; 111(1): 3–10.
- Ernst RL, Hay JW, Fenn C, et al. Cognitive function and the costs of Alzheimer disease. An exploratory study. *Arch Neurol* 1997; 54(6):687–693.
- Forman MS, Trojanowski JQ, Lee VM. Neurodegenerative diseases: a decade of discoveries paves the way for therapeutic breakthroughs. *Nat Med* 2004; 10(10):1055–1063.
- Basser PJ, Pierpaoli C. Microstructural and physiological features of tissues elucidated by quantitative-diffusion-tensor MRI. *J Magn Reson B* 1996; 111(3):209–219.
- Beaulieu C. The basis of anisotropic water diffusion in the nervous system—a technical review. *NMR Biomed* 2002; 15(7–8):435–455.
- Chenevert TL, Brunberg JA, Pipe JG. Anisotropic diffusion in human white matter: demonstration with MR techniques *in vivo*. *Radiology* 1990; 177(2):401–405.
- Albayram S, Melhem ER, Mori S, et al. Holoprosencephaly in children: diffusion tensor MR imaging of white matter tracts of the brainstem—initial experience. *Radiology* 2002; 223(3):645–651.
- Hoon AH, Jr., Lawrie WT, Jr., Melhem ER, et al. Diffusion tensor imaging of periventricular leukomalacia shows affected sensory cortex white matter pathways. *Neurology* 2002; 59(5):752–756.
- Reading SA, Yassa MA, Bakker A, et al. Regional white matter change in pre-symptomatic Huntington's disease: a diffusion tensor imaging study. *Psychiatry Res* 2005; 140(1): 55–62.
- Pajevic S, Pierpaoli C. Color schemes to represent the orientation of anisotropic tissues from diffusion tensor data: application to white matter fiber tract mapping in the human brain. *Magn Reson Med* 1999; 42(3):526–540.
- Wu YC, Field AS, Chung MK, et al. Quantitative analysis of diffusion tensor orientation: theoretical framework. *Magn Reson Med* 2004; 52(5):1146–1155.
- Xie S, Xiao JX, Gong GL, et al. Voxel-based detection of white matter abnormalities in mild Alzheimer disease. *Neurology* 2006; 66(12):1845–1849.
- Zhang H, Yushkevich PA, Gee JC. Deformable registration of diffusion tensor MR images with explicit orientation optimization. *Med Image Comput Comput Assist Interv Int Conf Med Image Comput Comput Assist Interv* 2005; 8:172–179.
- Rovaris M, Iannucci G, Cercignani M, et al. Age-related changes in conventional, magnetization transfer, and diffusion-tensor MR imaging findings: study with whole-brain tissue histogram analysis. *Radiology* 2003; 227(3): 731–738.
- Ge Y, Law M, Grossman RI. Applications of diffusion tensor MR imaging in multiple sclerosis. *Ann N Y Acad Sci* 2005; 1064:202–219.
- Steens SC, Admiraal-Behloul F, Schaap JA, et al. Reproducibility of brain ADC histograms. *Eur Radiol* 2004; 14(3): 425–430.
- Wang S, Poptani H, Woo JH, et al. Amyotrophic lateral sclerosis: diffusion-tensor and chemical shift MR imaging at 3.0 T. *Radiology* 2006; 239(3):831–838.
- Kanaan RA, Shergill SS, Barker GJ, et al. Tract-specific anisotropy measurements in diffusion tensor imaging. *Psychiatry Res* 2006; 146(1):73–82.
- Jones DK, Griffin LD, Alexander DC, et al. Spatial normalization and averaging of diffusion tensor MRI data sets. *Neuroimage* 2002; 17(2):592–617.
- Zhang H, Yushkevich PA, Alexander DC, et al. Deformable registration of diffusion tensor MR images with explicit orientation optimization. *Med Image Anal* 2006; 10(5):764–785.
- Jones DK, Symms MR, Cercignani M, et al. The effect of filter size on VBM analyses of DT-MRI data. *Neuroimage* 2005; 26(2):546–554.
- Mori S, Crain BJ, Chacko VP, et al. Three-dimensional tracking of axonal projections in the brain by magnetic resonance imaging. *Ann Neurol* 1999; 45(2):265–269.
- Stieltjes B, Kaufmann WE, van Zijl PC, et al. Diffusion tensor imaging and axonal tracking in the human brain-stem. *Neuroimage* 2001; 14(3):723–735.
- Virta A, Barnett A, Pierpaoli C. Visualizing and characterizing white matter fiber structure and architecture in the human pyramidal tract using diffusion tensor MRI. *Magn Reson Imaging* 1999; 17(8):1121–1133.
- Mori S, Kaufmann WE, Davatzikos C, et al. Imaging cortical association tracts in the human brain using diffusion-tensor-based axonal tracking. *Magn Reson Med* 2002; 47(2): 215–223.
- Mori S, van Zijl PC. Fiber tracking: principles and strategies—a technical review. *NMR Biomed* 2002; 15 (7–8):468–480.
- Ciccarelli O, Behrens TE, Altmann DR, et al. Probabilistic diffusion tractography: a potential tool to assess the rate of disease progression in amyotrophic lateral sclerosis. *Brain* 2006; 129(pt 7):1859–1871.

28. Behrens TE, Johansen-Berg H, Woolrich MW, et al. Non-invasive mapping of connections between human thalamus and cortex using diffusion imaging. *Nat Neurosci* 2003; 6(7):750–757.
29. Parker GJ, Stephan KE, Barker GJ, et al. Initial demonstration of in vivo tracing of axonal projections in the macaque brain and comparison with the human brain using diffusion tensor imaging and fast marching tractography. *Neuroimage* 2002; 15(4):797–809.
30. Jackowski M, Kao CY, Qiu M, et al. White matter tractography by anisotropic wavefront evolution and diffusion tensor imaging. *Med Image Anal* 2005; 9(5):427–440.
31. Staempfli P, Jaermann T, Crelier GR, et al. Resolving fiber crossing using advanced fast marching tractography based on diffusion tensor imaging. *Neuroimage* 2006; 30 (1):110–120.
32. Wakana S, Jiang H, Nagae-Poetscher LM, et al. Fiber tract-based atlas of human white matter anatomy. *Radiology* 2004; 230(1):77–87.
33. Mori S, Zhang J. Principles of diffusion tensor imaging and its applications to basic neuroscience research. *Neuron* 2006; 51(5):527–539.
34. Tournier JD, Calamante F, King MD, et al. Limitations and requirements of diffusion tensor fiber tracking: an assessment using simulations. *Magn Reson Med* 2002; 47 (4):701–708.
35. Brun A, Englund E. A white matter disorder in dementia of the Alzheimer type: a pathoanatomical study. *Ann Neurol* 1986; 19(3):253–262.
36. Iwanaga K, Hayashi S, Oyake M, et al. Neuropathology of sporadic amyotrophic lateral sclerosis of long duration. *J Neurol Sci* 1997; 146(2):139–143.
37. Englund E, Brun A. Frontal lobe degeneration of non-Alzheimer type. IV. White matter changes. *Arch Gerontol Geriatr* 1987; 6(3):235–243.
38. Englund E. Neuropathology of white matter changes in Alzheimer's disease and vascular dementia. *Dement Geriatr Cogn Disord* 1998; 9(suppl 1):6–12.
39. Neil J, Miller J, Mukherjee P, et al. Diffusion tensor imaging of normal and injured developing human brain—a technical review. *NMR Biomed* 2002; 15(7–8): 543–552.
40. Meier-Ruge W, Ulrich J, Bruhlmann M, et al. Age-related white matter atrophy in the human brain. *Ann N Y Acad Sci* 1992; 673:260–269.
41. Marner L, Nyengaard JR, Tang Y, et al. Marked loss of myelinated nerve fibers in the human brain with age. *J Comp Neurol* 2003; 462(2):144–152.
42. O'Sullivan M, Jones DK, Summers PE, et al. Evidence for cortical “disconnection” as a mechanism of age-related cognitive decline. *Neurology* 2001; 57(4):632–638.
43. Pfefferbaum A, Sullivan EV, Hedehus M, et al. Age-related decline in brain white matter anisotropy measured with spatially corrected echo-planar diffusion tensor imaging. *Magn Reson Med* 2000; 44(2):259–268.
44. Nusbaum AO, Tang CY, Buchsbaum MS, et al. Regional and global changes in cerebral diffusion with normal aging. *AJNR Am J Neuroradiol* 2001; 22(1):136–142.
45. Ardekani S, Kumar A, Bartzokis G, et al. Exploratory voxel-based analysis of diffusion indices and hemispheric asymmetry in normal aging. *Magn Reson Imaging* 2007; 25(2):154–167.
46. Camara E, Bodammer N, Rodriguez-Fornells A, et al. Age-related water diffusion changes in human brain: a voxel-based approach. *Neuroimage* 2007; 34(4):1588–1599.
47. Lehmbeck JT, Brassen S, Weber-Fahr W, et al. Combining voxel-based morphometry and diffusion tensor imaging to detect age-related brain changes. *Neuroreport* 2006; 17(5):467–470.
48. Salat DH, Tuch DS, Greve DN, et al. Age-related alterations in white matter microstructure measured by diffusion tensor imaging. *Neurobiol Aging* 2005; 26(8):1215–1227.
49. Krejza J, Melhem ER. Quantitative diffusion tensor imaging of the brain in young adults shows age-related structural changes in gray and white matter. *Acad Radiol* 2005; 12(3):265–267.
50. Khachaturian ZS. Diagnosis of Alzheimer's disease. *Arch Neurol* 1985; 42(11):1097–1105.
51. Hauw JJ, Duyckaerts C, Delaere P, et al. Alzheimer's disease: neuropathological and etiological data. *Biomed Pharmacother* 1989; 43(7):469–482.
52. Pearson RC, Esiri MM, Hiorns RW, et al. Anatomical correlates of the distribution of the pathological changes in the neocortex in Alzheimer disease. *Proc Natl Acad Sci U S A* 1985; 82(13):4531–4534.
53. Bozzali M, Falini A, Franceschi M, et al. White matter damage in Alzheimer's disease assessed in vivo using diffusion tensor magnetic resonance imaging. *J Neurol Neurosurg Psychiatry* 2002; 72(6):742–746.
54. Hanyu H, Sakurai H, Iwamoto T, et al. Diffusion-weighted MR imaging of the hippocampus and temporal white matter in Alzheimer's disease. *J Neurol Sci* 1998; 156(2): 195–200.
55. Kantarci K, Jack CR, Jr., Xu YC, et al. Mild cognitive impairment and Alzheimer disease: regional diffusivity of water. *Radiology* 2001; 219(1):101–107.
56. Ramani A, Jensen JH, Helpern JA. Quantitative MR imaging in Alzheimer disease. *Radiology* 2006; 241(1): 26–44.
57. Sandson TA, Felician O, Edelman RR, et al. Diffusion-weighted magnetic resonance imaging in Alzheimer's disease. *Dement Geriatr Cogn Disord* 1999; 10(2):166–171.
58. Sugihara S, Kinoshita T, Matsusue E, et al. Usefulness of diffusion tensor imaging of white matter in Alzheimer disease and vascular dementia. *Acta Radiol* 2004; 45(6): 658–663.
59. Folstein MF, Folstein SE, McHugh PR. “Mini-mental state”. A practical method for grading the cognitive state of patients for the clinician. *J Psychiatr Res* 1975; 12(3): 189–198.
60. Rose SE, Chen F, Chalk JB, et al. Loss of connectivity in Alzheimer's disease: an evaluation of white matter tract integrity with colour coded MR diffusion tensor imaging. *J Neurol Neurosurg Psychiatry* 2000; 69(4):528–530.
61. Reisberg B, Franssen EH, Hasan SM, et al. Retrogenesis: clinical, physiologic, and pathologic mechanisms in brain aging, Alzheimer's and other dementing processes. *Eur Arch Psychiatry Clin Neurosci* 1999; 249(suppl 3):28–36.

62. Taoka T, Iwasaki S, Sakamoto M, et al. Diffusion anisotropy and diffusivity of white matter tracts within the temporal stem in Alzheimer disease: evaluation of the "tract of interest" by diffusion tensor tractography. *AJNR Am J Neuroradiol* 2006; 27(5):1040–1045.
63. Hansen L, Salmon D, Galasko D, et al. The Lewy body variant of Alzheimer's disease: a clinical and pathologic entity. *Neurology* 1990; 40(1):1–8.
64. Spillantini MG, Crowther RA, Jakes R, et al. Filamentous alpha-synuclein inclusions link multiple system atrophy with Parkinson's disease and dementia with Lewy bodies. *Neurosci Lett* 1998; 251(3):205–208.
65. Bozzali M, Falini A, Cercignani M, et al. Brain tissue damage in dementia with Lewy bodies: an in vivo diffusion tensor MRI study. *Brain* 2005; 128(pt 7):1595–1604.
66. Hodges JR, Davies RR, Xuereb JH, et al. Clinicopathological correlates in frontotemporal dementia. *Ann Neurol* 2004; 56(3):399–406.
67. Larsson EM, Englund E, Sjöbeck M, et al. MRI with diffusion tensor imaging post-mortem at 3.0 T in a patient with frontotemporal dementia. *Dement Geriatr Cogn Disord* 2004; 17(4):316–319.
68. Yoshiura T, Mihara F, Koga H, et al. Cerebral white matter degeneration in frontotemporal dementia detected by diffusion-weighted magnetic resonance imaging. *Acad Radiol* 2006; 13(11):1373–1378.
69. Borroni B, Brambati SM, Agosti C, et al. Evidence of white matter changes on diffusion tensor imaging in frontotemporal dementia. *Arch Neurol* 2007; 64(2):246–251.
70. Prusiner SB. Prions. *Proc Natl Acad Sci U S A* 1998; 95(23):13363–13383.
71. Brown P, Cathala F, Castaigne P, et al. Creutzfeldt-Jakob disease: clinical analysis of a consecutive series of 230 neuropathologically verified cases. *Ann Neurol* 1986; 20(5):597–602.
72. Shiga Y, Miyazawa K, Sato S, et al. Diffusion-weighted MRI abnormalities as an early diagnostic marker for Creutzfeldt-Jakob disease. *Neurology* 2004; 63(3):443–449.
73. Ukitu R, Kushihashi T, Tanaka E, et al. Diffusion-weighted MR imaging of early-stage Creutzfeldt-Jakob Disease: typical and atypical manifestations. *Radiographics* 2006; 26(suppl 1):S191–S204.
74. Murata T, Shiga Y, Higano S, et al. Conspicuity and evolution of lesions in Creutzfeldt-Jakob disease at diffusion-weighted imaging. *AJNR Am J Neuroradiol* 2002; 23(7):1164–1172.
75. Young GS, Geschwind MD, Fischbein NJ, et al. Diffusion-weighted and fluid-attenuated inversion recovery imaging in Creutzfeldt-Jakob disease: high sensitivity and specificity for diagnosis. *AJNR Am J Neuroradiol* 2005; 26(6):1551–1562.
76. Ukitu R, Kushihashi T, Kitanosono T, et al. Serial diffusion-weighted MRI of Creutzfeldt-Jakob disease. *AJR Am J Roentgenol* 2005; 184(2):560–566.
77. Mittal S, Farmer P, Kalina P, et al. Correlation of diffusion-weighted magnetic resonance imaging with neuropathology in Creutzfeldt-Jakob disease. *Arch Neurol* 2002; 59(1):128–134.
78. Urbach H, Klisch J, Wolf HK, et al. MRI in sporadic Creutzfeldt-Jakob disease: correlation with clinical and neuropathological data. *Neuroradiology* 1998; 40(2):65–70.
79. Russmann H, Vingerhoets F, Miklossy J, et al. Sporadic Creutzfeldt-Jakob disease: a comparison of pathological findings and diffusion weighted imaging. *J Neurol* 2005; 252(3):338–342.
80. Yoshikawa K, Nakata Y, Yamada K, et al. Early pathological changes in the parkinsonian brain demonstrated by diffusion tensor MRI. *J Neurol Neurosurg Psychiatry* 2004; 75(3):481–484.
81. Scherfler C, Schocke MF, Seppi K, et al. Voxel-wise analysis of diffusion weighted imaging reveals disruption of the olfactory tract in Parkinson's disease. *Brain* 2006; 129(pt 2):538–542.
82. Padovani A, Borroni B, Brambati SM, et al. Diffusion tensor imaging and voxel based morphometry study in early progressive supranuclear palsy. *J Neurol Neurosurg Psychiatry* 2006; 77(4):457–463.
83. Blain CR, Barker GJ, Jarosz JM, et al. Measuring brain stem and cerebellar damage in parkinsonian syndromes using diffusion tensor MRI. *Neurology* 2006; 67(12): 2199–2205.
84. Nilsson C, Markenroth Bloch K, Brockstedt S, et al. Tracking the neurodegeneration of parkinsonian disorders—a pilot study. *Neuroradiology* 2007; 49(2):111–119.
85. Seppi K, Schocke MF, Esterhammer R, et al. Diffusion-weighted imaging discriminates progressive supranuclear palsy from PD, but not from the parkinson variant of multiple system atrophy. *Neurology* 2003; 60(6):922–927.
86. Rosas HD, Koroshetz WJ, Chen YI, et al. Evidence for more widespread cerebral pathology in early HD: an MRI-based morphometric analysis. *Neurology* 2003; 60(10): 1615–1620.
87. Ross CA. Huntington's disease: new paths to pathogenesis. *Cell* 2004; 118(1):4–7.
88. Mascalchi M, Lolli F, Della Nave R, et al. Huntington disease: volumetric, diffusion-weighted, and magnetization transfer MR imaging of brain. *Radiology* 2004; 232(3): 867–873.
89. Seppi K, Schocke MF, Mair KJ, et al. Diffusion-weighted imaging in Huntington's disease. *Mov Disord* 2006; 21(7): 1043–1047.
90. Rosas HD, Tuch DS, Hevelone ND, et al. Diffusion tensor imaging in presymptomatic and early Huntington's disease: selective white matter pathology and its relationship to clinical measures. *Mov Disord* 2006; 21(9):1317–1325.
91. Rowland LP. Diagnosis of amyotrophic lateral sclerosis. *J Neurol Sci* 1998; 160(suppl 1):S6–S24.
92. Brownell B, Oppenheimer DR, Hughes JT. The central nervous system in motor neurone disease. *J Neurol Neurosurg Psychiatry* 1970; 33(3):338–357.
93. Chan S, Kaufmann P, Shungu DC, et al. Amyotrophic lateral sclerosis and primary lateral sclerosis: evidence-based diagnostic evaluation of the upper motor neuron. *Neuroimaging Clin N Am* 2003; 13(2):307–326.
94. Abe K. Cognitive function in amyotrophic lateral sclerosis. *Amyotroph Lateral Scler Other Motor Neuron Disord* 2000; 1(5):343–347.

95. Nakano I. Frontotemporal dementia with motor neuron disease (amyotrophic lateral sclerosis with dementia). *Neuropathology* 2000; 20(1):68–75.
96. Sasaki S, Tsutsumi Y, Yamane K, et al. Sporadic amyotrophic lateral sclerosis with extensive neurological involvement. *Acta Neuropathol (Berl)* 1992; 84(2):211–215.
97. Abrahams S, Goldstein LH, Suckling J, et al. Frontotemporal white matter changes in amyotrophic lateral sclerosis. *J Neurol* 2005; 252(3):321–331.
98. Ringholz GM, Appel SH, Bradshaw M, et al. Prevalence and patterns of cognitive impairment in sporadic ALS. *Neurology* 2005; 65(4):586–590.
99. Ellis CM, Simmons A, Jones DK, et al. Diffusion tensor MRI assesses corticospinal tract damage in ALS. *Neurology* 1999; 53(5):1051–1058.
100. Graham JM, Papadakis N, Evans J, et al. Diffusion tensor imaging for the assessment of upper motor neuron integrity in ALS. *Neurology* 2004; 63(11):2111–2119.
101. Hong YH, Lee KW, Sung JJ, et al. Diffusion tensor MRI as a diagnostic tool of upper motor neuron involvement in amyotrophic lateral sclerosis. *J Neurol Sci* 2004; 227(1):73–78.
102. Toosy AT, Werring DJ, Orrell RW, et al. Diffusion tensor imaging detects corticospinal tract involvement at multiple levels in amyotrophic lateral sclerosis. In: *J Neurol Neurosurg Psychiatry* 2003; 74(9):1250–1257.
103. Ulug AM, Grunewald T, Lin MT, et al. Diffusion tensor imaging in the diagnosis of primary lateral sclerosis. *J Magn Reson Imaging* 2004; 19(1):34–39.
104. Abe O, Yamada H, Masutani Y, et al. Amyotrophic lateral sclerosis: diffusion tensor tractography and voxel-based analysis. *NMR Biomed* 2004; 17(6):411–416.
105. Sach M, Winkler G, Glauche V, et al. Diffusion tensor MRI of early upper motor neuron involvement in amyotrophic lateral sclerosis. *Brain* 2004; 127(pt 2):340–350.
106. Sage CA, Peeters RR, Gorner A, et al. Quantitative diffusion tensor imaging in amyotrophic lateral sclerosis. *Neuroimage* 2007; 34(2):486–499.
107. Wang S, Poptani H, Bilello M, et al. Diffusion tensor imaging in amyotrophic lateral sclerosis: volumetric analysis of the corticospinal tract. *AJNR Am J Neuroradiol* 2006; 27(6):1234–1238.
108. Bjartmar C, Trapp BD. Axonal and neuronal degeneration in multiple sclerosis: mechanisms and functional consequences. *Curr Opin Neurol* 2001; 14(3):271–278.
109. Bjartmar C, Trapp BD. Axonal degeneration and progressive neurologic disability in multiple sclerosis. *Neurotox Res* 2003; 5(1–2):157–164.
110. Trapp BD, Ransohoff R, Rudick R. Axonal pathology in multiple sclerosis: relationship to neurologic disability. *Curr Opin Neurol* 1999; 12(3):295–302.
111. Ingles M. Multiple sclerosis: new insights and trends. *AJNR Am J Neuroradiol* 2006; 27(5):954–957.
112. Trapp BD, Peterson J, Ransohoff RM, et al. Axonal transection in the lesions of multiple sclerosis. *N Engl J Med* 1998; 338(5):278–285.
113. Rovaris M, Gass A, Bammer R, et al. Diffusion MRI in multiple sclerosis. *Neurology* 2005; 65(10):1526–1532.
114. Schmierer K, Wheeler-Kingshott CA, Boultby PA, et al. Diffusion tensor imaging of post mortem multiple sclerosis brain. *Neuroimage* 2006; 35(2):467–477.
115. Castriota Scanderbeg A, Tomaiuolo F, Sabatini U, et al. Demyelinating plaques in relapsing-remitting and secondary-progressive multiple sclerosis: assessment with diffusion MR imaging. *AJNR Am J Neuroradiol* 2000; 21(5):862–868.
116. Filippi M, Cercignani M, Inglesi M, et al. Diffusion tensor magnetic resonance imaging in multiple sclerosis. *Neurology* 2001; 56(3):304–311.
117. Filippi M, Iannucci G, Cercignani M, et al. A quantitative study of water diffusion in multiple sclerosis lesions and normal-appearing white matter using echo-planar imaging. *Arch Neurol* 2000; 57(7):1017–1021.
118. Iannucci G, Mascalchi M, Salvi F, et al. Vanishing Ballo-like lesions in multiple sclerosis. *J Neurol Neurosurg Psychiatry* 2000; 69(3):399–400.
119. Roychowdhury S, Maldjian JA, Grossman RI. Multiple sclerosis: comparison of trace apparent diffusion coefficients with MR enhancement pattern of lesions. *AJNR Am J Neuroradiol* 2000; 21(5):869–874.
120. Castriota-Scanderbeg A, Fasano F, Hagberg G, et al. Coefficient D(av) is more sensitive than fractional anisotropy in monitoring progression of irreversible tissue damage in focal nonactive multiple sclerosis lesions. *AJNR Am J Neuroradiol* 2003; 24(4):663–670.
121. Werring DJ, Clark CA, Barker GJ, et al. Diffusion tensor imaging of lesions and normal-appearing white matter in multiple sclerosis. *Neurology* 1999; 52(8):1626–1632.
122. Cercignani M, Bozzali M, Iannucci G, et al. Magnetisation transfer ratio and mean diffusivity of normal appearing white and grey matter from patients with multiple sclerosis. *J Neurol Neurosurg Psychiatry* 2001; 70(3):311–317.
123. Ge Y, Law M, Johnson G, et al. Preferential occult injury of corpus callosum in multiple sclerosis measured by diffusion tensor imaging. *J Magn Reson Imaging* 2004; 20(1):1–7.
124. Guo AC, Jewells VL, Provenzale JM. Analysis of normal-appearing white matter in multiple sclerosis: comparison of diffusion tensor MR imaging and magnetization transfer imaging. *AJNR Am J Neuroradiol* 2001; 22(10):1893–1900.
125. Guo AC, MacFall JR, Provenzale JM. Multiple sclerosis: diffusion tensor MR imaging for evaluation of normal-appearing white matter. *Radiology* 2002; 222(3):729–736.
126. Cercignani M, Iannucci G, Rocca MA, et al. Pathologic damage in MS assessed by diffusion-weighted and magnetization transfer MRI. *Neurology* 2000; 54(5):1139–1144.
127. Ciccarelli O, Werring DJ, Wheeler-Kingshott CA, et al. Investigation of MS normal-appearing brain using diffusion tensor MRI with clinical correlations. *Neurology* 2001; 56(7):926–933.
128. Vrenken H, Pouwels PJ, Geurts JJ, et al. Altered diffusion tensor in multiple sclerosis normal-appearing brain tissue: cortical diffusion changes seem related to clinical deterioration. *J Magn Reson Imaging* 2006; 23(5):628–636.

129. Bozzali M, Cercignani M, Sormani MP, et al. Quantification of brain gray matter damage in different MS phenotypes by use of diffusion tensor MR imaging. *AJNR Am J Neuroradiol* 2002; 23(6):985–988.
130. Miller DH, Thompson AJ, Filippi M. Magnetic resonance studies of abnormalities in the normal appearing white matter and grey matter in multiple sclerosis. *J Neurol* 2003; 250(12):1407–1419.
131. Filippi M, Bozzali M, Comi G. Magnetization transfer and diffusion tensor MR imaging of basal ganglia from patients with multiple sclerosis. *J Neurol Sci* 2001; 183(1): 69–72.
132. Ciccarelli O, Toosy AT, Hickman SJ, et al. Optic radiation changes after optic neuritis detected by tractography-based group mapping. *Hum Brain Mapp* 2005; 25(3): 308–316.
133. Evangelou N, Konz D, Esiri MM, et al. Size-selective neuronal changes in the anterior optic pathways suggest a differential susceptibility to injury in multiple sclerosis. *Brain* 2001; 124(pt 9):1813–1820.

16

Perfusion Imaging

JONATHAN P. DYKE

Citigroup Biomedical Imaging Center, Weill Cornell Medical College, New York, New York, U.S.A.

INTRODUCTION

Perfusion-weighted imaging is a technique that allows assessment of blood flow at the level of the capillary bed. Various methods exist within MRI to measure the uptake of endogenous or exogenous tracers. This chapter will explore dynamic acquisition methods that supplement clinical information gained from traditional static contrast-enhanced images. Analysis of time intensity curves (TICs) that plot contrast uptake over time yields information about the angiogenic properties of the region that cannot be obtained with a single time point. Calculation of MRI perfusion parameters will be described and compared with “gold standard” physiological measures of perfusion and angiogenesis.

HISTORY

The arrival of the first Food and Drug Administration (FDA)-approved contrast enhancement agents in both MRI and CT can be heralded as major advances in the field of medical imaging. CT contrast enhancement agents such as bismuth and iodine were used in X-ray imaging soon after its inception by Roentgen in 1895. Imaging of soft tissues required the introduction of such agents to visualize structures that would otherwise be invisible to the technique. The first FDA-approved MRI contrast agent was not introduced until 1988. Currently, an estimated

30% of the 25 million MRI scans performed in the United States use an injection of an MRI contrast agent. Static contrast-enhanced imaging has proven to be a necessity in detecting vascular abnormalities and neoplasms throughout the body. Contrast accumulation also occurs in regions of ischemia, inflammation, and infection. Malignancies that appear iso-intense with surrounding tissues on standard unenhanced images often become apparent in the presence of contrast. MR contrast agents may then increase the diagnostic sensitivity of the examination.

Static vs. Dynamic Imaging Methods

The shift from static to dynamic imaging yields a wealth of information about perfusion within the tissue of interest. Dynamic imaging rapidly acquires signal from every voxel in the image at fixed intervals prior to and following contrast administration. In this manner, each voxel contains a time course reflective of the degree of contrast uptake in that specific volume of tissue. A contrast-enhanced dynamic scan is the accumulation of multiple static contrast-enhanced images over time. Analysis of the entire time course of contrast uptake provides information about the vascularity and tissue perfusion of the region that could not be obtained statically.

The choice of when to acquire a static contrast-enhanced image is of prime importance. Contrast studies that utilize positive enhancement techniques illustrate the

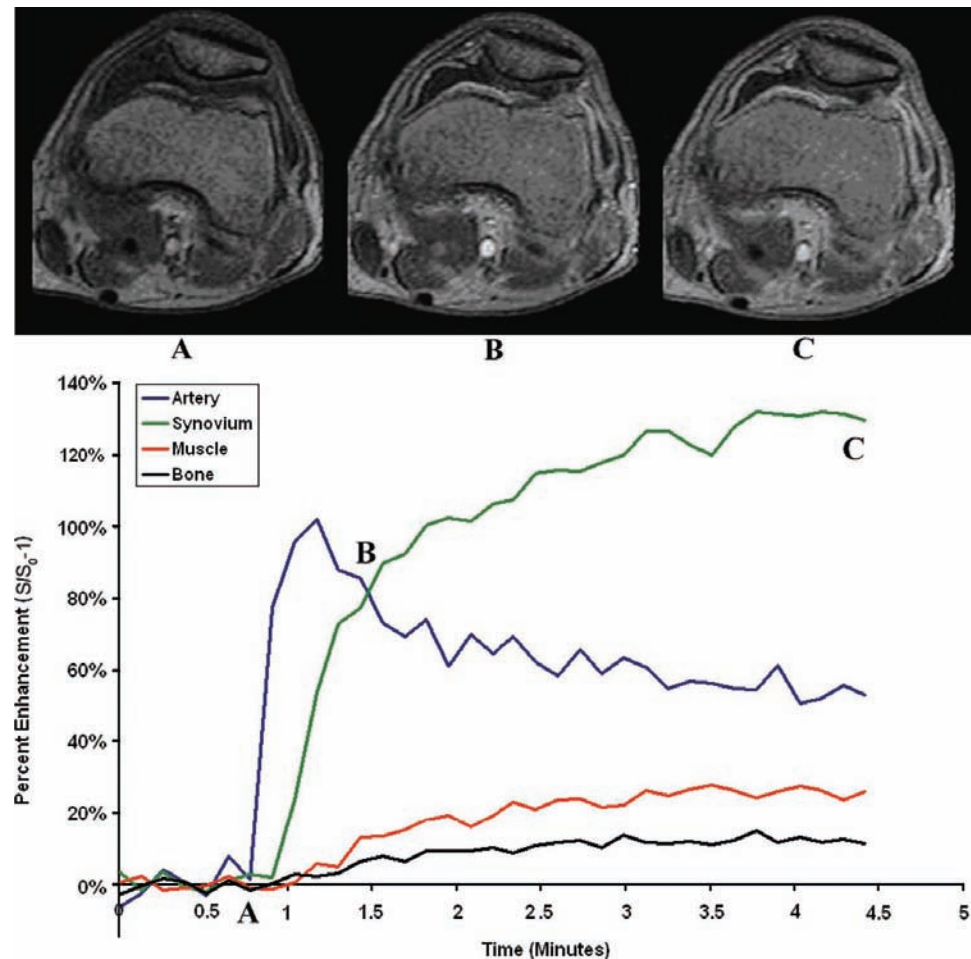


Figure 1 DCE perfusion data are shown from a patient with hemophilic arthropathy. Regions of interest were taken in the popliteal artery, synovium, muscle, and bone respectively. Static contrast-enhanced images are shown corresponding to time points taken at baseline (A), 1.5 minutes (B), and the end of the acquisition (C). Static contrast-enhanced images at a single time point cannot provide information on both the first-pass and washout characteristics of the contrast agent. Without adequate knowledge of the entire shape of the TIC, maximum contrast between the tissue of interest and the background may not be obtained. This example illustrates the complementary information that DCE MRI may provide to that of static contrast enhanced images. Abbreviations: DCE, dynamic contrast enhanced; TIC, time intensity curves; MRI, magnetic resonance imaging.

necessity of acquiring data dynamically. Figure 1 shows various TICs in a subject presenting with hemophilic arthropathy. Neovasculature has grown in the synovium of the knee to remove blood byproducts from the joint. A dynamic contrast-enhanced (DCE) study was used to assess the degree of tissue perfusion in this region. A 3-D gradient-echo (GE) sequence was acquired covering 24 slices at a thickness of 4 mm with a time resolution of 7.5 seconds. Acquisition parameters included a 256×128 matrix, a 4.5-ms repetition time (TR), and a 2.2-ms echo time (TE). A rectangular phase field of view as well as a fractional echo were employed. A series of seven baseline images was acquired serially prior to manual injection of 0.1 mM/kg gadolinium-diethylenetriamine

penta-acetic acid (Gd-DTPA) followed by a saline flush as shown in Figure 1A. At 45 seconds post-injection, the percent enhancement of the synovium was equivalent to that of the popliteal artery (Figure 1B). However, at four minutes postinjection (Fig. 1C), the synovium continued to enhance while the popliteal artery began to wash out. Static contrast-enhanced images at a single time point cannot provide information on both the first-pass and washout characteristics of the contrast agent. Without adequate knowledge of the entire shape of the TIC, maximum contrast between the tissue of interest and the background may not be obtained. This example illustrates the complementary information that DCE-MRI may provide to that of static contrast-enhanced images.

Dynamic perfusion-weighted imaging differs from angiography, although both employ techniques to image the vasculature. Angiography acquires images related to macroscopic blood flow in the arteries and the veins. However, many central nervous system (CNS) pathologies do not alter macroscopic circulation but display pathophysiological changes at the level of the capillary bed, arterioles, and venules (39). Perfusion imaging acquires data from contrast uptake in the capillary bed instead of within the major vessels. For example, blood flow in the carotid artery may be measured in mL/min using phase contrast angiography. Perfusion imaging measures cerebral blood flow (CBF) in units of mL/100 g tissue/min.

Tissue perfusion performs tasks of vital importance including the delivery of oxygen and nutrients and removal of waste at the level of the capillary bed as shown in Figure 2. Dynamic perfusion studies may also provide indirect information on the growth of neovasculation and microvessel density (MVD) within a tumor. (1,2) Perfusion studies also allow indirect assessment of angiogenic markers such as vascular endothelial growth factor (VEGF) in response to antiangiogenic treatments that specifically target the tumor blood supply (3,4).

The techniques needed to extract clinically relevant parameters from perfusion-weighted imaging will be discussed. MR contrast-enhanced studies with exogenous tracers can be classified into positive or negative enhancement techniques, depending on the effect the agent has on the signal intensity. Dynamic susceptibility contrast (DSC)-enhanced MR is a negative enhancement technique. These methods provide estimates of blood flow, blood volume, and mean transit time (MTT). T₁-weighted dynamic contrast enhanced (DCE)-MRI produces positive enhancement of image intensity following contrast administration. These studies provide information on vascular

permeability, extravascular extracellular space (EES), as well as clearance and extraction rates. Likewise, arterial spin labeling (ASL) uses magnetically labeled water in the blood as an endogenous tracer to produce a positive enhancement effect. ASL studies provide a noninvasive estimate of blood flow that may be acquired in a serial manner. Compared with static contrast-enhanced images, the addition of a dynamic component to a study allows more information to be gathered from the same region of interest without change in the dose of contrast administered.

Prescription of Spatial and Temporal Acquisition Parameters

The choice of spatial resolution requires prescription of the field of view, matrix size, and slice thickness. These parameters are chosen such that the tissue of interest is covered while ensuring that specific structures within the tissue can be delineated without sacrificing signal or introducing partial volume effects. Often, a reduced phase field of view and matrix are chosen to increase temporal resolution while preserving spatial resolution. Compensation for the reduced matrix size in the phase direction is usually accomplished by zero filling the matrix in k-space to match the matrix size in the frequency-encoding direction.

Attainable temporal resolution depends on how rapidly the MRI scanner can acquire the images at the chosen spatial resolution within a given TR. Spiral and echo-planar sampling techniques as well as centric k-space acquisitions are used to increase temporal resolution. However, these techniques increase blurring in the image, incur a slight loss in spatial resolution, and may increase susceptibility distortions. Acquisition parameters for DCE-MRI using standard GE sequences currently allows obtaining a series of 2-D slices or a single 3-D slab in approximately 5 to 10 seconds without compromising spatial resolution. This fulfills the Nyquist sampling criterion, which requires that an event must be sampled at twice the frequency of occurrence. The first pass of contrast through a tissue lasts approximately 7 to 15 seconds (5). Likewise, sampling in DSC-MRI imaging should optimize signal-to-noise ratios while maximizing sensitivity to T₂/T₂* effects. Nyquist sampling criterion requires the TR to be less than two seconds while greater than 0.5 seconds is required to remain sensitive to susceptibility effects (39).

Several additional techniques are available to reduce the image acquisition time. Many parameters may be modified to increase the temporal resolution. However, the effects on the resulting signal-to-noise ratio and image contrast as well as their interdependence must be

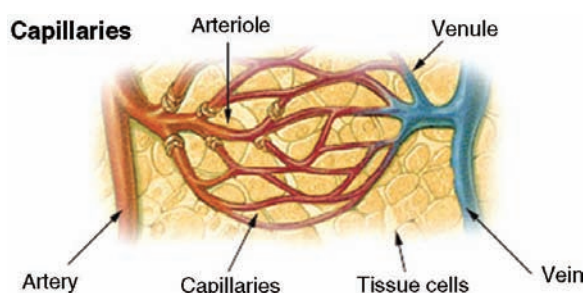


Figure 2 A pictorial diagram of the vascular structure at the level of the capillary bed is shown. Tissue perfusion takes place in this region and performs tasks of oxygen and nutrient delivery as well as waste removal. Contrast-enhanced studies model the pharmacokinetic exchange and diffusion of water molecules between the plasma and EES within the capillary bed.

Abbreviation: EES, extravascular extracellular space.

considered. For example, increasing the receiver bandwidth (RBW) of the scan reduces the acquisition time at the cost of a reduced signal-to-noise ratio. Reducing the RBW will increase the signal-to-noise ratio while intensifying chemical shift artifacts in the region. Equation 1 shows a signal-to-noise relationship that relates spatial resolution parameters, RBW, and the number of excitations.

$$SNR \propto \frac{\Delta X \Delta Y \Delta Z \sqrt{N_x N_y N_z} \sqrt{NEX}}{\sqrt{RBW}} \quad (1)$$

Another technique for reducing the scan time is that of rectangular image acquisition, which allows the phase field of view to be a fraction of that acquired in the frequency direction. This is accomplished by sampling alternate lines of k-space in the phase encode direction while leaving the maximum and minimum amplitudes of the phase-encoding gradient the same (66). The signal-to-noise ratio is slightly reduced and care must be given to ensure that the anatomy of interest does not wrap around into the center of the rectangular field of view. The advantage of reducing the field of view in the phase encode direction is that the scan time is reduced by the same factor without loss of spatial resolution.

Imaging options are routinely available for fractional echo and fractional number of excitations. In fractional or asymmetric echo imaging, all phase-encoding steps are acquired, but, in general, only the back half of the echo is sampled and the remaining points are reconstructed using the conjugate symmetry property of k-space. An advantage of using fractional echo imaging is that the TE can be shortened to the extent that the free induction decay actually overlaps with the echo and increases T₁ weighting of the image while reducing the acquisition time. A reduction in signal will occur, although this is partially offset by the shortened TE. The acquisition of a fractional excitation is also known as partial Fourier imaging. It reduces the scan time up to 50% by utilizing the phase conjugate symmetry of k-space. Slightly more than half of the k-space lines need to be sampled to reconstruct an entire image. A reduction in the number of excitations though is also reflected in a decrease in signal-to-noise ratio, as shown in Equation 1.

Lastly, the introduction of sensitivity-encoding parallel imaging techniques across multiple MRI vendors has allowed for decreased acquisition times at the price of decreased signal-to-noise ratios (6). The use of a multi-channel-phased array coil allows each coil to independently sample a different portion of the field of view. A low-resolution scan of coil sensitivities allows for reconstruction or unfolding of the data in either the frequency or spatial domains. A reduction factor (R) in time is also the factor by which the number of k-space samples is reduced. The reduction in the signal-to-noise ratio is proportional to the square root of R.

Mechanisms of Exogenous Contrast Enhancement

Standard clinical MRI contrast agents use gadolinium-based paramagnetic compounds of low molecular weight that remain intravascular in an intact blood-brain barrier (BBB). However, the contrast mechanism resulting in negative image enhancement is not due to direct detection of the agent *in vivo*. The contrast-enhanced signal detected in MRI results from the relaxation of water molecules in the tissue of interest adjacent to the agent. Gadolinium contains seven unpaired electrons, giving it a large magnetic moment. Paramagnetic compounds reduce both the spin-lattice (T₁) and spin-spin (T₂) relaxation times of the water adjacent to the contrast agent. Shortening of T₁ increases signal intensity, whereas shortening of T₂ broadens the line width and decreases signal intensity. In addition, thermal agitation of the molecules adjacent to the contrast agent propagates these shortened relaxation effects far beyond the vicinity of the contrast agent. Signal intensity from MR contrast agents may produce positive or negative enhancement, depending on the concentration, vasculature, and sequence used to acquire the data.

While both T₁ and T₂ relaxation times are reduced, a dominant method of contrast enhancement arises. Figure 3 shows representative TICs from both DCE and DSC studies on the same axis. The same dose of contrast was given to patients in both studies, resulting in positive enhancement in one study and negative enhancement in the other. However, the pulse sequence, weighting and the properties of the vasculature, which are being interrogated, are different between these studies. The underlying mechanisms causing these differences will be discussed such that a better overall understanding of contrast enhancement will be gained.

The vascular system within a voxel is either flow or permeability limited in low molecular weight compounds (7). The BBB is a vast network of capillary endothelial cells that protects the brain from harmful substances in the bloodstream. Endothelial junctions in the normal BBB are very tightly bound. In this low-permeability regime, the contrast agent remains completely contained within the vasculature. Containment of a high concentration of the paramagnetic agent causes a sharp local field gradient that causes spin dephasing far beyond the vessel walls (66). A susceptibility-weighted pulse sequence, such as a GE, can then be used to detect the effect in which the T₂ relaxation effect dominates. This negative enhancement effect occurs rapidly and signal typically returns to near baseline levels in less than 30 seconds (8). Full recovery of the signal to precontrast levels is dependent on the degree of BBB permeability, as can be seen in DSC studies of various tumor systems. T₂ or T₂^{*}-weighted pulse sequences used to

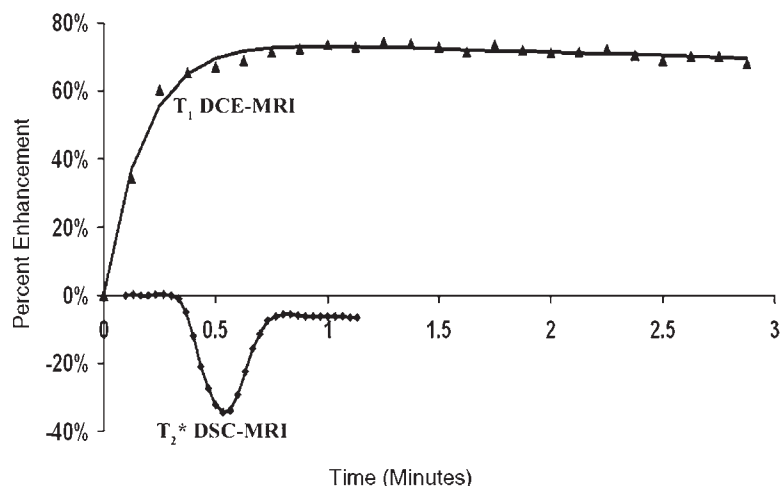


Figure 3 Representative time intensity curves plot signal intensity (S/S_0-1) against time for both DCE and DSC acquisitions. Identical doses of 0.1 mM/kg of Gd-DTPA were given to patients in both studies. The positive enhancing DCE curve shows the dominant T_1 -weighting mechanism in an osteosarcoma patient, acquired using a fast GRE sequence. The negative enhancing DSC curve emphasizes the T_2^* susceptibility effect seen in normal brain, acquired using a GRE-EPI sequence. Abbreviations: DCE, dynamic contrast enhanced; DSC, dynamic susceptibility contrast; Gd-DTPA, gadolinium-diethylenetriamine penta-acetic acid; GRE, gradient-recalled echo; EPI, echo-planar imaging.

study this effect utilize fast sampling techniques such as echo-planar imaging to adequately sample contrast uptake in a period of one to two seconds.

Capillary endothelial cells outside the brain are traditionally “leaky,” having an increased permeability that allows passage of the contrast beyond the vessel walls into the interstitial space. Additionally, this occurs under various pathological CNS conditions and tumors, which unless accounted for is a source of error in determination of perfusion parameters using DSC-MRI. Diffusion distributes the gadolinium beyond the vessel wall into the EES, where the long-range spin-lattice or T_1 relaxation effect dominates.

T_1 -WEIGHTED DCE-MRI

Positive enhancing T_1 -weighted MRI contrast studies are traditionally referred to as DCE acquisitions. With the approval of the first FDA-approved MRI contrast agent in 1988, dynamic acquisition and analysis techniques soon followed in the research community (9–11). The ability to dynamically monitor the uptake of contrast in various CNS disorders and tumor systems has yielded physiologically relevant information regarding the angiogenic properties of the tumor vasculature. Knowledge of the vascular permeability in tumor systems is essential in determining therapeutic drug delivery as well as in assessing tumor cell migration (12). DCE remains a prominent method for assessing perfusion within a wide variety of tumor systems

and has been correlated with various outcome measures such as histopathology and survival (8).

DCE-MRI Acquisition Methods

Acquisition of DCE-MRI data requires a fast T_1 -weighted pulse sequence that ideally offers high spatial resolution without compromising temporal resolution. The sequence of choice for many groups has been a fast 2-D or 3-D spoiled gradient echo (GE) sequence [fast spoiled GRASS (FSPGR), fast low-angle shot (FLASH), fast field echo (FFE) with short TE (<5 ms) and short TR times (<10 ms)]. The “spoiling” refers to gradient or RF techniques that destroy any remaining magnetization in the transverse plane at the end of each acquisition, which in turn maximizes T_1 weighting. The ability to cover the anatomy of interest with adequate spatial resolution and a high signal-to-noise ratio in as short a time as possible has been the challenge of this method. Representative DCE acquisition parameters from Weill Medical College of Cornell University are given in Table 1. In specifying DCE acquisition parameters, there will always be a compromise between spatial and temporal resolutions. Unfortunately, an increase in one traditionally results in a decrease in the other.

Serial acquisition of the entire volume at several time points prior to injection of the contrast agent is necessary to allow estimation of the baseline signal intensity. An injection of contrast is administered traditionally in the antecubital vein using a power injector followed with a

Table 1 Representative MR Perfusion Acquisition Parameters at 3T

	DCE-MRI T ₁ weighted	DSC-MRI T ₂ /T ₂ * weighted	ASL
Sequence	3-D spoiled GRE	Gradient echo EPI	3-D fast spin echo
TR	4.6 ms	1.6 sec	5.5 sec
TE	2.2 ms	65 ms	24 ms
Flip angle	12°	60°	90°
Matrix	256 × 128	128 × 128	512 × 128
Field of view	20 cm	24 cm	24 cm
Thickness	3.5 mm	6 mm	3.8 mm
Number of Slices	20	12	48
Number of Time points	40	40	—
Voxel size	~2 mm ³ a	~20 mm ³	~0.8 mm ³ a
Time resolution	~7 sec	1.6 sec	

^aImages are zero-filled in k-space prior to reconstruction, using Fourier transformation to yield a square matrix.

Abbreviations: DCE, dynamic contrast enhanced; MRI, magnetic resonance imaging; ASL, arterial spin labeling; GRE, gradient-recalled echo; EPI, echo-planar imaging; TR, repetition time; TE, echo time.

saline flush. The use of a power injector provides stable and reproducible injection rates that become an asset in modeling and comparison of arterial input functions (AIFs). The rate of contrast administration is dependent on the type of study, the patient condition, and whether a bolus or continuous infusion input function is desired. Traditionally, a bolus injection at a rate of 2 to 5 cc/sec is chosen, but knowledge of a better-defined function administered in time via a constant infusion of 30 to 60 seconds may also be desirable for analysis (13). Repeated acquisition of the volume over time then allows serial study of the first-pass and washout characteristics of the contrast agent, resulting in a TIC.

DCE-MRI Analysis Methods

Qualitative DCE Analysis

Analysis of the TIC can be done in either a qualitative or semiquantitative manner. Qualitative or heuristic estimates of contrast uptake provide parameters such as percentage enhancement, signal enhancement ratio (SER), initial slope, and the area under the curve. These measures have the advantage of being simple to derive and reproducible between patients and institutions. Relative changes in these qualitative parameters are an indirect measure of tissue perfusion. Several studies have correlated MVD with uptake parameters of time to peak, maximum slope, and SER in both breast and colorectal tumors (14,15).

The percentage enhancement reflects an estimate of the product of the permeability and the surface area in as much as the amount of contrast that has not been cleared from the interstitial space at later time points is assumed to have diffused out of the vasculature. Similarly, simple static subtraction images will also qualitatively exhibit the amount of residual contrast at various time points after injection. The SER has been used to characterize contrast uptake in tumors and correlate with MVD (15). Three specific time points are chosen to characterize the entire TIC. A point is taken prior to contrast injection (S_0), one at early enhancement (S_1) (~three minutes), and one at late enhancement (S_2) (~nine minutes). The SER is calculated as $(S_1 - S_0)/(S_2 - S_0)$, and incorporates data from the initial first pass as well as the washout phase of the TIC. This three-time point (3TP)-DCE-MRI method has been expanded to yield additional pharmacokinetic parameters via compartmental modeling techniques. This method has been used to characterize contrast uptake in breast lesions and may increase the diagnostic accuracy of the examination (16).

One asset of qualitative analysis relates to the rapid generation of parametric images that can be produced in a clinical setting in the MR suite. For example, a parametric image is shown in Figure 4 that displays the maximum slope of uptake in units of percent/min of the same slice depicted in Figure 1. The slope is a qualitative estimator of tissue permeability at early times after initial injection

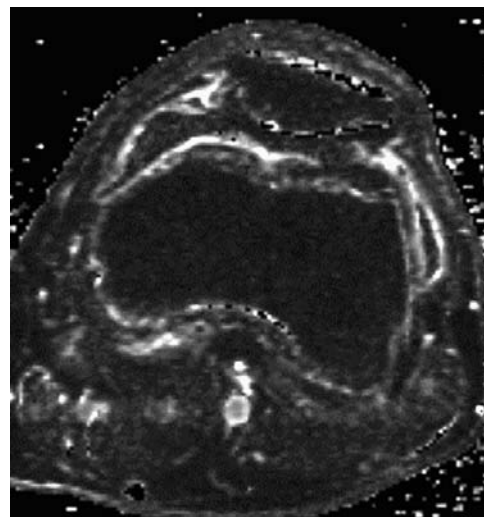


Figure 4 A parametric slope image is displayed of a hemophilic arthropathy patient for the same slice as shown in Figure 1. MRI signal intensity in each voxel is replaced with the maximum initial slope value in units of percent/min. Regions with increased initial slope may be visually assessed in a rapid qualitative manner through the use of parametric image maps. Increased slope may be seen in the synovium as well as arterial regions. *Abbreviation:* MRI, magnetic resonance imaging.

of contrast (17). It is believed that neovasculature develops in the synovium of hemophilic arthropathy patients, whereas normal synovial spaces are not well perfused. A quick visual assessment of contrast uptake may be viewed in the region of abnormality from the parametric slope image. However, there is not a direct relation between these qualitative uptake parameters and physiological markers of angiogenesis, given MR signal intensity is not equivalent to absolute concentration of the contrast agent. The utility of qualitative analysis techniques will always retain its simplicity to visualize the validity of the acquisition, to confirm more advanced modeling techniques, and to see regions of enhancement that would be confounding on simple static subtraction images.

Semiquantitative DCE Analysis

The choice to perform a more quantitative analysis using compartmental modeling is based on several reasons. Firstly, it is known that the signal intensity in MRI does not directly reflect the absolute concentration of contrast agent in that voxel as it does in CT. Knowledge of absolute concentration eliminates discrepancies between acquisition methods and assumptions that are included in raw signal intensity measures (18). Variances in field strength result in changes of precontrast T_1 and T_2 tissue relaxation times, which would not be accounted for even in a ratio of raw signal intensities. Changes in contrast dose and agent would also have an effect on raw signal intensity data if compared directly (17).

Conversion of Signal Intensity to Concentration

The equations relating the tissue relaxation prior to the addition of a contrast agent of known concentration with that following contrast administration are shown in Equation 2:

$$\frac{1}{T_1} = \frac{1}{T_{10}} + r_1 C_t; \frac{1}{T_2} = \frac{1}{T_{20}} + r_2 C_t, \quad (2)$$

where r_1 , and r_2 represent the relaxivity of the contrast agent in units of $\text{mM}^{-1}\text{s}^{-1}$, C_t is the concentration of contrast in the tissue in units of mM, and T_{10} and T_{20} are the native relaxation times in seconds prior to injection of contrast (19). These equations also emphasize the fact that a bolus injection of contrast delivers the highest concentration per unit time, yielding the greatest change in relaxation times. Relaxivities have recently been published for various gadolinium-based contrast agents at differing field strengths in human blood plasma (20).

Measurement of native relaxation times in tissue (T_{10}) prior to injection of contrast must be performed to convert

signal intensity to absolute concentration. Several groups have proposed methods for rapid in-vivo measurement of T_1 , including multiangle 3-D GE, look-locker-based methods, and by using the ratio of a proton density image to that of a T_1 -weighted image (21,22). In all of these methods, care must be taken to account for spatial non-uniformity in the flip angle, imperfections in the R slice profile, and spatial variations in the transmitted R field intensity, resulting in flip angle deviations (23,80). Inaccuracies in the measurement of T_{10} present one of the most significant sources of error in semiquantitative analysis of DCE-MRI data.

Once the dependence of T_1 on concentration is known, this may be substituted into the Bloch equations specific to the pulse sequence used to derive the resulting signal intensity. For example, the solution of the Bloch equations for a spoiled GE sequence, assuming that $\text{TE} \ll T_2^*$, is given by

$$S = \frac{S_0(1 - e^{-\frac{\text{TR}}{T_1}}) \sin \theta}{1 - \cos \theta e^{-\frac{\text{TR}}{T_1}}}, \quad (3)$$

where S_0 is a constant that includes factors relating to the proton density, coil sensitivity, and scanner gains. Substitution of the Solomon-Bloembergen equations into the above equation then gives a relationship between MRI signal intensity and concentration of the contrast agent *in vivo*.

An assumption in semiquantitative analysis methods is that a fast-exchange regime exists, whereby equilibrium of molecules interacting between the intravascular and extravascular compartments is achieved within a single time period T_1 (17,24). Fast imaging sequences traditionally acquire data with TRs much less than the native T_1 relaxation times of the tissue of interest. Depending on the permeability between the two compartments, this assumption may or may not be an accurate depiction of the true exchange regime. Studies have shown that an underestimation by a factor of 2 or 3 may occur in determination of pharmacokinetic perfusion parameters if an accurate measurement of the mean intracellular molecule lifetime is not obtained (24).

At times immediately following the bolus injection for contrast doses seen in the clinic, phantom studies and theory both confirm that a linear relation exists between signal intensity and concentration:

$$S(t) = S(0)[1 + gC(t)], \quad (4)$$

where g is a constant that depends on the native tissue relaxation time and relaxivity of the contrast agent (20,25). A signal intensity time course may be converted to relative concentration by plotting

$$\frac{S(t)}{S_0} - 1 = gC(t) \quad (5)$$

Absolute concentration must be estimated through knowledge of the in-vitro contrast agent relaxivity and native tissue relaxation time as discussed.

Choice of Compartmental Model

Once the relationship between MR signal intensity and concentration of the contrast agent is known, these results may be utilized within the framework of a pharmacokinetic model to derive estimates of physiologically relevant parameters from the data. The standard form of the compartmental model in use for DCE analysis dates back to the work of Kety and Schmidt in 1948 (26). They derived a general rate equation that modeled the freely diffusible flow of a tracer through the vasculature. This work laid the foundation for measurement of CBF across multiple modalities. It also formed the link between the blood oxygen level-dependent (BOLD) effect caused by deoxyhemoglobin in functional MRI (fMRI) with its oxygen metabolism and blood flow precursors (27).

Figure 5 shows a generalized compartmental model used to characterize the inflow of tracer into the region as well as the diffusion of tracer from the plasma compartment (C_p) into the EES compartment (C_e). The volumes of the plasma and EES compartments are respectively, v_p and v_e . The physiological significance of K^{trans} depends on whether the system is flow or permeability limited. If blood flow exceeds the rate of vascular permeability ($F >> PS$), then K^{trans} characterizes the product of the permeability surface area multiplied by the tissue density ($PS\rho$) per unit volume of tissue in units of 1/min (7). If, however, in regions such as necrosis having reduced

blood flow ($PS >> F$), then K^{trans} is directly related to the product $Fp(1-Hct)$, where F represents blood flow in units of mL/g min and Hct is the blood hematocrit. Additional assumptions are traditionally made concerning the fact that K^{trans} is directionally invariant.

Equation 6 describes the rate of change of contrast in the EES and becomes the basis for DCE-MRI modeling work.

$$v_e \frac{dC_e(t)}{dt} = K^{trans}[C_p(t) - C_e(t)] \quad (6)$$

The composition of an MRI voxel contains approximately 2% to 4% vasculature in normal brain. The changes in signal intensity due to contrast enhancement are a result of a combination of effects from both intra-vascular and extravascular components. A single voxel in tissue encompasses a fraction of vasculature as indicated by the dashed line in Figure 5. The resulting concentration time course within tissue is given as a combination of these two compartments:

$$C_t(t) = v_p C_p(t) + v_e C_e(t), \quad (7)$$

where the sum of the plasma and EES volumes, v_p and v_e , is always equal to unity. Substituting Equation 6 into Equation 7 and solving the differential equations for $C_t(t)$ yields a general solution of the concentration of contrast in the tissue:

$$C_t(t) = v_p C_p(t) + C_p(t) \otimes K^{trans} e^{-\frac{K^{trans}}{v_e} t}, \quad (8)$$

which provides the basis for many of the compartmental models in use within the research community today (9–11). Three unknown parameters must be fitted using the concentration time curves obtained from an AIF as well as from the tissue of interest. The AIF should ideally be a TIC derived from a voxel exhibiting no partial volume averaging that is placed entirely within the artery that feeds the tissue of interest.

The choice of an AIF in DCE analysis in neurological applications has traditionally been taken from an average data set of concentration measurements from direct arterial blood samples taken from healthy volunteers (28). These data were fitted with a biexponentially decaying plasma curve given by

$$C_p(t) = 3.99 \frac{kg}{L} e^{-0.144t/\text{min}} + 4.78 \frac{kg}{L} e^{-0.0111t/\text{min}}. \quad (9)$$

When Equation 9 is multiplied by the dose (D) of the contrast agent in units of mmol/kg, the resulting plasma curve is in concentration units of mM (17). However, the use of a generalized plasma curve does not provide information on specific fluctuations because of physiological factors including variances in cardiac output.

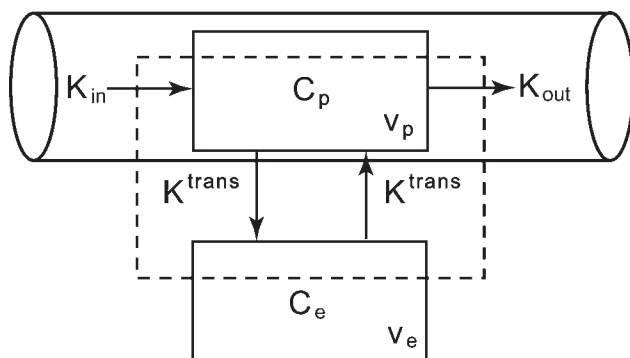


Figure 5 A generalized compartmental model is shown that may be used to derive estimates of physiologically relevant parameters such as the directionally invariant estimate of product of the permeability surface area (K^{trans}), the extravascular extracellular space volume (v_e) and the plasma volume (v_p).

Additional variations are produced by the time-of-flight inflow effect of blood, which shortens the apparent T_1 of vessels (29). This effect increases with the flow velocity and may cause overestimation of the AIF. Optimally, the AIF should be measured for each patient to provide a more accurate representation of peak concentration and timing of the plasma curve.

Knowing the native T_1 of tissue prior to contrast administration and using the plasma curve given in Equation 9, a solution to the concentration of contrast agent in the tissue is given according to the compartmental model proposed by Tofts and Kermode (11).

$$C_t(t) = Dk_{in}^{PS\rho} \sum_{i=1}^2 a_i^T \frac{e^{-(k_{out}^{PS\rho}/v_e)t} - e^{-m_i t}}{m_i - (k_{out}^{PS\rho}/v_e)} + v_p D \sum_{i=1}^2 a_i^T e^{-m_i t} \quad (10)$$

Fitting of the model solution to the data then produces estimates of $k^{PS\rho}$ (K^{trans}), v_e , and v_p . A clinical example applying this compartmental model to a patient with multiple sclerosis (MS) lesions is shown in Figure 6. The more acute MS lesion shows a greater permeability and a reduced EES than the less severe lesion.

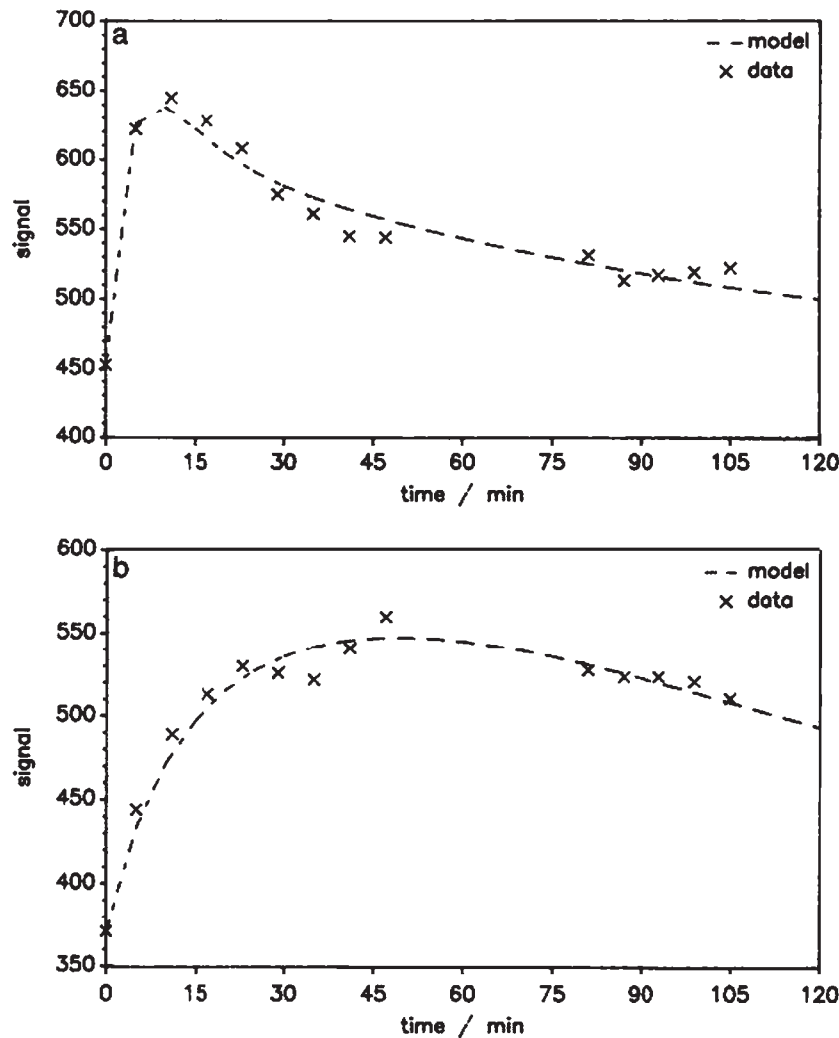


Figure 6 DCE signal intensity changes are shown from two different MS patients acquired for nearly two hours after injection of the contrast agent. In the first example, from an acute MS lesion, peak enhancement is relatively early (about 12 minutes), and the fitted model parameters are permeability $K^{trans} = 0.050/\text{min}$, extracellular space $v_e = 21\%$. In the second example, from a chronic lesion, enhancement is slower, reaching a peak at about 50 minutes. Fitting the model shows a much lower permeability $K^{trans} = 0.013/\text{min}$, and a much larger extracellular space $v_e = 49\%$, both consistent with what is known from postmortem studies. Abbreviations: DCE, dynamic contrast enhanced; MS, multiple sclerosis. Source: Paul Tofts, Ph.D., Brighton and Sussex Medical School.

Alternatively, several compartmental models approximate the plasma curve as a single or double exponential function that is fitted along with the transfer coefficients. Such a model was proposed for use in CNS and breast tumor cases (9,13). A solution describing the tissue concentration, is

$$\frac{S(t)}{S(0)} - 1 = A^H k_{ep} \left(\frac{e^{-k_{ep}t} - e^{-k_{el}t}}{k_{el} - k_{ep}} \right), \quad (11)$$

where k_{ep} is defined as the transfer rate from the EES to the C_p in units of 1/min and is equivalent to k^{PSp}/v_e in the Tofts and Kermode model. The elimination of contrast by the kidneys is given by k_{el} in units of 1/min. Note that the native T_{10} of tissue is not measured but contained in the constant A^H and that raw MRI signal intensities and not absolute concentrations are used. This model assumed that the plasma curve given in Equation 9 is sufficiently approximated by a single exponential function for times less than 20 minutes.

An example of this model applied to clinical data may be seen in Figure 7. Patients were studied with DCE-MRI methods that presented with various grades of osteogenic or Ewing's sarcomas following chemotherapy (30). Representative TICs are shown from two patients with differing degrees of necrosis as determined by histology. The grade II responder (50% tumor necrosis following induction chemotherapy) shows a faster initial uptake of contrast, measured by $A^H k_{ep}$, compared with that of the grade IV responder (100% tumor necrosis following induction chemotherapy). Additionally, the TIC of the grade IV

responder to chemotherapy was still increasing and had not reached a plateau by the end of the scan. DCE analysis in this population was used to estimate prior to surgery whether patients had responded to chemotherapy, as gauged by greater than or equal to 90% tumor necrosis.

Validation

DCE-assessed physiological parameters are primarily qualitative, although some semiquantitative parameters may be derived. Indirect measurement of increased MVD or angiogenic activity may be detected through contrast-enhanced MRI techniques. One such proangiogenic molecule is VEGF, which induces signaling in endothelial cells and preserves tumor endothelium. There is a scarcity of studies positively correlating DCE parameters with increased MVD or VEGF expression. A large study of breast lesions compared DCE-MRI parameters with MVD and determined that changes in contrast enhancement patterns in the center compared with the periphery were not entirely due to increased MVD (31).

DCE also has utility in determining changes in tissue perfusion following administration of antiangiogenic drugs in various tumor systems. DCE perfusion parameters such as initial slope and $A^H k_{ep}$ were significantly reduced in mice carrying a human non-small cell lung carcinoma seven days after treatment with an antiangiogenic agent (3). DCE was able to detect an effect of treatment that was not seen via overall changes in tumor volume. Likewise, we studied VEGF expression in patients with osteogenic sarcomas and showed an increasing trend in $A^H k_{ep}$ estimates

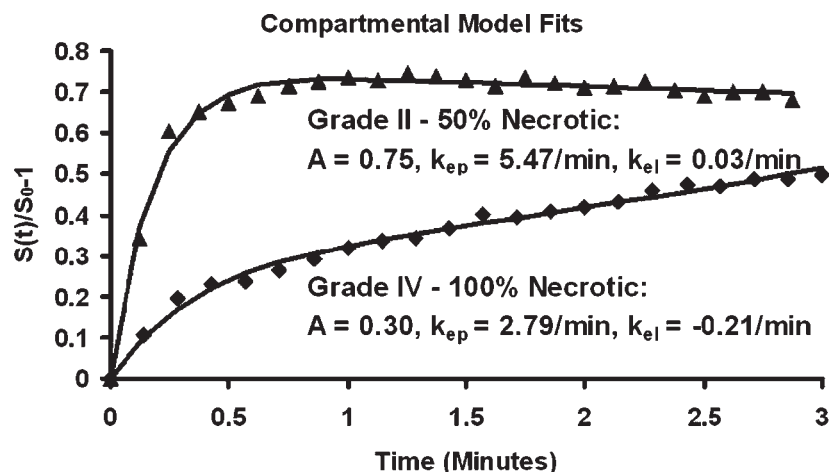


Figure 7 DCE-MRI time intensity curves are shown for two osteosarcoma patients with differing histologically confirmed necrotic fractions. Compartmental model fits of the TICs are shown using the Brix-Hoffman model. The grade II responder (50% necrosis following induction chemotherapy) shows increased uptake and clearance of the contrast compared to the grade IV tumor, as given by $A^H k_{ep}$ and k_{el} , respectively. The grade IV responder (100% necrosis following induction chemotherapy) continues to slowly enhance throughout the scan while the grade II tumor has reached a plateau. Abbreviations: DCE, dynamic contrast enhanced; MRI, magnetic resonance imaging; TIC, time intensity curve.

of vascular permeability with immunohistochemical detection of VEGF expression (4). The utility of DCE may not lie directly in the physiological accuracy of the method but in the ability to increase the sensitivity and specificity of a diagnostic examination as compared with standard static contrast-enhanced or subtraction techniques.

T₂/T₂^{*}-WEIGHTED DSC-MRI

Villringer et al. (32), in 1988, reported the first description of DSC-enhanced MRI. Subsequently, the first report of DSC-MRI to assess cerebral hemodynamics in humans was by Rosen et al. (33). Since then, the technique has been used to estimate CBV, CBF, and MTT in patients presenting a myriad of CNS pathologies such as stroke, aphasia, and various tumor types. One of the primary clinical applications of DSC-MRI is in conjunction with diffusion-weighted imaging (DWI) in the early detection of stroke. DWI is known to detect early infarction in the hyperacute phase within a few minutes of onset of symptoms and is superior to routine MRI sequences and CT. DSC-MRI provides complementary information on possible early ischemia in the region of interest. A mismatch may develop between the region of high intensity on the DWI and that of increased MTT as calculated from the DSC-MRI time course (34). This region may be classified as ischemic penumbra and illustrates tissue that may benefit from thrombolytic or neuroprotective therapies.

DSC-MRI Acquisition Methods

The choice of pulse sequence depends on several factors including sensitivity to field strength-related susceptibility changes and specificity to vessel diameters (39). T₂-weighted spin echo (SE) and T₂^{*}-weighted GE sequences may both utilize an echo-planar readout method suitable for perfusion-weighted imaging, which is inherently T₂^{*}-sensitive due to the rapid readout scheme (35). Advantages of SE sequences include the property that they are more sensitive to changes in the microvasculature than GE sequences (36). This is beneficial in detecting angiogenic changes within tumor neovasculature, capillary deoxygenation, or neoplastic disorders (37,39). Cerebrovascular diseases alter regulatory mechanisms at the level of the capillary bed or arterioles. SE sequences are more sensitive than GE sequences in detecting changes because of contrast enhancement at that level. Decreased distortion with SE sequences also allows for increased anatomical precision when examining regions at air-tissue interfaces within the brain.

GE sequences carry a double-edged sword with regard to detecting susceptibility-related changes. As DSC is inherently a T₂^{*}-weighted effect that dephases the signal

surrounding the contrast agent, a GE sequence is more sensitive to detecting signal changes because of susceptibility effects than a-T₂-weighted SE sequence. This signal-to-noise-advantage traditionally results in the ability to administer half the dose of contrast when using a GE instead of an SE sequence (37). However, with a GE sequence, large vessels exhibit CBVs of 100%. If the vessels are adjacent to white or gray matter areas of interest with CBVs of 2% to 4%, respectively, changes may be obscured because of the close proximity of the vessel. It is also possible to obtain more slices within a given TR using a GE than an SE sequence allowing more complete coverage of the brain.

However, the advantage that a GE sequence provides in detecting DSC becomes a detriment when examining regions near differing tissue boundaries. Tissues having different magnetic susceptibilities interact, producing local field inhomogeneities or distortions such as at an air-tissue interface. These distortions are more prominent using a GE than an SE sequence and this effect is intensified with increased field strength, (e.g., 1.5–3.0 T). Distortions are especially pronounced at air-tissue interfaces in the posterior fossa, skull base, orbits, and paranasal sinuses. Other distortions can occur at bone-tissue interfaces such as at the cortical bone and brain parenchyma boundary (38).

The choice of pulse sequence, whether SE or GE, must maximize temporal resolution (< 2 sec/time point), obtain the needed coverage of the brain with adequate spatial resolution, and remain sensitive to contrast-induced T₂/T₂^{*} changes in susceptibility while reducing contributions from T₁-weighted effects. Representative DSC acquisition parameters are given in Table 1 from Weill Medical College of Cornell University. In addition, Sorenson gives an excellent discussion of all pertinent DSC parameters and their effects on scan quality (39). As in DCE imaging, the availability of multichannel-phased array coils utilizing sensitivity-encoding parallel imaging techniques may reduce acquisition times while obtaining adequate signal-to-noise resolution. The ability to rapidly sample and capture the actual peak of the concentration curve has a significant effect on semiquantitative calculations of cerebral perfusion parameters. Partial k-space sampling techniques may also aid in obtaining faster temporal resolution, although a reduction in signal-to-noise or spatial resolution may occur.

Physiological Description of Perfusion Parameters

Prior to discussing methods of estimating physiologically relevant perfusion parameters using DSC, a basic understanding of the significance and normative values

of these parameters should be discussed. The simplest perfusion parameter to measure from the DSC concentration curve is that of regional cerebral blood volume (*rCBV*), which is an estimate of the volume of blood contained in the microvasculature. This may be defined as either a mass or volume fraction reporting the volume of blood in a voxel divided by the mass or volume of the voxel, respectively (40). Typically, the volume fraction is reported as a percentage with normal values determined by $H_2^{15}O$ positron emission tomography (PET) to be $5.2\% \pm 1.2\%$ and $2.7\% \pm 0.5\%$ in gray and white matter, respectively (41).

rCBF is an estimate of the net blood flow through the voxel divided by the mass of the voxel and is typically reported in units of mL/100 g brain tissue/min (40). CBF as reported by $H_2^{15}O$ PET methods is reported to be 55 ± 12 mL/100 g/min and 22 ± 5 mL/100 g/min in gray and white matter, respectively (41). CBF is tightly regulated to meet metabolic demands, and blood flow less than approximately 20 mL/100 g/min causes ischemia while flow less than 10 mL/100 g/min causes tissue death (42). Conversely, abnormally increased CBF above 60 mL/100 g/min is termed “hyperemia” and may cause an increase in intracranial pressure.

The regional mean transit time (rMTT) describes the average amount of time it takes the tracer to pass through the vasculature contained within a single voxel, given an idealized input function. The MTT reported in adult brain using $H_2^{15}O$ PET methods is 5.6 ± 2 seconds and 7.2 ± 3 seconds in gray and white matter, respectively (41). Note that all normal values deviate slightly when placed in various regions of the brain as well as with patient age. Quoted values represent only approximate estimates of these parameters averaged over multiple patients.

DSC-MRI Analysis Methods

Indicator dilution techniques for determination of cerebral hemodynamic parameters have been investigated since the turn of the 19th century (43). A bolus injection of a dye into the bloodstream and the subsequent collection of the diluted sample formed the basis of the resulting formalism. Estimation of physiologically relevant parameters such as CBF, CBV, and MTT was derived from these equations. The central volume theorem gives the relation between these parameters as $MTT = CBV/CBF$ (44). This allows determination of the MTT via knowledge of the flow per unit weight and blood volume. Methods of determining accurate estimates of these parameters may again be classified as either qualitative or semiquantitative, similar to those discussed in the previous section on DCE-MRI.

Conversion of Signal Intensity to Concentration

A central assumption in DSC perfusion imaging is that a linear relation exists between the relaxation time in tissue and the concentration of contrast. This relation is given by $R_2(t) = rc(t)$, where $R_2(t) = 1/T_2(t)$, r is the relaxivity of the contrast agent in units of $\text{mM}^{-1}\text{s}^{-1}$ and $c(t)$ is the concentration of contrast in units of mM (45). The solution of the Bloch equations for both SE and GE sequences reduces to the following equations, assuming that $TR >> T_2$.

$$S(t) \approx \rho e^{-\frac{TE}{T_2}}; S(0) \approx \rho e^{-\frac{TE}{T_{20}}} \quad (12)$$

The above equations assume a single exponential relation describing the T_2/T_{20} relaxation effects, which, depending on the exchange regime with the surrounding water, may not be a completely accurate description of the processes involved (34,45). Combining these equations with Equation 2, relating relaxation times with the concentration of contrast agent, yields

$$C(t) = -\frac{1}{r \cdot TE} \cdot \ln\left(\frac{S(t)}{S(0)}\right) \quad (13)$$

Raw MR signal intensity may then be transformed to units of concentration of the contrast agent in mM. Figure 8 displays an AIF taken from the average of two voxels placed on the right internal cerebral artery (ICA). Time course curves are also shown for regions of interest placed on gray and white matter regions in the same study. Data were acquired at 3.0 T, while setting the relaxivity of the contrast agent r to unity.

Qualitative

As in DCE-MRI, image analysis of the TICs can be rapidly accomplished to yield qualitative perfusion parameters. A first approximation for the *rCBV* may be estimated by determining the area under the concentration time curve (AUC) for the voxel of interest as given by

$$rCBV = \int_0^t \Delta R_2(\tau) d\tau \quad (14)$$

The integration may be performed numerically for the curve shown in Figure 8. The range of integration must specify the last precontrast image, which would be used to define the start of the integral. Alternatively, a baseline signal intensity level may be calculated by averaging the precontrast images that have achieved equilibrium. Determination of the signal intensity baseline prior to first-pass contrast administration should be done after the signal achieves steady state, which is typically three to four

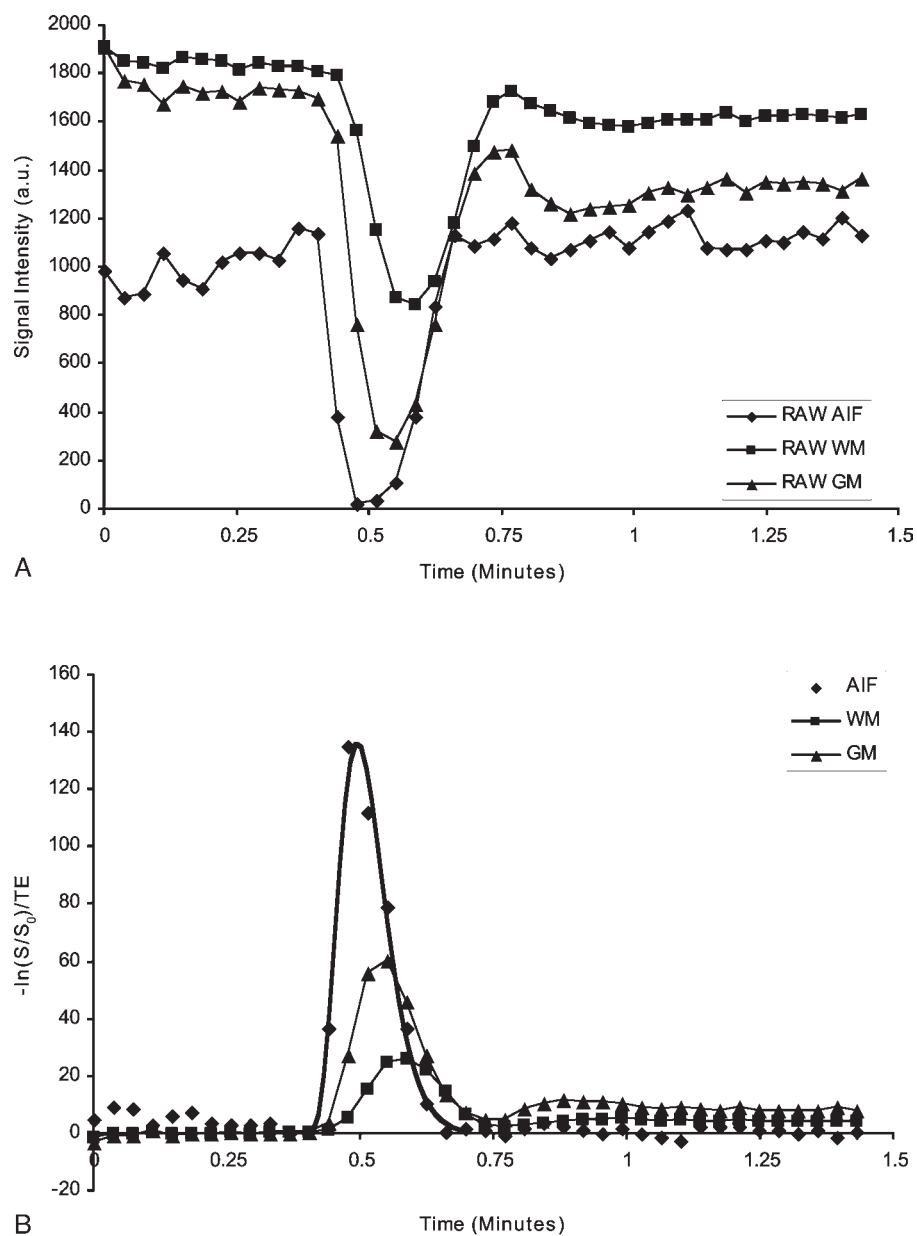


Figure 8 DSC TICs are shown for an AIF placed on the right ICA as well as for ROIs taken from gray and white matter. (A) Displays the raw MRI signal intensities over time for each ROI, showing the reduction in signal due to the T_2^* -susceptibility effect. (B) Displays a concentration time curve for each ROI, assuming a value of unity for the relaxivity. A γ -variate fit of the AIF concentration time curve is also displayed. Abbreviations: DSC, dynamic susceptibility contrast; TIC, time intensity curve; AIF, arterial input function; ICA, internal cerebral artery; ROI, region of interest.

seconds after the start of acquisition (46). The AUC could be measured for the entire time course; however, this would not account for recirculation effects, which would be compounded in cases where the BBB is compromised. Recirculation effects are typically apparent as a smaller

second peak in the concentration time curve. An incomplete return of the signal to baseline levels may also be due to leakage into the extravascular space during the first pass of contrast, representing diffusion of the contrast through a permeable BBB.

A method of correcting for recirculation effects involves fitting the concentration time curve with a γ -variate function defined as follows:

$$C_a(t) = \begin{cases} 0 & t \leq t_0 \\ C_0(t - t_0)^{\alpha} e^{-(t-t_0)/\beta} & t > t_0 \end{cases}, \quad (15)$$

where the parameters C_0 , α , β , and t_0 are determined for each curve fit (34). The solid line in Figure 8 displays a γ -variate fit, using the above equation to an AIF located in the right ICA acquired at 3.0 T. An additional advantage of using the γ -variate function is that the area under the curve is analytically given by

$$rCBV = \int_0^{\infty} C(\tau) d\tau = C_0 \beta^{\alpha+1} \Gamma(\alpha + 1), \quad (16)$$

resulting in an estimate of rCBV that accounts for recirculation effects.

As mentioned previously, one major assumption in DSC is that the vasculature remains nonpermeable because of an

intact BBB. If the BBB is compromised, then estimates of rCBV, even with γ -variate fitting, will be overestimated due to leakage and T_1 effects (47). Although qualitative measures of rCBV do not yield absolute quantitation, various groups have shown clinical utility in measurement of relative CBV values. Relative CBV measures are taken as a ratio to a specific region found in normal contralateral brain such as white matter (46,47). This technique further corrects for recirculation and leakage by normalizing results to an internal tissue standard. Figure 9 shows an example of DSC TICs from an anaplastic astrocytoma and a meningioma. Normal contralateral white matter is used as a reference for semiquantitative estimates of rCBV. Additionally, although not discussed here, measurement of rCBV may also be determined by steady-state methods assuming an intact BBB (48).

The rMTT is traditionally derived following estimates of rCBV. Numerous qualitative parameters have been proposed to describe the delay or passage of contrast through the tissue. Figure 10 displays several qualitative estimators of rMTT including the time to peak (TTP),

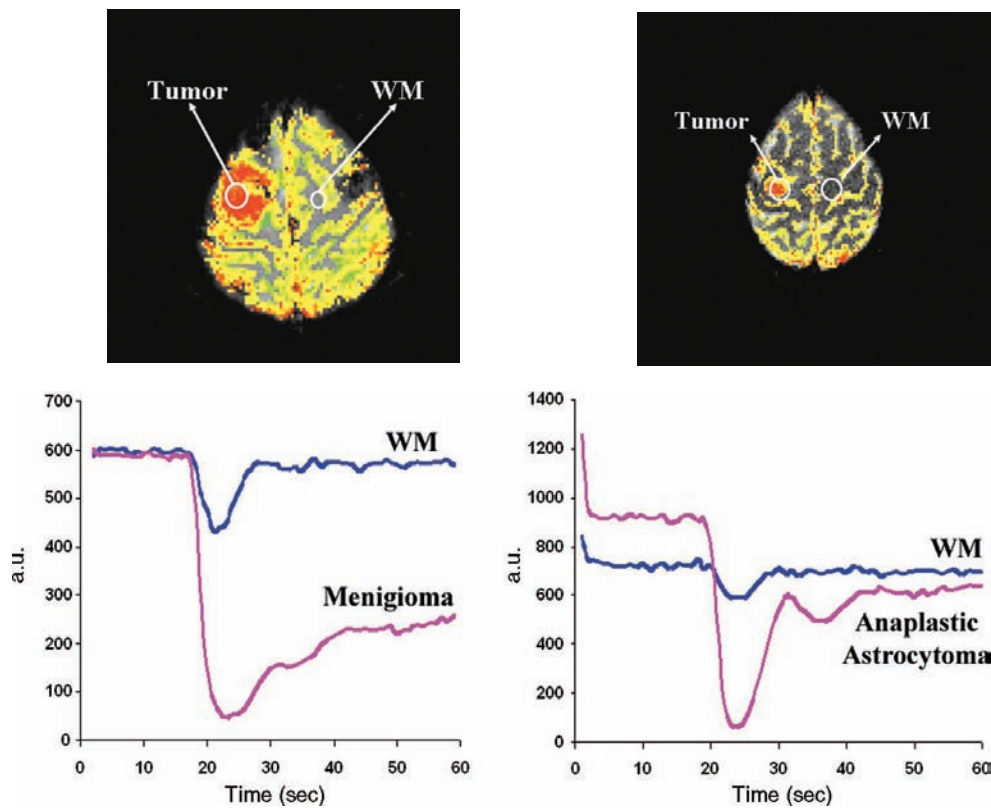


Figure 9 DSC TICs are shown for ROIs taken in a meningioma as well as an anaplastic astrocytoma. Corresponding contralateral white matter ROIs are also displayed, which are used for calculation of qualitative rCBV ratios. The lack of signal return to baseline in the meningioma is representative of increased vascular permeability. Semiquantitative estimation of perfusion parameters without correction for this increased permeability would result in inaccurate results. The parametric images for both tumors display relative rCBV values normalized to white matter. Abbreviations: DSC, dynamic susceptibility contrast; TIC, time intensity curve; AIF, arterial input function; ICA, internal cerebral artery; ROI, region of interest; rCBV, regional cerebral blood volume. Source: Meng Law, M.D., New York University Medical School.

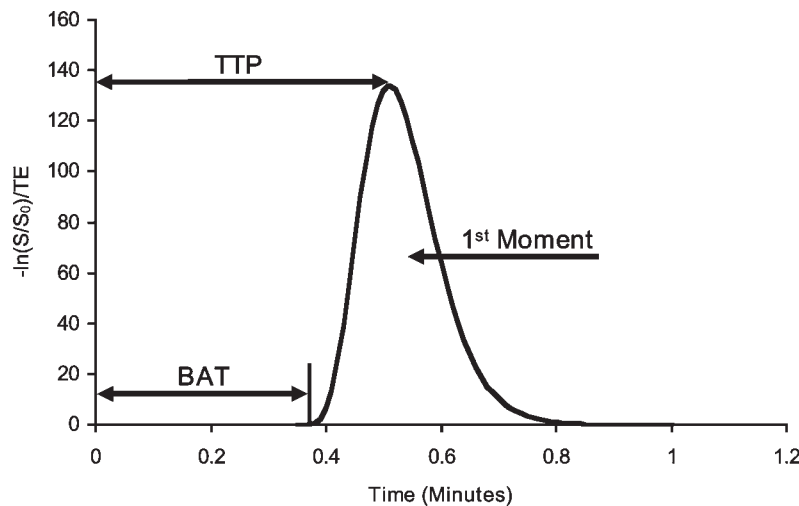


Figure 10 Qualitative estimates characterizing the delay time of a DSC concentration time curve are shown. The TTP, BAT, and MRT defined as the first moment of the curve are given. These qualitative perfusion parameters may be used to rapidly assess regions of abnormal perfusion. However, in regions of slow or pathological flow, they are also known to inaccurately model true changes in the MTT. Abbreviations: DSC, dynamic susceptibility contrast; TTP, time to peak; BAT, bolus arrival time; MRT, mean residence time; MTT, mean transit time.

bolus arrival time (BAT), and the first moment of the concentration time course, which may be referred to as the mean residence time (MRT). Calculation of the MRT is taken as the ratio of the area under the moment curve (AUMC) to that of the AUC.

$$MRT = \frac{\int_0^{\infty} tC(t)dt}{\int_0^{\infty} C(t)dt} = \frac{AUMC}{AUC} \quad (17)$$

Additionally, the use of a γ -variate function to fit the concentration time curve results in an estimate of the MRT given by $MRT = t_0 + \beta(\alpha + 1)$. The MRT is only equivalent to the physiological MTT following an instantaneous AIF (49). However, a δ -function bolus injection of zero width is never achieved *in vivo* as dispersion of the AIF occurs because of passage of the contrast through vessels of varying degrees of tortuosity, stenosis, and mean path length.

Traditionally, qualitative estimates of perfusion parameters determine the rCBV and rMTT as explained above and then an estimate of rCBF is taken as the ratio of the two parameters utilizing the central volume theorem. Advantages to qualitative estimates of these parameters include the speed of processing and the necessity of not having to choose an AIF. However, it has been shown that qualitative estimates of rCBF do not correlate with $H_2^{15}O$ PET measures (50), though ratios of qualitative rCBF in diseased regions with those of contralateral brain were found to correlate with similar $H_2^{15}O$ PET ratios. Additionally, Sorenson points out that in cases of unilateral stenosis such as seen in stroke, qualitative maps of

MRT may be abnormal for the entire hemisphere while semiquantitative estimates of rMTT may show little or no tissue at risk (39).

Semiquantitative

AIF Determination

The determination of more accurate estimates of CBV, CBF, and MTT is driven by the desire to obtain more reliable estimates of physiological perfusion changes that may be routinely used in the clinical setting. Two major tasks are currently performed to increase the accuracy of this technique. The first task requires the choice of an accurate AIF and the second involves a mathematical deconvolution of this AIF from the tissue curve. The requirement for incorporating an AIF into calculation of the perfusion parameters results from the lack of an instantaneous bolus injection and dispersion of the bolus within the vasculature. Ideally, a voxel at the center of a vessel should be chosen that incurs no partial volume effects. In practice, this may be difficult to accomplish given the susceptibility artifacts at air-tissue interfaces acquired using, echo-planar imaging (EPI) techniques. Vessels such as the middle cerebral artery (MCA) run parallel to axially placed slices not only making them easily identifiable but also incorporating partial volume signal from normal brain due to a smaller vessel diameter than slice thickness. Rausch et al. determined that AIF peak amplitudes taken in the MCA are a factor of 3, lower than those taken from the ICA or vertebral artery (VA) (51).

The dose of contrast should also be examined when prescribing a DSC protocol. The dose will ideally provide the maximum decrease in signal intensity at the lowest concentration that may be administered to the patient. The AIF shown in Figure 8 nearly reaches zero but remains positive during the bolus peak of 0.1 mM/kg Gd-DTPA acquired at 3.0 T. However, complete signal cancellation is possible using a GE sequence, whereby the contrast dephases the signal to the extent that the intensity remains zero during the true peak of the bolus (52). This results in inaccurate determination of the peak and area of the AIF, affecting all subsequent calculations of perfusion parameters.

Frequency shifts along the phase encode direction are also induced by susceptibility changes seen during the influx of contrast into a vessel. These frequency changes translate into spatial shifts of an AIF during the first-pass injection of contrast. Because of the low bandwidth of echo-planar readout techniques in the phase encode direction, this may result in a shift of several voxels or more during the peak of the injection. If the AIF is placed near the rim of the vessel, the peak signal may actually occur outside the chosen voxel as seen in the decrease at peak amplitude shown in Figure 11. Corrections for this effect have been proposed via modeling the changes in phase due to the contrast injection (53). Analysis of both phase and amplitude components of the signal also allow performing a correction to remove the static contribution of the partial volume background signal (54). Underestimation of the true AIF will result in greatly increased measures of rCBF. These factors must be considered when choosing an AIF for semiquantitative measures.

Semiquantitative estimates of rCBV may be performed once the concentration time course has been chosen from an appropriate AIF.

$$rCBV = \frac{k_H}{\rho} \frac{\int_0^{\infty} C_{\text{Tissue}}(t)dt}{\int_0^{\infty} C_{\text{AIF}}(t)dt}, \quad (18)$$

where C_{Tissue} represents the concentration time curve taken from the voxel of interest and C_{AIF} the concentration time curve of the chosen AIF. Rempp et al. (55) derived a correction factor k_H to take into account the differences in hematocrit levels between large and small vessels. The factor was given the form

$$k_H = \frac{1 - H_{LV}}{1 - H_{SV}}, \text{ where } H_{LV} = 0.45 \text{ and } H_{SV} = 0.25 \quad (19)$$

to approximate the changes in hematocrit due to variances in vessel size. The constant k_H then yields a unitless value of 0.733. Additionally, the density of brain tissue is given as 1.04 g/mL such that the units of rCBV are reported as a percentage (mL/100 g brain tissue). Assumptions are also made equating the relaxivity of contrast in blood to that in tissue when converting signal intensity to concentration. However, recent studies have shown that further inaccuracies in semiquantitative estimates of rCBV may result from this assumption (45).

The steps needed to determine rCBF must now incorporate the fact that the bolus injection is not ideal and that dispersion and delay of the bolus has occurred in vivo. The transport function $h(t)$ describes the distribution of transit times within a voxel for all particles of contrast that have passed through (Fig. 12). In the general case, it is known that

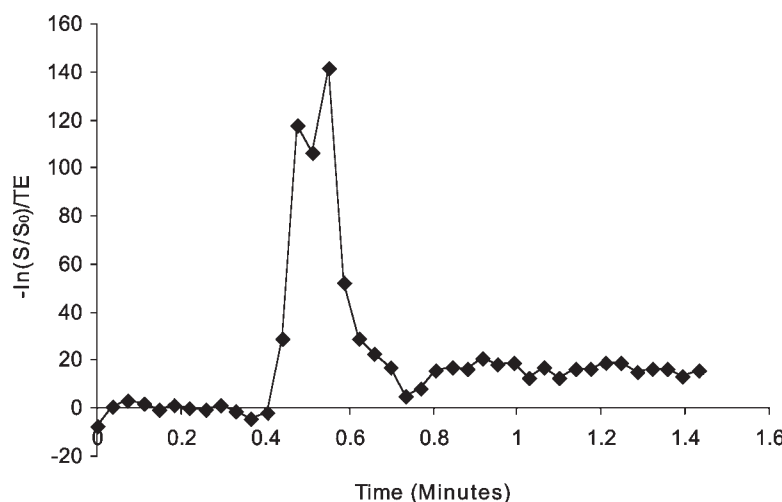


Figure 11 An AIF is shown that incorrectly characterizes the peak of the concentration time curve. This curve was generated by placing a single voxel near the vessel rim. A susceptibility-induced frequency shift displaced the peak of the bolus injection outside the range of this voxel incorrectly, resulting in a decrease at the time to peak. Abbreviation: AIF, arterial input function.

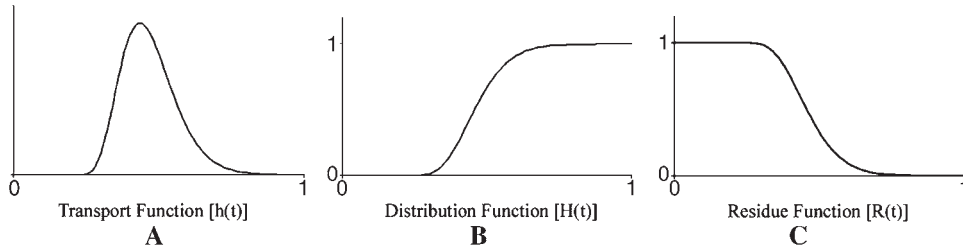


Figure 12 Semiquantitative estimates of DSC perfusion parameters require knowledge of the distribution of contrast over time in each voxel. The transport function $[h(t)]$ is shown in (A), which is typically an asymmetric distribution of times needed for all molecules of contrast to pass through the voxel. The integral of the transport function $[H(t)]$ is the cumulative distribution function (B) and physically represents the amount of contrast that has left the voxel. The MRI-measured signal intensity is then described by the residue function $[R(t)]$ or $1-H(t)$, which physically is the amount of contrast remaining in the voxel. Abbreviations: DSC, dynamic susceptibility contrast; MRI, magnetic resonance imaging.

the concentration measured in a voxel of interest is the result of a convolution of the AIF with this transport function.

$$C_{\text{Tissue}}(t) = C_{\text{AIF}}(t) \otimes h(t) \quad (20)$$

However, in MRI, the amount of contrast agent remaining in a voxel is what is actually measured over time. The cumulative distribution function shown in Figure 12 is the integral of the transport function over time and represents the fraction of contrast that has left the voxel at time (t). Subsequently, the amount of contrast remaining in the voxel after time (t) is then defined as the residue function $R(t)$ and is given by $1-H(t)$ (Fig. 12) (43). Ostergaard et al. showed through the use of the residue function that the CBF is then derived from the following equation, which is central to all semiquantitative approaches in DSC-MRI (56,57).

$$C_{\text{Tissue}}(t) = \frac{\rho}{k_H} F \int_0^t C_{\text{AIF}}(\tau) R(t - \tau) d\tau \quad (21)$$

The solution to this equation requires isolating the residue function for each voxel.

Numerous methods have been proposed to accomplish this task, but a mathematical deconvolution technique is traditionally chosen. As these methods are sensitive to noise, smoothing of the data prior to deconvolution is suggested. Recently, a circular deconvolution technique was proposed that is invariant to time delays incurred by the AIF, which might alter estimates of rCBF (58). Correction for this is essential as delays in concentration time curves may result in the AIF incorrectly lagging behind various tissue curves. Deconvolution of the AIF from the tissue concentration curve will then yield the product of rCBF ($\rho F/k_H$) and the residue function. As the residue function is unity at time zero, the initial height of $R(0)$ then becomes the estimate of rCBF. Practically though, as the deconvolved curve may display delay and dispersion, the maximum value of the residue function should be taken as a more robust estimate of rCBF (34,57). Lastly, the central volume

theorem may be applied, knowing that $rMTT = rCBV/rCBF$. Additionally, by definition, the MTT may also be determined as the total area under the residue function.

A clinical example of DSC perfusion maps derived using circular singular value decomposition methods is shown in Figure 13 of a patient presenting with a left MCA-occluded stroke. A primary clinical use of DSC perfusion-weighted imaging is in stroke patients to detect regions of impaired blood flow. Increased rMTT is an indicator of the presence of infarcted tissue. The region of infarct on a perfusion-weighted imaging may be larger than that seen on a DWI leading to a “diffusion-perfusion mismatch.” It is thought that the perfusion-weighted imaging may predict the location of viable tissue that is at risk for future infarct. The ischemic penumbra is that region that may then be salvaged by appropriate treatment.

Validation

The difficulties and assumptions required to obtain semiquantitative measures of CBV, CBF, and MTT traditionally have precluded absolute quantitation from the clinical setting. Several studies have compared perfusion parameters acquired via DSC-MRI techniques with those from single photon emission computed tomography (SPECT), CT, and PET. Ostergaard et al. compared DSC-MRI with $H_2^{15}\text{O}$ PET estimates of rCBF in six normal subjects and derived a linear regression factor of 0.87 between the methods (59). MRI estimates of rCBV were slightly higher than those found via PET. rMTT values in this study were equivalent between DSC-MRI and $H_2^{15}\text{O}$ PET acquisitions. A similar study found that DSC estimates of rMTT were approximately 30% lower than those obtained by PET (60). DSC-MRI measures of rMTT are more accurate than rCBV or rCBF estimates as they are formed from the ratio of two parameters. Various constants and scaling factors cancel out producing a more accurate estimation of rMTT via DSC-MRI.

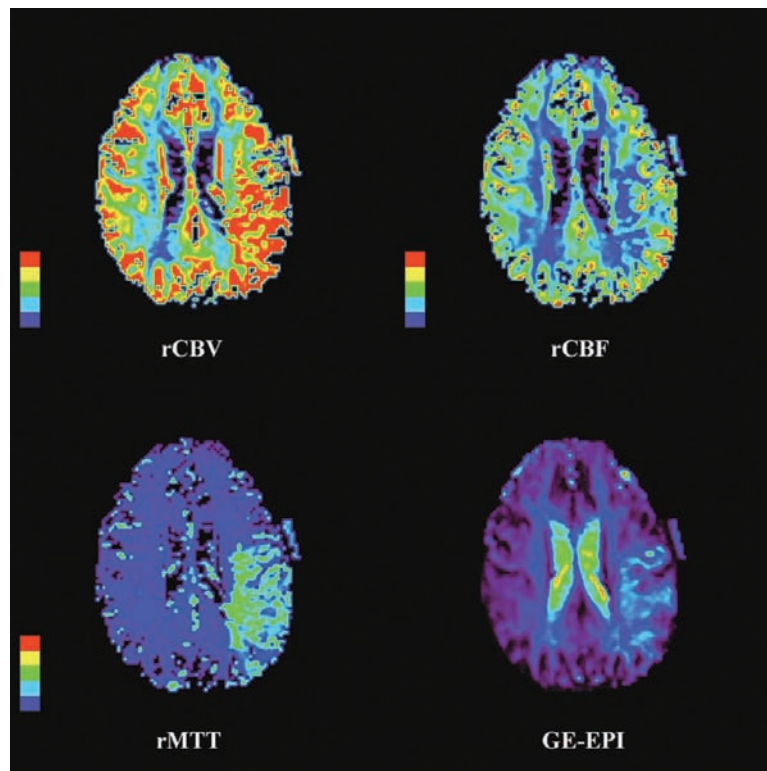


Figure 13 DSC perfusion-weighted imaging parametric maps. DSC perfusion maps are shown from a 62-year-old female presenting with a left MCI stroke. Data were acquired at 3.0 T with parameters given in Table 1. The AIF was chosen as a single voxel from the right ICA. Increased rMTT can be clearly seen in the region of infarct. Abbreviations: DSC, dynamic susceptibility contrast; MCA, middle cerebral artery; ICA, internal cerebral artery; rMTT, regional mean transit time.

ASL MRI

ASL utilizes knowledge of the inflow of magnetically labeled or “tagged” blood into a region of interest to derive a semiquantitative measure of rCBF (34). Labeled blood flowing into the tissue of interest exchanges spins with the water molecules in the surrounding tissue, altering the resulting magnetization in the region. Images are acquired with and without spin labeling and are subtracted to generate a perfusion-weighted imaging. Endogenous blood water is assumed to be a freely diffusible tracer except that ASL is only sensitive to the rate of delivery and not to exchange and clearance of the tracer such as with H_2^{15}O PET (61). A monoexponential flow-dependent exchange term describing single compartmental tracer kinetics is added to the Bloch equations as shown below:

$$\frac{dM_t(t)}{dt} = \frac{M_{t,0} - M_t(t)}{T_{1t}} + rCBF \left(M_a(t) - \frac{M_t(t)}{\lambda} \right) \quad (22)$$

All measures of rCBF result from the solution of the steady-state magnetization as given by a modified version of the Bloch equations.

ASL differs from DCE and DSC techniques in that no injection of an exogenous contrast agent is administered, making ASL completely noninvasive. This allows ASL to acquire serial studies on the same patient, which cannot be done using DCE or DSC methods. Similarly, patients with renal pathologies, pediatric patients, or those with allergies to contrast may be imaged with ASL. Additionally, semiquantitative estimates of rCBF are produced without subjective determination of voxels representing an AIF or the need for deconvolution techniques. The fast exchange of the tagged spins with neighboring water molecules in the tissue is also assumed as in DCE and DSC methods. However, ASL cannot provide estimates of rCBV or rMTT, which have proven clinical significance in assessment of stroke, tumor, and other CNS diseases.

Advantages in acquiring perfusion images using ASL include a higher spatial resolution than DSC images typically acquired using EPI techniques. Higher anatomic resolution of perfusion maps is a benefit in diagnosis of cerebral vascular diseases as well as in delineating regions of abnormal flow in infarct or tumor systems. Additionally, estimates of rCBF may provide complementary information to that of the BOLD effect in fMRI. The BOLD effect

does not directly measure neuronal activation but the hemodynamic response, which is governed by CBF, CBV, and cerebral metabolic rate of oxygen (CMRO₂) (62). Regions of increased CBF, caused by breathing CO₂, produce reduced levels of the BOLD response compared with identical stimuli under normal conditions (62). Correctly interpreting fMRI data relies on understanding the interaction between neuronal activation and the underlying factors affecting the hemodynamic response.

ASL Acquisition Methods

Although there are several ASL methods in use today, the basic underlying mechanisms are the same. Arterial blood flowing into the slice of interest is inverted by 180° and relaxes at a rate given by T_1 . A delay is given and a tagged image is acquired that incorporates signal from static tissue as well as tagged blood that has entered the slice during the delay time. A “control” image is then acquired in which blood entering the slice has not been inverted. The tagged image is subtracted from the control image to yield a perfusion-weighted image with intensities related only to the effects of the inflowing blood while removing those of static tissue. A typical increase in signal intensity compared with that of static tissue is only 1%, and repeated measurements must be performed and averaged to obtain an adequate signal-to-noise ratio (61).

Continuous ASL Methods

The two ASL methods in use today are continuous (CASL) and pulsed (PASL) techniques. Advantages, limitations, and assumptions differ between methods and will be discussed. Williams and Detre et al. first utilized CASL in the rat brain to determine estimates of rCBF under normocapnic conditions (63,64). Initially a train of RF pulses was used to saturate inflowing blood which then freely exchanged with water molecules in the capillary bed. Current CASL methods apply continuous adiabatic 180° inversion pulses to the major arterial vessels feeding the brain (34). As the spins are continuously inverted, they reach a steady-state level of magnetization, which is directly related to the rCBF in the region. This method provides a factor-of-2 increase in signal compared with that obtained via saturation pulses. rCBF may be estimated using the following equation that remains central to ASL.

$$rCBF = \frac{\lambda}{T_{\text{lapp}}} \frac{M_{\text{control}} - M_{\text{tagged}}}{2M_{\text{control}}}, \quad (23)$$

where λ represents the brain-blood partition coefficient quantifying the distribution of water between intravascular and extravascular compartments and is given the value of 0.9 mL/g (65). The partition coefficient has been

reported to have different regional values throughout the brain as well as variances with hematocrit levels. The apparent T_1 of tissue as altered by the labeled blood is given by $T_{1\text{app}}$. The longitudinal magnetization per gram of brain tissue for the control and tagged acquisitions (M_{control} , M_{tagged}) reflect values of MRI signal intensity (66).

CASL techniques suffer from two inherent problems related to transit time and magnetization transfer effects. The transit time is defined as the time it takes the labeled spins to travel from the labeling plane to the imaging plane. This time is nonzero, and T_1 relaxation effects may produce underestimations of rCBF in regions of reduced flow (34). Additionally, a long (two to four seconds) off resonance RF pulse is applied to label the spins. This produces magnetization transfer (MT) effects, saturating macromolecules in the imaging slice, and thereby reducing the contrast between the control and tagged images. These effects are only seen in the tagged image and not in the control image, complicating quantitation of flow.

Alsop et al. proposed an alternative solution to these problems by introducing a fixed delay time between the end of the labeling period and the image acquisition (67). A delay of between 0.9 and 1.5 seconds renders the CASL technique almost invariant to transit time delays (68). Greater time delays may be chosen for patients known to have reduced flow, collateral flow, or cerebrovascular disease. Although this delay reduces contrast between the control and tagged images, if the delay time is greater than the arterial transit times in the image, then the resulting rCBF will be almost completely invariant to delays in transit times. A clinical example of this technique is shown in Figure 14, showing rCBF perfusion maps in glioblastoma patients using the CASL technique. Figure 14A shows 32 slices acquired at 3.0 T with 3.8-mm³ isotropic resolution over the entire brain. Comparison of rCBF maps with static postcontrast T_1 -weighted images shows representative tumor slices with increased rCBF throughout the lesion.

Pulsed ASL Methods

Pulsed ASL techniques vary from CASL methods in the manner by which the spins of the inflowing blood are tagged prior to entering the imaging slice. CASL continuously labels a single thin slice using saturation or inversion pulses. PASL sequences apply a single short (< 10 ms) adiabatic pulse over a thick (10–15 cm) slab, minimizing MT effects. However, imperfections in the slice profile of the adiabatic pulse will produce incomplete subtraction of the static tissue (61). Edelman et al. proposed the first PASL sequence, echo-planar imaging with signal targeting using alternating RF (EPISTAR), to measure rCBF in hypercapnic pigs (69). In EPISTAR, the inversion pulse is applied proximal to the tagging plane and applied again distal to the control plane to

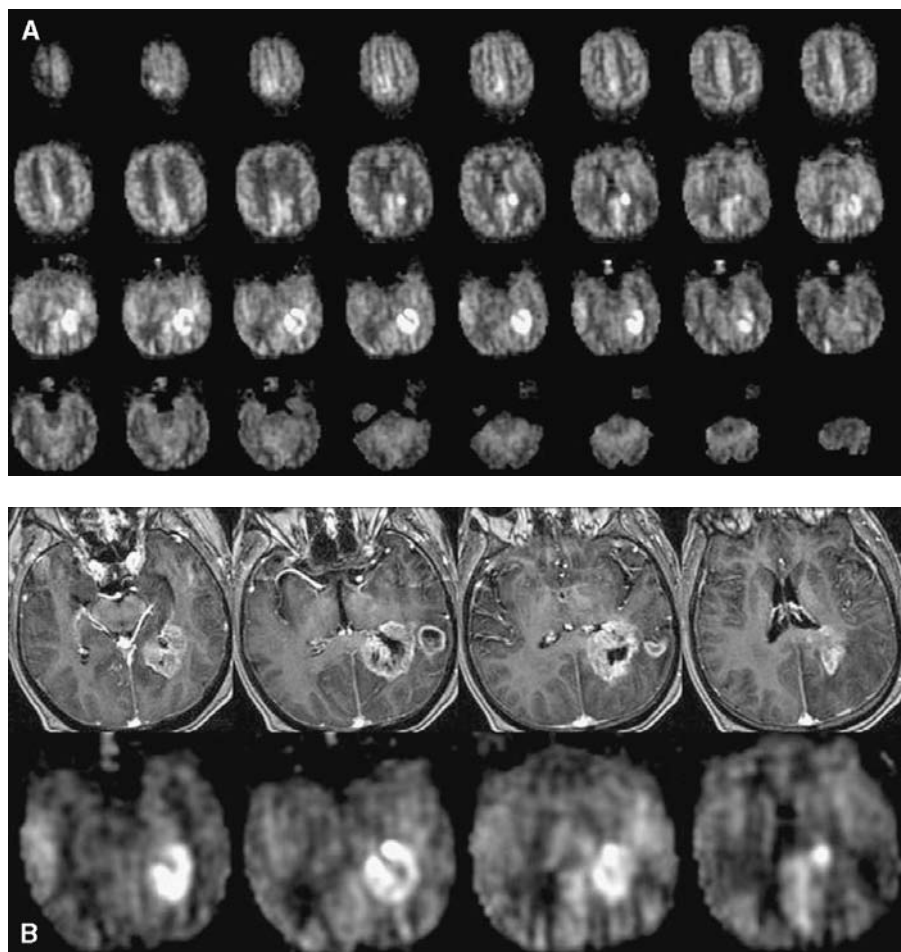


Figure 14 rCBF parametric images are generated using ASL techniques in a patient with a glioblastoma. Data were acquired at 3.0 T using a 3-D fast SE sequence with 3.8-mm isotropic resolution. **(A)** Images were acquired at 6-mm intervals covering the entire brain. **(B)** Regions of increased rCBF in the tumor as seen in the ASL study are displayed beneath static T₁-weighted postcontrast images. ASL measures of rCBF provide complementary information on tissue perfusion to that gained from static imaging methods. Abbreviations: SE, spin echo; rCBF, regional cerebral blood flow; ASL, arterial spin labeling. Source: David Alsop, Ph.D., Beth Israel Deaconess Medical Center/Harvard Medical School.

produce identical MT effects. A subsequent PASL sequence utilizing flow alternating inversion recovery (FAIR) was proposed that compensated for MT effects because of the symmetric nature of the sequence (68,70,71). A nonselective inversion pulse labels inflowing spins while the control image uses a concurrent slice-selective gradient pulse.

Difficulties in rCBF quantitation using PASL techniques arise from assumptions used in estimation of the arterial transit time (τ_a) *in vivo*. PASL acquires information on the transit time at a single inversion time point or assumes it to be zero throughout the region. These assumptions reduce the accuracy of rCBF measures and nullify comparative estimates of flow among various regions of the brain by assuming equivalent transit times in all voxels (68). These effects are compounded with

increased transit times seen in slow flow and pathologic vasculature. A solution to this difficulty may be obtained by sampling the transit time at multiple inversion times. This allows visualization of perfusion images at different transit times, creating a time course curve that may be fit using a compartmental model to estimate rCBF.

Method Comparisons and Difficulties

Comparison between continuous and pulsed ASL methods shows that CASL provides an advantage in signal-to-noise ratio over PASL. T₁ relaxation of the spins during the delay time in PASL contributes to this difference. CASL techniques can also be used to acquire more inferior slices than PASL, as only a single plane must be inverted. PASL

requires that the transmit RF field covers the entire imaging slab (61).

Clinical implementation of CASL typically produces a large amount of RF deposition, leading to increased specific absorption rates (SAR). At 3.0 T, this may tend to limit the application of a continuous RF pulse for an extended duration of time. A pulse train having a reduced duty cycle of 75% to 90% may be used to overcome this limitation (34).

The degree of inversion, or inversion efficiency, must also be accurately determined to produce semiquantitative estimates of rCBF using ASL techniques. The inversion efficiency is more velocity-dependent in CASL methods than PASL and may require calibration for each individual site. PASL inversion efficiencies remain upward of 97% at even high-flow rates such as 100 cm/sec. Typical CASL inversion efficiencies range from 80% to 95% across a clinically relevant range of flow velocities (68). Inversion efficiency is also dependent on angulation of the vessel and RF and gradient pulse characteristics (68). Partial volume contamination of voxels containing CSF may theoretically produce an underestimation of rCBF on the order of 30%, depending on the slice thickness. Both ASL methods assume that tagged blood fully exchanges with tissue water in the capillary bed, which may be incorrect in high flow-situations (Elster).

Validation

ASL methods provide a noninvasive estimate of rCBF *in vivo*, using continuous- or pulsed-labeling techniques. Validation of CASL methods in humans with H₂¹⁵O PET CBF

measurements showed a linear correlation between methods ($R = 0.85$). A nonsignificant 15% increase in ASL gray matter cortical rCBF values was seen in comparison with PET (72). Additionally, estimates of white matter rCBF values were 30% lower for ASL methods than those of PET. Transit time differences, BBB permeability and exchange and the assumption of equivalent partition coefficients in gray and white matter may all contribute to these differences. A similar validation study was performed in rats using quantitative autoradiography (QAR) (73). rCBF was estimated in rats with unilateral cerebral ischemia using both CASL and QAR methods. ASL results were linearly correlated with QAR estimates of flow. However, an overestimation of rCBF of 34% was observed in ASL methods compared with those of QAR.

A clinical application of comparing ASL methods with that of fluoro-2-deoxy-D-glucose (FDG)- PET is shown in Figure 15. Parkinson's disease (PD) is characterized by an abnormal metabolic PD-related spatial covariance pattern (PDRP), which is expressed in the FDG-PET of patients relative to healthy control subjects. PDRP scores (a measure of pattern expression) have been found to correlate with disease severity and duration (74–76). PDRP expression can also be quantified in radionuclide-based cerebral perfusion scans (77,78). In a pilot study, PD-related network activity was quantified in the ASL MRI scans of eight early-stage PD patients and four healthy volunteer subjects. The data in Figure 15A indicate that PDRP values computed in ASL MRI scans are similar to those obtained with FDG PET and could differentiate between the patient and control groups. The data in Figure 15B indicate that PDRP expression

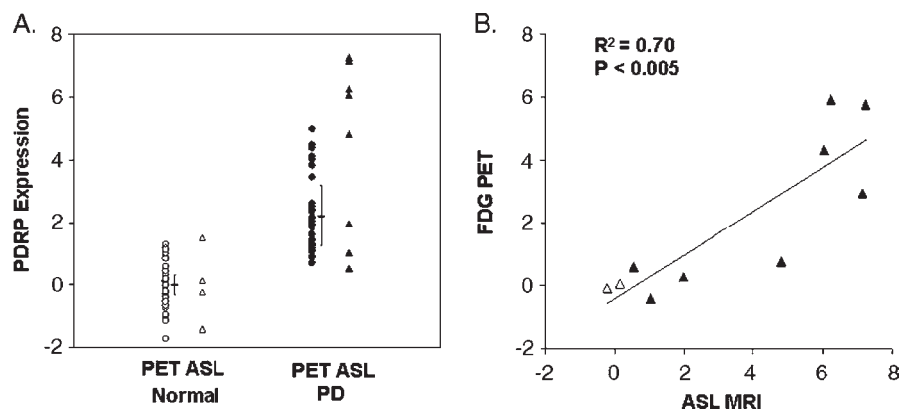


Figure 15 (A) Subject scores for the PDRP that was identified in the FDG PET scans of 30 PD patients (filled circles) and 30 control subjects (open circles). Accurate group discrimination ($p < 0.001$) was achieved with these pattern scores in the PET data. The expression of this disease-related pattern was subsequently computed in the ASL MRI scans of eight PD patients (filled triangles) and four control subjects (open triangles). These PDRP scores were similar to the values for each group that were obtained with FDG PET. (Error bars indicate standard errors for PDRP scores obtained by PET). (B) Correlation between PDRP scores computed prospectively in FDG PET and ASL MRI scans from the same subjects. A significant correlation ($p < 0.005$) was present between the two network measures. (Open circles denote normal volunteers; filled circles denote PD patients). Abbreviations: PD, Parkinson's disease; PDRP, PD-related spatial covariance pattern; FDG, fluoro-2-deoxy-D-glucose; PET, positron emission tomography; ASL, arterial spin labeling; MRI, magnetic resonance imaging. Source: David Eidelberg, M.D., North Shore—Long Island Jewish Medical System.

computed in the ASL MRI scans is highly correlated with values computed with FDG-PET. These preliminary results suggest that abnormal PDRP expression can be detected noninvasively using ASL MRI. This method may have potential use in image-based differential diagnosis as well as in the objective assessment of novel therapies for this disorder (79).

CONCLUSION

MR perfusion-weighted imaging offers the clinician a variety of tools to examine various CNS pathologies. Exogenous (DCE, DSC) or endogenous (ASL) techniques may be applied in a qualitative or semiquantitative manner, depending on the requirements. Factors affecting the choice of perfusion technique include the permeability of the vasculature within the region of interest as well as the perfusion parameters desired. Dynamic perfusion studies complement information gained by static contrast-enhanced imaging. They also provide novel information regarding the angiogenic properties of the tissue of interest. Although absolute quantitation of perfusion parameters using MRI is still being refined, the clinical utility of these techniques has been shown to increase diagnostic accuracy in multiple disease states, making them an essential part of a clinical protocol.

ACKNOWLEDGMENTS

The author would like to thank those researchers who provided additional figures illustrating clinical applications of MR perfusion imaging for this work: Paul Tofts, Brighton and Sussex Medical School; Meng Law, New York University School of Medicine; David Eidelberg, North Shore—Long Island Jewish System; and David Alsop, Beth Israel Deaconess Medical Center/Harvard Medical School. Additional appreciation goes to Thomas Yankelev, Vanderbilt University, for his help in editing this work.

REFERENCES

- Padhani AR. MRI for assessing antivascular cancer treatments. *Br J Radiol* 2003; 76 Spec No 1:S60–S80.
- Jackson A. Imaging microvascular structure with contrast enhanced MRI. *Br J Radiol* 2003; 76 Spec No 2:S159–S173.
- Muruganandham M, Lupu M, Dyke JP, et al. Preclinical evaluation of tumor microvascular response to a novel antiangiogenic/antitumor agent RO0281501 by dynamic contrast-enhanced MRI at 1.5 T. *Mol Cancer Ther* 2006; 5: 1950–1957.
- Hoang BH, Dyke JP, Koutcher JA, et al. VEGF expression in osteosarcoma correlates with vascular permeability by dynamic MRI. *Clin Orthop Relat Res* 2004; 426:32–38.
- Verstraete KL, Van der Woude HJ, Hogendoorn PC, et al. Dynamic contrast-enhanced MR imaging of musculoskeletal tumors: basic principles and clinical applications. *J Magn Reson Imaging* 1996; 6:311–321.
- Blaimer M, Breuer F, Mueller M, et al. SMASH, SENSE, PILS, GRAPPA: how to choose the optimal method. *Top Magn Reson Imaging* 2004; 15:223–236.
- Tofts PS, Brix G, Buckley DL, et al. Estimating kinetic parameters from dynamic contrast-enhanced T1-weighted MRI of a diffusible tracer: standardized quantities and symbols. *JMRI* 1999; 10:223–232.
- Taylor JS, Tofts PS, Port R, et al. MR imaging of tumor microcirculation: promise for the new millennium. *J Magn Reson Imaging* 1999; 10:903–907.
- Brix G, Semmler W, Port R, et al. Pharmacokinetic parameters in CND Gd-DTPA enhanced MR imaging. *J Comput Assist Tomogr* 1991; 15:621–628.
- Larsson HBW, Stubgaard M, Frederiksen JL, et al. Quantitation of blood-brain barrier defect by magnetic resonance imaging and gadolinium-DTPA in patients with multiple sclerosis and brain tumors. *Magn Reson Med* 1990; 16: 117–131.
- Tofts PS, Kermode AG. Measurement of the blood-brain barrier permeability and leakage space using dynamic MR imaging. 1. Fundamental concepts. *Magn Reson Med* 1991; 17:357–367.
- Verhoeve M, van der Sanden BP, Rijken PF, et al. Assessment of the neovascular permeability in glioma xenografts by dynamic T(1) MRI with Gadomer-17. *Magn Reson Med* 2002; 47:305–313.
- Hoffman U, Brix G, Knopp MV, et al. Pharmacokinetic mapping of the breast: a new method for dynamic MR mammography. *Magn Reson Med* 1995; 33:506–514.
- Tuncbilek N, Karakas HM, Altaner S. Dynamic MRI in indirect estimation of microvessel density, histologic grade, and prognosis in colorectal adenocarcinomas. *Abdom Imaging* 2004; 29:166–172.
- Esserman L, Hylton N, George T, et al. Contrast-enhanced magnetic resonance imaging to assess tumor histopathology and angiogenesis in breast carcinoma. *Breast J* 1999; 5:13–21.
- Degani H, Gusis V, Weinstein D, et al. Mapping pathophysiological features of breast tumors by MRI at high spatial resolution. *Nat Med* 1997; 3:780–782.
- Tofts PS. Modeling Tracer Kinetics in Dynamic Gd-DTPA MR Imaging. *JMRI* 1997; 7:91–101.
- Taylor JS, Reddick WE. Evolution from empirical dynamic contrast-enhanced magnetic resonance imaging to pharmacokinetic MRI. *Adv Drug Deliv Rev* 2000; 41:91–110.
- Donahue KM, Burstein D, Manning WJ, et al. Studies of Gd-DTPA relaxivity and proton exchange rates in tissue. *Magn Reson Med* 1994; 32:66–76.
- Pintaske J, Martirosian P, Graf H, et al. Relaxivity of Gadopentetate Dimeglumine (Magnevist), Gadobutrol (Gadovist), and Gadobenate Dimeglumine (MultiHance) in human blood plasma at 0.2, 1.5, and 3 Tesla. *Invest Radiol* 2006; 41:213–221.
- Parker GJ, Suckling J, Tanner SF, et al. Probing tumor microvasculature by measurement, analysis and display of contrast agent uptake kinetics. *J Magn Reson Imaging* 1997; 7:564–574.

22. Gowland P, Mansfield P, Bullock P, et al. Dynamic studies of gadolinium uptake in brain tumors using inversion-recovery echo-planar imaging. *Magn Reson Med* 1992; 26:241–258.
23. Parker GJ, Barker GJ, Tofts PS. Accurate multislice gradient echo T(1) measurement in the presence of non-ideal RF pulse shape and RF field nonuniformity. *Magn Reson Med* 2001; 45:838–845.
24. Yankelev TE, Rooney WD, Huang W, et al. Evidence for shutter-speed variation in CR bolus-tracking studies of human pathology. *NMR Biomed* 2005; 18:173–185.
25. Port RE, Knopp MV, Brix G. Dynamic contrast-enhanced MRI using Gd-DTPA: interindividual variability of the arterial input function and consequences for the assessment of kinetics in tumors. *Magn Reson Med* 2001; 45:1030–1038.
26. Kety SS, Schmidt CF. The nitrous oxide method for the quantitative determination of cerebral blood flow in man: Theory, procedure and normal values. *J Clin Invest* 1948; 27: 476–483.
27. Small SA. Quantifying cerebral blood flow: regional regulation with global implications. *J Clin Invest* 2004; 114: 1046–1048.
28. Weinmann HJ, Laniado M, Mutzel W. Pharmacokinetics of GdDTPA/dimeglumine after intravenous injection into healthy volunteers. *Physiol Chem Phys Med NMR* 1984; 16:167–172.
29. Ivancevic MK, Zimine I, Montet X, et al. Inflow effect correction in fast gradient-echo perfusion imaging. *Magn Reson Med* 2003; 50:885–891.
30. Dyke JP, Panicek DM, Healey JH, et al. Osteogenic and Ewing sarcomas: estimation of necrotic fraction during induction chemotherapy with dynamic contrast-enhanced MR imaging. *Radiology* 2003; 228:271–278.
31. Teifke A, Behr O, Schmidt M, et al. Dynamic MR imaging of breast lesions: correlation with microvessel distribution pattern and histologic characteristics of prognosis. *Radiology* 2006; 239:351–360.
32. Villringer A, Rosen BR, Belliveau JW, et al. Dynamic imaging with lanthanide chelates in normal brain: contrast due to magnetic susceptibility effects. *Magn Reson Med* 1988; 6:164–174.
33. Rosen BR, Belliveau JW, Vevea JM, et al. Perfusion Imaging with NMR Contrast Agents. *Magn Res Med* 1990; 14:249–265.
34. Calamante F, Thomas DL, Pell GS, et al. Measuring cerebral blood flow using magnetic resonance imaging techniques. *J Cereb Blood Flow Metab* 1999; 19:701–735.
35. Heiland S, Kreibich W, Reith W, et al. Comparison of echo-planar sequences for perfusion-weighted MRI: which is best? *Neuroradiology* 1998; 40:216–221.
36. Boxerman JL, Hamberg LM, Rosen BR, et al. MR contrast due to intravascular magnetic susceptibility perturbations. *Magn Reson Med* 1995; 34:555–566.
37. Simonsen CZ, Ostergaard L, Smith DF, et al. Comparison of gradient- and spin-echo imaging: CBF, CBV, and MTT measurements by bolus tracking. *J Magn Reson Imaging* 2000; 12:411–416.
38. Keston P, Murray AD, Jackson A. Cerebral perfusion imaging using contrast-enhanced MRI. *Clin Radiol* 2003; 58:505–513.
39. Cerebral MR Perfusion Imaging: Principles and Current Applications. A. Gregory Sorenson, P. Reimer, Georg Thieme Verlag, New York, 2001.
40. Barbier EL, Lamalle L, Decops M. Methodology of brain perfusion imaging. *JMRI* 2001; 13:496–520.
41. Leenders KL, Perani D, Lammertsma AA, et al. Cerebral blood flow, blood volume and oxygen utilization. Normal values and effect of age. *Brain* 1990; 113:27–47.
42. Baron JC. Perfusion thresholds in human cerebral ischemia: historical perspective and therapeutic implications. *Cerebrovasc Dis* 2001; 11:2–8.
43. Zierler KL. Equations for measuring blood flow by external monitoring of radioisotopes. *Circ Res* 1965; 16:309–321.
44. Meier P, Zierler KL. On the theory of the indicator-dilution method for measurement of blood flow and volume. *J Appl Physiol* 1954; 6:731–744.
45. Kiselev VG. On the theoretical basis of perfusion measurements by dynamic susceptibility contrast MRI. *Magn Reson Med* 2001; 46:1113–1122.
46. Knopp EA, Cha S, Johnson G, et al. Glial neoplasms: dynamic contrast-enhanced T2*-weighted MR imaging. *Radiology* 1999; 211:791–798.
47. Law M, Yang S, Babb JS, et al. Comparison of cerebral blood volume and vascular permeability from dynamic susceptibility contrast-enhanced perfusion MR imaging with glioma grade. *AJNR Am J Neuroradiol* 2004; 25: 746–755.
48. Speck O, Chang L, Itti L, et al. Comparison of static and dynamic MRI techniques for the measurement of regional cerebral blood volume. *Magn Reson Med* 1999; 41:1264–1268.
49. Diffusion and Perfusion Magnetic Resonance Imaging. Denis Le Bihan, editor. Raven Press, Ltd., New York, NY, 1995.
50. Mihara F, Kuwabara Y, Yoshiura T, et al. Semi-quantitative CBF and CBV ratios obtained using perfusion-weighted MR imaging. *Neuroreport* 2003; 14:725–727.
51. Rausch M, Scheffler K, Rudin M, et al. Analysis of input functions from different arterial branches with gamma variate functions and cluster analysis for quantitative blood volume measurements. *Magn Reson Imaging* 2000; 18: 1235–1243.
52. Manka C, Traber F, Gieseke J, et al. Three-dimensional dynamic susceptibility-weighted perfusion MR imaging at 3.0 T: feasibility and contrast agent dose. *Radiology* 2005; 234:869–877.
53. Akbudak E, Conturo T. Arterial input functions from MR phase imaging. *Magn Reson Med* 1996; 36:809–815.
54. van Osch MJP, Vonken EPA, Bakker CJG, et al. Correcting partial volume artifacts of the arterial input function in quantitative cerebral perfusion MRI. *Magn Reson Med* 2001; 45:477–485.
55. Rempp KA, Brix G, Wenz F, et al. Quantification of regional cerebral blood flow and volume with dynamic susceptibility contrast-enhanced MR imaging. *Radiology* 1994; 193:637–641.
56. Østergaard L, Weisskoff RM, Chesler DA, et al. High resolution measurement of cerebral blood flow using intravascular tracer bolus passages. I. Mathematical approach and statistical analysis. *Magn Reson Med* 1996; 36:715–725.

57. Østergaard L, Sorensen AG, Kwong KK, et al. High resolution measurement of cerebral blood flow using intravascular tracer bolus passages. II. Experimental comparison and preliminary results. *Magn Reson Med* 1996; 36: 726–736.
58. Wu O, Ostergaard L, Weisskoff RM, et al. Tracer arrival timing-insensitive technique for estimating flow in MR perfusion-weighted imaging using singular value decomposition with a block-circulant deconvolution matrix. *Magn Reson Med* 2003; 50:164–174.
59. Ostergaard L, Johannsen P, Host-Poulsen P, et al. Cerebral blood flow measurements by magnetic resonance imaging bolus tracking: comparison with [(15)O]H₂O positron emission tomography in humans. *J Cereb Blood Flow Metab* 1998; 18:935–940.
60. Ibaraki M, Ito H, Shimosegawa E, et al. Cerebral vascular mean transit time in healthy humans: a comparative study with PET and dynamic susceptibility contrast-enhanced MRI. *J Cereb Blood Flow Metab* 2007; 27:404–413.
61. Wong E, Buxton RB, Frank LR. Quantitative Perfusion Imaging Using Arterial Spin Labeling. *Neuroimaging Clin N Am* 1999; 9:333–342.
62. Buxton RB, Uludağ K, Dubowitz DJ, et al. Modeling the hemodynamic response to brain activation. *NeuroImage* 2004; 23:S220–S233.
63. Williams DS, Detre JA, Leigh JS, et al. Magnetic resonance imaging of perfusion using spin inversion of arterial water. *Proc Natl Acad Sci U S A* 1992; 89:212–216.
64. Detre JA, Leigh JS, Williams DS, et al. Perfusion imaging. *Magn Reson Med* 1992; 23:37–45.
65. Herscovitch P, Raichle ME. What is the correct value for the brain–blood partition coefficient for water? *J Cereb Blood Flow Metab* 1985; 5:65–69.
66. Questions & Answers in Magnetic Resonance Imaging. A. Elster, J. Burdette. Mosby, St. Louis, 2001.
67. Alsop DC, Detre JA. Reduced transit-time sensitivity in noninvasive magnetic resonance imaging of human cerebral blood-flow. *J Cereb Blood Flow Metab* 1996; 16: 1236–1249.
68. Petersen ET, Zimine I, Ho YC, et al. Non-invasive measurement of perfusion: a critical review of arterial spin labelling techniques. *Br J Radiol* 2006; 79:688–701.
69. Edelman RR, Siewert B, Darby DG, et al. Qualitative mapping of cerebral blood flow and functional localization with echo-planar MR imaging and signal targeting with alternating radio frequency. *Radiology* 1994; 192: 513–520.
70. Kwong KK, Chesler DA, Weisskoff RM, et al. MR perfusion studies with T1-weighted echo planar imaging. *Magn Reson Med* 1995; 34:878–887.
71. Kim SG. Quantification of relative cerebral blood flow change by flow-sensitive alternating inversion recovery (FAIR) technique: application to functional mapping. *Magn Reson Med* 1995; 34:293–301.
72. Ye FQ, Berman KF, Ellmore T, et al. H(2)(15)O PET validation of steady-state arterial spin tagging cerebral blood flow measurements in humans. *Magn Reson Med* 2000; 44:450–456.
73. Ewing JR, Cao Y, Knight RA, et al. Arterial spin labeling: validity testing and comparison studies. *J Magn Reson Imaging* 2005; 22:737–740.
74. Eidelberg D, Moeller JR, Dhawan V, et al. The metabolic topography of parkinsonism. *J Cereb Blood Flow Metab* 1994; 14:783–801.
75. Eidelberg D, Moeller JR, Ishikawa T, et al. Assessment of disease severity in parkinsonism with fluorine-18-fluorodeoxyglucose and PET. *J Nucl Med* 1995; 36: 378–383.
76. Asanuma K, Tang C, Ma Y, et al. Network modulation in the treatment of Parkinson's disease. *Brain* 2006; 129:2667–2678.
77. Ma Y, Tang C, Spetsieris PG, et al. Abnormal metabolic network activity in Parkinson's disease: test-retest reproducibility. *J Cereb Blood Flow Metab* 2007; 27:597–605.
78. Eckert T, Van Laere K, Lewis DE, et al. Quantification of PD-related network expression with ECD SPECT. *Eur J Nucl Med Mol Imaging* 2007; 34:496–501.
79. Spetsieris PG, Ma Y, Dhawan V, et al. Highly automated computer-aided diagnosis of neurological disorders using functional brain imaging. *Proceedings of the International Society for Optical Engineering*, 2006; 6144: 61445M1–12.
80. Quantitative MRI of the Brain: Measuring Changes Caused by Disease. Paul Tofts, editor. John Wiley & Sons LTD., Sussex, England, 2003.

Perfusion Imaging: Physical Principles and Applications in the Brain

MENG LAW

Departments of Radiology and Neurosurgery, Mount Sinai Medical Center, New York, New York, U.S.A.

INTRODUCTION

PATHOPHYSIOLOGY OF BRAIN TUMOR PERfusion: ANGIOGENESIS AND VASCULAR PERMEABILITY

Perfusion MRI is able to characterize brain tumor biology and other central nervous system (CNS) disorders due to the underlying pathologic and physiologic changes that occur with tumor vasculature. Although the biology underlying brain tumor angiogenesis and vascular recruitment along with the feedback loop with tumor hypoxia and necrosis are extremely complex, there are some physiologic mechanisms that can be quantified using perfusion MRI. In particular, there are some perfusion metrics that can be used as surrogate markers of tumor angiogenesis and vascular permeability. The previous chapter describes the various techniques available for acquiring perfusion MRI data. The two major techniques currently used in both clinical and research settings are a T1-weighted steady-state dynamic contrast-enhanced MRI (DCE MRI) and a T2*-weighted dynamic susceptibility contrast (DSC) MRI (DSC MRI) method. The advantages and disadvantages of each technique with regard to characterizing tumor biology will be discussed; however, the majority of clinicians and investigators are currently utilizing the DSC MRI technique for brain tumor perfusion MRI.

The effects of vascular endothelial growth factor/vascular permeability factor (VEGF/VPF) and other growth factors on vascular permeability have been under investigation since Folkman first described the association of tumoral growth with angiogenesis (1). Recent evidence suggests that vascular permeability and the presence of VEGF/VPF are important mediators of tumor growth in addition to angiogenesis (2–4). There has been recent interest also in the characterization of vascular permeability in brain tumors. Perfusion MRI can now measure parameters such as cerebral blood volume (CBV) and vascular permeability, which can be directly correlated with these histopathologic changes (5–7). The metrics that have been utilized to measure brain tumor perfusion include relative CBV (rCBV), cerebral blood flow (CBF), mean transit time (MTT), blood plasma volume (V_p) and vascular permeability (K^{trans}).

The relationship between some of these metrics can be described by the central volume theory equation:

$$\text{CBF} = \frac{\text{CBV}}{\text{MTT}}$$

In brain tumors, increases in vessel diameter, vessel wall thickness, and vessel number (microvascular density) should lead to increased CBV measurements taken with DSC MRI. The diameter of normal cerebral capillaries has a limited range of 3 to 5 μm , whereas cerebral capillaries of gliomas contain tortuous hyperplastic vessels ranging between 3 and

40 μm in diameter (2). Furthermore, the endothelial thickness in glioma vessels is approximately 0.5 μm versus 0.26 μm in normal cerebral vessels. The increase in vessel wall thickness reduces the cross-sectional luminal area of the vessels. As a result, one may expect reduced rCBV. However, gradient-echo sequences exploit the local paramagnetic susceptibility within the vessel lumen, the vessel wall, and surrounding tissues, resulting in intra- and extravascular spins undergoing reduction of T2* signal (8). In view of this, it is not surprising that rCBV measurements have been shown to correlate reliably with tumor grade and histologic findings of increased tumor vascularity (9–20).

The degree of vascular proliferation is one of the most critical elements in the histopathologic characterization of tumor biology and determination of prognosis for several reasons. First, the degree of vascular proliferation, or angiogenesis, is one of the most important histologic criteria (along with cellularity, mitosis, pleomorphism, and necrosis) for determination of the degree of malignancy and grade of a glioma. Second, vascular networks are not only the principal route for delivery of oxygen and nutrients to the neoplastic cells but also serve as paths for tumor infiltration along perivascular spaces. Third, the cerebral capillary endothelium (site of the blood-brain barrier, which is composed of a continuous homogeneous basement membrane, numerous astrocytic processes, and tight junctions, and an important host defense mechanism responsible for the regulation of movement of molecules) is frequently destroyed by malignant tumor cells. Fourth, a hyperpermeable blood-brain barrier associated with or without immature angiogenic vessels allows for contrast agent enhancement, extravasation, and hence, measurement of vascular permeability.

These pathophysiologic changes have been shown to provide good correlation between tumor biology and rCBV, CBF, CBV K^{trans} , and V_p measurements. Due to an increase in CBV from microvascular density, as well as many collateral and tortuous vessels (from angiogenesis), it is felt that the MTT should be prolonged. However, MTT may decrease because of the immense heterogeneity of the tumor microvasculature in some regions. MTT may also decrease because of increased CBF, particularly at the tumor margins, where there is rapid shunting of blood flow (21). These metrics and correlations will be further described.

IMAGING TECHNIQUES, PULSE SEQUENCES, PERfusion MODELS, TECHNICAL PITFALLS, ARTIFACTS, AND LIMITATIONS

Methodology for Brain Tumor Perfusion MRI

Dynamic Susceptibility Contrast-enhanced Perfusion MRI

The most common methods for measurement of DSC-enhanced perfusion MRI (DSC MRI) metrics in brain tumors are the indicator dilution methods for

nondiffusible tracers (22) and the pharmacokinetic modeling approach developed by Tofts and Kermode (23–25). In DSC MRI, the signal measured is due to the susceptibility T2 or T2* effect induced by the injected contrast agent.

Indicator Dilution Theory

The theory of nondiffusible tracer kinetics can be used to derive CBV values from the concentration-time curves. On injection of a contrast agent (gadopentetate dimeglumine), a signal intensity versus time curve is obtained. CBV is proportional to the area under the contrast agent concentration, signal intensity-time curve, in the absence of recirculation and contrast leakage. The gadopentetate dimeglumine concentration is proportional to the change in relaxation rate [i.e., change in the reciprocal of T2* ($\Delta R2^*$)], which can be calculated from the signal by using the following equation: $\Delta R2^* = [-\ln(SI_t/SI_0)/TE]$, where SI_t is the pixel signal intensity at time t , SI_0 is the precontrast signal intensity, and TE is the echo time (26). This equation is valid only if T1 enhancement associated with blood-brain barrier disruption has negligible effect on signal intensity, which can be achieved by using either a long repetition time, a small flip angle, or both, to reduce T1 effects. In general, the assumptions of negligible recirculation and contrast agent leakage are violated. The effects of this violation can be reduced by fitting a γ -variate function to the measured $\Delta R2^*$ curve. The γ -variate function approximates the curve that would have been obtained without recirculation or leakage. Despite this correction, CBV is overestimated in regions where there is blood-brain barrier disruption due to leakage and T1 effects. Therefore, in clinical practice, CBV measurements are made relative to the contralateral normal-appearing white matter, which acts as a standard internal reference. As a result, CBV measurements become a relative measure and is denoted by relative CBV or rCBV (and has no unit). In the literature, rCBV has also been utilized to denote regional CBV or CBV relative to an arterial input function. The term cCBV is also sometimes used to denote corrected CBV, which corrects for the effect of leakage on CBV measurements.

First-Pass Pharmacokinetic Modeling

First-pass pharmacokinetic modeling (FPPM) is used to calculate vascular permeability (K^{trans}) from the same DSC MRI data used to calculate rCBV. FPPM uses an exact expression for tissue contrast concentration, assuming that contrast exists in two interchanging compartments (plasma and extravascular extracellular space) (24,25). An estimate of vascular contrast concentration is acquired from normal white matter and fitted to the tissue

concentration expression to derive K^{trans} . Other notations utilized to denote endothelial vascular permeability include K_{ps} (endothelial transfer constant), K_{fp} , and K_2 . Color overlay maps of the fractional signal intensity drop at 25 seconds (25 seconds is chosen as an arbitrary time point from the bolus peak to represent vascular permeability) after the bolus (SD25 maps) can be calculated. If vascular permeability is high, residual contrast concentration is also high after the bolus has passed, and the SD25 value is also high. The SD25 maps therefore provide a simple index related to vascular permeability (27,28). However, it has been demonstrated that the blood flow through tumor vasculature is extremely variable and heterogeneous within any given region of a tumor (2,29). Indeed, there are multiple factors that can influence the leakiness of a blood vessel. These include body temperature, steroid administration, luminal surface area, permeability of the vessel wall, blood flow, and hydrostatic, interstitial, and osmotic gradients across the endothelium (2,29–31). Hence, K^{trans} may be underestimated if there is extremely slow flow or low hydrostatic/osmotic gradients in a group of extremely tortuous vessels or where there is substantial vasogenic edema.

Sequence Consideration—Spin-Echo Vs. Gradient-Echo DSC-Perfusion MRI

Gradient-echo sequences are much more sensitive in detecting paramagnetic changes in local magnetic susceptibility between vessels and the surrounding tissue, resulting in intra- and extravascular spins undergoing a reduction of T2*. The passage of gadolinium through the microvasculature results in changes in both T2 and T2* so that both spin-echo and gradient-echo sequences will provide reliable and reproducible CBV measurements. With a standard dose of contrast agent (0.1 mmol/kg of body weight), there is a transient signal loss of approximately 25% in normal white matter. T2-weighted spin-echo images are less sensitive and require a double or even quadruple dose of contrast agent to yield substantial signal changes during the bolus passage. Perfusion imaging at higher field strengths (3 T and above) can be performed using smaller doses of contrast agent.

The advantages of utilizing spin-echo sequences include less susceptibility to artifacts, particularly near the skull base or at brain-bone-air interfaces and the increased sensitivity to spin-echo perfusion to contrast within the capillaries (32). It has been demonstrated that spin-echo sequences are mainly sensitive to smaller vessels ($<20\ \mu m$) and hence may provide more optimal imaging of tumor capillaries. However, gradient-echo sequences appear to be sensitive to both capillary and larger vessel perfusion (12,33). At our institution, echo-planar gradient-echo imaging provides excellent signal to

noise using a standard dose of contrast (0.1 mmol/kg of body weight, typically 20 mL of contrast) for brain tumor perfusion studies. Susceptibility artifact can be reduced by reducing slice thickness (12,34). The degree of susceptibility effect using 0.1 mmol/kg of gadolinium with gradient-echo sequences is similar in magnitude to using 0.2 mmol/kg with spin-echo sequences (32). The echo-planar imaging (EPI) also allows for at least 10 MR slices or sections at one-second intervals providing good spatial and temporal resolution. With new parallel imaging techniques, more rapid scan times can be achieved for whole-brain coverage and be achieved using both rapid gradient-echo and spin-echo techniques.

First-Pass T2* DSC MRI Vs. Steady-State T1 DCE MRI (Combined Approach)

Due to the complexity of angiogenesis, the accuracy and reproducibility of different perfusion MRI techniques for the measurement of vascular permeability has been under discussion recently. The primary issues are that vascular permeability may be “nonflow limited” or “flow limited” (35) and that the first pass of contrast measures only the permeability in the first pass that is likely to be different to permeability measured in the steady state, where measurement of bidirectional exchange between two interchanging compartments (plasma and extravascular extracellular space) can be characterized.

Recently Cha et al. compared vascular permeability measurements, K^{trans} , using steady-state T1-weighted (ssT1) with a first-pass T2*-weighted (fpT2*) MRI methods in gliomas and meningiomas (36). There are theoretical and practical considerations that were outlined in this study, which are summarized in Table 1. Our study demonstrates that the microvascular permeability measurements, K^{trans} , derived from ssT1 and fpT2* methods were more predictive of glioma grade than rCBV derived from fpT2* method. The fpT2* K^{trans} was highly correlated with ssT1 K^{trans} in gliomas but not in meningiomas likely because of extremely leaky vessels in meningiomas, which complicate K^{trans} calculation by using both methods. In tumors that are extremely permeable, the assumptions and algorithms utilized for measuring K^{trans} may be affected. Further investigation is likely to demonstrate two types of vascular permeability, very high permeability (which is flow related and can be characterized in the first pass) versus lower permeability (which is non-flow limited and more proportional to the surface area product that may be characterized using steady-state techniques). As a result some centers are utilizing both ssT1 and fpT2* methods for obtaining perfusion metrics in gliomas (37).

Table 1 Comparison Between ssT1 and fpT2* Methods: Theoretical and Practical Considerations

	ssT1 method	fpT2* method
Theoretical considerations		
Shape of contrast agent concentration-time curve	Biexponential decay	γ variate
Concentration of intravascular contrast agent	Lower	Higher
K^{trans} for normal brain tissue	Zero	Negligible or very small, but not zero
Rate of contrast agent movement from intravascular to extravascular space within a single voxel of tissue	Slower	Faster
Practical considerations		
Spatial resolution	Higher	Lower
Subjectivity to susceptibility artifact	No	Yes
Imaging time	Longer (>6 min)	Shorter (<1.5 min)
Postprocessing algorithm complexity	Higher	Lower

Abbreviations: ssT1, steady-state T1-weighted; fpT2*, first-pass T2*-weighted.

Source: From Ref. 36.

Technical Pitfalls and Limitations

Even though DSC MRI is the most commonly utilized and easily applied technique for studying brain tumor perfusion, there are a number of important limitations of using a gradient-echo sequence (38). First, because the technique is weighted to measure susceptibility, it is extremely sensitive to structures of lesions that cause magnetic field inhomogeneity such as blood products, calcium, bone, melanin, metals, or lesions near the brain-bone-air interface such as the skull base. This becomes important in characterizing both high-grade gliomas (HGG) where sometimes there are blood products as well as low-grade gliomas (LGGs) where there may be calcification present. Solutions to reduce the inhomogeneity and susceptibility include decreasing the slice thickness, which also reduces the signal to noise ratio (SNR) and slice coverage. Parallel imaging methods can also reduce both susceptibility and the scan time to allow for more brain coverage and SNR. If there is a larger lesion that requires increased brain coverage, then the interslice gap can be increased while maintaining thinner

slices to reduce susceptibility. Second, as discussed above, the quantification of perfusion metrics such as CBV and K^{trans} can be inaccurate in lesions where there is a very leaky blood-brain barrier, such as glioblastoma multiforme, choroids plexus tumors, and meningiomas. Therefore, extremely low- or high-perfusion values must be taken with caution. Third, DSC MRI and DCE MRI require high-performance gradients, ultrafast EPI techniques, and a power injector. These can be issues in terms of acquiring the hardware and also workflow in a busy clinical environment. Last, the algorithms for postprocessing ssT1 perfusion data are not trivial and may require the knowledge and technical assistance of an MR physicist.

BRAIN TUMOR CLINICAL MRI PROTOCOL

Typical parameters for brain tumor imaging at 1.5 T are shown in Table 2. The imaging parameters utilized at our institution for DSC MRI are repetition time (TR)/TE:1000/54; field of view, 210 × 210 mm; section thickness, 3 to 8 mm (typically 5 mm); matrix, 128 × 128; in-plane voxel size, 1.8 × 1.8 mm; intersection gap, 0% to 30%; flip angle, 30°; signal bandwidth, 1470 Hz/pixel. Ten slices are usually obtained to cover the entire lesion volume as identified on T2-weighted images. A series of 60 multi-slice acquisitions are acquired at one-second intervals. The combination of a 1000-ms repetition time and a 30° flip angle ensures that T1 effects are minimized. The first 10 acquisitions are performed prior to the contrast agent injection to establish a precontrast baseline. At the 10th acquisition, gadopentetate dimeglumine (0.1 mmol/kg) is injected with the power injector at a flow rate of 3 to 5 mL/sec through the intravenous catheter (18–22 gauge), the contrast agent injection is immediately followed by a bolus injection of saline (total of 20 mL at the same rate) (12,28,39–41).

CLINICAL APPLICATIONS OF PERFUSION MRI

Primary Gliomas

Histologic Grading: Limitations with Neuropathology and WHO Classification in Measuring Tumor Angiogenesis with CBV, CBF, and Permeability

In 2000, World Health Organization (WHO) revised the classification of CNS neoplasms. On the basis of the histologic features, this classification system is dependent on the visual assessment of the microscopic appearance of a tumor specimen. This raises concern for intraobserver and interobserver subjectivity. There have been numerous publications demonstrating the relatively low reproducibility of this system. Coons et al. demonstrated that four

Table 2 A Brain Tumor Imaging Protocol with Typical Parameters

Sequence	TR (ms)	TE (ms)	Flip angle /TI	Acq/NEX	Thickness (mm)	No. slices	Matrix	FOV (mm)	Acq time (min.sec)
Scout/localizer	15	6	NA	1	8	3	256	280	0.19
Axial T1	600	14	90	2	5	20	256	210	3.36
Axial FLAIR	9000	110	180/2500	1	5	20	256	210	3.56
Axial T2	3400	119	180	1	5	20	256	210	1.36
(1) Dual echo/PD	3400	16	180	1	5	26	256	256	7.59
Diffusion/ADC	3400	95	NA	3	5	20	128	210	1.15
(2) DTI ^a	4000	95	NA	4	5	20	128	210	1.56
DSC MRI	1000	54	30°	60 (1/s)	3 to 8	10	128	210	1
Post-Gd T1	600	14	90	1	5	20	256	210	3.36
MRSI	1500	144	90 2D CSI	3	10	1	16 × 16	160	6.05
		30	90 3D CSI	2	10	8	16 × 16	160	7.53
(3) MPRage ^a	1100	4.38	15	1	0.9	192	256	230	3.33

Total imaging time is approximately 30 minutes.

^aThe optional sequences are

(1) dual echo T2—PD for patients in a stereotactic headframe acquired instead of the FLAIR. Higher FOV and square FOV (256 × 256) to match the software in the operating room for stereotactic biopsy or resection. No angulation.

(2) DTI in 12 directions.

(3) MPRage—reconstructed in the axial, coronal, and sagittal planes.

These parameters are manufacturer specific at 1.5 Tesla. TI denotes inversion time.

Abbreviations: TR, repetition time; TE, echo time; Acq/NEX, acquisitions; FOV, field of view; Acq time, acquisition time; FLAIR, fast fluid-attenuated inversion recovery; PD, proton density; ADC, apparent diffusion coefficient; DTI, diffusion tensor imaging; DSC MRI, dynamic susceptibility contrast MRI; Post-Gd T1, postgadolinium T1; MRSI, MR spectroscopic imaging; MPRage, magnetization prepared-rapid gradient echo.

observer concordance is 52%, three observer concordance is 60%, and after three common reviews and agreement on pathologic features, the four observer concordance improved minimally to 69% and the three observer concordance to 75%. Furthermore, there are other issues affecting pathologic reproducibility that must also be considered. For example, (i) since only a few small samples of tissue are assessed, particularly from stereotactic biopsy, the most malignant portion of a tumor may not be sampled; (ii) it may be difficult to obtain a range of samples if the tumor is inaccessible to the surgeon (in eloquent brain); (iii) there are numerous classification/grading systems used among different institutions; and (iv) the dynamic nature of CNS tumors, with at least 50% dedifferentiating into more malignant grades (42–44).

Despite these shortcomings, the WHO classification scheme remains the standard reference for guiding therapy and predicting prognosis in patients with brain tumors. Recently, Law et al. (39) has compared the value of rCBV measurements in predicting tumor biology, using patient outcome as the gold standard. In this study, patients with the histopathologic diagnosis of LGG (from stereotactic biopsy and resection) could be stratified into two groups on the basis of rCBV. A Kaplan Meier curve (Fig. 1) demonstrated that lesions with rCBV less than 1.75 ($n = 16$) had a median time to progression of 4620 ± 433 days, and lesions with rCBV more than 1.75 ($n = 19$) had a

median time to progression of 245 ± 62 days ($p < 0.005$). Lesions with low baseline rCBV (<1.75) demonstrated stable tumor volumes when followed over time and lesions with high baseline rCBV (>1.75) demonstrated progressively increasing tumor volumes over time (Figs. 2 and 3). This demonstrates that perhaps rCBV measurements from DSC MRI may overcome some of the limitations of the current histologic methods to provide added value in predicting tumor biology.

Several studies have demonstrated that rCBV measurements have clinical utility in glioma grading. Comparison of rCBV measurements between LGG and HGG has demonstrated LGG to have maximal rCBV values of between 1.11 and 2.14 and HGG to have maximal rCBV values of between 3.54 and 7.32 (9,13,16,17, 41,45) (Table 3). These values have been significantly different statistically ($p = 0.05$ –0.0001). One study of 30 patients was able to differentiate between grade III/IV and grade IV/IV gliomas with rCBV values of 7.32, 5.84, and 1.26 for glioblastomas, anaplastic astrocytomas, and LGGs, respectively (17). A larger study ($n = 160$) demonstrated LGG to have rCBV values of 2.14 and HGG to have rCBV values of 5.18 (41).

DSC MRI increases the sensitivity and predictive value in predicting glioma grade compared with conventional contrast-enhanced MRI (41). In a comparison to conventional MRI and DSC MRI, sensitivity, specificity, positive

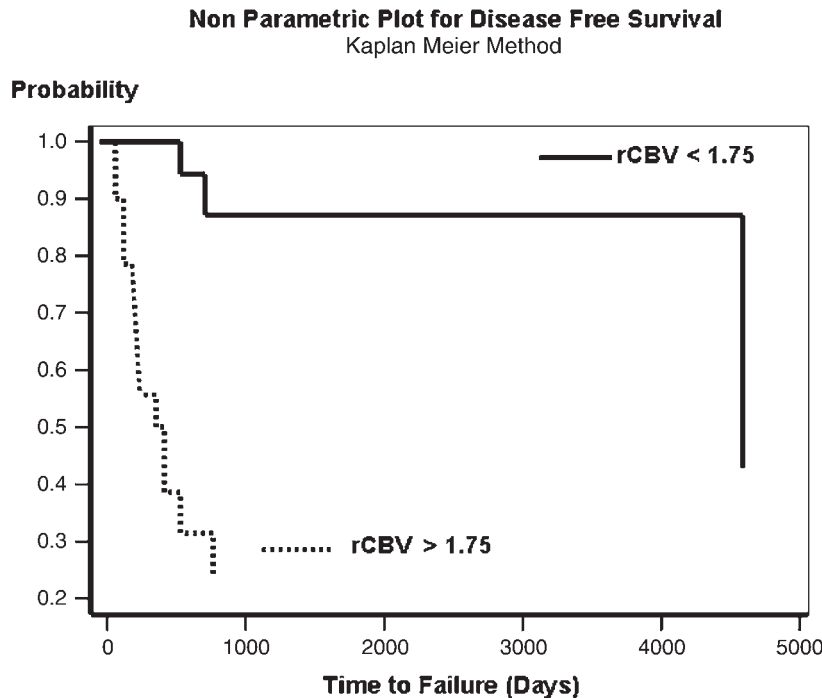


Figure 1 Kaplan-Meier survival curves for demonstrating the probability of time to progression at the most recent clinical follow-up. LGGs with $rCBV < 1.75$ had a median time to progression of 4620 ± 433 days (black solid curve which is far right shifted). LGGs with $rCBV > 1.75$ had a median time to progression of 245 ± 62 days (black dashed curve which is far left shifted) ($p < 0.005$). The data suggest that baseline $rCBV$ may be a stronger predictor of patient outcome than the initial histopathologic diagnosis because if these were all true LGGs, the median time to progression should be much longer than 245 days (eight months). Abbreviations: LGG, low-grade glioma; $rCBV$, relative cerebral blood volume. Source: From Ref. 39.

and negative predictive values of 72.5%, 65.0%, 86.1%, and 44.1 %, respectively, were obtained for conventional MRI in predicting an HGG compared with 95.0%, 57.5%, 87.0% and 79.3%, respectively, using $rCBV$ alone. In clinical practice, 95% to 100% sensitivity has been reported for differentiating high-grade from LGGs, using thresholds of 1.75 and 1.5 for $rCBV$, respectively (14,41). In the same studies, 57.5% to 69% specificity can be achieved using the same threshold values. Lev et al. (14) reviewed 32 consecutive glioma patients of whom 100% (13 of 13 astrocytomas) were correctly categorized as HGGs. Of the nine low-grade astrocytomas, seven were correctly classified. Law et al. (41) reviewed 160 glioma patients, of whom 120 were HGGs and 40 were LGGs. Using a different level of statistical error calculation, (16,41) threshold values of 2.93 and 2.97 from receiver-operating characteristic curve analysis were obtained in two independent studies (Table 3). The relatively lower specificity is due in part to the high number of false positives. A number of LGGs with elevated $rCBV$ can be misclassified as HGGs, giving more false positives.

The role of VEGF, also known as VPF, as a mediator of tumor growth and angiogenesis, has also resulted in a number of investigators demonstrating good correlation

between vascular permeability and glioma grade (5–7,46). LGGs demonstrate low permeability and HGGs demonstrate higher permeability (Figs. 4–7). However, measuring $rCBV$ and vascular permeability must be approached with some caution. Gliomas, particularly HGGs, are characterized by bizarre and extreme tortuosity in the morphology of the angioarchitecture. It has been demonstrated that the blood flow through the tumor vasculature is extremely variable and heterogeneous within any given region of a tumor (2,29). Indeed, there are multiple factors that influence the leakiness of a blood vessel. These include luminal surface area; permeability of the vessel wall; blood flow; and hydrostatic, interstitial, and osmotic gradients across the endothelium (29–31). Vascular permeability measurements may be underestimated if there is extremely slow flow or low hydrostatic/osmotic gradients in a group of extremely tortuous vessels or where there is substantial vasogenic edema.

Guiding Stereotactic Biopsy and Radiosurgery

The rationale for using perfusion MRI to guide stereotactic brain biopsy is again based on the utility of these techniques in defining the most vascular regions of the tumor,

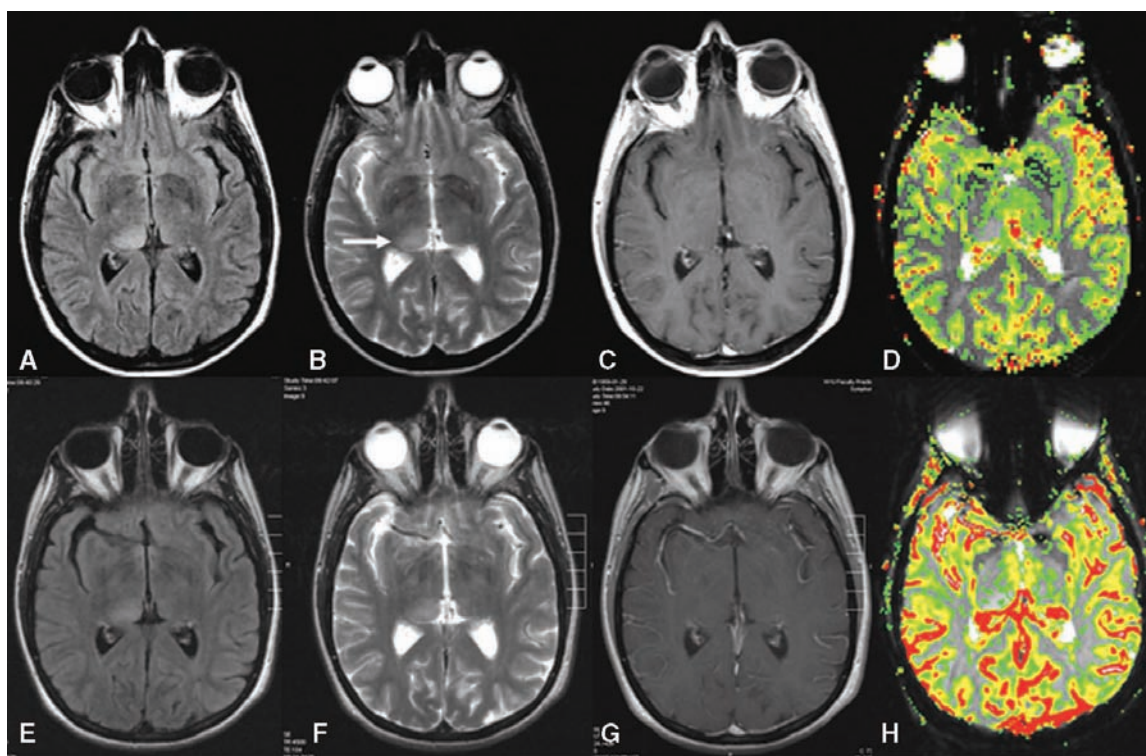


Figure 2 A 41-year-old female with a pathology proven LGG with a low baseline rCBV (1.42).

Top Row (A) Axial FLAIR image [9000/110/2500(TR/TE/TI)]. (B) Axial T2-weighted image (3400/119) shows increased signal within the posterior right thalamus with minimal mass effect (*arrow*). (C) Contrast-enhanced axial T1-weighted image (600/14) demonstrates subtle decrease in signal in the corresponding region without contrast enhancement. The lack of enhancement suggests a LGG on conventional MRI. (D) Gradient-echo (TR/TE 1000/54) axial DSC MRI image with rCBV color overlay map shows a lesion with relatively low perfusion with a rCBV of 1.42 in keeping with a LGG.

Bottom Row (E) MRI at 473 days (68 weeks) follow-up. Axial FLAIR image [9000/110/2500(TR/TE/TI)]. (F) Axial T2-weighted image (3400/119) both demonstrating very minimal change in tumor volume and signal abnormality. (G) Contrast-enhanced axial T1-weighted image (600/14) again demonstrating the lesion to be nonenhancing. Overall, remaining stable 473 days follow-up, suggesting a true low-grade lesion without malignant transformation/components. (H) Gradient-echo (TR/TE 1000/54) axial DSC MRI image, with rCBV color overlay map, shows a lesion with stable perfusion with a rCBV of 1.01. Abbreviations: LGG, low-grade glioma; FLAIR, fast fluid-attenuated inversion recovery; TR, repetition time; TE, echo time; rCBV, relative cerebral blood volume; MRI, magnetic resonance imaging; DSC MRI, dynamic susceptibility contrast MRI. Source: From Ref. 39.

particularly after radiation or chemotherapy (47). Most biopsies are guided with contrast-enhanced T1-weighted MR or CT images (48), which only reflect blood-brain barrier disruption and may not indicate the most malignant or vascular region of the tumor. Some institutions are utilizing chemical shift imaging (47) and perfusion imaging (12) to target regions of the highest cellularity and the highest vascularity, respectively. Often the region of highest vascularity and hence malignancy is found within the region of T2 signal abnormality and not necessarily within the region of contrast enhancement (Fig. 8). A decrease in CBV is able to predict treatment response to radiosurgery (RS) with a sensitivity of more than 90%. Tumor volume alone from contrast-enhanced MRI has a sensitivity of 64% (49).

Pilocytic Astrocytoma and Gliomatosis Cerebri

The prediction of tumor biology using perfusion MRI has a number of caveats. Generally, HGGs exhibit higher rCBV and K^{trans} ; however, pilocytic astrocytomas (JPA), which are designated as WHO grade I tumors can also have high rCBV and mimic HGGs (50), particularly if the enhancing nodule is sampled. Gliomatosis cerebri is characterized by involvement of at least two lobes of the brain by a glial cell tumor of neuroepithelial origin with relative preservation of neuronal architecture (51). Gliomatosis cerebri, which refers to the contiguous involvement of different regions of the brain must be differentiated from multicentric glioma that is defined as multiple foci of tumor in different sites. Histopathologically,

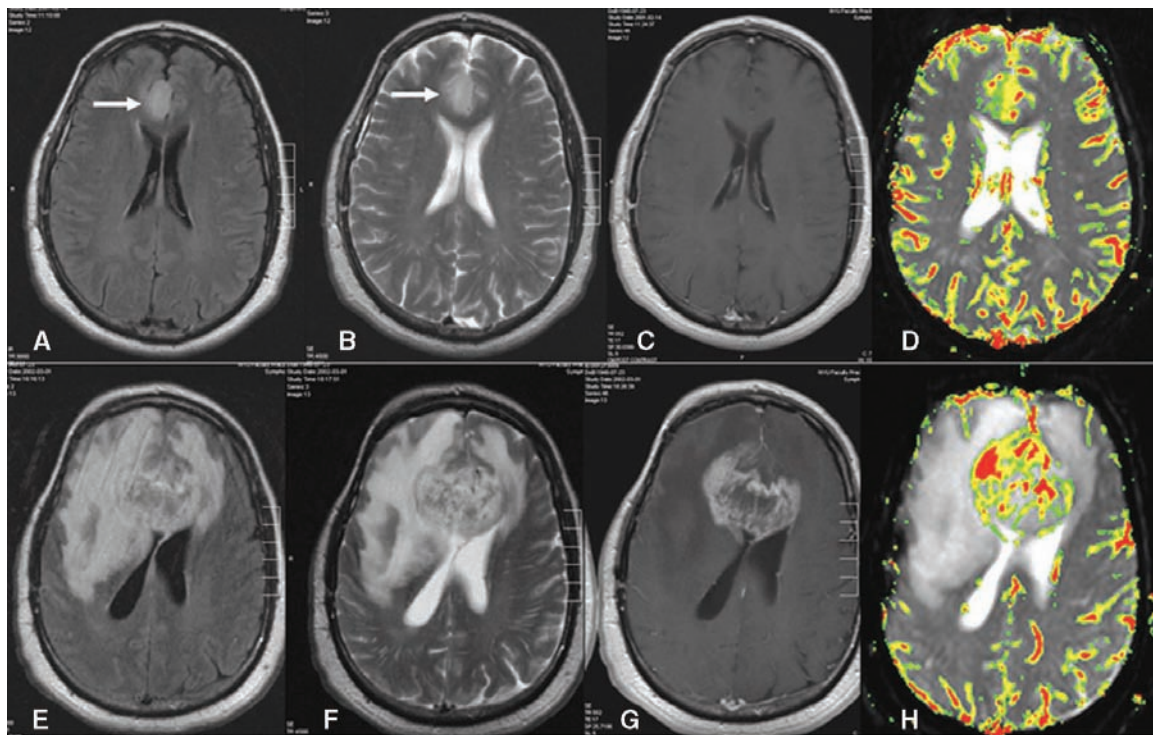


Figure 3 A 53-year-old male with pathology proven low-grade mixed oligoastrocytoma with a high baseline rCBV (4.29). **Top Row** (A) Axial FLAIR image [9000/110/2500(TR/TE/TI)]. (B) Axial T2-weighted image (3400/119) shows increased signal within the right mesial frontal lobe (arrow) with some mass effect on the adjacent genu of the corpus callosum. (C) Contrast-enhanced axial T1-weighted image (600/14) demonstrates no appreciable enhancement compatible with an imaging and pathologic diagnosis of LGG. (D) Gradient-echo (TR/TE 1,000/54) axial DSC MRI image, with rCBV color overlay map, shows a lesion with high initial perfusion with an rCBV of 4.23 more in keeping with an HGG than an LGG. **Bottom Row** (E) MRI at 127 days (18 weeks) follow-up. Axial FLAIR image [9000/110/2500(TR/TE/TI)]. (F) Axial T2-weighted image (3400/119) shows a substantial increase in tumor volume and volume of T2 signal abnormality by 220.97 cm³. There is now obvious evidence of tumor crossing the corpus callosum to the contralateral left frontal lobe. (G) Contrast-enhanced axial T1-weighted image (600/14) demonstrates an increase in enhancing tumor volume by 58.23 cm³. There is also more mass effect with almost complete effacement of the frontal horns. (H) Gradient-echo (TR/TE 1,000/54) axial DSC MRI image, with rCBV color overlay map, demonstrating progressively increasing rCBV from 4.23 to 13.37. Abbreviations: FLAIR, fast fluid-attenuated inversion recovery; LGG, low-grade glioma; DSC MRI, dynamic susceptibility contrast MRI; rCBV, relative cerebral blood volume; HGG, high-grade glioma; TR, repetition time; TE, echo time. Source: From Ref. 39.

Table 3 Differentiating Between Low-Grade and High-Grade Gliomas Using rCBV

Author (ref.)	Number (N)	Low-grade rCBV	High-grade rCBV	p value	Optimal threshold
Law et al. (41)	160	2.14	5.18	<0.0001	1.75/2.97 ^b
Sugahara et al. (17)	30	1.26	5.84/7.32 ^a	<0.002/<0.001 ^a	NA
Aronen et al. (9)	19	1.11	3.64	0.0001	NA
Knopp et al. (13)	29	1.44	5.07	0.001	NA
Yang et al. (45)	17	1.75	6.1	<0.05	NA
Shin et al. (16)	17	2.00	4.91	<0.05	2.93
Lev et al. (14) Range	32	NA 1.11–2.14	NA 3.64–7.32	NA	1.5

^a5.84 and 7.32 corresponds to rCBV values for anaplastic astrocytoma and glioblastoma multiforme, respectively.

^bThe values 1.75 and 2.97 are rCBV threshold values corrected for C2 and C1 type errors, respectively.

Abbreviations: rCBV, relative cerebral blood volume; NA, not available.

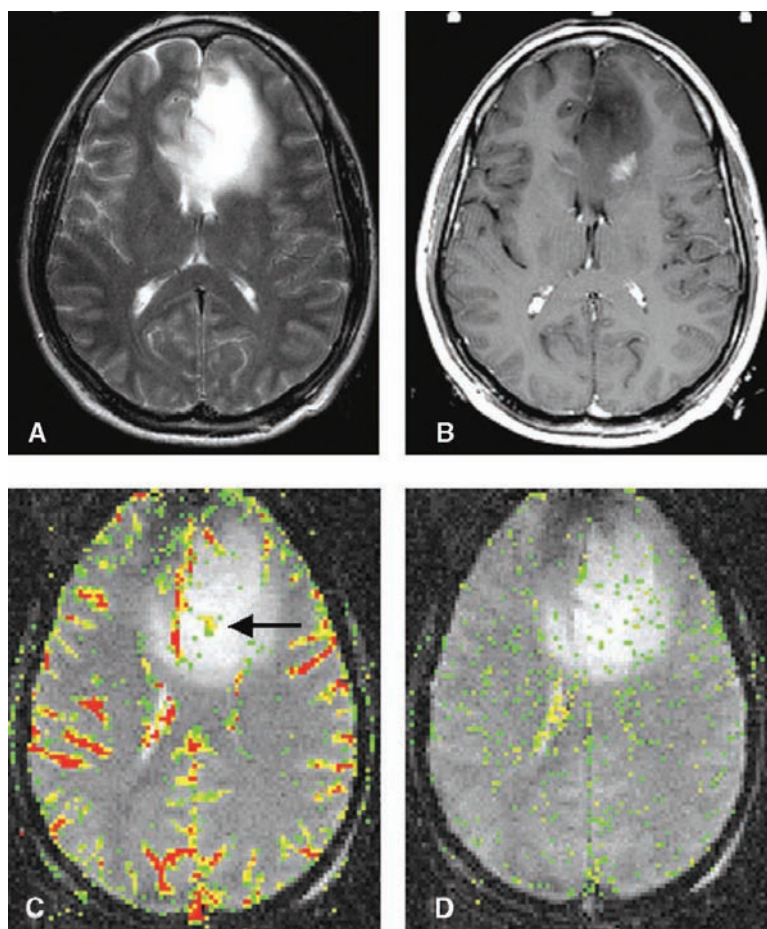


Figure 4 A 30-year-old woman with a low-grade astrocytoma (WHO Grade II). (A) T2-weighted image demonstrates bifrontal signal abnormality, centered primarily in the left frontal lobe. (B) T1-weighted postgadolinium image demonstrates an ill-defined focus of enhancement in the posterior aspect of the lesion. (C) Gradient-echo axial DSC MRI with (rCBV) color overlay map demonstrates a few foci of mildly elevated perfusion (arrow) that is seen in a different location to the region of maximal enhancement in Figure 2 (B). (D) SD25 color overlay map suggests low vascular permeability throughout the lesion. Abbreviations: rCBV, relative cerebral blood volume; DSC MRI, dynamic susceptibility contrast MRI. Source: From Ref. 28.

there is a lack of vascular hyperplasia in gliomatosis cerebri, which results in the relatively low rCBV measurements, mean 1.02 ± 0.42 (52). Normal Cho, elevated myo-Inositol, and decreased N-acetylaspartate has also been demonstrated with MR spectroscopy (MRS) in gliomatosis cerebri (53). The combination of these spectroscopy findings and reduced perfusion suggests that gliomatosis cerebri can be differentiated from high-grade multicentric glioma.

Therapeutic Monitoring

Therapy-Induced Necrosis and Recurrent Tumor

Treatment options for brain tumors include surgical resection, chemotherapy, and radiation therapy such as γ -knife RS, brachytherapy, and intensity-modulated radiation therapy. The differentiation of therapy-induced necrosis (by radiation or chemotherapy) from recurrent or residual tumor is

challenging. In the clinical setting it is best to simplify these two entities into two diagnoses that are potentially separable with DSC MRI, namely, delayed radiation necrosis (DRN)/ chemotherapy-induced necrosis versus recurrent tumor. Unfortunately, most of the time in clinical practice and also at histopathology, both of these entities coexist. After all, it is primarily in the setting of residual tumor that the patient is receiving adjuvant radiation or chemotherapy.

Some investigators have suggested, particularly in the first six months after initiation of treatment, that a combination of residual tumor and treatment effects or radiation leukoencephalopathy (RLE) must coexist in the same patient. By clinical definition, there must be residual disease within the surgical cavity for the patient to receive postoperative radiation therapy. Delayed radiation necrosis (DRN), however, is a very distinct entity from RLE and diffuse radiation injury. DRN results in vascular and myelin

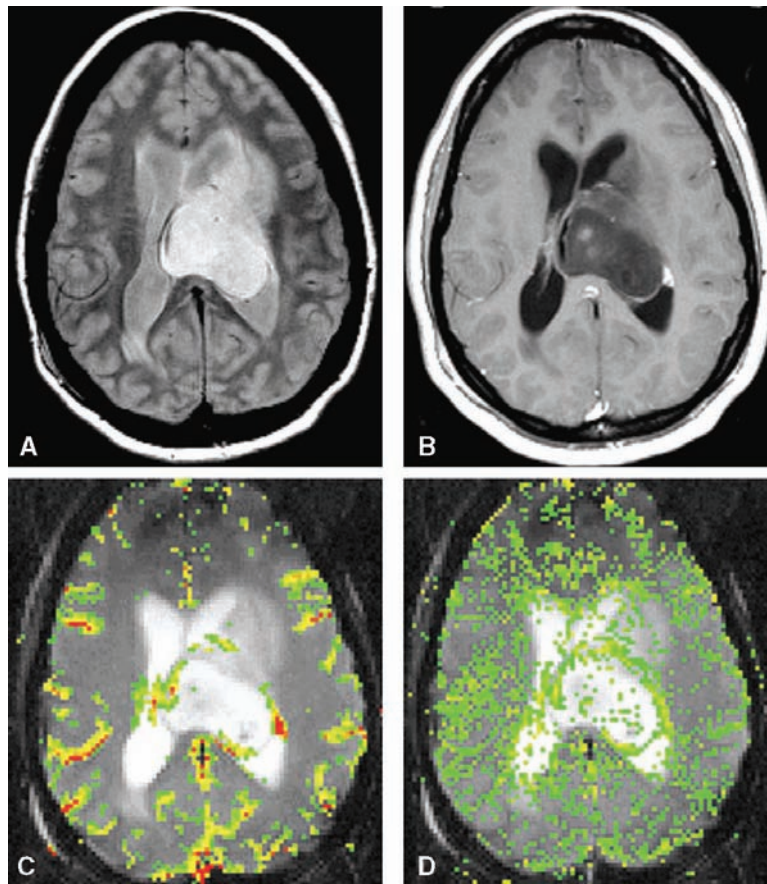


Figure 5 A 45-year-old woman with an anaplastic astrocytoma (WHO Grade III). **(A)** Proton density image demonstrates heterogeneous left-sided paraventricular lesion, extending into the left lateral ventricle. There is a small amount of vasogenic edema anterolaterally. **(B)** T1-weighted postgadolinium image demonstrates a small focus of peripheral enhancement. **(C)** Gradient-echo axial DSC MRI with relative rCBV map demonstrates elevated perfusion, on this occasion corresponding to the enhancing focus seen in Figure 3 **(B)**. **(D)** SD25 color overlay map suggests intermediate vascular permeability within the solid portions of this tumor. Abbreviations: rCBV, relative cerebral blood volume; DSC MRI, dynamic susceptibility contrast MRI. Source: From Ref. 28.

damage and occurs from a few months to several years and even decades after the end of therapy.

Posttherapeutic conventional MRI often depends on enhancement patterns, edema patterns, and interval change in dimensions to discriminate between gliosis, DRN, and recurrent tumor. These variables are often nonspecific and confusing. Six months following the initiation of therapy is when DSC MRI can help in determining if there is good or poor response to treatment. At any one point in time if there is substantial elevation in rCBV, there is recurrent tumoral disease (12,54,55).

DSC MRI is proving to be a sensitive technique in differentiating DRN, and maybe even RLE, from recurrent tumor (12,54,55). Histopathologically, DRN is an occlusive vasculopathy that results in ‘stroke-like episodes.’ Endothelial proliferation can be seen in the early phase of DRN, which may result in obliteration of the vessel lumen. The endothelial injury from radiation leads to fibrinoid necrosis

of small vessels, endothelial thickening, hyalinization, and vascular thrombosis.

Antiangiogenesis Therapies and Surrogate Biomarkers

DSC MRI has been utilized for evaluating antiangiogenic therapy of recurrent malignant glioma. In patients treated with carboplatin and thalidomide, the rCBV correlated better than conventional MRI with the clinical status of the patient and response to therapy (56).

More recently, we have demonstrated a decreased rCBV and K^{trans} in patients treated with Avastin (a new antiangiogenic agent). Interestingly, there appears to be a marked effect on reducing perfusion and contrast-enhancing tumor volume but an opposite effect on tumor cellularity. There is increasing evidence both pathologically and on imaging that tumors treated with antiangiogenic agents appear to behave more invasively. We have demonstrated, using diffusion imaging, that tumors treated

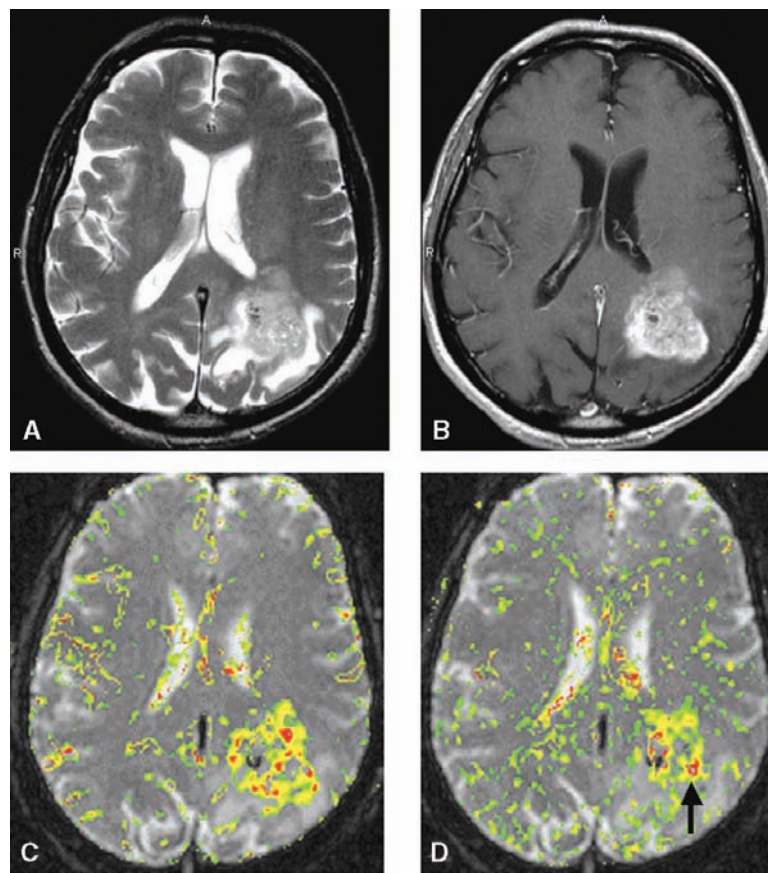


Figure 6 A 72-year-old man with a glioblastoma multiforme (WHO Grade IV). (A) T2-weighted image with a left parietal lesion demonstrating mass effect, edema, and signal heterogeneity, features of a glioblastoma multiforme. (B) T1-weighted postgadolinium image with extensive heterogeneous contrast enhancement. (C) Gradient-echo axial DSC MRI with rCBV map shows markedly elevated perfusion within the lesion. (D) SD25 color overlay map suggesting markedly elevated vascular permeability. Note that the areas of highest rCBV elevation do not correspond exactly with the regions of highest vascular permeability (arrow). Abbreviations: rCBV, relative cerebral blood volume; DSC MRI, dynamic susceptibility contrast MRI. Source: From Ref. 28.

with Avastin demonstrate a decrease in the diffusion [apparent diffusion coefficient (ADC)], which is thought to be correlated with increased tumor cellularity.

Oligodendrogloma and Correlation of Perfusion with Molecular Signatures

Numerous investigators have characterized the DSC MRI findings in oligodendroglial tumors. Oligodendroglomas are slowly growing, typically low-grade tumors. Oligodendroglomas have been shown to demonstrate high CBV even in the lower-grade tumors (57,58). The histologic appearance of oligodendroglomas consists of a dense network of branching capillaries that produce a vascular pattern resembling chicken wire in addition to the “fried-egg” appearance of the tumor cells, which in part accounts for the increase in rCBV (59,60).

The increased microvascular proliferation as indicated by the increased rCBV may also be partly responsible for

the chemosensitivity displayed by oligodendroglomas. Recently, there has been promise in the treatment of oligodendroglomas with the discovery of the association between 1p 19q chromosomal arm deletions and improved responsiveness to chemotherapy (61–63). Given that there is histopathologic and molecular evidence to support increased neovascularity in gliomas with oligodendroglial components, the association between 1p 19q deletions and increased perfusion seems to warrant further investigation. We found that elevated rCBV raises the possibility of a 1p 19q chromosomal deletion in human gliomas. Thus, rCBV may serve as an important physiologic imaging biomarker for identifying gliomas, with 1p 19q chromosomal deletions conferring higher chemosensitivity (Fig. 9). Furthermore, DSC MRI may provide non-invasive physiologic imaging markers of potential molecular signatures that identify microvascular proliferation, malignant transformation, patient outcome, and response to therapy.

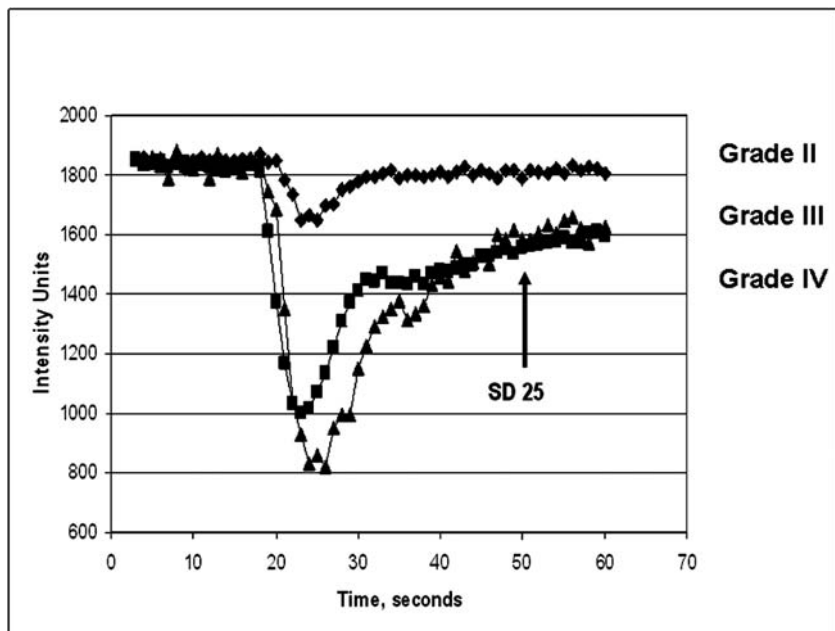


Figure 7 Typical normalized signal intensity curves for three different glioma grades. Grade II glioma (diamond) demonstrates a shallow perfusion signal intensity curve with the signal drop at 25 seconds (SD25) after the bolus peak, seen to be relatively close to the prebolus baseline, suggesting relatively low permeability. Grade III glioma (square) demonstrates a more substantial initial signal drop, indicating higher rCBV with slower return to baseline. SD25 is considerably larger than that seen in Grade II gliomas. Grade IV glioma (triangle) shows a larger area above the curve indicating very high rCBV with again a similarly delayed return to baseline, suggesting high vascular permeability. This figure suggests a positive correlation between rCBV and vascular permeability with glioma grade. Abbreviation: rCBV, relative cerebral blood volume. Source: From Ref. 28.

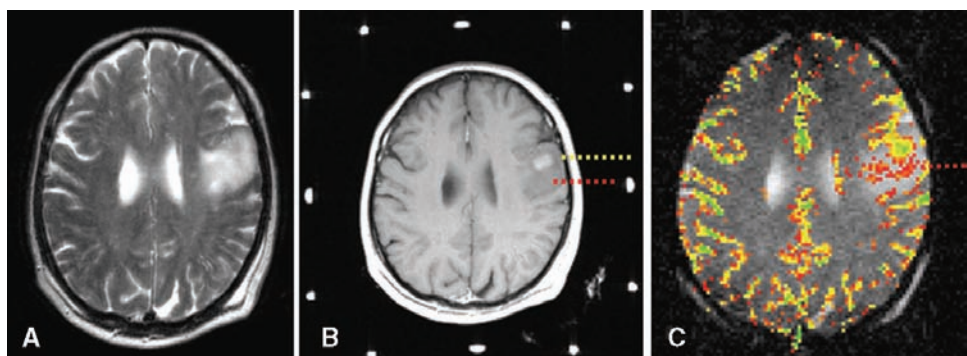


Figure 8 Minimally enhancing left frontal lobe tumor in a 50-year-old man. (A) Axial T2-weighted image shows a hyperintense mass in the left frontal region with minimal surrounding edema. (B) Axial T1-weighted image postgadolinium in a stereotactic headframe shows a small nodule of enhancement anteriorly within the tumor. (C) DSC MRI color overlay imaging as seen by the neurosurgeon in the operating room at the time of surgery, demonstrating increased perfusion posterior to the focus of enhancement. Two separate stereotactic biopsies were performed. The biopsy of the enhancing nodule revealed a low-grade glioma (yellow biopsy), whereas the biopsy of the focus of increased perfusion posteriorly (red biopsy) demonstrated an anaplastic astrocytoma. This was confirmed at subsequent surgical resection of the tumor. Abbreviation: DSC MRI, dynamic susceptibility contrast MRI.

Mixed Neuronal-Glial Tumors—Ganglioglioma

Gangliogliomas are neoplasms comprised of both neuronal and glial elements of varying proportion. The glial cells in gangliogliomas are typically astrocytes and their degree of

abnormality dictates the WHO classification of these tumors. Grade I signifies that the glial element is comprised of normal astrocytes. Grade II suggests that there is cellular and nuclear pleomorphism as well as high cellularity of the glial cells. Grade III is used to describe a combination of

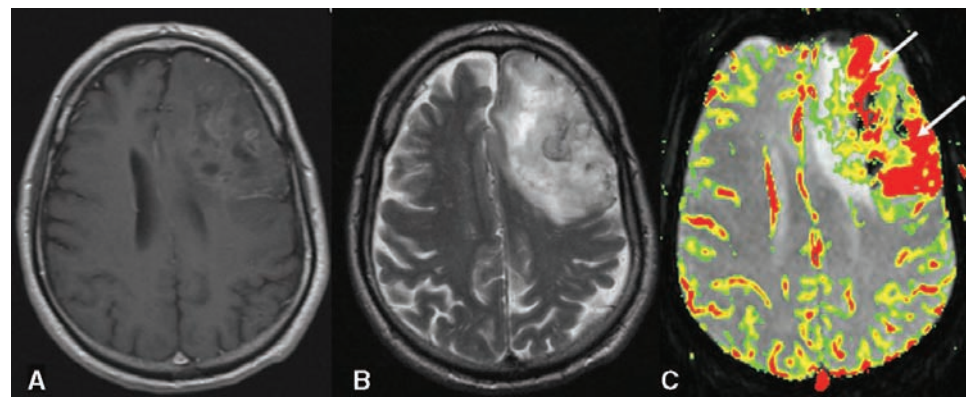


Figure 9 A 63-year-old male (patient no. 6) with a pathology proven anaplastic oligodendrogloma with high-perfusion rCBV of 8.08 and 1p19q allelic deletions. (A) Contrast-enhanced axial T1-weighted image (600/14) demonstrates a mass in the left frontal region with patchy contrast enhancement. (B) Axial T2-weighted image (3400/119) demonstrating mass effect with midline shift and some mass effect on the left lateral ventricle. (C) Gradient-echo (TR/TE 1,000/54) axial DSC MRI perfusion image, with rCBV color overlay map, shows a lesion with very high perfusion, rCBV of 8.08 (arrows). Key for color map: No color depicts baseline white matter perfusion; green depicts threshold gray matter perfusion; yellow depicts increased perfusion; red depicts maximal perfusion (the cortical vessels also demonstrate normal perfusion). Abbreviations: rCBV, relative cerebral blood volume; TR, repetition time; TE, echo time; DSC MRI, dynamic susceptibility contrast MRI.

high cellularity, necrosis, abundant mitoses, and, especially, vascular proliferation. Grade III implies a tumor that fulfills these criteria for anaplasia (51). Grade I and II gangliogliomas have been found to demonstrate higher rCBV than other LGGs (64). Finding rCBV elevation in gangliogliomas compared with other LGGs may indicate that some of these mixed neuronal-glial tumors may behave differently from other LGGs (65). It may be that the mixed glial-neuronal component confers a different behavior with higher cellularity, vascularity, and malignant potential, which we are measuring with DSC MRI.

Nonglial Neoplasms (Medulloblastoma, PNETs, Lymphoma)

Embryonal tumors compose of a group of primitive neuroepithelial tumors that include primitive neuroectodermal tumor (PNET), medulloblastoma, medulloepithelioma, ependymoblastoma, pineoblastoma, peripheral neuroepithelioma, esthesioneuroblastoma, and retinoblastoma (66). These are considered to be high-grade (grade IV) tumors and the DSC MRI and MRS findings are in keeping with this classification. PNETs have been shown to demonstrate vascular endothelial proliferation histopathologically (66–71). As a result, the rCBV and vascular permeability are elevated in PNETs (72). Lymphoma, like the PNET group of tumors, are also typically very cellular tumors. However, unlike the PNETs, the dense cellularity and lymphocytic perivascular invasion causes narrowing of the cerebral vasculature, resulting in reduced rCBV in intracerebral lymphomas (primary and secondary) (73–75). The destruction of the blood-

brain barrier however may affect CBV measurements, and as a result, some lymphomas could demonstrate increased vascular permeability and CBV.

Extra-Axial Neoplasms (Meningioma, Schwannoma)

In differentiating extra-axial from intra-axial lesions in the brain, rCBV may not be reliable, as substantial contrast leakage from lack of a blood-brain barrier in extra-axial lesions can give erroneously low or high uncorrected CBV values. However, evaluating the signal intensity-time curve and determining the degree of permeability may be helpful in the clinical setting. In extra-axial lesions, the signal intensity time curve demonstrates immediate and continued leakage of contrast compared with intra-axial lesions (12). Meningiomas are the most common extra-axial tumors and are usually a straightforward diagnosis on conventional MRI, obviating the need for DSC MRI or biopsy. The rCBV and vascular permeability (K^{trans}) are usually elevated in meningiomas. Meningiomas are known pathologically and also at angiography to be vascular tumors. There also appears to be good correlation between the K^{trans} and the histologic grade of meningiomas (27) (Fig. 10). Pathologically, higher K^{trans} measurements may be related to the degree of micronecrosis found in atypical meningiomas. Because the atypical and typical variants of meningioma have different recurrence rates, measurement of K^{trans} provides a prospective measure of tumor behavior, and this information could help avoid surprises such as brain invasion that could be successfully planned for if this information were available to the neurosurgeon preoperatively (76).

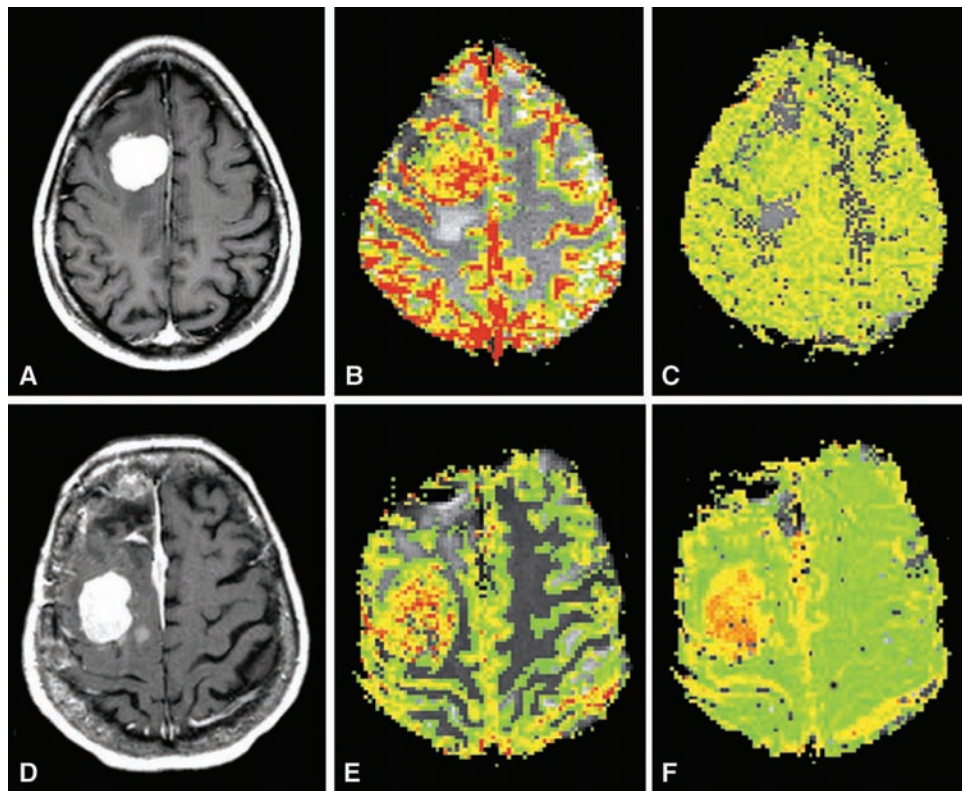


Figure 10 Pathologically confirmed meningioma, (WHO Grade I). (A) Axial T1-weighted postgadolinium image. (B) Gradient-echo axial DSC MRI with rCBV color overlay demonstrates high rCBV throughout the lesion. (C) Gradient-echo axial DSC MRI with SD25 color overlay depicts signal intensity drop after 25 seconds indicating mild increased vascular permeability. (D) Pathologically confirmed atypical meningioma, (WHO Grade II). Axial T1-weighted postgadolinium image. (E) Gradient-echo axial DSC MRI with rCBV color overlay demonstrates high rCBV throughout the lesion. (F) Gradient-echo axial DSC MRI with SD25 color overlay. Red indicates regions of highest signal drop, correlating to areas of marked increased vascular permeability. Qualitatively, this is the best way that this atypical meningioma can be differentiated from the typical meningioma seen in Figure 8 (C). Abbreviations: rCBV, relative cerebral blood volume; DSC MRI, dynamic susceptibility contrast MRI. Source: From Ref. 27.

DSC MRI can increase the sensitivity of diagnosis in extra-axial masses. Differentiating between a meningioma and acoustic neuroma at the cerebello-pontine angle can sometimes be a challenge. Lower vascular permeability was found in typical meningiomas as compared with acoustic neuromas (46). Some parafalcine chondrosarcomas may have a similar conventional MRI appearance to parafalcine meningiomas. Classical chondrosarcomas have been shown to demonstrate reduced rCBV (77).

Metastatic Neoplasms

Solitary brain metastases may be indistinguishable from a primary glioma by conventional MRI. The intratumoral rCBV is also not able to reliably differentiate between the metastases and glioma.

The differences in the pathophysiology of the peritumoral region of gliomas and metastases results in differences in rCBV, which can differentiate between these two

pathologies. HGGs are known to be infiltrating tumors, with tumoral tissue infiltrating along vascular channels, whereas in metastases the peritumoral region contains no infiltrating tumor cells or vascular endothelial proliferation and is almost purely vasogenic edema (78,79). In differentiating glioma from metastases, finding high rCBV in the peritumoral region of a lesion (Fig. 11) is more likely to represent a glioma rather than a metastases (80) (Table 4).

CNS Infections: Bacterial, Tuberculous, Parasitic

A major differential diagnosis for ring-enhancing lesions is the presence of intracranial abscesses, which may be bacterial, tuberculous, or parasitic. Usually the diagnosis of a brain abscess is made by reviewing the clinical, hematologic, and conventional imaging findings. In some instances where the diagnosis is not straightforward, combining MR spectroscopic imaging (MRSI) and DSC

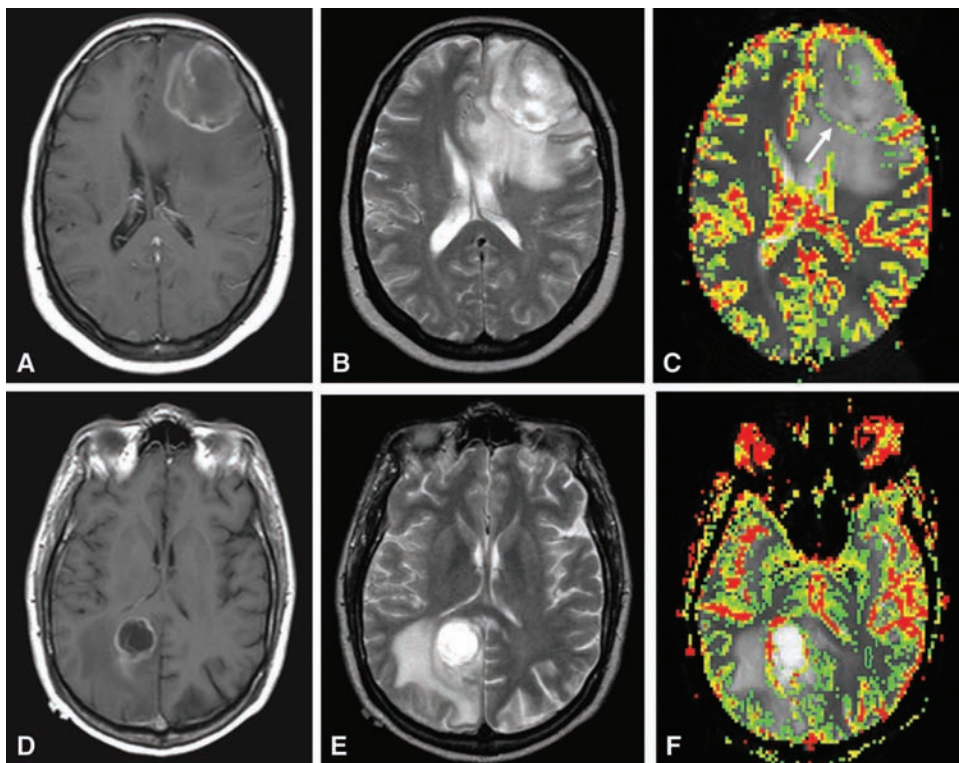


Figure 11 A 40-year-old woman with a metastasis from a lung carcinoma in the left frontal region. (A) Axial T1-weighted image postgadolinium shows a peripherally enhancing mass in the left frontal region with mass effect. (B) Axial T2-weighted image demonstrates moderate edema with questionable involvement of the corpus callosal genu seen more typically with infiltrating primary gliomas. Conventional MRI may sometimes be nonspecific in the setting of a solitary metastasis. (C) Gradient-echo axial DSC MRI with rCBV color overlay map demonstrates some increase in perfusion at the rim of enhancement (arrow); however, there is hypovascularity in the peritumoral region suggesting vasogenic edema without infiltrating tumor. (D) A 54-year-old man with a glioblastoma multiforme in the right mesial occipital lobe. Axial T1-weighted image postgadolinium shows a ring-enhancing mass with central necrosis. (E) Axial T2-weighted image demonstrates moderate edema with questionable involvement of the splenium of the corpus callosum. (F) Gradient-echo axial DSC MRI with rCBV color overlay map demonstrates increase in perfusion at enhancing tumoral as well as peritumoral regions, suggesting hypervascularity in the peritumoral region in keeping with infiltrating primary high-grade glioma. Abbreviations: DSC MRI, dynamic susceptibility contrast MRI; rCBV, relative cerebral blood volume. Source: From Ref. 80.

MRI may increase the specificity of neurodiagnosis. There is decreased perfusion within the central portion of an abscess and in the regions of surrounding edema when compared with a neoplasm. There may be a very thin rim of increased perfusion between the enhancing capsule and the region of surrounding edema (12). Typically bacterial abscesses will demonstrate some restriction of diffusion on diffusion-weighted imaging (DWI) (Fig. 12). Detection of multiple amino acids at either short or long echo time in MRSI would differentiate a bacterial abscess from other cystic, ring-enhancing masses. Polymorphonuclear cells within bacterial abscesses have numerous proteolytic enzymes that break down large amounts of amino acids. Lactate and lipids are also demonstrated as a result of anaerobic glycolysis. Glucose is metabolized via the Embden-Meyerhof pathway to produce pyruvate. The pyruvate is

converted to lactate or acetate via acetyl coenzyme A. A bacterial abscess may demonstrate leucine, isoleucine, valine (0.9 ppm); lactate/lipids (1.33 ppm); alanine (1.48 ppm); acetate (1.92 ppm); succinate (2.4 ppm); and glycine (3.55 ppm) (83–88). Similar findings have been reported in nonbacterial infections such as cysticercosis (84,89). Tuberculous abscesses may be differentiated from bacterial abscesses by demonstrating only lactate and lipid peaks (Fig. 13) without the presence of glycine, succinate, acetate, and alanine (85). In vivo studies have demonstrated lipids at 0.9, 1.3, 2.0, 2.8 ppm and phosphoserine at 3.7 ppm (90). Gupta et al. also recently demonstrated that rCBV measurements correlate with microvascular density and the expression of VEGF in excised tuberculomas. There was also a significant decrease in rCBV in response to antituberculous therapy (91).

Table 4 Summary of Perfusion Parameters (rCBV and Vascular Permeability) of Some Common Intracranial Tumors

Author (ref.)	Pathology	Number	rCBV	Vascular permeability (s^{-1})
Law et al. (41)	Grade II/IV	31	1.75	0.00053
Law et al. (41)	Grade III/IV	16	3.79	0.0011
Law et al. (41)	Grade IV/IV	26	6.05	0.002
Unpublished	Radiation necrosis	9	0.47	0.00206
Cha et al. (81)	TDL	12	0.88	NA
Yang et al. (52)	Gliomatosis cerebri	7	1.02	NA
Cha et al. (12)	Lymphoma	19	1.44	NA
Law et al. (41)	Gangliogliomas	20	3.66	0.00180
Yang et al. (82)	Metastases	19	3.79	0.002
Law et al. (72)	PNETs	12	4.76	0.00330
Yang et al. (27)	Meningioma I/III	15	8.02	0.0016
Yang et al. (27)	Meningioma II/III	7	10.5	0.00259

Abbreviations: rCBV, relative cerebral blood volume; TDL, tumefactive demyelinating lesion; PNETs, primitive neuroectodermal tumor; NA, not available.

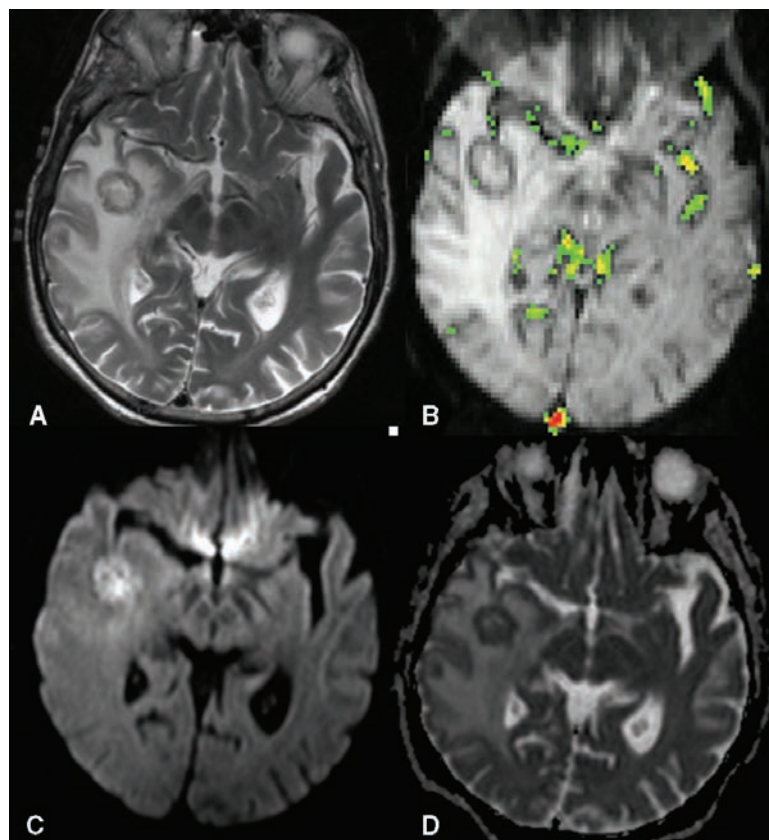


Figure 12 A 45 year-old-woman with a bacterial abscess. (A) Axial T2-weighted image demonstrates substantial vasogenic edema surrounding the mass but minimal mass effect. (B) Gradient-echo axial DSC MRI with rCBV color overlay demonstrates reduced rCBV within the lesion. There may be a thin rim with very minimally increased rCBV immediately adjacent to the enhancing edge of the abscess capsule. (C/D) Diffusion-weighted imaging with corresponding ADC map demonstrates some diffusion restriction seen in bacterial abscesses. Abbreviations: DSC MRI, dynamic susceptibility contrast MRI; rCBV, relative cerebral blood volume; ADC, apparent diffusion coefficient.

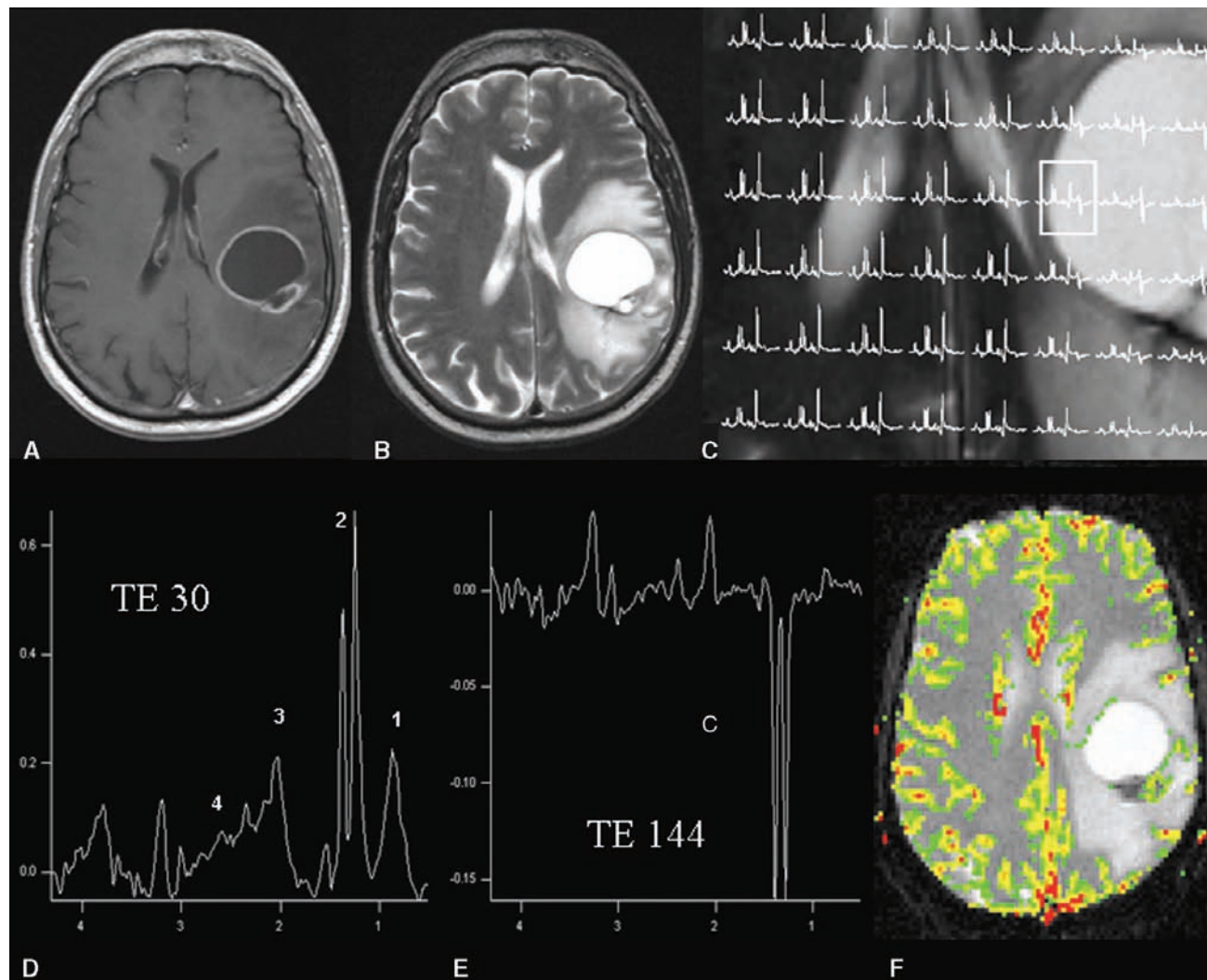


Figure 13 A 53-year-old woman with a tuberculous abscess. (A) Axial T1-weighted image postgadolinium shows a well-defined mass in the left frontoparietal region with a thin rim of enhancement. The irregularity in the posterior margin is from a stereotactic biopsy. (B) Axial T2-weighted image demonstrates substantial vasogenic edema surrounding the mass but minimal mass effect. (C) MRSI (TE 144 ms) shows presence of lipids and lactate within the lesion but no elevation of Cho in the adjacent regions of T2 signal hyperintensity suggesting a well-defined, noninfiltrating lesion. The vasogenic edema results in some diminution of metabolites around the lesion. (D) Spectrum (TE 30 ms) demonstrates various lipid and lactate resonances at (1) 0.9 ppm, (2) 1.3 ppm doublet, (3) 2.0 ppm, and (4) 2.8 ppm. Phosphoserine (3.7 ppm) not seen in this spectrum has also been demonstrated (90). (E) MRSI at intermediate echo time (TE 144 ms), the presence of lactate is confirmed by the inverted doublet at 1.33 ppm (85). (F) Gradient-echo axial DSC MRI with rCBV color overlay demonstrates reduced rCBV with a thin rim with very minimally increased rCBV, which may be a measure of angiogenesis adjacent to the tuberculous abscess (91). The focus of increased rCBV in the posterolateral aspect of the lesion represents some reactive perfusion from the biopsy site. The reduced perfusion is in keeping with a nonneoplastic lesion (12). The combination of finding lipid, lactate, phosphorine, and reduced rCBV is consistent with a tuberculous abscess. Abbreviations: MRSI, MR spectroscopic imaging; TE, echo time; DSC MRI, dynamic susceptibility contrast MRI; rCBV, relative cerebral blood volume.

Nonneoplastic Mimics

Tumefactive Demyelinating Lesions

The conventional MRI features of tumefactive demyelinating lesions (TDLs) can mimic that of a HGG. Both lesions may exhibit variable contrast enhancement, perilesional edema, varying degrees of mass effect, and central necrosis. One fairly characteristic sign of a TDL is that

these lesions often demonstrate an incomplete ring of enhancement (Fig. 14). The imaging similarities may stem from histopathologic similarities between TDLs and gliomas that include the presence of hypercellularity, reactive astrocytes, mitotic figures, and areas of necrosis. Stains for myelin and axons are usually required to help distinguish between TDL and tumor. However, the key pathologic difference between TDLs and HGGs is the

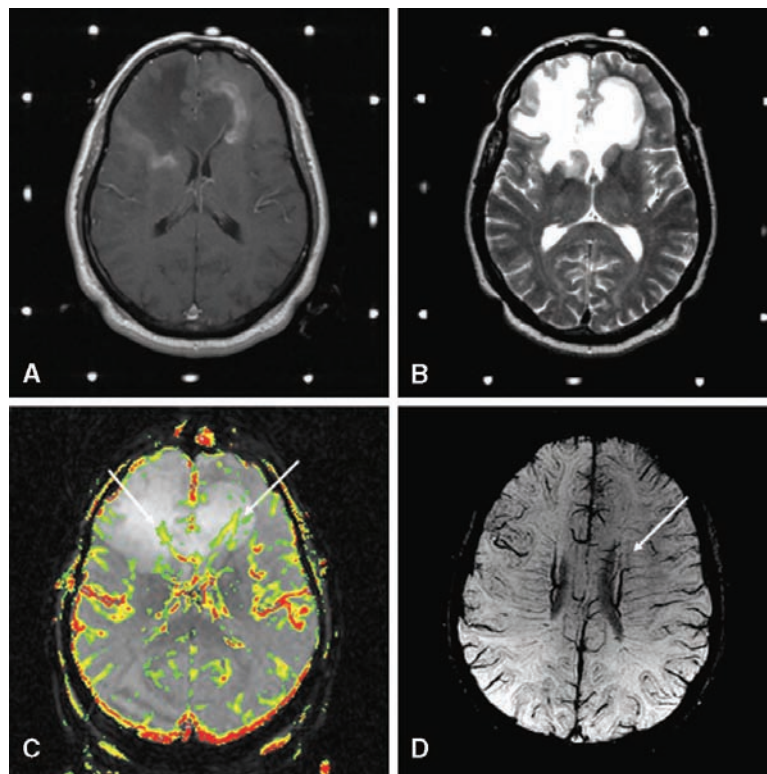


Figure 14 A 57-year-old man with a TDL. (A) Axial T1-weighted image postgadolinium in the stereotactic headframe shows a peripherally enhancing mass in the frontal regions with involvement of the corpus callosum. The mass-like appearance and “butterfly” configuration prompted the neurosurgeon to stereotactic surgical resection. The incomplete ring of enhancement is sometimes seen in TDLs. (B) Axial T2-weighted image demonstrates increased T2 signal within the lesion with minimal edema. (C) Gradient-echo axial DSC MRI with rCBV color overlay demonstrating reduced vascularity within the lesion, even at the enhancing so-called leading edge. Prominent vessel-like structures (veins) are identified within the lesion. These TDLs are known to arise along vascular or venular structures (12,81). (D) (SWI) demonstrates association of these lesions with prominent periventricular venules. Abbreviations: TDL, tumefactive demyelinating lesion; DSC MRI, dynamic susceptibility contrast MRI; rCBV, relative cerebral blood volume; SWI, susceptibility weighted imaging;

absence of angiogenesis in TDLs. TDLs demonstrate a mean rCBV of 0.88 (81). In contrast, gliomas are characterized by neovascularization and angiogenesis that contribute to a significant elevation in rCBV of 6.47. Prominent venous structures are also identified in association with large TDLs and on careful inspection of some smaller multiple sclerosis plaques, not only confirming that primary demyelination is closely related to venous structures but that it may be also related to venous inflammation (12,81,92) (Fig. 14). These venous structures are seen best on the gradient-echo DSC MRI at the time of the contrast bolus peak or with a new sequence called susceptibility-weighted imaging (SWI).

Other Inflammatory Mimics/Encephalitis

Inflammatory lesions of the CNS such as cerebritis and encephalitis can also mimic tumor. Typically brain inflammation is associated with an element of vasculitis.

A full discussion of all the etiologies of vasculitis is beyond the scope of this chapter. Noninfectious vasculitides are characterized by inflammatory cell infiltrate, with varying degree of multinucleated giant cells, granuloma formation, and fibrinoid necrosis (93). Several of these vasculitides result in vessel wall fibrosis if the disease state becomes chronic. There is variation within the vasculitides in terms of involvement of what part of the vessel wall (intima, media, adventitia) and within what type of vessel (large vessel, medium vessel, small vessel, or vein) is involved. The systemic vasculitides can cause neurologic symptoms by either primarily affecting cranial vessels or secondarily by causing vascular occlusion or embolism. Consequently, inflammatory lesions of the brain usually result in reduced rCBV because of the perivascular infiltrate causing some vascular narrowing (Figs. 15 and 16). The caveat is when there is substantial blood-brain barrier breakdown, which may artifactually cause an elevation in rCBV.

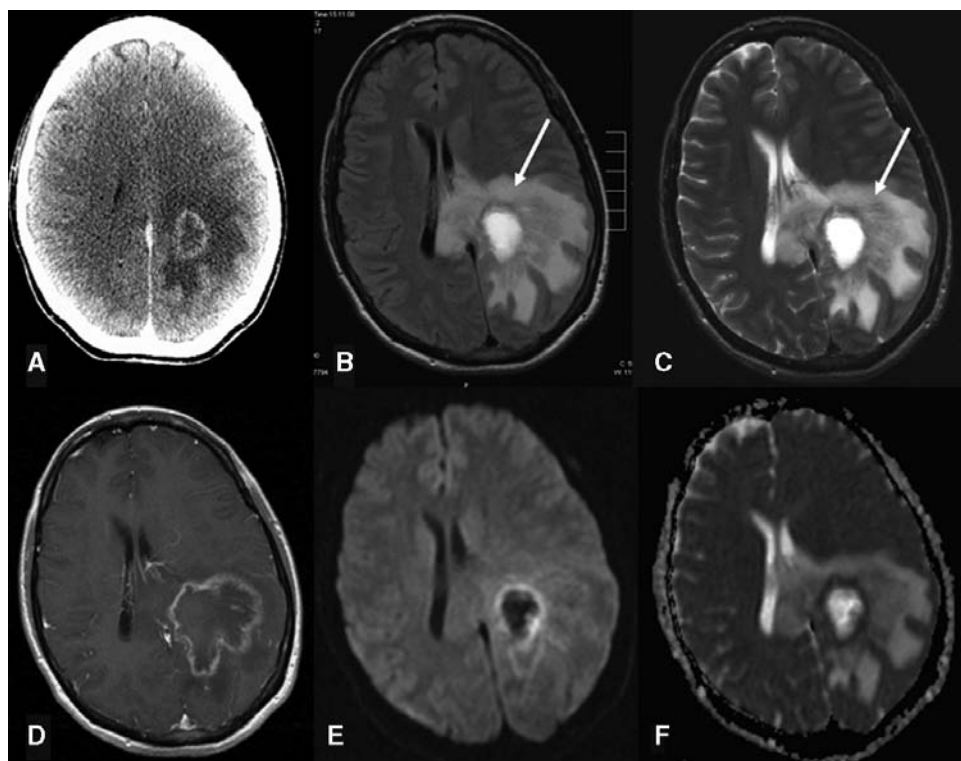


Figure 15 A 43-year-old woman who presented to her physician with a progressive visual disturbance and headache for several weeks with a final diagnosis of necrotizing cerebritis. (A) Post-contrast CT and conventional MRI, (B) FLAIR, (C)T2-weighted, and (D) Post-gadolinium T1-weighted images, in the transverse plane, demonstrating increased T2 signal intensity within the left temporoparietal region extending into splenium of the corpus callosum (arrow), with associated mass effect and effacement of the left lateral ventricle. There is peripheral enhancement with central areas of what appears to be necrosis. (E) DWI and (F) ADC map demonstrates a ring of high signal on diffusion with a corresponding ring of low signal on the ADC map. The conventional MR and the DWI findings proved to be a diagnostic dilemma, with the most likely differential diagnoses of glioblastoma multiforme, lymphoma, or a necrotizing cerebritis. Abbreviations: FLAIR, fast fluid-attenuated inversion recovery; DWI, diffusion-weighted imaging; ADC, apparent diffusion coefficient; MR, magnetic resonance; MRI, magnetic resonance imaging.

Cerebrovascular Injury (Acute Ischemic Stroke Vs. Tumor)

The differentiation between ischemia and tumoral disease is important for the timely administration of thrombolytic therapy/endovascular therapy or surgical treatment, respectively. Surgery in the setting of an ischemic lesion has significant avoidable morbidity and mortality. But unfortunately, these entities may sometimes share similar imaging findings on conventional MRI, such as abnormal T2 hyperintensity, ill-defined margins on T1W1, hemorrhage, contrast enhancement, mass effect, and even heterogeneous signal on DWI. Although a lesion with a typical vascular territory distribution, gray and white matter involvement, gyral enhancement combined with the abrupt onset of symptoms favors a diagnosis of infarction, in many cases these criteria are not fulfilled, and the exclusion of a surgical lesion, like glioma, can be challenging, sometimes even impossible (94). Both lesions may demonstrate variable contrast enhancement, due to varying

degrees of blood-brain barrier disruption and vascular permeability, which is partly related to the duration of ischemia with reperfusion in acute or subacute ischemic strokes (95). Due to this variability, contrast enhancement may not be helpful in the differential diagnosis.

In recent years, DWI has been shown to be the most sensitive MRI technique in making a diagnosis of hyperacute and acute ischemic stroke, by demonstrating regions of restricted diffusion as increased signal intensity areas, along with corresponding decreased signal intensity on the ADC map. But as the infarct continues to evolve into the subacute stage, there is pseudonormalization of the ADC, attributed to the combination of persistent cytotoxic edema and vasogenic edema, which results in a gradual decrease in the hyperintensity and a heterogeneous appearance on DWI. This heterogeneity in signal can also be seen in many gliomas (96). Furthermore, measurements of water diffusivity and cellularity in lymphomas and high-grade astrocytomas indicate that higher cellularity can result in restricted diffusion (96). These findings suggest that in

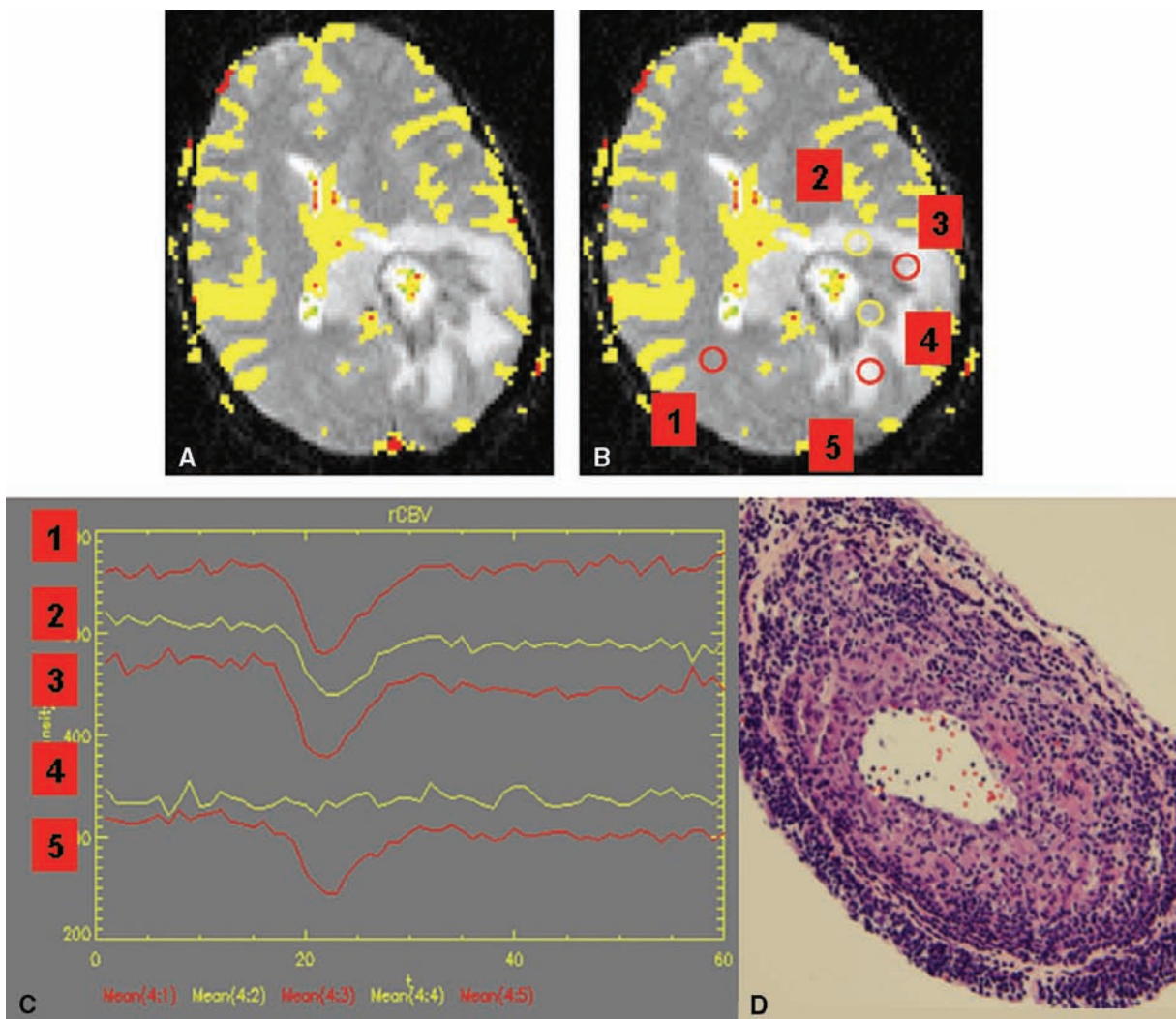


Figure 16 (A) Gradient-echo axial DSC MRI with rCBV color overlay map and (B) Gradient-echo axial DSC MRI with rCBV color overlay map demonstrating the location of five ROIs placed within (1) normal appearing contralateral brain (2) the anterior portion of the lesion (3) the lateral portion of the lesion (4) the darker necrotic portion of the lesion, and finally, (5) the posterior portion of the lesion within the edema. The rCBV in these four ROIs relative to the contralateral normal brain were 0.85, 1.11, 0.31, and 1.1, respectively. (C) Signal intensity versus time curves numbered according to the five yellow and red ROIs placed on the rCBV map demonstrates the rCBV to be approximately the same as the contralateral normal brain with reduced rCBV within the edge of the necrotic region ROI (4). The combination of decreased or normal rCBV and decreased metabolites on MRSI in the lesion and the perilesional regions was highly suggestive of a nonneoplastic diagnosis. The final diagnosis was necrotizing encephalitis. (D) Higher-power hematoxylin and eosin (H & E) ($\times 200$) demonstrates necrosis of the intima, media, and adventitia in keeping with a panvasculitis resulting in vascular narrowing. Abbreviations: DSC MRI, dynamic susceptibility contrast MRI; rCBV, relative cerebral blood volume; ROI, region of interest.

some lesions DWI may not be able to provide a conclusive diagnosis of an infarct, particularly in the subacute and sometimes even in the acute phase (Fig. 17).

Acute ischemia generally results in decreased CBF and increased/prolonged MTT or time to peak (TTP) from DSC MRI measurements (97). CBV measurements can be increased or decreased depending on the level of hypoperfusion (vasodilation due to autoregulation or collateral

vascularization can result in an increase in CBV, while with more severe hypoperfusion and chronic ischemia, CBV is decreased). Furthermore, CBV can be elevated in some nonacute pathophysiologic states, such as unilateral carotid artery occlusion, and in areas of reperfusion ("luxury perfusion") there is also increased CBV. Although CBV measurements (usually elevated in HGGs and variable in infarction) cannot always differentiate between the two entities, CBF

and MTT are more helpful. Prolongation in MTT, with decreased CBF, is considered a sensitive indicator of ischemia (Fig. 18). In HGGs, MTT can be low/fast with high flow larger vessels/arteriovenous shunts, or prolonged with small angiogenic vessels/collateral supply.

The degree of angiogenesis and vascular proliferation has been linked to tumor biology in human gliomas (41). Perfusion MRI, with its sensitivity to the capillary bed, is therefore ideally suited for differentiating tumor from acute ischemic stroke. Gliomas contain an elevated number of hyperplastic vessels with greater diameter and endothelial wall thickness compared with normal vessels (98), resulting in elevated CBV and CBF measurements (Figs. 19 and 20). An important pitfall is that MTT/TTP can be decreased or elevated because of increased flow or

increased vascular tortuosity, respectively, so this metric is not useful in characterizing tumors (21). This can be useful in differentiating a lesion that may be ischemic or represent a HGG glioma.

COMBINING CONVENTIONAL MRI WITH DIFFUSION MR, PERFUSION MRI, AND MRS TO INCREASE DIAGNOSTIC SPECIFICITY IN BRAIN TUMORS: MULTIPARAMETRIC ALGORITHMIC APPROACH

The recent advances in MRI hardware and software has allowed many advanced MRI techniques such as DWI, diffusion tensor imaging, perfusion-weighted imaging,

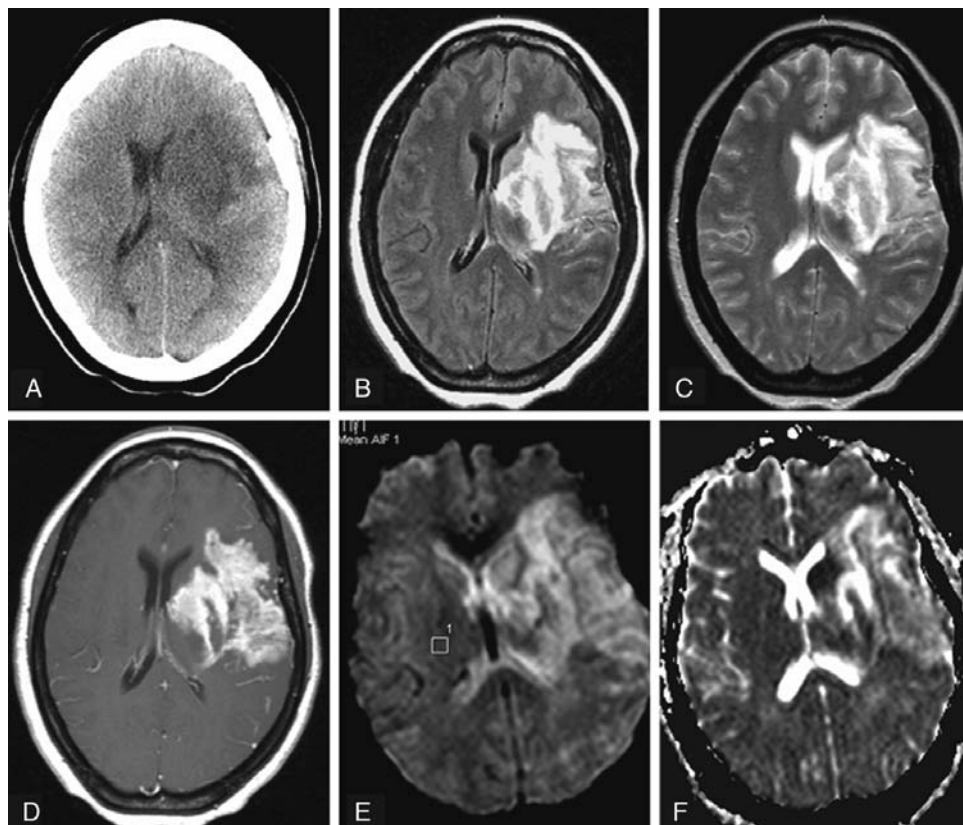


Figure 17 A 45-year-old female presented with a 10-day history of right-sided upper and lower extremity weakness. (A) Noncontrast CT and conventional MRI; (B) FLAIR; (C) T2-weighted; and (D) Axial post-Gd T1-weighted images demonstrating an irregularly enhancing mass in the left frontotemporal region involving gray and white matter, with a small amount of edema and slight mass effect; (E) DWI (b -value = 1000) demonstrated heterogeneous diffusion with some areas of high signal; (F) There is decreased signal on the ADC map due to restricted diffusion (including the head of the left caudate nucleus), possibly indicating ischemia, while other areas of high signal on DWI also demonstrates increased signal on the ADC map, representing T2-shine through. Although the clinical history suggested infarction at the left MCA territory, the conventional MRI and the diffusion pattern were inconclusive, seen in some heterogenous high-grade gliomas and also in subacute evolving infarcts. Abbreviations: CT, computed tomography; MRI, magnetic resonance imaging; FLAIR, fast fluid-attenuated inversion recovery; postGd, postgadolinium; DWI, diffusion-weighted image; ADC, apparent diffusion coefficient; MCA, middle cerebral artery.

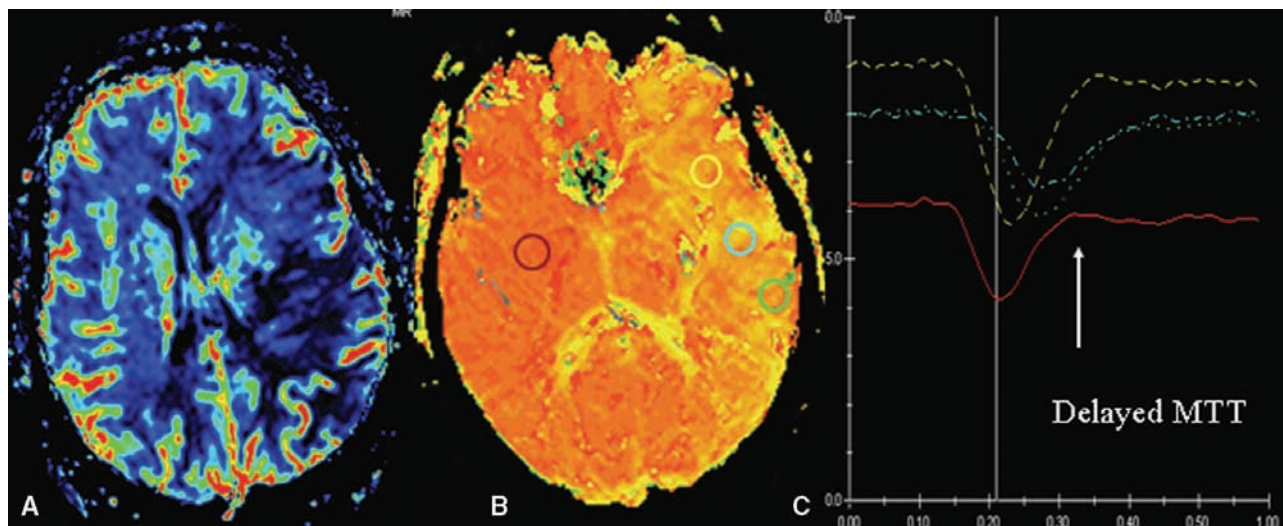


Figure 18 (A) Gradient-echo axial DSC MRI with CBF color overlay. (B) Gradient-echo axial DSC MRI with MTT color overlay maps demonstrating decreased CBF and prolongation in the MTT throughout the entire left MCA territory in keeping with left MCA ischemia. (C) Signal intensity versus time curves color coded to the four ROIs placed on the MTT maps, demonstrating prolongation in MTT in the green, blue, and to a lesser extent the yellow ROIs. The red ROI indicates normal MTT in the contralateral hemisphere. The prolonged MTT and reduced CBF in the MCA distribution are in keeping with an ischemic stroke. CBF and MTT are more specific than CBV in differentiating infarct from tumor. Abbreviations: DSC MRI, dynamic susceptibility contrast MRI; CBF, cerebral blood flow; MCA, middle cerebral artery; MTT, mean transit time; ROIs, regions of interest.

and MRS to be incorporated into not just research protocol but also in routine clinical practice. There have also been numerous publications demonstrating the utility of these techniques in characterizing intracranial pathology. These techniques provide insight into the various physiologic and metabolic changes that occur in different pathologies. It would then be useful to combine the information available from all of these techniques to provide useful functional data to ultimately increase our diagnostic specificity. As is the case with conventional MRI, rarely do we only just review the T1-weighted, T2-weighted, or diffusion-weighted images alone to make the final diagnosis, it would make sense then to eventually combine all of these advanced imaging tools to increase our diagnostic specificity.

The ring-enhancing mass lesion in the brain can have a number of differential diagnosis. These include a HGG, metastases, infarct, radiation necrosis, abscess or a TDL. In differentiating these pathologies, one can use an algorithmic, multiparametric approach combining findings from each of the advanced MRI techniques (Table 5) (Fig. 21). A potential approach to a mass lesion would first be to evaluate the CBV relative to the contralateral normal brain and also the choline levels relative to the contralateral brain Cho(n). If there is significant elevation of Cho/Cho(n) and rCBV, then the lesion is likely to represent either a HGG or a metastases. Then evaluation

of the peritumoral or perienhancing region may help differentiate these two pathologies. An HGG would demonstrate elevated peritumoral CBV and Cho because, pathologically, these are lesions that infiltrate the peritumoral region, resulting in elevated peritumoral cellularity as well as vascularity. An exception is the rarely seen, circumscribed glioma. Metastases, on the other hand, are usually circumscribed lesions with negligible tumoral infiltration. As a result the peritumoral Cho and CBV will not be elevated.

If the lesion demonstrates reduced Cho/Cho(n) and rCBV, then the lesion is likely to represent either an infarct, radiation necrosis, an abscess, or a giant TDL. When reviewing the perfusion images or using new techniques such as SWI, TDLs have a predilection for the periventricular white matter and will demonstrate venous structures running through the lesion. These periventricular veins maintain their normal architecture and are not disrupted or destroyed as one would expect in a glioma. If an acute ischemic stroke is considered a likely differential and the findings are not conclusive on DWI, then review of the signal intensity curves from perfusion MRI should demonstrate prolongation in the MTT/TTP (Fig. 18). If radiation necrosis is a consideration, then because of the vascular narrowing the CBV and CBF is typically low. The vascular permeability (K^{trans}) may be

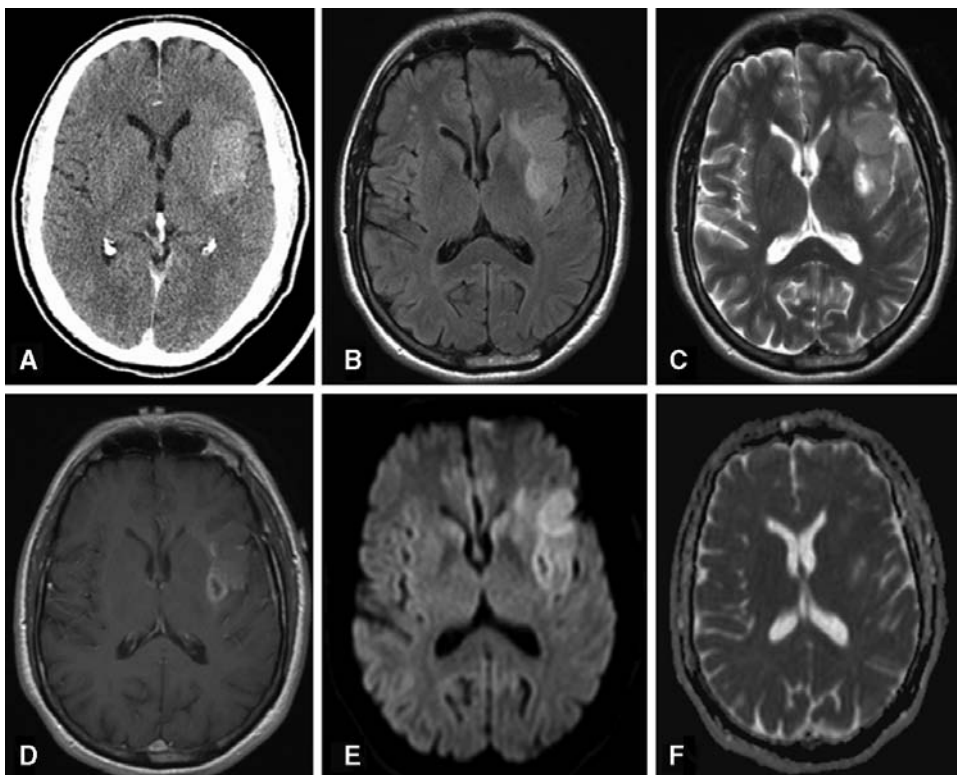


Figure 19 A 56-year-old male presented with a four-week history of right-sided weakness. (A) Post-contrast CT and conventional MRI, (B) FLAIR, (C) T2-weighted, and (D) Post-gadolinium T1-weighted images, in the axial plane, demonstrating increased T2 signal intensity within the left frontal operculum extending into the insular cortex and subinsular white matter, with associated effacement of the sulci and also some irregular patchy enhancement. There is some mass effect with the insula appearing somewhat mass-like. The lesion also conforms to a vascular territory involving the insula branches of the left MCA. (E) DWI and (F) ADC map demonstrate heterogeneous diffusion with some areas of low signal on the ADC map that may indicate either ischemia or tumor cellularity. Both the conventional MR and the DWI were inconclusive, with the most likely diagnosis of either subacute infarction versus glioma. Abbreviations: CT, computed tomography; MRI, magnetic resonance imaging; FLAIR, fast fluid-attenuated inversion recovery; MCA, middle cerebral artery; DWI, diffusion-weighted imaging; ADC, apparent diffusion coefficient.

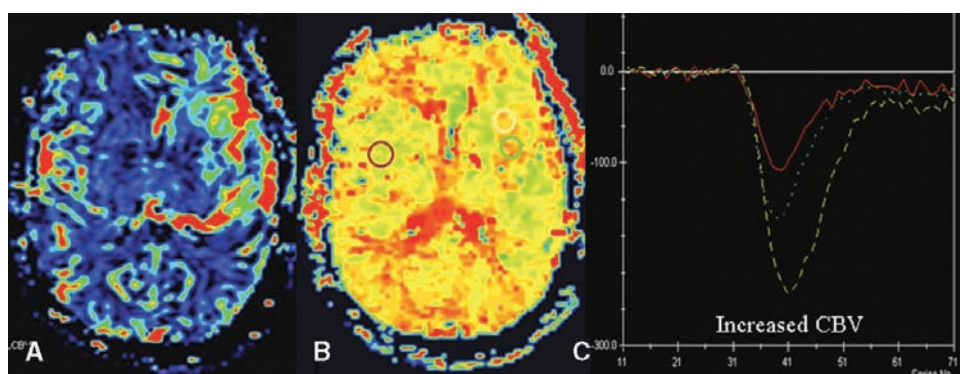


Figure 20 (A) Gradient-echo axial DSC MRI with rCBV color overlay map, and (B) MTT color overlay map demonstrates a high CBV in the lesion and the perilesional regions. (C) Signal intensity versus time curves color coded to the three ROIs placed on the MTT map demonstrates high CBV (area under the signal intensity curves) in the yellow ROI and to a lesser extent in the green ROI, which have been placed at the lesion, compared with the red ROI of the contralateral normal parenchyma. Increased CBV in the lesion and the perilesional regions was highly suggestive of a high-grade glioma with tumor infiltration into the surrounding tissues. In tumoral disease MTT/TTP may be increased or decreased and is less specific. The final diagnosis was anaplastic astrocytoma. Abbreviations: DSC MRI, dynamic susceptibility contrast MRI; rCBV, relative cerebral blood volume; MTT, mean transit time; ROI, region of interest; CBV, cerebral blood volume; TTP, time to peak.

Table 5 Summary of DSC MRI And MRSI Findings for Common Ring-Enhancing Brain Lesions

	MRSI	MRSI	MRSI	MRSI	DSC MRI	DSC MRI	CBV and Cho
Pathology	Cho/Cr	Cho/Cho(n)	NAA/Cr	Other	CBV	Other	Peritumoral
High grade glioma	V. high	V. high	V. low	Lipid/lac	V. high	K^{trans} /CBF	High
Radiation necrosis	Low	Low	Low	Lipid/lac	Low	High K^{trans}	Low
Metastases	High	High	Low	Lipids/lac	High	High K^{trans}	Low
Abscess	Mod	Mod	Low	Suc/acc ^a	Low	Rim of CBV	Low
Demyelination/TDL	High	High	Sl. low	Lipid/lac	Low	Venous	Normal
Infarct	High	Low	Low	Lipid/lac	Variable	High MTT	Normal
Contusion/hematoma	Mod	Mod	Low	Wide peaks	Variable	Susceptibility	Normal

^aMRSI in bacterial abscess will also demonstrate succinate, acetate, leucine and isoleucine (see reference 85).

Abbreviations: MRSI, MR spectroscopic imaging; Cho/Cr, choline/creatinine; Cho(n), normal contralateral choline; NAA, *N*-acetylaspartate; DSC MRI, dynamic susceptibility contrast MRI; CBV, cerebral blood volume; TDL, tumefactive demyelinating lesion; V.high, very high; Sl. low, slightly low; Mod, moderate; MTT, mean transit time; lac, lactate.

Algorithmic-Multiparametric Approach

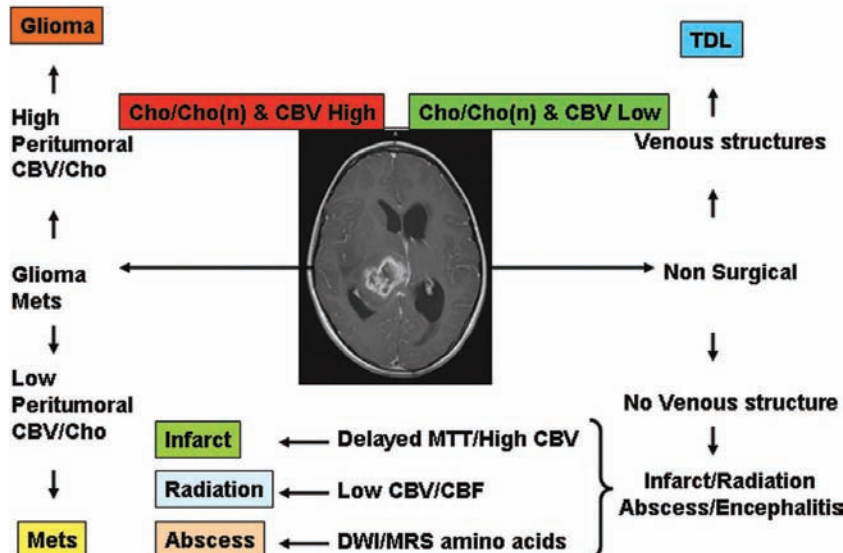


Figure 21 An algorithmic/multiparametric approach to increasing specificity in making a differential diagnosis of intracranial mass lesions using diffusion, perfusion, and MR spectroscopy. Abbreviations: CBV, cerebral blood volume; Cho, choline; Mets, metastases; Cho(n), normal contralateral choline; TDL, tumefactive demyelinating lesion; MTT, mean transit time; CBF, cerebral blood flow; DWI, diffusion-weighted imaging; MRS, MR spectroscopy.

elevated because the blood-brain barrier is usually disrupted in radiation necrosis. Finally, in the setting of a bacterial abscess, there is often diffusion restriction on DWI and MRS will demonstrate amino acids such as leucine, isoleucine, valine (0.9 ppm); lactate/lipids (1.33 ppm); alanine (1.48 ppm); acetate (1.92 ppm); succinate (2.4 ppm); and glycine (3.55 ppm) (83–88). The combination of multiple parameters can improve our diagnostic specificity. This is an evolving process as we learn more about what information these functional tools are able to provide us.

ARTERIAL SPIN-LABELING PERfusion MRI IN BRAIN TUMORS

DSC MRI techniques employ exogenous tracers (gadopentetate dimeglumine or deuterium oxide). Methods utilizing endogenous tracers include signal targeting with alternating radiofrequency or echo-planar imaging and signal targeting with alternating radio frequency; and flow-sensitive alternating inversion-recovery or UNFAIR techniques. Arterial spin labeling (ASL) is an endogenous

method for determining CBF, which utilizes water as a freely diffusible tracer. Arterial blood is tagged by an inversion pulse proximal to the imaging slice of interest. By measuring signal changes between tagged images and baseline untagged images, absolute CBF measurements can be made. The advantage of this technique is that there is no need for contrast agent injection. The main disadvantage (due primarily to the delay between the labeling pulse and the arrival of labeled blood in the imaging slice of interest) is the relatively low SNR and contrast-to-noise ratios, particularly at 1.5 T. This has prevented these techniques from gaining popularity in clinical practice. Recently, investigators have examined brain tumors using ASL techniques (99–101). ASL can (on the basis of CBF measurements) differentiate between LGGs and HGGs (99). There is also linear correlation between parameters acquired from the more commonly utilized DSC MRI techniques and ASL (linear regression coefficient, $r = 0.83$; $p < 0.005$). However, another potential disadvantage is that blood flow is underestimated with ASL at low flow rates, which is often encountered in the extremely heterogeneous tumor microenvironment. Wolf et al. utilized a continuous arterial spin-labeled (CASL) perfusion MRI technique at 3 T to provide a quantitative, noninvasive alternative to DSC perfusion MR methods for evaluating gliomas. The improved SNR and spin-labeling effect at 3 T was able to differentiate glioma grade on the basis of blood flow measured using CASL perfusion MRI (102).

STANDARDIZED METHODS FOR PERFORMING PERfusion MRI, AUTOMATED METHODS FOR CLINICAL TRIALS, AND ENDPOINTS

Reliable and reproducible determinations of tumor angiogenesis and neovascularity are important in the clinical management of patients with cerebral gliomas. This is also becoming increasingly important in the numerous clinical trials investigating the efficacy of antiangiogenic agents in cancer. Reliable, reproducible data may be obtainable by experienced operators in a research setting or in the clinics of large radiology departments. Simple, objective methods with the highest intra- and interinstitutional reproducibility are necessary to detect subtle changes, especially since perfusion MRI is being used to determine the efficacy of antiangiogenic therapies (103). Certainly, pharmaceutical companies are motivated by having reproducible methods that governmental agencies such as the Food and Drug Administration (FDA) can acknowledge as imaging biomarkers in the determination of therapeutic efficacy and safety. Furthermore, agencies that ultimately determine which MR techniques are applicable clinically and can be reimbursed will need to have methods that are easily

reproducible in the clinical setting. Determination of perfusion metrics is currently undertaken in the research and clinical settings using software that relies on accurate region-of-interest (ROI) analysis. Any ROI measurement still remains operator dependent and somewhat subjective with an unavoidable component of interobserver and intraobserver variability.

Histogram analysis is a quantitative technique used in a number of neuroimaging studies but most commonly used in magnetization transfer ratio studies of patients with diffuse cerebral disease such as multiple sclerosis. Histogram analysis of DSC MRI data in focal disease such as primary glial neoplasms has not been previously well studied. Recently, we have utilized histogram analysis for quantifying perfusion data in cerebral gliomas. The histogram can be applied to the rCBV color map to display the pixel values from the magnitude image. The interval between the minimum and maximum pixel values was divided into 40 equally spaced bins. Each pixel was assigned to the bin that surrounds its value. The number of pixels corresponding to each bin was counted and frequency counts plotted as a function of the bin locations. The peak height was normalized by dividing each histogram frequency value by the total number of voxels in the sample. A total of 14 different measures were obtained from the rCBV map by histogram analysis: mean, median, standard deviation (SD), mean of the top 50% of the histogram (mean_{50}), SD of the top 50% (SD_{50}), mean of the top 25% (mean_{25}), SD of the top 25% (SD_{25}), mean of the top 10% (mean_{10}), SD of the top 10% (SD_{10}), skewness (skew), kurtosis (kurt), peak height of the histogram, peak position (i.e., the mode), and area under the histogram curve within 1 SD. These measures are collectively referred to as rCBV_T and illustrated in Figure 22. Histograms are formed of tumor pixels defined by a single ROI drawn around the maximal tumor diameter on any single axial slice, regardless of lesion heterogeneity or radiologic suggestion of necrosis. Only a single slice from the perfusion data set was used to determine the rCBV_T . The tumor margins were determined to be the entire contrast-enhancing lesion as usually seen in high-grade tumors and the entire T2 signal abnormality for non-enhancing, usually low-grade tumors.

Histogram analysis of rCBV data was found to be as effective as rCBV_{\max} derived from an ROI analysis in the correlation with glioma grade. Inexperienced operators may obtain perfusion metrics using histogram analysis that are comparable to those obtained by experienced operators using ROI analysis. Representative cases of LGG and HGG are shown in Figures 23 and 24. We also examined the reproducibility of histogram-based versus ROI-based techniques and found the interobserver and intraobserver reproducibility of rCBV was acceptable

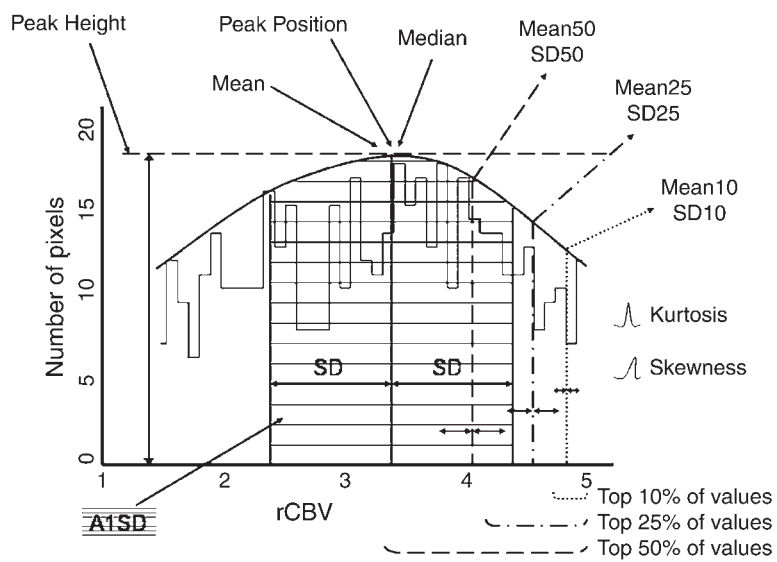


Figure 22 Sample histogram. Centile mean and SD measures are calculated from the top 50%, 25%, and 10% of the histogram curve. Skewness is zero if the data are distributed symmetrically around the mean, negative if the data are more spread out on the left of the mean, and positive if the data are more spread out on the right of the mean. Kurtosis is a measure of how “peaked” the histogram is; it equals zero if the histogram is Gaussian, is positive if the histogram has a sharper peak, and is negative if it has a flatter top. Abbreviation: SD, standard deviation.

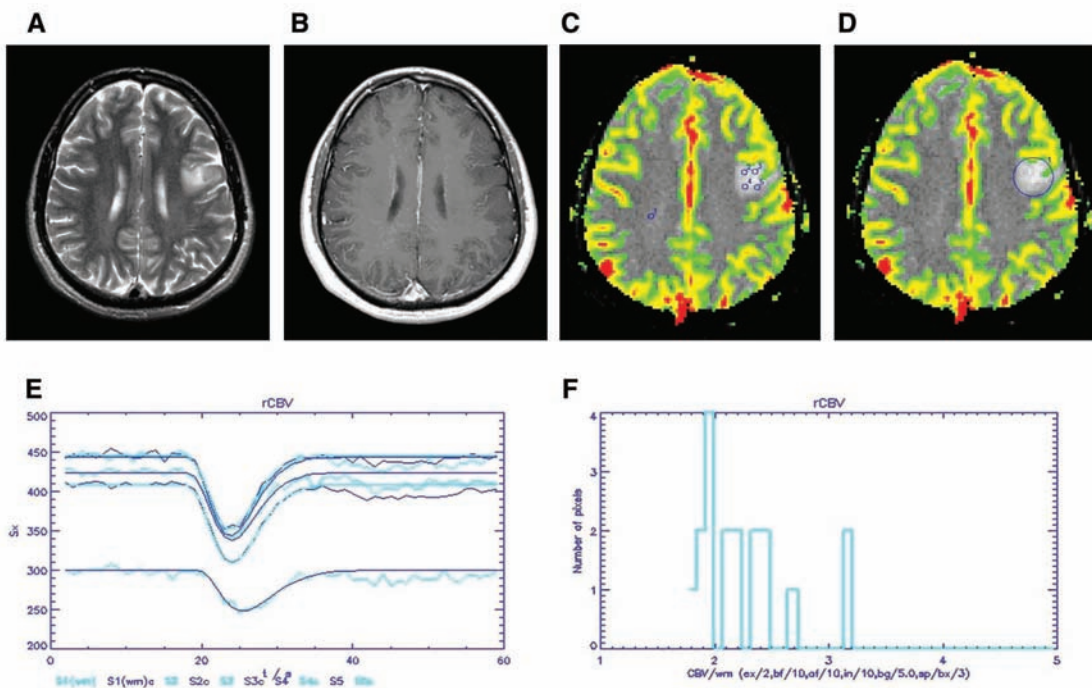


Figure 23 Low-grade glioma (grade II/IV) in left frontal lobe, (A) T2-weighted and (B) contrast T1-weighted images. The $rCBV_{max}$ method uses four small ROIs targeted to foci of greatest perfusion on (C) rCBV map, with the maximal $rCBV$ recorded from the subsequent (E) perfusion curves. Each of the signal intensity curves from each of the five ROIs are denoted by S1, S2, S3, S4, and S5, where S1 is the signal intensity curve for the ROI placed in normal brain and S2-S5, the other ROIs placed in the tumoral tissue. These five signal intensity curves were obtained from a single slice from the perfusion data set. The rCBV histogram method uses (D) a single ROI that encompasses the maximal tumor diameter to generate (F) the histogram curve, from which multiple metrics are derived. Abbreviations: rCBV, relative cerebral blood volume; ROI, region of interest. Source: From Ref. 111.

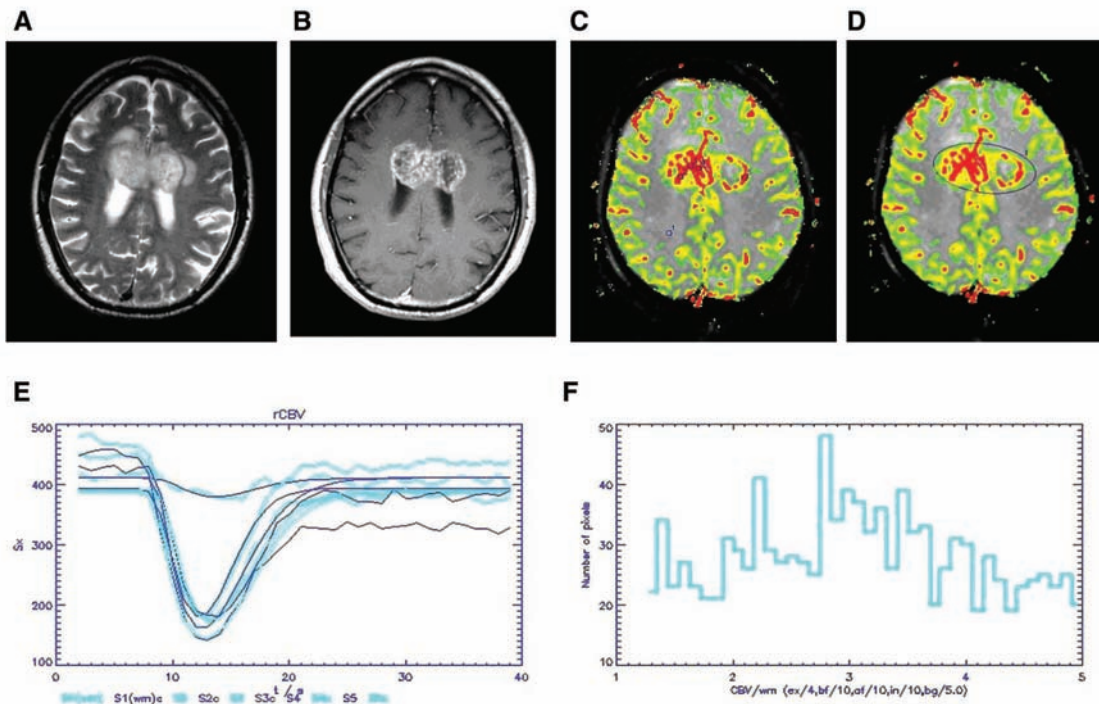


Figure 24 High-grade glioma, glioblastoma multiforme (grade IV/IV) in frontal lobes spanning the corpus callosum. (A) T2-weighted and (B) contrast T1-weighted images are shown along with (C) rCBV_{max} map with ROIs targeted to avoid areas of radiologic necrosis to determine (E) perfusion curves. (D) rCBV histogram map and (F) histogram curve are derived from the maximal tumor diameter regardless of heterogeneity. Abbreviations: rCBV, relative cerebral blood volume; ROI, region of interest. Source: From Ref. 111.

using ROI and non-ROI histogram techniques. Total tumoral histogram analysis, a non-ROI technique, outperformed ROI techniques and achieved the highest reproducibility. Further refinement of non-ROI analysis of perfusion MR data may lead to standardized, automated methods for tumor quantification. This will be critical in both single and multi-institutional studies involving quantification of perfusion metrics for both predicting glioma biology and also for assessing therapeutic response to novel antiangiogenic agents.

Perfusion MRI as Biomarkers for Novel Antiangiogenic Agents

Malignant gliomas, particularly recurrent anaplastic gliomas and glioblastoma multiforme (GBM), are highly refractory to therapy. A key feature of malignant gliomas, such as GBM, is their tendency to infiltrate surrounding tissues. This invasive property often precludes total surgical resection and makes it difficult to treat with radiation without damaging normal brain parenchyma. Because of

the difficulty in obtaining total eradication, patients with GBM have a median survival of less than one year, despite aggressive treatment. Of the approximately 35,000 Americans diagnosed with primary brain cancer each year, almost half with high-grade (WHO class III and IV) gliomas will succumb to their disease within two years if treated and in less than six months if untreated. This extremely poor prognosis has not changed despite 30 years of research, technological progress, and clinical trials. These gliomas are highly vascular and are likely the result of the tumoral upregulation of angiogenic growth factors, such as VEGF. Angiogenesis appears to play a major role in the recurrent and refractory nature of these high-grade tumors. As a result, pharmaceutical companies have invested heavily into researching and developing effective antiangiogenesis agents. One of the few agents currently approved by the FDA is Avastin or Bevacizumab.

Bevacizumab (Avastin) is a humanized murine monoclonal antibody against the VEGF receptor and was approved in February 2004 for the first-line use against metastatic colorectal cancer when used with 5-FU-based chemotherapy. There are promising data regarding its use

in other cancers as well, including renal cell carcinoma, nonsmall cell lung, pancreatic, and breast cancer (104). Current phase II and phase III studies are testing its efficacy in these and other tumor types. However, published data on Avastin's role in primary brain tumors are much more limited. One study demonstrated a 50% conventional MRI response rate in 14 patients with recurrent HGGs. Of these patients, four died (mean survival after treatment: 116 days), two of them had what the authors described as "mixed progressive disease" and the other two with "partial response," suggesting that radiographic improvement does not correlate well with clinical outcome (105).

Our initial studies with antiangiogenic agents such as thalidomide demonstrated that perfusion imaging was able to more accurately predict overall survival and progressive disease than conventional MRI (56). More recently, we have utilized CBV and permeability measurements to follow patients on Avastin. So far, it seems, as though radiographically, most patients demonstrate a response to treatment with a decrease in the enhancing volume, CBV, and vascular permeability; however, many of these patients do not demonstrate significant improvement in time to progression or overall survival (Figs. 25 and 26). Pathologically, it may be that treatment with antiangiogenic agents alters glioma biology and result in the tumor

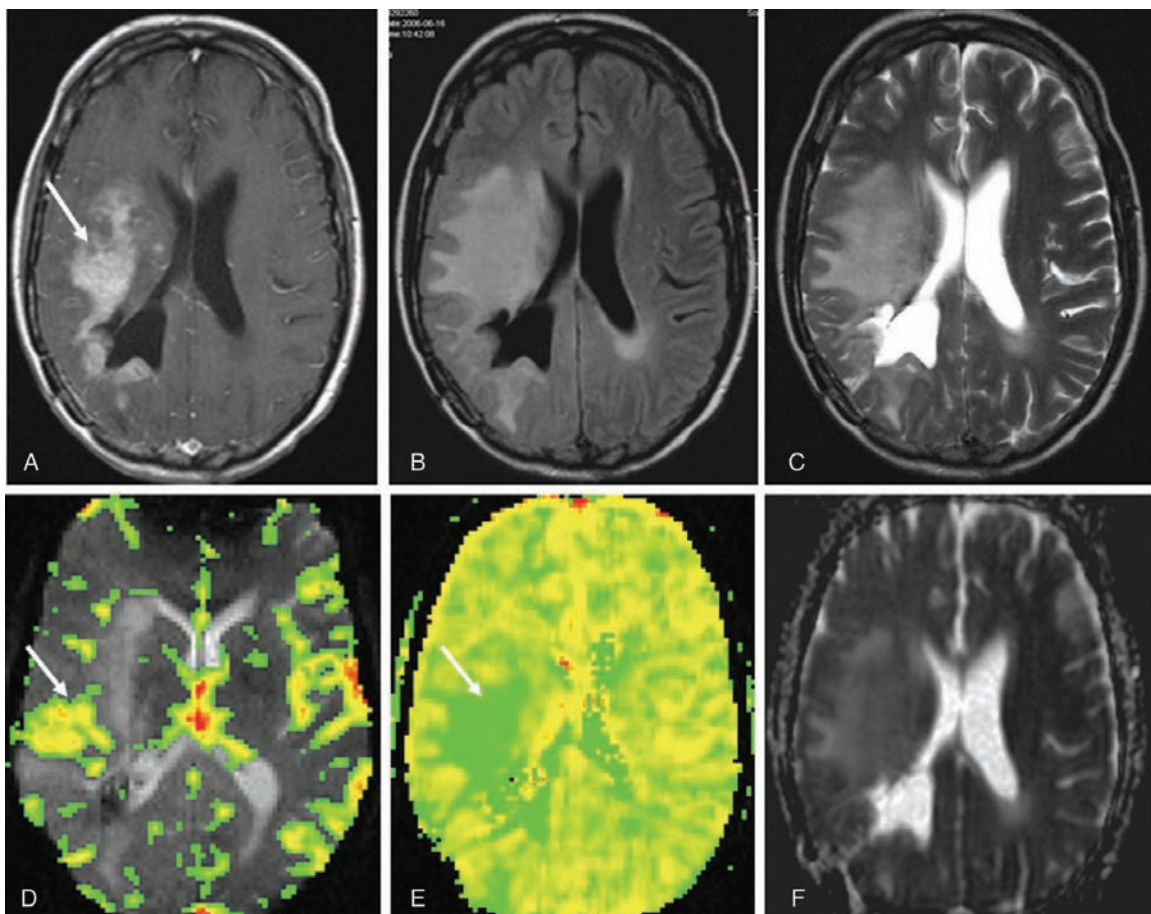


Figure 25 Pathologically recurrent glioblastoma multiforme (WHO grade IV). (A) Axial T1-weighted post-gadolinium image. (B/C) Axial FLAIR and T2-weighted images demonstrating recurrent enhancing glioma in the right frontoparietal region (white arrow). There is also substantial associated T2 signal abnormality with mass effect on the right lateral ventricle. (D) Gradient-echo axial DSC MRI with rCBV color overlay demonstrates high rCBV within the lesion (white arrow). (E) Gradient-echo axial DSC MRI with SD25 color overlay depicts signal intensity drop after 25 seconds indicating increased vascular permeability (white arrow). (F) Diffusion-weighted ADC image demonstrates some decrease in signal in keeping with some tumor cellularity within the recurrent glioma. Abbreviations: FLAIR, fast fluid-attenuated inversion recovery; DSC MRI, dynamic susceptibility contrast MRI; ADC, apparent diffusion coefficient.

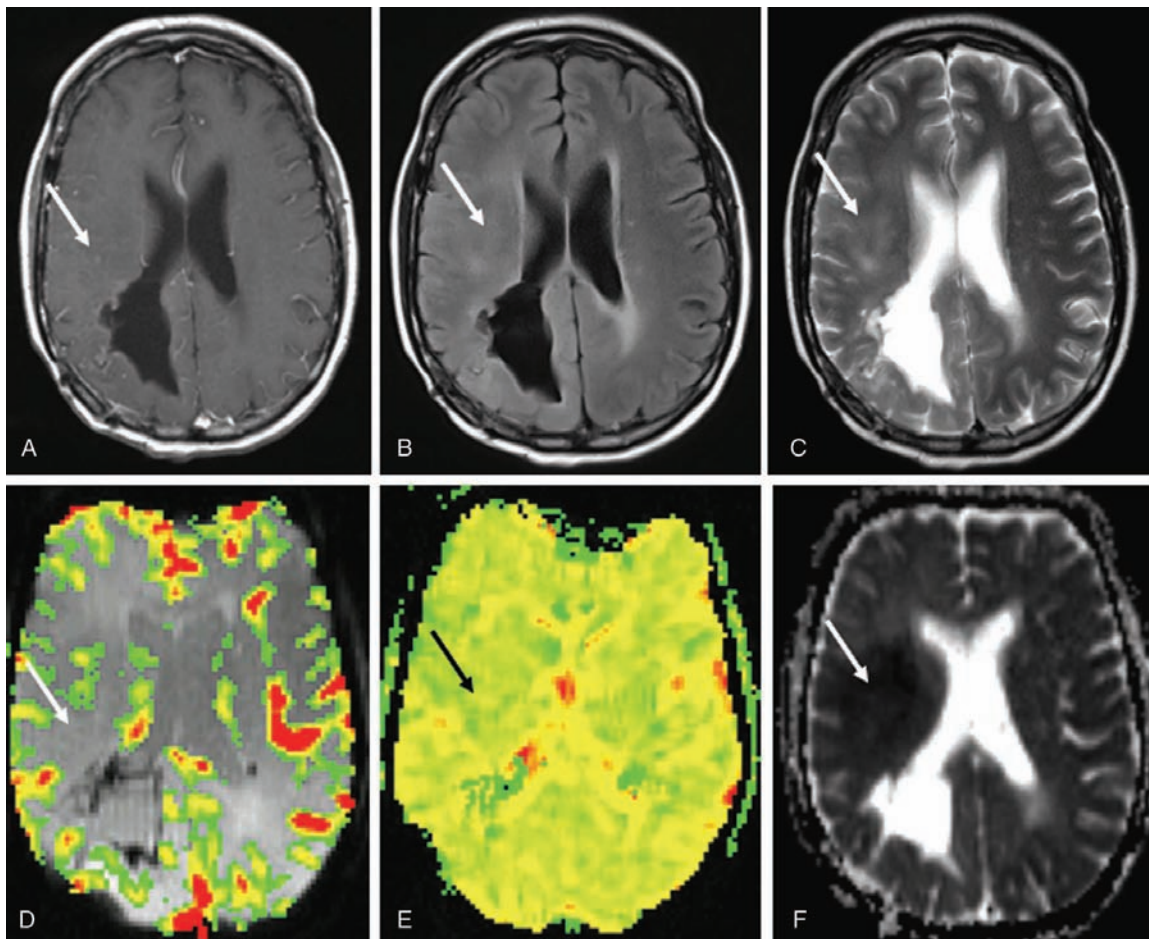


Figure 26 Pathologically recurrent glioblastoma multiforme, the same patient as in Figure 25 following two months of therapy with Avastin. (A) Axial T1-weighted post-gadolinium image. (B/C) Axial FLAIR and T2-weighted images demonstrating radiographic response to antiangiogenesis therapy, Avastin. There is almost complete resolution of contrast enhancement as well as associated T2 signal abnormality (white arrows). (D) Gradient-echo axial DSC MRI with rCBV color overlay demonstrates reduction in rCBV within the lesion (white arrow). (E) Gradient-echo axial DSC MRI with SD25 color overlay depicts signal intensity drop after 25 seconds, indicating decreased vascular permeability (black arrow). These findings are in keeping with a decrease in perfusion and permeability in response to Avastin therapy. (F) Diffusion-weighted ADC image demonstrates further decrease in signal, suggesting possible increase in tumor cellularity and possible invasiveness within the recurrent glioma, which may be a biologic response to the removal of the angiogenic component. Abbreviations: FLAIR, fast fluid-attenuated inversion recovery; DSC MRI, dynamic susceptibility contrast MRI; rCBV, relative cerebral blood volume; ADC, apparent diffusion coefficient.

become more invasive and cellular in response to the deprivation of angiogenesis. DWI and/or DTI is beginning to demonstrate the increased cellularity in some of these treated gliomas.

In the future, it is likely, as with many other disease processes such as HIV and tuberculous infection, that there will be a combination of drugs that will target different components of glioma biology that will be most effective. Regardless of therapy, it will be evident that quantitative MR measures of perfusion, diffusion, and other pathophysiologic parameters will become early surrogate biomarkers of therapeutic response.

FUTURE DIRECTIONS—COMBINING MRI METHODS TO MEASURE BLOOD VOLUME WITH FUNCTIONAL ACTIVATION

Recently, investigators have combined methods to detect changes in blood volume in conjunction with functional activation (106–108). Our own group had developed such a technique, termed “Vascular-Space-Occupancy (VASO)-dependent fMRI” (109). It uses a non-slice-selective inversion recovery sequence and an optimal inversion time (TI) to null the blood signal, resulting in an MR image that reflects the volume of extravascular

tissue. However, because of the signal weighting from tissue T_1 , such an image does not give information about the absolute CBV in the voxels, and therefore, the application has been mainly limited to the context of measuring blood volume changes in functional imaging (110). However, combining VASO MRI with the intravascular T_1 -shortening effects of the contrast agent Gd-DTPA also estimates absolute CBV in humans. Two VASO experiments with identical imaging parameters are performed before and after contrast agent administration. Since the T_1 effect of the contrast agent is restricted to the blood compartment (provided the blood-brain barrier is intact or leakage is negligible), the tissue MR signal does not change between the two experiments, whereas the blood signal increases. Therefore, the absolute CBV can be calculated from the signal difference between post and precontrast VASO images. The theoretical framework is presented, and experiments were performed on human

subjects at two commonly used magnetic field strengths, namely, 1.5 T and 3 T. Absolute CBV values for typical brain regions can be obtained using this technique and the VASO approach was found to be comparable to the conventional DSC MRI method (110). In predicting glioma biology, T_1 subtraction VASO imaging is comparable to T_2^* DSC MRI. We found that taking a ratio of the tumoral VASO (VASO_T) over the normal contralateral VASO to derive the relative VASO (VASO_R) provided improved performance (Figs. 27 and 28). This is likely due to partial correction for blood-brain barrier disruption and permeability effects. Their utility as independent predictors of grade suggests that they may be characterizing different perfusion properties. Work is underway to determine if this method can be used to derive blood volume, vascular permeability in the steady state, as well as functional activation in patients with brain tumors.

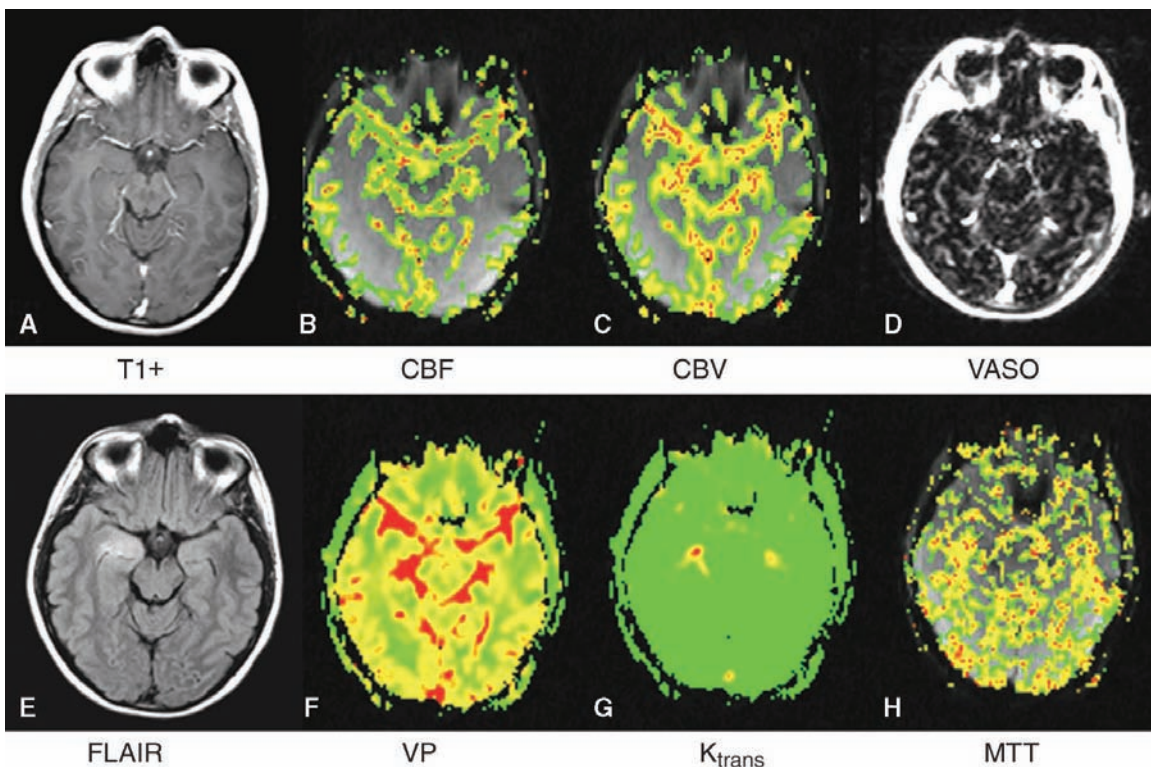


Figure 27 Pathologically proven right mesial temporal low-grade glioma. (A) Axial T1-weighted postgadolinium image. (B/C) Gradient-echo axial DSC MRI, CBF, and CBV overlay images demonstrating a lack of increased perfusion. (D) Vasoperfusion image also confirming that there is no increased perfusion within the low-grade glioma. (E) Axial FLAIR image demonstrating increased signal within the right mesial temporal lobe. (F/G/H) Gradient-echo axial DSC MRI with V_p , K^{trans} , and MTT color overlay demonstrates no increase in V_p , K^{trans} , or MTT. Abbreviations: FLAIR, fast fluid-attenuated inversion recovery; DSC MRI, dynamic susceptibility contrast MRI; CBF, cerebral blood flow; CBV, cerebral blood volume; V_p , blood plasma volume; K^{trans} , vascular permeability; MTT, mean transit time. Source: From Ref. 112.

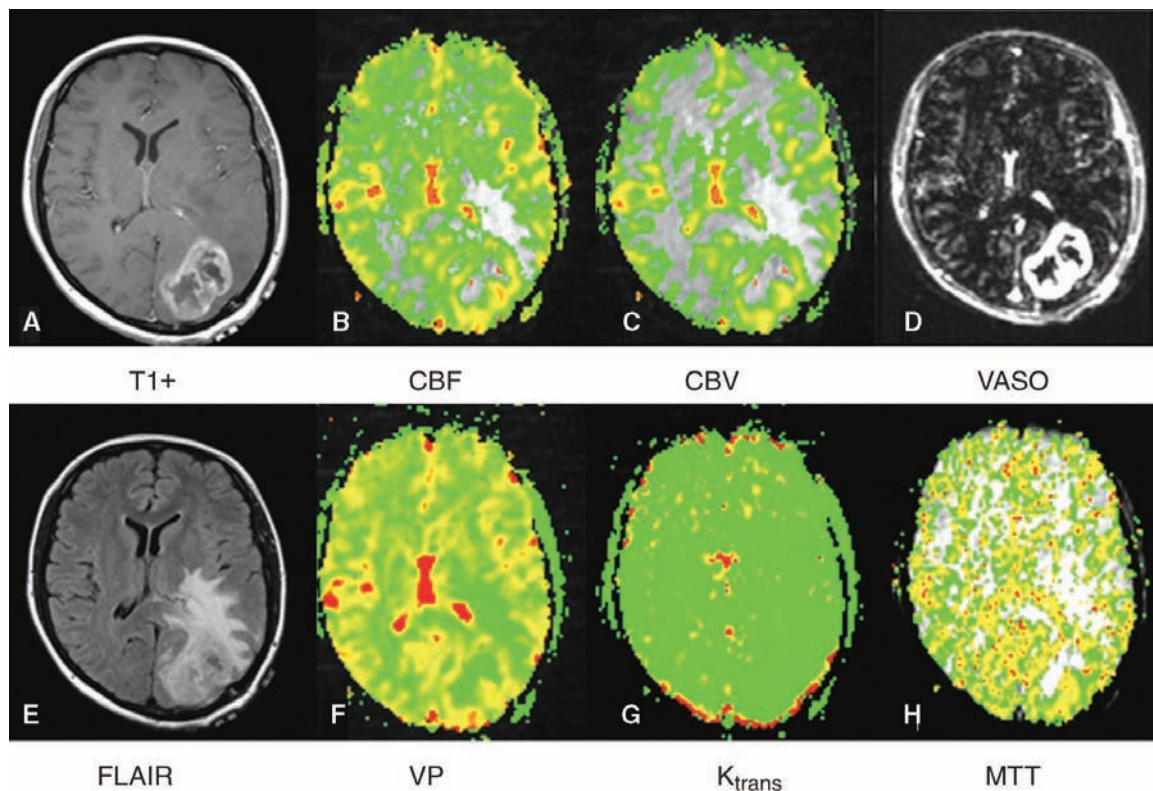


Figure 28 Pathologically proven left parieto-occipital high-grade glioma. (A) Axial T1-weighted postgadolinium image. (B/C) Gradient-echo axial DSC MRI, CBF, and CBV overlay images demonstrating increased CBF and CBV. (D) Vasoperfusion image also confirming that there is increased perfusion within left parieto-occipital lesion. (E) Axial FLAIR image demonstrating increased signal surrounding the left parieto-occipital lesion. (F/G/H) Gradient-echo axial DSC MRI with V_p , K^{trans} , and MTT color overlay demonstrates an increase in V_p , K^{trans} and MTT. Abbreviations: FLAIR, fast fluid-attenuated inversion recovery; DSC MRI, dynamic susceptibility contrast MRI; CBF, cerebral blood flow; CBV, cerebral blood volume; V_p , blood plasma volume; K^{trans} , vascular permeability; MTT, mean transit time. Source: From Ref. 112.

REFERENCES

1. Folkman J. Tumor angiogenesis: therapeutic implications. *N Engl J Med* 1971; 285:1182–1186.
2. Vajkoczy P, Menger MD. Vascular microenvironment in gliomas. *J Neurooncol* 2000; 50(1–2):99–108.
3. Dvorak HF, Brown LF, Detmar M, et al. Vascular permeability factor/vascular endothelial growth factor, microvascular hyperpermeability, and angiogenesis. *Am J Pathol* 1995; 146(5):1029–1039.
4. Dvorak HF, Nagy JA, Feng D, et al. Vascular permeability factor/vascular endothelial growth factor and the significance of microvascular hyperpermeability in angiogenesis. *Curr Top Microbiol Immunol* 1999; 237:97–132.
5. Provenzale JM, Wang GR, Brenner T, et al. Comparison of permeability in high-grade and low-grade brain tumors using dynamic susceptibility contrast MR imaging. *AJR Am J Roentgenol* 2002; 178(3):711–716.
6. Roberts HC, Roberts TP, Ley S, et al. Quantitative estimation of microvascular permeability in human brain tumors: correlation of dynamic Gd-DTPA-enhanced MR imaging with histopathologic grading. *Acad Radiol* 2002; 9(suppl 1):S151–155.
7. Roberts HC, Roberts TPL, Brasch RC, et al. Quantitative measurement of microvascular permeability in human brain tumors achieved using dynamic contrast-enhanced MR imaging: correlation with histologic grade. *AJNR Am J Neuroradiol* 2000; 21(5):891–899.
8. Sorensen AG, Reimer P. Cerebral MR Perfusion Imaging: Principles and Current Applications. 152nd ed. New York: Thieme, 2000.
9. Aronen HJ, Gazit IE, Louis DN, et al. Cerebral blood volume maps of gliomas: comparison with tumor grade and histologic findings. *Radiology* 1994; 191(1):41–51.
10. Bruening R, Kwong KK, Vevea MJ, et al. Echo-planar MR determination of relative cerebral blood volume in human brain tumors: T1 versus T2 weighting. *AJNR Am J Neuroradiol* 1996; 17(5):831–840.
11. Cha S, Johnson G, Wadghiri YZ, et al. Dynamic, contrast-enhanced perfusion MRI in mouse gliomas: correlation with histopathology. *Magn Reson Med* 2003; 49(5):848–855.

12. Cha S, Knopp EA, Johnson G, et al. Intracranial mass lesions: dynamic contrast-enhanced susceptibility-weighted echo-planar perfusion MR imaging. *Radiology* 2002; 223(1):11–29.
13. Knopp EA, Cha S, Johnson G, et al. Glial neoplasms: dynamic contrast-enhanced T2*-weighted MR imaging. *Radiology* 1999; 211(3):791–798.
14. Lev MH, Rosen BR. Clinical applications of intracranial perfusion MR imaging. *Neuroimaging Clin N Am* 1999; 9(2):309–331.
15. Petrella JR, Provenzale JM. MR Perfusion imaging of the brain: techniques and applications. *Am J Roentgenol* 2000; 175(1):207–219.
16. Shin JH, Lee HK, Kwun BD, et al. Using relative cerebral blood flow and volume to evaluate the histopathologic grade of cerebral gliomas: preliminary results. *Am J Roentgenol* 2002; 179(3):783–789.
17. Sugahara T, Korogi Y, Kochi M, et al. Correlation of MR imaging-determined cerebral blood volume maps with histologic and angiographic determination of vascularity of gliomas. *AJR Am J Roentgenol* 1998; 171(6):1479–1486.
18. Sugahara T, Korogi Y, Shigematsu Y, et al. Value of dynamic susceptibility contrast magnetic resonance imaging in the evaluation of intracranial tumors. *Top Magn Reson Imaging* 1999; 10(2):114–124.
19. Wong ET, Jackson EF, Hess KR, et al. Correlation between dynamic MRI and outcome in patients with malignant gliomas. *Neurology* 1998; 50(3):777–781.
20. Wong JC, Provenzale JM, Petrella JR. Perfusion MR Imaging of Brain Neoplasms. *Am J Roentgenol* 2000; 174(4): 1147–1157.
21. Law M, Young R, Babb J, et al. Comparing perfusion metrics obtained from a single compartment versus pharmacokinetic modeling methods using dynamic susceptibility contrast-enhanced perfusion MR imaging with glioma grade. *AJNR Am J Neuroradiol* 2006; 27:1975–1982.
22. Zierler KL. Circulation times and the theory of indicator-dilution methods for determining blood flow and volume. *Handbook of Physiology*. Baltimore, MD: Williams & Wilkins, 1962:585–615.
23. Johnson G, Wetzel SG, Cha S, et al. Measuring blood volume and vascular transfer constant from dynamic, T(2)*-weighted contrast-enhanced MRI. *Magn Reson Med* 2004; 51:961–968.
24. Tofts PS, Kermode AG. Measurement of the blood-brain barrier permeability and leakage space using dynamic MR imaging. 1. Fundamental concepts. *Magn Reson Med* 1991; 17(2):357–367.
25. Tofts PS, Brix G, Buckley DL, et al. Estimating kinetic parameters from dynamic contrast-enhanced T(1)-weighted MRI of a diffusible tracer: standardized quantities and symbols. *J Magn Reson Imaging* 1999; 10(3): 223–232.
26. Rosen BR, Belliveau JW, Vevea JM, et al. Perfusion imaging with NMR contrast agents. *Magn Reson Med* 1990; 14:249–265.
27. Yang S, Law M, Zagzag D, et al. Dynamic contrast-enhanced perfusion MR imaging measurements of endothelial permeability: differentiation between atypical and typical meningiomas. *AJNR Am J Neuroradiol* 2003; 24(8): 1554–1559.
28. Law M, Yang S, Babb JS, et al. Comparison of cerebral blood volume and vascular permeability from dynamic susceptibility contrast-enhanced perfusion MR imaging with glioma grade. *AJNR Am J Neuroradiol* 2004; 25(5): 746–755.
29. McDonald DM, Choyke PL. Imaging of angiogenesis: from microscope to clinic. *Nat Med* 2003; 9(6):713–725.
30. McDonald DM, Blank P. Significance of blood vessel leakiness in cancer. *Cancer Res* 2002; 62:5381–5385.
31. Li KL, Zhu XP, Checkley DR, et al. Simultaneous mapping of blood volume and endothelial permeability surface area product in gliomas using iterative analysis of first-pass dynamic contrast enhanced MRI data. *Br J Radiol* 2003; 76(901):39–51.
32. Aronen HJ, Perkio J. Dynamic Susceptibility Contrast MRI of Gliomas. *Neuroimaging Clin N Am* 2002; 12: 501–523.
33. Weisskoff RM, Zuo CS, Boxerman JL, et al. Microscopic susceptibility variation and transverse relaxation: theory and experiment. *Magn Reson Med* 1994; 31:601–610.
34. Young IR, Cox IJ, Coutts GA, et al. Some consideration concerning susceptibility, longitudinal relaxation time constants and motion artifact in vivo human spectroscopy. *NMR Biomed* 1989; 2:329–339.
35. Padhani AR, Dzik-Jurasz A. Perfusion MR imaging of extracranial tumor angiogenesis. *Top Magn Reson Imaging* 2004; 15(1):41–57.
36. Cha S, Yang L, Johnson G, et al. Comparison of Microvascular Permeability Measurements, K(trans), Determined with Conventional Steady-State T1-Weighted and First-Pass T2*-Weighted MR Imaging Methods in Gliomas and Meningiomas. *AJNR Am J Neuroradiol* 2006; 27(2): 409–417.
37. Parks LD, Choma MA, York GE, et al. Correlation of DCE and rCBV values for patients with high grade glial neoplasms. *Proceedings, Radiological Society of North America*, Chicago 2005, III:346.
38. Cha S. Dynamic susceptibility-weighted contrast-enhanced perfusion MR imaging in pediatric patients. *Neuroimaging Clin N Am* 2006; 16(1):137–147, ix.
39. Law M, Oh S, Babb JS, et al. Low-grade gliomas: dynamic susceptibility-weighted contrast-enhanced perfusion MR imaging—prediction of patient clinical response. *Radiology* 2006; 238(2):658–667.
40. Law M, Oh S, Johnson G, et al. Perfusion magnetic resonance imaging predicts patient outcome as an adjunct to histopathology: a second reference standard in the surgical and nonsurgical treatment of low-grade gliomas. *Neurosurgery* 2006; 58(6):1099–1107; (discussion 1099–1107).
41. Law M, Yang S, Wang H, et al. Glioma grading: sensitivity, specificity, and predictive values of perfusion MR imaging and proton MR spectroscopic imaging compared with conventional MR imaging. *AJNR Am J Neuroradiol* 2003; 24(10):1989–1998.
42. Gilles FH, Brown WD, Leviton A, et al. Limitations of the World Health Organization classification of childhood

- supratentorial astrocytic tumors. Children Brain Tumor Consortium. *Cancer* 2000; 88(6):1477–1483.
- 43. Jackson RJ, Fuller GN, Abi-Said D, et al. Limitations of stereotactic biopsy in the initial management of gliomas. *Neuro-oncol* 2001; 3(3):193–200.
 - 44. Shaw EG, Wisoff JH. Prospective clinical trials of intracranial low-grade glioma in adults and children. *Neuro-oncol* 2003; 5(3):153–160.
 - 45. Yang D, Korogi Y, Sugahara T, et al. Cerebral gliomas: prospective comparison of multivoxel 2D chemical-shift imaging proton MR spectroscopy, echoplanar perfusion and diffusion-weighted MRI. *Neuroradiology* 2002; 44(8):656–666.
 - 46. Uematsu H, Maeda M, Sadato N, et al. Vascular Permeability: Quantitative Measurement with Double-Echo Dynamic MR Imaging—Theory and Clinical Application. *Radiology* 2000; 214(3):912–917.
 - 47. Martin AJ, Liu H, Hall WA, et al. Preliminary assessment of turbo spectroscopic imaging for targeting in brain biopsy. *AJNR Am J Neuroradiol* 2001; 22(5):959–968.
 - 48. Kelly PJ, Daumas-Duport C, Scheithauer BW, et al. Stereotactic histologic correlations of computed tomography- and magnetic resonance imaging-defined abnormalities in patients with glial neoplasms. *Mayo Clin Proc* 1987; 62(6):450–459.
 - 49. Essig M, Waschkies M, Wenz F, et al. Assessment of brain metastases with dynamic susceptibility-weighted contrast-enhanced MR imaging: initial results. *Radiology* 2003; 228(1):193–199.
 - 50. Ball WS Jr., Holland SK. Perfusion imaging in the pediatric patient. *Magn Reson Imaging Clin N Am* 2001; 9(1):207–230, ix.
 - 51. Kleihues P, Cavane P. WHO Classification of Tumors: Pathology and Genetic of Tumours of the Nervous System. Lyon: IARC Press, 2000.
 - 52. Yang S, Wetzel S, Law M, et al. Dynamic contrast-enhanced T2*-weighted MR imaging of gliomatosis cerebri. *AJNR Am J Neuroradiol* 2002; 23(3):350–355.
 - 53. Saraf-Lavi E, Bowen BC, Pattany PM, et al. Proton MR Spectroscopy of Gliomatosis Cerebri: Case Report of Elevated Myoinositol with Normal Choline Levels. *AJNR Am J Neuroradiol* 2003; 24(5):946–951.
 - 54. Wenz F, Rempp K, Hess T, et al. Effect of radiation on blood volume in low-grade astrocytomas and normal brain tissue: quantification with dynamic susceptibility contrast MR imaging. *Am J Roentgenol* 1996; 166(1): 187–193.
 - 55. Fuss M, Wenz F, Scholdei R, et al. Radiation-induced regional cerebral blood volume (rCBV) changes in normal brain and low-grade astrocytomas: quantification and time and dose-dependent occurrence. *Int J Radiat Oncol Biol Phys* 2000; 48(1):53–58.
 - 56. Cha S, Knopp EA, Johnson G, et al. Dynamic, contrast-enhanced T2*-weighted MR imaging of recurrent malignant gliomas treated with thalidomide and carboplatin. *Am J Neuroradiol* 2000; 21(5):881–890.
 - 57. Cha S, Tihan T, Crawford F, et al. Differentiation of low-grade oligodendroglomas from low-grade astrocytomas by using quantitative blood-volume measurements derived from dynamic susceptibility contrast-enhanced MR imaging. *AJNR Am J Neuroradiol* 2005; 26(2):266–273.
 - 58. Lev MH, Ozsunar Y, Henson JW, et al. Glial tumor grading and outcome prediction using dynamic spin-echo MR susceptibility mapping compared with conventional contrast-enhanced MR: confounding effect of elevated rCBV of oligodendroglomas (corrected). *AJNR Am J Neuroradiol* 2004; 25(2):214–221.
 - 59. Engelhard HH, Stelea A, Cochran EJ. Oligodendrogloma: pathology and molecular biology. *Surg Neurol* 2002; 58(2):111–117 (discussion 117).
 - 60. Watanabe T, Nakamura M, Kros JM, et al. Phenotype versus genotype correlation in oligodendroglomas and low-grade diffuse astrocytomas. *Acta Neuropathol (Berl)* 2002; 103(3):267–275.
 - 61. Bauman GS, Ino Y, Ueki K, et al. Allelic loss of chromosome 1p and radiotherapy plus chemotherapy in patients with oligodendroglomas. *Int J Radiat Oncol Biol Phys* 2000; 48(3):825–830.
 - 62. Buckner JC. Factors influencing survival in high-grade gliomas. *Semin Oncol* 2003; 30(6 suppl 19):10–14.
 - 63. Cairncross J, Ueki K, Zlatescu M, et al. Specific genetic predictors of chemotherapeutic response and survival in patients with anaplastic oligodendroglomas. *J Natl Cancer Inst* 1998; 90(19):1473–1479.
 - 64. Law M, Meltzer DE, Wetzel SG, et al. Conventional MR imaging with simultaneous measurements of cerebral blood volume and vascular permeability in ganglioglioma. *Magn Reson Imaging* 2004; 22(5):599–606.
 - 65. Bowles AP Jr., Pantazis CG, Allen MB Jr., et al. Ganglioglioma, a malignant tumor? Correlation with flow deoxyribonucleic acid cytometric analysis. *Neurosurgery* 1988; 23(3):376–381.
 - 66. Hart MN, Earle KM. Primitive neuroectodermal tumors of the brain in children. *Cancer* 1973; 32(4):890–897.
 - 67. Kosnik EJ, Boesel CP, Bay J, et al. Primitive neuroectodermal tumors of the central nervous system in children. *J Neurosurg* 1978; 48(5):741–746.
 - 68. Duffner PK, Cohen ME, Heffner RR, et al. Primitive neuroectodermal tumors of childhood. An approach to therapy. *J Neurosurg* 1981; 55(3):376–381.
 - 69. Bellis EH, Salzman M, Bastian FO. Primitive neuroectodermal tumor in a 57-year-old man. *Surg Neurol* 1983; 20(1):30–35.
 - 70. Gaffney CC, Sloane JP, Bradley NJ, et al. Primitive neuroectodermal tumours of the cerebrum. Pathology and treatment. *J Neurooncol* 1985; 3(1):23–33.
 - 71. Masuda K, Yutani C, Akutagawa K, et al. Cerebral primitive neuroectodermal tumor in an adult male. A case report. *Acta Cytol* 2000; 44(6):1050–1058.
 - 72. Law M, Kazmi K, Wetzel S, et al. Dynamic susceptibility contrast-enhanced perfusion and conventional MR imaging findings for adult patients with cerebral primitive neuroectodermal tumors. *AJNR Am J Neuroradiol* 2004; 25(6):997–1005.
 - 73. Law M, Teicher N, Zagzag D, et al. Dynamic contrast enhanced perfusion MRI in mycosis fungoides. *J Magn Reson Imaging* 2003; 18(3):364–367.

74. Hartmann M, Heiland S, Harting I, et al. Distinguishing of primary cerebral lymphoma from high-grade glioma with perfusion-weighted magnetic resonance imaging. *Neurosci Lett* 2003; 338(2):119–122.
75. Sugahara T, Korogi Y, Shigematsu Y, et al. Perfusion-sensitive MRI of cerebral lymphomas: a preliminary report. *J Comput Assist Tomogr* 1999; 23(2):232–237.
76. Berger MS. Perfusion MR and the evaluation of meningiomas: is it important surgically? *AJNR Am J Neuroradiol* 2003; 24(8):1499–1500.
77. Kothary N, Law M, Cha S, et al. Conventional and perfusion MR imaging of parafalcine chondrosarcoma. *AJNR Am J Neuroradiol* 2003; 24(2):245–248.
78. Burger PC. Classification, grading, and patterns of spread of malignant gliomas. In: Apuzzo ML, eds. *Neurosurgical Topics: Malignant Cerebral Glioma*. Park Ridge, Ill: America Association of Neurological Surgeons, 1990:3–17.
79. Burger PC, Vogel FS, Green SB, et al. Glioblastoma multiforme and anaplastic astrocytoma: pathologic criteria and prognostic implications. *Cancer* 1985; 56:1106–1111.
80. Law M, Cha S, Knopp EA, et al. High-grade gliomas and solitary metastases: Differentiation by using perfusion and proton spectroscopic MR imaging. *Radiology* 2002; 222(3): 715–721.
81. Cha S, Pierce S, Knopp EA, et al. Dynamic contrast-enhanced T2*-weighted MR imaging of tumefactive demyelinating lesions. *AJNR Am J Neuroradiol* 2001; 22(6):1109–1116.
82. Yang S, Law M, Yu D, et al. Differentiation between high grade gliomas and solitary metastases using relative CBV and vascular permeability measurements from DCE MRI. Proceedings, Annual Meeting of the American Society of Neuroradiology, Washington, D.C., 2003.
83. Dev R, Gupta RK, Poptani H, et al. Role of in vivo proton magnetic resonance spectroscopy in the diagnosis and management of brain abscesses. *Neurosurgery* 1998; 42(1): 37–43.
84. Chang KH, Song IC, Kim SH, et al. In vivo single-voxel proton MR spectroscopy in intracranial cystic masses. *AJNR Am J Neuroradiol* 1998; 19(3):401–405.
85. Gupta RK, Vatsal DK, Husain N, et al. Differentiation of tuberculous from pyogenic brain abscesses with in vivo proton MR spectroscopy and magnetization transfer MR imaging. *AJNR Am J Neuroradiol* 2001; 22(8):1503–1509.
86. Shukla-Dave A, Gupta RK, Roy R, et al. Prospective evaluation of in vivo proton MR spectroscopy in differentiation of similar appearing intracranial cystic lesions. *Magn Reson Imaging* 2001; 19(1):103–110.
87. Kadota O, Kohno K, Ohue S, et al. Discrimination of brain abscess and cystic tumor by in vivo proton magnetic resonance spectroscopy. *Neurol Med Chir (Tokyo)* 2001; 41(3):121–126.
88. Burtscher IM, Holtas S. In vivo proton MR spectroscopy of untreated and treated brain abscesses. *AJNR Am J Neuroradiol* 1999; 20(6):1049–1053.
89. Pandit S, Lin A, Gahbauer H, et al. MR spectroscopy in neurocysticercosis. *J Comput Assist Tomogr* 2001; 25(6): 950–952.
90. Gupta RK, Roy R, Dev R, et al. Finger printing of mycobacterium tuberculosis in patients with intracranial tuberculomas by using in vivo, ex vivo, and in vitro magnetic resonance spectroscopy. *Magn Reson Med* 1996; 36(6): 829–833.
91. Gupta RK, Haris M, Husain N, et al. Relative cerebral blood volume is a measure of angiogenesis in brain tuberculoma and its therapeutic implications. *Proceedings, ISMRM*, 2006:181.
92. Law M, Hamburger M, Johnson G, et al. Differentiating surgical from non-surgical lesions using perfusion MR imaging and proton MR spectroscopic imaging. *Technol Cancer Res Treat* 2004; 3(6):557–566.
93. Graham D, Lantos PL. *Vascular Diseases*. Greenfields Neuropathology, New York: Oxford University Press, 1997.
94. Morgenstern LB, Frankowski RF. Brain tumor masquerading as stroke. *J Neurooncol* 1999; 44(1):47–52.
95. Jiang Q, Ewing JR, Ding GL, et al. Quantitative evaluation of BBB permeability after embolic stroke in rat using MRI. *J Cereb Blood Flow Metab* 2005; 25(5):583–592.
96. Holodny AI, Ollenschlager M. Diffusion imaging in brain tumors. *Neuroimaging Clin N Am* 2002; 12(1):107–124, x.
97. Sorensen AG, Copen WA, Ostergaard L, et al. Hyperacute stroke: simultaneous measurement of relative cerebral blood volume, relative cerebral blood flow, and mean transit time. *Radiology* 1999; 210(519–527).
98. Vajkoczy P, Ullrich A, Menger MD. Intravital fluorescence videomicroscopy to study tumor angiogenesis and microcirculation. *Neoplasia* 2000; 2(1–2):53–61.
99. Warmuth C, Gunther M, Zimmer C. Quantification of blood flow in brain tumors: comparison of arterial spin labeling and dynamic susceptibility-weighted contrast-enhanced MR imaging. *Radiology* 2003; 228(2):523–532.
100. Silva AC, Kim SG, Garwood M. Imaging blood flow in brain tumors using arterial spin labelling. *Magn Reson Med* 2000; 44:169–173.
101. Gaa J, Warach S, Wen P, et al. Noninvasive perfusion imaging of human brain tumors with EPISTAR. *Eur Radiol* 1996; 6:518–522.
102. Wolf RL, Wang J, Wang S, et al. Grading of CNS neoplasms using continuous arterial spin labeled perfusion MR imaging at 3 Tesla. *J Magn Reson Imaging* 2005; 22(4): 475–482.
103. Akella NS, Twieg DB, Mikkelsen T, et al. Assessment of brain tumor angiogenesis inhibitors using perfusion magnetic resonance imaging: quality and analysis results of a phase I trial. *J Magn Reson Imaging* 2004; 20(6): 913–922.
104. de Gramont A, Van Cutsem E. Investigating the potential of bevacizumab in other indications: metastatic renal cell, non-small cell lung, pancreatic and breast cancer. *Oncology* 2005; 69(suppl 3):46–56.
105. Pope WB, Lai A, Nghiemphu P, et al. MRI in patients with high-grade gliomas treated with bevacizumab and chemotherapy 10.1212/01.wnl.0000208958.29600.87. *Neurology* 2006; 66(8):1258–1260.
106. Lu H, Golay X, Pekar JJ, et al. Sustained poststimulus elevation in cerebral oxygen utilization after vascular recovery. *J Cereb Blood Flow Metab* 2004; 24(7):764–770.

107. Lu H, van Zijl PC, Hendrikse J, et al. Multiple acquisitions with global inversion cycling (MAGIC): a multislice technique for vascular-space-occupancy dependent fMRI. *Magn Reson Med* 2004; 51(1):9–15.
108. Lu H, Golay X, Pekar JJ, et al. Functional magnetic resonance imaging based on changes in vascular space occupancy. *Magn Reson Med* 2003; 50(2):263–274.
109. Lu H, Law M, Johnson G, et al. Novel approach to the measurement of absolute cerebral blood volume using vascular-space-occupancy magnetic resonance imaging. *Magn Reson Med* 2005; 54(6):1403–1411.
110. Lu H, van Zijl PC. Experimental measurement of extravascular parenchymal BOLD effects and tissue oxygen extraction fractions using multi-echo VASO fMRI at 1.5 and 3.0 T. *Magn Reson Med* 2005; 53(4): 808–816.
111. Law M, Young R, Babb J, et al. Histogram analysis versus region of interest analysis of dynamic susceptibility contrast perfusion MR imaging data in the grading of cerebral gliomas. *AJNR Am J Neuroradiol* 2007; 28: 761–766.
112. Lu H, Pollack E, Young R, et al. Predicting Grade of Cerebral Glioma Using Vascular-Space Occupancy MR Imaging. *AJNR Am J Neuroradiol* 2008; 29(2):373–378.

18

Magnetoencephalography

TIMOTHY P.L. ROBERTS, CHRISTOPHER EDGAR, and ERIN SIMON SCHWARTZ

Children's Hospital of Philadelphia, Philadelphia, Pennsylvania, U.S.A.

INTRODUCTION

Many of the determinants of brain function (normal and abnormal) are influenced by the genetic codes, giving rise to structural and functional features of the brain. Our immediate interaction with the world however is electrochemical in nature—release of neurotransmitters, action potentials in neurons, and synaptic events. Electromagnetic activity occurs on a timescale measured in fractions of a second, and such rapid processing and transmission of information is needed to successfully interact with our environment. Thus, understanding the brain necessitates the use of noninvasive technologies that are (*i*) sensitive to activity at the neuronal level and (*ii*) sufficiently fast to track dynamic processes with millisecond or better temporal resolution.

Although magnetic resonance imaging (MRI)-based functional imaging has advanced considerably over recent years, an inherent limitation of functional MRI (fMRI) is the poor temporal resolution intrinsic to hemodynamic phenomena (blood oxygenation and blood flow). As such, fMRI is unable to track rapidly changing neural activity within and across brain regions. Alternative imaging methods are needed that complement fMRI in evaluating brain activity in the healthy brain as well as in patients with neurologic and psychiatric disorders. Magnetoencephalography (MEG) measures electromagnetic neural activity. The temporal resolution of MEG is limited only

by the data acquisition rate, thus allowing real-time assessment of brain electrophysiology. As such, MEG has the temporal resolution needed to detect ongoing oscillatory activity as well as isolated bursts of electrical discharge (e.g., interictal epileptiform activity). Propagation of brain activity can also be assessed.

This chapter describes the use of MEG in the clinical assessment of brain activity in patients referred for pre-surgical mapping of eloquent cortex and the identification of zone(s) of interictal discharge in seizure disorders. While the ability of MEG to resolve and localize brain activity is under continuous discussion, evaluation, and improvement, numerous studies have demonstrated the utility of MEG source localization, and this technique is now commonly used in the clinical definition of eloquent cortex prior to neurosurgical procedures (1–5), as well as in the localization of the source(s) of interictal epileptiform activity (6). MEG technology, MEG clinical applications, and the future of MEG as a clinical tool are considered.

MEG—THE TECHNOLOGY

MEG instrumentation and technology are briefly described. For readers with an interest in MEG instrumentation and technology, Lewine and Orrison (7) provide a detailed but accessible review. Hämäläinen et al. (8) provide a more extensive and technical review.

Like electroencephalography (EEG), MEG measures electromagnetic activity. Whereas EEG results from the extracellular volume currents triggered mainly by postsynaptic potentials, MEG is thought to arise from the intracellular branch of this process—from the currents flowing from the dendritic tree to the soma (7). As a result, MEG is mainly sensitive to the currents flowing tangentially to the surface of the scalp (9) and to a lesser degree to radial sources.

In patients referred for a presurgical examination, accurate localization of eloquent cortex and epileptic foci is needed. Accurate localization of brain activity using EEG is compromised by the smearing of electrical brain activity due to the varying electrical conductivities of intervening tissues (e.g., cerebrospinal fluid, scalp, skull). The magnetic fields associated with neural activity however are not distorted as they pass through tissues with varying conductivity. As such, MEG, the “magnetic cousin” of EEG, provides a methodology with high temporal resolution (~ms) and reasonable spatial resolution (~mm), especially for cortical activity. Leahy et al. (10) showed an average spatial localization error of 3 mm with 61-channel MEG and 7 to 8 mm with up to 64-channel EEG across 32 dipole sources.

First recorded in the late 1960s (11,12), MEG technology has evolved through increasingly dense sensor arrays, from single-channel detector systems that required repositioning to fully sample magnetic field patterns, through partial coverage systems (7 or 37 spatially distinct sensors, allowing coverage of lobar anatomy) (13,14), to whole-cortex sensor arrays with several hundred sensors covering the entire head (15). Figure 1 shows a 275-channel system.

MEG sensors detect the neuromagnetic fields produced by current flow within neurons. Specifically, the neuromagnetic signals induce an electric current within the wire loops of a detection coil. The detection coil is coupled to a superconducting quantum interference device (SQUID), which produces a voltage output proportional to the current flowing in the input coil. To detect the weak magnetic fields generated by neural activity (10 fT–1 pT), detection coils and sensors are maintained at superconducting temperatures, accomplished by bathing the sensors in liquid helium, contained within a cryogenically insulated dewar (Fig. 1). Thus, unlike EEG, MEG sensors are located at a distance from the patient’s head. Because the MEG sensors are sensitive to any magnetic activity, MEG recordings are performed in a room with walls made of materials of high magnetic permeability and electrical conductivity to shield the sensors from external magnetic fields (e.g., power lines, computers, moving metal carts).

The neuromagnetic field associated with a single postsynaptic event is too weak to produce a magnetic field that MEG sensors can detect. Thus, distinct from single-unit

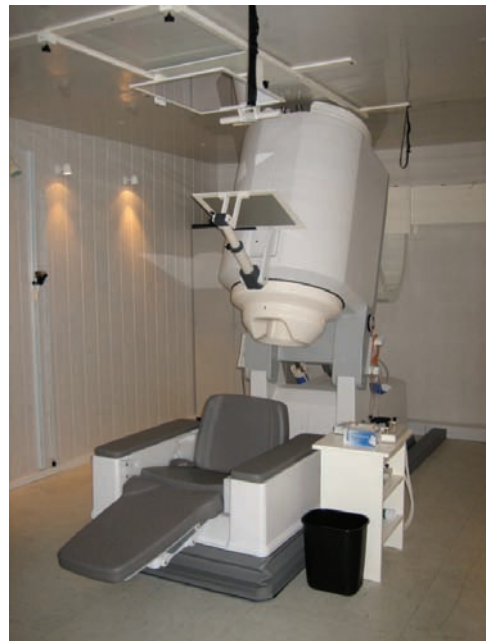


Figure 1 This whole-head biomagnetic recording instrument (at the Children’s Hospital of Philadelphia) contains 275 sensors. The sensors are housed within a cryogenic dewar filled with liquid helium. During recordings, the patient sits on the chair and his/her head is placed within the helmet-shaped dewar. The MEG system is housed in a MSR made of mu-metal and aluminum that shields the sensors from external magnetic fields. Abbreviations: MEG, magnetoencephalography; MSR, magnetically shielded room.

electrophysiology, MEG only observes magnetic fields generated by the synchronous activity of some tens of thousands of neurons. Consequently, it is widely assumed that MEG is not sensitive to action potentials but rather to postsynaptic excitatory or inhibitory potentials (PSEP, PSIP). In addition to a need for a large number of synchronously active neurons, magnetic signals are not observed at MEG sensors unless the neurons are oriented in such a way that the magnetic fields superimpose constructively. Thus, whereas synchronous activity in neurons oriented roughly parallel to each other linearly sum and produce an external signal (open-field configuration), synchronous activity in neurons arranged in a spherically symmetric fashion produce cancellation of the magnetic fields generated by the individual cells (closed-field configuration). Given the above, it is generally thought that MEG is most sensitive to current flow in the dendritic processes of pyramidal cells of layer IV of the cortex, in the banks of sulci (as opposed to radially oriented cells in the gyral crown, or the less appropriately organized cells of other layers). Because MEG is relatively “blind” to nontangentially oriented sources, sulcal brain activity is “highlighted.” In addition, as magnetic field

signal intensity is inversely proportional to the cube of the distance from the source, the MEG signal tends to highlight cortical activity over activity from deeper structures.

OBTAINING MEG DATA

In most clinical cases, spontaneous electromagnetic activity is recorded to examine endogenous rhythmic activity as well as abnormal epileptiform discharges in patients with seizure disorders. In cases where identification of eloquent cortex or other brain regions is desired, sensory stimuli are presented (sometimes also requiring a behavioral response), and MEG data are collected time locked with respect to each stimulus. Single epochs can be subjected to single-trial analysis techniques or averaged together to obtain event-related fields (ERFs), analogous to the event-related potentials (ERPs) derived from EEG recordings.

With the high sensitivity of the MEG detectors and the very low signal of neuromagnetic brain activity, spontaneous recordings and ERFs are extremely sensitive to contaminating signals such as activity from 50- or 60-Hz electrical power lines, moving metallic bodies (e.g., dental braces, jewelry, piercings), implanted prosthetic devices [vagal nerve stimulators (VNS), cardiac pacemakers], and “noise” arising from muscle activity, eyeblinks, arterial pulsations, and the electrical activity of the heart.

In addition to the need to obtain MEG data in a shielded room to reduce external magnetic artifact, a number of strategies are used to mitigate artifact (in practice, several different strategies are applied in combination to remove different types of artifact). A general approach is time-domain filtering. Notch filtering 60-Hz (or 50 Hz in Europe) activity is an effective way of eliminating power-line noise. High-pass filtering at 0.1 or 1 Hz removes baseline drift and eliminates low-frequency noise (arising, for example, from the movement of nearby elevators). Cardiac and blink artifacts may be eliminated manually (which may be time-consuming), by pattern-recognition (first defining a “typical” template and then searching for and removing similar events), or blind methods such as independent components analysis (ICA) (16). Extracranial artifact sources such as those arising from VNS implants and/or dental work may be eliminated via signal space separation (SSS) and its temporal extension (tSSS) (17). SSS and tSSS algorithms mathematically identify distinct intra- and extracranial sources and thus provide a method to remove extracranial artifact. Appropriately used, the above approaches almost entirely eliminate cardiac and eye-blink activity from the MEG signal and have an estimated efficacy of 50% to 80% in extracting useable signal embedded in noise from dental work or implanted VNS stimulators. To date, the presence of a cardiac pacemaker remains a contraindication for MEG.

SPONTANEOUS RECORDINGS AND MAPPING

One of the principal clinical applications of MEG is the detection and localization of interictal epileptiform activity in patients with seizure disorders, accomplished by simply recording spontaneous activity. Recording of spontaneous interictal activity requires no stimulus, and a conventional approach is to collect data while subjects passively relax seated or supine. By identifying the distribution of epileptiform activity (focal, multifocal, generalized) as well as its anatomic substrate, MEG promises to assist in patient management by distinguishing candidates for resective surgery from those for whom focal surgery is less promising. In addition, in some patients, although a confident determination cannot be made, MEG is still used to direct placement of intracranial or subdural electrodes used to confirm the ictal-onset zone.

MEG data can be acquired while patients are awake, drowsy, or asleep. Unless the patient is placed under general anesthesia, it is recommended that the patient stay awake the night before the examination and then try to sleep during the MEG examination. This procedure increases the chance of observing epileptiform activity. For presurgical mapping of eloquent cortex (detailed below), it is generally necessary for the patient to remain awake. For both epilepsy and presurgical evaluations, it is common to obtain an initial data set where the patient is asked to rest, blink his/her eyes, clench his/her teeth, swallow, and make mild head movements. This is done to record the “signature” of commonly appearing artifacts.

Spontaneous MEG is typically collected in two-minute segments (a single continuous segment could be obtained, but the size of the file would become unwieldy). As required by Nyquist’s rule, MEG data are sampled more than twice the fastest frequency present in the original waveform (18). Because of possible errors in estimating the highest frequencies in real-world data, noise introduced by amplifiers and analog/digital (A/D) converters, and the nonsinusoidal nature of many physiologic signals, many have suggested that the sample rate be as much as 5 to 10 times higher than the Nyquist’s rule suggests (19).

In many MEG laboratories, MEG data is typically digitally sampled at per-channel rates of 600 to 1200 Hz, providing a Nyquist’s frequency of 300 and 600 Hz, respectively. During data acquisition, analog filtering is performed (e.g., bandwidths of 0.1–70 or 0.1–300 Hz), with higher sampling rates naturally accommodating broader bandwidth acquisitions. Whereas high-pass cutoff frequencies of 1 to 3 Hz are sometimes applied in settings with considerable low-frequency “urban” or environmental noise, because digital filtering is easily applied offline, in most cases it is better to obtain the original MEG data using a broad bandwidth and then digitally filter offline.

In many MEG clinics, EEG is collected simultaneously with MEG. EEG-compatible electrodes are placed on the scalp in either standard 10–20 montages or in higher-density 64- or 128-channel arrangements. Several manufacturers make MEG-compatible EEG systems. Aside from the EEG sensors being compatible with MEG, MEG-compatible high-density EEG systems use thin adaptors to hold the electrodes, allowing placement of the MEG sensors as close to the head as possible. Picton et al. (20) provide EEG data collection and analysis guidelines. In most cases, the Picton et al. (20) guidelines apply also to MEG data collection and analysis procedures. If simultaneous EEG is not desired, it is still recommended that the electrooculogram (EOG) and electrocardiogram (ECG) be obtained for easy identification of eyeblink and heartbeat activity.

Interpretation of the magnetic activity detected by MEG is usually dependent on some form of source modeling (a few different methods are discussed below) to determine the location of the underlying neuronal generator(s). The value of source modeling, however, is most apparent when source localization results are displayed in some anatomic context, usually provided by cross-sectional anatomic imaging such as structural MRI. Thus, once the MEG data are obtained, some way of registering “MEG space” to “MRI space” is required. In addition, whereas EEG sensors are attached directly to the patient’s head and thus remain fixed with respect to the patient’s head during head movement, the MEG sensors are located at a distance. This necessitates the need to define the relationship between the MEG sensors and the patient’s head. Head position-locating coils, generally placed at nasion and left and right periauricular locations, are used as fiducial landmarks to define the 3-D space, relating the MEG sensors to the individual head. This information is also used to coregister the MEG data to the patient’s structural MRI. The coil/fiducial landmarks are identified (typically manually) on the MRI, and a transformation matrix relates the MEG coordinate system to the MRI reference frame.

Whereas older generation MEG systems required that the patient remain stationary across the examination to ensure a constant relationship between the MEG sensors and the patient’s head, in recent hardware implementations the head position-locating coils are activated and detected continuously throughout the recording. As such, head position and head motion can be monitored in real time, and postprocessing algorithms can be used to correct for a limited amount of head movement during the recording.

For clinical epilepsy examinations, once the data are collected, the spontaneous MEG (and sometimes EEG) data are reviewed to identify characteristic sharp wave and spike and wave activity. A 1 to 8 Hz band-pass filter also may be applied to examine δ and θ slow wave activity.

Manual review of the spontaneous data is arduous and time consuming. Consequently, several semiautomated and fully automated approaches have been proposed. Semiautomated approaches tend to rely on temporal pattern matching, where a characteristic event is defined and then an automated pattern search is applied to the entire data set to locate morphologically similar activity. For example, a typical spike and wave event is identified and then the continuous recording is searched by computing correlation coefficients between the search and the target pattern (analogous to strategies used for identifying recurring sources of artifact such as eyeblink activity). Once similar events are identified, the detected events can be averaged to obtain an averaged spike and wave event with good signal-to-noise. Alternatively, once identified, each unique event can be modeled and clusters of activity identified.

A single equivalent current dipole (ECD) model is typically used to estimate the source of the detected spike and wave activity. Standard dipole-fitting procedures use a model in which the magnetic field pattern at the relevant sensors is forward-modeled as though it were generated by a point source current dipole embedded within a spherical, homogeneously conducting medium (7). The dipole-modeling algorithm uses iterative minimization procedures to determine the spatial position, orientation, and strength of the hypothetical current dipole that best accounts, in a statistical sense, for the magnetic field actually measured by each sensor within the specified time window. Figure 2 shows an example of MEG recording of an interictal epileptiform spike and shows the magnetic field topography as well as the single ECD source model overlaid on structural MRI.

In general, consensus is emerging that modeling the onset of epileptiform activity rather than its peak is more likely to reveal the anatomic origin of the discharge rather than its spread. In some cases, multiple dipole models are used when the data suggest multiple spatially distinct areas of temporally overlapping source activity (21). In general, moving dipole models allow the depiction of the time-varying spatial patterns of activity through the evolution of the interictal event. Given the spread or propagation of spike and wave activity, spatiotemporal dipole models (using a dipole source to describe activity over an extended latency window) may not be favored.

Whereas the above describes a semiautomated approach to localizing seizure foci, more automated approaches have been proposed. Robinson et al., (22) describe a two-step approach using beamformers. A beamformer in MEG is a set of spatial filters based on the MEG lead fields. The basic principle of beamformer design is to allow the neuronal signal of interest to pass through in certain source locations and orientations, called passbands, while suppressing noise or unwanted signal in

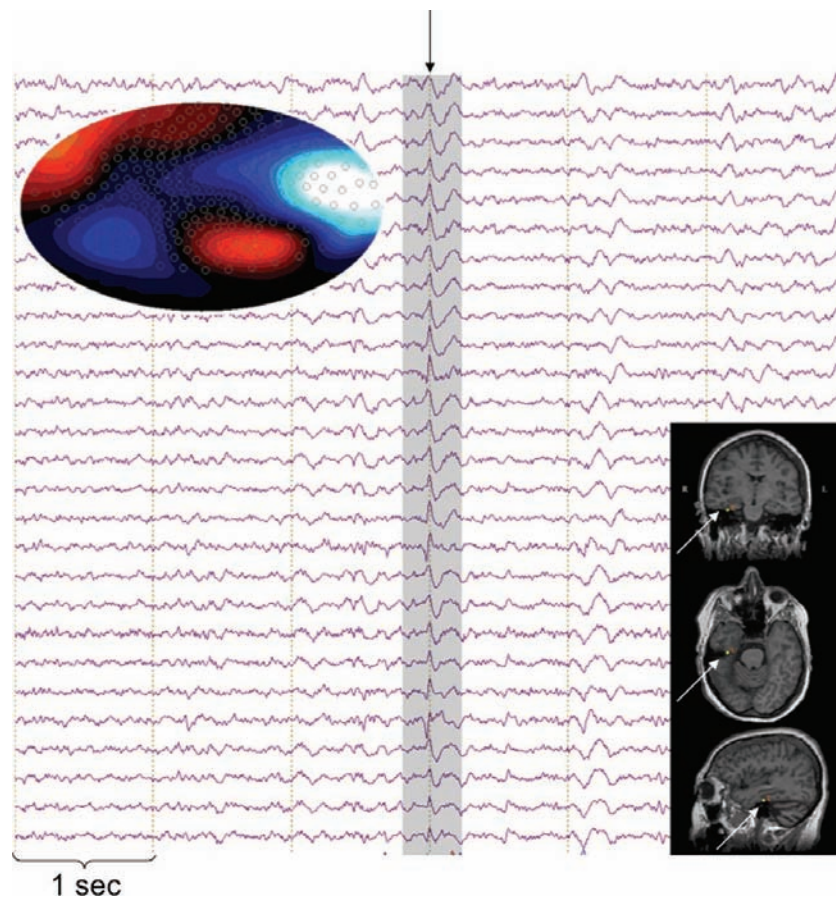


Figure 2 A spike and wave activity during the interictal recording is highlighted (a subset of channels over right temporal regions shown). The spike event is marked by shading (black arrow). The topographic representation is shown on the upper left. Single dipole localization of the onset of the spike and wave event is shown on the lower right on coronal, axial, and sagittal MRI views (white arrows). Abbreviation: MRI, magnetic resonance imaging.

other source locations, called stopbands (23). The beam-former approach, outlined by Robinson et al. (22), first identifies the time-activity profiles of each brain voxel (at an arbitrary resolution, typically 5 mm isotropic), examining activity between approximately 20 and 70 Hz. Second, the time-activity profile at each voxel is analyzed across the recording for the presence of kurtosis. Kurtosis is a mathematical reflection of “spikiness,” defined as the deviation in a continuous signal from static or smoothly varying behavior. Spikiness is used to identify interictal epileptiform activity. Voxels with statistically significant evidence of spikiness are displayed as a color overlay on the individual’s MRI to identify possible seizure foci (Fig. 3). Time-varying source electrical activity profiles can be displayed for each voxel within the brain, reflecting regional activity; these may be considered as “virtual sensors,” placed within the brain.

The study of spontaneous activity detected by MEG is not restricted to interictal epileptiform discharges. The study of electrical brain activity in humans in fact began

with the analysis of spontaneous EEG oscillations. The German neurophysiologist Hans Berger (24) first described a dominant oscillation of approximately 10 Hz, which he termed α activity. Berger and other investigators (25 coined terms still used today to designate brain activity within specific frequency bands: δ (0–4 Hz), θ (4–8 Hz), α (8–12 Hz), β (12–30 Hz), and γ (~40 Hz).

Whereas the spontaneous EEG and MEG of healthy subjects are dominated by α activity (Fig. 4a), patients with brain damage show increased δ and θ slow wave activity (Fig. 4b). Aside from epileptiform activity, clinical MEG examinations often assess spontaneous activity in the δ or θ bands, often generically called “slowing.” Although much studied with EEG in the past, there is renewed interest in abnormal slow wave activity due to the ability to localize the source(s) of slow wave activity.

In the waking state, slow waves generated in a circumscribed brain region typically characterize pathologic or dysfunctional neural tissue and appear in the vicinity of structural lesions like cerebral infarcts, tumors, and

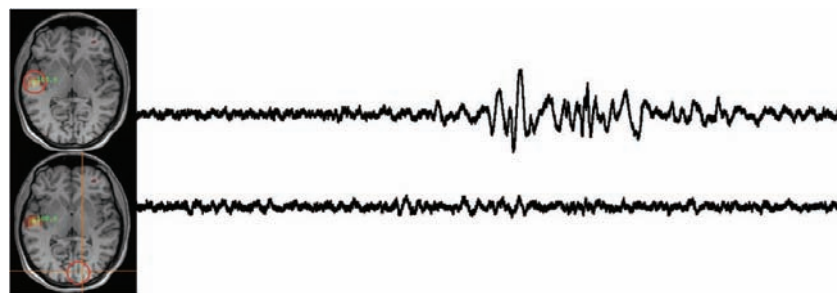


Figure 3 Beamforming used to identify epileptiform activity. Voxels with statistically significant evidence of “spikiness” (SAMg2) are displayed as a color overlay on the patient’s MRI and identifies possible seizure foci. The peak of statistical significance (along with a numeric t-statistic) is marked. Plotted to the side, a virtual sensor placed at the center of the localized “seizure” activity (*upper waveform*) shows epileptiform activity (the “virtual sensor” simply extracts the time activity of brain within a single voxel; approximately five seconds of data are displayed). A virtual sensor placed at an occipital “control” site (*lower waveform*) shows normal low-amplitude background activity. Abbreviation: MRI, magnetic resonance imaging.

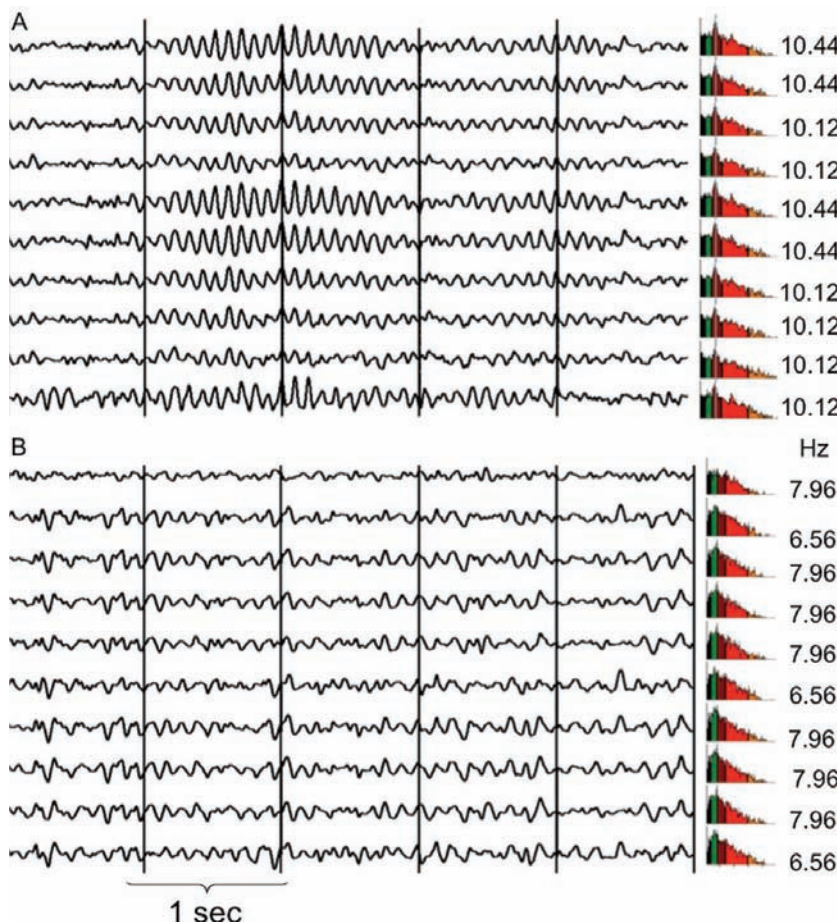


Figure 4 (A) Spontaneous oscillatory α activity (8–12 Hz) in a control subject awake and resting. Power spectra at the right indicate greatest power in the α band (dark red), and less power in the δ (black), θ (green), β (light red), and γ bands (orange). (B) Abnormal spontaneous low-frequency oscillatory activity in a patient. As shown in the power spectrum, the largest magnitude oscillatory activity is observed between 6 and 8 Hz.

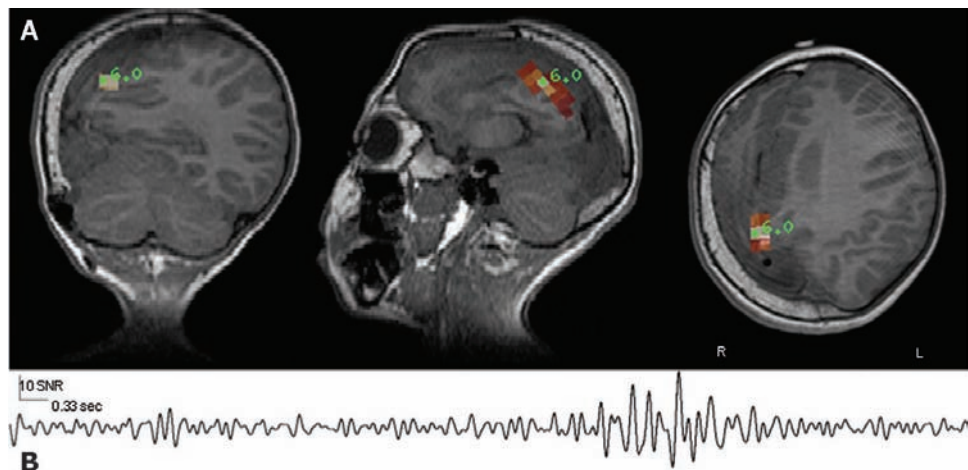


Figure 5 (A) A child with a severely dysplastic right cerebral hemisphere and marked parenchymal loss. Using a beamformer approach, significant abnormal low-frequency slow wave activity is localized to perilesional tissue in the right hemisphere, indicating compromised but active tissue. (B) Plotted below the MRI, a virtual sensor placed at the center of the localized slow wave activity shows activity at this location across time. Abbreviation: MRI, magnetic resonance imaging.

degenerative defects (7). Abnormal slow wave activity is described as being due to a “dysfunctional state” of the neuronal tissue (7), perhaps due to loss of afferent input and/or a primary metabolic change within neurons at or near the lesion border (26). MEG is used to localize abnormal slow wave activity to identify areas that are active but damaged. MEG is preferred over EEG, as with EEG the spread of volume currents affects even distant electrodes, making it more difficult to model focal activity when background activity is present (27). In addition, as previously noted, MEG better identifies focal sources in sulci, which comprise two-thirds of the cortex.

Abnormal slow wave magnetic activity is examined from the spontaneous MEG. Typically, the data are bandpass filtered to emphasize δ and θ activity. In most studies to date, single ECDs are fitted to each time point in the nonartifact spontaneous data, and dipole density across brain regions examined. Lewine and Orrison (7) describe general approaches to assessing abnormal slow wave activity. Weinbruch (28) outlines a comprehensive approach. Figure 5 shows slow wave activity localized in a patient using beamformer methods. Beamforming methods are emerging in combination with appropriate image-based statistical mapping as an alternative to analysis of clusters of single dipole solutions.

MEG studies have observed increased δ and θ activity in temporal and parietal regions in patients with schizophrenia (29–32). Canive et al. (30) observed augmented slow wave activity in patients with schizophrenia with higher scores on psychopathology [Positive and Negative Syndrome Scale (PANSS)]. Fehr et al. (32) reported a significant correlation between the number of temporal delta dipoles and the amount of negative symptoms in

patients with schizophrenia (PANSS-N scale). Increased abnormal slow wave activity also has been observed in patients with neurologic conditions. For example, increased temporal and parietal slow wave activity was observed in individuals with Alzheimer’s disease, and slow wave activity predicted cognitive and functional status (33).

Given the absence of structurally obvious lesions in many psychiatric populations, localization of focal abnormal slow wave activity may be especially useful in identifying areas of dysfunction. Such analyses might also identify slow wave signatures specific to individual psychiatric disorders. For example, Rockstroh et al. (34) observed increased frontal and central abnormal slow wave activity in patients with schizophrenia compared with a patient group with affective/neurotic diagnoses (e.g., major depressive episode, neurotic, reactive, and somatoform disorders) and a group of healthy controls (Fig. 6). In contrast, the affective/neurotic group showed less slow wave activity than the other two groups in frontal and central areas. In both patient groups, frontal slow wave activity was associated with effective symptoms.

Assessment of abnormal slow wave activity may also be used to track changes in the course of recovery or treatment. Lewine et al. (35) observed an association between symptom resolution and slow wave reduction in patients with minor traumatic brain injury. Meinzer et al. (36) observed left hemisphere slow wave clusters in aphasic patients suffering from ischemic or hemorrhagic lesions affecting the left hemisphere. Following the initial MEG examination, the aphasic patients received extensive language training. A comparison of abnormal slow wave activity pre- and posttraining indicated that the

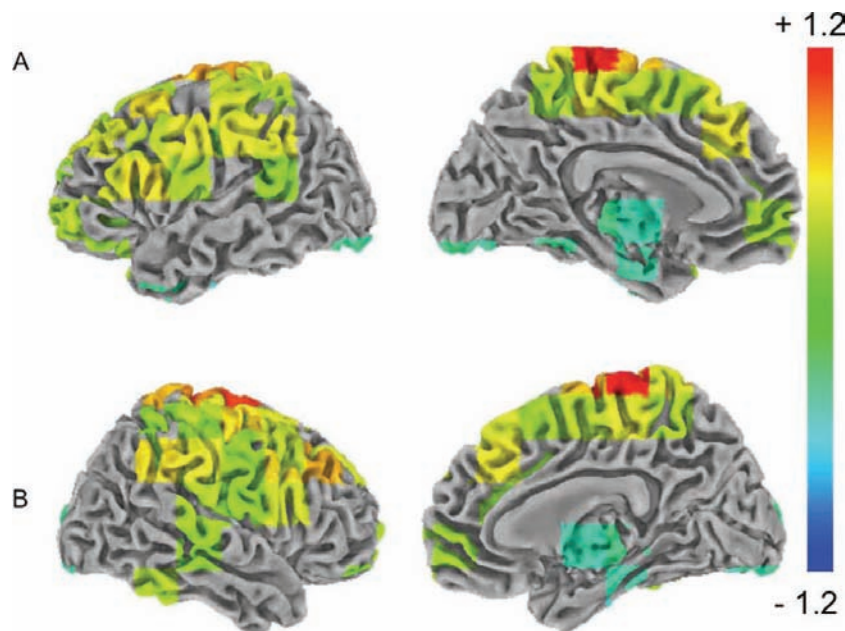


Figure 6 Areas of increased (red) and decreased (blue) slow wave activity in patients with schizophrenia compared with controls. (A) left hemisphere. (B) right hemisphere. Maximal differences (Z-scores) were observed in frontal and central areas. Abbreviation: MRI, magnetic resonance imaging.

magnitude of change of slow wave activity was associated with the amount of change in language function.

EVOKED RECORDINGS AND MAPPING

In addition to recording spontaneous activity, MEG is also collected in paradigms where sensory stimuli are presented (e.g., auditory tones, visual images). In some instances, the subject is instructed to rest while stimuli are presented. In other instances, the subject makes a response each time a stimulus is presented (e.g., a button press). MEG data are time locked to the presentation of each stimulus and/or button press. As previously noted, because the response to a single stimulus is weak, an averaged response to multiple stimuli is often obtained, creating the ERF. Typically, over one hundred stimuli in each condition (e.g., 100 left visual field stimuli, 100 right visual field stimuli) are presented to obtain an ERF with a signal-to-noise ratio (SNR) sufficient for source localization.

In this section, stimulus presentation and recording/analysis approaches are described for commonly used sensory and cognitive tasks. Whereas in some cases the types of analyses presented are widely used, in other cases, less traditional analyses are presented to show the great range of options available. This field is rapidly developing and advances in cognitive neuroscience will undoubtedly influence the paradigms used and the analyses applied.

Nonetheless, the general principles discussed will continue to apply.

Somatosensory

Somatosensory-evoked potentials (SEPs) are obtained during intraoperative electrocorticography to locate the central sulcus, identified by locating the phase reversal on electrodes placed on the exposed dural surface. The central sulcus divides precentral and postcentral gyri, allowing identification of primary motor and somatosensory cortices. SEPs are widely used in this way because of the importance of identifying the location of primary somatosensory and motor cortex during neurosurgery and because of the relatively simple morphology of the somatosensory-evoked response, with a well-defined primary somatosensory component occurring approximately 20 ms postelectrical stimulation of the median nerve (37,38).

Similar to intraoperative procedures, somatosensory-evoked fields (SEFs) are obtained by applying a tactile stimulus to the body surface. Whereas median and tibial nerve responses are typically obtained, tactile stimuli applied to almost any region of the body will generate a SEF. MEG somatosensory activity at 20 ms (M20) reflects activity in primary somatosensory cortex (39–42). M20 is thought to reflect activity from area 3b of somatosensory cortex, from pyramidal cells lying on the posterior bank of the central sulcus, oriented tangentially to the cortical

surface (42). M20 activity is focal and well modeled with a single source (41,43).

During a clinical MEG examination, one of two types of stimuli are presented to obtain SEFs: (i) electrical stimulation (typically of the median and/or tibial nerve), using a electrical pulse of ~0.2-ms duration, with sufficient current to obtain a thumb- or toe-twitch or (ii) pneumatic stimulation, using a pulse of compressed air into a diaphragm clipped to the stimulated body part (typically the digits of the hand, the toes, and/or the lips) (44) for complete homuncular mapping). As described above, since single-trial-evoked response amplitudes have poor SNR, it is common to repeat stimulation several hundred times to improve the SNR. The interstimulus interval (ISI) for somatosensory electrical stimuli is typically 300 to 500 ms. As such, 200 stimuli can be presented in less than two minutes. As in most ERF paradigms, it is common to randomly vary (or jitter) the ISI to avoid averaging unwanted periodic activity, such as artifacts from arterial pulsation and background endogenous α activity.

Once obtained, the averaged response is digitally filtered to remove low-frequency drift or baseline oscillation, as well as high-frequency noise. A common pass-band filter for pneumatic stimuli ERFs is 1 to 40 Hz. Evoked responses elicited by electrical stimulation tend to exhibit higher-frequency response behavior and may be

pass-band filtered at 20 to 300 Hz. For pneumatic and electrical SEFs, single dipole modeling of the first well-defined component (approximately 20 ms for electrical stimuli —M20) identifies primary somatosensory cortex. A single dipole typically accounts for 95% to 99% of the variance in the observed data, indicating no other activity (Fig. 7). By mapping multiple digits, the toes, and the lips, it is possible to define the somatosensory homunculus, from which the identity of the central sulcus can be inferred along with the presumed location of motor cortex in the precentral gyrus.

This approach is widely used in clinical studies and validated against anatomic methods of delineating central sulcus (45) as well as against intraoperative cortical stimulation mapping (3,46,47). In general, cortical stimulation tends to define sites at the cortical surface. Although MEG localizes activity in the deep banks of a sulcus, the agreement between cortical recordings and MEG localization is extremely good, and errors are within the variability associated with the intraoperative mapping procedure itself.

Motor Mapping

Whereas identification of tissue subserving motor function is a crucial goal in presurgical planning to help guide the

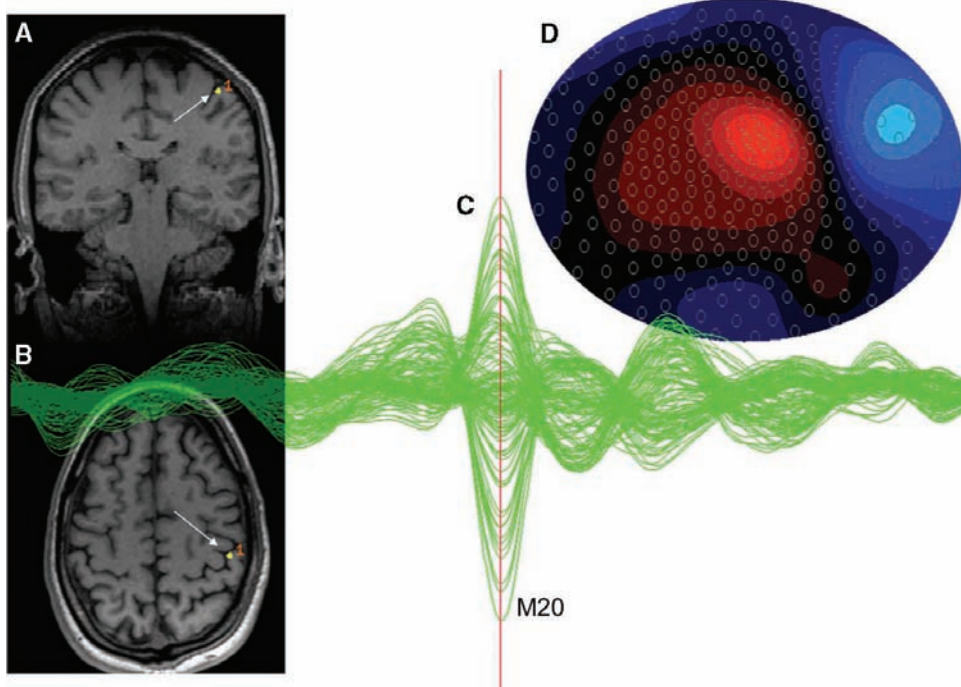


Figure 7 Somatosensory stimulation, evoked responses, and localization. Data from all 275 channels (*overlaid*) show a large response at ~20 ms (M20) to median nerve stimulation (C). The topographic color map (D) shows the magnetic field distribution at the time of the M20 peak. The field pattern is dipolar, with clearly defined regions of emerging (red) and entering (blue) magnetic flux. As shown in the (A) coronal and (B) axial MRI, M20 dipole source localization identified activity in primary somatosensory cortex (postcentral gyrus) (arrow).

neurosurgeon and thus avoid postoperative motor deficits, mapping motor cortex via motor ERFs is more complicated than localizing SEF activity. Firstly, unlike the passive somatosensory clinical tasks, motor tasks require that the patient reliably lift or tap their finger (sometimes difficult for individuals with brain lesions). Secondly, even when executing a simple motor task, brain activity related to the motor task starts some hundreds of milliseconds prior to the motor movement (bereitschaft-potential, bereitschaft-field), includes a motor field component near the time of movement, and is associated with larger motor ERFs (MEF-I, MEF-II, and MEF-III), approximately 100, 200, and 400 ms postmovement. These later ERF components (which may reflect proprioceptive feedback) often localize to postcentral gyrus and are generally associated with somatosensory representations and functions. Given temporally overlapping activity, motor-elicited neuromagnetic activity has not lent itself to simple dipole modeling and has seen little clinical implementation. In the majority of clinical cases, location of the primary motor strip is inferred from SEF recordings via the expected neuroanatomic relationship—one gyrus anterior to somatosensory cortex.

Recent advances in beamformer approaches may offer a robust means to map primary motor areas. Immediately preceding and following a button press, a decrease in β -band activity is observed (12–30 Hz) (48). Using a beamformer approach, at each brain voxel (at arbitrary 5-mm resolution), β -band power can be assessed during a latency window surrounding voluntary self-paced button presses. By comparing β -band activity during the period surrounding the button press with β -band activity during a baseline period (several seconds away from a button press), brain regions showing a significant decrease in β -band activity with respect to the baseline period are identified. This decrease in power is termed event-related desynchronization (ERD). Typical beamformer analyses consider β -band activity from approximately -300 to +200 ms relative to the button press and contrast this to a baseline period. In a clinical setting, beamformer localization of primary motor cortex is often displayed (by identifying voxels with statistically significant ERD exceeding a chosen t-threshold) in combination with images of the corticospinal fiber tracts derived from diffusion tensor MRI (Fig. 8)

Visual Stimulation

Visual-evoked fields (VEFs) are also more complex than SEFs, reflecting concurrent activation of multiple visual cortical regions. Despite this added complexity, primary visual cortex can be localized using short-duration, small-patterned visual stimuli presented to each visual field (large foveal stimuli activate too large a region of primary

visual cortex). Using well-designed stimuli, primary visual areas can be identified in most subjects (2,49).

Figure 9 shows localization of primary visual cortex in the left hemisphere (blue dipole). Instead of plotting MEG results on MR slices, MEG results can be plotted on an inflated brain (Fig. 9a) or an inflated and flattened brain (Fig. 9b). In some instances, inflated and flattened brain images are preferred; as such, images allow simultaneous examination of lateral and medial brain surfaces.

In addition to identification of primary visual cortex, other visual areas can be identified. Figure 9 shows localization of secondary visual (pink dipole) and fusiform activity (orange dipole) in response to face stimuli. A fusiform face response is observed at 170 ms in most subjects (50–52). The 170-ms response has a dipolar field pattern and is easily localized using single dipole methods. At present, there is no barrier to extend mapping of visual areas to include identification of fusiform face areas in presurgical cases.

Language Function

The attempt to localize language functions in the cerebral cortex dates back to at least 1825 when Bouillaud argued before the Royal Academy of Medicine in France that specific functions are localized in the neocortex, and specifically, that speech is localized in the frontal lobes. This claim was later substantiated when Broca (53) showed that lesions in the posterior portion of the left frontal lobe cause expressive aphasia in right-handed patients.

On examination of the occurrence of aphasia in individuals with unilateral brain damage, it appears that at least 95% of the total population has left-hemisphere representation of language (54). This mirrors the results of speech lateralization determined by the Wada (intracarotid sodium amytal) test in which between 90% to 95% of right-handers and 70% of non-right-handers show left-sided speech representation (55).

Aside from merely “academic interest,” accurate knowledge of the lateralization of language is often of practical importance, especially when considering neurosurgical procedures for lesions above the tentorium. The intracarotid amobarbital (Wada) test is currently the only method that reliably determines language representation in both hemispheres (55). The test was found to predict the side of speech production, as assessed by whether patients showed dysphasia after surgery or the Wada test predicted nondominant hemisphere with between 95% (56) and 98% accuracy (57).

Several MEG laboratories have sought to develop an MEG-based and thus noninvasive alternative to Wada testing. As with motor function, the brain activity associated with language tasks is distributed. Consequently,

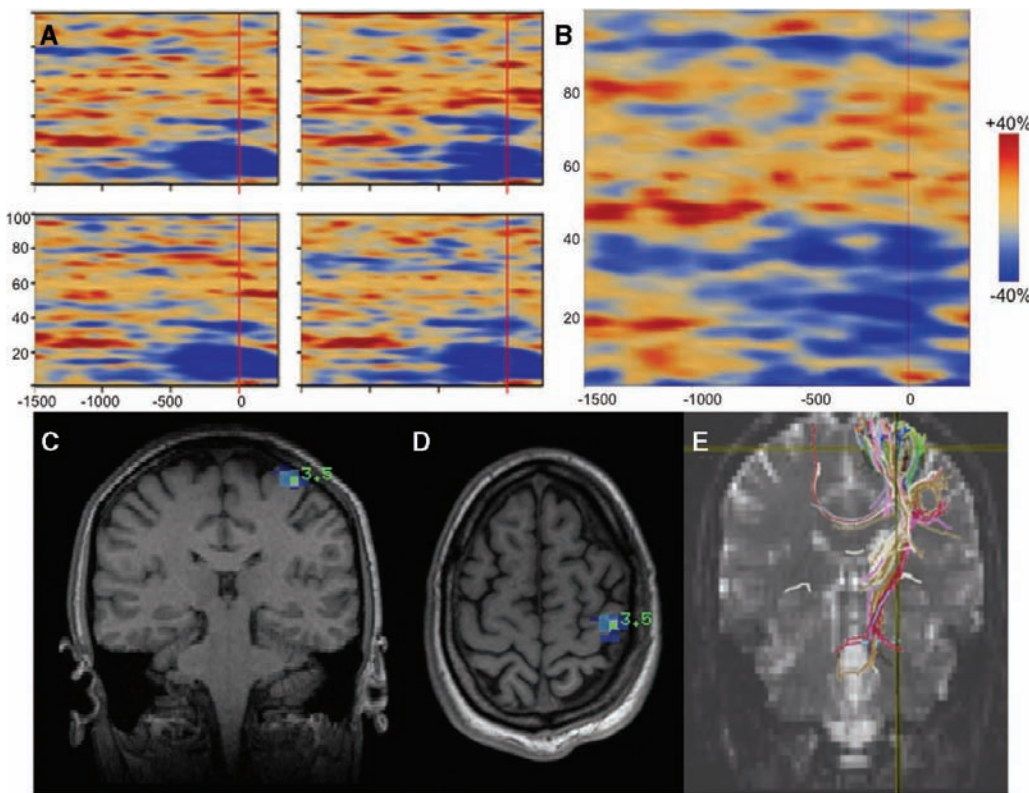


Figure 8 Beamformer localization of primary motor areas. Compared with a -1500- to -1000-ms baseline period, decreased β -band activity (shown in blue) is observed immediately preceding and following finger movement (red line). Time-frequency activity is shown for individual MEG sensors near primary cortex (A) and in a dipole source placed in primary motor cortex (B). The color bar indicates percentage change from baseline. Maps of statistically significantly decreased β -band power in the latency range -300 to +200 ms (with respect to the right index finger button press) are overlaid on MRI in the coronal (C) and axial (D) views. The voxel with maximum significance (t-value) is marked (along with the numeric t-statistics). Corresponding corticospinal fiber tracts derived from diffusion tensor MRI are shown in (E), based on a seed voxel defined in (C, D) by MEG. Abbreviations: MRI, magnetic resonance imaging; MEG, magnetoencephalography.

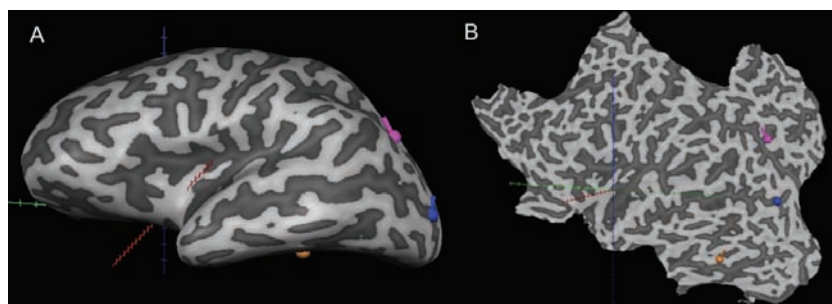


Figure 9 Localization of primary visual cortex in the left hemisphere (blue dipole) shown on an inflated brain (A) and an inflated and flattened brain (B). In addition to identification of primary visual cortex, localization of secondary visual (pink dipole) and fusiform activity (orange dipole) in response to face stimuli is shown.

unlike the short-latency ERPs associated with simple somatosensory stimulation, “language-”evoked responses have a long latency and likely include activity from multiple brain areas.

A variety of MEG language paradigms have been evaluated. These include verb generation, stem completion, picture-naming, and word recall tasks. Merrifield et al. (58) and Papanicolaou (59) describe a word recall task

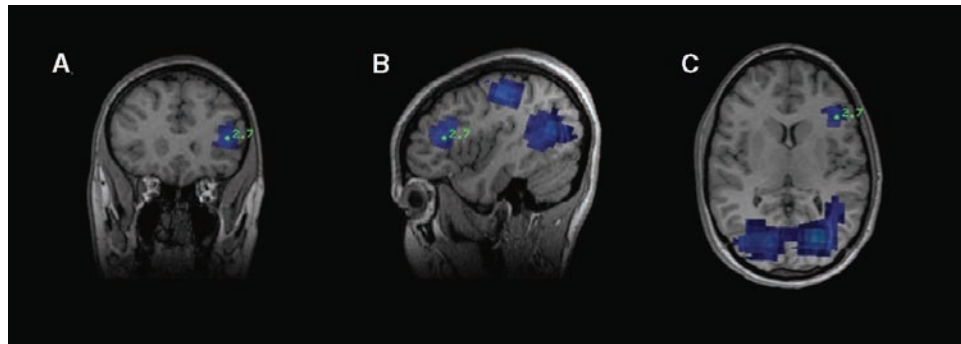


Figure 10 Similar to mapping of motor cortex, a beamforming approach can be used to identify the neural substrates of language processing. In this example, a patient is presented with novel and familiar words (visually) and must make a familiarity judgment. β -Band power is compared during an “active” period (200–700 ms poststimulus presentation) compared with baseline. Significantly decreased β power (ERD) is shown in left hemisphere frontal and posterior temporal sites, overlaid on (A) coronal, (B) sagittal, and (C) axial MRI. A left inferior frontal pixel is identified as exhibiting maximally significant ERD and its associated t-statistic is displayed. Additionally, left motor cortex and bilateral visual cortex areas show ERD, corresponding to the motoric response (to indicate familiarity) as well as visual processing of the stimuli. The sensitivity of MEG to multiple brain processes can be considered as expeditious for multisite mapping or as an important criterion/challenge for focused experimental design (to eliminate confounding activity depiction). Abbreviations: ERD, event-related desynchronization; MRI, magnetic resonance imaging; MEG, magnetoencephalography.

employed at several MEG clinics. During this task, prior to the MEG examination, subjects are presented with a series of words they are asked to remember. During the MEG examination, familiar and novel words are presented and the subject performs a familiarity task (stimulus presentation may be auditory or visual).

Two main strategies have been proposed for assessing language-related MEG activity, with a primary goal of assessing lateralization of language functions and sometimes a secondary goal of identifying Broca’s and Wernicke’s area (often simplistically associated with expressive and receptive language functions, respectively). The first strategy (“dipole counting”) defines a poststimulus window (approximately 200–700 ms). A single equivalent dipole in each hemisphere is fit at each digitized sample point throughout the window. The number of successful fits across the window (i.e., the dipole fits with a small residual error between the model and the data) are counted in each hemisphere, and a laterality index is computed as

$$LI = \frac{N_L - N_R}{N_L + N_R},$$

where N_L and N_R are the total number of successful fits in the left and right hemisphere. The LI ranges from -1 (fully rightward) to +1 (fully leftward). LI values in the range -0.1 to +0.1 are generally considered to show bilateral representation of language (58) for a detailed description of dipole counting analysis procedures). A limitation of this method is that it assumes the presence of a single underlying source at each data point, even though multiple areas of activity are likely present.

A second emerging strategy is the use of beamformer approach. Similar to the motor beamformer analyses described above, active and control baseline periods are defined and the percentage change in oscillatory activity within a frequency band from baseline to the active condition examined. β and low γ activity after the processing of stimulus properties beyond simple acoustic features are typically of interest (after ~200 ms). In addition to localizing language areas, like the dipole counting procedure, an estimate of hemispheric dominance or lateralization can be computed, based on the relative magnitude of the peak statistical significance of activation in each hemisphere (such as the peak t-values). For example, the beamformer laterality index is computed as

$$LI = \frac{\max t_L - \max t_R}{\max t_L + \max t_R},$$

where $\max t_L$ and $\max t_R$ are the maximum t-statistic values. Using a beamformer approach to examine inferior and middle frontal gyrus hemispheric asymmetry in β - and γ -band activity, Hirata et al. (60) show strong concordance with this approach for assessment of hemispheric dominance in comparison with the gold standard Wada test.

PRESENT CLINICAL UTILIZATION—ILLUSTRATIVE CASE STUDIES

MEG is clinically indicated for presurgical mapping of eloquent cortex and for the identification of the source of abnormal epileptiform electrical activity. MEG can play several roles in the preoperative assessment of patients with medically refractory epilepsy. In cases where

alternative imaging modalities, including ictal EEG, are nonlocalizing, MEG can help determine if the origin of the discharges is focal (offering a potential surgical management), multifocal, or generalized (typically precluding surgery). If surgery is deemed possible, MEG data may suggest a reduced-coverage phase II intracranial or subdural electrode placement. In patients with focal and nonfocal activity, information on the functional organization of the patient's brain obtained through functional MEG mapping can guide patient management away from or toward a surgical solution by identifying the proximity between the ictal-onset zone and eloquent cortex (especially in cases where cortical reorganization is possible). The following case studies illustrate the role MEG may play in (i) guiding a decision to perform surgery in a previously ineligible patient, (ii) guiding a decision against surgery by identification of multifocal activity, and (iii) identifying cortical reorganization and indicating the possibility for surgery when a decision based on anatomical location alone might have precluded surgery.

Case 1: A six-year-old right-handed boy was referred for MEG after suffering for two years with medically refractory epilepsy. Brain MRI was essentially unremarkable, showing only a slightly small right hippocampal head. The hippocampus however maintained its normal internal architecture and did not display abnormal signal intensity. EEG

favored a right anterior temporal ictal-onset zone, while ictal and interictal single photon emission computed tomography (SPECT) favored a more medial and posterior onset in right posterior temporal/temporoparietal regions. SPECT also identified a region of abnormal activity in the medial left temporal lobe, perhaps indicating an independent seizure focus in this area.

MEG identified spatially and temporally independent spikes in the anterior and posterior aspects of the right temporal lobe (Fig. 11). No abnormal interictal left hemisphere activity was observed. Subdural grid placement was significantly influenced by MEG findings, as coverage was extended more posteriorly than suggested by EEG. Intracranial EEG analysis confirmed the MEG anterior and posterior findings. Both regions were resected, resulting in freedom from seizures.

Case 2: An 18-year-old right-handed male was referred for MEG for medically refractory epilepsy, which was felt to be generated in the right frontal lobe, on the basis of seizure semiology and EEG. Brain MRI did not demonstrate a structural abnormality.

MEG showed multifocal and bilateral interictal sharp activity (Fig. 12). Independent foci were seen medially and laterally within the anterior aspect of the right parietal lobe, abutting the central sulcus. Additional foci were present in the lateral aspect of the left posterior frontal/

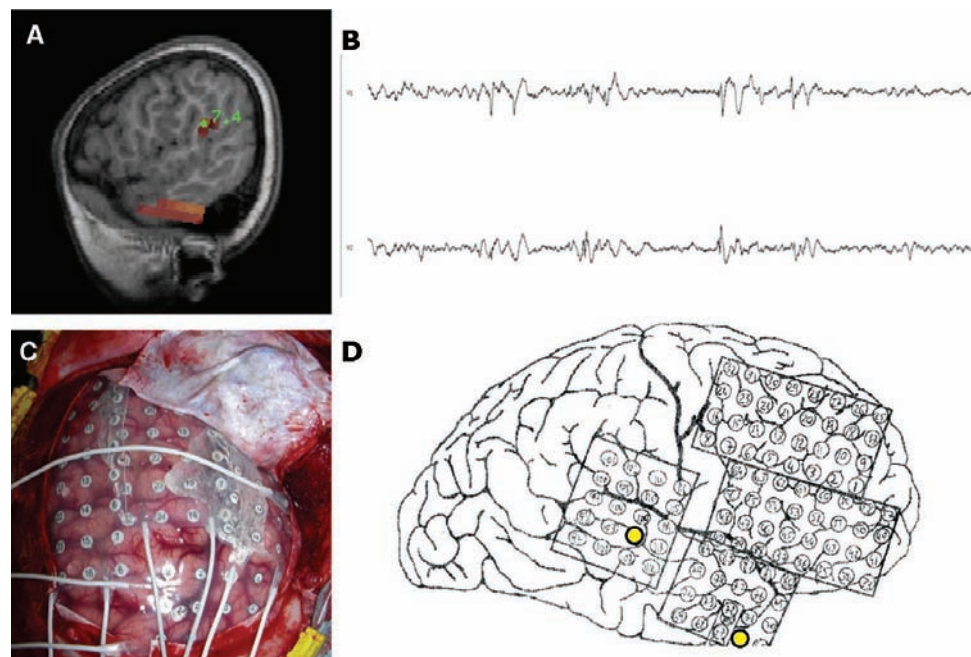


Figure 11 A six-year-old right-handed boy was referred for MEG after suffering for two years with medically refractory epilepsy. **(A)** MEG identified spatially and temporally independent spikes in the anterior and posterior aspects of the right temporal lobe. **(B)** Epileptiform activity is observed on virtual sensor MEG channels placed at each locus. **(C)** Subdural grid placement was significantly influenced by MEG findings, as coverage was extended more posteriorly than suggested by EEG. **(D)** Intracranial EEG analysis confirmed the MEG anterior and posterior findings, with two electrodes (shaded yellow) showing maximum activity. Abbreviations: MEG, magnetoencephalography; EEG, electroencephalography.

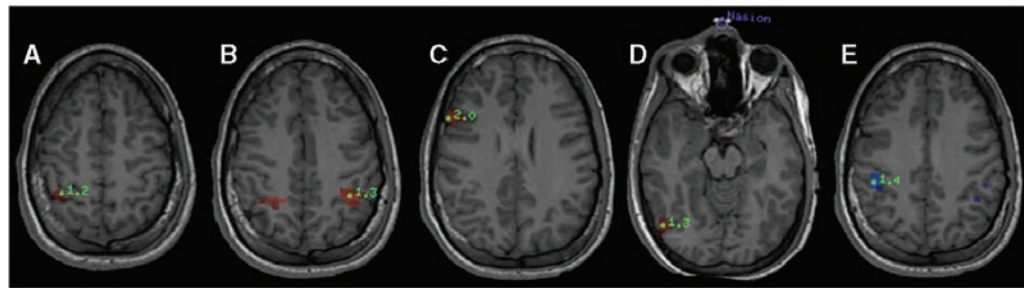


Figure 12 An 18-year-old right-handed male was referred for MEG for medically refractory epilepsy. MEG showed multifocal and bilateral interictal sharp activity localized using the beamforming approach to identify significant kurtosis in the time-activity profiles (A–D). The multifocal MEG sharp activity, as well as the relationship of the foci to eloquent brain regions—motor mapping results are displayed in (E)—indicated that a surgical cure was highly unlikely, and intracranial EEG lead placement was not offered. Abbreviations: MEG, magnetoencephalography; EEG, electroencephalography.

anterior parietal lobe, straddling the central sulcus, as well as in the right anterior inferior frontal gyrus and the posterior aspect of the right temporal lobe.

The multifocal MEG sharp activity as well as the relationship of the foci to eloquent brain regions indicated that a surgical cure was highly unlikely, and intracranial EEG lead placement was not offered.

Case 3: A 17-year-old female with a mild right hemiparesis was referred for MEG given a history of medically refractory epilepsy. As a young child, the patient had intracranial complications from leukemia, resulting in bilateral multifocal cystic encephalomalacia and parenchymal volume loss. An EEG showed right posterior quadrant polymorphic slowing, maximal at T6 and O2. Positron-emission tomography (PET) scanning did not identify a seizure focus.

Analogous to the EEG findings, MEG demonstrated abnormal interictal sharp activity, primarily centered in the right posterior temporal/occipital junction. Marked volume loss in the left posterior frontal lobe was seen on correlative MRI, and functional testing demonstrated reorganization of motor representation due to the early childhood injury. Functional motor mapping of the left index finger showed the expected ERD in the right precentral gyrus. In contrast, motor mapping of the right index finger showed ERD in the nearly identical region in the ipsilateral precentral gyrus (Fig. 13).

Whereas the motor representation showed reorganization, the somatosensory representation remained orthotopic, in keeping with the structurally unaffected postcentral gyri seen on MRI.

PERSPECTIVE ON THE FUTURE OF CLINICAL MEG

Clinical MEG laboratories are a recent phenomenon. The evolution of clinical MEG reflects a growing sensitivity among clinicians to the practical problems of assessment

and treatment of patients with neurologic maladies. Neurologists and neurosurgeons are increasingly requesting MEG evaluations to aid in diagnosis and treatment. As noted, clinical MEG examinations currently involve

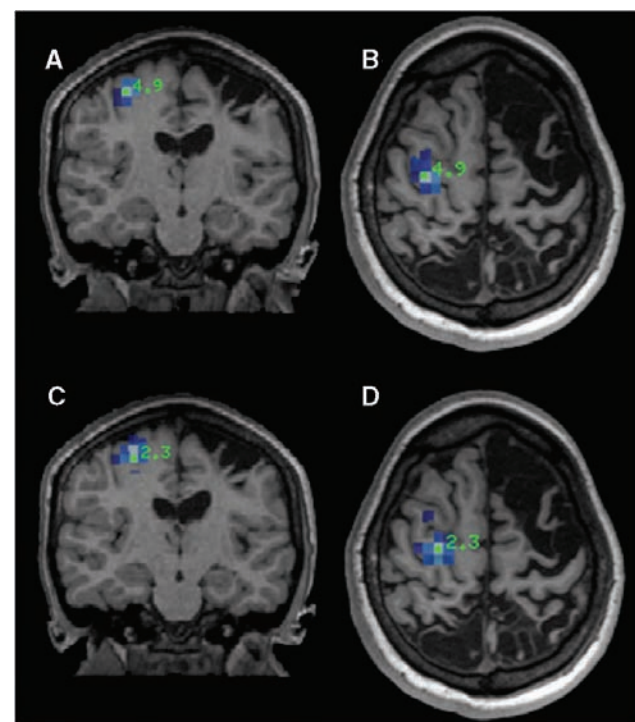


Figure 13 A 17-year-old female with a mild right hemiparesis was referred for MEG given a history of medically refractory epilepsy. As shown in the upper panels, functional motor mapping of the left index finger showed the expected ERD in the right precentral gyrus (A,B). In contrast, as shown in the lower panels, motor mapping of the right index finger showed ERD in the nearly identical region in the ipsilateral precentral gyrus (C,D). Abbreviations: MEG, magnetoencephalography; ERD, event-related desynchronization.

preoperative localization of functional areas in patients with lesions (e.g., neoplasms, cavernous hemangioma, or arteriovenous malformation), within or near eloquent cortex, and preoperative identification of epileptic foci/presurgical planning for epilepsy.

Staffing a clinical MEG site is demanding, as a great range of expertise is needed. Physicists, neuropsychologists, radiologists, neurologists, cognitive psychologists, anesthesiologists, nurses, and neuroscientists are all usually encountered in a fully functioning MEG laboratory, largely due to the challenge of any one individual mastering the needed expertise in physics, signal-processing, experimental design and data analysis, diagnosis, clinical neuropsychology, etc. Aside from professional staff, MRI and/or EEG technicians typically collect the MEG data. In most cases, MEG scientists are involved in clinical and research work, aided by graduate and postdoctoral students. A fully operational MEG laboratory truly is a collaborative effort.

Compared with EEG and fMRI, MEG laboratories are comparatively rare. As Miller et al. (61) note, a primary factor holding back clinical application of MEG is limited access (relatively few systems) and a small expert user community. As such, there is not a large established base of EEG users or a flourishing growth of fMRI users who play a critical role in translational research, moving the technology into the clinic.

Aside from the need to develop a larger user base, the future of clinical MEG also depends on increased standardization and a gradual move from a qualitative to an actuarial framework. At present, clinical MEG assessment primarily relies on careful and intensive examination of each subject's MEG data. MEG is a child of its time and place, and this qualitative approach likely reflects the development of MEG as a tool to localize epileptiform activity in patients with epilepsy. Clinical, theoretical, and actuarial approaches can be thought of as extremes on a continuum of quantification (62). At the qualitative end are assessment approaches built on detailed observations of MEG activity, with particular attention paid to the manner in which MEG activity is abnormal, but which lack objective standardization. On the other hand, actuarial systems rely exclusively on statistical evaluations of scores, derived from a standard set of protocols and analysis methods. Whereas at present much more emphasis on quantitative approaches is needed, Lezak (62) notes that "... to do justice to a field of inquiry as complex as brain-behavior relationships in adult human beings requires an adaptable assessment methodology that incorporates the strengths of both quantitative and qualitative approaches" (pg. 4).

At present there are no standard MEG clinical protocols, and clinical MEG examinations vary across laboratories. For example, whereas some laboratories use

electrical stimuli to obtain median and tibial nerve responses, other laboratories use pneumatic stimuli. Even for spontaneous resting data, laboratories differ in how resting data are obtained. Similar variability is observed in data analysis procedures. Whereas most laboratories use single dipole strategies to localize epileptiform activity (63,64), as detailed above, the use of beamformer techniques to localize epileptiform activity is also considered (65). Whereas such variability is expected in a developing field, the field is gradually maturing and over the last few years there has been increasing interest in the development of a standard set of stimuli presentation and analysis protocols. Concurrently, there also is a move to develop a more quantitative (statistical) approach to identifying abnormal brain activity as well as assigning diagnoses.

Development in this area requires a multipronged approach and includes standardization of protocols, data collection, and data analyses procedures. Whereas some standardization is possible, variability will remain as MEG hardware, software, and other site-specific factors (e.g., noise levels) differ across laboratories. An ongoing study conducted by the Mental Illness and Neuroscience Discovery (MIND) Institute is currently examining these issues. Weisend et al. (66) obtained MEG data from the same subjects at three different sites with different MEG arrays: Elekta-NeuroMag Vectorview, VSM MedTEch Omega275, and 4D Neuroimaging Magnes 3600 WH. Data were collected from each subject run twice at each site, using the same stimulus delivery equipment in simple somatosensory, visual, and auditory paradigms. Although analyses are ongoing, somatosensory data show excellent test-retest results within subjects across instruments and software packages. Weisend et al. (66) noted that initial results indicate that pooling data across machine types and sites is possible.

The establishment of standard presentation and analysis protocol allows merging of data across sites and the eventual development of normative databases. Development of normative databases in turn allows a quantitative approach to clinical interpretation. As an example, as described above, although slow wave activity during the waking state is indicative of compromised brain tissue, some δ and θ activity is seen in most awake controls and is thought to reflect a "normal" range of low-frequency neuronal network communication. Weinbruch (28) describes a method to apply a Z-score-based analysis of single subjects and group results. In a large sample of controls, Weinbruch (28) demonstrated a range of normal slow wave dipole density distributions across subjects, with male subjects exhibiting more focal slow waves in frontocentral regions than females. Weinbruch (28) noted that once a normative database is established, comparison of individual data against scores from a demographically



Figure 14 Prototype of a multichannel neonatal MEG system for assessing brain function in newborns and infants (baby SQUID). To assess brain function, the baby's head is placed on the headrest, with MEG sensors directly below. Abbreviations: MEG, magnetoencephalography; SQUID, superconducting quantum interference device. Source: From Ref. 67.

matched control group allows for the potential to make fine distinctions and comparisons that would be unattainable by clinical observation alone.

Whereas development of standard MEG clinical protocol for adults will be difficult, even more difficult is similar development in infant, child, and young adolescent populations. Given the difficulty children have sitting still during an MEG examination, less demanding protocols will be required. For very young children, only passive protocols will be possible. In conjunction with the development of optimal clinical protocols for children, continued development of robust motion correction algorithms is needed to correct for the increased head motion in children.

As an alternative to adapting an adult MEG system to meet the needs of a child, private groups and companies are developing MEG systems for infants and young children (67). For neonates, MEG is preferred over EEG, as anterior fontanel and suture skull opening or gaps significantly distort EEG but not MEG signals (68,69). In addition, as in neonates the combined thickness of the scalp and skull is about 3 to 4 mm (70), brain activity can be measured a few millimeters above the brain surface if the MEG sensors are close to the scalp. Figure 14 shows a schematic representation of a recently developed prototype neonatal MEG system.

Additional issues make development of MEG normative databases for nonadult populations difficult. For example, whereas there is general consensus how to score auditory components in adults, the latency and

morphology of auditory components across development are only recently being defined. Paetau et al. (71) discuss the changing form of electrophysiologic responses to auditory stimulation (using both tones and speech elements) as a function of typical childhood and adolescence development. They noted that auditory components differ as a function of age and observed a tendency for major ERPs (e.g., N1) to become stronger and to occur at an earlier latency with increasing age. Although longitudinal data in the same subjects are not yet available for a broad age range, horizontal snapshots across subjects of different ages confirm these broad observations (72). For research and clinical work in this area to develop, understanding the normal changes in the auditory ERPs/ERFs as a function of age is needed so that findings can be properly assessed. DeBoer et al. (73) discuss the problems associated with studying brain activity in younger populations more generally.

SUMMARY

Whole-cortex biomagnetometer systems offer a sensitive measure of brain electrical activity, providing spatial, temporal, and spectral information. Spontaneous and evoked activity can be obtained to provide time-varying descriptions of the neural networks involved in brain function and dysfunction. Clinical applications have emerged in the form of presurgical mapping of eloquent cortex (useful in neurosurgical candidates, especially those in whom alternative

functional mapping techniques such as fMRI may be compromised by physiologic limitations to neurovascular coupling) and in the identification of the origin of abnormal epileptiform discharges. Emerging technologies allow a spatiotemporal mapping of these networks of activity, effectively yielding movies of brain function.

Focus on the spectral domain allows examining the modulation of oscillatory brain activity and may indicate pathologic processes (e.g., focal slow wave activity), localization of brain function (e.g., language lateralization), or disruptions in higher cognitive functions (e.g., abnormal γ oscillations). Time-frequency methods promise a detailed assessment of complex brain functions (74), and may eventually help elucidate the neural substrates as well as the nature of neuronal system dysfunction in complex psychiatric disorders.

In addition to the considerable and ongoing improvements in spatial localization underway in MEG research, additional work is needed to develop a more quantitative approach to assigning diagnoses and/or identifying abnormal brain activity. Although not reviewed in the present chapter, since brain regions do not operate in isolation, another current challenge is the development of tools to evaluate functional connectivity among brain regions. Finally, it is hoped MEG evaluations will eventually document the course of acquired brain disorders (e.g., head trauma), developmental psychiatric disorders (such as autism spectrum disorders), and the effects of treatment (cognitive behavioral and pharmaceutical).

REFERENCES

1. Nakasato N, Yoshimoto T. Somatosensory, auditory, and visual evoked magnetic fields in patients with brain diseases. *J Clin Neurophysiol* 2000; 17:201–211.
2. Alberstone CD, Skirboll SL, Benzel EC, et al. R.R. Magnetic source imaging and brain surgery: presurgical and intraoperative planning in 26 patients. *J Neurosurg* 2000; 92:79–90.
3. Schiffbauer H, Berger MS, Ferrari P, et al. Preoperative magnetic source imaging for brain tumor surgery: a quantitative comparison with intraoperative sensory and motor mapping. *J Neurosurg* 2002; 97:1333–1342.
4. Ganslandt O, Buchfelder M, Hastreiter P, et al. Magnetic source imaging supports clinical decision making in glioma patients. *Clin Neurol Neurosurg* 2004; 107:20–26.
5. Lee D, Sawrie SM, Simos PG, et al. Reliability of language mapping with magnetic source imaging in epilepsy surgery candidates. *Epilepsy Behav* 2006; 8:742–749.
6. Knowlton RC, Elgavish R, Howell J, et al. Magnetic source imaging versus intracranial electroencephalogram in epilepsy surgery: A prospective study. *Ann Neurol* 2006; 59: 835–842.
7. Lewine JD, Orrison WW. Magnetoencephalography and magnetic source imaging. In: Orrison WW, Lewine JD, Sanders JA, et al., eds. *Functional Brain Imaging*. St. Louis: Mosby, 1995:369–417.
8. Hämäläinen MS. Functional localization based on measurements with a whole-head magnetometer system. *Brain Topogr* 1995; 7:283–289.
9. Williamson JS, Kaufman L. Theory of neuromagnetic fields. In: Grandori F, Hoke M, Romani GL, eds. *Auditory Evoked Magnetic Fields and Electric Potentials 1990*; Vol. 6, *Advances in Audiology*. Basel: Karger, 190: 1–39
10. Leahy RM, Mosher JC, Spencer ME, et al. A study of dipole localization accuracy for MEG and EEG using a human skull phantom 1998 (Los Alamos Tech. Rep. No. LA-UR-98-1442). Los Alamos, NM: Los Alamos National Laboratories, 1998.
11. Cohen D. Magnetoencephalography: evidence of magnetic fields produced by alpha-rhythm currents. *Science* 1968; 161: 784–786.
12. Cohen D. Magnetoencephalography: detection of the brain's electrical activity with a superconducting magnetometer. *Science* 1972; 175:664–666.
13. Sams M, Näätänen R. Neuromagnetic responses of the human auditory cortex to short frequency glides. *Neurosci Lett* 1991; 121:43–46.
14. Maclin EL, Rose DF, Knight JE, Orrison WW, et al. Somatosensory evoked magnetic fields in patients with stroke. *Electroencephalogr Clin Neurophysiol* 1994; 91:468–475.
15. Hämäläinen MS. Functional localization based on measurements with a whole-head magnetometer system. *Brain Topogr* 1995; 7:283–289.
16. Jung TP, Makeig S, Humphries C, et al. Removing electroencephalographic artifacts by blind source separation. *Psychophysiology* 2000; 37:163–178.
17. Taulu S, Kajola M, Simola J. Suppression of interference and artifacts by the Signal Space Separation Method. *Brain Topogr* 2004; 16:269–275.
18. Edgar JC, Stewart J, Miller GA. Digital filters in ERP research. In: Handy TC, ed. *Event-Related Potentials: A Methods Handbook*. Cambridge: MIT Press 2005.
19. Coles MGH, Gratton G, Kramer A, et al. Principles of signal acquisition. In: Coles MGH, Donchin E, Porges W, eds. *Psychophysiology: Systems, processes, and applications – A Handbook*. New York: Guilford Press, 1986:183–221.
20. Picton TW, Bentin S, Berg P, et al. Guidelines for using human event-related potentials to study cognition: Recording standards and publication criteria. *Psychophysiology* 2000; 37:127–152.
21. Sherg M, Bast T, Berg P. Multiple source analysis of interictal spikes: goals, requirements, clinical value. *J Clin Neurophysiol* 1999; 16:214–224.
22. Robinson SE, Nagarajan SS, Mantle M, et al. Localization of interictal spikes using SAM(g2) and dipole fit. *Neurology Clin Neurophysiol* 2004; 30,74.
23. Huang MX, Shih J, Lee RR, et al. Commonalities and differences among vectorized beamformers in electromagnetic source imaging. *Brain Topogr* 2004; 16:139–158.
24. Berger H. Über das Elektrenkephalogramm des Menschen. *Arch Psychiat Nervenkr* 1929; 87:52–570.

25. Adrian E. Olfactory reactions in the brain of the hedgehog. *J Physiol (London)* 1942; 100:459–473.
26. Kamada K, Saguer M, Möller M, et al. Functional and metabolic analysis of cerebral ischemia using magnetoencephalography and proton magnetic resonance spectroscopy. *Ann Neurol* 1997; 42:554–563.
27. Elbert T. Neuromagnetism. In: André W, Nowak H, eds. *Magnetism in medicine*. New York: John Wiley and Sons, 1988:190–262.
28. Weinbruch C. Abnormal low wave mapping (ASWAM) – a tool for the investigation of abnormal slow wave activity in the human brain. *J Neurosci Methods* 2007; 163:119–127.
29. Cañive JM, Lewine JD, Edgar JC, et al. Magnetoencephalographic assessment of spontaneous brain activity in schizophrenia. *Psychopharmacol Bull* 1996; 32(4):104–110.
30. Cañive JM, Lewine JD, Edgar JC, et al. Magnetoencephalographic examination of the effect of OPC-14597 in schizophrenia patients. *Psychopharmacol Bull* 1998; 34(1):101–105.
31. Fehr T, Kissler J, Moratti S, et al. Source distribution of neuromagnetic slow waves and MEG-delta activity in schizophrenia patients. *Biol Psychiatry* 2001; 50:108–116.
32. Fehr T, Kissler J, Weinbruch C, et al. Source distribution of neuromagnetic slow-wave activity in schizophrenic patients – effects of activation. *Schizophr Res* 2003; 63: 63–71.
33. Fernández A, Maestú F, Amo C, et al. Focal temporoparietal slow activity in Alzheimer's disease revealed by magnetoencephalography. *Biol Psychiatry* 2002; 52:764–770.
34. Rockstroh B, Wienbruch C, Ray WJ, et al. Abnormal oscillatory brain dynamics in schizophrenia: a sign of deviant communication in neural network? *BMC Psychiatry* 2007; 7:44.
35. Lewine JD, Davis JT, Sloan JH, et al. Neuromagnetic assessment of pathophysiologic brain activity induced by minor head trauma. *Am J Neuroradiol* 1999; 20:857–866.
36. Meinzer M, Elbert T, Wienbruch C, et al. Intensive language training enhances brain plasticity in chronic aphasia. *BMC Biol* 2004; 2:20.
37. Allison T. Scalp and cortical recordings of initial somatosensory cortex activation to median nerve stimulation in man. *Ann N Y Acad Sci* 1982; 112:671–677.
38. Wood CC, Spencer DD, Allison T, et al. Localization of human sensorimotor cortex during surgery by cortical surface recording of somatosensory evoked potentials. *J Neurosurg* 1988; 68:99–111.
39. Okada YC, Tanenbaum R, Williamson SJ, et al. Somatotopic organization of the human somatosensory cortex revealed by neuromagnetic measurements. *Exp Brain Res* 1984; 56:197–205.
40. Wood CC, Cohen D, Cuffin BN, et al. Electrical sources in human somatosensory cortex: Identification by combined magnetic and potential recordings. *Science* 1985; 227: 1051–1053.
41. Romani GL, Rossini PM. Neuromagnetic functional localization: principles, state of the art and perspectives. *Brain Topogr* 1988; 1:5–21.
42. Allison T, McCarthy G, Wood CC, et al. Potentials evoked in human and monkey cerebral cortex by stimulation of the median nerve. *Brain* 1991; 114:2465–2503.
43. Hari R, Kaukoranta E. Neuromagnetic study of somatosensory system: principles and example. *Prog Neurobiol* 1985; 24:233–256.
44. Nakamura A, Yamada T, Goto A, et al. Somatosensory homunculus as drawn by MEG. *Neuroimage* 1998; 7:377–386.
45. Sobel DF, Gallen CC, Schwartz BJ, et al. Locating the central sulcus: comparison of MR anatomic and magnetoencephalographic functional methods. *American J Neuroradiol* 1993; 14:915–925.
46. Roberts TP, Rowley H, Kucharczyk J. Applications of magnetic source imaging to presurgical brain mapping. *Neuroimaging Clin N Am* 1995; 5:251–266.
47. Roberts TP, Ferrari P, Perry D, et al. Presurgical mapping with magnetic source imaging: comparisons with intraoperative findings. *Brain Tumor Pathol* 2000; 17:57–64.
48. Pfurtscheller G, Lopes da Silva FH. Event-related EEG/MEG synchronization and desynchronization: basic principles. *Clin Neurophysiol* 1999; 110:1842–1857.
49. Aine CJ, Supek S, George JS, et al. Retinotopic organization of human visual cortex: departures from the classical model. *Cereb Cortex* 1996; 6:354–361.
50. Halgren E, Raji T, Marinkovic K, et al. Cognitive response profile of the human fusiform face area as determined by MEG. *Cereb Cortex* 2000; 10:69–81.
51. Sams M, Hietanen JK, Hari R, et al. Face-specific responses from the human inferior occipito-temporal cortex. *Neuroscience* 1997; 77:49–55.
52. Lewis S, Thomas RJ, Lanoue MD, et al. Visual processing of facial affect. *Neuroreport* 2003; 14:1841–1845.
53. Broca P. Sur le siège de la faculté du langage articulé. *Bulletins de la Societe d'Anthropologie de Paris* 1965; 6: 377–393.
54. Zangwill OL (1967). Speech and the minor hemisphere. *Acta Neurol of Belgium* 1967; 67:1013–1020.
55. Wada J, Rasmussen T. Intracarotid injection of sodium amytal for the lateralization of cerebral speech dominance: experimental and clinical observations. *J Neurosurg* 1960; 17:266–282.
56. Davis AE, Wada JA. Lateralization of speech dominance by spectral analysis of evoked potentials. *J Neurol Neurosurg Psychiatry* 1977; 40:1–4.
57. Branch C, Milner B, Rasmussen T. Intracarotid sodium amytal for the lateralization of cerebral speech dominance. *J Neurosurg* 1964; 21:399–405.
58. Merrifield WS, Simos PG, Papanicolaou AC, et al. Hemispheric language dominance in magnetoencephalography: sensitivity, specificity, and data reduction techniques. *Epilepsy Behav* 2007; 10:120–128.
59. Papanicolaou AC, Simos PG, Breier JI, et al. Magnetoencephalographic mapping of language-specific cortex. *J Neurosurg* 1999; 90:85–93.
60. Hirata M, Kato A, Taniguchi M, et al. Determination of language dominance with synthetic aperture magnetometry: comparison with the Wada test. *NeuroImage* 2004; 23:46–53.
61. Miller GA, Elbert T, Sutton BP, et al. Innovative clinical assessment technologies: challenges and opportunities in neuroradiology. *Psychol Assess* 2007; 19:58–73.
62. Lezak MD. *Neuropsychological Assessment*. 3rd ed. Oxford University Press: New York, 1995.

63. Barth DS, Sutherling W, Engel J, et al. Neuromagnetic evidence of spatially distributed sources underlying epileptiform spikes in the human brain. *Science* 1984; 223: 293–296.
64. Imai K, Otsubo H, Sell E, et al. MEG source estimation from mesio-basal temporal areas in a child with a porencephalic cyst. *Acta Neurol Scand* 2007; 116:263–267.
65. Kato A, Ninomiya H, Saitoh Y, et al. Seishin Shinkeigaku Zasshi 2003; 105:425–432.
66. Weisend MP, Hanlon FM, Montañ, R, et al. Paving the way for cross-site pooling of magnetoencephalography (MEG) data. *Int Congr Ser* 2007; 1300:615–618.
67. Okada Y, Pratt K, Atwood C, et al. BabySQUID: a mobile, high-resolution multichannel magnetoencephalography system for neonatal brain assessment. *Rev Sci Instrum* 2006; 77, 024301.
68. Okada YC, Lähteenmäki A, Xu C. Experimental analysis of distortion of magnetoencephalography signals by the skull. *Clin Neurophysiol* 1999a; 110:230–238.
69. Okada YC, Lähteenmäki A, Xu C. Comparison of MEG and EEG on the basis of somatic evoked responses elicited by stimulation of the snout in the juvenile swine. *Clin Neurophysiol* 1999b; 110:214–229.
70. Hansman CF. Growth of interorbital distance and skull thickness as observed in roentgenographic measurements. *Radiology* 1966; 86:87–96.
71. Paetav R, Ahonen A, Salonen O, et al. Auditory evoked magnetic fields to tones and pseudowords in healthy children and adults. *J Clin Neurophysiol* 1995; 12:177–85.
72. Oram Cardy JE, Ferrari P, Flagg EJ, et al. Prominence of M50 auditory evoked response over M100 in childhood and Autism. *Neuroreport* 2004; 15:1867–1870.
73. DeBoer T, Scott LS, Nelson CA. ERPs in developmental populations. In: Handy TC, ed. *Event-related Potentials: A methods handbook*. Cambridge, MA: The MIT Press, 2005:263–298.
74. Makeig S, Debener S, Onton J, et al. Mining event-related brain dynamics. *Trends Cogn Sci* 2004; 8:204–210.

Index

- Acoustic noise, 40–42
Acute ischemic stroke, 291–293.
 See also Strokes
Acute stroke
 diffusion MRI of, 178–179
 hemorrhagic transformation
 and, 184–185
 theories for decreased diffusion in,
 177–178
AD. *See* Alzheimer disease (AD)
ADC. *See* Apparent diffusion coefficient
 (ADC)
Adenosine triphosphate (ATP), 177
Adolescence, 219
Adrenoleukodystrophy (ALD), 221
Aging
 data interpretation of altered
 activation in, 131
 DTI in normal, 235
AIF. *See* Arterial input function (AIF)
Akinesia, 143–144
ALD. *See* Adrenoleukodystrophy (ALD)
ALS. *See* Amyotrophic lateral sclerosis
 (ALS)
Alzheimer disease (AD), 132–141
 DTI of, 235–237
 fMRI findings in, 133
 methodological considerations in, 133
Amino acids, detection, 287
Amyotrophic lateral sclerosis
 (ALS), 239–241
 fiber-tracking images of patient
 with, 242
Anaerobic glycolysis, 287
Anaplastic gliomas, 299
Anatomic imaging, cross-sectional, 312
Anisotropic diffusion, 166
Anisotropy, 206
Anisotropy map, color fractional, 99
Antiangiogenesis, 282–283, 299
Antiangiogenic agents, 299–301
Antituberculous therapy, 287
Anxiety, in pediatric fMRI, 107
Apolipoprotein E type 4 allele (APOE-
 epsilon 4), 140–141
Apparent diffusion coefficient (ADC),
 164–166, 234, 283, 291
 and fDM, 212–213
 maps and diffusion-weighted
 images, 202
 maps of MS, 243
 and time course of diffusion
 changes, 179–180
 and tumor grade, 210–211
 tumors maps of, 202–205
 tumor treatment and change
 in, 211–212
Arachnoid cysts, 202
Arterial input function (AIF)
 T2/T2*-weighted DSC-MRI, 263–265
 T1-weighted DCE-MRI, 256–257
Arterial spin labeling (ASL), 10, 251,
 296–297
 data acquisition methods
 continuous (CASL), 267
 pulsed ASL (PASL), 267–268
 validation of, 269–270
 MRI, 266–270
Arteriovenous malformation
 (AVM), 86
 induced neurovascular
 uncoupling, 77
Artifacts, 37–48
 image acquisition, 42–44
 motion, 44–45
 preprocessing, 45–48
ASD. *See* Autism spectrum disorders
 (ASD)
ASL. *See* Arterial spin labeling (ASL)
Astrocytomas, pilocytic, 279–281
Attention deficit hyperactivity
 disorder (ADHD), BOLD fMRI
 of, 118–120
Auditory stimulus presentation, 51–52
Auditory system, BOLD fMRI response
 to, 111–112
Autism spectrum disorders (ASD),
 BOLD fMRI of, 120–123, 124
Avastin, 282, 283, 299–300
AVM. *See* Arteriovenous malformation
 (AVM)
Balloon model, 3, 4
Baseline task, 19
BBB. *See* Blood-brain barrier (BBB)
Beamformers
 design, 312–313
 laterality index, 320
Berger, Hans, 313
Bevacizumab. *See* Avastin
β-galactocerebrosidase, 220

- Bilateral finger-tapping task
 BOLD fMRI for, 8–9
 boxcar paradigm, 6

Bilingual language representation, 62–63

Biofeedback, 109
 “bite bar,” 109

Bloch equations
 for GE and SE, 255, 260
 for rCBF, 266

Block design, 18, 51
 vs. event-related designs, 18–19

Blood-brain barrier (BBB), 252–253

Blood oxygenation level dependent (BOLD) fMRI, 51
 abnormal vasculature and, 84
 advantages over PET imaging, 94
 for a bilateral finger-tapping task, 8–9
 and neurovascular coupling, 130
 pediatric
 brain development, 110–115
 challenges in, 107–110
 common disorders, 115–124

physical principles of, 1–10
 practical considerations in, 7–8
 preoperative for glioblastoma
 multiforme (GBM), 83–84

signal measurements, 7
 signal sources, 82
 statistical analysis of data, 5–7
 unexpected results from, 81–82
 vs. routine MR imaging sequences, 3

BOLD fMRI. *See* Blood oxygenation level dependent (BOLD) fMRI

Boxcar paradigm, 3

Bradykinesia, 144

Brain
 activation identification, 29–33
 development as seen in BOLD fMRI, 110–115
 reading circuits, 117
 tumor. *See* Brain tumor

Brain atrophy, 129–130

Brain plasticity. *See* Cortical reorganization

Brain tumor
 advanced MRI techniques for, 293–296
 ASL perfusion MRI in, 296–297
 clinical MRI protocol, 276
 perfusion. *See* Perfusion MRI
 vs. acute ischemic stroke, 291–293

Broca’s area, 14
 effect of electrical stimulation in, 92

Brownian motion, 162

Camera-based navigational system, 94–95

Carboplatin, 282

Cardiac-induced noise, 39

Carotid endarterectomy, 193

Caveats, 279, 290

CBD. *See* Corticobasal degeneration (CBD)

CBF. *See* Cerebral blood flow (CBF)

CBV. *See* Cerebral blood volume (CBV)

CCBV matrix, 274

CEDD trials. *See* Convection-enhanced drug delivery (CEDD) trials

Central nervous system (CNS)
 infections, 286–289
 inflammation, 290

Cerebral blood flow (CBF), 3, 273
 perfusion fMRI methods to measure, 9–10

Cerebral blood volume (CBV), 273

Cerebral ischemia. *See* Acute ischemic stroke

Cerebral venous sinus thrombosis (CVT), 194–196

Cerebral sinus thrombosis, 194–196

Cerebrospinal fluid (CSF), motion of, 164

Childhood period, myelination in, 219

Chondrosarcomas, 286

CJD. *See* Creutzfeldt-Jakob disease (CJD)

CNS. *See* Central nervous system (CNS)

Cocktail party, 9

Cognition
 in abnormal population, 224
 in normal population, 224

Cognitive division, 118–119

Color fractional anisotropy map, 99

Compliance, in pediatric fMRI, 107

Conditioning head motion, 109

Continuous (CASL), 267, 297

Convection-enhanced drug delivery (CEDD) trials, 212

Correlation analysis, 5
 for fMRI data analysis, 30–31

Cortical reorganization, 81
 due to tumor growth, 84–86
 following stroke, 86–88

Cortical stimulation, 317

Cortical visual processing, 69–72

Corticobasal degeneration (CBD), 151

Corticospinal tracts (CST), 240
 in DTI-based color maps, 241
 location, 97–98

Creutzfeldt-Jakob disease (CJD), 194, 238

Crowding hypothesis, 113–114

Cysticercosis, 287

Cysts, arachnoid, 202

Data acquisition-related artifacts, 24

DCE MRI. *See* Dynamic contrast-enhanced MRI (DCE MRI)

Deconvolution analysis, 31, 32

Delayed radiation necrosis (DRN), 281–282

Dementia, 131–132

Dementia with Lewy bodies (DLB), 237–238

Deoxygenated hemoglobin (dHb), 2 paramagnetic, 3

Dermoid tumor, 202

Detection coils, 310

Developmental dyslexia, BOLD fMRI of, 115–118

Diffusion, 162, 201–202
 acute stroke and theories for decreased, 177–178
 anisotropic, 166
 anisotropy, 186
 imaging with avastin, 282–283
 isotropic, 164–166
 measurement with MRI, 162–164
 and pathology in neurodegenerative disorders, 235
 time course and change in, 179–180

tractography. *See* Diffusion tractography

Diffusion MRI, 287. *See also* Diffusion tensor imaging (DTI)

of acute stroke, 178–179

clinical diagnosis of tumors, 202–205

and clinical outcomes of stroke, 187–188

and diffusion tensor, 166

and DTI, 168, 185–187

false-positive DW images, 181

lesion and reversibility, 182–184

measurements, 162–164

physical principles of, 201–202

reliability to detect acute ischemic infarction, 180–182

of syndromes which clinically mimic strokes, 188–194

ischemic lesions, 188–192

nonischemic lesions, 188

vasogenic edema syndromes, 192–193

time course of stroke evolution, 179–180

of venous infarction, 194–96

Diffusion tensor, 164. *See also* Diffusion and anisotropic diffusion, 166

calculations, 166–167, 207–208

data acquisition of, 207–208

data visualization, 168

and fractional anisotropy maps, 207–208

limitations of, 171–172

quantities derived from, 167–168

tractography. *See* Diffusion tensor tractography

Diffusion tensor imaging (DTI), 61, 233–234

for AD, 235–237

of brain tumors, 225–226

[Diffusion tensor imaging (DTI)]
of CJD, 238
dataset on navigational software, 98, 99
to detect Wallerian degeneration, 187
and diffusion tensor tractography,
234–235
for disease pathophysiology, 226–227
in DLB, 237–238
dropout, 76–78
vs. DWI, 167
in FTD, 238
of HD, 239
of leukoencephalopathies, 220–223
measurement of basic parameters,
185–187
of MS, 241–244
for neuroanatomical structure, 227–228
of neurocognition and white matter
structure, 223–225
and neurodevelopmental maturation,
218–220
abnormal, 219–220
normal, 218–219
for normal aging, 235
optic radiations in, 69
of PD, 238–239
in pretreatment planning, 74, 75
quantitative, 172–174
Diffusion tensor tractography, 168–170,
234–235. *See also* Diffusion
tensor imaging (DTI)
combination with fMRI, 174
physical principles in, 206–207
techniques of, 174
Diffusion-weighted imaging (DWI). *See*
Diffusion MRI
Diffusion-weighting gradient, 164, 165
Digital filtering, 38, 311
Dihydropteridine reductase, 222–223
Dipole counting, 320
Dipole models, 312
Direct electrical cortical stimulation
(DECS) mapping, 57–60
DLB. *See* Dementia with Lewy bodies
(DLB)
Dorsal anterior cingulate cortex (dACC),
118–119
Draining vein effect, 32
DRN. *See* Delayed radiation necrosis
(DRN)
Drunkard's walk, 161–162
DSC MRI. *See* Dynamic susceptibility
contrast-enhanced perfusion MRI
(DSC MRI)
DTI. *See* Diffusion tensor imaging (DTI)
Dynamic contrast-enhanced MRI
(DCE MRI), 250, 273
acquisition spatial and temporal
parameters, 251–252

[Dynamic contrast-enhanced
MRI (DCE MRI)]
and mechanisms of exogenous con-
trast enhancement, 252–253
T2/T2 *-weighted, 259
analysis methods, 260–265
data acquisition, 259
perfusion parameters, 259–260
validation of, 265
T₁-weighted, 253
analysis methods, 254–258
data acquisition in, 253–254
validation of perfusion parameters,
258–259
vs. DSC MRI, 275–276
Dynamic susceptibility contrast-
enhanced perfusion MRI (DSC
MRI), 274–275
identifying physiologic imaging bio-
marker for gliomas, 283
for recurrent tumor detection, 282
vs. DCE MRI, 275–276

Eccentricity fMRI map, 75
Echo-planar imaging (EPI), 3, 7, 164, 275
data acquisition, 171
N/2 ghosting, 42
susceptibility artifacts in, 42
EEG. *See* Electroencephalography (EEG)
Einstein's equation of mean-squared
displacement, 162
Electrical stimulation, 317
Electrocortical stimulation (ECS), 92–94
Electrocorticography (ECOG), 92–94
Electroencephalography (EEG)
sensors, 312
vs. MEG, 310
Emden-Meyerhof pathway, 287
Embryonal tumors, 285
Encephalitis, 290
Encephalomalacia, 46
Encephalomyopathy, mitochondrial, 223
Endogenous tracers, 296
Endothelial proliferation, 282
EPI. *See* Echo planar imaging (EPI);
Echo-planar imaging (EPI)
Epidermoid tumor, 202
Epilepsy, medically refractory, 320–321
Equivalent current dipole (ECD) model,
312
Event-related designs, 18, 51
block design vs., 18–19
Event-related desynchronization
(ERD), 318
Event-related fMRI paradigms, 52
Executive functioning, in
autism, 122–124
Exogenous tracers, 296
Extracellular extravascular space (EES),
and DCE-MRI compartmental
model, 256–258

FA. *See* Fractional anisotropy (FA)
Face processing, in autism, 121–122, 123
Fast ForWord Language, 117
FDA. *See* Food and Drug Administration
(FDA)
FDG-PET. *See* 2-fluoro- 2-deoxy-d-
glucose positron emission
tomography (FDG-PET)
FDM. *See* Functional diffusion map
(fDM)
Fiber assignment by continuous tracking
(FACT), 168–170
Finger-tapping task, 18
First-pass pharmacokinetic modeling
(FPPM), 274–275
Fluid-attenuated inversion recovery
(FLAIR) images, 74, 75
of MS, 243
of patients with CJD, 238
2-fluoro- 2-deoxy-d-glucose positron
emission tomography
(FDG-PET), 210–211
Focal encephalomalacia, 46
Food and Drug Administration
(FDA), 297
Foot stimulation task, 18
FPPM. *See* First-pass pharmacokinetic
modeling (FPPM)
Fractional anisotropy (FA),
205–212, 234
clinical application of, 208–209
and diffusion tensor, 207–208
map of MS, 243
physical principles in, 206–207
temporal evolution in acute ischemia,
186–187
and tumor grade, 209–211
and tumor treatment response,
211–212
Frameless stereotaxy, 95
Frontal language areas, 14
functions, 98–102
Frontotemporal dementia (FTD),
141–143
DTI in, 238
Frontotemporal lobar degeneration
(FTLD), 141–143
FTD. *See* Frontotemporal dementia
(FTD)
FTLD. *See* Frontotemporal lobar
degeneration (FTLD)
Functional diffusion map
(fDM), 212–213
Functional field map (FFMap), 76, 77

Functional magnetic resonance imaging (fMRI)
BOLD. *See* Blood oxygenation level dependent (BOLD) fMRI
 functional neuroanatomy, 13–15
 localizations of speech for preoperative risk determination, 100–101
 monitoring patient’s performance, 20, 53
 paradigm selection for patients, 17–19
 postprocessing, 29–33
 preparing patient for, 19–20
 preprocessing, 23–29
 Functional neuroanatomy, fMRI of, 13–15
 Functional specialization, 69–72

Gadolinium-based contrasts, 10
 Gadolinium-diethylenetriamine penta-acetic acid (Gd-DTPA), 250, 302
 Ganglioglioma, 284–285
 GBM. *See* Glioblastoma multiforme (GBM)
 Gd-DTPA. *See* Gadolinium-diethylenetriamine penta-acetic acid (Gd-DTPA)
 GE. *See* Gradient-echo (GE) sequence
 General linear model (GLM), 31–32, 52
 Geometric distortions, 45
 Glial cells, 284
 Glioblastoma multiforme (GBM), 74, 75, 204, 299. *See also* Tumors
 preoperative BOLD fMRI for, 83–84
 Gliomas, 210. *See also* Tumors
 anaplastic, 299
 glioblastoma multiforme, 299
 high-grade, 276
 low-grade, 276
 malignant, 299
 perfusion metrics, 275
 recurrent
 antiangiogenic therapy, 282–283
 therapeutic monitoring, 281–282
 Gliomatosis cerebri, 279–281
 Global signal change, 39–40
 Globoid cell leukodystrophy, 220–221
 Glucose metabolism, 287
 Go/No-Go Test, 120
 Gradient echo (GE) sequence, 2, 275
 acquisition parameters for DCE-MRI using, 251, 253, 259
 Bloch equations for, 255, 260
 EPI, 7, 8
 Gray mantle, 109
 Gray matter, 186

“Hand omega” anatomy, 15, 16
 HD. *See* Huntington’s disease (HD)
 Head motion, 25–26
 correction, 26–28
 in pediatric fMRI, 108–109
 Head position–locating coils, 312
 Head stabilizer, 61
 Hemiplegic migraine, 192
 Hemodynamic response, 3
 time series, 6
 Hemodynamic response curve, 109, 110
 Hemodynamic response function (HRF), 3, 130–131
 Hemoglobin (Hb), 2
 Hemorrhagic transformation, 184–185
 Heschl’s gyrus, 14
 Hippocampal ROI, 130
 Histogram analysis, of DSC MRI data, 297
 HIV infection, 301
 Holoprosencephaly, 221–222
 Homunculus, motor
 BOLD fMRI of, 9
 fMRI maps representing three major areas on, 16
 HRF. *See* Hemodynamic response function (HRF)
 Humphrey perimetry charts, 76, 77
 Huntington’s disease (HD), 151–152
 DTI in, 239
 Hyperperfusion syndrome, 193
 Hypoglycemia, 192
 Hypothesis-driven analysis of fMRI data, 29–32

ICA. *See* Independent components analysis (ICA)
 Image reconstruction, 24
 Independent components analysis (ICA), 52, 311
 Indicator dilution theory, 274
 Inflammatory lesions, 290
 Injury, treatment-induced, 226
 Interstimulus interval (ISI), 317
 Intracarotid amobarbital test (IAT).
 See also Wada test
 Intraoperative mapping, 59, 60
 Intravenous bolus tracking, 9–10
 Intravoxel dephasing, 42
 Invasive mapping techniques, in neurosurgery, 92–94
 Ischemic lesions, 188–192
 Isotropic diffusion, 164–166

John Cunningham (JC) virus, 223
 Krabbe disease, 220–221

Language
 anatomy, 14
 in autism, 124
 BOLD fMRI during development of, 111–112
 fMRI paradigms, 17–18
 clinical validation of, 56–60
 future directions, 63–65
 research applications of, 63–65
 typically used in clinical practice, 52–56
 functions, 318–320
 laterality, 6, 52–53, 99–100
 mapping with fMRI, 15, 55
 potential pitfalls of, 60–62
 neuroanatomy, 13–14
 operations risking frontal function, 98–102
 reorganization following stroke, 86–87
 risks during rolandic region operations, 95–98
 Latency differences, 42–43
 Laterality, language, 52–53
 index, 6
 preoperative determination for risk assessment, 99–100
 Lesions
 diffusion MRI, 182–184
 ischemic, 188–192
 nonischemic, 188
 Leukoencephalopathies, 220–223
 Lexical orthography, 115
 Lexical phonology, 115
 Linear trend, 24–25
 Lobectomy, 102–103
 Localizations of speech, for preoperative risk determination, 100–101
 Local magnetic field inhomogeneities, 2
 Lou Gehrig’s disease. *See* Amyotrophic lateral sclerosis (ALS)
 Low-frequency noise, 38
 Lymphoma, 285

M20, 316, 317
 Magnet
 contrast mechanisms, 1–2
 MRI, 1
 Magnetic signals, 310
 Magnetic susceptibility, 42
 artifacts, 62
 Magnetoencephalography (MEG), 323
 clinical protocols, 323, 324
 data collection, 311
 for infants and young children, 324
 instrumentation and technology, 309–311
 laboratories, 323

- [Magnetoencephalography (MEG)]
for medically refractory epilepsy, 320–321
scientists, 323
sensors, 310
spontaneous recording, 311
vs. EEG, 310
- Magnocellular visual pathway theory of developmental dyslexia, 116
- Malignant phenylketonuria (PKU), 222–223
- Maple syrup urine disease (MSUD), 223
- Matrix diagonalization, 168
- MCI. *See* Mild cognitive impairment (MCI)
- Mean transit time (MTT), 293
- Medial temporal resection. *See* Lobectomy
- Medulloblastomas, 203, 285
- MEG. *See* Magnetoencephalography (MEG)
- Memory, fMRI paradigms, 102–103
- Meningioma, 285, 286
- Mental Illness and Neuroscience Discovery (MIND) Institute, 323
- Metastases, 294
- Metastatic neoplasms, 286
- Migraine, hemiplegic, 192
- Mild cognitive impairment (MCI), 132–141
fMRI findings in, 133–140
- Mini mental state examination (MMSE) scores, 132
- Mitochondrial encephalomyopathy, 223
- MMSE scores. *See* Mini mental state examination (MMSE) scores
- Molecular signature, 283
- Motion
artifacts, 44–45
correction, 25–28
- Motor areas
fMRI paradigms for, 18–19
functions, 317–318
homunculus
BOLD fMRI of, 9
fMRI maps representing three major areas on, 16
neuroanatomy, 15–17
- Motor neuron disease, 239–241
- Movement disorders, 143. *See also* Parkinson’s disease
DTI of, 238–239
- MRI. *See* specific entries
- FMRI. *See* Functional magnetic resonance imaging (fMRI)
- MRS. *See* MR spectroscopy (MRS)
- MRSI. *See* MR spectroscopic imaging (MRSI)
- MR spectroscopic imaging (MRSI), 286, 287
- MR spectroscopy
of demyelination abnormalities in ALD patients, 221
- MR spectroscopy (MRS)
MS. *See* Multiple sclerosis (MS)
- Multiple comparison correction, 33
- Multiple sclerosis (MS), 241–244
- Multiple system atrophy (MSA), 238, 239
- Myelination, 217
in adolescence, 219
in childhood period, 219
in perinatal period, 218–219
- Naming tasks, 54
- Necrosis
therapy-induced, 281–283
tumor, 204
- “Negative BOLD response,” 110
- Neoplasms
extra-axial, 285–286
metastatic, 286
nonglial, 285
- Neovasculature, tumor, 3
- Neuroanatomical structures, 227–228
- Neurocognition, 223–225
- Neurodegenerative diseases
data interpretation of altered activation in, 131
DTI of, 233–244
methodological challenges in patients with, 129–131
pathology and diffusion in, 234
- Neurodevelopmental maturation
abnormal, 219–220
normal, 218–219
- Neuromagnetic field, 310
- Neuromagnetic signals. *See* Magnetic signals
- Neuronal activity, and BOLD fMRI, 3–5
- Neurosurgery
applications of functional imaging in, 94–103
imaging revolution in, 91
invasive mapping techniques, 92–94
origins of functional mapping in, 91–92
- Neurovascular coupling, 130–131
- Neurovascular uncoupling, 60, 76–78, 83–84
- Newborn Individualized Developmental Care and Assessment Program (NIDCAP), 224–225
- N/2 ghosting. *See* Nyquist (N/2) ghosting
- Noise, 37, 38
due to physiologic activity, 38–39
scanner acoustic, 40–42
- Nonischemic lesions, 188
- Noun-verb semantic association task, 53, 55
- Nyquist (N/2) ghosting, 42, 43
- Oligodendrogloma, 283
- Orthographic lexical retrieval (OLR), 112
- Oxygenated hemoglobin (HbO₂), 2
- Paramagnetic deoxyhemoglobin, 3
- Parkinson’s disease (PD), 143–151
DTI in, 238–239
effects of dopaminergic treatment, 150
fMRI findings in, 151
monitoring surgical intervention in, 150–151
neural pathways in nondemented, 143–150
cognitive deficits, 144–150
motor deficits, 143–144
WCST in, 149
- Passbands, 312
- Passive listening paradigm, 54
activation on, 56
- Patients
fMRI paradigms selection for, 17–19
monitoring performance, 20, 53
preparation for fMRI study, 19–20
- PD. *See* Parkinson’s disease (PD)
- Pediatric BOLD fMRI
brain development, 110–115
challenges in, 107–110
common disorders, 115–124
- Performance intelligence quotient (IQ), 113
- Perfusion metrics, determination of, 297
- Perfusion MRI, 273–274
as biomarkers, 299–301
clinical applications
gliomatosis cerebri, 279–281
pilocytic astrocytoma, 279–281
radiosurgery, 278–279
stereotactic biopsy, 278–279
and molecular signatures, 283–284
standard methods for, 297–301
therapeutic monitoring with, 283
- Perfusion-weighted imaging
DCE-MRI. *See* DCE-MRI
static vs. dynamic, 249–251
- Perinatal insults, 220
- Perinatal period, 218–219
- PET imaging, 94
- Phenylalanine, 223
- Phenylketonuria (PKU), malignant, 222–223
- Phonemic fluency task, 18

Phonological (rhyming) language task, 53, 54, 55
areas of activation on, 56
Phonological theory of developmental dyslexia, 116–117
Physiologic noise, 38–39
PML. *See* Progressive multifocal leukoencephalopathy (PML)
PNETs. *See* Primitive neuroectodermal tumors (PNETs)
Pneumatic stimulation, 317
Polymorphonuclear cells, 287
Pontine tumors, 225–226
Positive and Negative Syndrome Scale (PANSS), 315
Posterior medial cortex (PMC), 136, 139–140
Posterior reversible encephalopathy syndrome (PRES), 192–193
Primary visual cortex, 318
Primitive neuroectodermal tumors (PNETs), 202–204, 285
Prion disease, 238
Progressive multifocal leukoencephalopathy (PML), 223
Progressive supranuclear palsy (PSP), 238, 239
Proteolytic enzymes, 287
Pseudoword rhyming, 117, 118
Pulsed ASL (PASL), 267–268
Pyruvate, 287

Quality assessment, 24–25

Radiation leukoencephalopathy (RLE), 281, 282
Radiation necrosis, 294, 296
Radiosurgery, 279
Rapoport and Grady model, 131
RBW. *See* Receiver bandwidth (RBW)
RCBF. *See* Regional blood flow (rCBF)
RCBV. *See* Regional cerebral blood volume (rCBV)
Reading
 BOLD fMRI response during development of, 114–115
 circuits in brain, 117
 disability. *See* Developmental dyslexia
Real-word rhyming, 117, 118
Receiver bandwidth (RBW), 252
Recombinant tissue plasminogen activator (rtPA), 180
Reference waveform, 30
Regional blood flow (rCBF)
 and ASL MRI, 266–267
 and T2/T2 *-weighted DSC-MRI, 260

Regional cerebral blood volume (rCBV), 260
AIFdetermination of, 264
matrix, measurement of, 274
qualitative analysis of, 260–262
Regional mean transit time (rMTT), 260, 265
and rCBV, 262–263
Regions of interest (ROI)
 analysis and quantitative DTI, 173, 234
 hippocampal, 130
Registration
 artifacts, 46
 for rigid-body motion correction, 44–45
Residual motion artifact, 45
Respiratory-induced noise, 39, 40
Response latency, 42
Restraint, head, 109
Retinotopy, 67–69
Rhyming language task, 53, 54, 55
 areas of activation on, 56
Rigid-body motion artifact, 44–45
RLE. *See* Radiation leukoencephalopathy (RLE)
ROI. *See* Regions of interest (ROI)
ROI (region-of-interest) analysis, 297
Rolandic region, operations in, 95–98
Root-mean-square (RMS)
 displacement, 162

Scanner acoustic noise, 40–42
Scanner drift, 38
Schizophrenia, 315
Schwannoma, 285
Scotomata, 68
SD25 maps, 275
SE. *See* Spin echo (SE)
Secondary speech areas, 102
SEFs. *See* Somatosensoryevoked fields (SEFs)
Segmentation
 artifacts, 46–47
Seizures, 191
Self-diffusion, 162
Semantic association tasks, 53, 54, 55
 areas of activation on, 56
Semantic fluency task, 18
Semantic processing, 114
SEPs. *See* Somatosensory-evoked potentials (SEPs)
Signal enhancement ratio (SER), 254
Signal space separation (SSS), 311
Signal targeting, 296
Signal-to-noise ratio (SNR), 37, 276, 316, 317
Single photon emission computed tomography (SPECT), 321

Single-shot echo-planar imaging (ssEPI), 52
Slice-timing correction, 25
Slice-timing effect, 42–44
SMA. *See* Supplementary motor area (SMA)
Smoothing artifact, 48
SNR. *See* Signal-to-noise ratio (SNR)
Socialization abnormalities in autism, 120–122
Somatosensoryevoked fields (SEFs), 316
Somatosensory-evoked potentials (SSEPs), 92, 316
 intraoperative mapping by, 93
Somatosensory homunculus, 317
Spatial normalization, and brain atrophy, 129–130
Spatial smoothing, 28–29
SPECT. *See* Single photon emission computed tomography (SPECT)
Speech
 fMRI integrated for navigation, 101–102
 localization, 100–101
Speech-correlated motion, 27–28
Spike in image, 25
Spin echo (SE) sequence, 1–2, 259, 275
 Bloch equations for, 260
 EPI, 7, 8
Spin-history effect, 45
SSS. *See* Signal space separation (SSS)
Statistical analysis
 of BOLD fMRI data, 5–7
 in postprocessing stage, 29–32
Statistical maps of brain activation, 29
 interpretation of, 32–33
Statistical parametric mapping (SPM), 52
Stejskal-Tanner diffusion-weighted imaging sequence, 163–164
Stereotactic brain biopsy, 278–279
Stereotaxy, frameless, 95
Stimulation mapping, cortical, 317
Stimulus presentation, 51–52
Stopbands, 313
Stop Signal Test, 120
Strokes
 acute. *See* Acute stroke
 acute ischemic with DWI
 reversibility, 183
 acute ischemic with hemorrhagic transformation, 185
 cortical reorganization following, 86–88
 diffusion MRI findings in, 179
 evolution and time course of diffusion, 179–180
 syndromes which clinically mimic, 188–192
Stroop test, 119

Structured noise, 37
Student's t test, for fMRI data analysis, 29–30
Subject-related artifacts, 24
Superconducting quantum interference device (SQUID), 310
Supplementary motor area (SMA), 16–17, 144
Susceptibility artifacts, 32–33, 42, 43
Susceptibility-weighted imaging (SWI), 290
Synaptic pruning, 110

Task-correlated motion artifacts, 27–28
T1 contrast mechanism, 1–2
T2 contrast mechanism, 1–2
T2* contrast mechanism, 1–2
and BOLD fMRI signal, 2–3
TDLs. *See* Tumefactive demyelinating lesions (TDLs)
Temporal language areas, 14, 15
TGA. *See* Transient global amnesia (TGA)
Thalamic lacune, 181
Thalidomide, 282, 300
Three-dimensional volume registration, 26–27
TIA. *See* Transient ischemic attack (TIA)
Time to peak (TTP), 293
T2*-induced intravoxel dephasing, 42
1.5T-MRI system, 53
3-T MRI system, 53, 54
Tofts and Kermode model, 257–258
Tongue movement task, 18
Tower of London test, 122
Tractography, diffusion, 168–170
Transcranial magnetic stimulation (TMS), 14
Transient global amnesia (TGA), 190–191
Transient ischemic attack (TIA), 188–190
Treatment-induced injury, 226
TSSS (temporal SSS), 311
Tuberculous infection, 301
Tuberous sclerosis (TS), 226
Tumefactive demyelinating lesions (TDLs), 289–290

Tumor grade, 209–211
Tumor necrosis factor-related apoptosis-inducing ligand (TRAIL), 212
Tumors, 202–205
cellularity, 225
dermoid, 202
DTI of brain, 225–226
epidermoid, 202
grade, 209–211
growth, 84–86
infarction, 204
infarction and necrosis, 204
necrosis, 204
neovasculature, 3
pontine, 225–226
primitive neuroectodermal, 202–204
response to therapy, 211–212
 T_1 -weighted DCE-MRI, 253
 T_2 -weighted images, 238

UNFAIR, 296

Vascular endothelial growth factor (VEGF), 278
Vascular permeability factor (VPF).
See Vascular endothelial growth factor (VEGF)
Vascular permeability (K_{trans}), 275
Vascular-Space-Occupancy (VASO)-dependent fMRI.
See VASO MRI
Vasculation, abnormal
and BOLD fMRI, 84
Vasculitides, noninfectious, 290
Vasogenic edema syndromes, 193
VASO MRI, 301–303
VEFs. *See* Visual-evoked fields (VEFs)
VEGF. *See* Vascular endothelial growth factor (VEGF)
Venous infarction, 194–196
Venous inflammation, 290
Ventral tegmental area (VTA), 144, 148
Verbal IQ, 113

Verb generation tasks, 54, 112–113
Virtual sensors, 313
Vision fMRI, clinical application of, 73–76
Visual attention, role of, 72–73
Visual cortex, 73–74
Visual-evoked fields (VEFs), 318
Visual field deficits, 68
maps, 67–69
Visual function, reorganization of, 78
Visual stimulus presentation, 51
Visual system
BOLD fMRI response to developmental, 111
clinical neuroimaging and principles of, 67–73
Voxel-based analysis (VBA), 173–174, 234
to evaluate WM integrity in ALS, 240
VTA. *See* Ventral tegmental area (VTA)

Wada test, 57–60, 93–94, 318
Wallerian degeneration, 188
WCST. *See* Wisconsin card sorting task (WCST)
Wechsler Intelligence Scale, 113
Wernicke's area, 14
dominant posterior temporal, 101–102
effect of electrical stimulation in, 92
White matter (WM)
changes vs. acute ischemic infarction, 183
diffusivity *versus* gray matter, 186
DTI of MS and normal appearing, 242
neurodegenerative diseases and, 235
in patients with AD, 236–237
structure, 223–225
WHO, 276
classification of gliomas, 276–278
Wisconsin card sorting task (WCST), 149
WM. *See* White matter (WM)
Word recall task, 319–320

Radiology and Nuclear Medicine

about the book...

The first text designed specifically with clinical practitioners in mind, including neuroradiologists, radiologists, neurologists, neurosurgeons, and clinical psychologists, **Functional Neuroimaging** demonstrates the clinical application and utilization of functional neuroradiology for early diagnosis, neurological decision-making, and assessing response to cancer therapy. Edited by the Founding President of American Society of Functional Neuroradiology, this guide expertly describes the incorporation of this technology into clinical practice, and showcases high-quality color images depicting the function and mechanisms of the brain.

Functional Neuroimaging:

- helps clinicians incorporate functional neuroradiology into their practice
- contains 320 intricate, full-color figures comprising the anatomy and function of the brain
- depicts current methods for imaging the central nervous system, as well as cutting-edge approaches for the imaging of brain function
- shows new advancements in functional brain imaging to benefit the diagnosis, management, and treatment of patients

about the editor...

ANDREI I. HOLODNY is Professor of Radiology at the Weill Medical College of Cornell University and Attending Neuroradiologist at Memorial Sloan-Kettering Cancer Center, New York, New York, USA. He is the Chief of the Neuroradiology Section and Director of the Functional MRI Laboratory at Memorial Sloan-Kettering. Dr. Holodny is the Founding President of the American Society of Functional Neuroradiology and past-President of the Eastern Neuroradiological Society. Dr. Holodny's studies concentrate principally on functional imaging of central nervous system tumors including blood oxygen level dependent functional MRI and diffusion tractography.

Printed in the United States of America

DK7056

ISBN 978-084937056-4



9 780849 370564

informa
healthcare
www.informahealthcare.com

52 Vanderbilt Avenue
New York, NY 10017
Telephone House
69-77 Paul Street
London EC2A 4LQ, UK